

Mushabbar A. Syed
Subha V. Raman
Orlando P. Simonetti
Editors

Basic Principles of Cardiovascular MRI

Physics and
Imaging Technique

Basic Principles of Cardiovascular MRI

Mushabbar A. Syed • Subha V. Raman
Orlando P. Simonetti
Editors

Basic Principles of Cardiovascular MRI

Physics and Imaging Technique

 Springer

Editors

Mushabbar A. Syed
Department of Medicine
Loyola University Medical Center
Maywood, IL
USA

Orlando P. Simonetti
The Ohio State University
Columbus, OH
USA

Subha V. Raman
The Ohio State University
Columbus, OH
USA

ISBN 978-3-319-22140-3 ISBN 978-3-319-22141-0 (eBook)
DOI 10.1007/978-3-319-22141-0

Library of Congress Control Number: 2015954859

Springer Cham Heidelberg New York Dordrecht London
© Springer International Publishing Switzerland 2015

This work is subject to copyright. All rights are reserved by the Publisher, whether the whole or part of the material is concerned, specifically the rights of translation, reprinting, reuse of illustrations, recitation, broadcasting, reproduction on microfilms or in any other physical way, and transmission or information storage and retrieval, electronic adaptation, computer software, or by similar or dissimilar methodology now known or hereafter developed.

The use of general descriptive names, registered names, trademarks, service marks, etc. in this publication does not imply, even in the absence of a specific statement, that such names are exempt from the relevant protective laws and regulations and therefore free for general use.

The publisher, the authors and the editors are safe to assume that the advice and information in this book are believed to be true and accurate at the date of publication. Neither the publisher nor the authors or the editors give a warranty, express or implied, with respect to the material contained herein or for any errors or omissions that may have been made.

Printed on acid-free paper

Springer International Publishing AG Switzerland is part of Springer Science+Business Media (www.springer.com)

To the source of my inspiration, my wife Humaira and my children Daneyal, Ameena, and Aleena.

Mushabbar A. Syed

To the mentors, colleagues, and students.

Subha V. Raman

To my loving wife, Lynn.

Orlando P. Simonetti

Preface

Cardiovascular magnetic resonance (CMR) has evolved into a routinely used imaging modality in clinical practice. Indications for CMR continue to expand which have led to the development of appropriate use criteria by the relevant medical societies including the American College of Cardiology, Society for Cardiovascular Magnetic Resonance, and the European Society of Cardiology. CMR is a relatively complex modality that requires good understanding of the basic principles including the relevant physics. Fellowship training programs have been developed to provide CMR training to cardiologists and radiologists using a combination of didactic teaching, clinical experience, and hands-on experience. Didactic training in the basic principles of CMR is mostly completed in the form of lectures and self-study. However, most of the available texts on MRI physics are not specific to CMR or are not up to date. The objective of writing this book was to develop a comprehensive and contemporary text on the basic principles and imaging techniques of CMR that will serve as a main reference source for both trainees and faculty. In doing so, we have chosen authors that are highly regarded as CMR experts, researchers, and teachers. Many authors direct CMR fellowship programs and are actively involved in training and education. We believe that this book will not only be useful for CMR fellowship trainees, cardiologists and radiologists who want to learn or expand their knowledge but also for CMR experts and physicists to use as a reference material.

The book is divided into two parts. Part one includes Chaps. 1 through 8 and focuses on the basic principles of CMR, MRI safety, and high field imaging. This part forms the basis for understanding of advanced techniques discussed in part two. Part two includes Chaps. 9 through 22 that discuss various techniques used in CMR including a review of advanced and emerging techniques. Tables and figures are included where appropriate and key references are included at the end of the chapter. This book is available in both print and electronic formats.

The success of any textbook depends on its ability to satisfy the needs of readers. We hope that readers will appreciate the clarity and thoroughness of each chapter and the hard work that went into developing this text. We will welcome any feedback comments to help improve the future editions.

Last but not the least, we want to extend our sincere thanks to Tracy Marton (Developmental Editor, Springer) for her invaluable help in completing this book and Grant Weston (Senior Editor, Medicine, Springer) for his insight, support, and overseeing this work to completion.

Maywood, IL, USA
Columbus, OH, USA
Columbus, OH, USA

Mushabbar A. Syed
Subha V. Raman
Orlando P. Simonetti

Contents

Part I Basic Principles of Magnetic Resonance Imaging

1 Signal Generation	3
Arunark Kolipaka	
2 k-Space	13
Michael Loecher and Oliver Wieben	
3 CMR Pulse Sequences	25
Rohan Dharmakumar, Behzad Sharif, and Hsin-Jung Yang	
4 Spatial, Temporal Resolution and Signal-to-Noise Ratio	41
Ning Jin, Haris Saybasili, and Xiaoming Bi	
5 Fast Imaging	63
Johannes Tran-Gia, Herbert Köstler, and Nicole Seiberlich	
6 High Field MRI for CMR	87
Yiu-Cho Chung	
7 Imaging Artifacts	97
Pedro Filipe Ferreira, Peter D. Gatehouse, Raad H. Mohiaddin, and David N. Firmin	
8 MRI Safety	115
Anja C.S. Brau, Christopher J. Hardy, and John F. Schenck	

Part II Cardiovascular Magnetic Resonance Techniques

9 Principles of ECG Gating for CMR	131
David Lopez and Michael Salerno	
10 Cardiac Cine Imaging	145
David C. Wendell and Robert M. Judd	
11 Black-Blood CMR	161
Henrik Engblom, Christos G. Xanthis, Sophie I. Mavrogeni, Suzanne M. Smart, and Anthony H. Aletras	
12 Tissue Characterization: T_1, T_2 and T_2^* Techniques	167
Marcus Carlsson, Christos G. Xanthis, Suzanne Smart, Sebastian Bidhult, and Anthony H. Aletras	
13 Perfusion	179
Daniel C. Lee, Neil R. Chatterjee, and Timothy J. Carroll	
14 Stress Testing	193
Amedeo Chiribiri, Islam Mahmoud, and Sven Plein	

15	Late Gadolinium Enhancement Imaging	211
	Rebecca E. Thornhill and Elena Peña	
16	Flow Imaging	227
	John N. Oshinski, Anurag Sahu, and Gregory R. Hartlage	
17	Magnetic Resonance Imaging of Coronary Arteries	245
	Mehmet Akçakaya and Reza Nezafat	
18	Cardiac Spectroscopy	261
	Ronald Ouwerkerk	
19	Contrast Media	271
	Lara Bakhos and Mushabbar A. Syed	
20	Contrast-Enhanced MR Angiography	283
	Parmede Vakil, Octavia Bane, Charles G. Cantrell, and Timothy J. Carroll	
21	Non-contrast Enhanced MRA	297
	Ioannis Koktzoglou, Ruth P. Lim, Oisín Flanagan, and Robert R. Edelman	
22	Advanced Cardiovascular Magnetic Resonance Techniques	315
	Florian von Knobelsdorff-Brenkenhoff, Matthias Alexander Dieringer, and Jeanette Schulz-Menger	
	Index	327

Contributors

Editors

Mushabbar A. Syed, MD, FACC Rolf & Merian Gunnar Professor of Medicine, Departments of Medicine – Cardiology, Radiology, Cell & Molecular Physiology, Director, Cardiovascular Imaging & Cardiology Fellowship Program, Stritch School of Medicine, Loyola University Medical Center, Maywood, IL, USA

Subha V. Raman, MD, MSEE, FACC, FAHA Professor and Joseph M. Ryan, MD Chair in Cardiovascular Medicine, Associate Division Director for Quality, and Medical Director, CMR/CT, The Ohio State University, Columbus, OH, USA

Orlando P. Simonetti, PhD, FISMRM, FAHA John W. Wolfe Professor in Cardiovascular Research, Professor of Cardiovascular Medicine and Radiology, Research Director, CMR/CT, The Ohio State University, Columbus, OH, USA

Contributors

Mehmet Akçakaya, PhD Department of Medicine, Beth Israel Deaconess Medical Center, Harvard Medical School, Boston, MA, USA

Anthony H. Aletras, PhD Department of Medicine, Laboratory of Medical Informatics, Aristotle University of Thessaloniki, Thessaloniki, Greece

Department of Clinical Physiology and Nuclear Medicine, Lund University Hospital, Lund, Sweden

Lara Bakhos, MD Department of Medicine-Cardiology, Stritch School of Medicine, Loyola University Medical Center, Maywood, IL, USA

Octavia Bane, PhD Departments of Biomedical Engineering and Radiology, Northwestern University, Chicago, IL, USA

Mount Sinai Hospital, Translational and Molecular Imaging Institute, New York, NY, USA

Xiaoming Bi, PhD MR R&D, Siemens Healthcare, Los Angeles, CA, USA

S. Bidhult, MSc Department of Clinical Physiology and Nuclear Medicine, Lund University Hospital, Lund, Sweden

Anja C.S. Brau, PhD GE Healthcare, Cardiac Center of Excellence, GE Global Research Center, Munich, Germany

Charles G. Cantrell Departments of Biomedical Engineering and Radiology,
Northwestern University, Chicago, IL, USA

Department of Radiology, Northwestern Memorial Hospital, Chicago, IL, USA

Marcus Carlsson, MD, PhD Department of Clinical Physiology
and Nuclear Medicine, Lund University Hospital, Lund, Sweden

Timothy J. Carroll, PhD Departments of Biomedical Engineering and Radiology,
Northwestern University, Chicago, IL, USA

Department of Radiology, Northwestern Memorial Hospital, Chicago, IL, USA

Neil R. Chatterjee, BS Northwestern University Feinberg School of Medicine,
Chicago, IL, USA

Yi-Cho Chung, PhD Paul C. Lauterbur Research Center for Biomedical Imaging,
Shenzhen Institutes of Advanced Technology, Chinese Academy of Sciences,
Shenzhen, China

Rohan Dharmakumar, PhD Biomedical Imaging Research Institute, Department of
Biomedical Sciences, Cedars-Sinai Medical Center, Los Angeles, CA, USA

Department of Medicine and Bioengineering, UCLA, Los Angeles, CA, USA

Matthias Alexander Dieringer, PhD Department of Cardiology and Nephrology,
Cardiovascular MRI – Experimental and Clinical Research Center, a joint cooperation
between Charité Medical Faculty and Max-Delbrueck Center for Molecular Medicine,
and HELIOS Clinics Berlin-Buch, Berlin, Germany

Robert R. Edelman, MD Department of Radiology, Evanston Hospital, NorthShore
University HealthSystem, Evanston, IL, USA

NorthShore University HealthSystem, Evanston, IL, USA

Henrik Engblom, MD, PhD Department of Clinical Physiology
and Nuclear Medicine, Lund University Hospital, Lund, Sweden

Pedro Filipe Ferreira, PhD Department of Cardiovascular BRU, Royal Brompton
Hospital, London, UK

David N. Firmin, PhD Department of Cardiac MRI, Royal Brompton Hospital,
London, UK

Oisin Flanagan, MD Northwestern University Feinberg School of Medicine,
Chicago, IL, USA

NorthShore University HealthSystem, Evanston, IL, USA

Peter Gatehouse, PhD Department of Cardiac MRI, Royal Brompton Hospital,
London, UK

Christopher J. Hardy, PhD GE Global Research, Niskayuna, NY, USA

Gregory R. Hartlage, MD Department of Internal Medicine, Division of Cardiology,
Emory University, Atlanta, GA, USA

Ning Jin, PhD MR R&D, Siemens Healthcare, Columbus, OH, USA

Robert M. Judd, PhD Department of Medicine, Duke University Medical
Center, Durham, NC, USA

Ioannis Koktzoglou, PhD Department of Radiology, Evanston Hospital,
NorthShore University HealthSystem, Evanston, IL, USA

The University of Chicago Pritzker School of Medicine, Chicago, IL, USA

Arunark Kolipaka, PhD Department of Radiology, The Ohio State University
Wexner Medical Center, Columbus, OH, USA

Herbert Köstler, PhD Department of Radiology, University of Würzburg, Würzburg,
Germany

Daniel C. Lee, MD Department of Medicine, Division of Cardiology,
Northwestern University Feinberg School of Medicine, Chicago, IL, USA

Ruth P. Lim, MD Department of Radiology, Austin Health,
Melbourne/Heidelberg, VIC, Australia

The University of Melbourne, Melbourne, Victoria, Australia

Michael Loecher, PhD Department of Medical Physics, University
of Wisconsin Madison, Madison, WI, USA

David Lopez, MD Department of Medicine, Cardiovascular Division,
University of Virginia Health System, Charlottesville, VA, USA

Sophie Mavrogeni, MD, FESC Department of Cardiology,
Onassis Cardiac Surgery Center, Athens, Attiki, Greece

Raad H. Mohiaddin, MD, FRCR, FRCP, FESC, PhD Department of Cardiology
and Imaging, Royal Brompton Hospital, National Heart and Lung Institute,
Imperial College London, London, UK

Reza Nezafat, PhD Department of Medicine, Beth Israel Deaconess
Medical Center, Harvard Medical School, Boston, MA, USA

John N. Oshinski, PhD Radiology and Imaging Sciences, Emory University
School of Medicine, Atlanta, GA, USA

Ronald Ouwerkerk, PhD The Biomedical and Metabolic Imaging Branch, National
Institute of Diabetes and Digestive and Kidney Diseases (NIDDK), Bethesda, MD, USA

Elena Peña, MD Department of Radiology, University of Ottawa, Ottawa, ON, USA

Department of Medical Imaging, The Ottawa Hospital, Ottawa, ON, Canada

Anurag Sahu, MD Division of Cardiology, Emory University Hospital, Atlanta, GA, USA

Michael Salerno, MD, PhD Department of Medicine, Cardiovascular Division,
Radiology and Biomedical Engineering, University of Virginia Health System,
Charlottesville, VA, USA

Haris Saybasili, PhD MR R&D, Siemens Healthcare, Chicago, IL, USA

John F. Schenck, MD, PhD GE Global Research, Niskayuna, NY, USA

Jeanette Schulz-Menger, MD Department of Cardiology and Nephrology, Cardiovascular
MRI – Experimental and Clinical Research Center, a joint cooperation between Charité
Medical Faculty and Max-Delbrueck Center for Molecular Medicine, and HELIOS Clinics
Berlin-Buch, Bavaria, Germany

Nicole Seiberlich, PhD Biomedical Engineering, Case Western Reserve University,
Cleveland, OH, USA

Behzad Sharif, PhD Biomedical Imaging Research Institute, Department of Biomedical Sciences, Cedars-Sinai Medical Center, Los Angeles, CA, USA

Suzanne Smart, BS Davis Heart and Lung Research Institute, Ohio State University Wexner Medical Center, Columbus, OH, USA

Rebecca E. Thornhill, PhD Department of Radiology, University of Ottawa, Ottawa, ON, Canada

Clinical Epidemiology Program, Ottawa Hospital Research Institute, Ottawa, ON, USA

Department Medical Imaging c/o Laura Lang, The Ottawa Hospital, Civic Campus, Ottawa, ON, USA

Johannes Tran-Gia, PhD Department of Radiology, University of Würzburg, Würzburg, Germany

Parmede Vakil, PhD Departments of Biomedical Engineering and Radiology, Northwestern University, Chicago, IL, USA

Department of Radiology, Northwestern Memorial Hospital, Chicago, IL, USA

Florian von Knobelsdorff-Brenkenhoff, MD, PhD Department of Cardiology and Nephrology, Cardiovascular MRI – Experimental and Clinical Research Center, a joint cooperation between Charité Medical Faculty and Max-Delbrueck Center for Molecular Medicine, and HELIOS Clinics Berlin-Buch, Berlin, Germany

David C. Wendell, PhD Department of Medicine/Cardiology, Duke University Medical Center, Durham, NC, USA

Oliver Wieben, PhD Departments of Medical Physics and Radiology, University of Wisconsin School of Medicine and Public Health, Madison, WI, USA

Christos G. Xanthis, PhD Department of Computer Science and Biomedical Informatics, University of Thessaly, Lamia, Greece

Hsin-Jun Yang, MS Biomedical Imaging Research Institute, Department of Biomedical Sciences, Cedars-Sinai Medical Center, Los Angeles, CA, USA

Department of Bioengineering, UCLA, Los Angeles, CA, USA

Part I

Basic Principles of Magnetic Resonance Imaging

Arunark Kolipaka

Abstract

This chapter provides some basic information regarding the origin of the MRI signal. The MRI signal is generated by the interaction of applied magnetic fields with the nuclei of hydrogen atoms in the body. Hydrogen nuclei (protons, or “spins”) tend to align themselves with the large static magnetic field generated by the MRI system, and rotate or precess about the direction of that field at a characteristic frequency called the Larmor frequency. The application of additional radiofrequency (RF) energy at the same frequency excites the magnetized protons causing them to tip into the plane perpendicular to the main field. The magnetized protons which have been perturbed in this fashion undergo a process of relaxation that returns them back into alignment with the main field. During the course of relaxation, a signal is emitted which is detected using receiver coils and digitally sampled. The relaxation of spins is governed by time constants known as T_1 and T_2 , and these time constants play a major role in determining the contrast between tissues in an image. The encoding of spatial information is accomplished using magnetic field gradients that alter the precession frequency of spins based on their position in the scanner. The Fourier transform is then used to reconstruct an image from the encoded data. Many of the basic concepts introduced in this chapter are covered in greater detail in later chapters.

Keywords

Larmor Frequency • T_1 relaxation • T_2 relaxation • Spatial encoding • Bloch Equations • Slice selection gradient • Phase encoding gradient • Readout gradient

The Magnetic Resonance Imaging (MRI) signal is generated by the hydrogen nuclei (protons) in human tissue. Three fourths of the human body consists of water, and each water molecule includes two hydrogen atoms; thus, water is the primary source of MRI signal in medical imaging applications. This chapter covers the important steps required to generate the signal used to create MR images.

The MRI Signal

Any modern digital imaging system requires a probe to interact with the tissue to be imaged; this interaction results in a signal that is detected, digitized, and further processed to generate an image as shown in Fig. 1.1. In magnetic resonance imaging (MRI), radiofrequency (RF) pulses are used to excite the tissue, and the resulting signal is detected by receiver coils. MRI is thus based on the absorption and emission of energy in the RF range of the electromagnetic spectrum. Although several chemical elements can interact with magnetic fields to emit an MRI signal, the large amount of hydrogen found in the body, and the relatively large signal it produces, has made hydrogen-based the most widely used MRI technique for clinical

A. Kolipaka, PhD
Department of Radiology, The Ohio State University Wexner
Medical Center, 395 W 12th Ave, 4th Floor Radiology,
Columbus, OH 43210, USA
e-mail: arunark.kolipaka@osumc.edu

diagnosis. The primary sources of MRI signal in the human body are the hydrogen nuclei found in tissues comprised mainly of water, and also fat (hydrocarbons). In the following discussion, the terms “hydrogen nuclei,” “protons,” and “spins” will be used interchangeably to describe the atomic particles that provide the primary source of the MRI signal.

Nuclear Spin in a Magnetic Field

Hydrogen has a nuclear property known as “spin” that results in a magnetic moment, μ . Because of this magnetic moment, when exposed to the static magnetic field (B_0) generated by the main magnet of the MRI system, hydrogen nuclei will align parallel or anti-parallel to the field as shown in Fig. 1.2. The energy difference (E) between these two orientations is $E=2\mu B_0$. The small preference for the hydrogen nuclei to align toward the parallel, lower energy state, over the anti-parallel orientation, contributes to the development of the net longitudinal magnetization [1]. The net magnetization is the vector sum of magnetic moments from many individual protons.

Larmor Frequency

When a hydrogen nucleus is exposed to a magnetic field of strength B_0 , it precesses at a frequency, ω , due to the interaction of its angular momentum and the field, as illustrated in Fig. 1.3. The frequency, ω , depends on B_0 and on the gyro-

magnetic ratio, γ , of the specific nucleus according to the Larmor Eq. 1.1.

$$\omega_L = \gamma B_0 \tag{1.1}$$

For hydrogen nuclei, $\gamma/2\pi=42.58$ MHz/T, and ω_L is termed the Larmor frequency. Thus, the Larmor frequency of precession is dependent on the applied magnetic field strength; for example, protons will precess at approximately 64 MHz at 1.5T, and 128 MHz at 3.0T.

Excitation of Spins

In a three-dimensional (x, y, z) coordinate system, let us assume by convention that the static magnetic field is oriented in the z -direction. As a result, the net longitudinal magnetization vector at equilibrium (M_0) will point in the z -direction as shown in Fig. 1.4a; this is due to the alignment of a majority of protons with the applied field.

Protons can be excited to the higher energy state by applying a radio frequency (RF) field oscillating at the

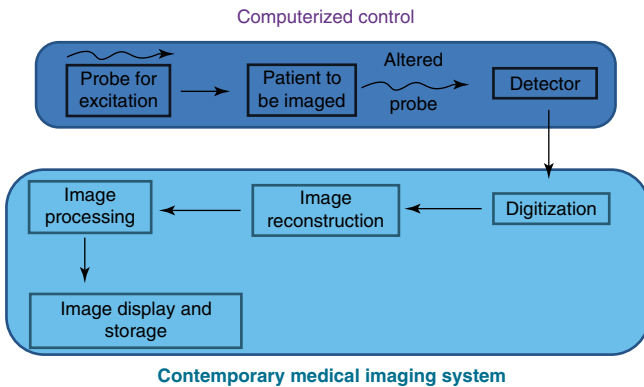


Fig. 1.1 The generic process behind any modern medical imaging system, including MRI

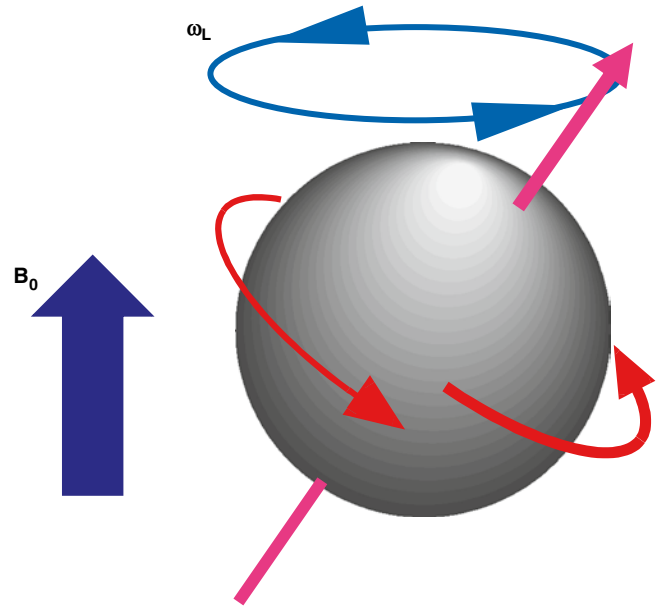
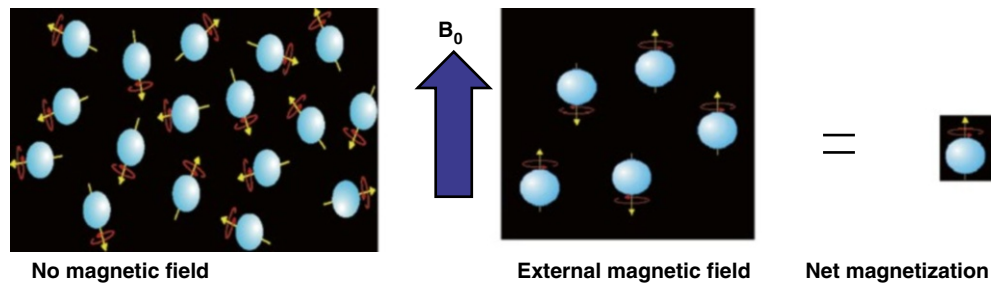


Fig. 1.3 Spins precess at a frequency, ω , that depends on the externally applied magnetic field, B_0 , and the gyromagnetic ratio, γ , of the particular nuclei. The gyromagnetic ratio for hydrogen is 42.58 MHz/T

Fig. 1.2 The alignment of a majority of spins (hydrogen nuclei, i.e., protons) with a strong magnetic field generates a net longitudinal magnetization



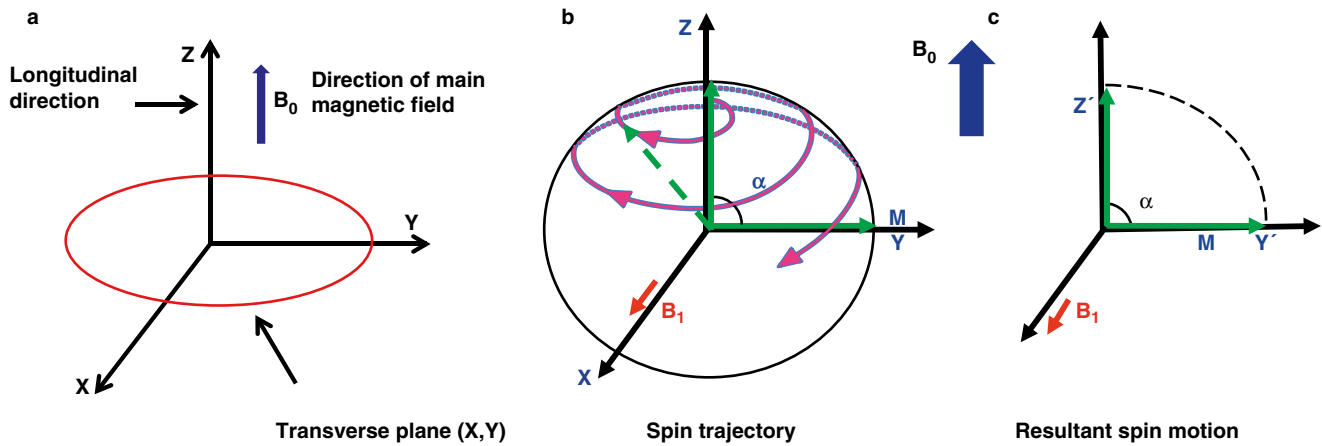


Fig. 1.4 Schematics showing (a) the direction of the main magnetic field and longitudinal magnetization, (b) nutation of a spin from the longitudinal axis to the transverse plane in response to an applied RF

field (B_1) (c) the final result of tipping all of the longitudinal magnetization by flip angle $\alpha=90^\circ$ into the transverse plane

Larmor frequency; this applied RF field is known as the B_1 field. The magnitude of the net longitudinal magnetization in the z-direction is extremely small compared to the magnetic field strength, B_0 , and is undetectable. In order to measure a detectable signal from protons, the magnetization is tipped out of alignment with B_0 and into the transverse plane. When an RF pulse is applied at the Larmor frequency, i.e., a B_1 field is switched on briefly as shown in Fig. 1.4b, the net magnetization vector will respond and be tipped away from the z-axis and towards the x-y transverse plane (Fig. 1.4c). The angle that the magnetization vector rotates away from the z-axis is known as flip angle (α), and can be approximated as

$$\alpha = \gamma\tau B_1 \quad (1.2)$$

where τ represents the length of time the RF pulse is applied with amplitude B_1 .

When the RF pulse is terminated, the net magnetization will begin to return back to the longitudinal axis as the protons return to equilibrium by releasing energy to the environment, a process known as relaxation as termed by Felix Bloch, one of the discoverers of the nuclear magnetic resonance phenomenon that forms the basis for MRI. Before the protons fully relax back to equilibrium, the signal generated by the transverse component of the precessing magnetization can be detected using an RF receiver coil.

MR Signal and Contrast Characteristics from Spin Relaxation

The MRI signal available from stationary tissue is determined by a combination of factors, including the density of protons and their relaxation rates; depending on the specific pulse sequence parameters, the image contrast will reflect these as

well as many other factors such as flow and motion, diffusion, local differences in magnetic susceptibility and field homogeneity. Two types of relaxation take place: longitudinal, spin-lattice or T_1 relaxation, and transverse, spin-spin, or T_2 relaxation. The extent that T_1 and T_2 -relaxations and proton density contribute to image intensity and contrast is controlled through manipulation of pulse sequence timing and RF pulse flip angles as explained in later chapters.

Longitudinal Relaxation (Spin-Lattice Relaxation)

The spin lattice relaxation time, or T_1 , is the characteristic tissue-specific exponential time constant that governs the regrowth of longitudinal magnetization (M_z) towards its equilibrium value, M_0 (Fig. 1.5). T_1 is the time required for M_z to regain 63 % of its equilibrium value when starting from zero, e.g., following the application of a 90° excitation pulse that tips the longitudinal magnetization completely into the transverse plane; this can be expressed as:

$$M_z = M_0 (1 - e^{-t/T_1}) \quad (1.3)$$

where t is the time following the excitation pulse.

Longitudinal, spin-lattice relaxation is caused by the transfer of thermal energy between excited nuclei and the surrounding atomic lattice [2]. Molecules that have an efficient means of energy transfer will exhibit a shorter T_1 relaxation time, while those without effective transfer mechanisms demonstrate a longer T_1 time. This is primarily dependent on the mobility of the lattice, and the related vibrational and rotational frequencies. The more closely these frequencies correspond to the energy gap, E , and the Larmor frequency, the more efficient is T_1 relaxation. Thus, T_1 relaxation is highly dependent on molecular motion, and

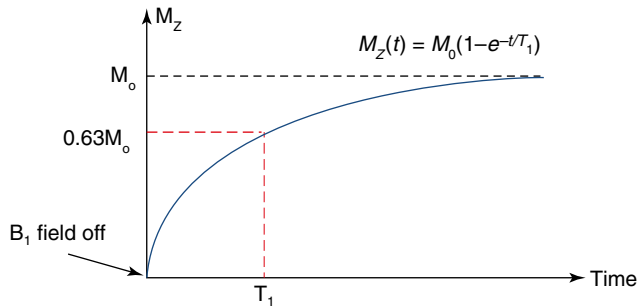


Fig. 1.5 Schematic illustrating T_1 recovery curve. T_1 relaxation constant defines the time to regain 63 % of longitudinal magnetization following a 90° excitation pulse

hence, on the size of the molecules. The motion of very large molecules generally occurs at a frequency too low for efficient energy transfer, and likewise extremely mobile nuclei such as those in free water are moving at frequencies too high to facilitate relaxation; thus the T_1 values of fluids are relatively long, while fat tissues demonstrate shorter T_1 values [3].

T_1 Differences Determine Image Contrast

As an example, consider tissues A and B shown in Fig. 1.6; tissue A has a shorter T_1 relaxation time than tissue B, i.e., the longitudinal magnetization of tissue A will recover and realign with the main magnetic field more quickly than tissue B following RF excitation. After a 90° RF pulse, the magnetization vectors for both tissues A and B are tipped into the transverse plane and from there the longitudinal magnetization begins to recover. Magnetic resonance imaging typically requires multiple excitation pulses to collect all of the data needed to form an image; if the next excitation pulse is applied before full recovery occurs (which takes approximately five times T_1), tissue A will have recovered more longitudinal magnetization than tissue B. Since tissue A has a larger longitudinal component prior to the next RF pulse, it will have a larger transverse component after the RF pulse, and therefore tissue A will have a higher signal than tissue B, and will appear brighter in the image as shown in Fig. 1.6. Thus, in a pulse sequence designed to generate image contrast sensitive to T_1 , i.e., a T_1 -weighted image [4], tissues with shorter T_1 will have higher signal than tissues with longer T_1 . Table 1.1 shows the T_1 values for various tissues at 1.5T [5].

Transverse Relaxation (Spin – Spin Relaxation)

The transverse magnetization created when an RF pulse is used to tip the longitudinal (M_z) magnetization into the transverse plane decays back to zero after the termination of the RF excitation pulse. The time constant, T_2 , describes the

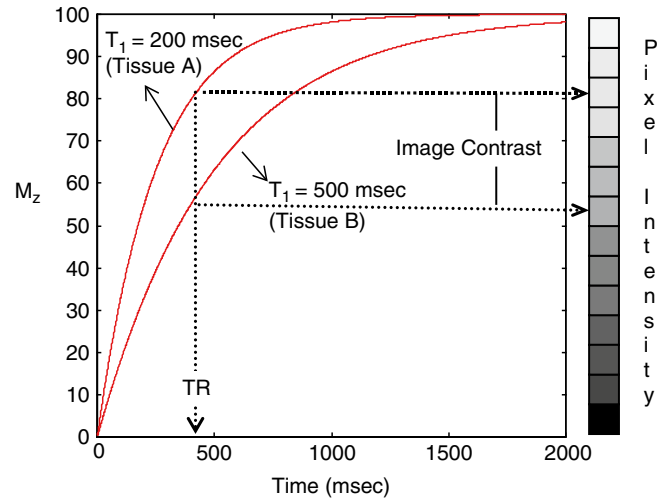


Fig. 1.6 Difference in T_1 relaxation times between example tissues A ($T_1=200$ ms) and B ($T_1=500$ ms) leads to a difference in longitudinal magnetization at time TR. This difference is used to generate contrast between the tissues in a T_1 -weighted image

Table 1.1 Typical T_1 and T_2 values for various tissues at 1.5 T

Tissue	T_2 (ms)	T_1 (ms)
Adipose tissue	80	260
Liver	40	490
Skeletal muscle	50	870
Myocardium	60	950
Blood	~180 (arterial)	1500
Cerebrospinal fluid	2000	4200

exponential rate of decay of the transverse magnetization (Fig. 1.7), which is given by:

$$M_{xy}(t) = M_{xy}(0) * e^{-t/T_2} \quad (1.4)$$

where t is the time following the excitation pulse, and M_{xy} is the component of the magnetization in the transverse plane. By this equation, T_2 is the time required for 63 % of the initial transverse magnetization to dissipate [6, p. 381].

Recall that the net magnetization vector is the sum of magnetic moments from many individual protons. To maintain a detectable net transverse magnetization, the protons must maintain phase coherence, that is, they must precess in phase with one another at exactly the same frequency. Over time, however, the individual precessing protons get out of sync with each other, or become “dephased” in the transverse plane; this means that the individual magnetic moments begin to point in different directions, decreasing the total net transverse magnetization [3]. Realizing from the Larmor Equation (Eq. 1.1) that the precession frequency of a proton is dependent on the magnetic field it experiences, it is easy to understand that the primary reasons for transverse dephasing are related to spatial and temporal variations in the magnetic field. One

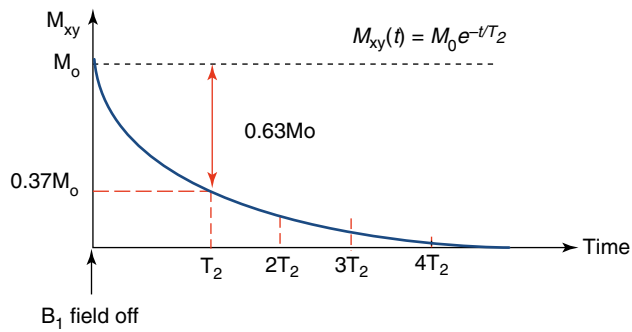


Fig. 1.7 Schematic illustrating T_2 decay curve. T_2 relaxation constant defines the time for transverse magnetization to decay to 37 % of its original value following an RF excitation pulse. T_2 is always shorter than T_1

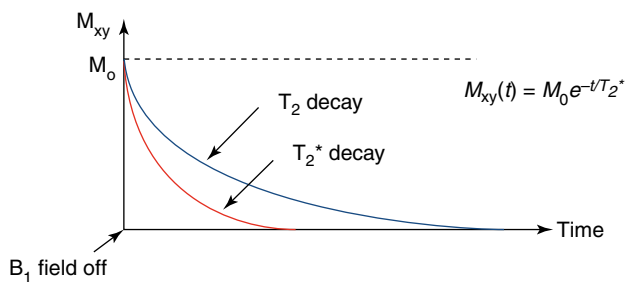


Fig. 1.8 T_2^* takes into account local, static field inhomogeneities, as well as spin-spin relaxation, and therefore is always shorter than T_2

of the factors contributing to the dephasing of the protons is the interaction between the magnetic fields of individual protons, or so-called “spin-spin” dephasing [6]. Similar to spin-lattice relaxation, spin-spin relaxation is inefficient in highly mobile protons, and thus the T_2 relaxation time tends to be longer in free water, and in tissue containing a high percentage of water. Besides these temporally varying spin-spin interactions, transverse phase coherence is also affected by static inhomogeneities in the local magnetic field; these can be caused by inhomogeneities in the applied field, or by local differences in the magnetization of tissues due to differences in their magnetic susceptibility. The effective transverse relaxation time (T_2^*) describes the exponential decay in signal that results from the combination of spin-spin relaxation (T_2) and static field inhomogeneities (T_2') [3] as shown in Fig. 1.8 and in the equation:

$$1/T_2^* = 1/T_2 + 1/T_2' \quad (1.5)$$

T_2 Differences Determine Image Contrast

Again, consider an example of two tissues, tissue A and tissue B; let tissue A have a shorter T_2 time than tissue B, indicating that its transverse magnetization relaxes or decays more rapidly than tissue B. At any time following an excitation pulse, the amount of transverse magnetization in tissue

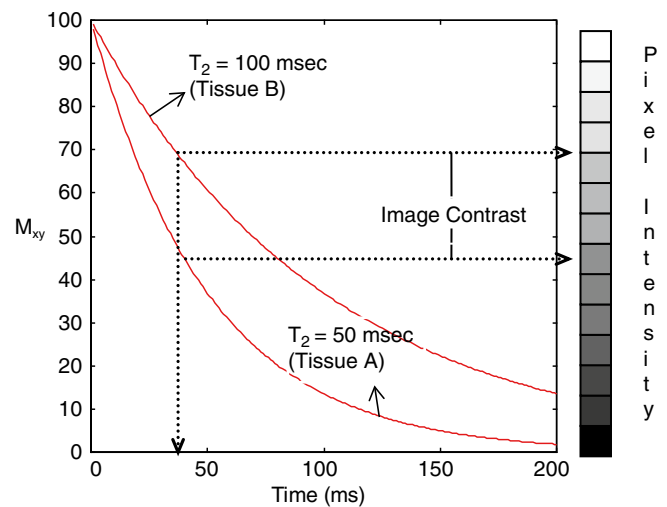


Fig. 1.9 Difference in T_2 relaxation times between example tissues A ($T_2 = 50$ ms) and B ($T_2 = 100$ ms) leads to a difference in transverse magnetization at time TE . This difference is used to generate contrast between the tissues in a T_2 -weighted image

A is less than tissue B, thus generating less signal in the image [4] as shown in Fig. 1.9. Thus, in a T_2 -weighted image, tissues with longer T_2 will appear brighter than tissues with shorter T_2 . Table 1.1 shows the T_2 relaxation times for different tissues.

Contrast Produced by Proton Density

Besides the tissue relaxation rates, contrast between tissues is also governed by differences in proton density. Proton density, as one would expect, is indicative of the number of protons per volume of tissue. The higher the number of protons in a given volume of tissue, the greater is the magnetization available to provide signal. Imaging pulse sequences can be designed to provide “proton density weighting,” i.e., to be sensitive to proton density and relatively insensitive to T_1 or T_2 relaxation [4], although this contrast mechanism is rarely used in cardiovascular MRI applications.

Signal Acquisition

Free Induction Decay

In the most basic example of a nuclear magnetic resonance signal, a 90° RF pulse is applied to rotate the net longitudinal magnetization vector completely into the x-y plane, where it can induce a signal in an RF receiver coil. This signal, which is a result of the free precession of the net magnetization in the transverse plane, is called the free induction decay, or FID, since it gradually decays due to the relaxation mechanisms previously described.

The FID in hydrogen magnetic resonance has the following characteristics:

1. It oscillates at the Larmor frequency determined by the gyromagnetic ratio of hydrogen, and the applied magnetic field strength.
2. It has an initial magnitude that is proportional to the density of protons (hydrogen nuclei) in the sample being measured.
3. It decreases in amplitude exponentially with a time constant T_2^* , due to the combination of spin-spin relaxation and magnetic field inhomogeneities [2].

Imaging Procedure

To generate an image, a sequence of RF pulses in combination with magnetic field gradients is implemented as detailed in later chapters. The specific sequence and timing of RF pulses, magnetic field gradient pulses, and delay times is designed to manipulate the transverse and longitudinal magnetization to generate a specific type of image contrast. It is typically necessary to repeat a pulse sequence a number of times to acquire enough data to form an image. Therefore, the time for one cycle of a pulse sequence is called the repetition time, or TR.

Spatial Localization

It is necessary to encode the emitted signal so that the spatial position of the nuclei contributing to the signal can be located through the image reconstruction process. To spatially encode the signal, sets of magnetic field gradients are applied during the imaging procedure. Using coils that are embedded in the bore of the MRI scanner, it is possible to superimpose a magnetic field gradient (variation in the magnetic field with respect to position) onto the static main magnetic field. These gradients are weaker magnetic fields oriented in the same direction as the B_0 field (i.e., the z-direction) and vary linearly with position. There are three independent gradient coils in the MRI system, each designed to create a linear variation in the static field along one of the Cartesian axes, x, y, and z; the gradients produced on each axis are respectively referred to as G_x , G_y , and G_z . Note that a linear gradient can be generated in any direction by appropriate combination of gradients along multiple axes simultaneously. This is what gives MRI the flexibility to generate images in any orientation.

As an example, G_x refers to a one-dimensional gradient superimposed on the B_0 field that causes a linear variation in

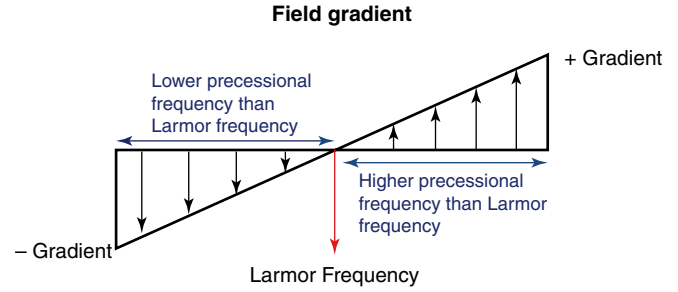


Fig. 1.10 Magnetic gradient field superimposes on the main magnetic field (B_0) to create a linear variation in field strength in the direction of the gradient. By the Larmor equation, this creates a linear variation in precessional frequencies as a function of location. This control over the spatial distribution of precessional frequencies enables spatial localization of the MR signal, and image encoding

the field in the x direction. In Fig. 1.10, the length of the vectors represents the magnitude of the gradient field that changes positively and negatively. Recalling that the Larmor Equation (Eq. 1.1) states that the precessional frequency is proportional to magnetic field strength, the gradient causes the precessional frequency to vary as a function of position along the direction of the gradient. Thus, the position of a particular spin along the direction of an applied gradient can be determined from its precessional frequency.

The imaging process can be divided into four fundamental operations:

1. Slice selection
2. Spatial encoding
3. Signal read-out
4. Image Reconstruction

Slice Selection

The slice selection gradient (G_z , by convention) and the RF pulse are applied simultaneously in order to excite (tip) the magnetization of protons only within a slice of discrete thickness (Fig. 1.11). The slice thickness is controlled by two factors: the amplitude of the magnetic field gradient, which affects the spatial distribution of the proton resonant frequencies, and the bandwidth of the RF pulse (i.e., the range of frequencies included in the pulse) [5] as shown in Fig. 1.12. We can see by Eq. 1.6,

$$\Delta z = \frac{2\pi\Delta f}{\gamma \bar{G}_z} \quad (1.6)$$

that the slice thickness, Δz , is proportional to the RF pulse bandwidth, Δf , and inversely proportional to the slice select gradient amplitude, G_z . That is, for a given bandwidth RF pulse, a stronger slice select gradient will excite a thinner

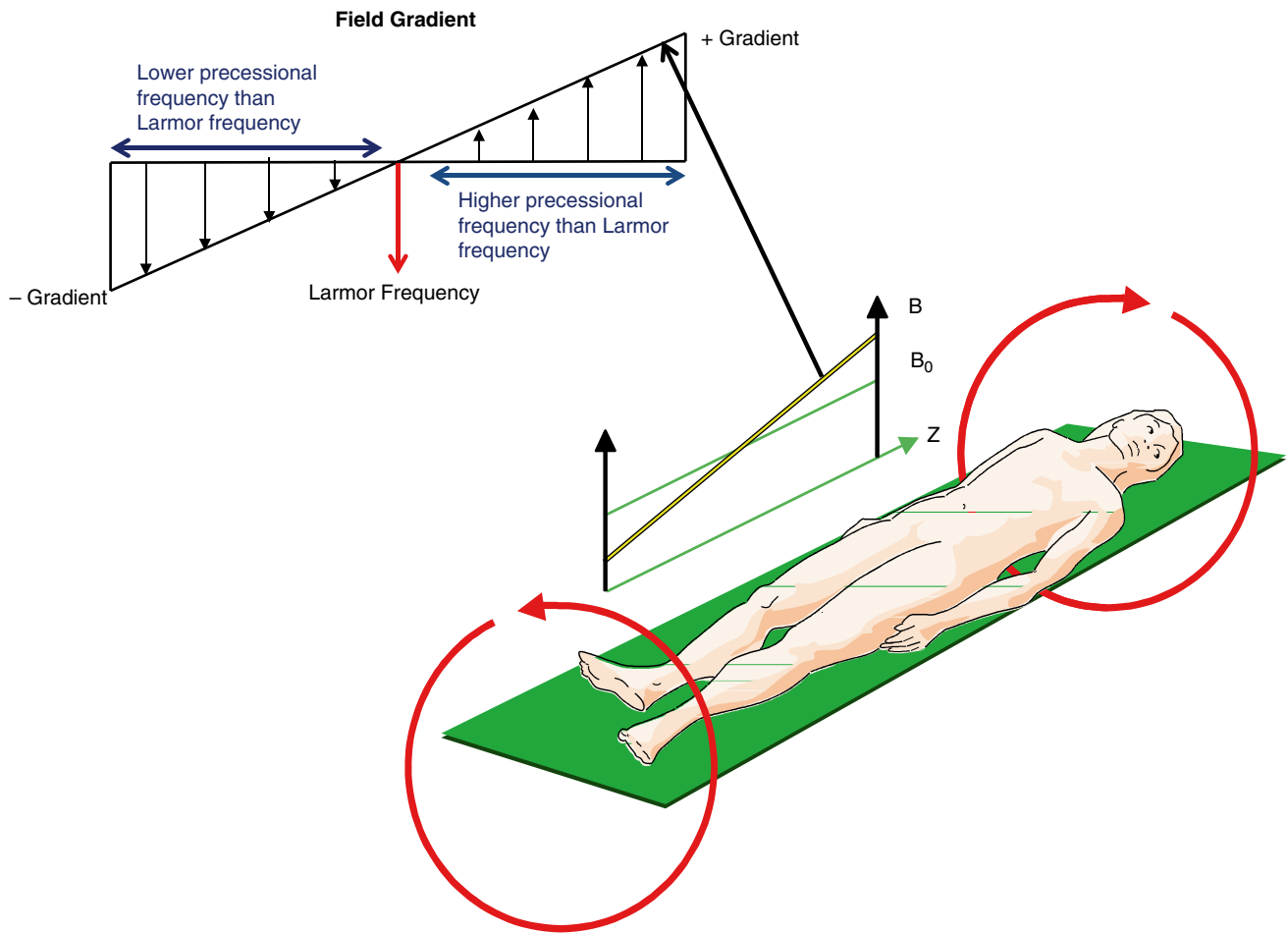


Fig. 1.11 Z-gradient coil, schematically represented by the red loops, generates a linear variation in the main magnetic field in the head to foot direction. Additional gradient coils create linear variations in the

main field in X and Y directions. Using all three coils it is possible to select and encode an image in any orientation

slice as compared to a weaker slice gradient, as shown in Fig. 1.13. The center frequency of the RF pulse is set to match the precessional frequency of protons at the location of the desired slice, as shown in Fig. 1.14. Therefore, the slice select gradient localizes the signals in one direction.

Spatial Encoding

The next step in the process of image formation is to localize the positions of the protons within the slice (that is, in the in-plane x- and y-directions). Two gradients are applied, one (G_y) in the phase-encoding direction (by convention, the y-direction) and one (G_x) in the frequency-encoding direction (by convention, the x-direction). The latter is also called the “read-out gradient”, because the signal is read or received during its application. When a phase-encoding gradient, G_y , is applied, the frequencies in the y direction are changed spatially. Similarly, when G_x is applied the frequencies in the x direction are changed spatially. This combination of gradients provides the basis for the application of the inverse

two-dimensional Fourier transform ($M(k_x, k_y)$) which reconstructs the final image as shown in Eq. 1.7

$$M(k_x, k_y) = \iint_{x,y} m(x, y) e^{-i2\pi[k_x x + k_y y]} dx dy \quad (1.7)$$

where k_x and k_y are spatial frequencies in the x and y directions respectively. The time integrals of the applied gradients, G_x and G_y , control the sampling of spatial frequencies, k_x and k_y , as shown in Eqs. 1.8 and 1.9;

$$k_x = \frac{\gamma}{2\pi} \int_0^t G_x(t) dt \quad (1.8)$$

$$k_y = \frac{\gamma}{2\pi} \int_0^t G_y(t) dt \quad (1.9)$$

These relationships between gradient pulses and k-space sampling will be described in more detail in later chapters.

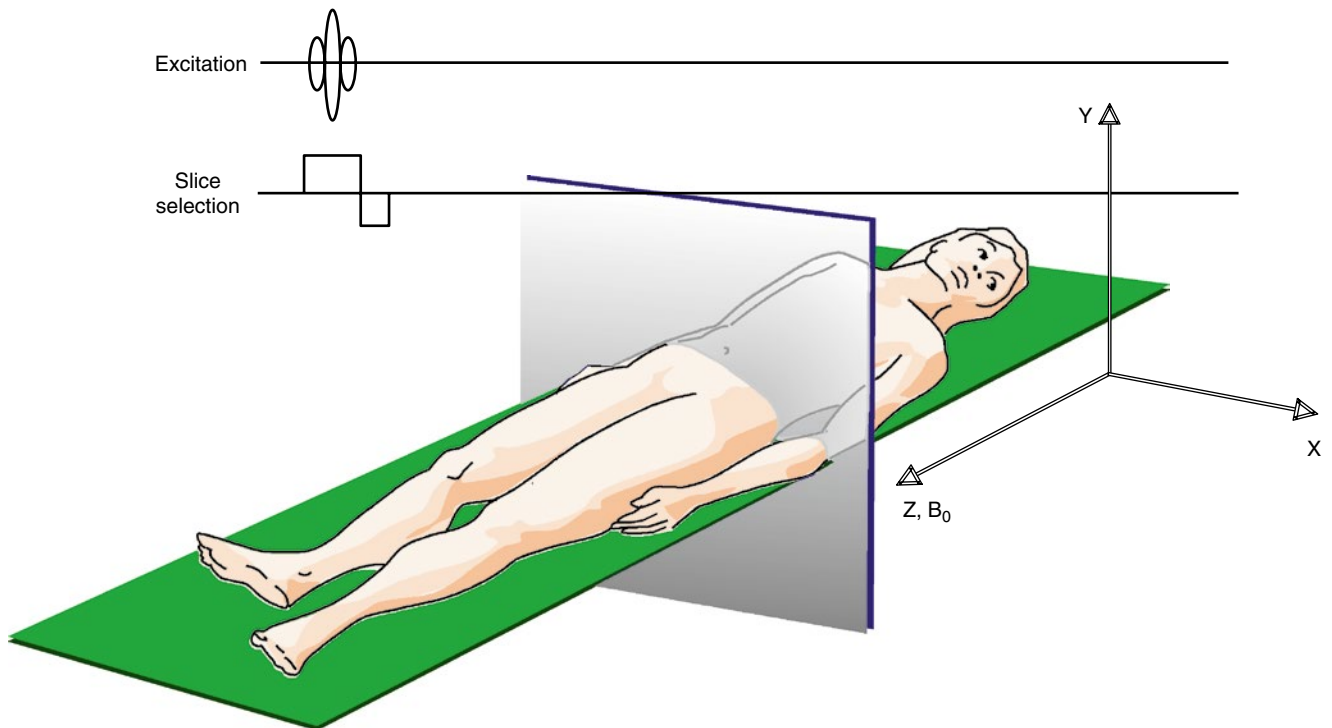


Fig. 1.12 RF excitation and slice select gradient are applied simultaneously to excite the spins only in the selected slice. The gradient creates a distribution of precessional frequencies along the direction of the

gradient, and a narrow band RF pulse is applied to excite spins only within a location based on their frequency

Fig. 1.13 Bandwidth of the RF pulse and the gradient strength (steepness of the change in magnetic field) together determine the thickness of the selected slice. For a given bandwidth RF pulse, the stronger gradient (*red line*) will excite a thinner slice compared to the weaker gradient (*green line*)

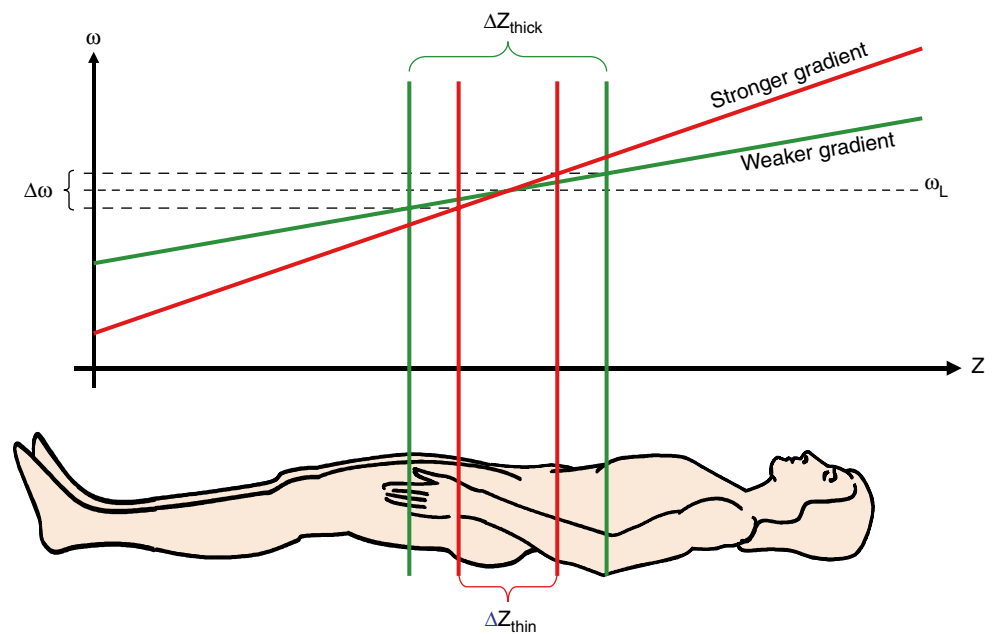
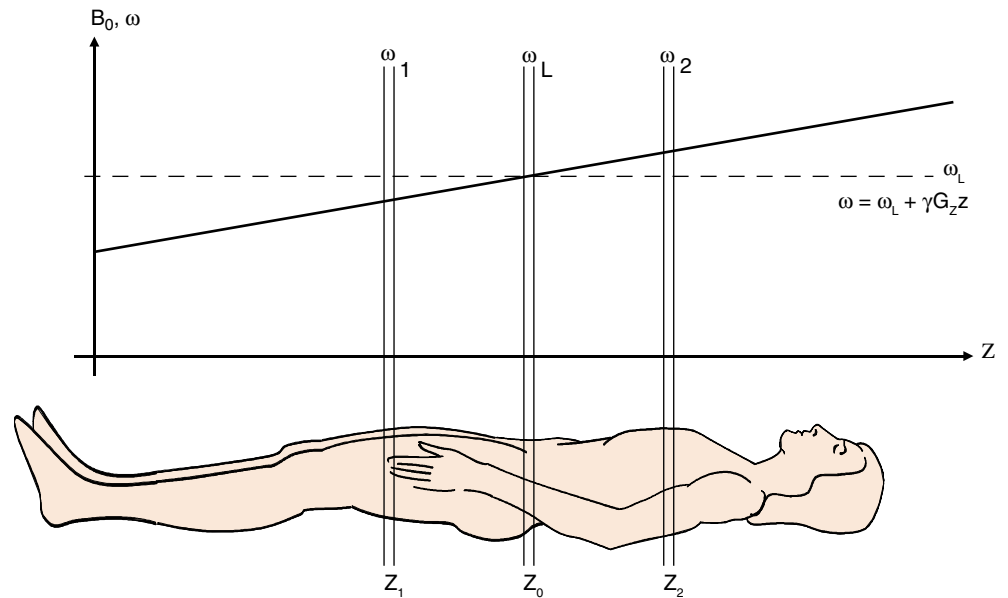


Fig. 1.14 The gradient creates a variation in magnetic field, which creates a variation in precessional frequency by the relationship described by the Larmor equation. This schematic shows how slices can be selected in different locations (z_1, z_0, z_2) by matching the frequency of the RF excitation pulse to the precessional frequency ($\omega_1, \omega_0, \omega_2$) of spins in a specific location



Signal Read-out

The MRI signal is sampled during the G_x gradient application. The time-varying signal is digitized and stored in a two-dimensional data matrix known as k-space. As will be described in detail in the following chapters, spatial frequencies k_x and k_y define the axes of k-space. The sampled signal typically fills k-space one row, or k_x -line, at a time. Low spatial frequency data fill the center of k-space and provide information about general shapes and contrast in the image, while high spatial frequency data are stored in the periphery of k-space that represents image resolution and detail.

Image Reconstruction

In its most basic form, MR images are reconstructed by applying a two-dimensional Fourier transform to the raw k-space data row by row and column by column. This process effectively decodes the spatial position of the excited hydrogen nuclei based on variations in frequency and phase [2]. In the reconstruction process, a relative signal intensity value for each image voxel, or volume element, is calculated based on

the strength of the signal from the hydrogen nuclei contained in the corresponding volume of tissue within the patient. The result is the final image, which illustrates spatial anatomical relationships and grayscale contrast between tissues based on the magnetization behavior of hydrogen within a slice of tissue [5]. Additional details on the process of image reconstruction are provided in the following chapters.

References

1. Slichter CP. Principles of magnetic resonance. 3rd ed. Berlin: Springer-Verlag; 1990.
2. Nishimura DG. Principles of magnetic resonance imaging. 11th ed. Raleigh: Lulu.com; 2010.
3. Elster AD, Burdette JH, editors. Questions and answers in magnetic resonance imaging. 2nd ed. Maryland Heights: Mosby; 1994.
4. Bushberg JT, et al. The essential physics of medical imaging. Philadelphia: Lippincott Williams & Wilkins; 1994.
5. Bernstein AM, et al. Hand book of MRI pulse sequences. Amsterdam: Elsevier; 2004.
6. Sprawls P. Physical principles of medical imaging. Philadelphia: Lippincott Williams & Wilkins; 1987.

Michael Loecher and Oliver Wieben

Abstract

This chapter will introduce the k-space formalism used in MR imaging for data encoding and image reconstruction via Fourier transforms (FT). Essentially, this formalism is a mathematical construct that allows for the description of acquired MRI data in a domain described as spatial-frequency space, or k-space, which is related to the desired image space representation via the Fourier transform. Representing the data as k-space converts the time varying signal acquired with the MR receiving coils into a 2D or 3D data space that can be readily reconstructed into an image representation by applying the well-known Fourier transform. Understanding MRI acquisitions and reconstructions in terms of k-space is a crucial step in understanding the basic relationships between the acquisition and the reconstructed images, most acceleration and reconstruction techniques, sources of artifacts and their appearance, and advanced acquisition strategies.

Keywords

k-space formalism • Fourier transform • Spatial resolution • Field-of-view • Sampling • Receiver bandwidth • Spatial frequency • Sampling trajectory

This chapter will review the principles of data acquisitions in frequency space along with the implications that the choice of acquisition parameters, such as sampling frequency and receiver bandwidth, have on the resulting image parameters such as spatial resolution, field-of-view (FOV), spatial aliasing, and others. The k-space formalism also allows for a convenient and intuitive interpretation of sampling patterns, usually referred to as k-space

trajectories, through the use of pulsed magnetic field gradients. This concept will be discussed along with standard rectilinear or Cartesian sampling and examples of echo-planar MRI as well as radial and spiral trajectories. For a more extensive derivation of these concepts and the underlying mathematics, the interested reader is referred to textbooks [1–3].

Introduction to k-Space

The ultimate goal in MR imaging is the generation of a diagnostically useful image that represents the spatial distribution of certain tissue properties as influenced by the spin distribution, relaxation parameters, and physiological factors such as flow, motion, and diffusion. Some early MRI approaches exploited pointwise scanning of the object [4]. This method is very time-consuming and extremely

M. Loecher, PhD

Department of Medical Physics, University of Wisconsin-Madison,
1111 Highland Ave, Suite 1127, Madison, WI 53705-2275, USA

O. Wieben, PhD (✉)

Department of Medical Physics, University of Wisconsin-Madison,
1111 Highland Ave, Suite 1127, Madison, WI 53705-2275, USA

Department of Radiology, University of Wisconsin-Madison,
1111 Highland Ave, Suite 1127, Madison, WI 53705-2275, USA
e-mail: owieben@wisc.edu

limited in its signal-to-noise ratio (SNR) because of the inherently low signal that arises from a single voxel. This approach somewhat resembles the use of a digital camera that has only a single sensor to acquire signal from each individual voxel one after another in a sequential digitization process, instead of the actual simultaneous use of many light receptors.

Instead, MR data acquisition is conducted in a transform domain called *Fourier space*, which is also called *frequency space*. In MRI, this domain is commonly referred to as *k-space* based on nomenclature established by physicists and mathematicians to describe spatial frequencies in equations that contain propagating waves such as light, sound, or radio waves [5]. This terminology precedes its use in MR imaging, and the letter ‘*k*’ is neither an abbreviation nor does it have a specific meaning.

Acquiring data in an alternative domain is not necessarily intuitive at a first glance, but can offer many advantages. This approach is not uncommon in medical imaging; consider, for example, the use of the Radon transform for Computed Tomography (CT) image reconstruction from projection data. One tremendous advantage of *k-space* acquisition is that the net magnetization in every voxel of the imaging volume contributes to the received signal simultaneously, thereby greatly amplifying the SNR and scan efficiency. While many transforms share this property, MR data acquisition is conducted in Fourier space because the time-varying gradient waveforms used for imaging give rise to a signal equation that directly resembles the Fourier transform (FT) and therefore ensures a straightforward image reconstruction using 2D or 3D FT as shown in Fig. 2.1. This is somewhat of a fortunate coincidence for the field of MRI and the realization of the *k-space* formalism [6–8] has greatly advanced the field.

Signal Equation and *k*-Space

We can represent an extremely simplified MRI signal equation as:

$$S(t) = \iiint I(\mathbf{r}) e^{i\gamma \mathbf{r} \cdot \int_0^t \mathbf{G}(t') dt'} d^3\mathbf{r} \quad (2.1)$$

Where $S(t)$ is the free-induction decay (FID) or echo detected by an RF receiver coil; $I(\mathbf{r})$ describes the signal associated with spatial location or point \mathbf{r} , which is dependent on several factors including proton density, T_1 and T_2 relaxation, as well as imaging parameters; i is the imaginary unit; γ is the nuclear gyromagnetic ratio; and $\mathbf{G}(t)$ is a vector quantity that represents the magnetic field gradient at time t after the magnetic excitation. We can then substitute:

$$\mathbf{k}(t) = \gamma \int_0^t \mathbf{G}(t') dt' \quad (2.2)$$

to simplify Eq. 2.1 and we obtain:

$$S(t) = \iiint I(\mathbf{r}) e^{i\mathbf{k}(t) \cdot \mathbf{r}} d^3\mathbf{r} \quad (2.3)$$

where we can see the relationship between the acquired signal, $S(t)$, the original object, $I(\mathbf{r})$, and the spatial-frequency distribution, $\mathbf{k}(t)$.

In this notation, the signal equation which links the data acquired with the RF receiver coil to the spatial distribution of the underlying MR signal sources resembles the Fourier transform. Mapping the acquired FID to its corresponding value of $\mathbf{k}(t) \cdot \mathbf{r}$ gives us our *k-space* representation, where the acquired time varying data is mapped onto a spatial frequency coordinate system relating it to the applied gradients. In this context, the *k-space* representation can be either two

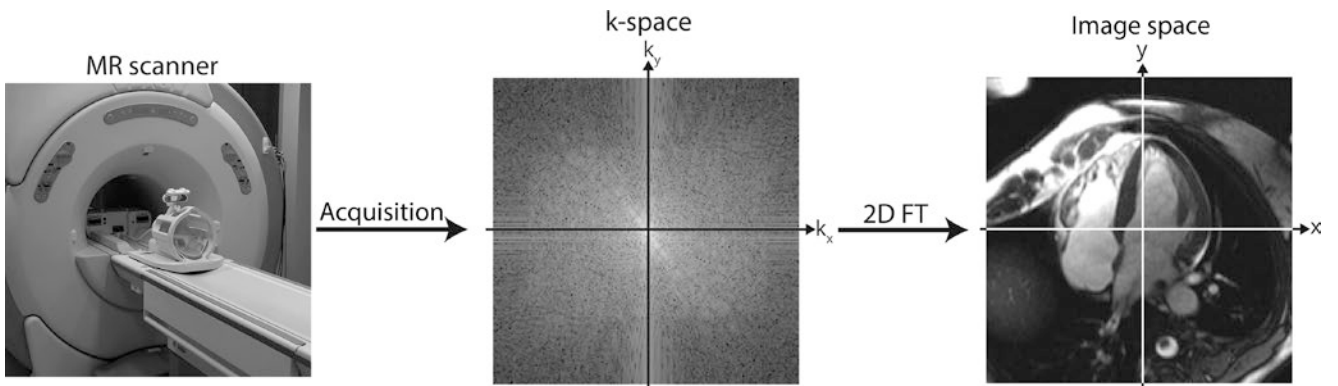


Fig. 2.1 The acquisition and reconstruction process for MR imaging. Data is collected using RF receiver coils. Through the use of time varying gradients, the data are acquired in Fourier space, also commonly

referred to as *k-space*. A Fourier transform (FT) is required to reconstruct the desired image that displays the signal distribution in spatial coordinates

or three dimensional, depending on the acquisition scheme. In general, $k(t)$ has three directional components, commonly notated as k_x , k_y , and k_z . The acquired k-space data points are complex valued and correspond to spatial frequencies with units of 1/distance.

Spatial Frequencies

The acquisition of the weighting coefficients of spatial frequencies is central to MR imaging as it is based on the concept that any image can be represented in Fourier space as a weighted sum of harmonic functions of multiple spatial frequencies and orientations. Thereby, the data representation in image space and frequency space are linked with the Fourier transform [3].

This relationship is illustrated in Fig. 2.2, where the underlying patterns of three representative spatial harmonics are explored in more detail. Datapoint (O) represents the weighting coefficient for a low spatial frequency in the k_y -direction and the zero spatial frequency in the k_x -direction. The spatial frequency is inversely proportional to the wavelength. Consequently, it represents a wave pattern of moderately long wavelength, λ_o , which is strictly oriented along the y-axis. Datapoint (P) has components in k_x and k_y and represents a diagonal wave pattern, here of higher spatial frequency with a shorter wavelength, λ_p . Datapoint (Q) is a special case as it represents the origin of the coordinate system, which corresponds to the sum of the signal in the image across all voxels, thereby reflecting the average

signal intensity of the image when properly scaled. The resulting image is composed of the sum of all wave patterns weighted by the coefficient (grayscale value) in the k-space representation. It can be shown that any image can be accurately decomposed into the sum of these weighted wave patterns with varying wavelengths and angle orientations. The weighting coefficients of the wave patterns are displayed in grayscale as the k-space representation of the image.

Data Properties in Image Space and k-Space

In MRI, the k-space data, also referred to as the raw MR data, are directly measured and the corresponding image space is reconstructed by performing an inverse 2D or 3D Fourier transform. It is noteworthy that the process is reciprocal: for a known image, forward FT can generate the corresponding k-space representation, a fact that can be important for example in certain iterative reconstructions. It is further important to note that the Fourier transform generally generates complex valued data in both domains. In MR imaging, the acquired k-space signal is complex valued as it is obtained with quadrature coils containing a real and an imaginary channel. The MR image is also complex valued due to various factors including magnetic susceptibility, chemical shift, data inconsistencies from motion and flow artifacts, acquisition imperfections such as eddy currents and gradient delays, and other factors that cause the image to deviate from what would ideally be real-valued.

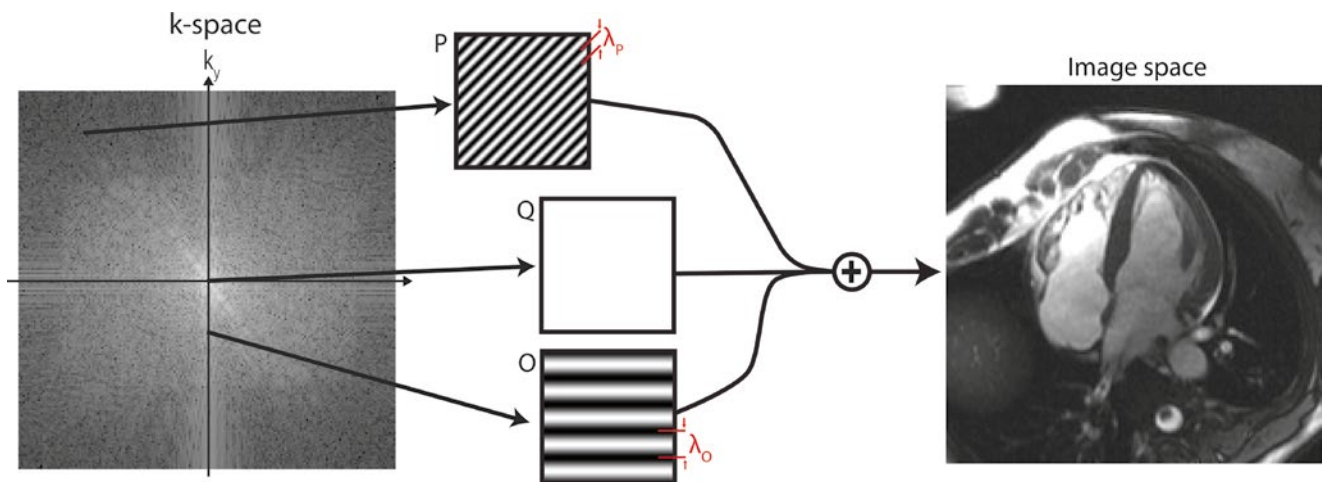


Fig. 2.2 A visual interpretation of the use of spatial harmonics to decompose an image. Every individual point in k-space represents a spatial frequency that can be represented as a wave of a certain frequency and corresponding wavelength, λ , as well as direction of the wave pattern. The image can be formed by the summation of all wave

patterns weighted by their k-space coefficient, which is represented as a grayscale value in the k-space map. Representative pictures of the spatial harmonics are shown for select points O, P, and Q, with their corresponding wavelengths, λ_o and λ_p .

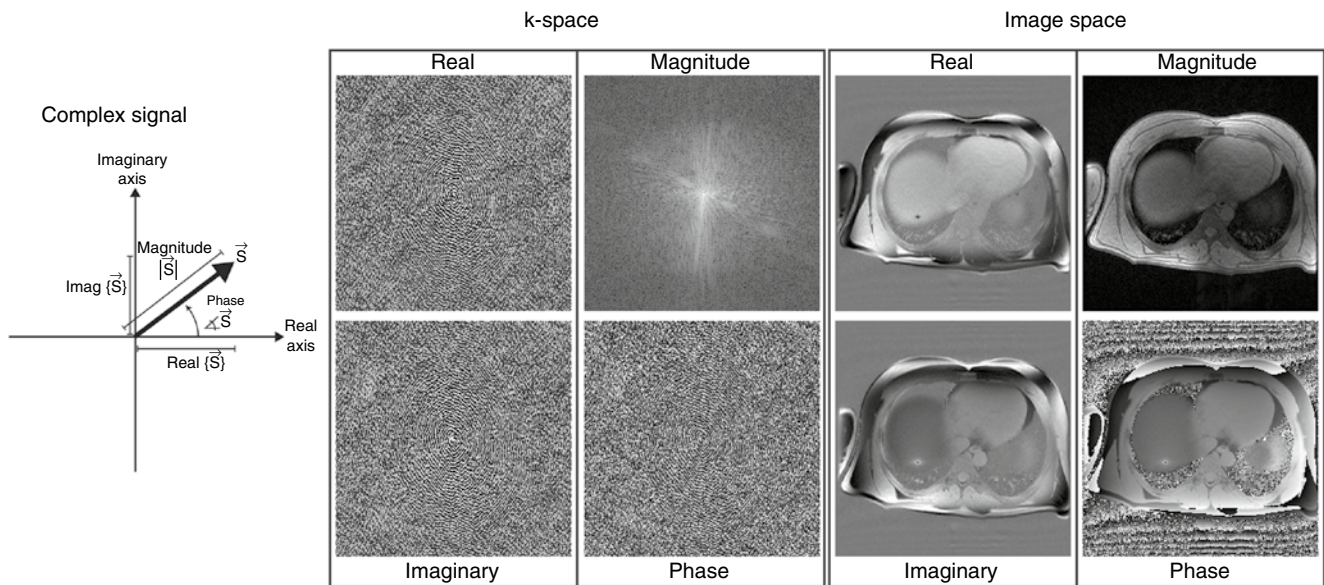


Fig. 2.3 All data from an MR system with quadrature RF coils are complex valued and can be described either by their magnitude and phase or by their real and imaginary components. Often, the image display and storage is reduced to the magnitude display. The in vivo head

scan shows that an MR image is not real valued as there are phase contributions from system imperfections and effects such as magnetic susceptibility, motion, and flow

Consequently, a complete data representation in k-space or in image space requires the display of either the real and imaginary channel, or an equivalent display of magnitude and phase of the complex valued signal as shown in Fig. 2.3. The reconstruction process always generates a complex valued image data set. However, in most clinical scans the phase image is discarded and only the magnitude image is utilized for diagnosis. There are some exceptions where diagnostic information is contained in the phase data, including phase contrast MRI, MR elastography, susceptibility weighted imaging, spectroscopy, and fat-water imaging approaches. These techniques require the processing of the phase data in image space in addition to the magnitude data. Alternatively, the data can be stored as a real and an imaginary channel from which magnitude and phase can be derived as shown in Fig. 2.3.

As described above, the center spatial frequency, also called the DC component because it reflects a non-varying image component similar to a direct current, represents the sum of the signal in all voxels in image space. Consequently, it is a very high signal, usually orders of magnitude higher than almost all other k-space coefficients. It is typical in MR images for most of the signal energy to be concentrated in the lower spatial frequencies because the imaging scene is dominated by large, high contrast objects. Therefore, the k-space data are commonly displayed with a logarithmic grayscale as shown in Fig. 2.4. Otherwise, the dynamic range of the display is not sufficient to distinguish signal variances in the lower signal regions, i.e., the outer regions of k-space.

The k-space data are usually displayed in the form of a magnitude representation since there is little added value to the human observer to display the k-space phase, or to display the real and imaginary channels. The most essential information, namely the distribution of energy in k-space, is contained in the magnitude component. Nonetheless, it is essential for the reconstruction engine to use complex-valued k-space data and not the magnitude alone.

Matrix Sizes and Artifacts

When using the Fourier transform, the matrix sizes in both domains are identical. In a 2D case, $M \times N$ k-space data points are mapped onto $M \times N$ image space data points. However, this one-to-one mapping does not always hold true as we introduce acceleration techniques, which allow us to reconstruct more image pixels from less acquired data under certain assumptions, as will be explored in greater detail in Chap. 5. It is important to note that this one-to-one mapping does not mean that a specific data point in k-space reconstructs to a specific data point in image space. In fact, each single point in k-space will influence *all* of the pixels in image space, because each value in k space represents a harmonic function over the whole image. This concept is essential in understanding and identifying some of the artifacts found in MRI, such as those described in Fig. 2.5.

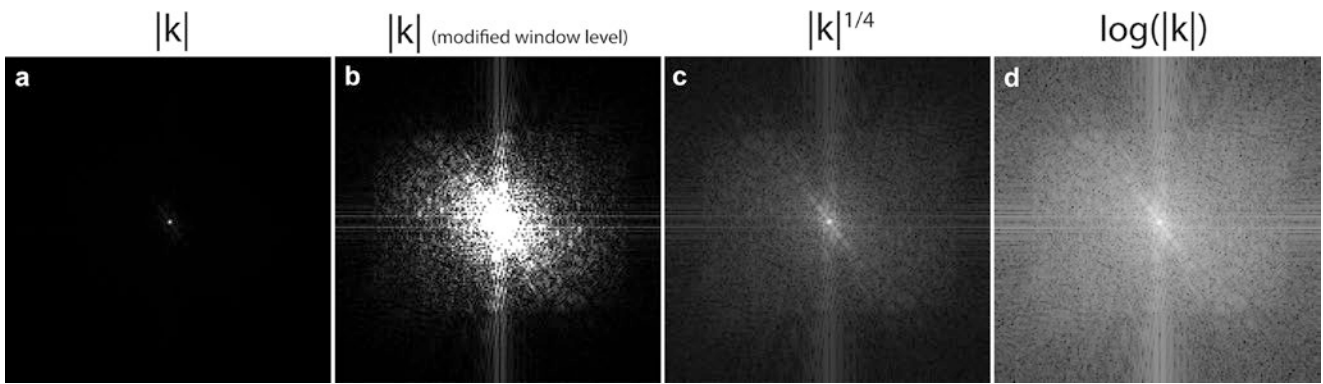


Fig. 2.4 k-space magnitude displays of the cardiac scan shown in Fig. 2.2 with various scaling schemes. As the center of k-space can be on the order of 10,000 times greater than the edges of k-space, a non-linear display of the grayscale can be advantageous. (a) k-space values linearly mapped to greyscale values and using the full dynamic range of the acquired data, which suppressed any signal outside the very center

of k space. (b) Same as (a), except window and level settings have been changed to cap off higher signals to better appreciate lower values. (c, d) Data scaling with an exponential or logarithm scale can improve the visualization of the smaller values as seen in the higher spatial frequency components

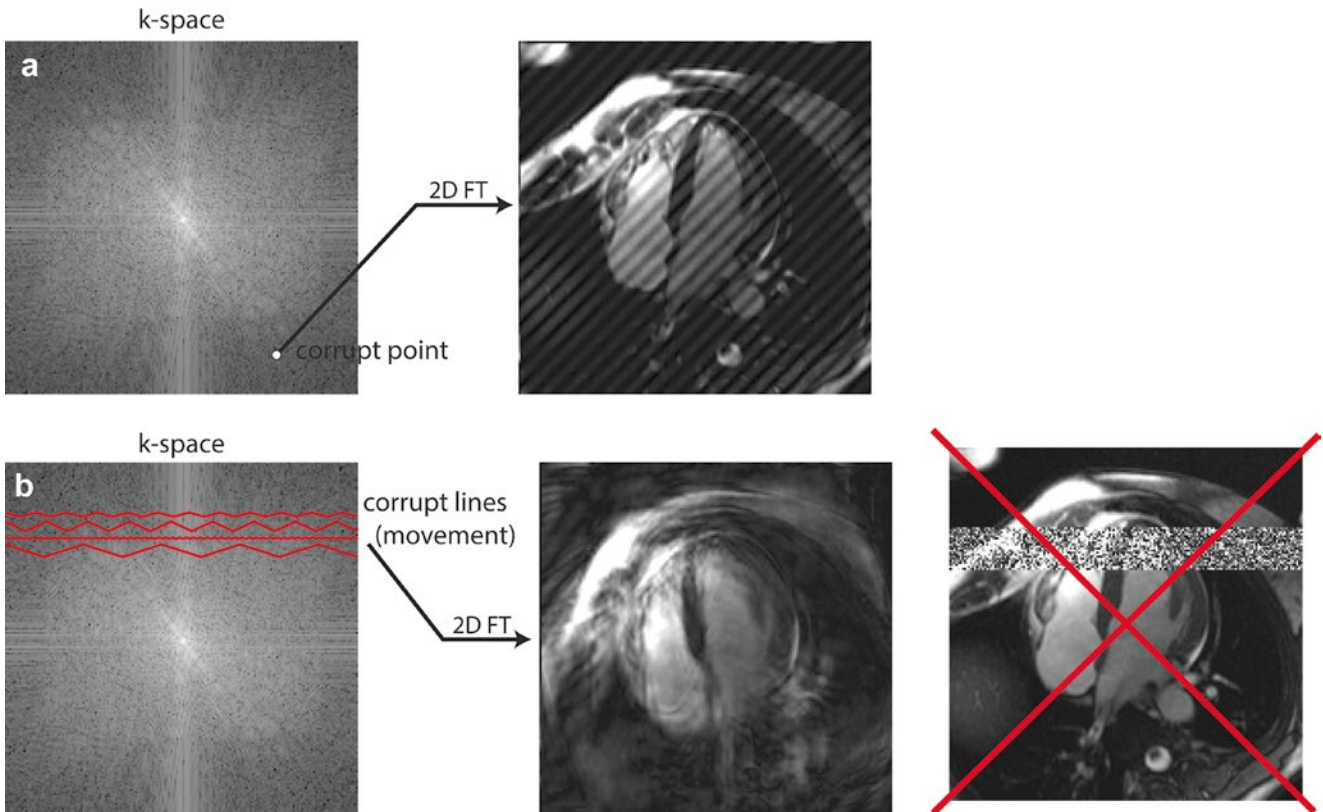


Fig. 2.5 Errors in k-space manifest in image space based on the spatial frequencies affected. (a) If a single point in k-space is corrupt, that particular spatial frequency will appear enhanced or reduced in the reconstructed image as shown in this “corduroy” or “spiking” artifact. (b) If a patient moves during an acquisition, those

portions of k-space will be corrupt and can lead to decreased image quality. These errors will be reflected in the whole image and not only in a single region of the image as shown here for illustration purposes

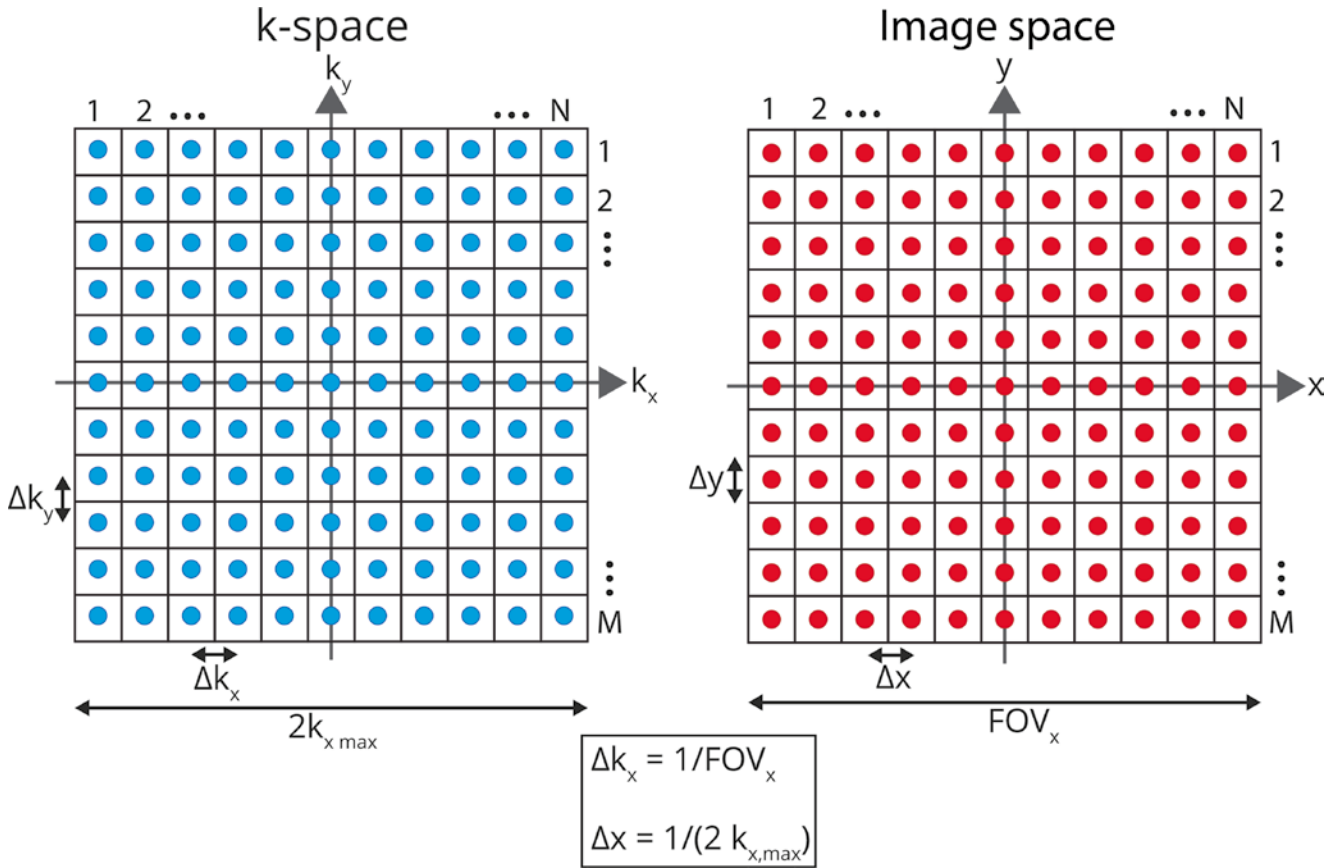


Fig. 2.6 Relationship between the sampling grids in k-space (*left*) and image space (*right*). $M \times N$ points are mapped from one domain to the other, and the relationship between the sample distance in k-space (Δk_x

and Δk_y) and the k-space coverage ($2k_{x,\text{max}}$ and $2k_{y,\text{max}}$) to the spatial resolution (Δx and Δy) and the covered field-of-view (FOV_x and FOV_y) is given in the equations above

Properties of k-Space

The Fourier transform is a commonly used tool in signal processing for signal filtering and conditioning. Therefore, an added advantage of the k-space formalism is that the impact that parameter choices in the sampling domain have on the resulting image are well characterized by the Fourier transform properties [3]. MR imaging involves the digitization of the acquired analog RF signal. Consequently, the fundamental laws of discrete data sampling and digital signal processing apply to MR data acquisition. The Nyquist-Shannon sampling theorem describes the k-space coverage required to reconstruct an image to the desired spatial resolution, as well the maximum separation between adjacent sampling points to ensure a field-of-view (FOV) without aliasing artifact. Figure 2.6 shows the relevant relations between the digital grids in k-space and in image space for the 2D case, which are explored in more detail here.

Spatial Resolution

The spatial resolution Δi in the resultant image is determined by the highest sampled spatial frequency ($k_{i,\text{max}}$):

$$\Delta i = 1 / (2k_{i,\text{max}}) \quad (2.4)$$

where Δi is the spatial resolution in direction i . In other words, the voxel dimensions in the resultant image become smaller as the coverage of k-space increases further out from the center. This also implies that a higher resolution image requires more data samples, which usually results in longer scan time.

The information content of k-space regions with respect to their distance from the k-space origin are further illustrated in a cardiac *in vivo* scan reconstructed from different data samples in Fig. 2.7. The data points that represent the center of k space contain the low spatial frequencies, while the outer portions of k space contain the high spatial frequency information. In practical terms, this means that most of the image contrast is contained near the k-space center, while the outer portions define edges and are necessary to resolve small objects. Figure 2.7 shows that an image reconstructed from only the central 1 % of k-space will provide a general outline of the imaged object and some very low resolution contrast. The second column of Fig. 2.7 shows the image when the remaining 99 % of the outer portions of k-space are used in the reconstruction process. Now all the detailed structure can be identified but much of the underlying

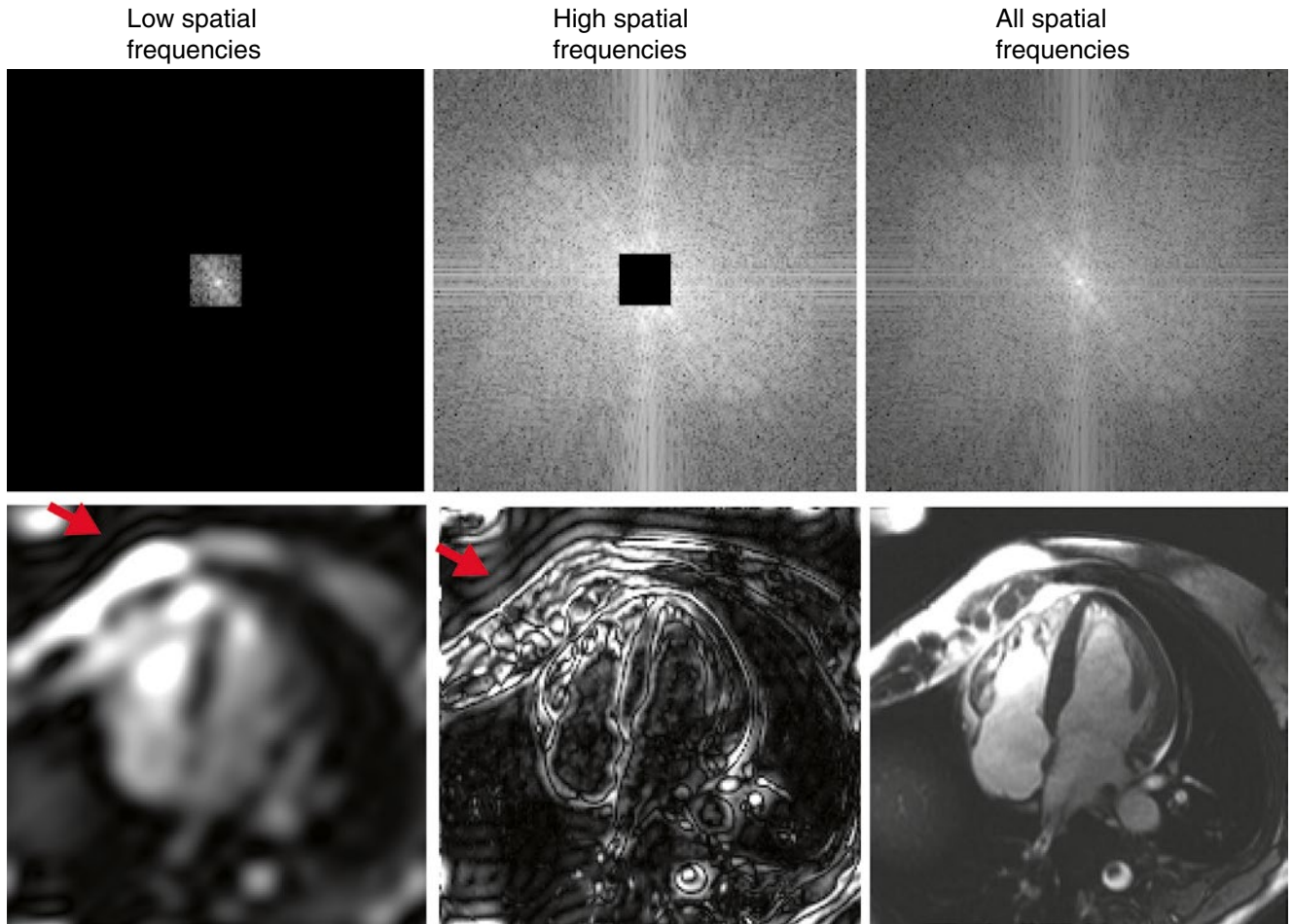


Fig. 2.7 Image contributions of low and high spatial frequencies in k-space. Low spatial frequencies are represented by the center of k-space, and define most of the image contrast, but lack edges or information on small objects. The periphery of k-space contains high spatial frequency information, which provides sharp edges in images. These

images were reconstructed with 1 % of the central k-space data (*left column*) and 99 % of the higher spatial frequency data (*center column*). The *red arrows* point out ringing artifacts due to the k-space truncation, which are further discussed in other chapters

contrast has disappeared. These are basically low-pass and high-pass filtered images as a result of the omission of k-space regions.

This concept is frequently exploited in accelerated cardiovascular imaging, where high spatial frequency data are often undersampled at a higher degree than the low spatial frequency data in order to reduce total scan times without sacrificing significant information content.

Field-of-View

The separation between points in k-space, Δk_i , is proportional to the inverse of the FOV_i in image space:

$$\Delta k_i = \left(\frac{1}{FOV_i} \right) \quad (2.5)$$

where i represents the spatial dimensions x or y .

In other words, as the distance between sampled points in k space increases, the FOV of the resultant image decreases. A sufficient FOV is required in order to ensure ample coverage of the imaged object. Note that the k-space sampling grid and resultant FOV are independent along the two or three dimensions, meaning that the FOV and resolution can be set independently for each dimension.

Gradients and k-Space

As shown in Eq. 2.3, the actual k-space trajectory, i.e., the position in k-space at any time during data acquisition, is directly related to the product of the applied gradient field multiplied by the time since RF excitation, or more generally to the time integral of the gradient waveform. This is a powerful framework that allows us to control the gradients to steer our acquisition on a desired trajectory through k-space until all required data points are sampled. Note that from Eqs. 2.2

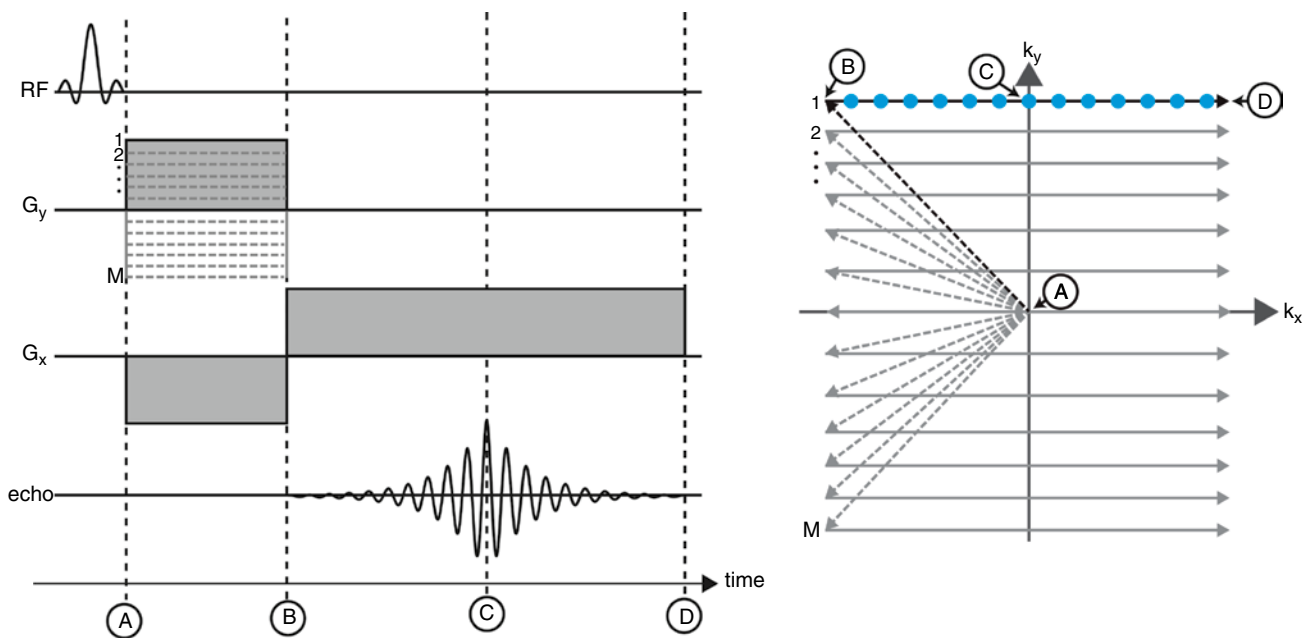


Fig. 2.8 Gradient waveforms are used to generate desired k-space trajectories, here shown for the spin warp acquisition of a simple 2D Cartesian trajectory using a gradient echo sequence. The k-space trajectory immediately after RF excitation always starts in the center of k-space (A). The use of a phase encoding gradient (G_y) and frequency encoding gradient (G_x), also referred to as the readout gradient, establishes the path on the k-space grid as shown on the right. After the pre-winding gradients are played out at time B, the trajectory location is on

the left edge of k-space and the acquisition is started. As the readout gradient is applied, data collection traverses through the center of k-space when the refocused echo occurs (time C). This point is also known as the echo time, or TE. Finally the acquisition of a single line is finished when the right edge of k-space is reached at time D. Data are sampled along lines parallel to the readout direction in equidistant spacing until all of k-space is covered

to 2.3, the k-space location of a given data point in the FID is located at $k_x = G_x * t$, $k_y = G_y * t$, and $k_z = G_z * t$, where G_x , G_y , and G_z are the gradients in the x , y , and z directions.

Figure 2.8 illustrates the use of time varying gradients for a simple 2D gradient echo sequence with the commonly used spin-warp encoding [9] where data are sampled on a rectilinear Cartesian grid in lines parallel to the readout direction, x , at an acquisition speed of one line per excitation. A total of M lines is acquired by repeating the pulse sequence shown on the left. Each k-space line represents data sampled during a single echo formation, here generated by the gradient echo waveform labeled G_x . The combination of a pre-winding gradient between time points A and B, and the subsequent readout gradient between time points B and D, generates a gradient echo with its maximum amplitude at time point C. Therefore, this gradient is called the *readout gradient* and by convention it is usually labeled as the x -gradient, G_x . This acquisition is repeated M times with the only difference being variation of the amplitude of the G_y gradient, which is played out as a short pulse simultaneously with the pre-winding lobe of G_x between time points A and B. Again by convention, this phase encoding gradient is usually labeled the y -gradient, G_y , and phase encoding in 3D scanning is explored in a similar fashion along the z axis. Note that the use of G_x and G_y is not meant to imply that the gradient coils on the x and y axis of the magnet are always used for readout

and phase encoding, respectively; this is by convention only. In practice, the direction of the readout and phase-encoding gradients, while always orthogonal to each other, will vary in direction based on the image orientation, and for oblique imaging planes will require some combination of gradients in the x and y directions.

This combination of gradient waveforms results in the k-space sampling pattern displayed on the right of Fig. 2.8. By convention, the readout direction is usually displayed in the left-to-right direction on the k-space map. In this example, the first acquired k-space line is represented by the top row with blue dots for each data sample. At time point A, the spins have been excited and the trajectory starts at the origin of k-space. Between time points A and B, the G_x and G_y gradients are both switched on with constant amplitude, thereby the k-space trajectory as determined by the product of gradient strength and time is steered towards the top left corner of the k-space map. Once that corner is reached at time point B, the phase encoding gradient is switched off and the frequency encoding gradient is inverted with identical amplitude. This leads to a trajectory parallel to the k_x axis traveling across k-space from left to right, during which data are acquired. The system then returns to a steady state and this experiment is repeated M times while the amplitude of the phase encoding gradient is varied to step through equidistant parallel lines until the bottom row is sampled.

Consequently, the sampling intervals along the frequency encoding direction are determined by the sampling frequency of the analog-to-digital (AD) converter in the receiving chain and the amplitude of the readout gradient, while the sampling intervals along the phase encoding direction are determined by the increments in gradient amplitude.

As we have shown, we can think of gradients as ‘driving’ the acquisition through k-space, moving at a speed along each gradient direction directly related to the amplitude of the gradients. The trajectory design is ultimately limited by the maximum gradient amplitude (speed along a line) and by the maximum slew rate of the gradients (change of direction). Modern gradient systems used for medical imaging have undergone remarkable improvements over the past two decades to the point that their maximum performance is determined by safety limits to avoid peripheral nerve stimulation caused by rapidly switching magnetic fields. An important point to note is that *all* gradients in the pulse sequence influence the actual position in k-space, though k space *data* are only being recorded when the MRI scanner is actually acquiring data during the readout period.

Receiver Bandwidth

The sampling intervals, or spacing of samples in k-space, are controlled distinctively differently in the phase encoding direction and the frequency encoding (readout) direction. In the phase encoding direction, the increments in the area under the phase encode pulses directly determine the spacing of samples in the k_y direction. In the readout direction, the sample spacing in time is ultimately dictated by the sampling frequency of the AD converter in the receiver chain. Once a desired spatial resolution and FOV is determined by the user, the number of data points in image space is established, which is identical to the number of k-space samples needed for each line. In the readout direction, not only the gradient strength but also the sampling rate can be adjusted to achieve the target sampling pattern in k-space. By increasing the amplitude G_x , we traverse faster through k-space. In order to maintain the proper number of samples and the desired distance in k-space, the sampling rate would also need to be increased and the duration of the acquisition window would be decreased. While this acquisition is identical in terms of k space sample points, there are several important implications in choosing the sampling frequency.

To avoid aliasing artifacts and decreased SNR performance due to external signal contributions, the receiver bandwidth has to be adjusted to the chosen sampling frequency, in practice by the operator. Depending on the system, this parameter is chosen either as a total bandwidth, e.g., 125 kHz, or in terms of Hz/pixel, the two being directly related as the product of Hz/pixel times the number of acquired data points (i.e., pixels across the FOV in the

readout direction). Either way, the system automatically adjusts the gradient amplitude and sampling rate accordingly, effectively defining the time between samples (dwell time) while keeping the FOV constant. One of the first and most obvious consequences of increasing the receiver bandwidth is a decrease in the echo time (TE) because the increased gradient strength means that the echo forms faster, i.e., the readout crosses the center of k-space earlier. Shorter echo times are often desirable as they can shorten scan time in rapid imaging as well as decrease artifacts from intravoxel dephasing.

However, there are several other implications of changes in the receiver bandwidth, most importantly in SNR performance and in sensitivity to chemical shift artifacts. By increasing the receiver bandwidth, the readout gradient strength is increased, and thus the range of frequencies being imaged increases. Since noise contributions come equally from all frequency components, as the bandwidth increases, the noise content increases and SNR decreases. By increasing the bandwidth and allowing a wider frequency spectrum to measure the desired signal, more noise is added to the acquisition. The relationship between SNR and bandwidth is $SNR \propto \frac{1}{\sqrt{\text{bandwidth}}}$; so, for example, increasing the bandwidth by a factor of four will decrease the image SNR by a factor of 2.

Additionally, the amount of spatial shifting in the image due to off-resonance (i.e., chemical shift) is inversely proportional to the receiver bandwidth. The common occurrence in clinical MRI of the chemical shift between fat and water illustrates this effect. When imaging at 1.5 T, the dominant fat peak has a frequency offset of about -220 Hz (3.5 ppm) as shown in Fig. 2.9. When imaging with a receiver bandwidth of ± 31.25 kHz and a readout of 256 data points, the bandwidth is 2×31.25 kHz/256 = 244 Hz/pixel, and the corresponding chemical shift for fat is 1.1 pixels (256 Hz/244 Hz/pixel). In this example, fat will appear to be shifted by 1.1 pixels relative to water. Thus, when the receiver bandwidth is decreased, the SNR improves but the chemical shift worsens.

k-Space Sampling Trajectories

The sampling pattern described as spin warp imaging in section “Gradients and k-space” is by far the most commonly used k-space trajectory. In essence, k-space samples collected on a rectilinear checker board pattern with equidistant sampling points along each direction provide a framework where the computationally efficient Fast Fourier Transform (FFT) can be used for image reconstruction [10]. However, many alternative methods for traversing through k-space exist with certain potential advantages and tradeoffs. In the standard method of acquiring MR data, lines in k-space are “rastered” through, i.e., sampled one after another in a manner

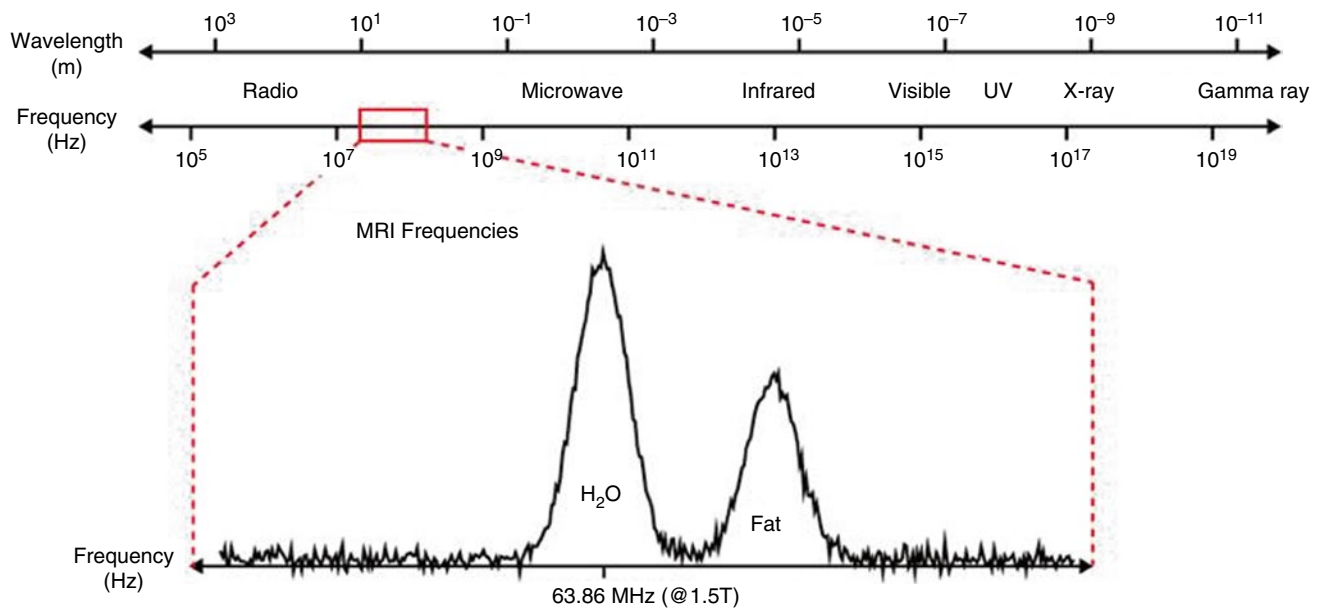


Fig. 2.9 Example of the MR imaging signal frequencies and their place in the entire electromagnetic spectrum. Here in this example, the spectrum is characterized by two peaks representing protons bound to water (on resonance) and fat (chemical shift of 3.5 ppm, corresponding to 220 Hz at 1.5 T)

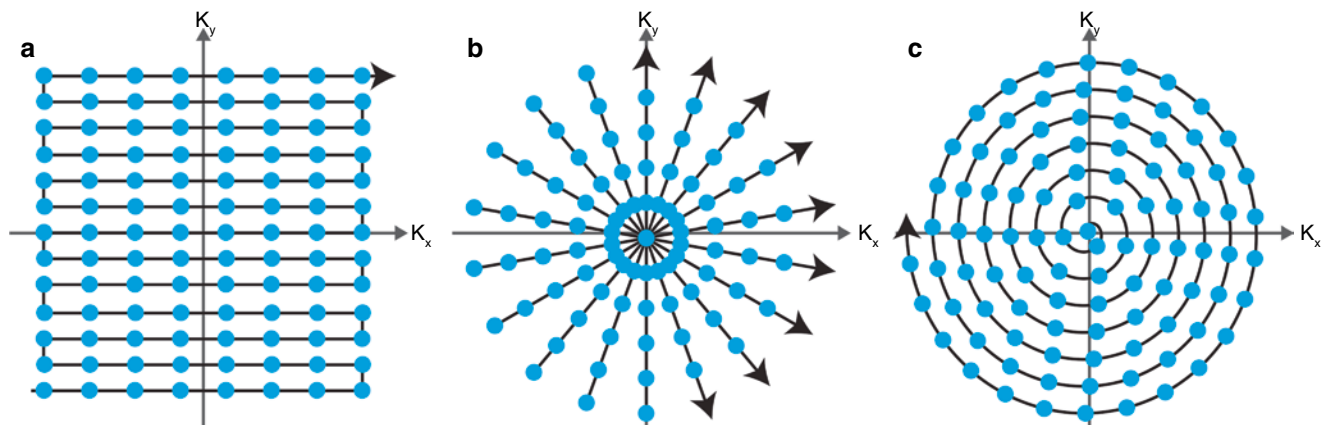


Fig. 2.10 Alternative k-space trajectories. (a) EPI, (b) radial, (c) spiral

reminiscent of cathode ray tube raster display systems, until k-space is fully sampled. Fully sampled, in this case, indicates that enough samples are acquired to reconstruct a full FOV image without aliasing artifact, while providing the desired spatial resolution. By deviating from this standard approach, k-space can be acquired at faster speeds with potential tradeoffs in image quality. The two main pathways for accelerated acquisitions with advanced sampling strategies are: (1) extending the readout duration, so that more k-space data can be sampled for each RF excitation, and (2) using sampling patterns to purposefully undersample k-space in a fashion that the resulting artifacts are acceptable and do not interfere with diagnosis. There are numerous alternative trajectory approaches including radial, spiral, echo-planar

imaging (EPI), PROPELLER, rosettes, cones, all in 2D and 3D, and many more. A complete review of these trajectories is beyond the scope of this chapter and instead, three methods frequently used in cardiovascular MRI will be briefly discussed: echo-planar imaging (EPI), radial, and spiral, which highlight the above two techniques for accelerating k-space acquisition and are shown in Fig. 2.10.

EPI

Echo-planar imaging is one of the most common forms of single-shot pulse sequences and was originally proposed in the very early days of MR imaging [11]. As the name implies,

single-shot imaging aims to acquire all of k-space with a single RF excitation and readout, as seen in Fig. 2.10a. The sequence works via a series of gradient or spin echoes, with ‘blips’ of the phase encode gradient in between to move between successive phase encode lines in k-space. The inherent limitation of EPI, and all single shot acquisitions, is that MRI signal decays rapidly due to various relaxation mechanisms, so the acquisition must be completed before extensive signal decay has occurred. This generally means that single-shot EPI images are of fairly low spatial resolution, but a single 2D image can be acquired extremely rapidly, in the range of 10–100 ms. EPI sequences can also lead to errors and artifacts due to phase inconsistencies such as chemical shift, susceptibility, and off-resonance effects, some of which can manifest inconsistently in the opposing readout directions caused by sampling during both positive and negative readout gradient lobes. These errors are more pronounced because spins are not necessarily being rephased on each readout line, causing some errors to accumulate and progressively worsen throughout the acquisition. The zigzag trajectory can also lead to cumulative trajectory errors that decrease image quality. Contrast in EPI sequences can be modified by using gradient-echo or spin-echo contrast mechanisms, or magnetization preparations such as saturation or inversion recovery. Multi-shot versions of EPI exist, where a smaller segment of k-space lines, i.e., less than required for the entire image, are acquired with each readout. This gives the user control over the trade-off between imaging speed and the resolution limitations/artifacts inherent with EPI.

Radial

Radial k-space trajectories, shown in Fig. 2.10b, are a non-Cartesian method, which means that points are not acquired on a rectilinear grid [12]. In the case of radial imaging, readout lines are designed as ‘spokes’ such that each pass through the center of k-space at different rotation angles. The inherent oversampling of the center of k-space where the spokes are naturally closer together leads to benefits for motion robustness and motion estimation, but also increases the total scan time when a fully sampled data set is desired. However, radial sequences are often accelerated by *undersampling*, which can be tolerable in high contrast imaging such as cardiac applications of balanced SSFP. Unlike fold-over artifact in Cartesian imaging, radial undersampling produces ‘streaking’ artifact, which can be minimal if moderate undersampling factors are chosen. The tradeoffs with radial acquisitions are twofold: the first is that reconstructions take longer because data must be gridded back onto a Cartesian k-space before a Fourier transform can be applied, and the second tradeoff is the increased sensitivity to trajectory errors that have to be carefully corrected for. Since the readout direction

changes with each echo, the center of k-space might be missed slightly due to minimal gradient delays or uncompensated eddy currents. These trajectory deviations add phase errors and blurring to the reconstructed image, though techniques can be used to measure these gradient offsets and compensate for them to mostly eliminate the errors.

Spiral

Spiral acquisitions combine both of the acceleration techniques described above: longer readouts to achieve higher k-space coverage with a single RF excitation, and a non-Cartesian trajectory so that aliasing is more benign [13]. There are various implementations of spiral trajectories but most spiral out from the center of k-space as shown in Fig. 2.10c. Single-shot versions of spiral exist and are used as an alternative to EPI, however multiple interleaved versions of spiral are also common. With multiple interleaves, each spiral starts in the center of k-space, while stepping through angles for each new interleave. Like EPI, spiral imaging is vulnerable to off-resonance effects due to the long TR, and like radial acquisitions it requires a computationally more demanding gridded reconstruction and can suffer from trajectory errors caused by eddy currents and gradient delays that must be accounted for.

References

- Bernstein MA, King KF, Zhou ZJ. Handbook of MRI pulse sequences. Amsterdam: Academic; 2004.
- Liang Z-P, Lauterbur P C, and IEEE Engineering in Medicine and Biology Society. Principles of magnetic resonance imaging: a signal processing perspective. Bellingham/New York: SPIE Optical Engineering Press/IEEE Press, 2000.
- Bracewell RN. The fourier transform and its applications. New York: McGraw-Hill; 2000.
- Hinshaw WS. Spin mapping – application of moving gradients to Nmr. Phys Lett A. 1974;A 48(2):87–8.
- Mezrich R. A perspective on K-space. Radiology. 1995;195:297–315.
- Likes R S. Moving gradient zeugmatography, US patent 430734, USA, 1981.
- Ljunggren S. A simple graphical representation of Fourier-based imaging methods. J Magn Reson. 1983;54:338–43.
- Twieg DB. The k-trajectory formulation of the NMR imaging process with applications in analysis and synthesis of imaging methods. Med Phys. 1983;10:610–21.
- Edelstein WA, Hutchison JM, Johnson G, Redpath T. Spin warp NMR imaging and applications to human whole-body imaging. Phys Med Biol. 1980;25(4):751–6.
- Brigham EO, Brigham EO. The fast Fourier transform and its applications. Englewood Cliffs: Prentice Hall; 1988.
- Mansfield P. Multi-planar image formation using NMR spin echoes. J Phys C Solid State Phys. 1977;10:L55.
- Lai CM, Lauterbur PC. True three-dimensional image reconstruction by nuclear magnetic resonance zeugmatography. Phys Med Biol. 1981;26(5):851–6.
- Meyer CH, Hu BS, Nishimura DG, Macovski A. Fast spiral coronary artery imaging. Magn Reson Med. 1992;28:202–13.

Rohan Dharmakumar, Behzad Sharif,
and Hsin-Jung Yang

Abstract

This chapter begins with a description of key components of a cardiac magnetic resonance (CMR) pulse sequence and then builds on the variations of these components that are commonly used in the field. Specifically, it considers common types of magnetization preparation schemes (T_1 -, T_2 -weighted, inversion recover and saturation recovery preparations, fat suppression and black-blood preparation) and the general class of base imaging schemes (gradient-recalled, spin-echo based, and steady-state methods) and their variations. The various combinations of the components forming different imaging approaches are compared and contrasted with respect to image characteristics (signal-to-noise ratio, contrast and artifacts) as well as acquisition speed and thermal dose.

Keywords

Pulse sequence • Magnetization preparation • Gradient-echo • Multi-gradient echo • Spin-echo • Fast spin echo • Balanced steady-state free precession • T_1 , T_2 , and T_2^*

In this Chapter we provide an overview of CMR pulse sequences. In section “[What is a pulse sequence?](#)” we consider the key features of CMR pulse sequences. In section

“[Common types of magnetization preparation](#)” we describe the commonly used methods to sensitize/prepare the CMR signals to generate desirable image contrast. In section “[General classes of sequences](#)” we explore the general classes of CMR imaging sequences and their variations. Relevant clinical examples will be provided along the way to illustrate the key aspects of the pulse sequences.

R. Dharmakumar, PhD (✉)
Biomedical Imaging Research Institute,
Department of Biomedical Sciences,
Cedars-Sinai Medical Center, Los Angeles, CA, USA

Department of Medicine and Bioengineering,
UCLA, Los Angeles, CA, USA
e-mail: rohandkumar@csmc.edu

B. Sharif, PhD
Biomedical Imaging Research Institute,
Department of Biomedical Sciences,
Cedars-Sinai Medical Center, Los Angeles, CA, USA
e-mail: Behzad.Sharif@cshs.org

H.-J. Yang, MS
Biomedical Imaging Research Institute,
Department of Biomedical Sciences,
Cedars-Sinai Medical Center, Los Angeles, CA, USA

Department of Bioengineering,
UCLA, Los Angeles, CA, USA
e-mail: Hsin-Jung.Yang@cshs.org

What Is a Pulse Sequence?

The pulse sequence is the fundamental operation module that controls the MR scanner in allowing one to capture the desired CMR image. It is a string of tightly timed and ordered operations that deliver various different magnetic fields to excite tissues of interest and spatially encode the signal from excited protons. The excitation is achieved with radiofrequency (RF) pulses (also referred to as the B_1 magnetic field) that are on the resonant frequency determined by the static magnetic field (B_0 magnetic field), and the spatial encoding is achieved with spatially varying (gradient) magnetic fields. When executed

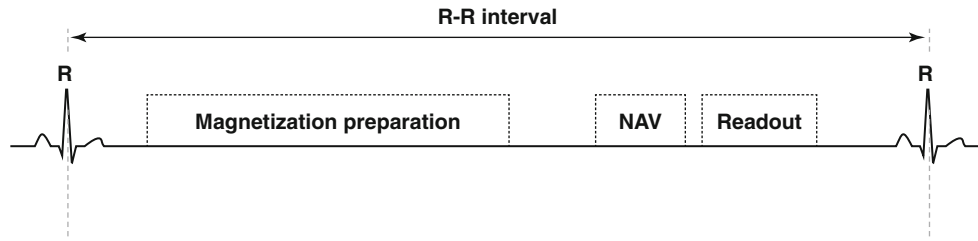


Fig. 3.1 General structure of a CMR pulse sequence. The key components (magnetization preparation, respiratory navigation (*NAV*) and imaging (readout)) are defined within two consecutive R waves (i.e. within an R-R interval). Magnetization preparation may not be present in pulse sequences that generate image contrast from the imaging

(i.e., Readout) block. Similarly, the NAV block is typically not present when imaging is performed with voluntary suspension of breathing. While the typical order of the blocks is as drawn, the duration and exact position of the blocks within the R-R interval can vary greatly between sequences

together, these operations control the imaging resolution, speed/temporal resolution of acquisition, and image contrast (contrast-to-noise ratio, CNR) and signal-to-noise ratio (SNR). The type of MR pulse sequence is determined on the basis of the nature of images one wishes to generate (2D, 3D, cine, etc.) within the constraints of acceptable acquisition time. The general structure of a CMR pulse sequence is shown in Fig. 3.1 and the various components of the sequence are elaborated in the following paragraphs.

One of the distinguishing features of CMR acquisitions, compared to imaging other organ systems, is that the acquisitions are typically timed relative to the electrocardiographic (ECG) signal within the nominal period between consecutive R waves referred to as the *R-R interval*. This permits data acquisition to take place at specific time frames within the cardiac cycle, which allows one to capture cardiac phase-dependent features in an image, as well as minimize imaging artifacts (such as, blurring or flow artifacts) from cardiac motion. For instance, cine acquisitions are captured over multiple frames by limiting the data acquisition period to approximately 50 ms or less depending on heart rate. On the other hand, most other (non-cine) CMR acquisitions take place during quiescent periods (typically, mid diastole), where data can be collected over a relatively long period of time (~200 ms) without motion artifacts.

Another important feature of CMR acquisition is that it must account for respiratory motion, which otherwise can also lead to significant image artifacts. The most common approach used to overcome respiratory motion is voluntary suspension of breathing for 10–15 s (breath-holding). In cases where subjects cannot suspend breathing over the acquisition period, particularly in acquisitions that are in excess of 10–15 s (e.g., 3D imaging), other forms of motion compensation are used. Of these approaches, navigator gating is the most common. Here a quick excitation (<30 ms) is applied in a direction perpendicular to the diaphragm and an echo is acquired, reconstructed, and analyzed to determine diaphragm position to estimate respiratory motion. Following image data acquisition, the data that falls within a pre-determined window of diaphragm motion, typically <5 mm, is

accepted and used for reconstructing the CMR image. Naturally this process can reduce the time-efficiency of acquisition, particularly if the subject's breathing pattern is highly variable, since sufficient data needs to be collected to reconstruct an artifact-free image.

RF excitations can be applied to “bias” the magnetization (signal) to different biophysical environments. These excitations are often referred to as *magnetization preparation* and typically precede the different imaging schemes. Common magnetization preparation schemes are explored in detail in section “[Common types of magnetization preparation](#)”. While magnetization preparation is a common and efficient means of sensitizing the protons to generate a desired image contrast, it is to be noted that it is not always necessary to have a separate magnetization preparation component to generate image contrast. In fact, the desired image contrast may be available through optimal scan parameter selection from sequences in which the magnetization preparation is effectively integrated into the imaging sequence itself. The general classes of imaging sequences will be described in section “[General classes of sequences](#)”. In general, the utilization of an isolated magnetization preparation scheme prior to imaging is often based on the need to optimize image contrast (CNR), image quality (SNR, spatial resolution, image artifacts), acquisition speed, and specific-absorption rate (SAR).

Common Types of Magnetization Preparation

In this Section we explore the most commonly used magnetization preparation schemes in CMR. In particular, we will look at T_1 - and T_2 -weighted preparations and then consider fat suppression and black-blood preparation.

T_1 -Weighted Preparations

The goal of T_1 -weighted preparation is to evaluate potential T_1 differences within and between tissues; these can be

prescribed as an *inversion-recovery* scheme or *saturation recovery* scheme. In the inversion-recovery (IR) approach, the equilibrium magnetization (M_0) is inverted by a 180° RF pulse which is immediately followed by large gradient pulses designed to spoil any residual transverse magnetization that may have been generated by imperfections in the inversion process. Then, following a waiting period of TI, also referred to as the *inversion time*, one or more k-space data lines are acquired using any of a variety of sequence types (e.g., spoiled gradient echo, balanced SSFP, or fast spin echo). During TI, the inverted longitudinal magnetization ($-M_0$) recovers towards equilibrium, with the rate of recovery determined by T_1 . The recovery of the excited spins back to equilibrium will be differentially altered by the T_1 distribution in specific tissues. For instance, the T_1 of myocardial tissue could be altered by the presence of heterogeneous tissue (healthy myocardium, fat, fibrotic tissue, or elevated free water (edema)), or by the variable distribution of T_1 -shortening exogenous contrast media. If the TI is selected to coincide with the time that the longitudinal magnetization for tissue of a specific T_1 is crossing zero, the tissue is effectively “nulled” and will appear black in the image. This approach is commonly exploited in late-gadolinium-enhanced (LGE) CMR to visualize and quantify infarcted myocardium by selectively nulling the non-infarcted myocardium (Fig. 3.2). This is possible because the infarcted myocardium tends to have a greater concentration of contrast agent (due to reduced contrast clearance), and therefore a shorter T_1 , than viable tissue.

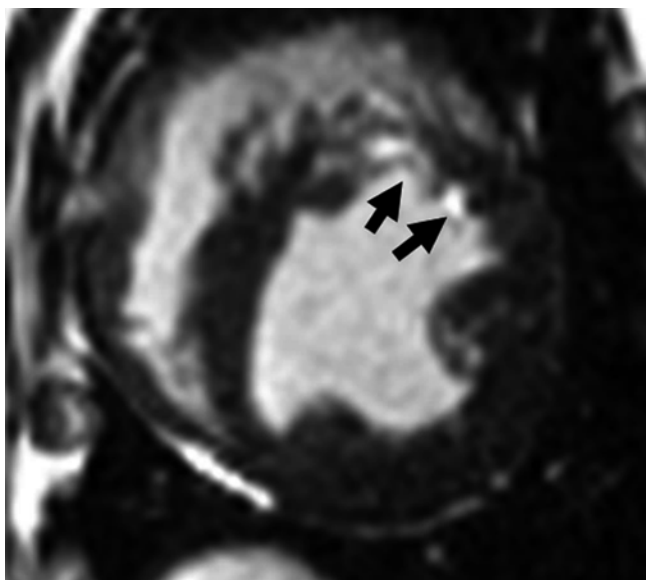


Fig. 3.2 Application of inversion-recovery preparation for imaging infarcted myocardium. Late gadolinium enhanced image obtained with IR-preparation with balanced steady-state free precession readout at TI of 330 ms is shown. The IR-preparation “nulls” the healthy myocardium while ensuring the infarcted myocardium (i.e., regions with higher concentration of T_1 -shortening agent (such as gadolinium chelate) indicated by *arrows*) appears bright

In the saturation recovery (SR) preparation, the equilibrium longitudinal magnetization is completely tipped into the transverse plane by a 90° RF pulse and is dephased (disordered) in the transverse plane by a magnetic field gradient (“spoiler” or “crusher” gradient) to annihilate the transverse magnetization. After a time delay of TI (in this case, a “saturation delay” although it is still often denoted as “TI”), one or more lines of k-space data are acquired. During TI, the magnetization recovers toward the equilibrium at a rate dependent on T_1 .

While both IR and SR preparations can be used to generate T_1 image contrast, there are some practical differences. In general, IR preparations provide nearly a twofold greater image contrast between tissues of different T_1 since the signal recovery following IR preparation spans the full range of $-M_0$ to $+M_0$, whereas following SR preparation the signal varies only over the range of zero to $+M_0$. A key difference between the two preparations is that the signal following an IR prep is dependent on the pre-existing longitudinal magnetization; that is, if the magnetization has not fully recovered from the last preparation or excitation pulses, this will affect the magnitude of longitudinal magnetization that is inverted, and thereby the inversion recovery signal trajectory. On the other hand, the SR prep destroys any existing longitudinal magnetization and starts the recovery from zero regardless of the past history of the magnetization. Because there is no need to wait for recovery of longitudinal magnetization, the recovery period between consecutive SR preparation modules can be kept relatively short, and SR-prepared acquisitions therefore tend to be faster as compared to IR-prepared acquisitions. Nonetheless, both methods can be used to generate a pixelwise map of the T_1 of the myocardium and other tissues in a process known as “ T_1 -mapping.” This is typically accomplished by acquiring images across a range of TI times and then fitting the signal from each voxel to a mono-exponential equation, the time constant of which is T_1 .

T_2 -Weighted Preparations

T_2 -weighted preparations are used to enhance the differences within myocardium that emerge from localized changes in free-water content (edema), blood oxygenation, or intramyocardial hemorrhage, among other factors. One of the most commonly used T_2 -weighted preparation schemes involves a composite set of RF pulses that are non-selective (i.e., all spins within the volume of the RF transmitter coil are excited by each of the RF pulses). This scheme, commonly referred to as T_2 preparation, involves the formation of one or more spin echoes and is designed to impart T_2 weighting on the longitudinal magnetization. It can be described as follows: first the longitudinal magnetization is tipped into the transverse plane with a 90° RF pulse and then

allowed to evolve in the transverse plane for a time, τ . During this period, the magnetization dephases at a rate dependent on the T_2^* of the tissue (i.e., with some spins precessing faster than others due to static local differences in magnetic field, as well as due to random spin-spin interactions). At time τ , a 180° pulse is applied which flips the transverse plane and effectively reverses the direction of phase evolution, leading to a coherent signal (echo) at time 2τ after the initial 90° RF pulse (which is also a time of τ after the 180° RF pulse). This echo is referred to as a *spin echo* and will be described in greater detail in section “[Spin-echo sequences](#)”. Subsequently, the magnetization, now weighted by T_2 decay rather than T_2^* , is rotated back to the longitudinal axis and any remaining transverse magnetization is spoiled before imaging. In practice, additional 180° pulses are typically incorporated to minimize refocusing errors due to blood flow and inhomogeneities in the B_0 and B_1 fields. The total duration between the first and second 90° RF pulses is referred to as the *T_2 -preparation period, or T_2 -prep time*. The longer the T_2 -prep time, the greater is the contrast between regions of myocardium with different T_2 values. In practice, the longest practical T_2 -prep time is typically under 60 ms at 1.5T, and shorter at 3.0T (<50 ms); beyond these times the overall signal loss due to T_2 decay can significantly degrade image quality. Among the variety of applications, T_2 preparation has been used to examine myocardial edema in acute myocardial infarction (Fig. 3.3a) and changes in myocardial blood oxygenation in the setting of coronary narrowing with-

out exogenous contrast agents (Fig. 3.3b). Using this approach iteratively (i.e., by acquiring a series of images with different T_2 -prep times) it is possible to generate a T_2 map of the myocardium. Fitting the signal intensities of the individual voxels at different T_2 -prep times to a mono-exponential decay curve, the time constant of which is T_2 , permits one to generate a T_2 map, i.e., an image in which the pixel values are equal to T_2 .

Fat Suppression

At times, signal from adipose tissue can confound image interpretation. To minimize this, it is often desirable to suppress adipose tissue, for example, to enable accurate visualization of coronary arteries or characterize myocardial tissue. For instance in post-contrast T_1 -weighted images, epicardial fat can appear bright which can confound the visualization of infarcted myocardium, especially when the infarction is transmural. In this scenario, suppressing the fat signal could reduce ambiguity regarding the presence and extent of infarcted myocardium. In other situations it may be useful to acquire images with and without fat suppression to aid in determination of whether a particular lesion is comprised of fat. Fat suppression, i.e., reducing or eliminating the signal from fat, may be performed in a number of different ways with each method carrying with it advantages and disadvantages. In this Section we will describe two of the most

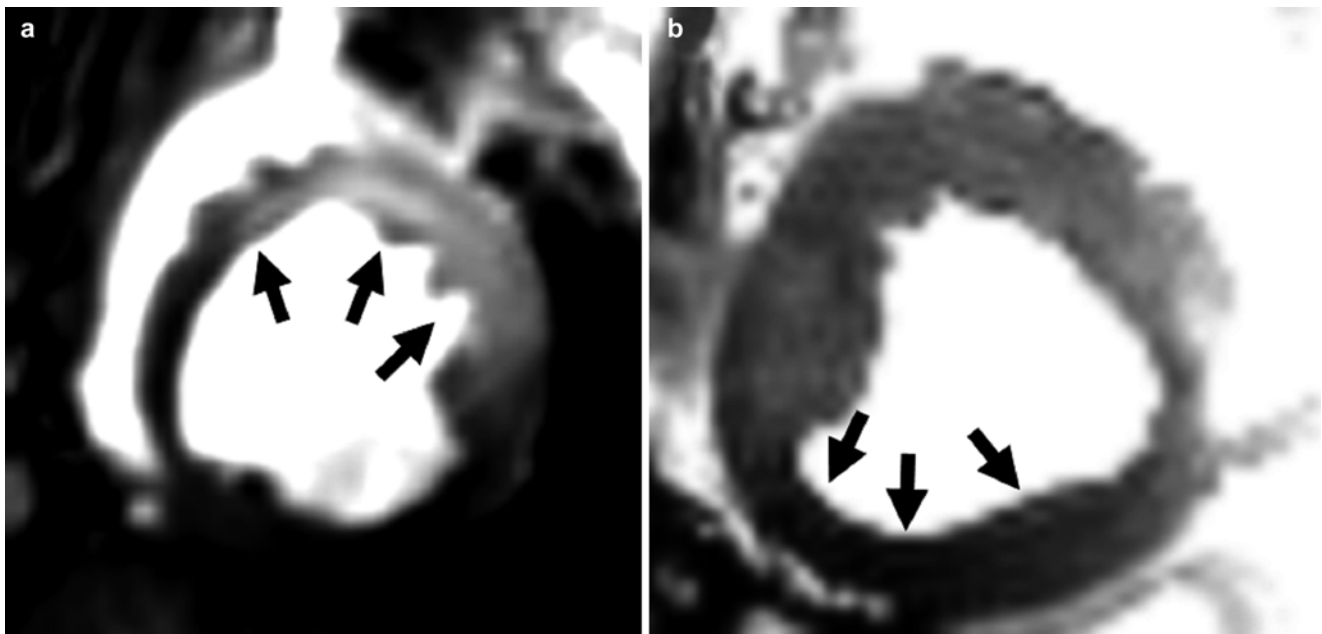


Fig. 3.3 Application of T_2 -preparation for imaging myocardial edema (a) and oxygenation (b). (a) T_2 -preparation is used to highlight the myocardial territory with increased T_2 (arrows) due to edema from acute myocardial infarction. (b) T_2 -preparation is used to highlight the

absence of increase in T_2 (blood oxygenation) during adenosine infusion from myocardial territories subtended by a stenotic epicardial coronary artery relative to healthy myocardium

commonly used preparations, namely, frequency-selective (FS) fat saturation, and short TI inversion recovery (STIR) preparation.

The FS preparation exploits the frequency difference between fat and water protons (-220 Hz at 1.5T and -440 Hz at 3T) to saturate the fat signal. Here an RF pulse with a resonance frequency centered on that of fat is used to saturate the signal from fat. That is, in similar fashion to SR described in section “**T₁-weighted preparations**”, a 90° RF pulse is used to selectively tip the magnetization of lipid protons into the transverse plane, followed by a spoiler gradient to dephase the transverse magnetization. The advantage of this method is that it is frequency selective and therefore only affects the lipid protons resonating at their unique frequency, while not affecting water protons. Thus, FS preparation is a good method for suppressing fat signals when T_1 shortening contrast agents are used, since the T_1 of fat (200–300 ms) and that of regions with high concentration of gadolinium (e.g., infarcted myocardium) can be similar. However, good suppression of fat signal with this technique requires fairly homogeneous B_0 field. If significant field inhomogeneities exist, frequency-selective saturation may not be effective since the RF pulse will only partially saturate the fat, or in the worst case may saturate the water protons instead; this leads to an overall reduction in SNR. Unfortunately, significant B_0 field inhomogeneities in and around the heart are not uncommon, especially at 3.0T, due to the large susceptibility gradients that exists at the heart-lung interface, or due to the presence of sternal wires, stents, or other metallic implants that have very different magnetic susceptibility from that of the heart. An example of FS applied to late-gadolinium imaging is shown in Fig. 3.4a.

Another approach to fat suppression is the Short-Tau Inversion Recovery, or STIR preparation, which exploits the difference in T_1 between fat and water-based tissues to suppress the fat signal. Here, a 180° IR preparation (as in section “**T₁-weighted preparations**”) is used to invert the magnetization of both fat and water, using a short TI (approximately 150 ms at 1.5T) specifically chosen to null the fat signal. By acquiring image data near the null point of fat, an appreciable signal from the protons in water-based tissues is realized while the signal from fat protons is effectively reduced to zero. The STIR preparation is not as dependent as FS on B_0 homogeneity, and is therefore the preferred method when field inhomogeneities are a problem. Because tissues with long T_1 tend to also have long T_2 , e.g., edematous myocardium, the STIR preparation also effectively enhances T_2 contrast by suppressing tissues with shorter T_1 ; hence the STIR technique has been useful for myocardial edema imaging. However, since the STIR preparation will reduce signal from any tissue with shorter T_1 , including water-based tissues, it can limit overall image SNR. Another disadvantage of this method is that it is generally ineffective following contrast injection, since the post-contrast T_1 of water-based tissues may become similar to fat. An example of STIR preparation for myocardial edema imaging is shown in Fig. 3.4b.

Black-Blood Preparation

In this preparation, the signal from flowing blood is nulled by a unique inversion recovery strategy, and hence blood appears dark. This is accomplished using a so-called “double IR” strategy in which a *non-selective* 180° inversion pulse is

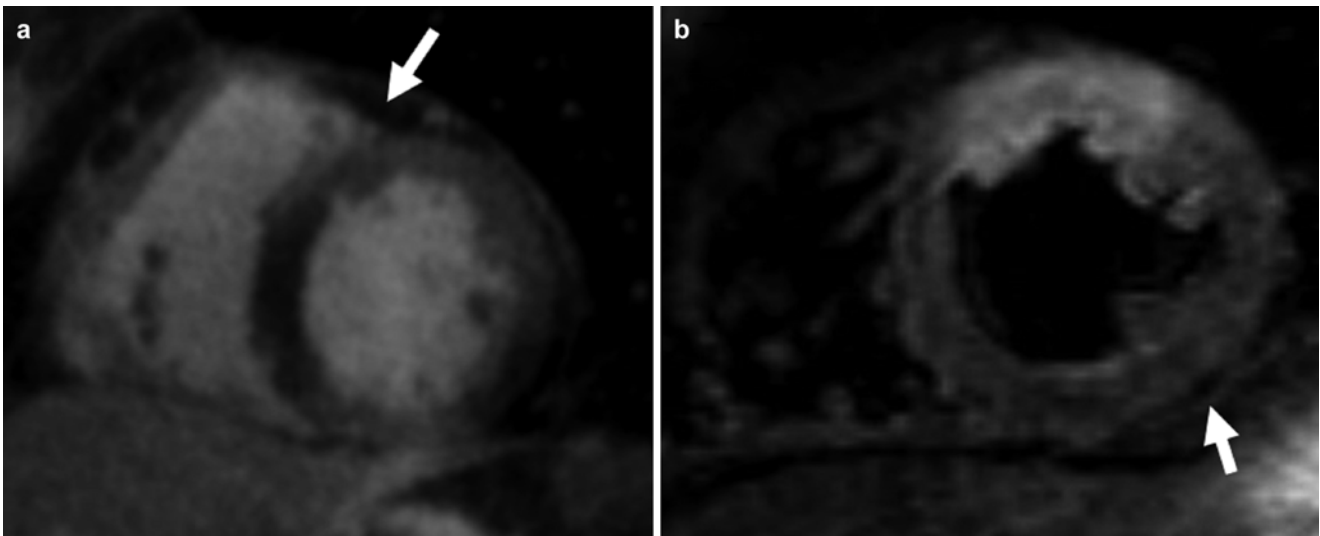


Fig. 3.4 Suppressing fat with frequency-selective preparation (a) and STIR preparation (b) at 1.5T. (a) Frequency-selective preparation is used to suppress the signal from epicardial fat (white arrow) as part of

a coronary artery imaging protocol. (b) Selective nulling of signal from fat protons using the STIR preparation with a $TI=170$ ms. Note the suppression of epicardial fat relative to the myocardium (arrow)

immediately followed by a *slice-selective* 180° RF inversion pulse that effectively rotates the spins within the image slice back up to the equilibrium position, i.e., $+M_0$, leaving all of the magnetization *outside* the slice inverted at $-M_0$. More specifically, (a) the first inversion pulse inverts all the spins within the body coil since it is non-selective; (b) the second slice-selective inversion pulse affects *only* those spins within the slice of interest, effectively rotating those spins back up to the equilibrium position, i.e., $+M_0$, leaving all of the magnetization *outside* the slice inverted at $-M_0$; and (c) a long TI period precedes image data acquisition to ensure that inverted blood has time to flow into the imaging slice, and that data are collected when the signal of inflowing blood is at its null point following the first (non-selective) inversion pulse. Commencement of imaging at this point will ensure that moving blood appears “black” while other structures that remained within the imaged slice have signal. An example of a black-blood prepared image is shown in Fig. 3.5. This approach can be combined with other preparation modules, such as STIR, to additionally suppress fat. In general, black-blood preparation is commonly employed to preferentially visualize the blood vessel walls, cardiac chambers, and the myocardium without any contribution from blood. While the advantages of black-blood preparation are widely recognized for visualizing anatomical structures, there are some limitations, foremost of which is the requirement that the



Fig. 3.5 Application of black-blood preparation for anatomic imaging. Short-axis image obtained with dark-blood prepared gradient-echo acquisition is shown. Note that the cardiac chambers (RV and LV) containing blood appear *black* due to selective nulling of moving blood, which otherwise would appear *bright* (refer to Fig. 3.3)

blood flow is sufficiently fast so that inverted blood moves into the slice of interest before the start of imaging. In black-blood prepared images, slow moving or stagnant blood can have high signal and may artifactually appear to be an extension of anatomical structures. Rapidly moving myocardium can also be problematic, as inverted myocardium may enter the imaged slice causing an artifactual reduction in myocardial signal.

General Classes of Sequences

In this Section, we will examine imaging pulse sequences that are commonly used in CMR as the “Readout” block illustrated in Fig. 3.1. First, we will review the basic structure of imaging sequences and key parameters in section “[Basic structure of imaging pulse sequences](#)”. Next, in section “[Gradient echo sequences](#)”, we will describe gradient-recalled echo (GRE) sequences starting with the basic gradient echo sequence, extending to the multi-gradient echo (mGRE) sequence, and concluding with the fast incoherent steady-state imaging sequence, also referred to as spoiled gradient echo. In section “[Spin echo sequences](#)”, we will review spin echo sequences, beginning with the simple spin echo (SE) sequence followed by the fast spin-echo (FSE) sequence. Finally, in section “[Balanced steady-state free precession](#)”, we will review the coherent steady-state sequence, referred to as balanced steady-state free precession (bSSFP).

Basic Structure of Imaging Pulse Sequences

CMR data acquisition for 2D or 3D imaging involves RF excitation of a prescribed slice or slab that includes the region or tissue of interest. In response to RF excitation, all of the tissue inside the excited slice/slab emits a signal referred to as an “echo.” Spatial localization of the echo signal is achieved using magnetic field gradients, which encode the spatial information into the phase and frequency of the echo signal. In general, acquisition of an MR image requires a series of RF and gradient pulses in combination with data acquisition periods that are synchronized to the timing of the echo signals; this is collectively referred to as a *pulse sequence*. It is often designed to provide the specific image contrast needed for a particular CMR application. For instance, the pulse sequence applied for edema imaging (Fig. 3.3a) is very different from the pulse sequence used to assess myocardial perfusion (described later in Fig. 3.9). The most commonly used CMR pulse sequences can be categorized as “gradient echo” and “spin echo”. Gradient echo sequences employ magnetic field gradients to produce an echo, whereas spin echo sequences use RF pulses to produce an echo.

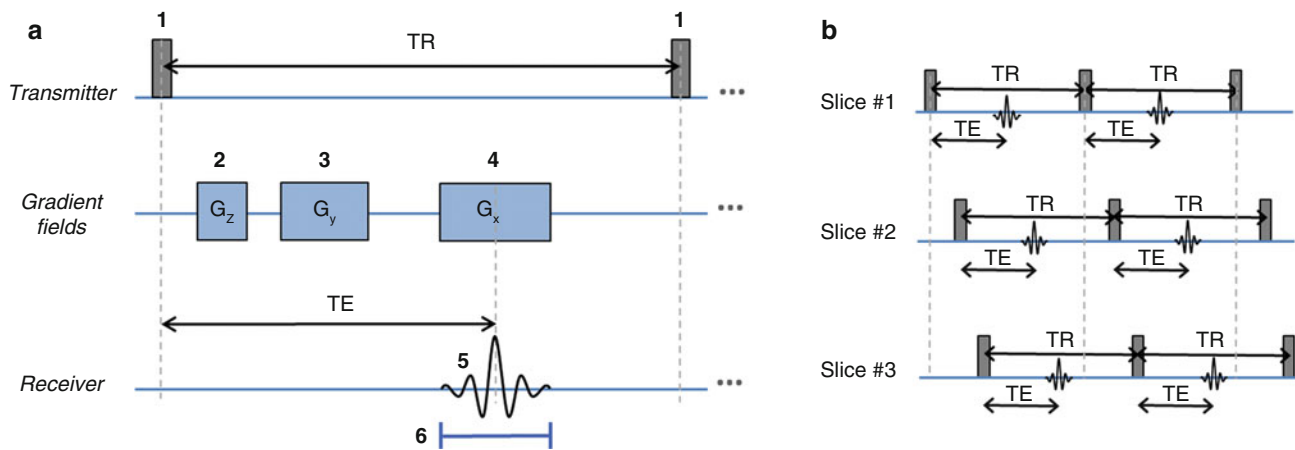


Fig. 3.6 Structure of a general pulse sequence. (a) Simple single-slice imaging; (b) multi-slice imaging. (a) the general structure of an MRI pulse sequence consisting of six components including: (1) transmitted RF pulses, (2) slice/slab-selection gradient (G_z), (3) phase encoding gradient (G_y), (4) frequency encoding gradient (G_x), (5) MR echo

Figure 3.6a shows a schematic of the structure of a simple pulse sequence illustrating a general implementation of the following six steps performed by the MR scanner hardware in chronological order from left to right:

1. Transmission of the slice/slab selective excitation RF pulse with a predetermined flip angle (α);
2. Switching of the slice/slab-selection magnetic field gradient, denoted by G_z ;
3. Phase-encoding gradient, denoted by G_y , which enables localization of the signal along y ;
4. Formation of the MR echo signal (either gradient echo or spin echo);
5. Frequency encoding gradient, denoted by G_x , which enables localization of the signal along x ;
6. Signal acquisition, which involves digital sampling of the detected echo signal.

The total time it takes to execute a single repetition of the above steps is referred to as the *repetition time*, denoted by TR. The *echo time*, denoted by TE, is defined as the time period between the RF pulse in step 1, and the peak of the echo signal in step 4. Each TR may be a few milliseconds (as short as 2 or 3 ms in certain CMR applications); however, a typical MRI scan includes tens or hundreds of TRs. The phase-encoding gradient varies across consecutive repetitions to create the desired number of shifts between the data readouts in k -space. In addition to the number of phase encodes required to cover the entire k -space (determined by the prescribed spatial resolution and field-of-view), the number of TRs in a CMR scan depends on multiple factors including: the prescribed temporal resolution (number of cardiac phases), the prescribed spatial coverage (number of slices), and the desired image quality

signal, (6) data acquisition period. (b) The general principle behind improving scanning efficiency through multi-slice imaging by using the long “wasted time” between consecutive RF pulses to excite and acquire data from other slices without adding to the TR

(e.g., the number of averages needed to achieve the requisite SNR at a given spatial resolution or CNR).

Most CMR applications acquire only a single 2D slice or 3D slab at a time; for example, cine imaging using the bSSFP sequence (section “[Balanced steady-state free precession](#)”) acquires a single 2D slice synchronized with the ECG signal and produces cardiac phase-resolved images for assessment of myocardial function. While multi-slice acquisitions as depicted in Fig. 3.6b are used routinely to image other organ systems, the constraints imposed by ECG synchronization and the need to typically complete data acquisition within a breath-hold have rendered this approach generally ineffective for CMR.

Gradient Echo Sequences

Gradient-Echo (also known as Gradient-Recalled Echo, or GRE) sequences are a commonly used class of imaging sequences in CMR. In this approach, after the RF excitation, a spatial magnetic gradient is used to first dephase and then refocus the magnetization to generate an echo signal which is digitally sampled. One of the key features of GRE imaging is that it typically employs small flip angles to excite the tissues ($\alpha < 90^\circ$), which permits the following: (a) very short TR ($\sim 2\text{--}50$ ms) since minimal time is needed for T_1 recovery between RF excitations; (b) enough transverse magnetization for imaging with minimal disturbance of the longitudinal magnetization; and (c) low SAR, even at higher field imaging (e.g. 3T). These advantages over other imaging methods make GRE imaging highly suitable for CMR, and it is used routinely in applications such as contrast-enhanced angiography, first-pass perfusion, late gadolinium enhancement, and phase velocity mapping. Nonetheless, the SNR of

GRE sequences can be limited by the combination of short TR and low flip angle. In this Section, we will first review the basic structure of a simple GRE sequence. We will then describe the multi-echo GRE sequence and conclude with the spoiled GRE sequence.

Basic Gradient-Recalled Echo

In a gradient-echo pulse sequence, also known as GRE or fast-field echo (FFE), a single RF excitation pulse is applied to the object being imaged during each TR period as illustrated in Fig. 3.7a. Concurrently, a slice- or slab-selective gradient is applied along G_z . Subsequently, a phase-encoding gradient and simultaneously a dephasing/pre-winder frequency-encoding gradient (with negative polarity) are applied along G_y and G_x , respectively. Note that the gradient directions (z = slice select, y = phase encode, x = frequency encode) are by convention only and do not correspond to the physical directions of the applied gradients; that will depend on the slice orientation and in-plane rotation of the field-of-view. Finally, this active/intentional dephasing is compensated by applying a rephasing/refocusing frequency-encoding gradient (with positive polarity) to generate a rephased signal (echo). The term *gradient echo* refers to this rephased signal that appears at the center of the acquisition period as shown

in Fig. 3.7a. The timing of the echo peak, i.e., TE, coincides with the moment that the area of the dephasing gradient (highlighted in gray in Fig. 3.7a) is compensated by the area of the rephasing gradient with the opposite polarity. The MR data is acquired during the readout of the entire echo signal.

As described in Fig. 3.7, TE as used in the context of GRE sequences is the interval between RF excitation and the center (peak) of the gradient echo. Among other factors, the image contrast in GRE acquisitions depends on the value of TE. Specifically, since the transverse magnetization is subject to T_2^* decay/dephasing during the generation of the echo signal, tissue with short T_2^* (relative to TE) will show a very low signal intensity and, tissue with longer T_2^* will have a relatively higher signal intensity. The degree of this T_2^* -weighting for the image contrast depends on TE: longer TEs accentuate the T_2^* contrast, which for example can be used to detect intra-myocardial hemorrhage or myocardial iron overloading. To minimize the T_2^* contrast, the shortest possible TE should be prescribed, which can be as short as 1–2 ms. On the other hand, GRE acquisitions often use very short TR values (as short as 2–3 ms), which implies that the image contrast also includes T_1 -weighting. That is, tissue with short T_1 appear brighter compared with tissue with longer T_1 . In addition to TR, the degree of the T_1 -weighting also

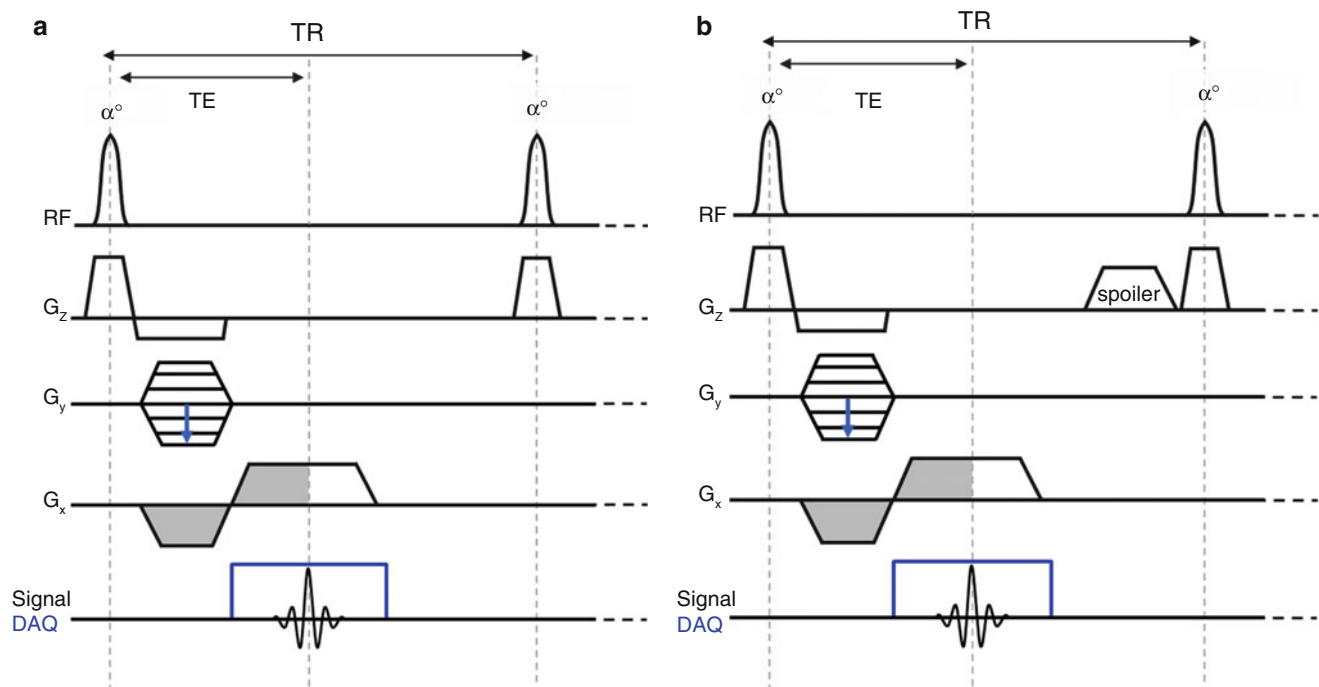


Fig. 3.7 Schematic for gradient-echo imaging sequences. (a) Simple gradient-recalled echo (GRE) sequence: after the excitation pulse, a phase-encoding gradient (varies in each repetition to encode different k -space lines along k_y) and simultaneously a dephasing/pre-winder frequency-encoding gradient are applied. The frequency-encoding gradient with negative polarity destroys the phase coherence of the spins, referred to as dephasing. To form the gradient echo, this

dephasing is compensated (i.e., spins are rephased) by applying a rephasing/refocusing gradient with positive polarity along the frequency-encode direction during the signal readout. (b) Spoiled gradient-recalled acquisition in the steady state (SPGR) sequence: GRE with low flip-angle excitation and spoiling of transverse magnetization after acquisition of a single phase encode; it is also referred to as *FLASH*, fast low-angle shot

depends on the flip angle. The flip angles typically used in GRE sequences range from $\sim 10^\circ$ – 40° , with the higher flip angles resulting in more T_1 weighting.

The key features of GRE imaging are summarized below:

- T_2^* decay – the magnitude of the echo formed by the reversal of the frequency encoding gradient is smaller than the signal in the transverse plane immediately after the excitation RF pulse because gradient dephasing cannot recover dephasing of spins from field inhomogeneities, susceptibility artifacts (heart-lung interface, metal clips etc), imperfections in B_0 field, phase variations among spins within an imaging voxel, and spin-spin relaxation (T_2). For this reason, to ensure adequate image quality TE is typically kept as short as possible, and generally less than 5 ms, depending on the application.
- *k-space filling* – only one k-space line is filled per TR and this process must be repeated the same number of times as the number of predetermined phase-encoding lines. However, this is typically accomplished quickly (compared to spin-echo imaging, section “[Spin echo sequences](#)”, since TR of GRE acquisitions are significantly shorter, typically on the order of 1–2 ms).
- SNR – GRE images tend to have modest SNR compared to spin-echo (section “[Spin echo sequences](#)”) or bSSFP (section “[Balanced steady-state free precession](#)”).
- *Multi-contrast imaging* – GRE image contrast can be adjusted with appropriate choice of TE, flip angle and TR. At longer TE (15–25 ms) and at low flip angles (5 – 10°) with TR long enough for full recovery, GRE images are T_2^* weighted. Under similar condition, except at shorter TEs (i.e. <3 – 5 ms), GRE images are proton density weighted. For short TEs (<3 – 5 ms), and large flip angles (~ 10 – 40°), at short TR (<50 ms), GRE images are T_1 weighted. Since GRE imaging cannot recover the signal lost from static field inhomogeneities, it cannot be used to generate T_2 weighting (refer to section “[Spin echo sequences](#)”).
- *Acquisition time* – is highly compatible with fast imaging since TR is relatively short.
- SAR – sequence typically has low SAR due to relatively small flip angles. The sequence can be SAR limited in some T_1 -weighted applications, however, depending on the choice of imaging parameters.
- T_2^* mapping – by collecting a set of images at different TEs and fitting the pixel intensities at the different TEs to a mono-exponential decay curve, it is possible to generate a pixelwise T_2^* map.

Multi-gradient Recalled Echo

GRE sequences can be extended to acquire multiple echoes in each repetition, i.e., having more than a single readout per TR period. The sequence diagram for such multi-

gradient-recalled echo (mGRE) pulse sequence is similar to the basic GRE sequence but with two or more repeat reversals of the frequency-encoding gradient, instead of just a single reversal as depicted in Fig. 3.7a. Following the first echo at $t=TE$, the second half of the positive gradient of the frequency-encoding gradient dephases the signal and the first half of the negative gradient lobe rephases the gradient to form a second echo. This process is repeated multiple times to generate multiple echoes, with the dephase/rephase gradient lobes for odd (3rd, 5th, 7th, etc.) echoes following the structure of the first echo, and the even (4th, 6th, etc.) echoes following the structure of the second echo. While this process can be repeated multiple times, in practice T_2^* decay will limit the duration of the echo train. In addition, the number of echoes that can be formed within the limits of T_2^* signal losses is limited by the rate at which the dephasing and rephasing gradients can be switched.

In CMR, mGRE sequences are used to rapidly acquire a set of images with different TEs, and therefore different T_2^* weightings. An important application of the multi-echo GRE sequence is “ T_2^* mapping” of the myocardium for assessment of iron overload; examples are shown in Fig. 3.8.

By separately phase encoding each echo to acquire a different line of k-space data, the mGRE sequence can also be used to accelerate data acquisition for ultrafast imaging. The classical single-shot echo planar imaging (EPI) sequence is an example of a single-shot GRE sequence in which a single RF excitation is applied and the entire k-space is traversed (i.e., all rows of the k-space matrix are filled) using multiple phase-encoded gradient echoes. While single-shot EPI is not

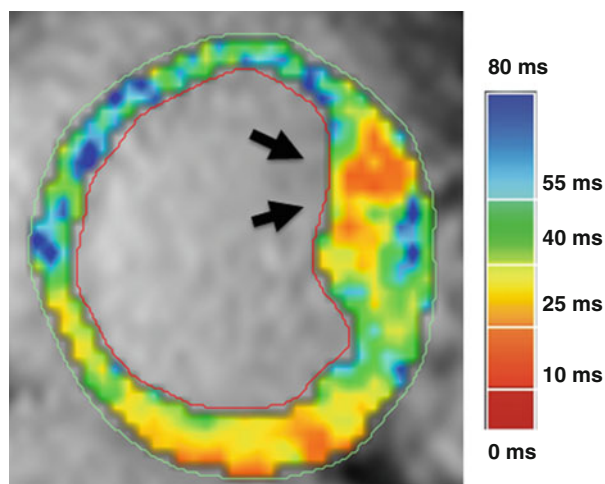


Fig. 3.8 Application of the mGRE approach for imaging regional chronic iron deposition following hemorrhagic myocardial infarction. By combining the information from multiple echoes, a T_2^* map is formed which enables assessment of iron overloading in the myocardium. As here for T_2^* map, all CMR maps (including T_1 and T_2) are typically color coded (with color bar provided) for ease of visualizing the exact value of the mapped pixel

commonly applied in CMR because it is very sensitive to field inhomogeneity, segmented EPI (sometimes called hybrid GRE-EPI) has found utility as a rapid readout strategy for first-pass perfusion imaging.

Fast Spoiled Gradient Echo

One of the assumptions of simple GRE and mGRE as described above is that the signal decays to zero between RF excitations. If $TR \ll T_2$, the transverse magnetization can persist for a longer period of time and can mix with the longitudinal magnetization on subsequent echoes. If the residual signal (transverse magnetization) from previous repetitions propagates and contributes to subsequent echoes, they may affect the desired image contrast or result in image artifacts. This residual MR signal must be eliminated, or “spoiled”, when T_1 -weighted imaging is desired. With spoiling, after a few RF excitations the signal will reach steady state, which is a balance between excitation and longitudinal magnetization. In other words, the longitudinal magnetization from one TR to the next will be equal. In this scenario, this signal will be a maximum at a flip angle, known as the Ernst angle (α_E), which is determined by the TR and T_1 of tissue. For flip angles lower than α_E , the steady state signal will have a greater proton density weighting; for flip angles greater than α_E , the steady-state signal will have greater T_1 weighting.

The spoiling of the residual signal can be accomplished by a spoiler gradient, which can be applied on the G_z (slice select) gradient direction to dephase the spins before the next repetition. As an alternative to spoiler gradients, the phase of the RF excitation pulse may be varied with every repetition to prevent the coherent accumulation of a steady state signal from residual transverse magnetization. The latter approach is referred to as RF spoiling and is accomplished by specially designed RF phase-increment schemes, which can be combined with a gradient spoiler. Figure 3.7b depicts the sequence diagram for the most commonly used spoiled GRE sequence in clinical settings, called the SPGR (spoiled gradient-recalled acquisition in the steady state) or FLASH (fast low-angle shot) sequence. The SPGR sequence is essentially a special case of a rapid GRE sequence with low flip angle excitation and spoiling of transverse magnetization after the acquisition of each phase-encode line, i.e., after each echo.

SPGR sequences include T_2^* weighting, which increases with TE but is negligible for very short TEs (section “Basic gradient-recalled echo”). The T_1 contrast of SPGR sequences can be manipulated by adjusting TR and α as follows: T_1 weighting increases as TR decreases, and/or as α increases. Therefore, T_1 weighting is minimized, i.e., images are effectively proton-density weighted, when TR is long (>100 ms) or a very low α is used (<5°), both in conjunction with a low TE (<2 ms). T_1 weighting is achieved by a short TR (<20 ms), short TE (1–2 ms), and a $\alpha > 10^\circ$, which can be optimized

based on SNR or CNR. The advantage of SPGR sequences with low α excitation is that the signal (image SNR) increases with short TR, which is in synergy with the requirement for rapid imaging (i.e., shorter TRs result in shorter scan times). Also, lower flip angles imply lower energy deposition in the body hence avoiding any SAR issues in CMR applications.

Besides 2D single- or multi-slice imaging, spoiled GRE sequences are often used to acquire 3D volumetric data, for example in contrast enhanced MR angiography. Volumetric acquisition enables imaging thin-slices without inter-slice gaps but comes at a cost of longer scan times. With the advent of improved gradient hardware, balanced steady state free precession (bSSFP) imaging (refer to section “Balanced steady-state free precession”) became possible, which allows one to generate steady-state signal without spoiling the transverse component of the magnetization. This permits marked improvement in SNR, which is diminished in SPGR images by spoiling the residual transverse magnetization at each TR. Nonetheless, since SPGR acquisitions are relatively insensitive to field inhomogeneities and have low SAR, SPGR imaging is a desirable means for amplifying T_1 image contrast when combined with magnetization preparation schemes, particularly at 3T where SAR can be a limiting factor for other pulse sequences such as bSSFP and fast spin echo.

Rapid spoiled GRE sequences can be easily integrated with the magnetization preparation schemes described earlier, such as IR or SR pulses applied prior to the data readout to enhance T_1 weighting. An important application of the magnetization-prepared SPGR sequence in CMR is SR-prepared first-pass myocardial perfusion imaging as demonstrated in Fig. 3.9. Panel (a) shows a proton-density weighted image acquired using the SPGR sequence with a very low flip angle. Panels (b–d) show the first-pass perfusion images capturing the signal dynamics following injection of gadolinium-based contrast, which acts as a T_1 -shortening agent (tissue with a higher contrast agent concentration will exhibit a lower T_1 and therefore a higher signal intensity). LGE imaging is another example of magnetization prepared SPGR; in this case an IR preparation is used to impart strong T_1 contrast.

Spin Echo Sequences

Spin echo (SE) imaging, especially the fast spin echo variant, is a commonly employed imaging method in CMR. The goal of spin echo imaging when compared to gradient echo imaging is to reduce the signal losses of excited spins from static field inhomogeneities and to extend the duration over which data can be acquired. In SE, an RF refocusing pulse is used to recover the phase coherence of spins following the initial excitation pulse, as opposed to gradient reversal to

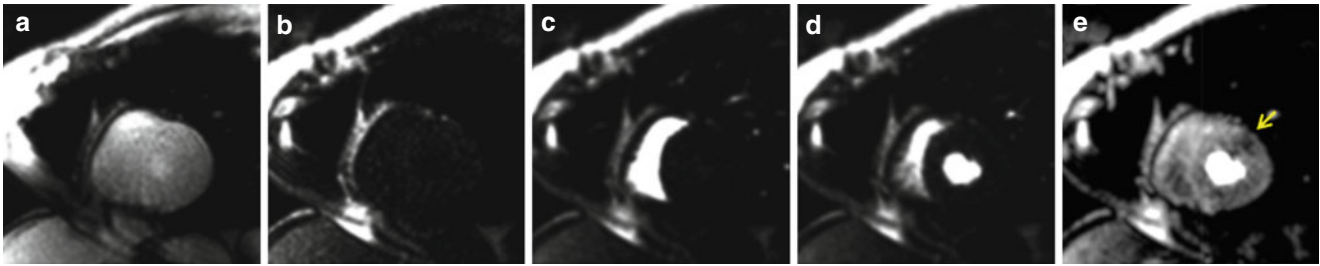


Fig. 3.9 Application of SPGR sequence for vasodilator-stress first-pass myocardial perfusion CMR at 3T. (a) Short-axis proton-density weighted image acquired using a SPGR sequence with $\alpha=4^\circ$; (b–e) perfusion images during injection of contrast agent acquired using a SR-prepared SPGR sequence with $TI=100$ ms and $\alpha=12^\circ$. (b) Pre-contrast image: before the gadolinium agent enters circulation, there is no contrast between the blood pool and the myocardium; (c) right-ven-

tricular enhancement phase; (d) left-ventricular enhancement phase, during which the T_1 -shortening gadolinium-based contrast arrives in the LV cavity thereby increasing the signal intensity in the blood pool; (e) myocardial enhancement phase, during which the myocardial contrast uptake is at its peak. A perfusion deficit (*arrow*) is observed in the LV myocardium, indicating stress-induced hypoperfusion

generate an echo as in GRE. This is the main distinguishing feature between spin echo and gradient echo imaging. In this Section, we first look at the simple spin echo imaging and then consider multi-echo spin echo imaging.

Spin Echo Imaging

In simple spin echo imaging, a 90° RF pulse is used to excite the spins by tipping the magnetization onto the transverse plane; a 180° RF pulse is then used to refocus the signal for imaging. A diagrammatic description of the spin echo formation following RF pulses is shown in Fig. 3.10. Following the 90° RF pulse, the excited magnetization begins to recover in the longitudinal direction (T_1 relaxation) and dephase in the transverse plane (due to T_2^* losses). If uninterrupted, the excited spins will fully recover to equilibrium with complete decay of signal in the transverse plane (in a time of $\sim 3T_2^*$) and regrowth in the longitudinal direction (in a time of $\sim 5T_1$). Since T_2^* is always smaller than T_1 , the complete dephasing of transverse magnetization will occur first prior to full recovery of the magnetization in the longitudinal direction. However, if a 180° RF pulse is applied at a time τ (typically >5 ms) after the 90° RF pulse, the dephasing can be reversed to form a coherent signal (echo) at a time 2τ (i.e. $TE = 2\tau$) after the initial 90° RF pulse. This signal can be encoded in space with phase and frequency encoding gradients before data acquisition. This leads to a few important consequences:

- T_2 decay – the magnitude of the spin echo is smaller than the signal in the transverse plane immediately after the 90° RF pulse because RF refocusing cannot recover the dephasing of spins from intrinsic T_2 losses which happen due to spin-spin interactions or fast diffusion in an inhomogeneous field;
- k -space filling – Similar to basic GRE sequences, only one k -space line can be filled per TR and this process must be repeated the same number of times as the number of predetermined phase-encoding lines;

- SNR – compared to gradient echo imaging, spin echo images tend to have greater SNR and reduced sensitivity to static (B_0) field inhomogeneities.
- *Multi-contrast imaging*– since SE is relatively insensitive to macroscopic field inhomogeneities, it offers flexibility to generate various (T_1 , T_2 and proton density) image contrast over a range of TE and TR. To generate T_1 contrast: TR and TE are kept short with TR ~ 300 – 600 ms and TE <20 ms; for T_2 contrast: TR and TE are set long with TR $>1,600$ ms and TE >60 ms; and for proton density (PD): TR is set long while TE is kept as short as possible, with long TR $>1,600$ ms and TE <20 ms.
- *Acquisition time* – Despite being robust to static field-inhomogeneity, spin echo sequences are relatively slow owing to long TRs, particularly when T_2 -weighting or proton density weighting are required. However, for T_1 weighting, the TRs are significantly shorter leading to shorter scan times (relative T_2 and PD weighted acquisition) along with relatively high SNR and immunity to static field inhomogeneities. In CMR applications, which typically use ECG triggering to synchronize data acquisition with the motion of the heart, the TR for spin echo sequences is typically restricted to multiples of the RR-interval.
- SAR – A SE sequence typically has greater SAR than a simple gradient echo sequence since it requires back-to-back 90° and 180° RF pulses, i.e., much higher flip angles than typically used in GRE sequences.
- T_2 mapping – by collecting a set of SE images at different TEs (i.e. changing τ) and fitting the pixel intensities at different TEs to a mono-exponential decay curve, it is possible to estimate the T_2 value for each image pixel (i.e. generate a T_2 map).

In a simple extension of spin-echo imaging, dual-echo spin-echo imaging can be used to generate a PD-weighted and T_2 -weighted image without any additional time penalty. Here two (instead of one) refocusing pulses are used with

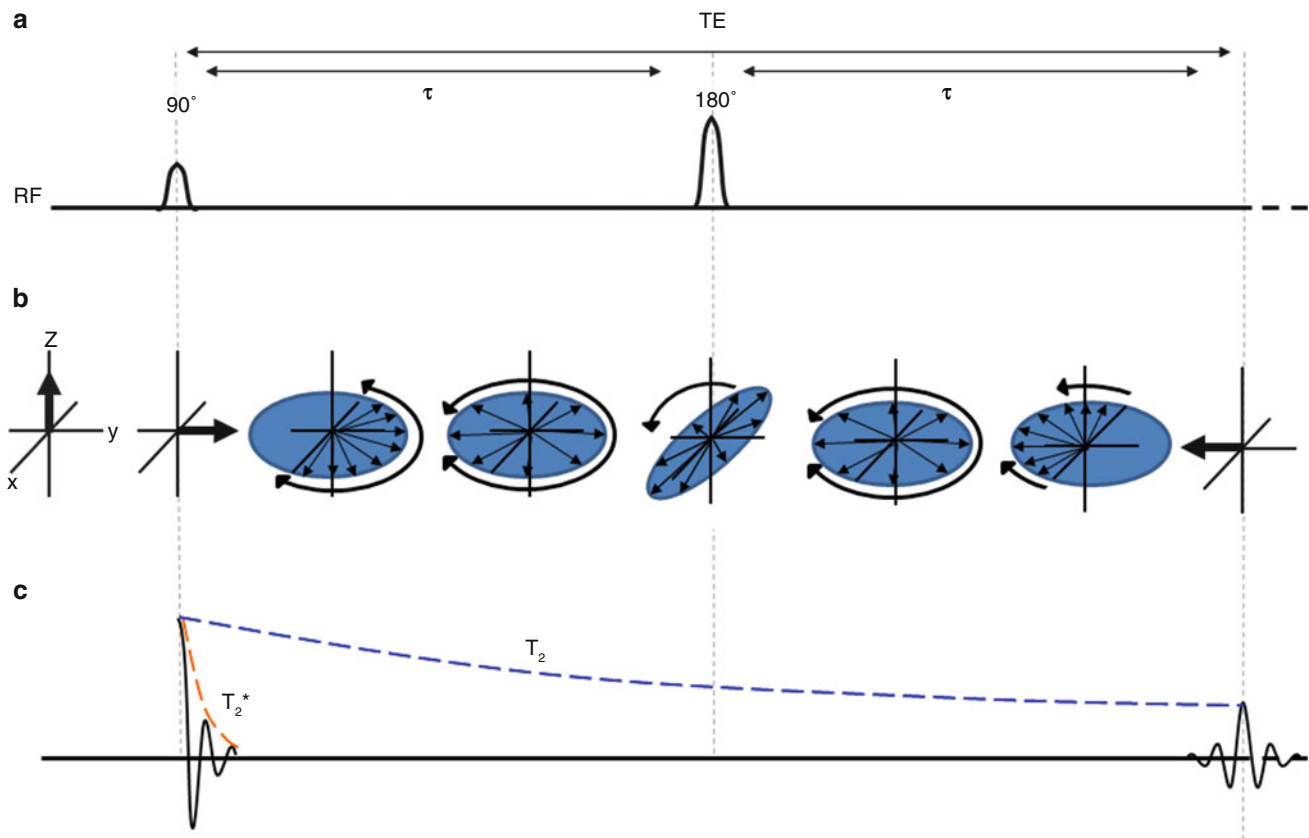


Fig. 3.10 Spin echo formation and T_2 relaxation. (a) A 90° RF excitation pulse is followed by a 180° RF pulse that is applied at a time of τ after the 90° RF pulse. (b) Shows a schematic of spins losing coherence due to T_2^* effects following the 90° RF pulse over the time period of τ . The 180° RF pulse reverses the direction of phase evolution to increase coherence over the next τ , forming an echo which peaks at time of 2τ

after the 90° RF pulse. (c) Shows the exponential decay of the echo peaks (blue curve) occurring over the period of 2τ , the time constant of which is T_2 . Also shown is the T_2^* decay curve (orange line). Note that spin-echo extends the time over which the transverse magnetization persists, without which T_2^* decay would more rapidly dephase the transverse magnetization

long TR to generate two echoes, one at a low TE and another at a longer TE by carefully positioning the refocusing RF pulses after the 90° RF pulse. Since both PD and T_2 -weighted imaging require that TR is kept long, the short and long TE echoes can be isolated to fill two different k-spaces. The k-space filled from echoes at the short TE can be used to generate a PD image, and the long TE can be used to generate a T_2 -weighted image. Nonetheless, both simple and dual spin-echo approaches are generally impractical for cardiac imaging since the acquisitions are too long to be executed with voluntary suspension of breathing or respiratory navigators; however, these techniques are still used in some instances with cardiac triggering and multiple averages to suppress respiratory motion artifact.

Fast Spin Echo Imaging

Fast spin-echo (FSE) sequences build on the simple spin-echo sequence described in section “Basic gradient-recalled echo” to significantly reduce the scan time. Here, instead of applying one refocusing RF pulse, multiple 180° RF refocusing pulses are applied in a consecutive fashion (as a

“train” of RF pulses). The timing diagram for the FSE sequence is shown in Fig. 3.11. The total number of echoes collected per TR is known as the echo-train length (ETL). Each echo from the refocusing pulse is encoded as a unique phase-encoding line. Since the total acquisition time is related to the number of phase-encode lines, a FSE sequence with an ETL of N reduces the scan time by a factor of N (i.e., if ETL = 10, the total scan time is reduced by a factor 10). In practice, ETL is limited by the tissue T_2 relaxation time and the inter-echo spacing (time between the consecutive RF pulses), 2τ (see section “Basic gradient-recalled echo”). In this scheme, not all k-space lines are acquired at the same TE; hence, combining the echoes to form a single image can create significant image artifacts caused by variations in signal across different lines of k-space. In particular, if the ETL is long and the echoes with short TE are encoded into the central k-space, which determines most of the image contrast, image blurring may result because the signal in the center of k-space is artificially amplified by the greater signal available at shorter TEs, and the signal is diminished in outer k-space lines if these are filled using

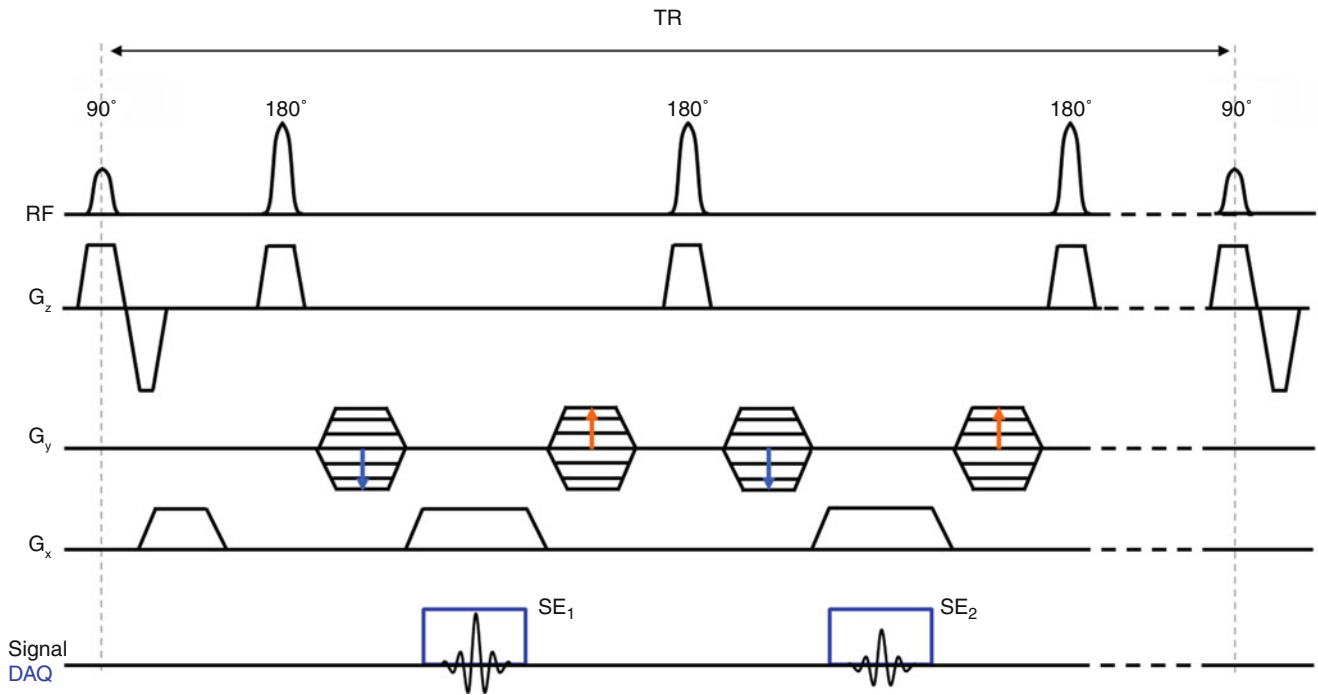


Fig. 3.11 Schematic for fast spin echo imaging sequence (FSE). This imaging sequence varies from the simple spin echo approach (Fig. 3.10) in that following the initial 180° refocusing RF pulse additional 180° RF pulses are applied to generate additional echoes. The echoes are formed at time of 2τ , 4τ , 6τ etc., where τ is the time between the time between the initial 90° and 180° RF pulses, respectively. Note that due to T_2 decay,

the echo peaks decrease in an incremental fashion with each subsequent echo. In addition, in FSE imaging the phase-encoding gradients are rewound after readouts (DAQ) to rephase the transverse magnetization to make it consistent between phase-encoding steps. Otherwise unlike in GRE, the subsequent 180° RF pulse would refocus the left over phase and interfere with accurate phase encoding of the next echo

later echoes. This is typically avoided by keeping the ETL short [3–7] to generate PD or T_1 weighting. However, this diminishes the value of FSE imaging which relies on long ETL to substantially decrease scan time. Thus the true benefit of FSE imaging is realized with T_2 -weighted imaging, where the echoes at long TEs are encoded in the central k-space. Since the TE of different phase-encode lines will vary in FSE imaging, an *effective TE* is identified in practice and is defined as the TE of the central phase-encode line of the FSE image. One of the common uses of FSE in CMR is for anatomic imaging (refer to Fig. 3.12). While the reduction in acquisition time from FSE, particularly for T_2 -weighted acquisitions, is significant, there are a few other limitations with this approach. Since multiple refocusing pulses are applied in a train, this sequence tends to have high SAR (especially when τ is small), and is sensitive to motion leading to image artifacts, particularly when ETL is long.

Balanced Steady-State Free Precession

Over the past decade, balanced steady-state free precession imaging (bSSFP) has emerged as an important imaging strategy, particularly for CMR. It has evolved into the method of choice for fast and accurate imaging of cardiac function

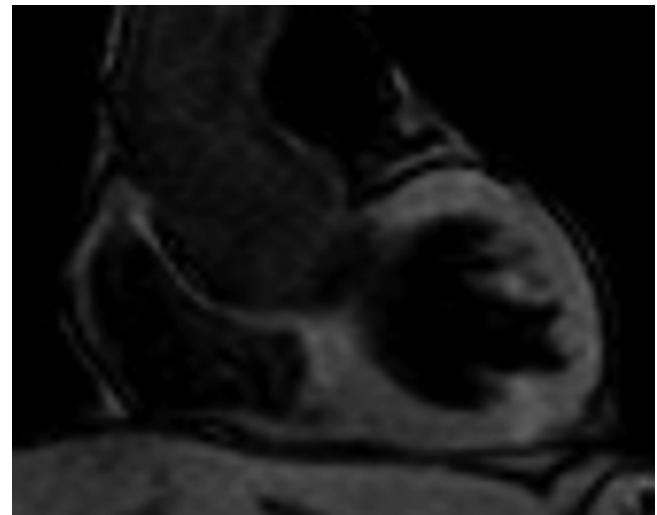


Fig. 3.12 Application of fast spin echo (FSE) to imaging the cardiac anatomy. FSE imaging permits clear visualization of cardiac anatomy (in this case a four chamber view of the heart) by suppressing the signal from moving blood

since it enables one to generate cardiac phase-resolved (cine) images with high contrast between blood and myocardium.

In this approach, the magnetization is repeatedly excited by RF pulses ($TR \sim 2\text{--}3$ ms) to reach a dynamic equilibrium between relaxation and excitation. This equilibrium is

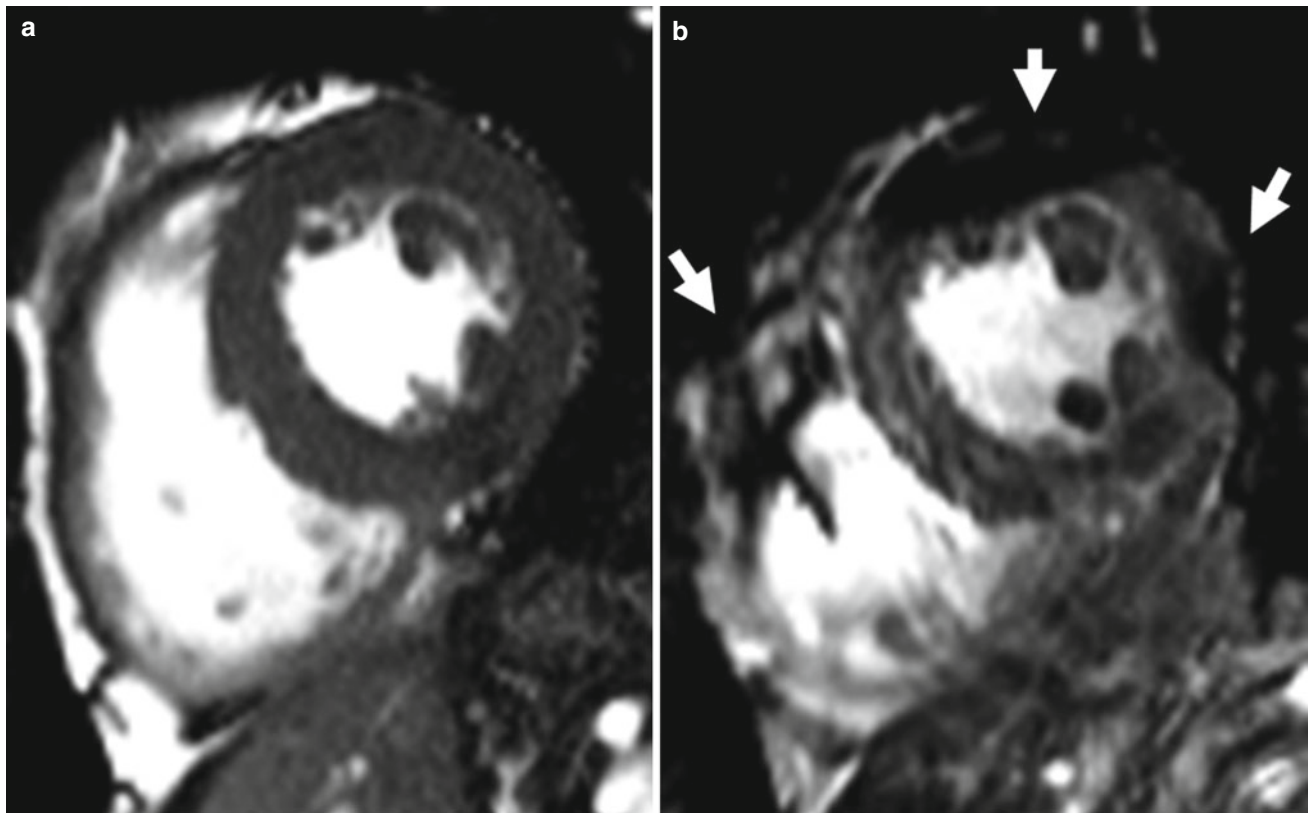


Fig. 3.13 Banding artifacts in bSSFP imaging. Short axis images of the heart at TR=3.2 ms (**a**) and TR=6.2 ms (**b**) are shown. Increasing the TR in bSSFP imaging increases the sensitivity to field inhomogene-

ity, which leads to banding artifacts (*arrows, b*) that appear as signal dropouts within the image

reached by minimizing the time between the RF pulses so that both the transverse dephasing and longitudinal recovery are relatively small (but not zero) between RF excitations. After a series of RF excitations, the equilibrium magnetization transitions into steady state magnetization, which is significantly smaller than M_0 , with a magnitude that is determined by the relaxation parameters (T_2 and T_1) and flip angle. At the optimal flip angle, bSSFP images are weighted by T_2/T_1 . The importance of bSSFP imaging in CMR may be understood simply from its signal properties. Since the T_2/T_1 ratio of blood is approximately threefold greater than that of myocardium, blood appears brighter than the myocardium in bSSFP images. This difference in signal intensities provides high image contrast that permits accurate delineation of the endocardial border between the myocardium and blood. In comparison, although SPGR imaging is also very fast (TR $\sim 2\text{--}3$ ms), the contrast between blood and muscle is weak ($<40\%$), rendering bSSFP imaging as the method of choice for fast and accurate assessment of cardiac function.

One of the unique characteristics of the bSSFP signal is that it can be very sensitive to magnetic field inhomogeneities which can be a profound source of image (banding) artifacts. In particular the bSSFP signal drops to zero at relatively well-defined field inhomogeneities (off-resonance frequencies) leading to signal nulls or dark bands in the image.

However, over a reasonable range of field homogeneity, the bSSFP signal can be relatively insensitive to these variations. Moreover, the range of field inhomogeneities causing these dark bands is inversely related to the TR. This lends a few ways to minimize the banding artifacts, but the first defense against banding artifacts begins with careful shimming of the static magnetic field around the heart to decrease inhomogeneities. Next, TR can be shortened as much as possible by, e.g., increasing sampling bandwidth, which can minimize the occurrence of nulls/bands and potentially restrict these artifacts only to poorly shimmed regions outside the heart. An example of the dependence of TR on banding artifacts is shown in Fig. 3.13. However, there are practical limits to how short the TR can be due to SAR limitations. In essence, decreasing TR is accompanied by an increase in SAR, which may require one to reduce the excitation flip angle (with the possibility of decreasing SNR and contrast) to keep SAR within acceptable limits. In addition to SAR issues, there are practical limitations imposed by the requirements of the imaging gradients as outlined below. Even at the shortest TR, banding artifacts are particularly problematic at 3T since the magnetic field inhomogeneities surrounding the heart (from the susceptibility differences between heart and lung as well as between the myocardium and cardiac veins) are amplified at 3T compared to

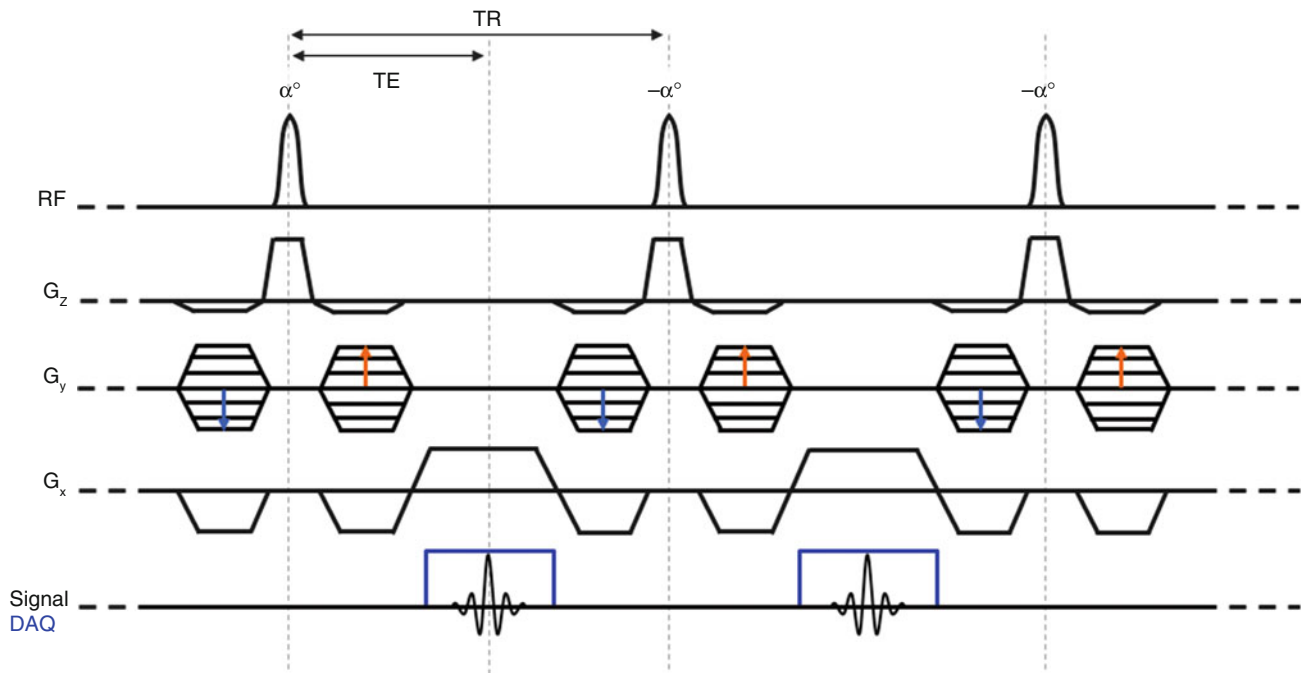


Fig. 3.14 Schematic for balanced SSFP (bSSFP) imaging sequence. The RF pulses are applied every TR and are typically phase-cycled (i.e., the RF phase is incremented by 180° each TR). This creates a more homogenous signal over an appreciable range of B_0 inhomogeneities

compared to repeated excitation with a train of α pulses without RF phase modulation. In addition, the G_z , G_y , and G_x are rewound at each TR. Since signal is collected in steady state, the echo peaks are of equal magnitude at each TR

1.5T. Moreover, the shortest possible TR may be critically limited by SAR and excitation flip angle at 3T more so than at 1.5T. In essence, SAR limitations scale up with cine imaging (which requires continuous, repeated application of RF pulses), increasing coverage (2D to 3D), and increasing field strength (e.g., from 1.5T to 3T); all of these factors force one to reduce flip angle, increase TR, or both, potentially resulting in suboptimal images (i.e., reduced SNR and/or increased image artifacts). For these reasons, cine imaging at 3T using bSSFP may not always yield desirable image quality and at times one may need to revert back to SPGR imaging for assessment of cardiac function at 3T.

The possibility of steady-state signal formation via interaction between RF excitation and relaxation was known for many decades before bSSFP imaging became practically feasible. The reduction of bSSFP concepts to practice was tied to improvements in gradient coil technology, which were necessary to satisfy key conditions critical for bSSFP imaging. In particular, in the bSSFP pulse sequence the imaging gradients (slice selection, phase and frequency encoding) need to be rewound every TR (2–3 ms). That is, in addition to maintaining a short TR (to ensure conditions suitable for steady-state signal formation and to minimize banding artifacts), the imaging gradients must be rapidly rewound before the next RF pulse; otherwise phase accumulation between TR can disturb the steady-state signal and degrade image quality. A timing diagram of the bSSFP pulse sequence that is commonly used for cine imaging is shown in

Fig. 3.14. Various acronyms are used by different vendors to designate balanced SSFP sequences including true FISP (Fast Imaging with Steady-state Precession by Siemens), FIESTA (Fast Imaging Employing STEady-state Acquisition by GE), and balanced FFE (Fast-Field Echo by Philips).

Currently bSSFP imaging is used for single-heartbeat bright-blood 2D imaging for slice localization, with navigator respiratory gating for 3D bright blood imaging of the thoracic vessels or coronary arteries, for cine imaging, or combined with a magnetization preparation module, for example, for inversion recovery or T_2 -prepared imaging. In the standard cine-imaging mode, typically prescribed with voluntary suspension of breathing, after ‘dummy’ excitation pulses (i.e. without data acquisition) typically lasting for one RR interval to transition the equilibrium magnetization to steady state, 2D data acquisition is performed continuously with k-space segmentation used to define relatively narrow time windows (temporal resolution) for reconstruction of multiple image frames (cardiac phases) representing the cardiac cycle. During this time window, cardiac motion is typically negligible and a number of phase-encode lines (i.e., temporal window/TR) are collected every heartbeat. Based on the imaging resolution (total phase-encode lines), this process is repeated over multiple heartbeats to fill all of k-space for each cardiac phase/image. This process is commonly referred to as *segmented imaging*, where the imaging process is segmented over multiple heartbeats as illustrated in Fig. 3.15.

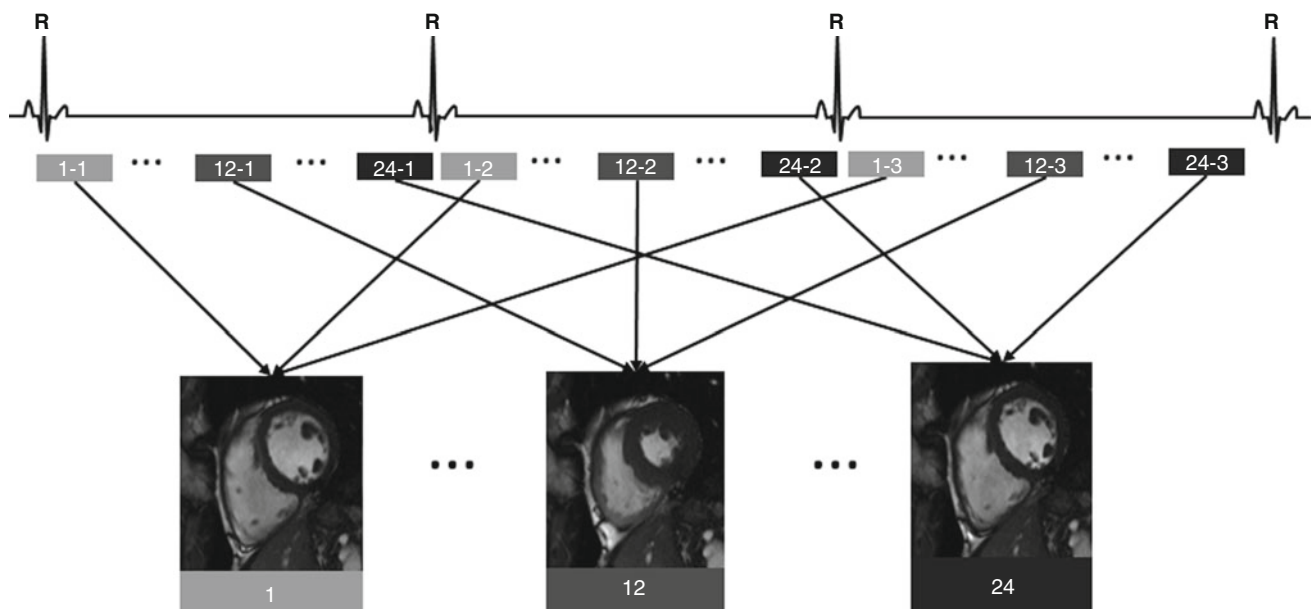


Fig. 3.15 Segmented 2D cine bSSFP. In segmented imaging data are collected over multiple heartbeats. This is shown for the case of 2D cine imaging with bSSFP. In this example 24 cardiac phases are collected within each R-R interval. However, at each R-R interval only a fraction of the k-space lines are collected. In this example, the complete k-space

data for each of the 24 images is collected over three heartbeats (R-R intervals). To form the image of the 12th cardiac phase, for example, phase encoding lines labeled as '12-1' (from the first heart beat), '12-2' (from second the heart beat) and '12-3' (from the third heart beat) are used to fill the corresponding k space

Given the excellent SNR efficiency of the bSSFP sequence, it has been successfully used in combination with common magnetization preparation schemes (section “Common types of magnetization preparation”), particularly at 1.5T where banding artifacts are typically not a significant problem. For instance, IR-bSSFP or SR-bSSFP are commonly used for infarct and perfusion imaging, respectively; and T_2 -prep bSSFP has been used for imaging myocardial edema, BOLD, and quantitative T_2 mapping.

Recommended Reading

- Bernstein MA, King KF, Zhou XJ. Handbook of MRI pulse sequences. Burlington: Elsevier Academic Press; 2004.
- Edelman RR. Contrast-enhanced MR imaging of the heart: overview of the literature. *Radiology*. 2004;232:653–68.
- Elster AD. Gradient-echo MR, imaging: techniques and acronyms. *Radiology*. 1993;186:1.
- Haacke EM, Frahm J. A guide to understanding key aspects of fast gradient echo imaging. *J Magn Reson Imaging*. 1991;1:621.
- Haacke EM, Brown RW, Thompson MR, Venkatesen R. Magnetic resonance imaging: physical principles and sequence design. New York: Wiley; 1996.
- Henning J, Nauerth A, Friedburg H. RARE-imaging: a fast imaging method for clinical MR. *MRM*. 1986;3:823–33.
- Mitchell DG. MRI principles. Philadelphia: W.B. Saunders Company; 1999.
- Reeder SB, Faranesh AZ, Boxerman JL, McVeight ER. In vivo measurement of T_2^* and field inhomogeneity maps in the human heart at 1.5T. *MRM*. 1998;39(6):988–98.
- Simonetti OP, Finn JP, White RD, et al. “Black blood” T_2 -weighted inversion-recovery MR imaging of the heart. *Radiology*. 1996;199:49–57.
- Simonetti OP, Kim RJ, Fieno DS, et al. An improved MR imaging technique for the visualization of myocardial infarction. *Radiology*. 2001;218(1):215–23.

Ning Jin, Haris Saybasili, and Xiaoming Bi

Abstract

Spatial resolution and temporal resolution refer to the smallest distance and temporal change that can be differentiated. Signal-to-noise ratio (SNR) is a reflection of signal intensity with reference to the background noise. In cardiac MR imaging, it is desirable to acquire images that have adequate spatial resolution to resolve fine structures in the heart, sufficient temporal resolution to visualize cardiac motion, and high SNR for good image quality. This chapter first covers spatial resolution in MRI, its relationship to k-space, the difference between nominal and apparent spatial resolution, and factors that affect spatial resolution. The chapter then discusses temporal resolution and image acquisition methods that can be used to change/improve temporal resolution, including view-sharing, segmented imaging, and real-time imaging. Finally, the chapter covers SNR and sources of noise, factors affecting SNR, how to measure SNR, and the tradeoffs between SNR, spatial resolution and temporal resolution.

Keywords

Spatial resolution • Temporal resolution • Signal-to-noise ratio

Spatial Resolution

The spatial resolution of an image refers to the smallest resolvable distance between two objects or features in an image [1]. This aspect of image quality is critical in that it determines the size of the smallest structures that can be

visualized, such as small lesions or tiny blood vessels. In general, images with higher spatial resolution can resolve smaller objects, while low spatial resolution will cause fuzzy edges, a pixelated appearance, and potentially the complete loss of smaller structures in the image.

MR images can be acquired in either two-dimensions (2D) or three-dimensions (3D). In 2D acquisitions, all the spins within the defined slice thickness are excited; therefore a 2D slice represents the summation of signal over the thickness of the prescribed slice. Resolution in the slice direction in a 2D acquisition is thus defined by the thickness of the excited slice. In 3D acquisitions, the MR data is acquired from a volume or thick “slab” rather than a single slice. The third dimension is referred to as the slice-encoded or partition-encoding direction. Compared to 2D multi-slice imaging, 3D volumetric imaging offers several advantages, including higher resolution in the slice direction, contiguous spatial coverage, and isotropic voxel dimensions, but 3D acquisition time is significantly longer than 2D.

Electronic supplementary material The online version of this chapter (doi:[10.1007/978-3-319-22141-0_4](https://doi.org/10.1007/978-3-319-22141-0_4)) contains supplementary material, which is available to authorized users.

N. Jin, PhD (✉)

MR R&D, Siemens Healthcare, Columbus, OH, USA
e-mail: ning.jin@siemens.com

H. Saybasili, PhD

MR R&D, Siemens Healthcare, Chicago, IL, USA
e-mail: haris.saybasili@siemens.com

X. Bi, PhD

MR R&D, Siemens Healthcare,
Los Angeles, CA, USA
e-mail: xiaoming.bi@siemens.com

The field of view (FOV) typically refers to the two-dimensional area of an image; each dimension is usually measured in centimeters (cm) or millimeters (mm). The in-plane dimensions are typically referred to as the frequency-encoding and phase-encoding directions. A typical FOV for a 2D image might be $400 \times 300 \text{ mm}^2$, for example, which means that the FOV in the frequency encoding direction is 400 mm and the FOV in the phase-encoding direction is 300 mm. The maximum FOV attainable is determined by the magnetic field homogeneity volume of the particular MRI system and typically ranges from 350 to 500 mm in all directions. In a 3D acquisition, FOV can also refer to the thickness in the slice-encoding or partition encoding direction.

The terms “pixel” (picture element) and “voxel” (volume element) are often used interchangeably to define the individual discrete units that make up an image; technically a pixel has only two dimensions, while a voxel also accounts for the slice thickness. The imaging matrix determines the number of voxels reconstructed to form the image and is expressed as the product of the number of voxels in each direction. For example, the imaging matrix for a 2D slice might typically be comprised of 256×256 voxels. The numbers of voxels in the frequency-encoding and phase-encoding directions do not need to be equivalent. For example, an imaging matrix might be 256×128 voxels; the smaller number is usually the number of voxels in the phase-encoding direction, since this directly impacts the total acquisition time. In 3D imaging, the imaging matrix might be $256 \times 128 \times 64$, where the smallest dimension typically represents the partition encoding direction, since the slab thickness usually covers less distance than the in-plane dimensions.

The pixel resolution in each dimension is determined by the FOV of the image and the number of the voxels in the imaging matrix:

Pixel resolution_x = FOV_x/number of voxels in the frequency-encoding direction

Pixel resolution_y = FOV_y/number of voxels in the phase-encoding direction

Pixel resolution_z = slice thickness in 2D imaging
or = FOV_z/number of voxels in the slice or slab direction in 3D imaging

Note that the designations of x = frequency encoding, y = phase encoding, and z = slice encoding are by convention only; in practice the frequency, phase, and slice directions, which while are always orthogonal to each other, can otherwise be defined with total flexibility.

It is a common mistake to think that the pixel resolution is equivalent to the spatial resolution; due to the nature of digital imaging techniques, the relationship between pixel size and spatial resolution is not always obvious. For example,

consider the digital zoom functionality on a digital camera; the digital zoom factor is only related to image enlargement and has little to do with the actual spatial resolution. A similar digital zoom technique can also be applied to MR acquisitions.

To understand the true spatial resolution of the image, we need to first understand how the MR signal is acquired.

k-Space

As discussed in earlier chapters, the MR signal is acquired in k-space, which is the Fourier transform of the object image. We refer to the MR image as the image domain, and k-space as the spatial frequency domain. For a two-dimensional acquisition, the MR signal, $s(t)$, as a function of time can be written as

$$s(t) = \iint_{-\infty}^{+\infty} S_0(x, y) e^{-2\pi i(k_x(t)x + k_y(t)y)} dx dy \quad (4.1)$$

where $S_0(x, y)$ represents the object, x and y are the image-domain position or distance variables in centimeters, and k_x and k_y are the spatial frequency domain variables (the frequency and phase-encoding directions, respectively) in 1/cm, or cycles per centimeter. This is equivalent to the 2D Fourier transform of the object $S_0(x, y)$. For 3D acquisitions, k-space is extended to the k_z direction.

K-space has measurable dimensions and an overall size. For each dimension, Δk (Δk_x , Δk_y , Δk_z) is a measure of the spacing between adjacent data points in k-space, and k_{\max} ($k_{x\max}$, $k_{y\max}$, $k_{z\max}$) is the highest spatial frequency sampled in each direction. The overall width of k-space W (W_x , W_y , W_z) in each direction is the product of the spacing between k-space sample points and the number of samples (Eq. 4.2):

$$\begin{aligned} W_x &= \Delta k_x \times \text{number of samples in } k_x \\ W_y &= \Delta k_y \times \text{number of samples in } k_y \\ W_z &= \Delta k_z \times \text{number of samples in } k_z \end{aligned} \quad (4.2)$$

If the k-space is sampled symmetrically around the k-space center (the origin) in each direction then

$$\begin{aligned} W_x &= 2 \times k_{x\max} \\ W_y &= 2 \times k_{y\max} \\ W_z &= 2 \times k_{z\max} \end{aligned} \quad (4.3)$$

MR data acquired in k-space is normally referred to as the *raw data*. The central region of k-space contains the low spatial frequency components of the image, such as the spatially slowly changing parts of the object and the overall contrast; the periphery of k-space contains the high spatial frequency

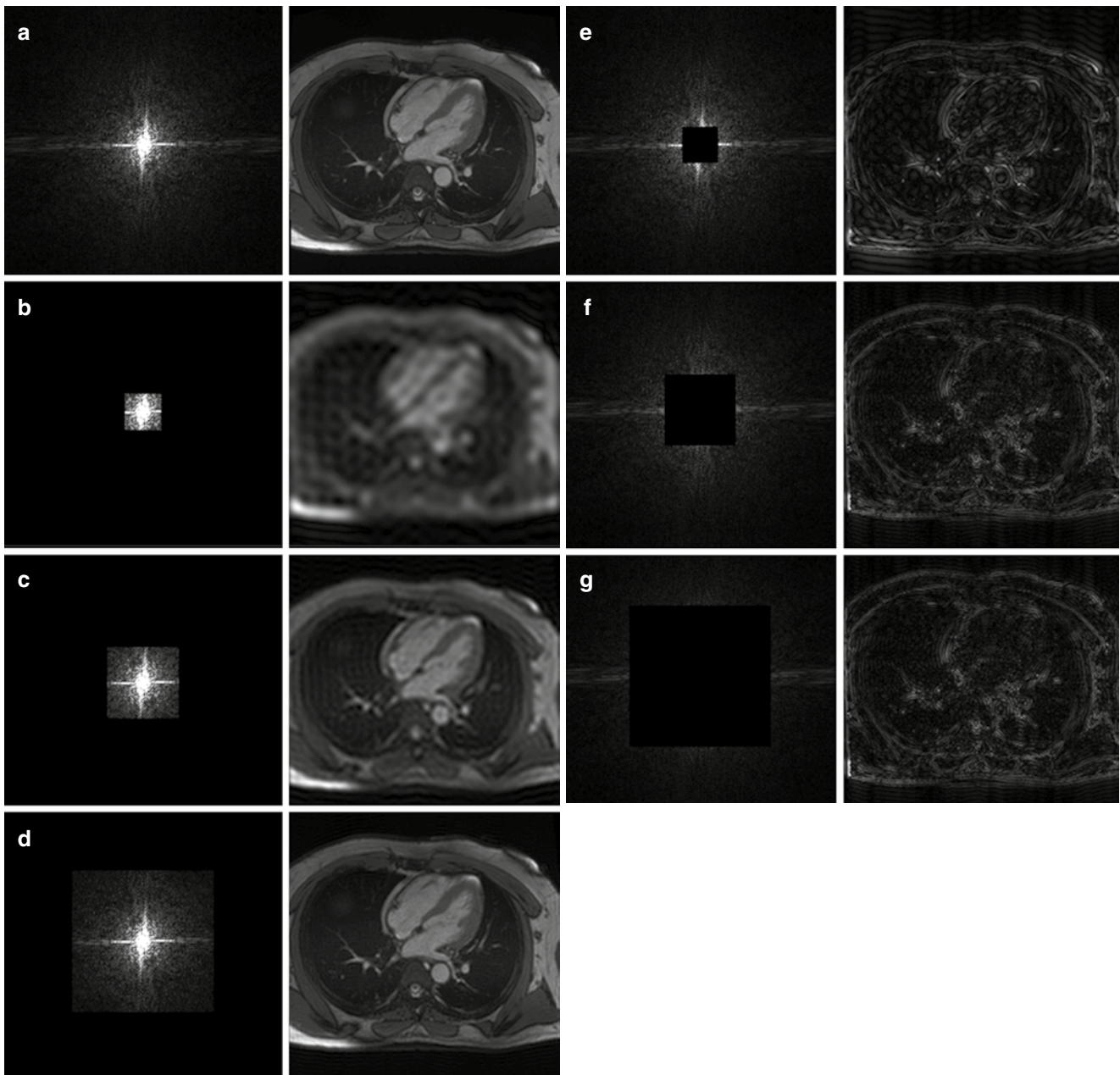


Fig. 4.1 The relationship between k-space and the reconstructed image. (a) The fully sampled k-space and its reconstructed image consisting of an FOV of $340 \times 340 \text{ mm}^2$ with an acquired matrix size of 256×256 . The effect of preserving the central 1/64th (b), 1/16th (c) and

1/4th (d) of k-space while filling the peripheral portions with zeros is demonstrated on the *left*. Conversely, the effect of filling the central 1/64th (e), 1/16th (f) and 1/4th (g) of k-space with zeros while preserving the peripheral portions is shown on the *right*

components of the image that provide the edge definition and finer structures.

All of the phantom and volunteer images in this chapter were acquired on a 1.5T scanner (MAGNETOM Aera, Siemens Healthcare, Germany). All the MR images of the heart were collected from the same normal volunteer. The relationship between k-space and the reconstructed image is illustrated in Fig. 4.1 using an MR image of the heart acquired in the four-chamber view. The original image was

acquired with a FOV of $340 \times 340 \text{ mm}^2$ and an acquired matrix size of 256×256 (a). In the lower left column, the central 1/64th (b), 1/16th (c) and 1/4th (d) portion of k-space were preserved and the peripheral portions were filled with zeros; conversely, in the lower right column the central 1/64th (e), 1/16th (f) and 1/4th (g) of k-space was filled with zeros and the peripheral portions preserved. As shown in the corresponding reconstructed images, the central portion of k-space mostly contains information about the overall image

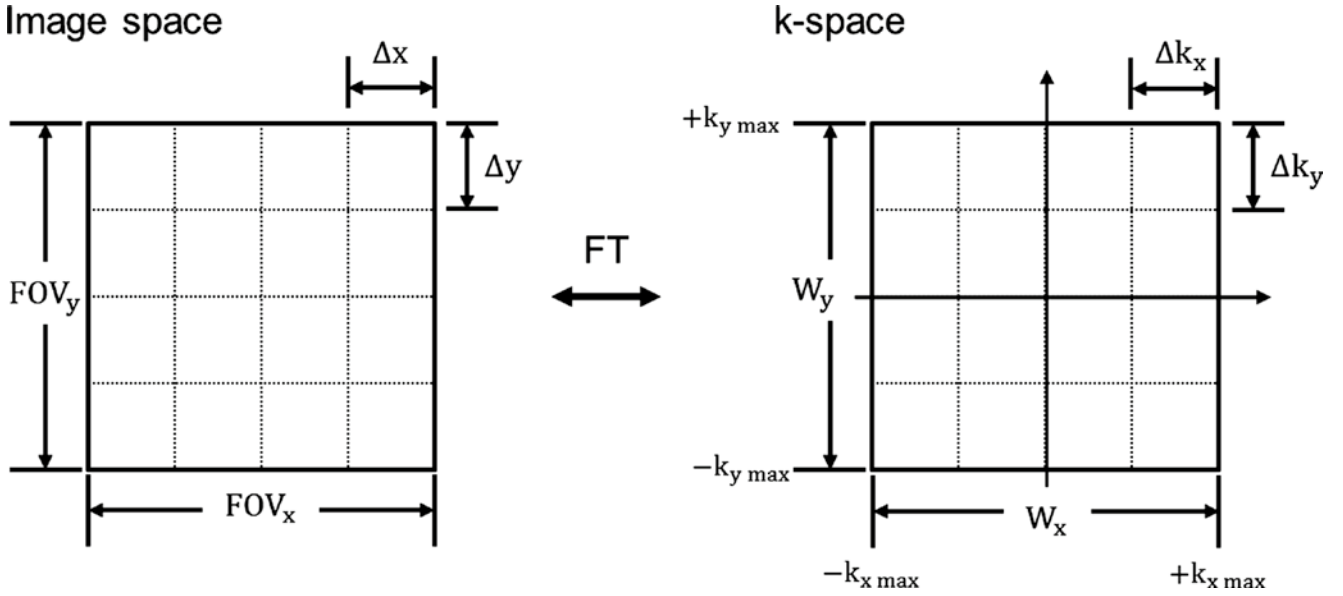


Fig. 4.2 The relationship between image space and k-space. The sampling interval between k-space points is inversely related to the FOV of the image and the spatial resolution is also inversely related to the overall size of k-space

contrast, while the peripheral portion of k-space mostly contains information about the fine details and edges.

The Relationship Between k-Space and Image Space

The desired in-plane spatial resolution is determined by selecting the FOV and number of sample points in the frequency- and phase-encoding directions. These selections in turn determine the sampling of k-space (the extent of coverage and sampling interval).

The spacing between k-space points is inversely related to the FOV of the image (Eq. 4.4). A larger FOV requires denser sampling in k-space, while a smaller FOV results from sparser sampling in k-space.

$$\begin{aligned} FOV_x &= \frac{1}{\Delta k_x} \\ FOV_y &= \frac{1}{\Delta k_y} \end{aligned} \quad (4.4)$$

Similarly, there is an inverse relationship between the spatial resolution and the overall extent of k-space (Eq. 4.5). Since k-space represents the spatial frequency content of the image, higher spatial frequencies are required to visualize the details of smaller objects. Increasing the extent of k-space results in reduced voxel size and therefore increased spatial resolution.

$$\begin{aligned} \Delta x &= \frac{1}{W_x} = \frac{1}{2k_{x,\max}} \\ \Delta y &= \frac{1}{W_y} = \frac{1}{2k_{y,\max}} \end{aligned} \quad (4.5)$$

The relationship between image space and k-space is shown in Fig. 4.2.

In Fig. 4.3, image *a* and image *b* have the same spatial resolution, but the FOV of image *b* is twice the size of the FOV of image *a*. The pixel size (spatial resolution) and extent of k-space coverage (W) are the same for both image *a* and image *b*; however, the k-space sampling interval (Δk) of image *a* is twice that of image *b*, and therefore the FOV of image *a* is only one half that of image *b*. On the other hand, image *a* and image *c* have the same FOV, but the spatial resolution of image *c* is twice that of image *a*, i.e., the pixel dimensions of image *c* are only half those of image *a*. As the result, the k-space sampling interval of image *a* is the same as that of image *c*, but the k-space of image *a* has twice the extent compared to that of image *c*. Figure 4.3 demonstrates that the extents of the acquired k-space (W_x and W_y) determine the pixel dimensions, while the sampling intervals of k-space (Δk_x and Δk_y) determine the image FOV.

Effect of Truncating k-Space on Image Quality

Because the object being imaged (typically a human or an animal) is of finite extent, by the properties of the Fourier Transform the corresponding k-space has infinite extent (Eq. 4.1). As the result, the measured k-space signal, which is of finite extent, is a truncated representation of the actual Fourier transform of the object. As shown in Fig. 4.1, the periphery of k-space contains the high spatial frequency information. With k-space truncation, some high spatial frequency information is unavoidably lost, leading to reduced image sharpness and loss of fine details in the image. Truncation of k-space is equivalent to multiplying the k-space by a rectangular function, which is

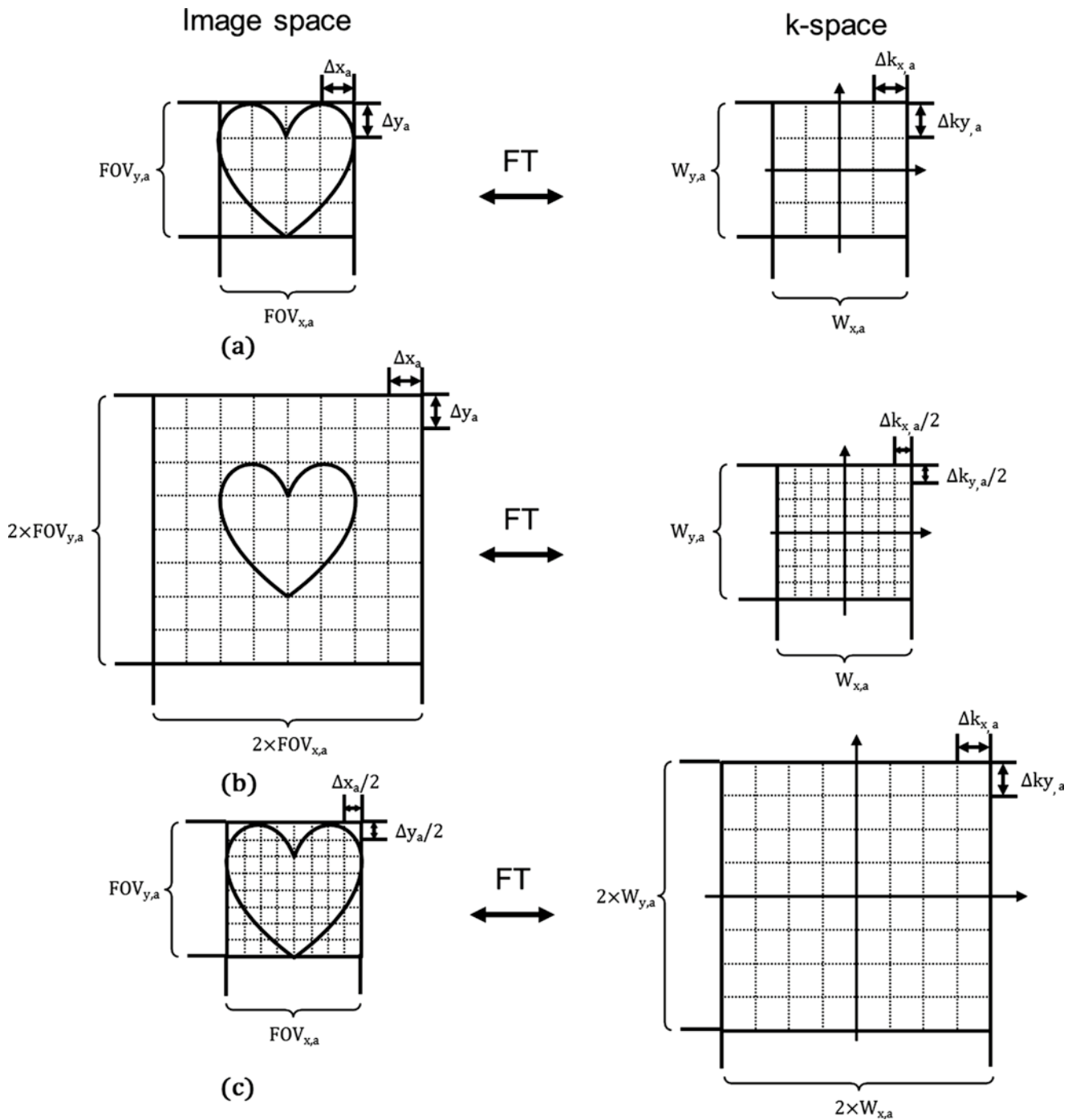


Fig. 4.3 Image (a) and image (b) have the same spatial resolution, but the FOV of image (b) is twice the FOV of image (a). Therefore the corresponding k-spaces for image (a) and image (b) have the same coverage (W), but the k-space sampling interval (Δk) of image (a) is twice that of

image (b). Image (a) and image (c) have the same FOV, but the spatial resolution of image (c) is twice the spatial resolution of image (a). As a result, the k-space sampling interval of image (a) is the same as that of image (c), but the k-space coverage of image (a) is twice that of image (c)

by the properties of the Fourier Transform equivalent to convolution of the image with a sinc function (the Fourier transform of the rectangular function). The sinc function ($\sin(x)/x$), has a main lobe of finite width, and an infinite number of sidelobes of diminishing amplitude, as shown in Fig. 4.4. Truncating the k-space causes image blurring and ringing artifacts around the edges of objects called Gibbs

ringing artifacts; these can be explained by the convolution of the image with the sinc function. For larger voxel size, the rectangular function is narrower and truncates k-space nearer to the center of k-space; this results in a sinc function with wide side lobes that produces a broader ringing artifact. The truncation artifacts become substantial when the width of an edge (the transition between tissues of

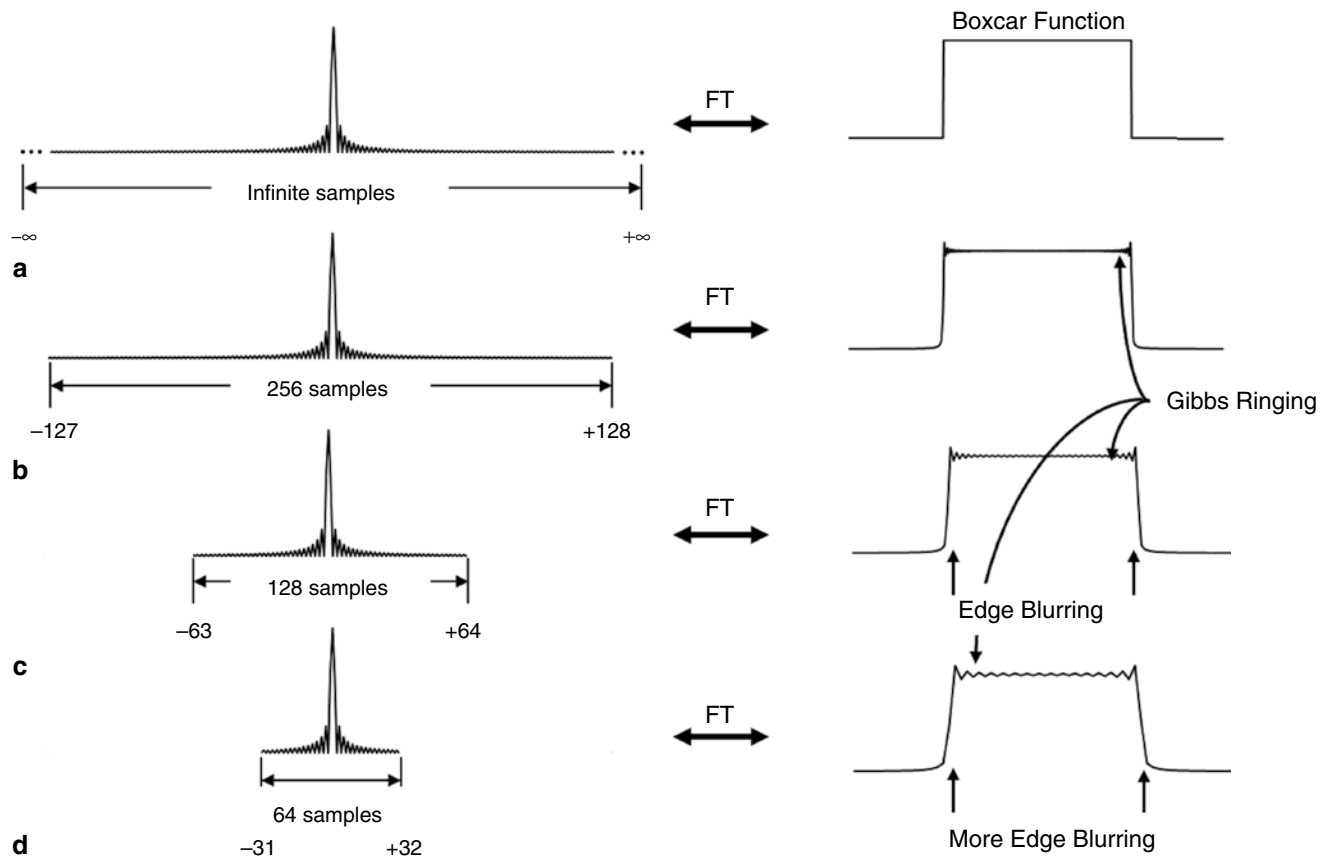


Fig. 4.4 The effect of frequency truncation on the boxcar function (a). With the decreased sampling in frequency space (b–d), blurring and Gibbs ringing are observed in the reconstructed signal

different image intensities) is on the order of or smaller than the voxel size.

Figure 4.4 demonstrates the effect of frequency space truncation using a 1D boxcar, which is another name for the rectangular function discussed earlier. The Fourier transform of the boxcar function has an infinite extent. If the entire frequency spectrum of the Fourier transform of the boxcar function could be sampled, its inverse transform would again result in a boxcar function with perfect edges. However, given that only a finite number of frequency components can be sampled, Gibbs ringing artifacts and edge blurring are observed in the reconstructed signal. As shown in Fig. 4.4b–d, with fewer points sampled in the frequency space, the edge becomes blurred and the Gibbs ringing artifact becomes broader. Figure 4.5 uses the same example as in Fig. 4.1. If only the central 64×64 of the k-space is acquired, the high-spatial-frequency information is lost and the reconstructed image shows edge blurring and ringing artifacts.

The Gibbs ringing artifacts can be minimized by multiplying the k-space data by a filter or window function that smoothly attenuates the high-frequency information, rather than sharply cutting off the data with a boxcar or rectangular function. However, the trade-off is reduced spatial

resolution due to the loss of additional high spatial frequency information [2].

Nominal Spatial Resolution vs. Apparent Spatial Resolution

Based on the concept of k-space and the relationship between k-space and image space, the nominal spatial resolution, which is also called *the true spatial resolution*, is determined by the extent of k-space coverage. Once the raw data are acquired, the nominal spatial resolution is defined and cannot be further improved. The nominal resolution determines the smallest structure that can be resolved in the image. Lesions or vessels smaller than the size of the nominal resolution cannot be distinguished from the background tissue since the information needed to visualize smaller structures is not contained in the raw data. On the other hand, the *apparent spatial resolution*, which is also called the display resolution, can be improved. It is determined by the image FOV and the number of pixels in the reconstructed image. Due to the nature of digital imaging, the display resolution may have little to do with the true spatial resolution, and can be improved by digital image interpolation.

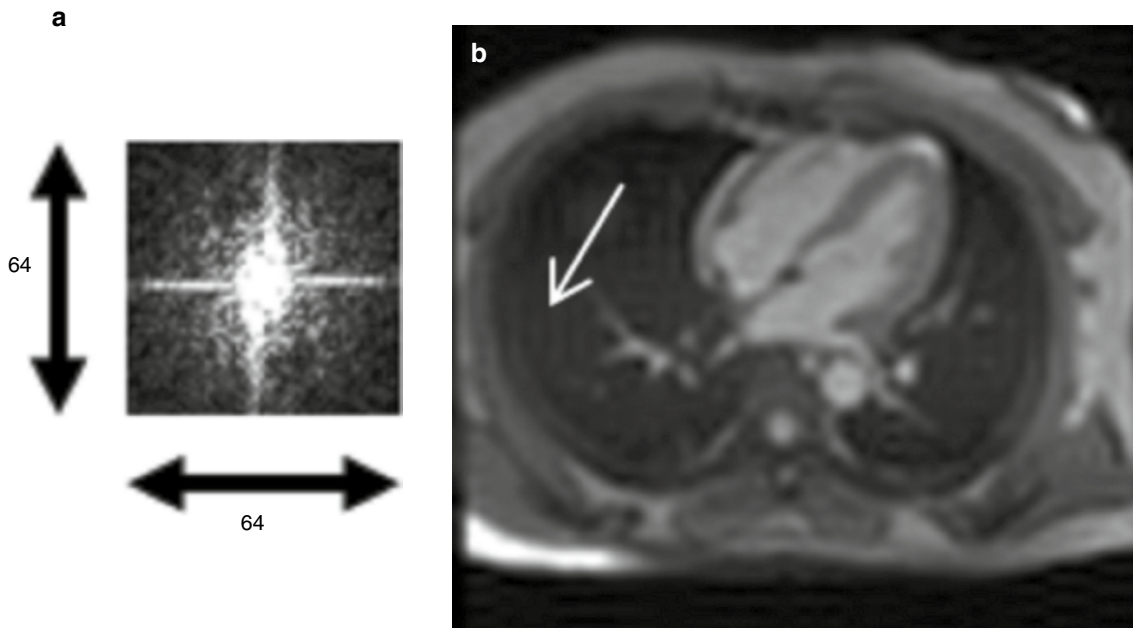


Fig. 4.5 If only the central 64×64 of the k-space (a) is sampled, the reconstructed image (b) shows blurring and Gibbs ringing artifacts (arrow)

Zero Filling

Digital image interpolation can be achieved by employing a strategy called zero padding or zero filling. It involves filling the uncollected peripheral regions of k-space with zeros before the Fourier transform to improve the apparent resolution.

The process is shown in Fig. 4.6. The original image is acquired on a FOV of 340 mm with an imaging matrix of 256×256 , resulting in a nominal or true spatial resolution roughly equal to 1.3×1.3 mm. A 512×512 matrix in k-space can be generated by filling the periphery of the 256×256 matrix with zeros to increase the raw data matrix size. Taking the Fourier transform of the 512×512 matrix in k-space creates an image with 512×512 pixels, cutting the pixel dimensions in half in each in-plane direction. Compared to the original image with 256×256 pixels, the new image with 512×512 pixels may appear smoother or less blocky; however, there is no additional true spatial resolution; the original pixels have merely been interpolated. Interpolation is roughly the equivalent of taking the average value of two adjacent pixels to make a new pixel in between the two. In the new image, the apparent resolution becomes 0.65×0.65 mm with zero filling, but the nominal resolution remains at 1.3×1.3 mm.

Zero filling is commonly used to increase the image matrix size in the phase-encoding direction or in the partition-encoding direction for 3D scans. In practice, zero-filling with a factor of 2 is used to improve the display resolution. Increasing the zero filling factors beyond 4 provides magnification of the image, but with diminishing returns.

One drawback of zero filling is the increase in reconstruction time due to the increased Fourier transform length. Also larger image files can burden the image archiving system: a 512×512 image requires four times the disk space compared to a 256×256 image. Finally, zero filling can increase the conspicuity of Gibbs ringing artifacts in the MR images due to the rapid signal changes in the high-spatial frequencies. Although zero filling has these minor drawbacks, it is still commonly used on commercial systems due to its computational convenience and the advantage of increasing apparent spatial resolution without a scan time penalty.

Partial Fourier

Partial Fourier acquisition is another method used to reduce acquisition time while maintaining spatial resolution. This technique is based on the fact that if an object is real (vs. complex valued), its Fourier transform (k-space) has a particular symmetry that reflects the relationship between the real and imaginary components. This symmetry is referred to as Hermitian conjugate symmetry, in which the data located diagonally from each other across the origin of k-space have identical amplitudes but opposite phases. In Fig. 4.7, point A and point B are located symmetrically across the k-space center. If point A is a complex number with its value equals to $a+bi$, where a is its real number and b is its imaginary number, and then based on the Hermitian conjugate symmetry, point B is known to be $a-bi$. Mathematically, Hermitian 2D k-space data obeys the equation (Eq. 4.6):

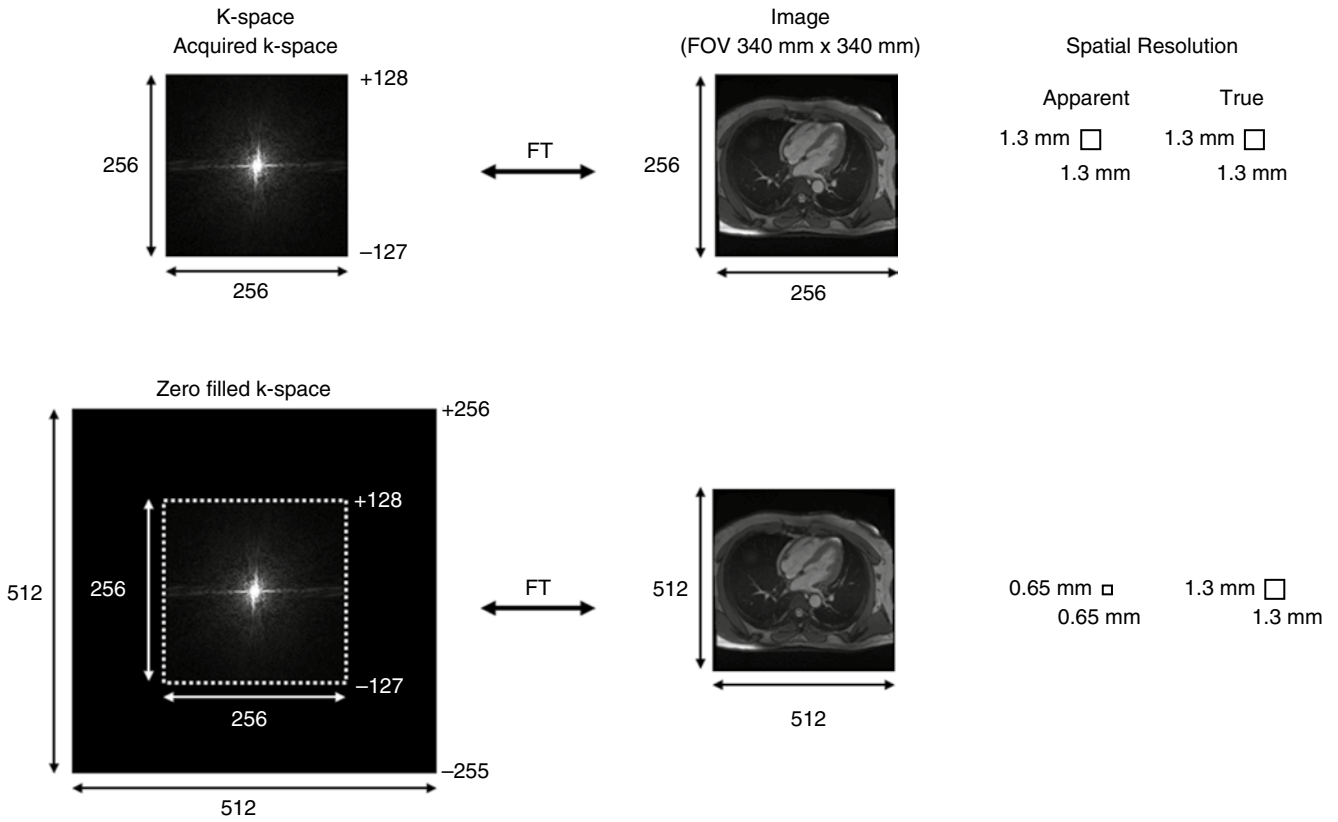


Fig. 4.6 Zero filling of an imaging matrix of 256×256–512×512 and its effect in image interpolation. The apparent spatial resolution of the reconstructed image improves by a factor of 2 due to interpolation, but the nominal spatial resolution does not change

$$S(-k_x, -k_y) = S^*(k_x, k_y) \tag{4.6}$$

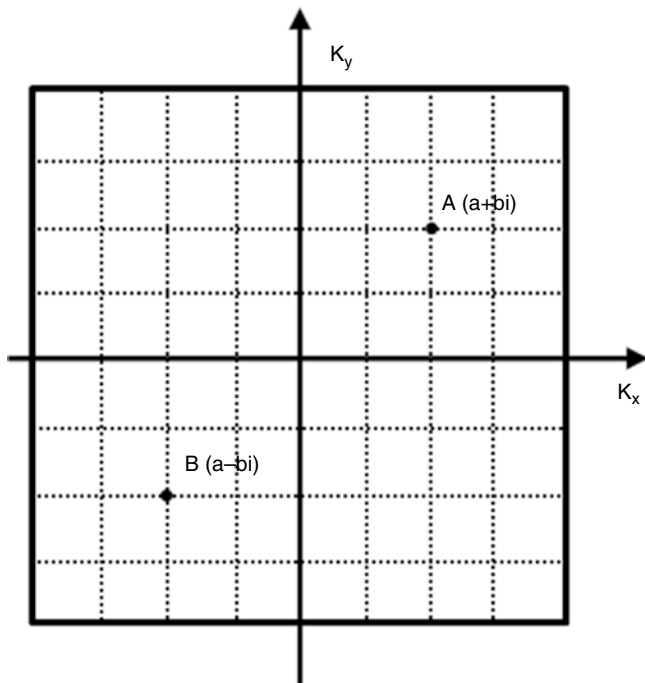
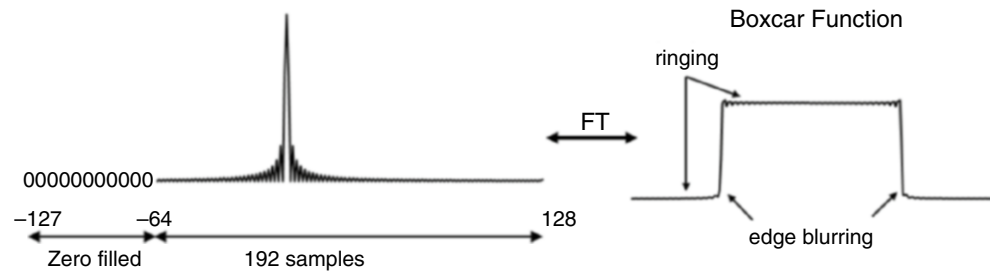


Fig. 4.7 Hermitian conjugate symmetry of k-space. Point A and point B are located diagonally from each other across the k-space center. If point A is a complex number with its value equals to $a+bi$, where a is its real number and b is its imaginary number, and then based on the Hermitian conjugate symmetry, point B is known to be $a-bi$

where $*$ denotes complex conjugation. As the result, theoretically, to reconstruct an image of a real object, only one half of k-space is needed, while the other half can be synthesized based on Hermitian symmetry. However, in MR imaging, unwanted phase shifts resulting from motion, B_0 and B_1 inhomogeneities, eddy currents, and hardware delays, cause the reconstructed images to be complex (real and imaginary parts), instead of strictly real; as a result, the Hermitian conjugate symmetry is no longer perfect.

Partial Fourier acquisition takes advantage of Hermitian conjugate symmetry to collect data asymmetrically around the center of the k-space. One half of k-space is collected completely, while the other half of k-space is only partially filled. Collection of partial k-space can be implemented in either the frequency-encoding or the phase-encoding direction. Partial Fourier acquisition in the frequency-encoding direction is called *fractional echo*, or *partial echo*, or *asymmetric echo* sampling. Its primary advantages are reduced TE, and also reduced frequency encoding gradient moment, which can reduce flow and motion artifacts. Partial Fourier in the phase-encoding direction is often called partial NEX (number of excitations). Its primary advantage is reduced total scan time. Similarly, partial Fourier can be applied in the partition-encoding direction for 3D scans.

Fig. 4.8 Zero filling reconstruction in partial Fourier acquisition



The partial Fourier fraction, defined as the ratio between the partially acquired k-space data size and the full k-space data size, can be used to characterize the k-space acquisition in partial Fourier. For example, a full Fourier acquisition has a matrix size of 256. A partial Fourier acquisition in the phase-encoding direction may only acquire 192 phase-encoding lines asymmetrically with respect to the center of the k-space. One hundred twenty-eight lines are fully sampled in one half of k-space, while only 64 lines are sampled in the other half of the k-space; this results in a partial Fourier fraction of 0.75 (192/256). In practice, we always sample at least slightly more than one-half of k-space, despite the common use of the term “half-Fourier acquisition” to mean any partial Fourier sampling. For example, in Half-Fourier Acquisition Single-shot Turbo spin Echo imaging (HASTE), typically at least eight lines of data are acquired on the undersampled side of k-space.

Zero filling is the simplest way to reconstruct data acquired with partial Fourier. It is implemented by substituting zeros for the uncollected portion of k-space data, followed by conventional Fourier transform reconstruction. The process is demonstrated in Fig. 4.8. In this example, each line of k-space would normally contain 256 data points, 128 on either side of the center peak. The right side of the k-space is fully sampled, while only 64 out of 128 points on the left side are sampled, and the missing samples are filled with zeros. After zero filling, the standard Fourier transform can be used. The advantage of zero filling is that it gives a relatively faithful representation of the object over the low spatial-frequency range. The phase of most large structures is therefore accurate and allows zero filling to be used for phase-sensitive reconstruction, but because some of the signal power is lost at higher spatial frequencies, zero filling introduces blurring and reduces spatial resolution. Other advanced methods, such as Homodyne reconstruction [2], or iterative partial Fourier reconstruction such as Projection onto Convex Sets, POCS [3], exploit the Hermitian conjugate symmetry of k-space to estimate the missing data. Those methods use a phase map generated from the fully sampled central region of k-space to correct for phase errors produced by the reconstruction of incomplete k-space data. Compared with zero filling, these methods do a better job of preserving the true spatial resolution, but add some computational complexity and reconstruction time.

When k-space is sampled using partial Fourier and zero filled, the true spatial resolution becomes more difficult to

determine. The true spatial resolution depends on the degree of asymmetry, i.e., how much data was skipped. However, for the same number of sample points, partial Fourier with zero filling generally improves the spatial resolution compared with symmetric sampling at the expense of SNR. This effect is demonstrated using a resolution phantom in Fig. 4.9. The image has an FOV of 384 mm. Symmetric sampling collects 384 phase encoding lines symmetrically to the center of k-space, i.e., 192 points on each side, generating an image with a true spatial resolution of 1 mm square. If only half of the k-space is acquired (partial Fourier fraction of 0.5), the true spatial resolution is expected to be between 1 and 2 mm in the phase-encoding direction. Compared to symmetric sampling with 96 points on each side of the k-space and a spatial resolution of 2 mm along the phase-encoding direction, partial Fourier improves spatial resolution.

Temporal Resolution

Introduction

In general terms, temporal resolution can be defined as the “*precision of a measurement with respect to time*” [4]. In medical imaging, temporal resolution is a fundamental parameter that defines our ability to evaluate dynamic processes. Functional MRI [5] aims to capture dynamic changes in blood oxygenation levels in the brain to analyze neural activity. Cine cardiac MRI captures the movement of the heart to assess cardiac function. Perfusion MRI captures the dynamic changes in image intensity following injection of contrast agent. Flow imaging measures blood flow dynamics. All of these various applications have a basic requirement in common; sufficient temporal resolution is needed to evaluate the dynamic physiological process of interest [6–8].

For cardiac MRI, the required temporal resolution could be defined as the shortest time per temporal frame required to capture cardiac dynamics. However, this is somewhat ambiguous as it could potentially be defined by the number of frames displayed per second, or by the acquisition time required to gather enough data to reconstruct one single image. In practice, temporal resolution in MRI can be difficult to define precisely for a particular acquisition. Going back to the general definition for temporal resolution, it is clear that higher temporal resolution should allow us to

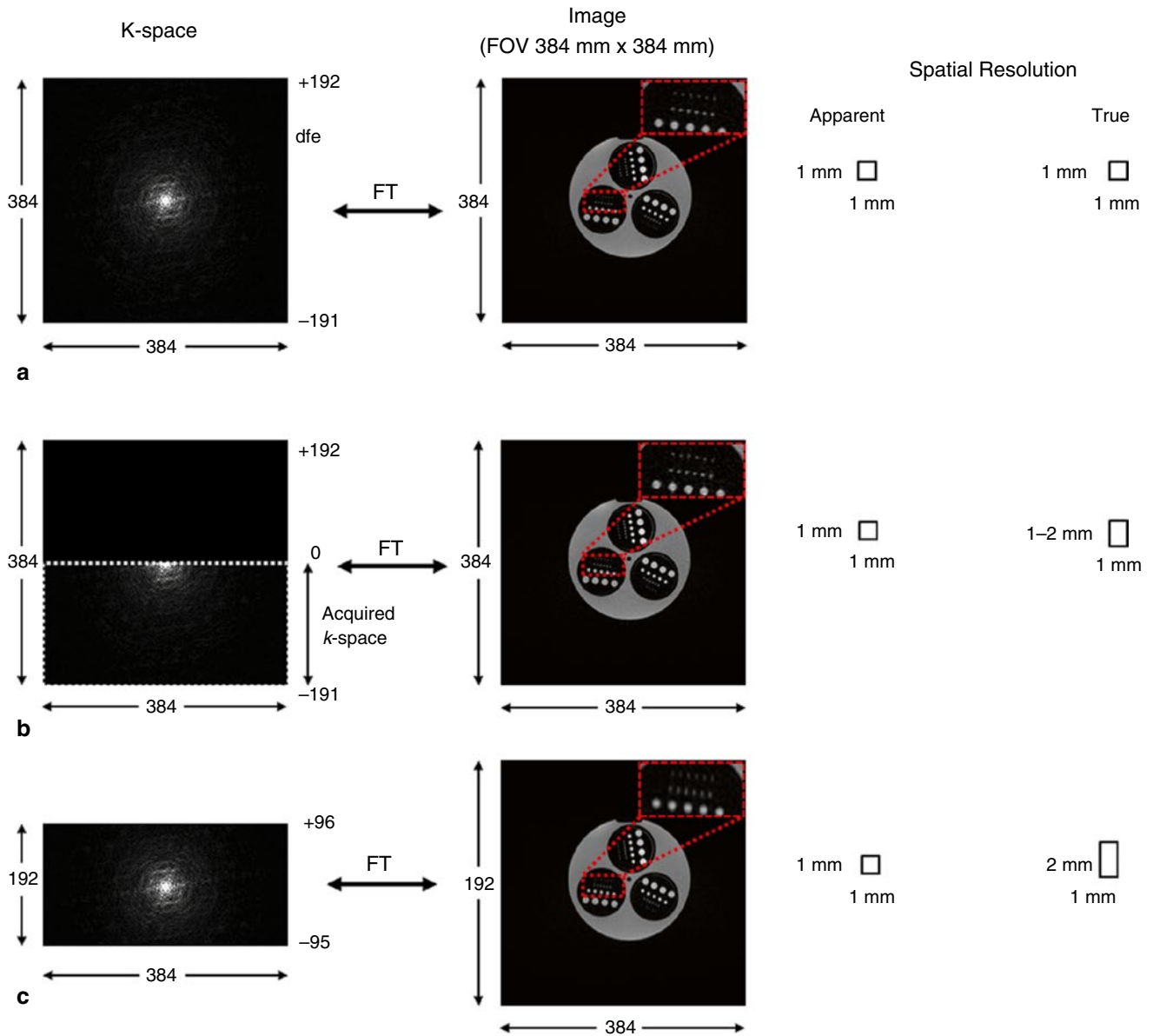


Fig. 4.9 The apparent and true spatial resolution of symmetric sampling and partial Fourier sampling. (a) 384 lines of k-space were acquired symmetrically to the center of k-space, resulting 1 mm of apparent and true spatial resolution. (b) 192 lines of k-space were acquired to fill only half of the k-space. The apparent spatial resolution in the phase-encoding direction is still 1 mm, but the true spatial resolu-

tion is expected to be between 1 and 2 mm due to partial Fourier acquisition. (c) 192 lines of k-space were acquired symmetrically to the center of k-space. Compared to (b), the same number of lines was acquired, but the true spatial resolution is now 2 mm in the phase-encoding direction

better distinguish motion without blurring. For cardiac cine MRI, the SCMR guidelines [9] suggest at least 50 ms temporal resolution for a nominal 1,000 ms R-to-R (RR) interval, which is equivalent to 20 frames per second.

Various image acquisition strategies have been used to improve temporal resolution for cardiac MRI. Some of these methods aim to improve the number of frames displayed per second (apparent temporal resolution) while keeping the acquisition times intact; others aim to decrease the acquisition time per frame (real temporal resolution). In the following sections, the aforementioned imaging methods

will be described in detail and their effects on apparent and real temporal resolutions will be illustrated. Due to difficulties visualizing the effects of temporal resolution on still images, video files from in-vivo cardiac scans covering different scenarios are provided.

View-Sharing

Temporally adjacent k-space frames tend to share a significant amount of information because many of the features in

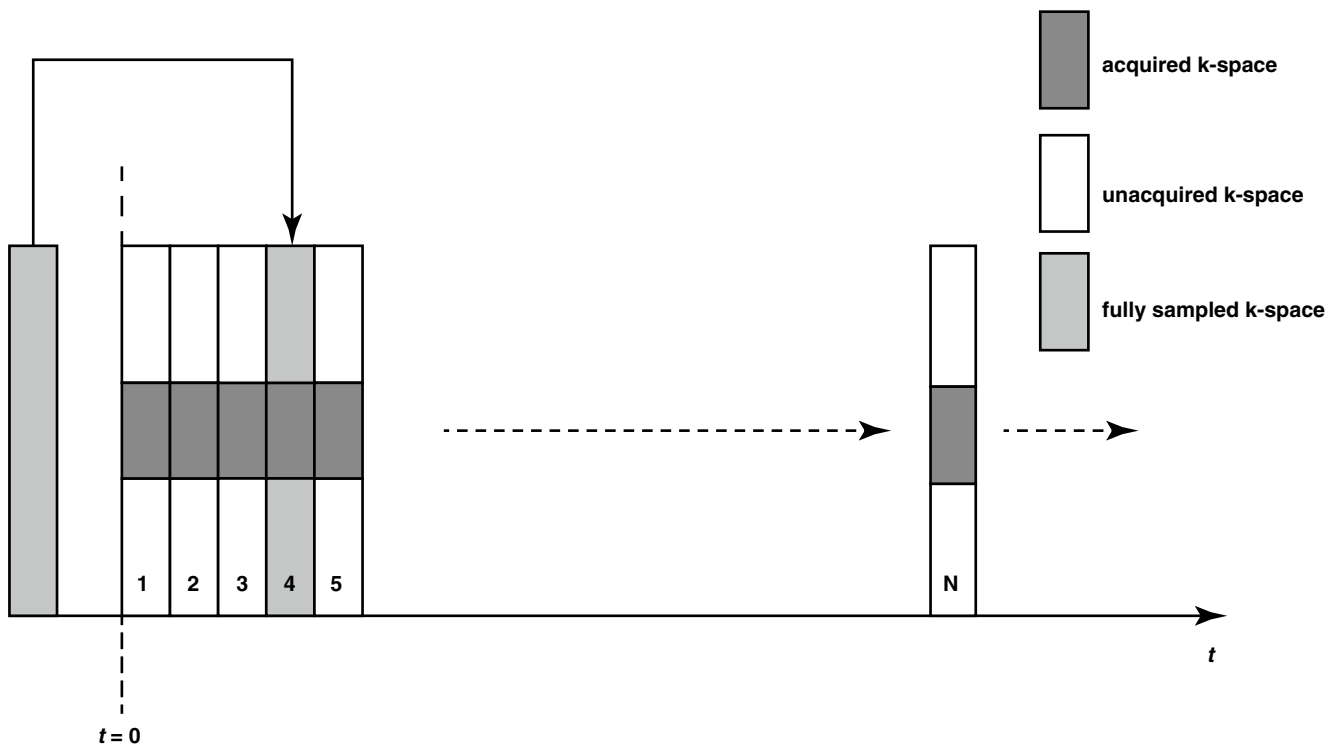


Fig. 4.10 Keyhole method. Data are partially acquired; for each frame, only a central portion of k-space is sampled. Outer k-space lines are filled using the fully sampled reference data acquired previously

sequential images remain unchanged. Therefore, in theory one could partially acquire each frame and recover the missing information from the adjacent frames. This strategy is broadly termed view-sharing [10]. View sharing improves the apparent temporal resolution by increasing image refresh rate; however, real temporal resolution may remain unchanged since the temporal information in the reconstructed images depends on the temporal window used to acquire the data. Please refer to Videos 4.1 (standard acquisition) and 4.2 (view-shared acquisition) to visualize the differences.

Over the years, various methods based on view-sharing principles had been presented; such as keyhole [11], blocked regional interpolation scheme for k-space (BRISK) [12], cardiac triggered phase-contrast examinations [13, 14], Continuous update with random encoding (CURE) [15] and TWIST [16].

Keyhole

The keyhole method dynamically acquires only a small portion of k-space for each reconstructed frame and fills the missing information from a fully sampled static reference image. Since some dynamic processes such as first-pass contrast enhancement are mostly represented by low-frequency information, central k-space lines are reacquired for each reconstructed frame. In practice, a factor of four acceleration (i.e., dynamically sampling only 25 % of k-space) may be

achieved. The unacquired high spatial frequency content in each frame is filled in using data from a previously acquired fully sampled reference frame¹ as depicted in Fig. 4.10. The choice of the k-space area to acquire has profound effects on image quality. Spraggins [17] showed that if the dynamic object is much smaller than the dynamically updated k-space region can depict, image intensity cannot be correctly estimated.

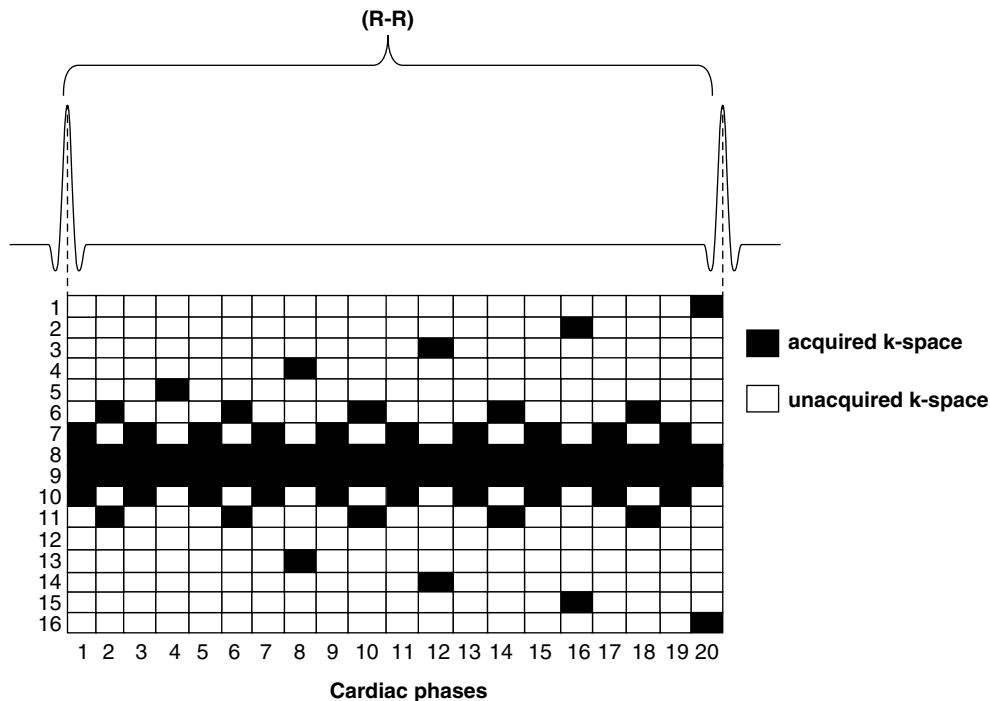
The most straightforward reconstruction scheme for a keyhole acquisition is to directly copy the missing high spatial frequency k-space content directly from the reference data (Eq. 4.7):

$$S_{full}(p) \begin{cases} S_k(p), & p \in K_A \\ S_{ref}(p), & p \notin K_A \end{cases} \quad (4.7)$$

Where S_{full} represents the full k-space, S_k represents keyhole k-space, and S_{ref} represents reference k-space frame, p is a specific phase encoding line, and K_A is the keyhole area acquired: missing phase encoding lines are directly copied from the reference frame to the keyhole frame to obtain the full k-space data.

¹For some applications, the reference frame may be acquired during or at the end of the actual acquisition.

Fig. 4.11 BRISK method. For each cardiac phase, central k-space is fully sampled. High spatial frequency content (outer k-space) is partially sampled in a temporally interleaved fashion; non-sampled k-space portions are estimated with Fourier interpolation of the acquired data



An alternative approach, reduced-encoding imaging by generalized-series reconstruction (RIGR), was presented by Webb et al. [18]. In this method the high spatial frequency information in the reconstructed image is forced to be continuous with the acquired low-frequency content to improve image quality.

While the apparent temporal resolution for keyhole methods can be fairly high, the real temporal resolution is still low. Despite high image quality, these methods may excessively smooth out some kinetic information due to large temporal footprint used for data acquisition, especially in smaller anatomical structures that are represented more strongly by outer lines of k-space [19].

BRISK

The Block Regional Interpolation Scheme for k-space (BRISK) [12] method extends the basic keyhole concept to shorten single-shot 2D cardiac MRI scans. Let N_{phases} depict the number of cardiac phases spanning one RR interval; in a single-shot acquisition, this would equal the number of consecutive k-space frames to acquire. However, fully sampling each k-space frame with high spatial resolution would typically result in temporal resolution so poor that it would be difficult or impossible to visualize cardiac motion. BRISK fully samples central k-space in each frame and partially samples outer k-space in an interleaved fashion as shown in Fig. 4.11. Subsequently, unsampled k-space locations are estimated by Fourier interpolation across time.

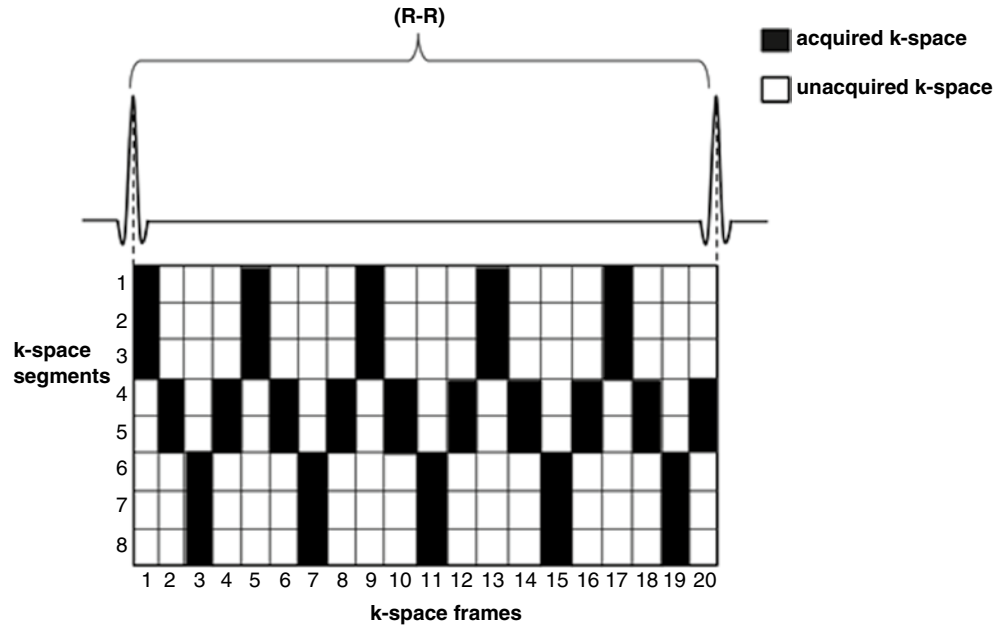
View-Sharing in Phase-Contrast Imaging

In phase-contrast imaging, bipolar encoding gradients are applied to differentiate moving spins from stationary spins along the desired direction. Two frames are acquired with alternating bipolar gradients; the effect of these bipolar gradients is to impart a phase shift on the moving spins that is proportional to velocity, while stationary spins remain unaffected. A pixelwise map of tissue and blood velocity acquired with good temporal resolution can be used to evaluate blood vessels and heart valves.

Temporal resolution is extremely important to properly resolve flow dynamics and to determine peak velocity. However, as is generally the case, balancing spatial resolution requirements with good temporal resolution can be challenging. Markl et al. [13], and Lin et al. [14], described different view-sharing concepts that can be applied to phase contrast imaging to improve spatial and/or temporal resolution.

Markl et al. analyzed the effects of view-sharing on phase contrast imaging strategies with more frequent sampling of the central k-space (Fig. 4.12). Based on the assumption that the flow dynamics are primarily presented by central k-space data, higher spatial frequency k-space lines were sampled less frequently and the missing data filled by view-sharing. This method achieved a 37.5 % increase in data acquisition performance and showed that while flow dynamics could be captured with great accuracy by properly adjusting the sampling frequency of the central k-space, peak velocities could

Fig. 4.12 Phase contrast imaging with view sharing. Central k-space is sampled every frame, while outer k-space is sampled less frequently in an alternating fashion. With each central k-space acquisition, an image is reconstructed by borrowing outer k-space data from the previous and next k-space frames



be underestimated in smaller vessels by about 20 % due to poor real temporal resolution.

Lin et al. proposed an alternative view-sharing approach for real-time phase-contrast imaging [14]. Unlike conventional view-sharing methods where k-space data are shared in between frames, in this scheme alternating (positive/negative) velocity encodings are shared. Positive (+) and negative (-) velocity encodings are alternated for each frame. The combination of any neighbor pair of acquisitions, either (+,-) or (-,+), provides updated velocity information. This method does not apply k-space interpolation to fill the missing information, and no specific k-space sampling scheme is required; it can be used with virtually any acquisition strategy. Since the velocity information is updated with every new frame rather than waiting for two full frames, the accuracy of peak velocity estimations is improved. This phase contrast imaging technique is depicted in Fig. 4.13.

This method improves image display rates without sacrificing dynamic content: only velocity encodings are shared and k-space data are left intact. Since alternating velocity encodings are used, each frame contains fresh velocity information. However, similarly to the previous method, real temporal resolution is only half of the apparent temporal resolution since two full k-space frames are required to reconstruct each image.

CURE

The pseudo-random k-space acquisition scheme dubbed CURE, proposed by Parrish et al. [15] to improve temporal resolution for dynamic 2D applications such as first-pass perfusion imaging. This method is similar to keyhole

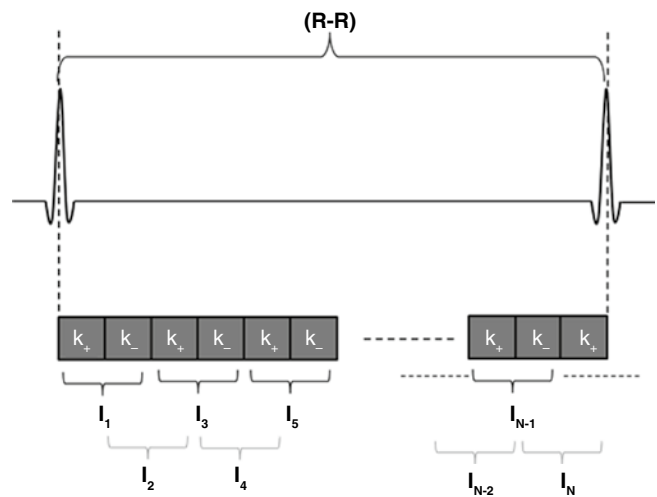
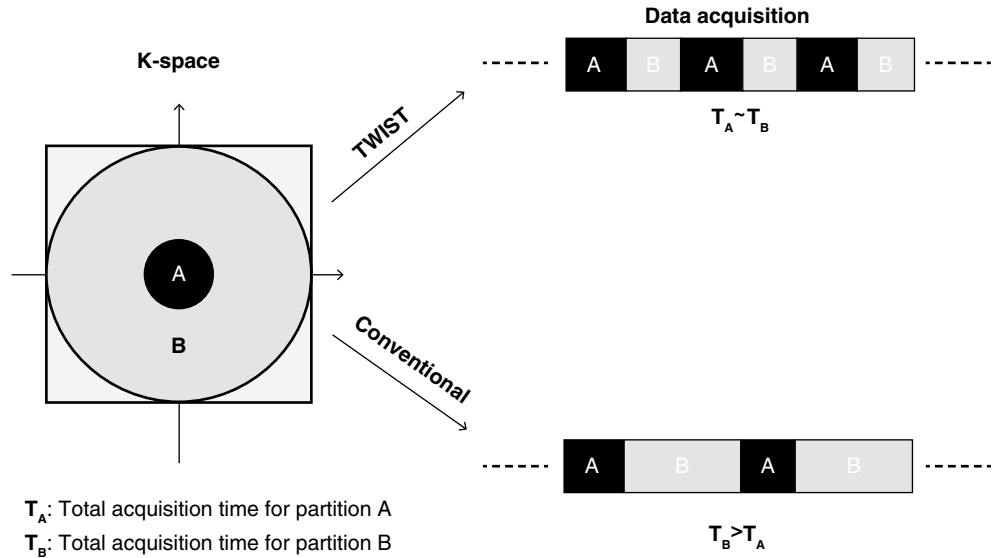


Fig. 4.13 Real-time phase contrast imaging with view sharing {Lin}. Positive (+) and negative (-) velocity encoding gradients are alternated for each frame. New velocity information is obtained from data acquired with gradient pairs of (+,-) or (-,+). This method does not share k-space data between frames; only alternating (positive/negative) velocity encodings are shared

methods since k-space data are shared across time. However, authors proposed a new sampling scheme where phase encoding steps are acquired in a randomized order, unlike the orderly and repetitive approaches used with other view-sharing methods. Central k-space is sampled more frequently than the outer k-space. An ultra-fast gradient echo sequence with no magnetization preparation is used to obtain T₁ weighted images.

Fig. 4.14 Schematic of the TWIST method. K-space is divided into two distinct regions, (a, b). (a) Represents low-frequency content (central k-space) that defines image contrast and (b) depicts the high-frequency content (outer k-space) that controls spatial resolution in the image. Regions (a, b) are tuned to attain desired temporal and spatial resolutions. (a) is sampled more frequently than (b). A variable sampling rate is used to acquire region (b) in multiple steps; each new acquisition in region (b) completes previously un-acquired samples in region (b). Therefore, fully sampled k-space is obtained by sharing data between a region (a) and two adjacent (b) regions



Data acquisition is performed as a stream with continuous excitation and phase-encoding is performed pseudo-randomly. Once the data acquisition is completed, a reconstruction window is defined that corresponds to the desired temporal resolution. The center of the reconstruction window is placed at the desired temporal location and k-space information is filled using data from the outer parts of the window. Since the low-frequency content is sampled more often, multiple instances of the same phase encoding line from the center of the k-space could be encountered in the reconstruction window. In such cases, the phase-encoding line closest to the center of the window is used, and the others were discarded. By moving the reconstruction window along the data stream, multiple images could be reconstructed. This method has been shown to be more accurate in depicting a dynamic process than the standard keyhole methods.

CURE was adopted and optimized for 3D dynamic angiography in 2006 by Laub et al. combining it with parallel MRI for improved temporal resolution and calling it “time-resolved angiography with stochastic trajectories (TWIST)” [16].

The TWIST method divides k-space into two distinct regions, A and B. A represents central k-space that defines image contrast and B depicts outer k-space that controls spatial resolution. The idea is to tune these regions to achieve a reasonable compromise between temporal and spatial resolution. A is sampled more frequently than B; a pseudo-random acquisition strategy is used to acquire data where all k-space samples are sorted by their radial distance and their azimuthal angle relative to the in-plane k-space center. A variable sampling rate is used to acquire region B in multiple steps; each new acquisition in region B completes previously un-acquired samples (Fig. 4.14). Therefore, a fully sampled k-space can be obtained by sharing data between region A and the two B regions acquired before

and after. Let T_{acq}^A denote the time spent to acquire region A, and $T_{acq}^B(i)$ region B(i) where $i \in \{1,2\}$. Then real temporal resolution would be $T_{res}^{real} = T_{acq}^A + \sum_i T_{acq}^B(i)$, and the apparent resolution $T_{res}^{real} = T_{acq}^A + T_{acq}^B(i)$. Hence, the real temporal resolution is actually lower than the apparent resolution, similar to other view-sharing techniques.

Segmented Imaging

Single-shot imaging strategies must necessarily reach some compromise between temporal and spatial resolutions for dynamic imaging, especially for cardiac cine imaging. With single-shot or real-time techniques, even with modern acceleration methods it is generally not possible to achieve high spatial resolution without sacrificing temporal resolution, or vice versa. Instead, k-space data are typically acquired in segments of several lines in each of multiple cardiac cycles and synchronized with cardiac motion using an ECG trigger signal. The multiple segments are then combined into fully sampled k-space frames to generate some predefined number of temporal frames (cardiac phases) spanning one cardiac cycle. This method is called segmented imaging [20]. Note that breath-holding is generally required, otherwise respiratory motion of the heart between cardiac cycles can lead to artifacts (see Fig. 4.15; still images in Fig. 4.15 are from Videos 4.3 (free breathing segmented) and 4.4 (breath-held segmented)).

In segmented imaging, the number of phase encodings acquired per k-space segment is generally referred to as the number of views per segment (NVS). Consider an image

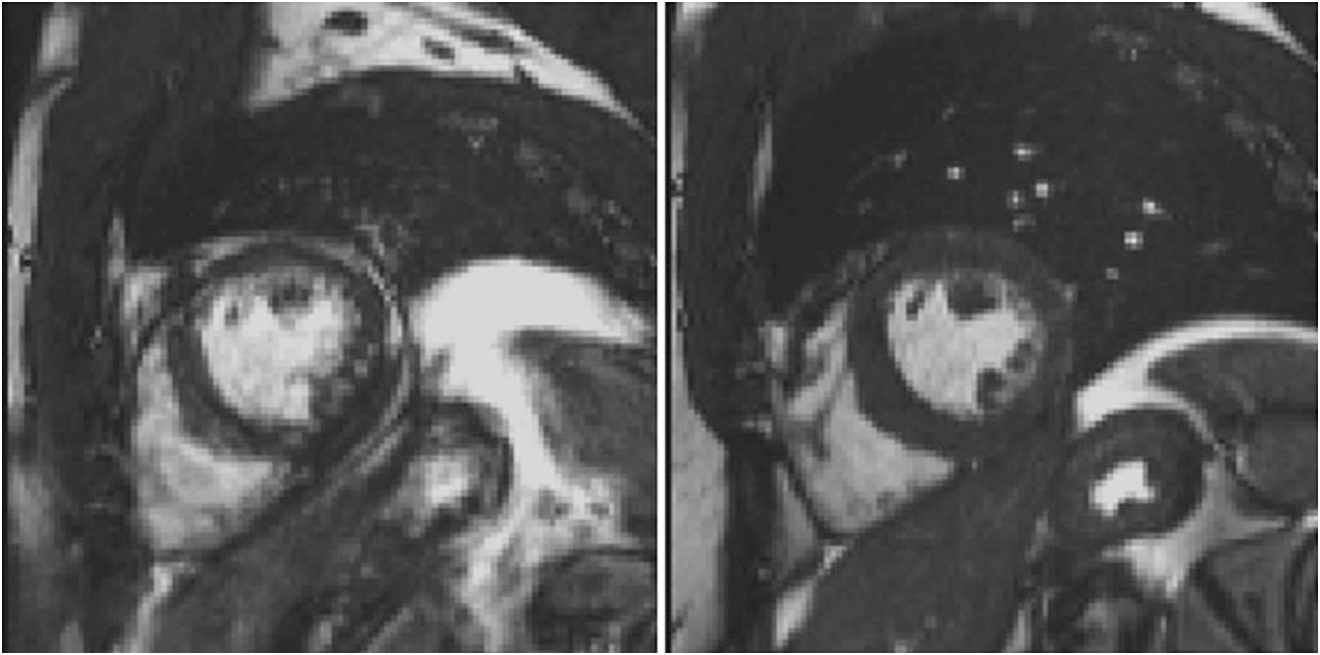


Fig. 4.15 Segmented CINE images acquired with (*right*) and without (*left*) breath-holding representing the same cardiac phase. In the *left*, image quality is highly degraded due to respiratory motion. Since segments

for the same cardiac phase are acquired during different respiratory positions, the image is corrupted by motion artifacts. On the other hand, breath-held images are free of respiratory motion, and thus are artifact free

matrix of 192×192 , 192 phase encoding lines would be required to fill all of k-space. If NVS is 12, $192/12 = 16$ segments would be required to reconstruct one cardiac phase. Since each segment of 12 views is acquired in a different heartbeat, 16 R-R intervals in total would be required to complete the acquisition. Moreover the breath-hold duration depends on the heart rate of the patient; for a patient with a heart rate of 80 beats per minute (750 ms per RR interval), a 12 s breath-hold will be required. The apparent temporal resolution of a segmented scan is defined by $(NVS \times TR)$, where TR stands for the repetition time.

ECG gating (or synchronization) during segmented imaging can be accomplished by two different methods: prospective and retrospective gating. With the prospective approach, data acquisition is triggered to start upon detection of the ECG R-wave, and usually covers 80–90 % of each cardiac cycle (see Fig. 4.16). End diastole is not fully covered to allow some variation in R-R interval and detection of the next trigger pulse. Once all the data from all the cardiac cycles are acquired, each cardiac phase is reconstructed. Due to limited RR coverage, end diastole is not well represented with the prospective gating strategy. Additionally, since the heart rate varies during data acquisition, improperly selected delay parameters may lead to skipped heart-beats, or inadequate diastolic coverage.

On the other hand, retrospective gating continuously acquires data though the whole cardiac cycle with ECG timing information stored in the header of the raw data. Once the acquisition finishes, phase encoding lines are

retrospectively binned to their corresponding cardiac phases using ECG timing data, and images are reconstructed. Retrospective ECG gating allows the reconstruction of any number of cardiac phases; therefore, the apparent temporal resolution is flexible. By increasing the number of reconstructed phases, the frame rate can be improved; however, the real temporal resolution in a retrospectively gated acquisition is still defined by the time spent acquiring one segment of k-space data, i.e., by $(NVS \times TR)$, similar to prospective reconstruction. Both prospective and retrospective segmented imaging acquisitions are represented in Fig. 4.16.

Segmented cine imaging is the gold standard for cardiac function assessment. It provides both good spatial and temporal resolution, although it requires the patient to hold their breath, and regular cardiac rhythm, and thus is not feasible in a large percentage of cardiac patients. For those cases, real-time cardiac MRI is a viable alternative.

Real-Time Imaging

In cardiac MRI, real-time imaging refers to continuous, single-shot data acquisition that is fast enough to capture each cardiac phase without the need for breath-holding, respiratory gating, or ECG synchronization (Fig. 4.17).

Cartesian sampling is preferred for real-time imaging, and generally for all CMR techniques, because (i) it provides for simple and fast image reconstructions, (ii) it supports the

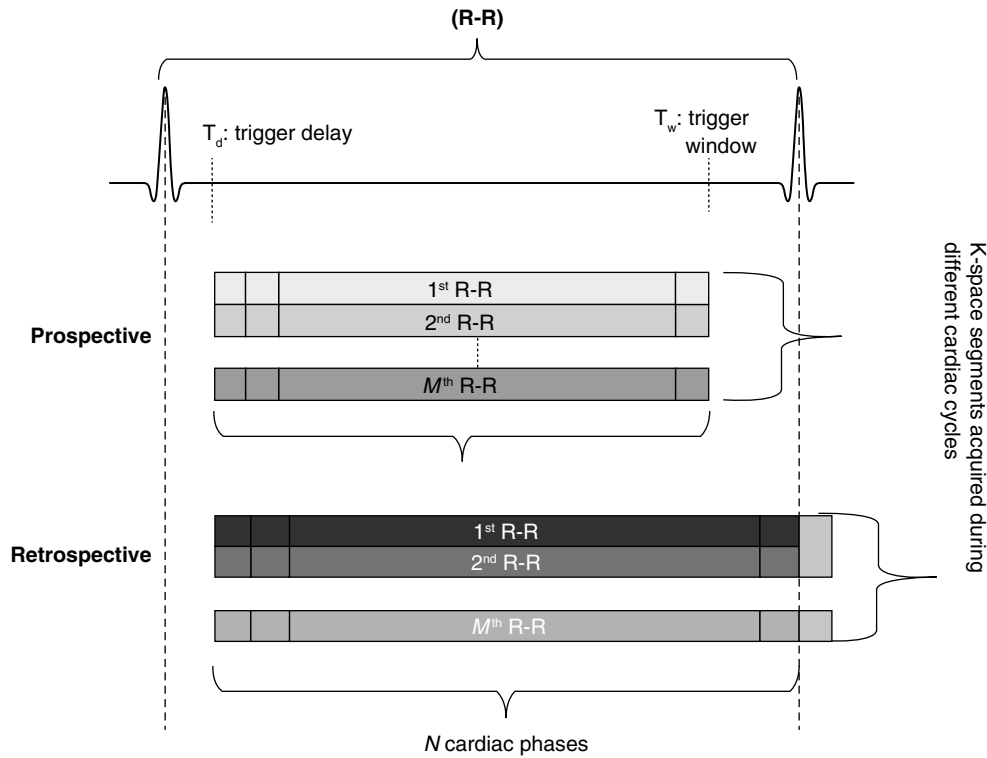
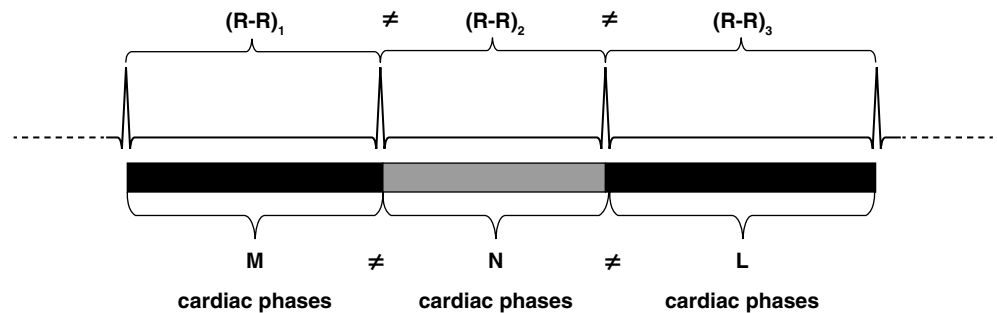


Fig. 4.16 Prospective and retrospective segmented cine imaging. Data are acquired in a segmented fashion during breath-holding across multiple R-R intervals; during each R-R interval, a k-space segment is filled for each cardiac phase. *Prospective triggering*: each cardiac phase is reconstructed from fully-sampled k-space data obtained by merging k-space segments acquired during different cardiac cycles. The number of cardiac phases to acquire and reconstruct are identical, and are fixed prior to acquisition. End diastole is not entirely covered with prospective triggering, and therefore cine imaging is typically performed using

retrospective gating. *Retrospective gating*: k-space is sampled continuously in a segmented fashion. At the end of the acquisition, k-space data are binned according to each R-R interval and the desired number of cardiac phases (temporal frames), and images are reconstructed. Retrospective gating allows for the reconstruction of any number of phases from a single acquisition. The effects of varying the number of phases retrospectively reconstructed from the same data can be visualized in Videos 4.5 (6 phases), 4.6 (12 phases), 4.7 (25 phases), and 4.8 (50 phases)

Fig. 4.17 Real-time MRI. Data are continuously acquired as a series of single-shot images; data may or may not be shared between temporal frames. There need not be any synchronization of the data acquisition with the ECG, although an R-wave trigger may be used to start the scan that can run for any predefined length of time



use of rectangular field-of-view (FOV) to improve temporal resolution, (iii) and there is general knowledge of common image artifacts and limitations. It has been shown that non-Cartesian acquisition strategies provide faster and more efficient sampling of k-space, especially combined with parallel imaging techniques [21–26]. However, reconstruction of such data sets is computationally more demanding, and image artifacts are less familiar and may be harder to evaluate than with standard Cartesian sampling. With the current

advances in computer hardware and optimized implementations, image reconstruction performance is improving for non-Cartesian imaging methods [27–30]. However, clinical evaluation of these methods is still limited; hence, Cartesian sampling remains the mainstay for CMR applications.

Since real-time cine image acquisition is performed in a single-shot often without data sharing between adjacent frames, real-time MRI provides true temporal resolution; one k-space frame is used to reconstruct only one imaging

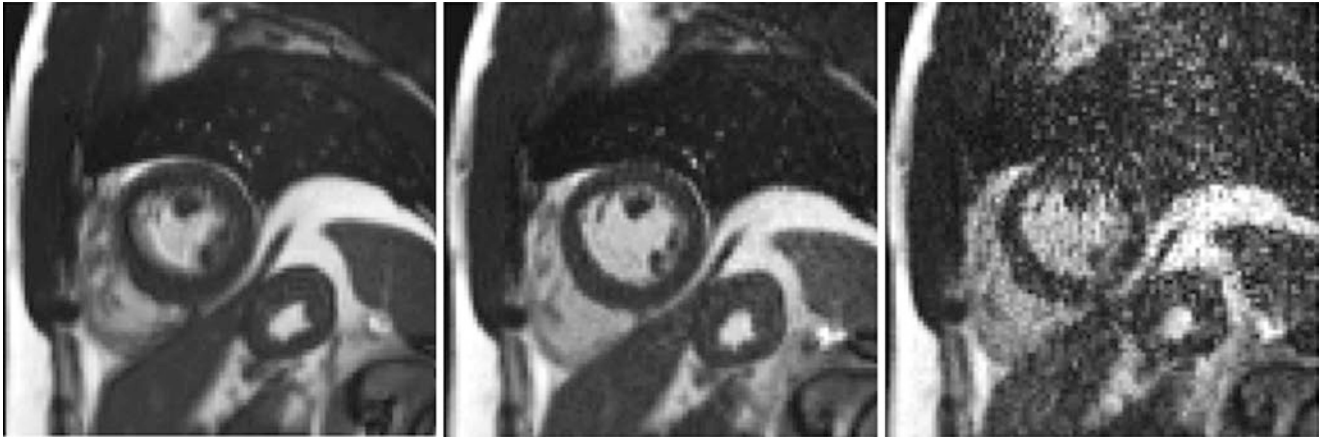


Fig. 4.18 Real-time cardiac short-axis images. *Left*: no parallel imaging (reference frame). *Middle*: threefold acceleration with parallel imaging. *Right*: fivefold acceleration with parallel imaging. Image on the *left* is blurred due to low temporal resolution, but it has significantly

higher SNR than the parallel imaging counterparts. *Middle* image is noisier, but significantly sharper due to threefold higher temporal resolution. Image on the *right* is the sharpest due to fivefold increase in temporal resolution, but with very high-degree of SNR loss

frame. The temporal resolution of a real-time image $T_{\text{res}} = \text{TR} \times N_{\text{pe}}$, where N_{pe} is the number of phase encoding lines, and TR is the repetition time, i.e., the time to acquire a single k-space line. Each reconstructed image represents the exact time period of T_{res} ; no temporal information is shared between individual imaging frames. Hence, real-time MRI is capable of realistically depicting the dynamics of cardiac function provided adequate temporal resolution can be achieved. It is possible to incorporate view-sharing approaches into real-time imaging to improve image refresh rate; however, real temporal resolution will remain the same. Please refer to Videos 4.1 (standard real-time) and 4.2 (view-shared real-time with approximately twofold increase in image refresh rates) for visual comparison.

Compared with segmented image acquisition, real-time imaging acquires data in single-shot fashion (i.e., with no data sharing across different heartbeats), and the need for patient breath hold can be eliminated since respiratory motion is negligible within the very short acquisition window. However, this comes at the price of lower spatial and/or temporal resolution.

Cine MRI requires a nominal temporal resolution of approximately 50 ms for accurate assessment of cardiac function. Since the data acquisition time mostly depends on the number of phase encodings, one could reach this goal with real-time MRI (single-shot, ungated data acquisition) by limiting the k-space coverage; for example, using a TR of 2.5 ms, the target temporal resolution can be reached by acquiring only 20 phase encoding lines. While 20 Cartesian phase encoding lines would be grossly insufficient for standard image reconstruction, parallel MRI (pMRI) methods which acquire data with multiple coil elements and undersample k-space in an interleaved fashion provides the means to reconstruct images with sufficient spatial and temporal

resolution to make real-time cine imaging practical. While pMRI methods have been tremendously successful, especially in CMR where the requirements of high temporal resolution and short scan time demand highly efficient data acquisition, the trade-offs of pMRI include decreased signal-to-noise ratio (SNR), and increased artifacts. Figure 4.18 and supplemental videos show examples of the effects of parallel acceleration on temporal resolution. More recently, techniques have been developed to combine pMRI with non-Cartesian trajectories to achieve very high acceleration rates [21–27], and a novel image reconstruction strategy called “compressed sensing” [31, 32] is promising to provide unparalleled acquisition speeds for real-time MRI. However, these subjects are out of the scope of this chapter, and will not be discussed in detail here.

Clinical real-time CMR protocols typically incorporate Cartesian pMRI methods such as (T)GRAPPA [33, 34] and (T)SENSE [35]. By combining rectangular FOV, partial Fourier, and pMRI acceleration, it is possible to obtain a reasonable compromise between temporal and spatial resolution in a real-time acquisition.

Real-time images are acquired in one shot, and the number of cardiac phases (frames) acquired and reconstructed is defined by the operator, typically to span one to three cardiac cycles. As the heart rate may vary due to arrhythmia, each cardiac cycle may contain a different number of phases (frames). Therefore, some practical concerns arise when trying to use real-time images for quantitative evaluation of global cardiac function. One technique uses simple interpolation along the time dimension to generate a predefined number of phases per slice and per heart beat [36], making the data more amenable to post-processing. Images from heart-beats acquired during the desired phase of respiratory motion (typically end expiration) can be selected and used

for data analysis. Interpolation may also help to increase the displayed cine frame rate by improving apparent temporal resolution; however, the real temporal resolution will still be defined by $T_{\text{res}} = \text{TR} \times N_{\text{pe}}$ as mentioned earlier.

Signal-to-Noise Ratio (SNR) and Sources of Noise

In MRI exams, it is always desirable to acquire images that have sufficiently high signal intensity, good image contrast, and adequate spatial resolution. Signal-to-noise ratio (SNR), which reflects signal intensity with respect to the background noise, is one of the most widely used measures to objectively assess the quality of an MR image and is commonly used to assess the performance of different pulse sequences and imaging protocols. High SNR is not only a necessity for good quality images, it can also be traded to improve spatial resolution, temporal resolution, or reduce scan time using various acceleration strategies (e.g., parallel imaging, compressed sensing, partial Fourier). Thus, SNR is often described as the “currency” of CMR, and can be spent to achieve any of a number of imaging goals.

The presence of excessive noise can lead to non-diagnostic MR images. Hoult and Lauterbur [37] elaborately discussed the various sources of noise in MRI in a 1979 paper. Using the fluctuation-dissipation theorem, they concluded that any dissipative medium, including the human body, generates thermally activated random fluctuations that contribute as the principle source of noise in MRI. Hayes and Axel [38] further analyzed SNR and concluded that tissue losses are the dominant source of noise of MRI at high field strength using surface coils. In addition, coil losses also add to total noise, although the contribution is smaller than that from tissue losses. For example, noise can be generated from imperfections in preamplifiers and RF coils. Noise can also originate in connectors between the preamplifier and the radio-frequency receiving electronics. Last but not least, noise can be amplified by suboptimal image reconstruction techniques and implementations.

Factors Affecting SNR

SNR depends on a few factors that cannot be modified by the operator, as well as some other parameters that can be adjusted by the user. Examples of fixed factors affecting SNR include the magnetic field strength, intrinsic relaxation properties of the imaged tissue, physical and physiological conditions of the patient such as body size, weight and heart rate. Ignoring differences in relaxation parameters, the MR signal induced in a receiver coil is proportional to the square of the magnetic field strength, while noise has a linear dependence on the field strength. Combining contributions of field

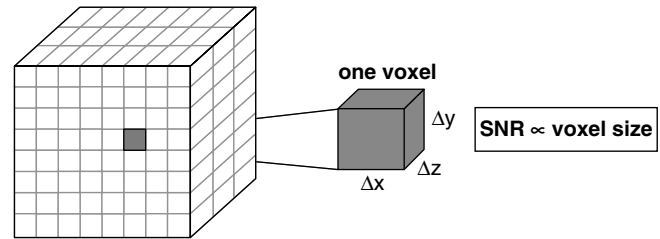


Fig. 4.19 SNR scales linearly with the voxel size in an image which is defined by voxel dimensions in the readout (Δx), phase-encoding (Δy) and slice directions (Δz)

strength to both signal and noise, one would expect SNR to be linearly scaled with the static magnetic field of an MR system; i.e., the SNR is theoretically two times higher at 3.0T as compared to 1.5T. In reality, such theoretical SNR gains are not always realized due to other constraints including changes in tissue relaxation properties and imaging parameters at different field strengths. For example, tissue longitudinal relaxation time (T_1) generally increases with field strength. On the contrary, transverse relaxation time (T_2) and T_2^* can decrease with increasing field strength. Such alterations in relaxation parameters cause deviation from the theoretically linear relationship between SNR and magnetic field strength. In practice, imaging parameters are tailored for specific field strength to account for different relaxation properties, specific absorption rate (SAR), chemical shift and other factors to optimize imaging results.

MR as a non-invasive imaging modality is extremely versatile. Protocol settings can be flexibly adjusted for specific applications to realize desired imaging contrast. With an existing MR system and coil configuration, protocol settings can be adjusted to influence the SNR in a predictable manner. Example imaging parameters affecting SNR include flip angle, imaging matrix size, voxel dimensions, readout bandwidth, and number of signal averages. Macovski [39] generalized that all of these parameters that affect SNR can be grouped into two basic factors: size of individual voxels, and the square root of the acquisition time.

The size of a voxel is governed by the image FOV, matrix size, and slice thickness as described previously; image SNR is inversely proportional to each voxel dimension (Δx , Δy , and Δz). Figure 4.19 illustrates the voxel dimensions in the readout, phase-encoding and partition-encoding directions. Increasing the voxel size, which is equivalent to decreasing spatial resolution, translates into higher SNR.

As described earlier, the spatial resolution determines the size of the smallest structures that can be visualized in an image. Applications that require higher spatial resolution (i.e., smaller voxel size) tend to be starved for SNR. In cardiac MRI, coronary artery imaging typically requires the highest spatial resolution (sub-millimeter voxel size) and SNR sometimes becomes the limiting factor for delineating such fine structures consistently.

$$\begin{aligned} \text{Acquisition time (TA)} = & \\ & \text{TR} \times \text{PE lines} \times \text{NEX (2D case)} \\ & \text{TR} \times \text{PE lines} \times \text{Number of Partitions} \times \text{NEX (3D case)} \end{aligned} \quad \boxed{\text{SNR} \propto \sqrt{\text{TA}}}$$

Fig. 4.20 SNR scales with the square root of the acquisition time (TA). TA is defined by the TR, number of PE lines, number of partitions (3D imaging) and number of averages (NEX)

Imaging acquisition time (TA) is another factor that affects the SNR. TA is determined by the repetition time (TR), and the total number of repetitions. TR is typically defined as the time required to apply RF pulse(s), encoding gradients, the readout module, and additional filling time between these elements. TA is calculated as following for 2D and 3D imaging cases: Fig. 4.20 shows SNR scales with the square root of TA.

These relationships imply that the imaging SNR can be improved by (1) increasing the imaging voxel size (i.e., decreasing spatial resolution), or by (2) increasing the total acquisition time.

An increase of imaging voxel size can be realized by reducing spatial resolution in one or more of the three spatial dimensions, for example by adjusting the slice thickness, FOV, or number of voxels acquired in each specific direction. The following strategies can be used to trade spatial resolution for SNR:

- Decrease the readout resolution by acquiring fewer sample points in each k-space line while keeping the same read FOV, or acquiring the same number of sampled points while increasing the read FOV;
- Decrease the phase-encoding resolution by collecting fewer phase-encoding lines, or increasing the phase-encoding FOV;
- Decrease the slice resolution by increasing the slice thickness (for the 2D case), or decreasing the number of partitions for the same spatial coverage in the partition direction (for the 3D case).

Image acquisition time can be increased to improve SNR by one or more of the following measures:

- Increase TR by decreasing the readout bandwidth, adding dead time within each TR, or using longer RF pulses or slower gradient ramping;
- Acquire more k-space lines by oversampling in the phase-encoding direction or partition-encoding direction;
- Acquire multiple signal averages;
- Use 3D versus 2D imaging to acquire more k-space data.

SNR Measurement

Mathematically, SNR is simply expressed as the ratio between measured signal and noise. However, it is not

trivial to measure image noise precisely in practice in part due to the spatially varying nature of noise. This becomes particularly problematic with the wide adoption of phased-array receiver coils and under-sampling of imaging data using various acceleration techniques such as parallel imaging.

Typically, signal intensity is directly measured from a region of interest in the actual anatomy. For cardiac MRI, blood pool in the ventricle and myocardium are widely selected targets for signal measurement. A few different approaches [40–42] have been proposed for the noise measurement in cardiac imaging; a comprehensive overview of this topic was provided by Kellman and McVeigh [43].

The most commonly used noise measurement approach estimates noise from a background region free of actual tissue [40]. A noise only region (e.g., background air) within the field-of-view is manually selected to calculate the standard deviation of all pixels in a region without signal. This method is easy to implement in practice and the calculation is straightforward using existing images. However, the accuracy of this noise measurement depends on the number of pixels within the user defined region-of-interest (ROI), and often for cardiac images it may not be feasible to define a large ROI free of tissues and/or artifacts. Furthermore, this simple method is not suitable for images acquired with parallel imaging techniques in which the noise distribution is spatially varying. Other alternatives for noise estimation include: subtracting images to cancel the stationary signal and retain noise only images [41], applying spatial differentiation to eliminate signal in homogeneous regions with constant signal intensity [42]. While these methods have some advantages, either highly stationary imaging objects are required, or relatively large regions with little intensity variation are required. Such requirements unfortunately impede their general application in cardiac MRI. Kellman and McVeigh proposed a general method that directly reconstructs images in SNR units with accurate and precise SNR measurement on a per pixel basis. It is applicable to clinical cardiac applications using parallel imaging acquisition and reconstruction. The procedure relies on a pre-scan noise measurement that eliminates the confounding of noise by signal from imaging objects in conventional methods. For this purpose an additional noise measurement and dedicated reconstruction routines are required to optimally scale signal and noise in the reconstruction routine, as well as proper treatment and combination of data from different elements of receiver coil arrays.

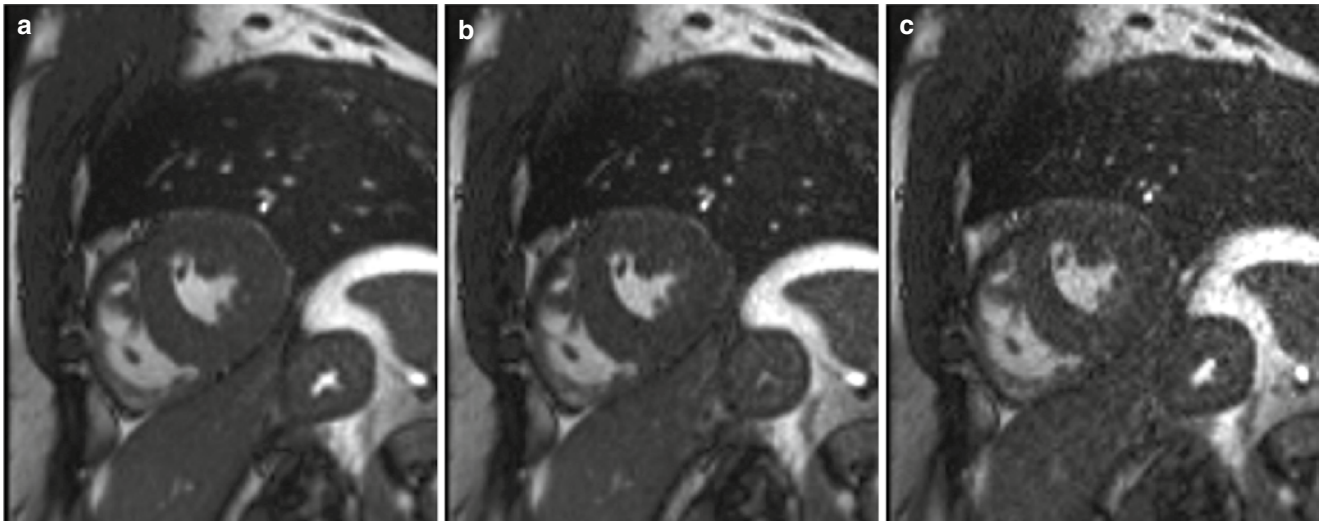


Fig. 4.21 Short-axis images of the heart acquired with identical spatial resolution and decreased imaging time resulting from increased parallel imaging acceleration factor: (a) PAT 2 (TA=4.2 s); (b) PAT 3 (TA=2.8 s); (c) PAT 4 (TA=2.1 s)

Tradeoff Between SNR, Spatial Resolution and Temporal Resolution

The SNR, temporal resolution, spatial resolution and imaging acquisition time are all inter-related. Although it is desirable to collect MR image with high SNR, high spatial and temporal resolution with minimal imaging time, practical issues have to be considered and compromises made to achieve reasonable imaging goals. With fixed scan time, increasing spatial resolution typically leads to decreased SNR and/or temporal resolution. The converse is also true, decreased spatial resolution can be traded for an increase in SNR and/or temporal resolution.

Figure 4.21 shows 1 out of 17 short-axis cine frames acquired in a healthy volunteer illustrating three different parameter combinations. Spatial resolution ($1.8 \times 1.8 \times 6.0 \text{ mm}^3$ voxel) was kept constant and TA was decreased using parallel imaging acceleration factors of 2 (a), 3 (b) and 4 (c), respectively. With identical spatial resolution and decreased imaging time, it is apparent image SNR is decreased from image (a) to (b) to (c).

Figure 4.22 illustrates 1 out of 17 short-axis cine frames. With four times increased spatial resolution from (a) to (b) (voxel size $1.8 \times 1.8 \times 6.0$ vs $0.9 \times 0.9 \times 6.0 \text{ mm}^3$), SNR is substantially decreased in (b) despite two times longer imaging time in (b).

Table 4.1 summarizes the typical tradeoffs between SNR, spatial resolution, acquisition time and spatial coverage. Depending on the specific application and the pertinent clinical questions, appropriate tradeoffs must be managed. In cine scans, for example, short acquisition time and temporal resolution are important; so spatial resolution may be traded in favor of temporal resolution and reduced breath hold duration. For coronary MRI, high spatial resolution is desired so the prolonged acquisition time is typically needed. A whole-heart coronary MRI measurement can take 5–15 min to account for cardiac motion, respiratory motion and sufficiently high spatial resolution.

In summary, SNR, spatial resolution and temporal resolution are all inter-related and can often be exchanged one for the other. Tradeoffs must be made and imaging parameters selected intelligently to make the best compromise based on the goals of the particular imaging application.

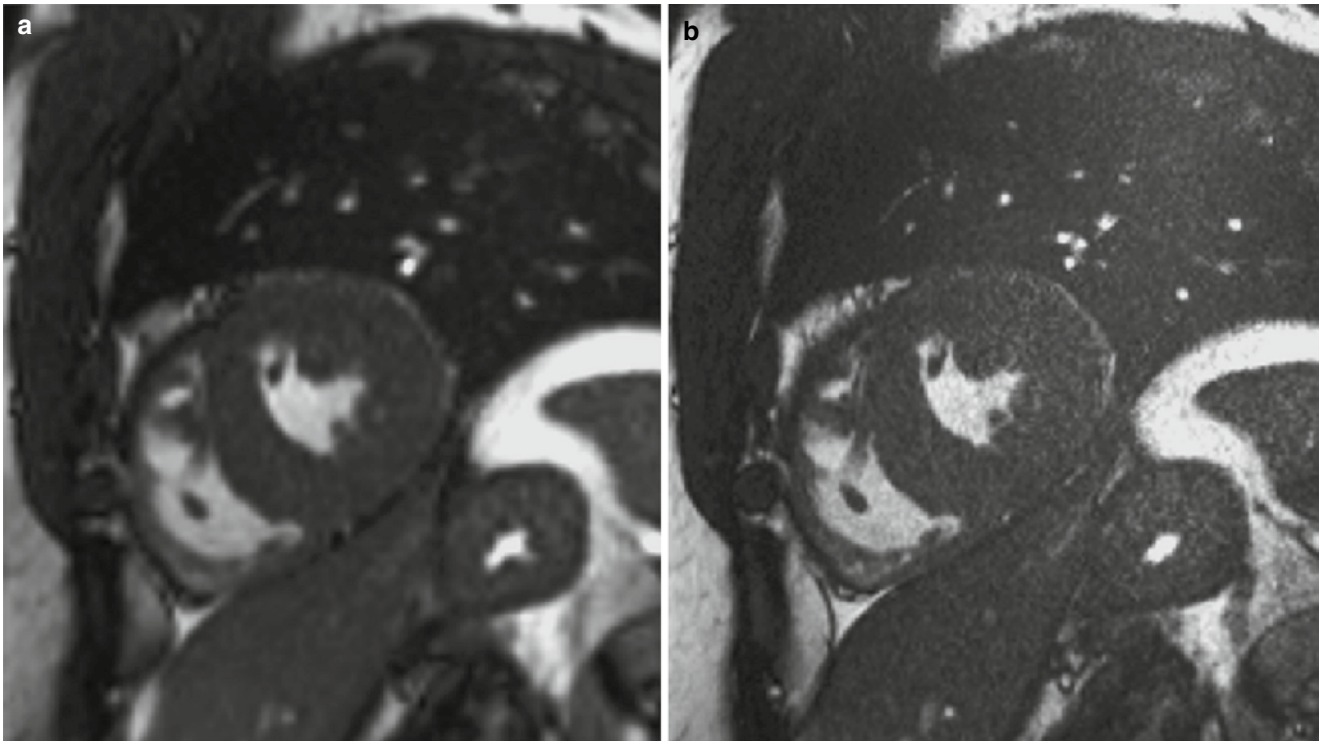


Fig. 4.22 Short-axis images of the heart acquired with fourfold increased spatial resolution in (b) as compared to (a). The SNR is substantially lower in (b) with 4× smaller voxel size despite 2× imaging time than (a) (TA=4.2 s for image a, and 8.4 s for image b)

Table 4.1 Typical tradeoffs among SNR, spatial resolution, acquisition time and spatial coverage

Increase parameters	SNR	Spatial resolution	Acquisition time	Spatial coverage
FOV	+	–	o	+
FOV and matrix size	+	o	+	+
Slice thickness	+	–	o	+
TR	+	o	+	o
TE	–	o	o	o
NEX	+	o	+	o
Matrix size	–	+	+	o
Readout BW	–	o	–	o
Partial Fourier	–	o	–	o
Asymmetric echo	–	o	–	o
Field strength	+	o	o	o
Phased-array coil	+	o	o	o

Icons in the table represent responses (+ increase; – decrease; o no difference) of these factors to the increase of parameters in the first column of the table

References

- Harris FJ. On the use of windows for harmonic analysis with the discrete Fourier transform. *Proc IEEE*. 1978;66:51–83.
- Noll DC, Nishimura GD, Macovski A. Homodyne detection in magnetic resonance imaging. *IEEE Trans Med Imaging*. 1991; 10(2):154–63.
- Lindskog ED, Haacke EM, Lin W. A fast, iterative, partial-fourier technique capable of local phase recovery. *J Magn Reson*. 1991; 92:126–45.
- Wikipedia. n.d. http://en.wikipedia.org/wiki/Temporal_resolution. Retrieved on Apr 2014.
- Ogawa S, Lee TM, Nayak AS, Glynn P. Oxygenation-sensitive contrast in magnetic resonance image of rodent brain at high magnetic fields. *Magn Reson Med*. 1990;14:68–78.
- Kellman P, Chellapaiah C, Lorenz CH, Mancini C, Arai AE, McVeigh ER. High-spatial and temporal resolution cardiac cine MRI from retrospective reconstruction of data acquired in real time using motion correction and resampling. *Magn Reson Med*. 2009; 62:1557–64.

7. Kim SG, Richter W, Ugurbil K. Limitations of temporal resolution in functional MRI. *Magn Reson Med*. 1997;37:631–6.
8. Thompson RB, McVeigh ER. High temporal resolution phase contrast MRI with multiecho acquisitions. *Magn Reson Med*. 2002;47:499–512.
9. Kramer CM, Barkhausen J, Flamm SD, Kim RJ, Nagel E. Standardized cardiovascular magnetic resonance (CMR) protocols 2013 update. *J Cardiovasc Magn Reson*. 2013;15:91.
10. Foo TK, Bernstein MA, Aisen AM, Hernandez RJ, Collick BD, Bernstein T. Improved ejection fraction and flow velocity estimates with use of view sharing and uniform repetition time excitation with fast cardiac techniques. *Radiology*. 1994;195:471–8.
11. van Vaals JJ, Brummer ME, Dixon WT, Tuithof HH, Engels H, Nelson RC, Gerety BM, Chezmar JL, den Boer JA. “Keyhole” method for accelerating imaging of contrast agent uptake. *J Magn Reson Imaging*. 1993;3:671–5.
12. Doyle M, Walsh EG, Blackwell GG, Pohost GM. Block regional interpolation scheme for k-space (BRISK): a rapid cardiac imaging technique. *Magn Reson Med*. 1995;33:163–70.
13. Markl M, Hennig J. Phase contrast MRI with improved temporal resolution by view sharing: k-space related velocity mapping properties. *Magn Reson Imaging*. 2001;19:669–76.
14. Lin HY, Bender JA, Chung YC, Hinton AM, Pennell ML, Whitehead KK, Raman SV, Simonetti OP. Shared velocity encoding: a method to improve the temporal resolution of phase-contrast velocity measurements. *Magn Reson Med*. 2012;68:703–10.
15. Parrish T, Hu X. Continuous update with random encoding (CURE): a new strategy for dynamic imaging. *Magn Reson Med*. 1995;33:326–36.
16. Lim RP, Shapiro M, Wang EY, Law M, Babb JS, Rueff LE, Jacob JS, Kim S, Carson RH, Mulholland TP, Laub G, Hecht EM. 3D time-resolved MR angiography (MRA) of the carotid arteries with time-resolved imaging with stochastic trajectories: comparison with 3D contrast-enhanced bolus-chase MRA and 3D time-of-flight MRA. *Am J Neuroradiol*. 2008;29:1847–54.
17. Spraggins TA. Simulation of spatial and contrast distortions in keyhole imaging. *Magn Reson Med*. 1994;31:320–2.
18. Webb AG, Liang ZP, Magin RL, Lauterbur PC. Applications of reduced-encoding MR imaging with generalized-series reconstruction (RIGR). *J Magn Reson Imaging*. 1993;3:925–8.
19. Bernstein MA, King KF, Zhou XJ. *Handbook of MRI pulse sequences*. Burlington: Elsevier/Academic; 2004.
20. Atkinson DJ, Edelman RR. Cineangiography of the heart in a single breath hold with a segmented turbo-FLASH sequence. *Radiology*. 1991;178:357–60.
21. Pruessmann KP, Weiger M, Bornert P, Boesiger P. Advances in sensitivity encoding with arbitrary k-space trajectories. *Magn Reson Med*. 2001;46:638–51.
22. Seiberlich N, Ehses P, Duerk J, Gilkeson R, Griswold MA. Improved radial GRAPPA calibration for real-time free-breathing cardiac imaging. *Magn Reson Med*. 2011;65:492–505.
23. Seiberlich N, Lee G, Ehses P, Duerk JL, Gilkeson R, Griswold M. Improved temporal resolution in cardiac imaging using through-time spiral GRAPPA. *Magn Reson Med*. 2011;66(6):1682–8.
24. Wild JM, Paley MNJ, Kasuboski L, Swift A, Fischele S, Woodhouse N, et al. Dynamic radial projection MRI of inhaled hyperpolarized ^3He gas. *Magn Reson Med*. 2003;49:991–7.
25. Nayak KS, Hargreaves BA, Hu BS, Nishimura DG, Pauly JM, Meyer CH. Spiral balanced steady-state free precession cardiac imaging. *Magn Reson Med*. 2005;53:1468–73.
26. Blaimer M, Breuer F, Mueller M, Heidemann RM, Griswold MA, Jakob PM. SMASH, SENSE, PILS, GRAPPA: how to choose the optimal method. *Top Magn Reson Imaging*. 2004;15:223–36.
27. Sørensen TS, Schaeffter T, Noe KØ, Hansen MS. Accelerating the nonequispaced fast Fourier transform on commodity graphics hardware. *IEEE Trans Med Imaging*. 2008;27:538–47.
28. Sørensen TS, Atkinson D, Schaeffter T, Hansen MS. Real-time reconstruction of sensitivity encoded radial magnetic resonance imaging using a graphics processing unit. *IEEE Trans Med Imaging*. 2009;28:1974–85.
29. Saybasili H, Derbyshire JA, Kellman P, Griswold MA, Ozturk C, Lederman RJ, Seiberlich N. RT-GROG: parallelized self-calibrating GROG for real-time MRI. *Magn Reson Med*. 2010;64:306–12.
30. Saybasili H, Herzka DA, Seiberlich N, Griswold MA. Real-time imaging with radial GRAPPA: implementation on a heterogeneous architecture for low-latency reconstructions. *Magn Reson Imaging*. 2014;32:747–58.
31. Lustig M, Pauly J. SPIRIT: iterative self-consistent parallel imaging reconstruction from arbitrary k-space. *Magn Reson Med*. 2010;64:457–71.
32. Lustig M, Donoho D, Pauly JM. Sparse MRI: the application of compressed sensing for rapid MR imaging. *Magn Reson Med*. 2007;58:1182–95.
33. Breuer FA, Kellman P, Griswold MA, Jakob PM. Dynamic auto-calibrated parallel imaging using temporal GRAPPA (TGRAPPA). *Magn Reson Med*. 2005;53:981–5.
34. Saybasili H, Kellman P, Griswold MA, Derbyshire JA, Guttman MA. HTGRAPPA: real-time B1-weighted image domain TGRAPPA reconstruction. *Magn Reson Med*. 2009;61:1425–33.
35. Kellman P, Epstein FH, McVeigh ER. Adaptive sensitivity encoding incorporating temporal filtering (TSENSE). *Magn Reson Med*. 2001;45:846–52.
36. Saybasili H, McNeal G, Zuehlsdorff S, Schmidt M, Kellman P, Zenge M. Temporal interpolation of real-time CINE images for ventricular function assessment. *Proceedings of SCMR, New Orleans*; 2014.
37. Hoult D, Lauterbur PC. The sensitivity of the zeugmatographic experiment involving human samples. *J Magn Reson*. 1979;34:425–33.
38. Hayes CE, Axel L. Noise performance of surface coils for magnetic resonance imaging at 1.5 T. *Med Phys*. 1985;12:604–7.
39. Macovski A. Noise in MRI. *Magn Reson Med*. 1996;36:494–7.
40. Henkelman RM. Measurement of signal intensities in the presence of noise in MR images. *Med Phys*. 1985;12:232–3.
41. Constantinides CD, Atalar E, McVeigh ER. Signal-to-noise measurements in magnitude images from NMR phased arrays. *Magn Reson Med*. 1997;38:852–7.
42. Sijbers J, den Dekker AJ, Van Audekerke J, Verhoye M, Van Dyck D. Estimation of the noise in magnitude MR images. *Magn Reson Imaging*. 1998;16:87–90.
43. De Wilde JP, Lunt JA, Straughan K. Information in magnetic resonance images: evaluation of signal, noise and contrast. *Med Biol Eng Comput*. 1997;35:259–65.
44. Kellman P, McVeigh ER. Image reconstruction in SNR units: a general method for SNR measurement. *Magn Reson Med*. 2005;54:1439–47.

Johannes Tran-Gia, Herbert Köstler, and Nicole Seiberlich

Abstract

Fast imaging is essential for cardiovascular Magnetic Resonance Imaging in order to avoid motion artifacts and capture the rapid motion of the heart and blood. Many different data collection and image reconstruction techniques are used to accelerate imaging in cardiovascular MRI. Basic methods involve synchronizing the collection of data to cardiac and respiratory cycles, such that artifacts due to motion are avoided. Other methods focus on collecting as much data as possible during one repetition time, and include the use of short pulse sequences such as bSSFP and multi-echo sequences. Rectangular fields-of-view can be used to encode only spatial information which is relevant to the clinician. Additionally, most clinical sequences speed up data acquisition by skipping lines of data and rely on image reconstruction techniques to generate an artifact-free image. Parallel imaging uses information from spatially varying receiver coil sensitivities to reconstruct images from undersampled datasets; acceleration rates of up to four are possible in the clinic using parallel imaging. Other techniques, including view-sharing or keyhole imaging, take advantage of the dynamic properties of many cardiovascular processes to reconstruct images from undersampled data. Although they are not yet available in most clinical sites, other techniques including non-Cartesian data sampling, k-t methods, and compressed sensing may also prove useful in accelerating cardiovascular MRI. This chapter provides an overview of all of these different methods for rapid cardiovascular MRI, and describes their implications for different applications.

Keywords

Fast imaging • bSSFP • Multi-echo sequences • Undersampling • Partial Fourier • Parallel imaging • Compressed sensing • Functional imaging • Myocardial perfusion • Viability imaging • Vascular imaging

J. Tran-Gia, PhD (✉) • H. Köstler, PhD
Department of Radiology, University of Würzburg,
Würzburg, Germany
e-mail: tran_j@ukw.de; koestler_h@ukw.de

N. Seiberlich, PhD
Biomedical Engineering, Case Western Reserve University,
Cleveland, OH, USA
e-mail: nes30@case.edu

Speed in Cardiovascular Magnetic Resonance Imaging

Imaging speed is one of the greatest challenges in cardiovascular imaging. In order to generate images which are not corrupted by motion artifacts, care must be taken to limit the amount of cardiac and respiratory motion that occurs during data acquisition. However, most MRI pulse sequences require a long time relative to the cardiac cycle to encode and collect the data needed for a single image. As an example, if a spatial resolution of 2 mm^2 and a Field-of-View (FoV) of 256 mm^2 are required for the visualization of cardiac anatomy, and the pulse sequence selected has a repetition time (TR) of 10 ms, data collection would take 1.28 s (128 phase encoding lines at 10 ms each). While respiratory motion could be suspended during this time by asking the patient to hold his breath, the resulting image would contain artifacts from cardiac motion, and not depict a single cardiac phase accurately. Thus, data collection in cardiovascular MRI must be accelerated and/or synchronized with patient motion using one of the techniques described below. The acceleration methods detailed in this chapter are meant to give an overview of different strategies used in a clinical setting to improve cardiovascular MRI, and include:

- Optimization of Pulse Sequences
- Cardiac and Respiratory Synchronization
- Multi-echo Pulse Sequences
- Segmented Acquisitions
- Partial Fourier Techniques
- Rectangular FoV
- View-Sharing/Keyhole Techniques
- Parallel Imaging
- Non-Cartesian Trajectories
- k-t Methods and Compressed Sensing

Optimization of Pulse Sequences

One simple way to accelerate image acquisition is to reduce the repetition time, TR, needed to acquire one line of k-space. While some pulse sequences require long repetition times in order to generate the desired contrast, other types of pulse sequences can be shortened in order to reduce the total acquisition time. For the second type of sequence, there are several different ways to reduce the TR (see Fig. 5.1), including:

1. Increasing gradient amplitudes and slew rates (Fig. 5.1b)
2. Employing shorter radio-frequency (RF) pulses (Fig. 5.1c)
3. Increasing the receiver bandwidth (Fig. 5.1d)

It is important to note that both the echo time, TE, and the repetition time can be shortened using these methods, and both can affect the image contrast. However, shortening the echo time without reducing the repetition time will not shorten the overall duration of the sequence, and thus reducing the TR is the focus of this section.

In order to shorten the TR while maintaining the gradient moments, higher gradient amplitudes and slew rates must be used (as in Fig. 5.1b). For instance, in order to halve the amount of time required for gradient encoding, the gradient amplitude has to be doubled, and the slew rate has to be quadrupled. While challenging, such gradient performance is possible given recent engineering advances, but the potential for peripheral nerve stimulation caused by rapidly changing fields limits the gradients that may be applied in a clinical examination. Current clinical sequences operate close to this limit, making further improvements in imaging speed through increased gradient amplitudes unlikely.

Another way of reducing the TR is to optimize the RF pulses used for slice excitation (the influence of a shorter RF pulse on TR is shown in Fig. 5.1c). A perfectly rectangular slice can only be selected using an infinitely long sinc pulse, and thus truncated sinc pulses with a considerably shortened duration but fewer side lobes are applied for slice selection. However, the truncation of the excitation pulse leads to a softening of the rectangular shape of the excited slice and a coarser slice definition. Instead, it is possible to use a high excitation bandwidth and a large slice selection gradient and compress the RF pulse. Such a compressed RF pulse has the same number of side lobes as an uncompressed RF pulse and leaves the profile of the selected slice unaffected, but the compression is limited by the maximum slice select gradient strength. The amplitude of the RF pulse must also be increased in order to shorten the RF duration while maintaining the flip angle. As larger amplitudes result in a higher deposition of energy which can potentially cause tissue heating, care has to be taken to limit the RF transmitter output. Another option is to use an asymmetric RF pulse, in which only one side of the RF pulse is truncated. In this case, a higher number of side lobes can be employed (on one side of the pulse) which can lead to an improved slice profile over a symmetric RF pulse with the same duration.

The third set of related parameters which influence the sequence timing includes the dwell time and receiver bandwidth (rBW) used for data collection. The dwell time describes the interval with which data points are sampled during the readout, and the rBW is the inverse of the dwell time. In general, the time needed to collect each line of k-space can be reduced by decreasing the time between sampled data points (in other words, increasing the rBW, as shown in Fig. 5.1d). If the total time needed for data sampling is reduced, the whole pulse sequence can be condensed, allowing the use of shorter TE and TR. However, an increase

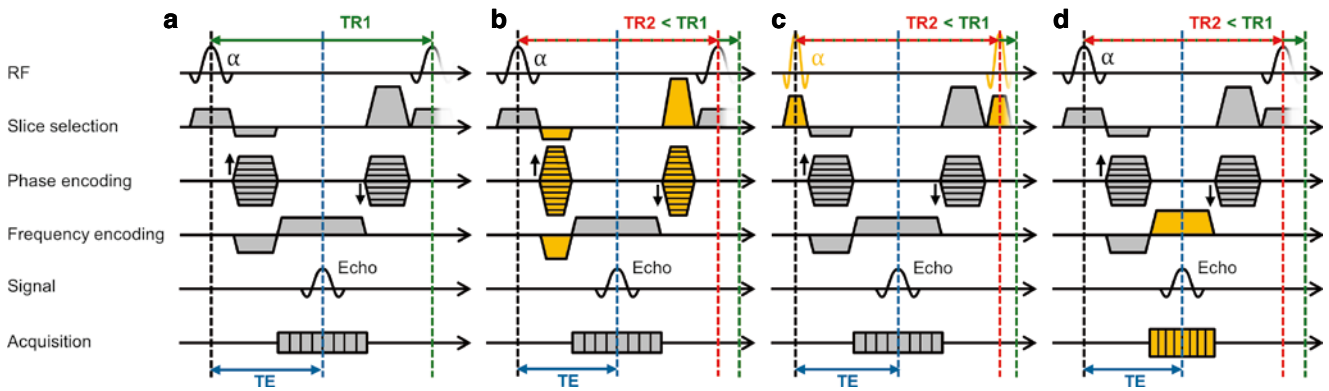


Fig. 5.1 Reducing TR. Several different ways to reduce the TR in a standard Fast Low-Angle SHot (FLASH) sequence, shown in (a): Shorter gradient durations with higher gradient strengths can be used

(b), the duration of the RF pulses can be shortened (c), or the acquisition bandwidth can be increased (sampling duration decreased) (d)

in rBW leads to a reduction in the signal-to-noise ratio (SNR), and the amount by which the scan can be accelerated by increasing the rBW is limited by the maximum read gradient strength. Another option is to employ an asymmetric readout, in which different numbers of readout points are collected before and after the echo, which can help shorten the readout portion of the pulse sequence.

If further reduction of the TR using approaches based on those described above is limited, for instance by nerve stimulation or specific absorption rate (SAR) related tissue heating, another option to shorten the scan time is to reduce the spatial resolution. The total scan time is directly related to the number of k-space lines collected, which is in turn directly related to the spatial resolution and the FoV. As the FoV is determined by the size of the patient, the only free parameter is the spatial resolution. Thus, if a lower spatial resolution can be tolerated, some k-space lines can be eliminated. While this trade-off between spatial and temporal resolution is inherent to all MRI acquisitions, it is of particular importance in cardiovascular MRI where moving anatomy limits the amount of time available for data collection. If no spatial resolution can be sacrificed, a longer scan with a lower temporal resolution must be used, and any motion that occurs during data collection can lead to artifacts.

Cardiac and Respiratory Synchronization

Although reducing the TR is an effective way to reduce the acquisition time, an approach often used to avoid artifacts when scanning in the presence of cardiac motion is to synchronize the acquisition to the patient's electrocardiogram (ECG). The ECG signal can be obtained using ECG electrodes and leads attached to the patient's chest. The QRS complex is detected and employed to trigger the start of the imaging sequence. The time between the QRS detection and the start of the sequence is called the trigger delay and can be

adjusted such that data are collected only when the heart is in the desired cardiac phase. By distributing the acquisition over multiple heartbeats and changing the phase encoding each time data are collected, a motion-free image of the selected cardiac phase can be reconstructed.

Using conventional cardiac synchronization as described above, only one line of k-space is acquired per heartbeat. In these cases, the repetition time, TR, is equal to the R-R interval of the patient. The acquisition of a complete dataset depicting one cardiac phase using conventional spin echo (SE) or gradient echo (GRE) sequences can take up to several minutes. For an image with a spatial resolution of 2 mm^2 and a FoV of 256 mm^2 acquired in a patient with a heart rate of 80 beats per minute (TR equals one heartbeat, or 0.75 s), data collection would take 1.6 min (128 phase encoding lines with a TR of 0.75 s). Because respiratory motion will change the position of the heart and large parts of the thorax, the reconstructed images would be strongly affected by motion artifacts, and respiratory compensation methods would have to be applied.

The simplest and therefore most common method for avoiding respiratory motion artifacts is to ask the patient to perform a breath-hold during data acquisition. In cases where patients have problems holding their breath long enough for the scan to be performed, the sequence can be triggered by a respiratory bellows wrapped around the patient's chest. The breathing motion of the chest leads to expansion and contraction of the bellows, which can be detected for respiratory gating or compensation. As in cardiac gating, respiratory gating involves using the respiratory signal to directly trigger the start of the sequence. Data are then only acquired when the heart and lungs are in the proper cardiac and respiratory phases. In respiratory compensation, the respiratory signal is recorded in order to retrospectively select the k-space lines that are sampled within the selected portion of the respiratory cycle. Both methods require the patient's respiration to remain regular throughout the scan, and can lead to long scan times.

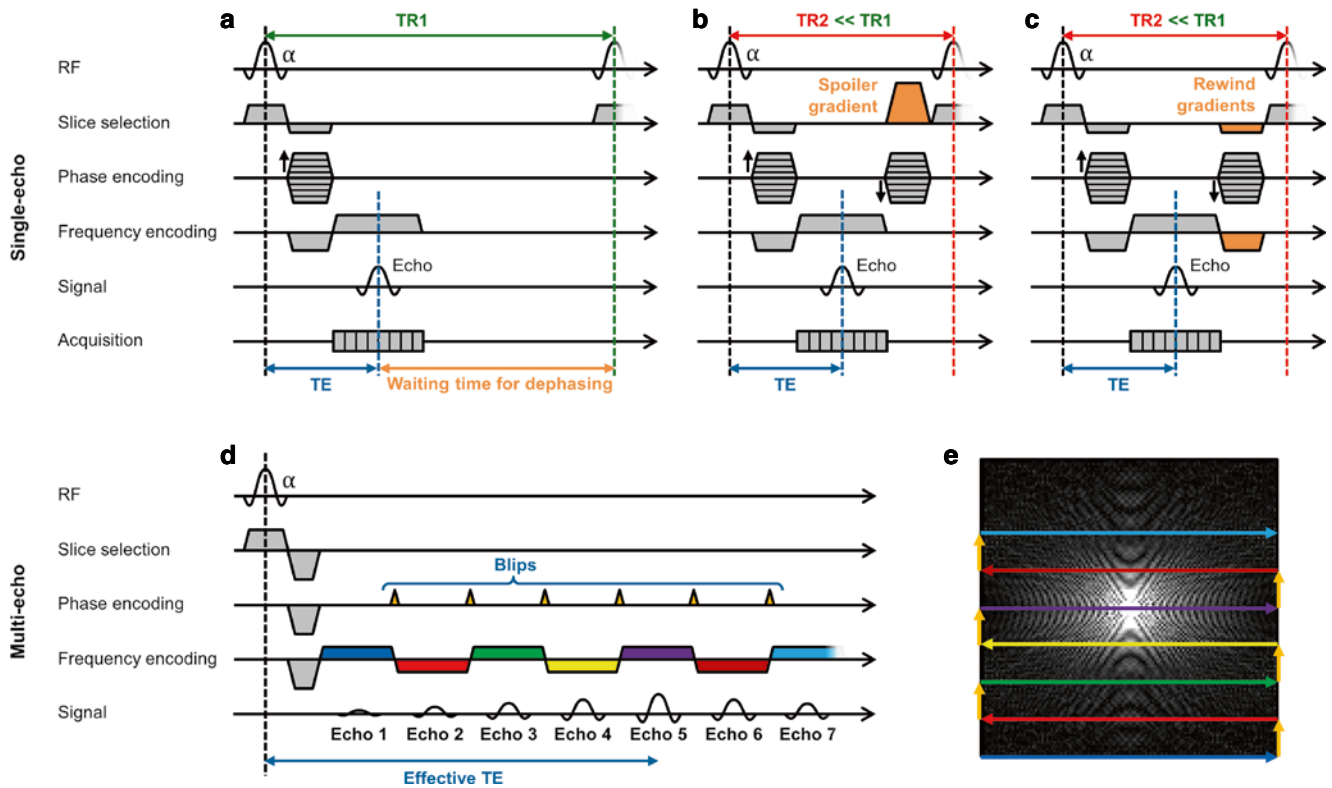


Fig. 5.2 Accelerating Gradient Echo (GRE) sequences. Sequence diagram of a conventional gradient echo sequence (a). The repetition time, TR, in a single-echo GRE sequence can be reduced by using spoiler gradients (b) or rewinding gradients (c). Multiple echoes can be created using an Echo-Planar Imaging (EPI) sequence (d): diagram,

and (e): corresponding k-space pattern. After the excitation pulse, the alternation of repeatedly reversed readout gradients and small phase encoding gradients (blips) generates a series of echoes. The echo with the smallest gradient moment (echo 5 in the diagram) defines the effective echo time TE

From Single-Echo to Multi-echo Acquisitions

In single-echo SE or GRE sequences, one RF excitation pulse is combined with a series of other RF pulses and gradients to create a single echo. In these sequences, one line of k-space is acquired in each TR, followed by a delay time to allow the longitudinal magnetization to recover. The delay time depends on the tissue-dependent longitudinal relaxation time, T_1 , and can be on the order of seconds for SE sequences, leading to extremely long TR unsuitable for cardiac imaging. Additionally, if only one k-space line is encoded for each heartbeat and breath-holding is used to reduce respiratory motion, the number of k-space lines and therefore image resolution would be severely restricted by the breath-holding time.

Accelerating Single-Echo GRE Sequences

In GRE sequences, gradients are used instead of RF pulses to refocus the magnetization to form an echo. The generation of the gradient echo can be performed quite rapidly (on the order of a few milliseconds), but the TR is determined by the time needed for the recovery of the longitudinal magnetization as well as for the dephasing of the residual transverse

magnetization. A typical pulse diagram of a conventional GRE sequence is shown in Fig. 5.2a. Instead of waiting for T_2 relaxation to dephase the transversal magnetization, there are two widely used techniques to significantly reduce the waiting time needed before the next excitation can be performed:

- Use spoiler gradients to dephase the remaining transversal magnetization (Fig. 5.2b)
- Use rephasing gradients to rewind the residual transversal magnetization (Fig. 5.2c)

Spoiled gradient echo sequences (General Electric: Spoiled Gradient echo, SPGR | Philips: T_1 Fast Field Echo, T_1 FFE | Siemens: Fast Low-Angle SHot, FLASH) apply spoiler gradients to ensure that the transversal magnetization from one excitation is completely dephased before the next excitation [1–3]. Subsequently, successive excitations can be performed without any additional recovery time. Relatively small flip angles are typically used to ensure that enough longitudinal magnetization will be present for excitation despite the short TR used. Because the longitudinal magnetization is greatly reduced when using FLASH sequences, there is a corresponding loss in SNR.

Instead of dephasing the remaining transverse magnetization, rewind or balanced gradient echo sequences

(introduced as balanced Steady-State Free Precession, bSSFP | General Electric: Fast Imaging Employing Steady-state Acquisition, FIESTA | Philips: Balanced Fast Field Echo, b-FFE | Siemens: TrueFISP) apply rephasing gradients of opposite signs to rewind any residual transverse magnetization left after data collection [4]. After every excitation, these coherent transverse components add to the “freshly” excited transverse magnetization. This leads to a steady-state with a higher signal than FLASH sequences, but also a more complicated contrast, with a combination of T_1 and T_2 weighting. Additionally, the avoidance of lengthy dephasing times enables a larger reduction of the TR compared to FLASH. The combination of high SNR and excellent contrast between blood and myocardium make bSSFP sequences among the most widely used in cardiovascular MRI.

The use of spoiling or balanced gradients are two of the most effective ways of accelerating gradient echo sequences. In the case of an image with a spatial resolution of 2 mm^2 and a FoV of 256 mm^2 , the use of a fast GRE sequence would typically result in a reduced TR of about 3 ms, and data collection could be performed in about 0.4 s (128 phase encoding lines with a TR of 3 ms). With such acquisition times shorter than the cardiac cycle period, these sequences can be used without additional acceleration during diastole to generate images with minimal motion artifacts.

Multi-echo Sequences

An efficient way to further accelerate the acquisition process is to generate multiple echoes after a single excitation, which drastically reduces the number of TR intervals needed to acquire an image and enables the acquisition of several

k-space lines in rapid succession. These multi-echo extensions exist for spin echo as well as gradient echo based sequences and are known as turbo or fast pulse sequences.

Turbo Spin Echo/Fast Spin Echo

In the standard SE sequence, one RF excitation pulse is combined with an RF refocusing pulse to generate one spin echo, which is encoded to form one line of k-space. The fast/turbo spin echo sequence (introduced as: Rapid Acquisition with Relaxation Enhancement, RARE | General Electric: Fast Spin Echo, FSE | Philips, Siemens: Turbo Spin Echo, TSE) is a modification of the standard SE sequence which employs additional RF refocusing pulses to generate several spin echoes, called an echo train [5, 6]. The pulse diagram of a typical TSE sequence is illustrated in Fig. 5.3. The number of echoes within the echo train is often denoted as the turbo factor, TF (Philips, Siemens), or echo train length, ETL (General Electric), and the time between echoes as the echo spacing, ES. By changing the magnitude of the phase encoding gradient applied to each of these echoes, several different k-space lines can be encoded and collected. Because a total of TF k-space lines can be collected after one RF pulse, the scan time can be shortened by a factor of TF. This acceleration is often used to reduce the number of heartbeats needed for data collection, making data acquisition during a single breath-hold possible. If $TF = 16$, and a total of 128 k-space lines are required, only eight heartbeats are needed to collect all of the data for the image. This would reduce the acquisition time from 1.6 min to 6 s (from 128 to 8 heartbeats at 80 beats per minute). However, the total amount of time required to collect all TF lines of k-space is $TF \cdot ES$. For instance, if a turbo factor of $TF = 16$ is used, and the ES is 3 ms, the total “acquisition window” is 48 ms. This “acquisition window”

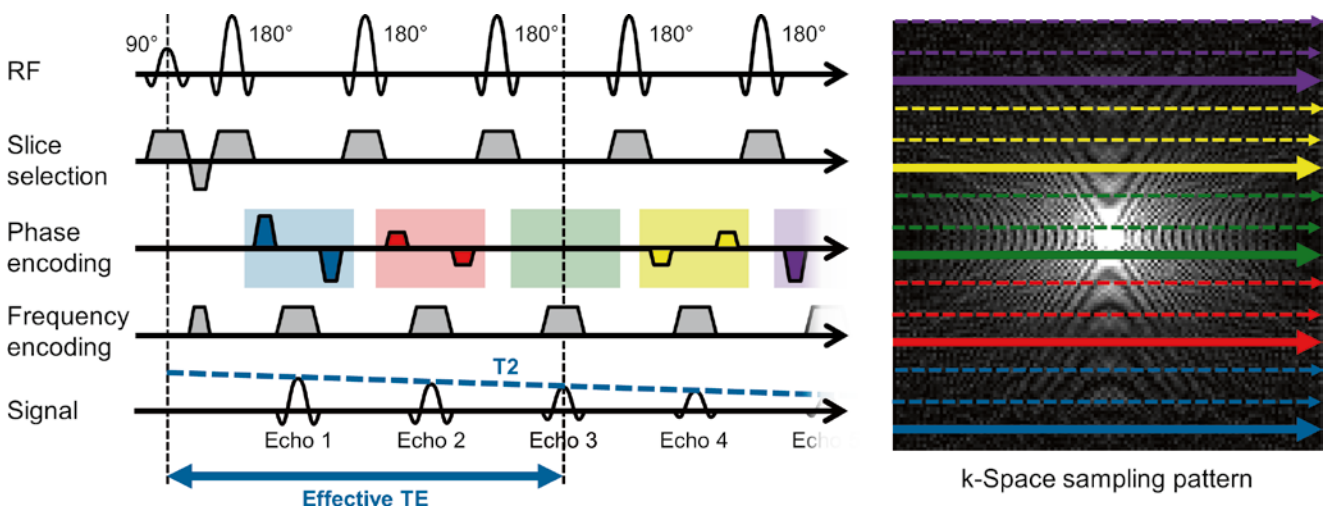


Fig. 5.3 Spin Echo (SE) to Turbo Spin Echo (TSE). Sequence diagram of a TSE sequence (*left*) with an echo train length (ETL) of 5, and the corresponding k-space sampling pattern (*right*) where the lines collected in one TR are shown in bold. After the 90° excitation pulse, the repeated application of 180° refocusing pulses generates a series of

echoes. The echo with the smallest gradient moment (echo 3 in the diagram) defines the effective echo time TE. The TSE sequence is repeated until the k-space is filled; three shots are needed in this case. Note the interleaving of the acquired k-space lines to avoid discontinuities in k-space due to T_2 relaxation

must be kept short enough to avoid image artifacts due to cardiac motion, and to minimize relaxation effects.

When a spin echo train is used, the echo time TE, and thus the T_2 weighting, changes with each k-space line collected. For TSE sequences, an effective echo time is defined as the TE of the k-space line that is acquired closest to the center of k-space, which carries the majority of the image contrast. Because different k-space lines have slightly different contrasts, blurring can occur in the phase encoding direction due to T_2 decay if the echo train is long. Similarly, if significant relaxation occurs during the collection of the echoes, the resulting images can have a low SNR. Another important consideration is the potential for discontinuities in k-space if significant differences in T_2 relaxation exist between the end of one echo train and the start of the next. To avoid such discontinuities, which can lead to artifacts, k-space is generally filled in an interleaved fashion to avoid large T_2 contrast jumps which could occur if a long echo train is used and the k-space filled sequentially.

Besides the extreme reduction in scan time, an additional advantage of TSE sequences is a signal increase in some tissues compared to conventional SE sequences. The reason lies in the interaction between hydrogen nuclei in molecules with long carbon chains known as J-coupling, usually reducing T_2 relaxation times. The rapidly repeated 180° pulses of TSE sequence break up this interaction, leading to longer effective T_2 times and therefore an increase in signal.

Single-Shot TSE/FSE

The highest acceleration possible for a TSE sequence can be achieved when the TF is equal to the number of k-space lines required for the entire image. This extreme case is known as single-shot TSE. For multi-slice acquisitions, the single-shot TSE sequence is applied sequentially to acquire one complete slice in a single heartbeat, before moving on to the next one. Due to the extremely high TF, significant T_2 decay occurs during the acquisition of one slice, and unless combined with additional steps to shorten the echo train, such as partial Fourier acquisition, its clinical use is limited to imaging of primarily fluid structures with extremely long T_2 relaxation times.

Multi-echo GRE: Echo-Planar Imaging (EPI)

Due to the possibility to dramatically shorten the repetition times in GRE based sequences with gradient spoiling and balancing in FLASH and bSSFP, these single-echo sequences are used in most cardiac imaging applications. However, as in single-shot TSE, it is possible to obtain multiple echoes after a single RF excitation pulse in GRE based sequences using Echo-Planar Imaging (EPI, [7]) which is illustrated in Fig. 5.2d–e. After the excitation pulse, the alternation of repeatedly reversed readout gradients and small phase encoding gra-

dients (blips) generates a series of echoes. The timing of the echo with the smallest gradient moment defines an effective TE determining the contrast of the image. Although EPI sequences enable the acquisition of an entire image in only a fraction of a second, the acquisition scheme is prone to a variety of artifacts such as image distortions and signal dropouts that limits the use of single-shot EPI in cardiac MRI. However, segmented EPI, sometimes called hybrid gradient echo – echo planar imaging (GRE-EPI), in which only a relatively few echoes are acquired after each RF pulse, has found utility in CMR for first-pass perfusion and velocity quantification. A more detailed description of EPI sequences can be found in [8].

Segmented Acquisitions

As described above, a combination of cardiac and respiratory synchronization can be used to obtain motion-free images of a desired cardiac phase. The main disadvantage that TR depends on the relatively long heart rate and T_1 relaxation can be overcome using the fast imaging sequences described in the previous section. Instead of using conventional GRE or SE sequences, which can produce only one echo per heartbeat, more rapid sequences such as TSE, FLASH or bSSFP can be used to generate multiple echoes in every heartbeat. By using the shortest TR possible, a group of k-space lines (typically referred to as one shot) can be acquired while the heart is in the desired cardiac phase. This series of events is repeated over successive heartbeats to acquire different groups of k-space lines until an entire k-space corresponding to the desired cardiac phase is filled. As these methods divide the acquisition of one image into multiple segments, they are often referred to as segmented measurements. Most importantly, segmented measurements are usually short enough that they can be performed during a breath-hold, greatly reducing motion artifacts.

Cine Imaging

Instead of acquiring only one cardiac phase over successive heartbeats, ECG gated segmented measurements can further be extended by acquiring partial k-spaces of multiple phases of the cardiac cycle (the so-called cine frames) during every heartbeat. This principle is illustrated in Fig. 5.4. As in segmented imaging, the k-space lines acquired in every group and every cardiac phase (indicated by different colors) are changed for consecutive heartbeats until a full k-space is available for each cine frame. The images of all cardiac phases can be viewed as a movie sequence or cine, allowing functional assessment of the heart and its wall motion, and a visual, qualitative assessment of blood flow.

The number of cine frames depends on the number of k-space lines collected per cardiac phase and the subject's

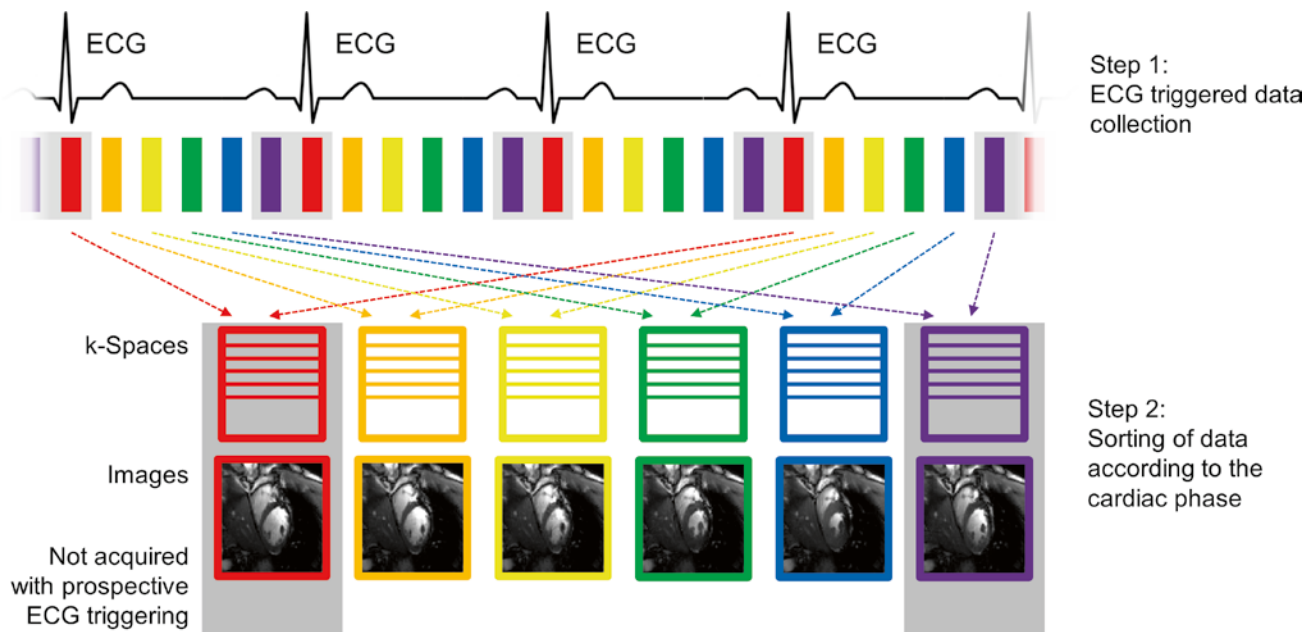


Fig. 5.4 Cine imaging. Prospective triggering: After an ECG triggered acquisition, the data are sorted into different k-spaces according to the acquisition order (indicated by different colors). Different parts of the k-space are filled in subsequent heartbeats. Because the prospectively triggered acquisition requires a small time window at the end of diastole to accommodate arrhythmic heartbeats (indicated by the *gray box* around

the *red* and *violet* cardiac phases), these phases of the cardiac cycle are lost for image acquisition. Retrospective gating: Data are continuously acquired over multiple heartbeats. The ECG signal is recorded during the entire acquisition, and the data can retrospectively be sorted according to their cardiac phase. This enables imaging all cardiac phases including end-diastolic cine frames

heart rate, which determines the total acquisition window. For example, if the subject has a heart rate of 80 beats per minute, the acquisition window is 750 ms. If 16 k-space lines with $TR=3$ ms are collected per cardiac phase, each frame requires 48 ms (16×3 ms) of data collection time per heartbeat and approximately 15 cine frames ($750 \text{ ms}/48 \text{ ms}$) can be defined. To fill up a complete k-space with 128 lines, a total of eight heartbeats would be required. Acquiring a larger number of k-space lines for each cardiac phase leads to both a reduced temporal resolution, as a longer time is needed to collect all of the lines, and a reduced number of cine frames, potentially leading to artifacts due to cardiac motion. Taking the previous example, if 32 k-space lines are collected for each cardiac phase in each heartbeat, the data acquisition for each cardiac phase would be 96 ms (32×3 ms), and only 7 cardiac phases could be collected. However, the overall acquisition time would be shorter, as fewer heartbeats (only four) are required to fill up the respective k-spaces. Because the total acquisition time is typically limited by the length of time the patient can hold his or her breath, an optimal balance between the number of cardiac phases to be acquired and the temporal resolution should be found by the operator.

Because cine imaging relies on very short repetition times, TR, it can only be used in conjunction with gradient echo based sequences such as FLASH and bSSFP. The particular choice depends on the field strength and the specific application.

Prospectively Triggered Cine Imaging

In prospectively triggered cine imaging, the acquisition is started at the R-wave of the ECG and no trigger delay is used in order to maximize the acquisition window. Typically, the last 10% of the cardiac cycle is not included in the acquisition window and thus not used for sampling to allow for variations in the R-R interval. This period is known as the arrhythmia rejection (AR) window. For a heart rate of 80 beats per minute (an R-R interval of 0.75 s), a TR of 3 ms and a shot consisting of 16 k-space lines per cine frame, a total of 14 cine frames could be acquired in every heartbeat (90% of 0.75 s time window divided by an acquisition time of 16×3 ms for each shot). The AR window is indicated by the gray boxes during end-systole in Fig. 5.4. In prospective gating, this part of the cardiac cycle is lost for image acquisition, and diastolic features of the cardiac cycle such as atrial contraction can be missed.

Retrospectively Gated Cine Imaging

A major disadvantage of prospectively triggered cine imaging is that the AR window between the end of the acquisition and the next trigger pulse is lost for image acquisition. One way to overcome this problem is to use retrospective gating [9], where data are continuously acquired over multiple heartbeats. By recording the ECG signal, each line of k-space can retrospectively be sorted into separate k-spaces corresponding to predefined cardiac phases. This results in

a set of cine frames covering the entire cardiac cycle without the AR gap present in prospectively triggered acquisitions. This is again illustrated by Fig. 5.4, where the two end-diastolic cine frames indicated by the gray boxes would now be included by the acquisition. The main challenge of this gating technique is the retrospective binning of the acquired data. For arrhythmic heartbeats, systole usually remains relatively constant while the duration of diastole varies. Linearly stretching or contracting the data is therefore physiologically not realistic and has to be replaced by computationally more complex models. Alternatively, data acquired during significantly abnormal heartbeats can be re-acquired, but this can result in long breath-hold times, and increases the potential for respiratory motion artifacts. Nevertheless, retrospectively gated cine imaging is indispensable for imaging mitral tricuspid valve function or atrial contraction. For the same heart rate, shot size, and TR used in the prospective triggering example, a total of 15 cine frames per heartbeat could be acquired using retrospective gating, adding one end-diastolic frame to the cine movie sequence.

Reducing the Number of k-Space Lines

In addition to optimizing sequences and using segmented imaging to reduce the acquisition time, there are a few easy ways to speed up the acquisition by reducing the number of k-space lines collected. In this section, techniques which rely on the acquisition of fewer k-space lines will be explained along with their advantages and disadvantages.

Zero-Filling

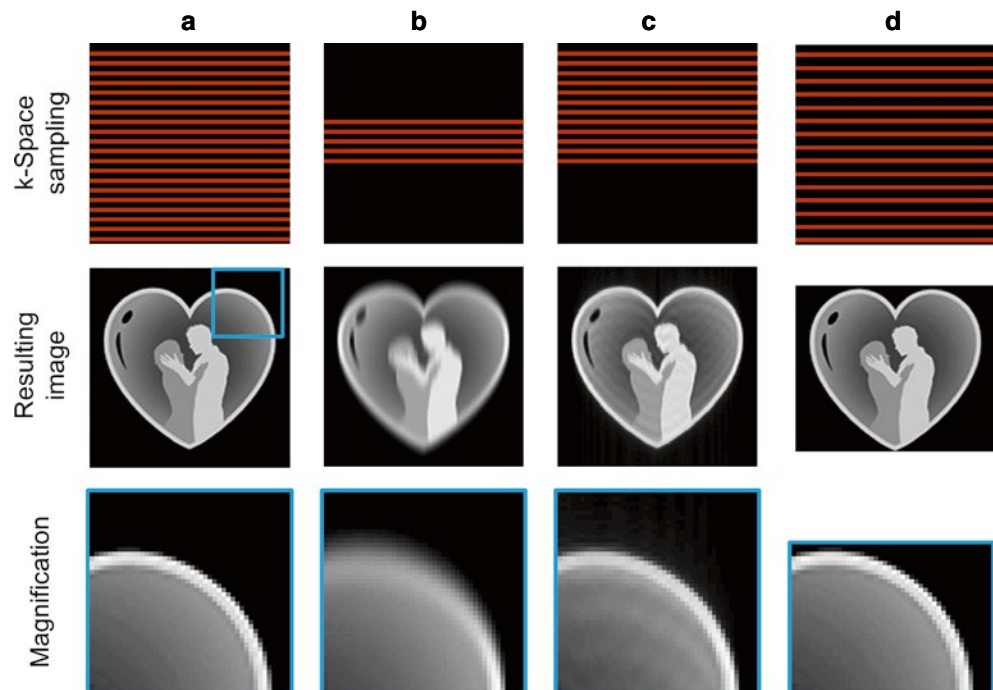
The simplest way to speed up the acquisition is to acquire fewer phase encoding lines in the k-space periphery. Because the extent of k-space determines the image resolution, such an image would have a reduced spatial resolution in the phase encoding direction. However, the acquisition time is reduced by a factor equal to the proportion of phase encoding lines which were not collected. For example, if 16 phase encoding lines at both edges of a fully sampled k-space of 128 lines are skipped, the acquisition would be accelerated by 25 %.

Instead of directly using the smaller k-space and the lower resolution image, the missing parts of k-space are often filled with zeros before Fourier reconstruction in order to maintain the desired matrix size. This operation is equivalent to interpolating the original image with a small imaging matrix to fill a larger image matrix. As no information is generated in this process, the resulting image will have a larger matrix size but the actual image resolution will not be increased. An example where only one fourth of the central k-space is used for reconstructing the full FoV image with zero-filling is shown in Fig. 5.5b. A deterioration of the resolution in the phase encoding direction is clearly visible.

Partial Fourier or Half Fourier

Another way to speed up data acquisition is known as partial or half Fourier imaging [10]. In these techniques, the spacing between k-space lines is left unchanged, but some of the lines on one side of the center of k-space are not acquired.

Fig. 5.5 Reducing the number of k-space lines. A fully-sampled k-space (*top*) and image (*bottom*) are shown in (a). Simply omitting outer parts of k-space during data collection, and replacing these pixels by zeroes to maintain the digital resolution, leads to an irreversible loss in spatial resolution (b). Instead, only slightly more than half the k-space is sampled in partial Fourier imaging, resulting in undersampling artifacts which can be greatly reduced by exploiting k-space symmetry (c). By acquiring fewer k-space lines spaced further apart (d), the FoV can be made smaller in the phase encoding direction to better fit the object and save scan time (rectangular FoV)



The reduction in scan time is directly proportional to the number of k-space lines left out of the acquisition. If, for example, only slightly more than half the k-space is acquired, the scan time can be reduced by approximately 50 %. Because each k-space line contributes to the overall imaging signal level, partial Fourier techniques result in a reduction in SNR. In practice, at least 5/8 of the data are collected to avoid SNR losses.

One way of reconstructing images from the resulting partial k-spaces is to simply insert zeros in place of the uncollected data, i.e., the technique known as zero-filling described in the previous section. The image quality obtained is similar to the fully-acquired image if the collected k-space fraction is close to one. However, a significant amount of blurring in the phase encoding direction occurs as this ratio approaches 0.5. An example of a partial Fourier acquisition where only 5/8 of the k-space has been acquired followed by a zero-filling reconstruction is illustrated in Fig. 5.5c.

In order to correct for this blurring, the sampled parts of k-space can be used to estimate the signal in the missing k-space parts in what is known as a homodyne reconstruction [11]; the symmetry properties of the k-space are exploited to synthesize the missing data after a correction is performed to account for any non-zero phase in the image, which can be caused by flow or motion. The homodyne reconstruction works well if the phase changes slowly over the image, but can lead to artifacts in areas with more rapidly changing phases. In these cases, the phase correction and the subsequent synthesis of uncollected data can be repeated in an iterative fashion. This algorithm, known as Projection Onto Convex Sets (POCS, [12]), reduces artifacts caused by rapidly changing image phase, and is often preferred over simple zero-filling or the homodyne reconstruction.

The partial Fourier technique is often used to reduce the turbo factor (TF), in single-shot TSE sequences [13]. By acquiring only slightly more than half of the k-space lines, the TF and therefore the acquisition time can be reduced by almost half. This technique, known as Half Fourier Acquisition Single-shot TSE (HASTE), enables acquisition times of less than 1 s per slice. However, the extremely long echo train leads to a significant T_2 decay during the acquisition of one slice. This signal decay in turn causes considerable blurring in the reconstructed images, resulting in a deterioration of the spatial resolution. Therefore, HASTE is mainly used in cases where respiratory motion must be avoided and a low spatial resolution can be tolerated, for example to look at gross cardiac and vascular structures in the chest and abdomen.

Rectangular Field-of-View

In most standard views in cardiovascular imaging, such as the four chamber view, the dimensions of the patient's body can be better described as a rectangle than as a square. In these cases,

acquiring a square FoV would be a waste of acquisition time. Instead, the acquisition time can be shortened by using a rectangular FoV, in which the size of the FoV and matrix in the phase encoding direction are less than in the frequency encoding direction. By reducing the FoV in the phase encoding direction, fewer phase encoding lines are required, and the scan time is reduced compared to imaging with a square FoV. It should be noted that in order to maintain the image resolution, the highest phase encoding gradients should be left unchanged, but the distance between neighboring k-space lines increased instead.

View-Sharing

Another simple but powerful technique to accelerate dynamic MRI acquisitions is known as view-sharing. In a dynamic acquisition, such as the previously described cine imaging technique, it would be advantageous to keep the temporal resolution of each cine frame constant while doubling the total number of cine frames. In principle, this means that a larger number of k-spaces have to be "filled up" with acquired data. Instead of attempting to collect this additional data, which would generally not be possible if the acquisition window had been optimally selected, each of the available k-space lines is used for two consecutive cine frames, which is indicated in Fig. 5.6a. Instead of achieving a better temporal resolution, view-sharing can also be used to increase the spatial resolution or other imaging parameters. Although this technique involves the introduction of redundant information in the image reconstruction, the visual appearance of the cine movie generated with these data can be significantly improved due to the considerable increase in the reconstructed cine frames.

Keyhole Imaging

Another effective technique for the acceleration of dynamic acquisitions is the keyhole method [14, 15]. This technique is used to increase the temporal resolution of a series of images with changing contrast but similar features, such as contrast-enhanced MR angiography. In such datasets, it is assumed that most of the changes over time occur in the central portions of k-space, which contain the information about image contrast. The keyhole method works by acquiring only the central k-space lines for every frame, and filling up the rest of the k-space with a previously (or subsequently) acquired set of peripheral k-space lines. Because only the central lines are updated for each frame, and the outer lines are updated less frequently, the scan time for each frame is effectively reduced. The keyhole technique is illustrated in Fig. 5.6b. While keyhole methods can be used to obtain a higher temporal resolution without sacrificing spatial resolution, the longer temporal footprint of the entire dataset can lead to a blurring of temporal dynamics. If the outer lines of k-space are acquired signifi-

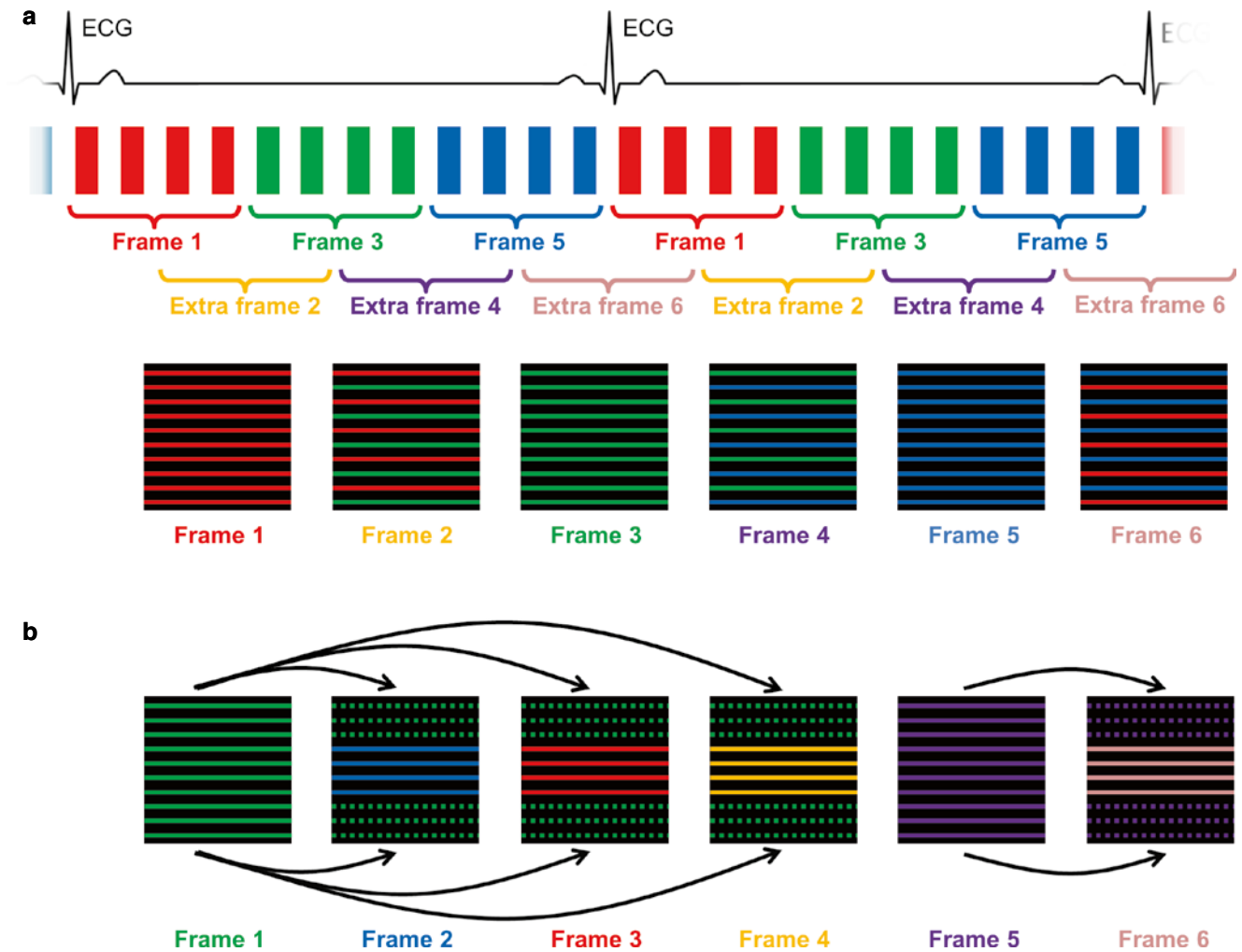


Fig. 5.6 View-sharing and keyhole techniques. In the view-sharing approach (a), each of the available k-space lines acquired in a dynamic image series is used for two consecutive cine frames. In this way, the apparent temporal resolution can be doubled without changing the spatial resolution. Keyhole imaging (b) can be used to accelerate the acquisition of a series of images where only the contrast changes over time. The assumed redundant information in the periphery of k-space is

acquired infrequently (here only every fourth frame), while the contrast-relevant central parts of k-space are collected for each frame, leading to a high temporal resolution. The outer portions of k-space for these frames are filled using lines from the full acquisition. Because k-space lines are taken over a longer time frame, the temporal resolution for such an acquisition can be difficult to define

cantly prior to or following the central lines of k-space, such that large image changes occur between the acquisitions, image artifacts can appear. For this reason, keyhole methods are only applicable in cases where the changes from image to image are minimal. Such methods are generally not used to capture motion but are limited to dynamic contrast changes, as in first-pass perfusion or dynamic angiography.

Parallel Imaging

As described in the previous section, acquisition time can be reduced by collecting fewer k-space lines. For instance, the rectangular FoV approach works by increasing the dis-

tance between lines of k-space, resulting in a reduced FoV in the phase encoding direction. This smaller FoV is beneficial in cases where the object to be imaged is smaller in the phase encoding direction than in the frequency encoding direction. However, if the object is larger than the reduced FoV, the parts of the object that extend beyond the FoV will fold over, as shown at the bottom of Fig. 5.7. This phenomenon is known as aliasing, or fold-over artifact. When the anatomy that aliases is not essential to the scan (i.e. the chest wall), such an artifact is tolerable and even encouraged to reduce the scan time. However, in cases where relevant anatomy is obscured by aliasing, dedicated image reconstruction techniques must be applied in order to eliminate the aliasing.

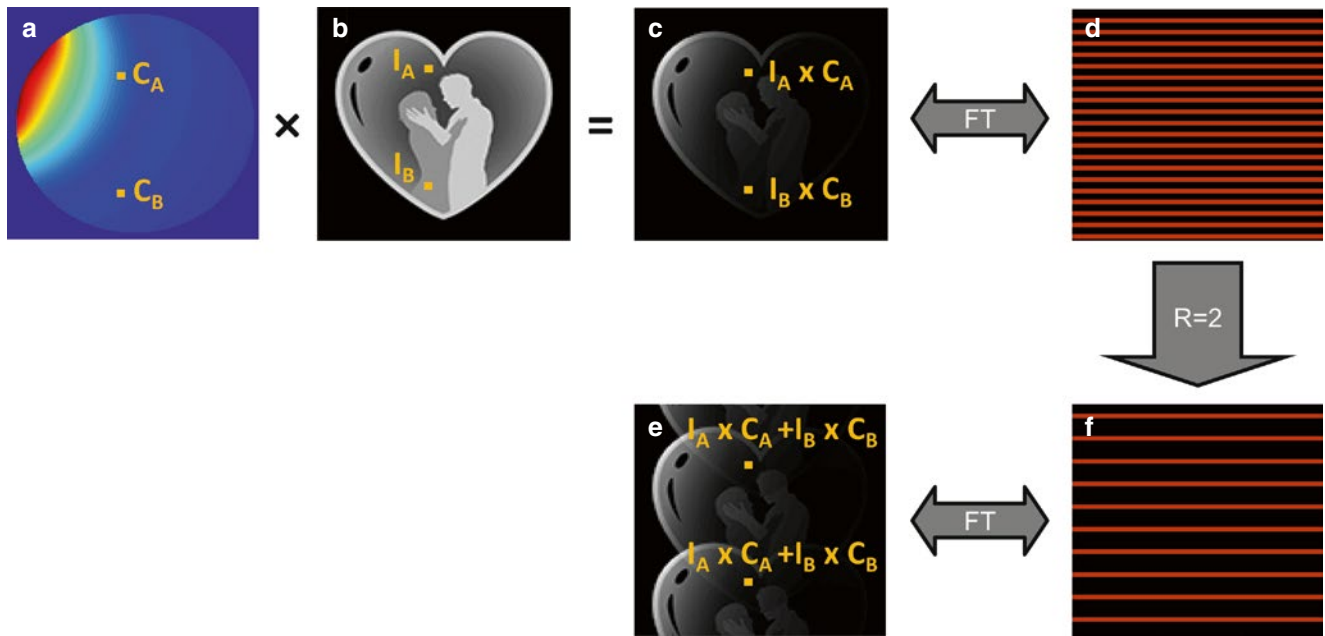


Fig. 5.7 Formation of aliased images in a parallel imaging acquisition with multiple coils. The pixel-wise multiplication of the coil sensitivity profile from a single coil in an array (a) and the image (b) results in the image acquired with that single receiver coil sensitivity (c), the data for

which is collected in k-space (d). If the k-space data are undersampled by a factor of $R=2$ to save scan time (e), the resulting image contains aliasing artifacts (f). Note that the two distinct pixels in the top row, which are separated by $\text{FoV}/2$, alias together in the image shown in the *bottom row*

With the development of the phased-array technology and the design of coils with up to 32 or more receiver channels, a number of ways have been proposed to eliminate this aliasing, known collectively as parallel imaging methods. These methods make use of the fact that each of the individual receiver elements is sensitive to a different part of the FoV depending on its position. Parallel imaging uses these differences in what each coil “sees”, or the coil sensitivity variations, to reconstruct unaliased images from undersampled data. Therefore, acceleration using parallel imaging can only be realized in directions with coil sensitivity variations. Figure 5.7 depicts a coil sensitivity profile (a), an image (b), and the single coil image that would be obtained in one receiver channel of a multi-channel array used for image acquisition (c).

Mathematically, the intensity of a pixel A in the single coil image is the product of the signal intensity, I_A , in the original image and the coil sensitivity, C_A , of the receiver coil at that pixel location:

$$A = I_A \cdot C_A.$$

For a second pixel B, this leads to a second equation

$$B = I_B \cdot C_B.$$

In parallel imaging, k-space lines are skipped in order to reduce the total scan time. An acceleration or reduction factor, R , is defined according to the ratio of fully sampled to undersampled k-space data. For example, if only every sec-

ond phase encoding step of a desired matrix size is acquired (as in Fig. 5.7e), the acceleration factor for that scan is $R=2$. As pixel A and pixel B are half a FoV away from each other, they fold together to make a new pixel with intensity

$$F = I_A \cdot C_A + I_B \cdot C_B.$$

The aliasing is illustrated in Fig. 5.7f. The parallel imaging algorithm works to undo this aliasing in order to recover the original pixels, A and B, to generate a fully-sampled and unaliased image.

As parallel imaging reconstructions are always performed after image acquisition, they are independent of the imaging sequence and can be combined with most of the previously described acceleration techniques, including view-sharing, keyhole imaging, and partial Fourier acquisitions [16, 17]. While all parallel imaging techniques use coil sensitivity variations, there are many different ways of actually performing the parallel imaging reconstruction process. Three important variations, which highlight different aspects of parallel imaging reconstructions, will be described here.

PILS (Parallel Imaging with Localized Sensitivities)

To provide an intuitive understanding of the concepts used in parallel imaging, a simplified example will be given first.

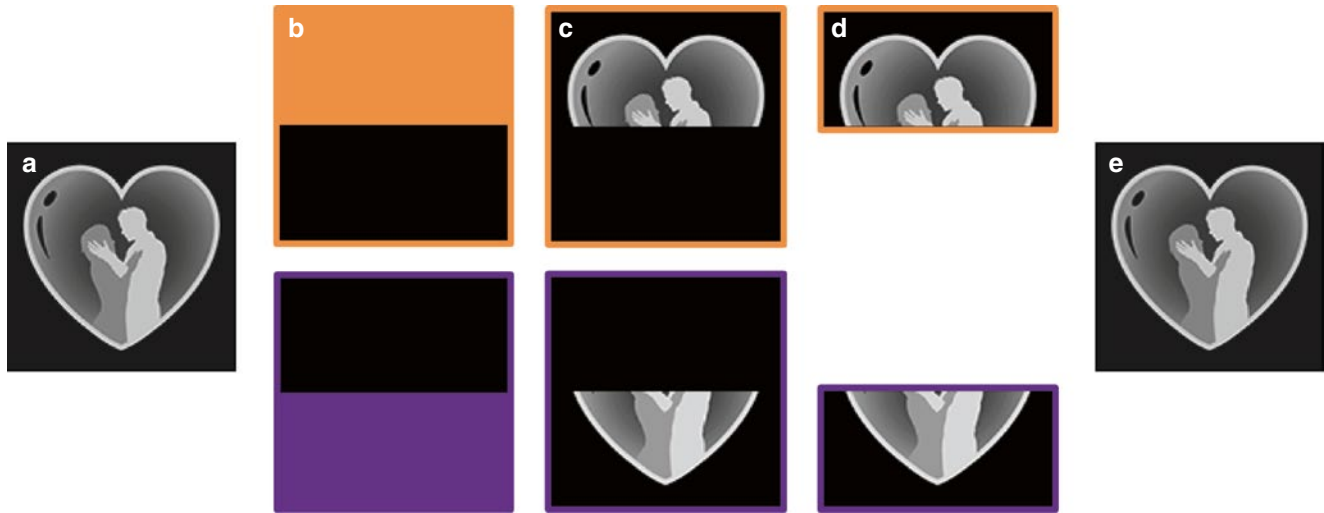


Fig. 5.8 Illustration of the Parallel Imaging with Localized Sensitivities (PILS) reconstruction. A multiplication of the full FoV image (a) with the coil sensitivities (b) results in the images seen by each coil (c). In these coil images, half of the FoV contains no signal and no aliasing

occurs if the images are undersampled with $R=2$ (d). Therefore, merging the two smaller FoV images results a good estimate of the initial image in this idealized example (e)

Imagine a simple array of two independent receiver coils each covering exactly half of the FoV, and each with a rectangular sensitivity profile in the phase encoding direction as depicted in Fig. 5.8b. Each coil is only sensitive to the colored area, and cannot collect signal from the black areas shown in the coil sensitivity maps. As described above, a standard acquisition would involve the acquisition of a certain number of phase-encoding steps to obtain a full FoV image of the desired resolution. By leaving out every second line of k-space during image acquisition, both the scan time and the FoV would be halved, leading to aliasing of all parts of the object outside the now smaller FoV. However, as each of the two coils is only sensitive to the signal generated from one half of the object, no aliasing will be visible in the images reconstructed from each of the coils (see Fig. 5.8c). Instead, the image from the first coil will only show the portion of the object that is covered by that coil, while the image from the second coil will show only the other half of the object (see Fig. 5.8d). By merging these two images, a fully-sampled image (Fig. 5.8e) can be reconstructed from a twofold undersampled dataset ($R=2$), which is equivalent to a twofold acceleration of the image acquisition time.

The basic method described above is called Parallel Imaging with Localized Sensitivities (PILS, [18]). This technique makes use of the fact that receiver coils generally have sensitivities which are localized to distinct regions of the desired FoV. Despite the simplicity of the reconstruction, most real-world receiver coils have more complicated coil sensitivity geometries, so PILS is not often used in a clinical setting, and other more complex reconstruction techniques are generally preferred for cardiovascular imaging.

SENSE (SENSitivity Encoding)

A more robust and commonly-used parallel imaging method is SENSitivity Encoding (SENSE, [19]). SENSE works by “unfolding” aliased pixels in the undersampled images. In Fig. 5.9, the k-space has been undersampled by a factor of $R=2$, which means that both the FoV in the phase encoding direction and the data collection time have been reduced by a factor of 2. As illustrated in Fig. 5.9, the result is a half-sized image with two copies of the initial image shifted by a distance of $\text{FoV}/2$ in the phase encoding direction (right column of Fig. 5.9). As described above, the intensity F_1 received in coil 1 can simply be written as the sum of the two intensities I_A and I_B of the original image weighted with the sensitivity profiles C_{A1} and C_{B1} of coil 1 at positions A and B:

$$F_1 = I_A \cdot C_{A1} + I_B \cdot C_{B1}.$$

Assuming that the coil sensitivity values C_{A1} and C_{B1} are known, there are two unknowns I_A and I_B and only one known F_1 in this equation. Thus with this one equation, it is not possible to find the unique pixel values I_A and I_B from the aliased pixel F_1 . However, as the signal is acquired using multiple receiver channels, one equation can be written for each of the coil elements used, leading to the following set of equations:

$$\begin{aligned} F_1 &= I_A \cdot C_{A1} + I_B \cdot C_{B1} \\ F_2 &= I_A \cdot C_{A2} + I_B \cdot C_{B2} \\ F_3 &= I_A \cdot C_{A3} + I_B \cdot C_{B3} \\ F_4 &= I_A \cdot C_{A4} + I_B \cdot C_{B4} \end{aligned}$$

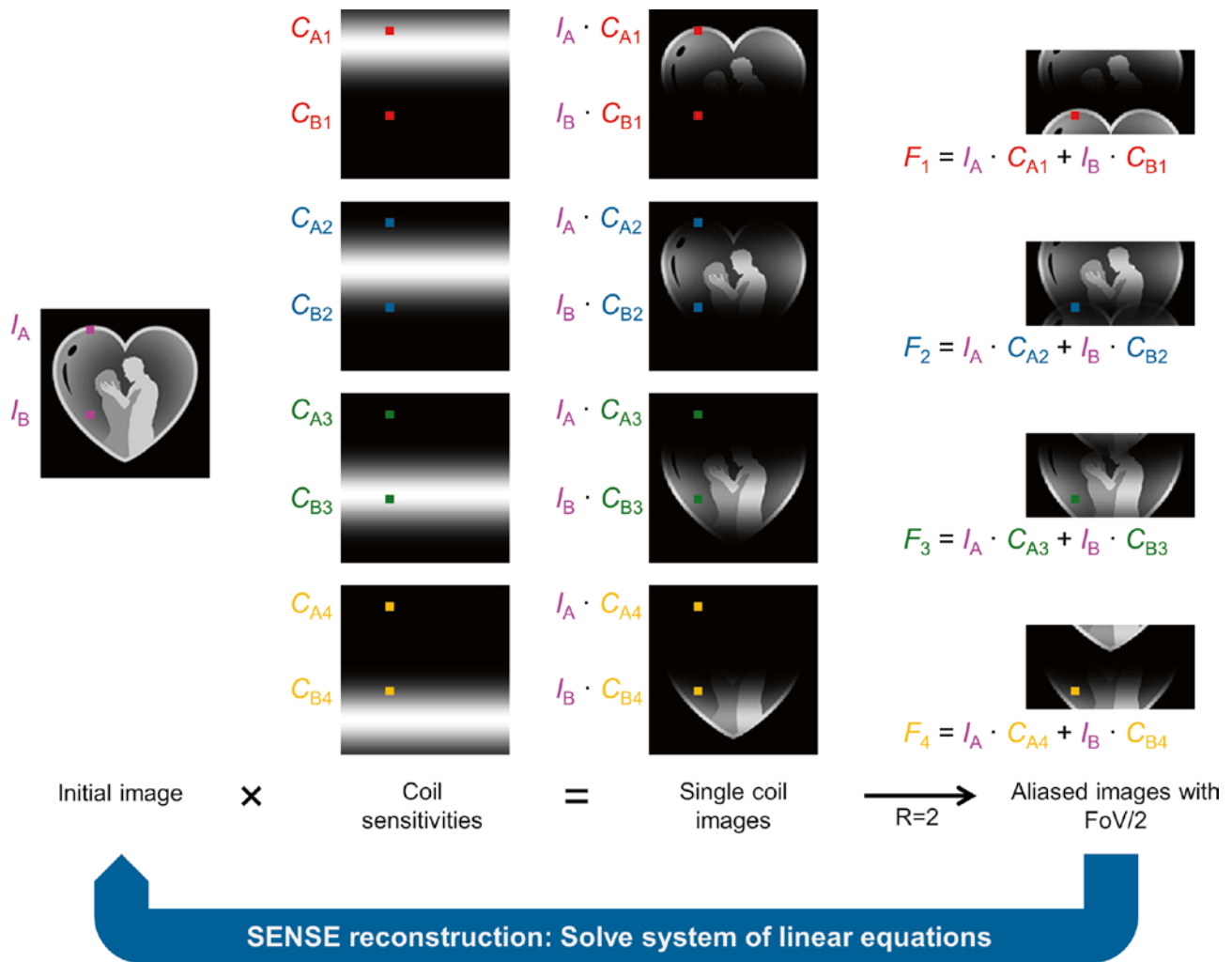


Fig. 5.9 SENSitivity Encoding (SENSE). The full FoV images seen by the individual receiver coils can be obtained by multiplying the initial image (I) with the sensitivity of each coil (C). If these images are under-sampled with $R=2$ (F), the signal of each pixel in the smaller FoV

image is the sum of two pixels of the full FoV images. As aliased images F are available for multiple coils, this corresponds to a set of linear equations which is solved in a SENSE reconstruction

As there are four equations and only two unknowns, this system of equations can be solved uniquely for the pixels A and B in the least-squares sense. The same procedure is used to unfold each of the aliased pixels, leading to a single full FoV image.

As any errors in the coil sensitivities can result in residual aliasing artifacts in the reconstructed images, the main challenge in SENSE reconstruction is the accurate determination of coil sensitivity maps. These maps are usually obtained by performing a pre-scan at the beginning of the MRI examination. Inaccuracies in the coil sensitivity maps can arise from many different sources, and can lead to image artifacts. In cardiovascular MRI, a significant source of error in the coil sensitivity maps is patient movement, which can change the position of the coil array and even the coil sensitivities themselves. This error can be partially mitigated by using TSENSE [20, 21], in which coil sensi-

tivity maps are generated by merging temporally adjacent undersampled datasets in a series of dynamic images. It can also be challenging to accurately determine the coil sensitivities in regions of low signal, including the lungs, which are difficult to avoid in cardiac images. Despite these minor challenges, SENSE and its variations are amongst the most robust and extensively used parallel imaging techniques in clinical MRI.

GRAPPA (GeneRALized Autocalibrating Partially Parallel Acquisition)

Both PILS and SENSE work by using coil sensitivity maps and aliased images to generate the unfolded image. However, other approaches use the information from the undersampled k-space to reconstruct a fully-sampled k-space. The most

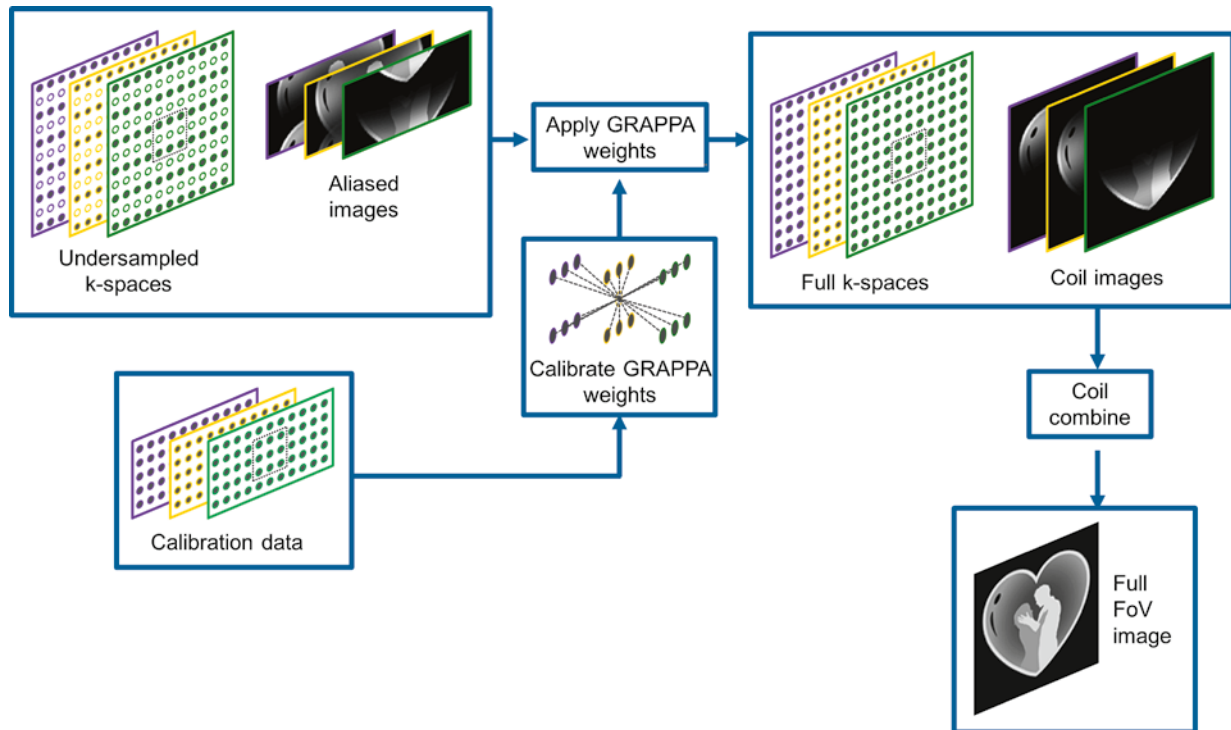


Fig. 5.10 GeneRalized Autocalibrating Partially Parallel Acquisition (GRAPPA). *Top left:* k-Space lines are acquired with three channels (denoted in different colors) using an acceleration factor of $R=2$ (skipped points are denoted as *empty circles*). The acceleration leads to aliasing in the images. *Bottom left:* An additional portion of fully-sampled data, the auto-calibration signal (ACS), is acquired. *Center:* Using the calibration data, the relationship between the acquired points and the missing points in a specified kernel is determined separately for

each channel. This relationship is known as the GRAPPA weights. The kernel shown here is a 2×3 kernel, which spans three read points and two phase encoding lines (*dotted box* in undersampled and calibration data). *Top right:* Once the GRAPPA weights have been calculated, they are applied to reconstruct the missing points in each k-space, resulting in unaliased images. The single-channel images are combined together to generate a single image without aliasing artifacts

widely used k-space based parallel imaging technique is known as GeneRalized Autocalibrating Partially Parallel Acquisition (GRAPPA, [22]). As any other parallel imaging technique, the k-space data are first undersampled in order to reduce the total scan time. GRAPPA reconstructs these missing k-space points by assuming that k-space points acquired near a missing point contain information about that missing point. This assumption is true if receiver coils with sufficient variations in the coil sensitivity profiles are used to collect the k-space data. The GRAPPA algorithm finds a mathematical relationship between a missing k-space point and its neighbors to estimate that missing point. When all the missing points have been reconstructed, and the k-space no longer contains missing points, a Fourier transform is applied to generate an unaliased image.

Figure 5.10 shows a schematic diagram of GRAPPA. In the GRAPPA language, acquired k-space points are typically called source points, and missing k-space points are called target points. The signal in one of the target points can be recovered by multiplying neighboring source points with a set of weights (GRAPPA weights). These GRAPPA weights are the same throughout regularly undersampled k-space, and they can be calculated using a

small part of a fully-sampled k-space known as auto-calibration signal (ACS) lines. In Fig. 5.10, three neighboring readout points of two phase encoding lines and the three coils used in the acquisition (differently colored frames) form the GRAPPA kernel of source points to reconstruct the target points. All occurrences of this kernel in the ACS dataset are used to determine the GRAPPA weights. Once the weights have been determined for this kernel, they can be applied to the undersampled k-space to reconstruct the missing data. The result is one full k-space for each coil used for signal acquisition, which can be converted into single-channel images and combined to make a final reconstructed image.

The ACS lines used for calibration in GRAPPA reconstructions are the k-space counterpart of the coil sensitivity maps used in SENSE, as both contain the coil sensitivity information needed for the parallel imaging reconstruction. An advantage of using ACS lines is that the coil sensitivity information that they contain is less affected by patient motion and areas with low signal than actual coil sensitivity maps. This can be beneficial in cardiovascular applications, where motion is difficult to avoid. Additionally, the ACS lines can directly be acquired dur-

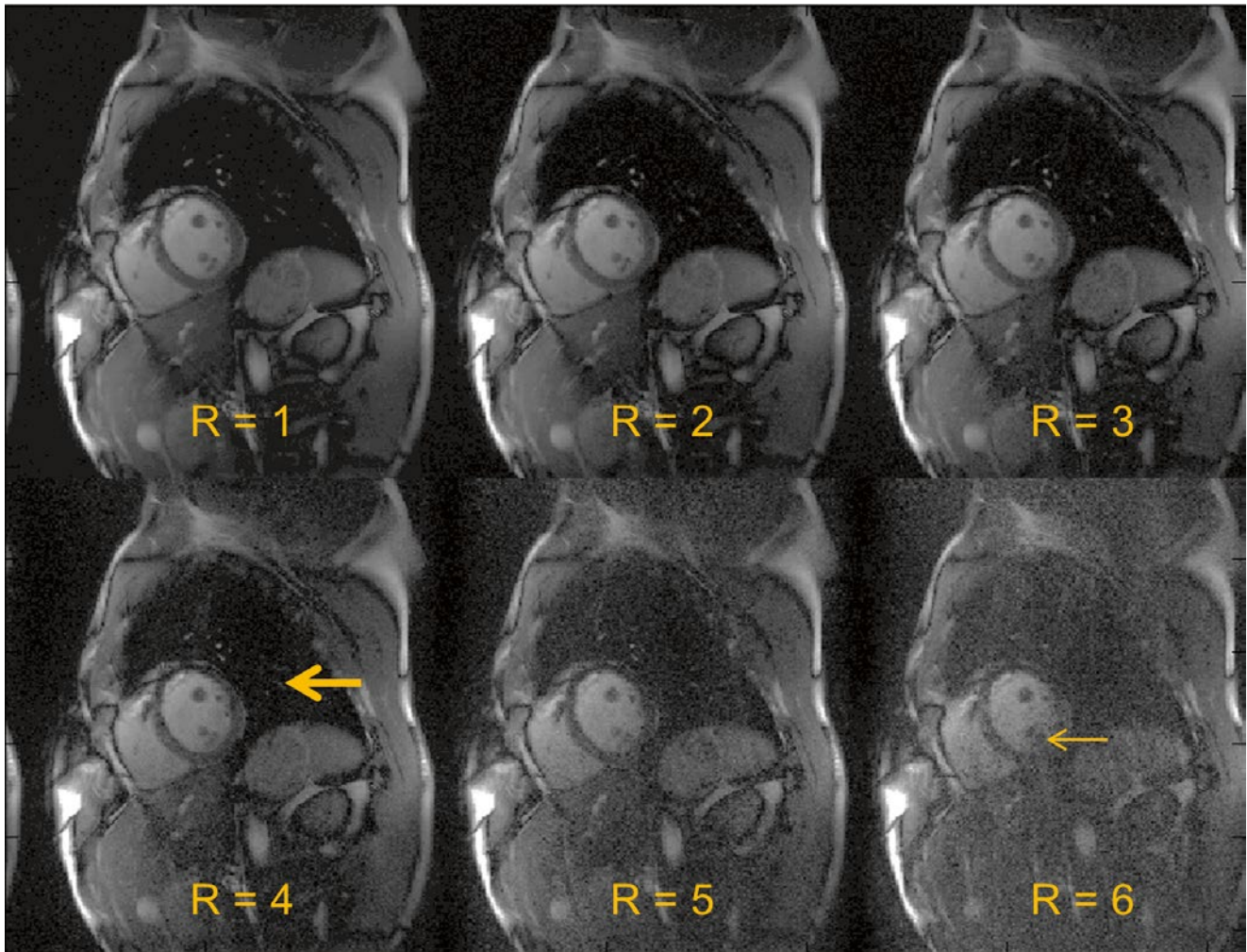


Fig. 5.11 Limitations of parallel imaging. Cardiac images acquired with a 32-channel receiver array, retrospectively undersampled and reconstructed using GRAPPA. Note that as the acceleration factor

increases, the SNR is reduced (for instance, near the *thick arrow*); at high acceleration factors, residual aliasing obscures relevant anatomy (for instance, near the *thin arrow*)

ing the accelerated scan, so GRAPPA can be performed without any pre-scans. The ACS data typically consists of multiple k-space lines acquired in the central portion of k-space, and these lines can be included in the final reconstruction in order to improve the stability of the reconstruction. Finally, as in TSENSE, the ACS lines can be generated from undersampled data collected in an interleaved fashion in dynamic imaging using TGRAPPA [23], eliminating the need for additional ACS data. For these reasons, GRAPPA and its variations are also widely used in clinical cardiovascular MRI.

Limitations of Parallel Imaging

In order for a parallel imaging reconstruction to be successful, the maximum reduction factor (R) should generally not be larger than the number of receiver coils used for the acquisition in this direction. In standard clinical practice, R is

typically chosen to be much smaller than the number of coils to avoid residual aliasing artifacts or severe SNR degradation. The loss in SNR in parallel imaging is due to two factors. The first is that R times fewer data points are acquired, reducing the SNR by a factor of \sqrt{R} . Additionally, there is a loss of SNR which depends on the geometry and properties of the receiver coil array, and the SNR is further reduced by the so-called coil geometry factor, g . The geometry factor varies across the reconstructed image, leading to non-uniform SNR which is generally lower in areas where many pixels overlap in the aliased image. Residual aliasing occurs when the acceleration factor is chosen to be too high, and the coil sensitivities cannot completely resolve the aliasing. As an example, Fig. 5.11 shows images where GRAPPA has been used to reconstruct datasets retrospectively undersampled by acceleration factors between $R=2$ and $R=6$. As the acceleration factor increases, the background noise also increases. At $R=5$ and $R=6$, the coil sensitivity variations are not capable of completely removing the aliasing, leading

to residual artifacts in these images. Thus, for cardiac imaging and typical receiver coils, acceleration factors of up to $R=4$ are currently employed in a clinical setting.

Up-and-Coming Methods

The methods discussed in this chapter thus far are all routinely used for clinical cardiac MRI. However, these methods all still require breath-holding and/or ECG gating, which can limit the application of cardiac MRI in clinical practice. Thus, many techniques have recently been introduced to further accelerate MRI scans; while most have yet to be validated for clinical use, the development of novel rapid imaging techniques is one of the most active fields of research in MRI. Several promising future methods will be described in the following section.

Non-Cartesian Trajectories

Non-Cartesian trajectories represent a promising opportunity for the further reduction of scan time. Instead of traversing k-space in a series of parallel raster lines, non-Cartesian techniques use alternative paths to collect k-space data. Although this opens the way for an infinite number of sampling trajectories, two non-Cartesian trajectories have emerged for rapid imaging, namely the radial trajectory, which is also known as projection reconstruction [24], and the spiral trajectory [25]. In these trajectories, the center of

k-space containing most of the image contrast is sampled with every readout, which can make them more robust in the presence of motion or flow. Another major difference is the appearance of undersampling artifacts when scanning along non-Cartesian trajectories. In contrast to Cartesian sampling, where aliasing artifacts appear as replicas of the image, non-Cartesian aliasing artifacts have a more noise-like appearance and often do not obscure the image. Figure 5.12 illustrates the undersampling artifacts of various non-Cartesian trajectories. Because such images can still be useful despite a high acceleration factor, non-Cartesian trajectories have great potential for cardiovascular imaging.

Although radial and other non-Cartesian trajectories have many advantages over Cartesian acquisitions, they come along with disadvantages which have limited their use in clinical routine. One challenge is the need to perform data gridding or a non-uniform Fourier transform in order to generate images from non-Cartesian data [26]. Thus, compared to the straight-forward two-dimensional Fourier transform used in Cartesian imaging, more sophisticated methods have to be used for the reconstruction of non-Cartesian datasets. In addition, phenomena such as trajectory errors and off-resonance effects can lead to pronounced artifacts which are not present in Cartesian imaging [27].

Another challenge when working with non-Cartesian trajectories is that it is difficult to combine them with parallel imaging. The main difficulty lays in the fact that most Cartesian parallel imaging algorithms require regularly undersampled Cartesian data, which leads to well-defined aliasing artifacts. In contrast, images generated from unders-

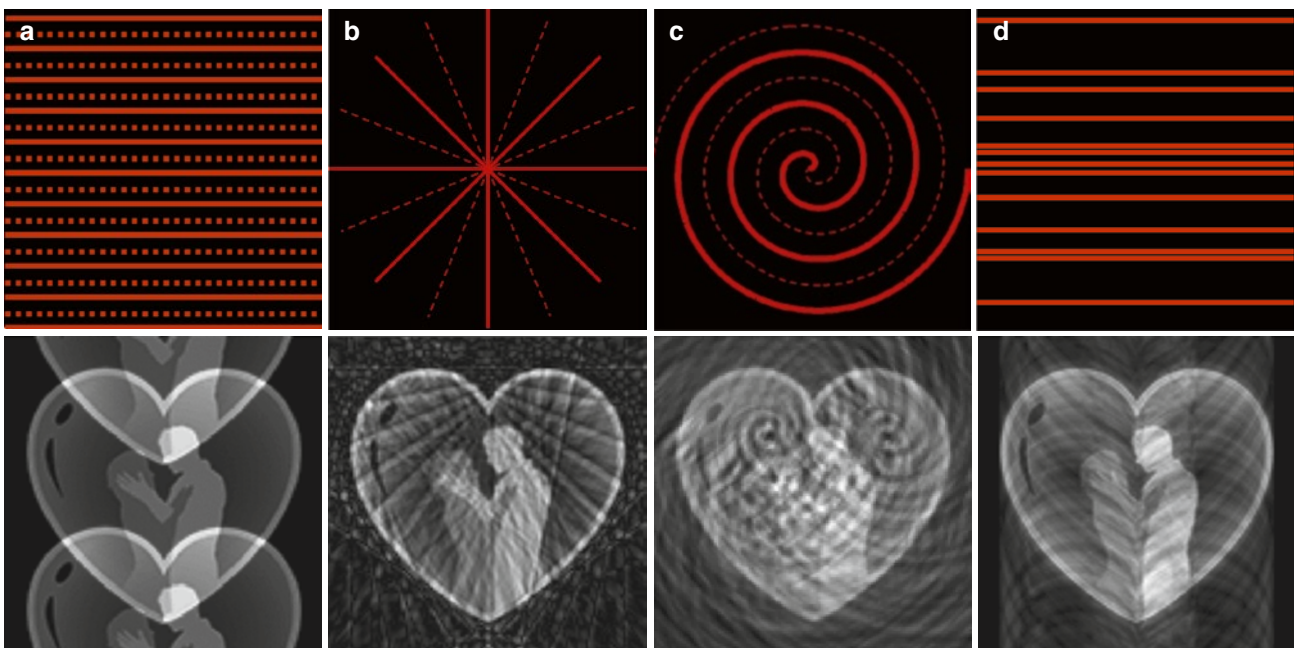


Fig. 5.12 Sampling trajectories and undersampling artifacts. Different sampling trajectories (*top*) and images showing typical aliasing artifacts from these trajectories (*bottom*): undersampled Cartesian (a), radial (b), spiral (c), and irregular Cartesian (d)

ampled non-Cartesian datasets exhibit complex aliasing artifacts as shown in Fig. 5.12, and each voxel in the image can potentially alias with all of the other voxels. However, it is possible to combine parallel imaging techniques with non-Cartesian trajectories using methods such as CG-SENSE [28], SPIRiT [29], or non-Cartesian GRAPPA techniques [30, 31]. While non-Cartesian parallel imaging is possible and enables significantly faster imaging than Cartesian parallel imaging, it has not yet become standard for clinical MRI examinations.

VIPR/HYPR

As seen in Fig. 5.12b, undersampled radial trajectories can result in images with streak artifacts where the underlying anatomy is still visible. By using 3D radial trajectories that distribute the radial projections in all three k-space dimensions in what is known as Vastly undersampled Isotropic PRojection imaging (VIPR, [32]), the acquisition can be even further accelerated to undersampling factors of about 50. These images can be used without any further reconstruction due to the diffuse nature of the aliasing artifacts in 3D.

However, in some cases it may be beneficial to further accelerate a 3D radial scan or remove some of the streaking artifacts in these images. The HighLY constrained back-PRojection (HYPR, [33]) reconstruction method can be used if the images are sparse and contain mostly contrast changes. Dynamic MR angiography images have these properties, and HYPR is typically employed with such datasets. HYPR works by continuously collecting data using a 3D radial trajectory during the administration of a contrast agent. By combining all of the acquired projections, a composite image with a high spatial resolution, but no temporal dynamics can be generated. The temporal dynamics can be understood by using small numbers of temporally adjacent projections to make highly undersampled (and therefore streaky) images which show the passage of the contrast agent. By combining the high spatial resolution composite image with these highly undersampled images showing the temporal dynamics using filtered back-projection, high resolution, temporally resolved 4D images can be created.

k-t Methods

Another class of recently introduced methods takes advantage of the fact that much of the image remains virtually unchanged in most dynamic cardiac acquisitions. In a breath-held cine acquisition of a short axis view, one of the most common acquisitions in cardiac MRI, the signal of the chest wall, the lungs, the spine as well as the muscles remains almost the same between two consecutive frames. Information about this static signal could theoretically be used for each of the time frames in the dynamic series, and

does not need to be reacquired for each image. The need for less information about each image corresponds with the ability to accelerate the scan by acquiring fewer k-space lines, which allows scan time to be decreased.

k-t Broad-use Linear Acquisition Speed-up Technique (k-t BLAST) uses the idea that dynamic images that are related to one another can be reconstructed from undersampled k-space data if some information about the temporal dynamics (or changes in the images over time) is known [34]. As in parallel imaging, lines of k-space are skipped using a special interleaved undersampling scheme in k-t BLAST, resulting in a series of undersampled images with aliasing artifacts. To unfold these images, a training dataset consisting of a similar series of images with a low spatial resolution but a high temporal resolution is collected. This set of training data can be used to estimate the temporal dynamics of the image series without the aliasing present in the undersampled images. By enforcing the temporal dynamics of the training data on the undersampled dynamic data, a movie of high spatial as well as temporal resolution can be generated.

k-t SENSE is a further extension of the k-t BLAST technique which also uses parallel imaging to further accelerate the measurement, allowing even higher acceleration factors. In both techniques, the time savings can be used to increase the coverage of the cardiac cycle (acquire more cine frames) or improve the spatial resolution. Other more complex k-t techniques including k-t PCA [35] and k-t SPARSE SENSE [36] have been proposed for rapid cardiovascular imaging, which use similar ideas to allow even faster data acquisition.

Compressed Sensing

Another way to accelerate image acquisition is to make use of the compressibility of natural images. Figure 5.13a shows an uncompressed short axis image in the bitmap format, as it is typically obtained in MRI. Using a simple JPG compression, the file size of the original can be reduced to 2 % of its initial size with no visual loss of information even in the magnified images. The example illustrates the fact that medical images are compressible and that theoretically, fewer points in k-space should be sufficient to generate a clinical quality image. This observation has led to the theory of compressed sensing (CS), which is one of the most active fields of research in MRI [37–39]. CS holds the potential of greatly accelerating data acquisition, and because the principles of CS are different from, but compatible with those of parallel imaging, these two types of methods can be combined to achieve even higher acceleration factors such as $R=8$ [40].

For compressed sensing to be able to reconstruct unaliased images from undersampled MRI data, several

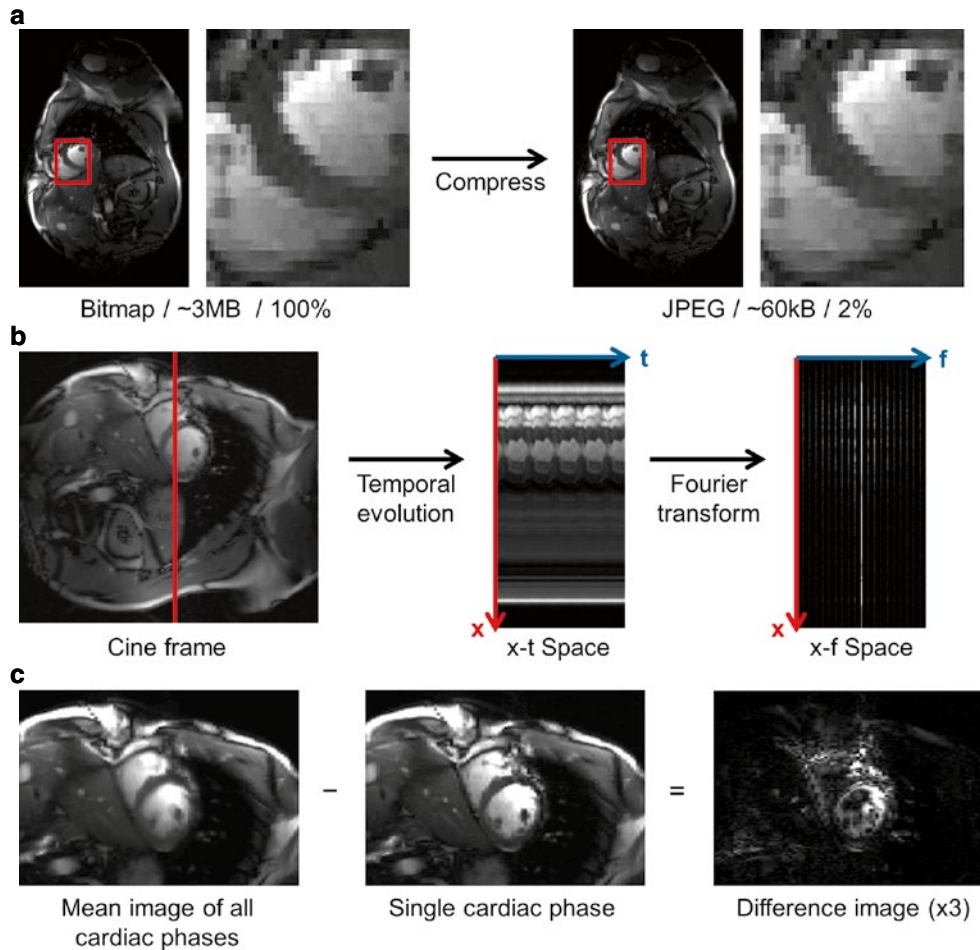


Fig. 5.13 Compressed Sensing (CS). (a) The size of an image in the bitmap format can be reduced to 2 % of its original size using the JPEG compression. Even in the magnified areas (*red*), no differences between the images are apparent. (b) The variations in a vertical line across the short heart axis image is first depicted in what is known as the x-t space. A Fourier transform in the time domain yields a sparse x-f space con-

taining the temporal frequencies of the cardiac cycle. (c) The images from each cardiac phase are subtracted from the mean image of all cardiac phases. These difference images show only information about parts of the image that move and can be sparse enough to be used with compressed sensing

requirements must be met. The first is that the image must have a sparse representation, or in other words, the image must be made up of only a few non-zero pixels. Although some MR images, such as angiograms, are inherently sparse, cardiac images do not have this property. Before a CS reconstruction can be applied, a transformation must be applied to such an image to make it sparse. One widely used transform domain is the x-f space, which is the type of transform used in k-t BLAST and which is depicted in Fig. 5.13b. Standard images reside in x-t space (where x is spatial position and t is time), and these images can contain a considerable amount of redundant information. By applying a Fourier transform in the temporal domain, the images are transformed from the x-t space to the x-f space (f is frequency). The representation in the x-f space is sparse, as all static portions of the image are found only at the center frequency. Another way to generate a sparse representation

of cardiac images is to take the difference between each single cine frame and a mean image of all frames of the entire cardiac cycle. This approach, which is depicted in Fig. 5.13c, results in a set of images which show only the information about cardiac motion and which are sufficiently sparse for the application of CS.

Another requirement for CS to be applied is that the aliasing artifacts resulting from data undersampling must be incoherent. As shown in Fig. 5.7, regular undersampling patterns lead to clear fold-over artifacts, known as coherent aliasing. In contrast, irregular undersampling patterns lead to irregular aliasing artifacts that visually appear like noise, which are also known as incoherent artifacts. To obtain these incoherent artifacts, some k-space lines can be pseudo-randomly omitted in Cartesian sampling, as illustrated in Fig. 5.12d. Alternatively, many non-Cartesian trajectories, such as radial trajectories, result in incoherent artifacts and are often used

in CS applications. An example of the incoherent artifacts in a radially undersampled sampling scheme is shown in Fig. 5.12b.

If the requirements of a sparse image (or image which can be made sparse) and incoherent aliasing artifacts are met, a compressed sensing reconstruction algorithm can be applied to remove the aliasing artifacts, yielding an artifact-free image. While there are many different types of CS algorithms, all involve a non-linear reconstruction that is most often applied iteratively to separate the sparse signals from the noise-like artifacts. These iterative algorithms seek to find an image that is both consistent with the k-space data that has been acquired, and with the requirement that the final image is sparse. For a better understanding of these types of algorithms, a simple explanation of the non-linear reconstruction algorithm is given in [39].

There are several challenges to the use of compressed sensing in clinical routine. One is that the type of transform used to sparsify the undersampled images is highly dependent on the particular application. The use of an inadequate sparsifying transformation can lead to the removal of some image features or the retention of artifacts in the final images. Another challenge lies in the long reconstruction times that are typically encountered for CS algorithms. Additionally, the unusual nature of CS artifacts, which differ based on the specific transform and reconstruction algorithm, have not yet been fully explored by radiologists. However, due to the high demand for further acceleration in cardiac MRI as well as the great redundancy in dynamic cardiac imagines, CS will continue to be explored, both alone and in conjunction with parallel imaging.

Applications of Fast Imaging in Cardiovascular MRI

Cardiovascular imaging in the clinic is nearly always accelerated using one or more of the techniques described above. Some examples of how rapid imaging is essential for clinical cardiovascular MRI are discussed in this section.

Morphological Imaging

Morphological cardiac imaging is one of the common applications of fast imaging sequences in clinical MRI. Its goal is the acquisition of a cardiac “snapshot” depicting one phase of the cardiac cycle, without any cardiac or respiratory motion. Additionally, the distinction between tissue and blood is of great importance for a reliable delineation of the heart chambers and the vascular lumen. A suppression of the blood signal can be achieved by using TSE sequences. A black-blood preparation scheme is additionally applied to

further enhance the intrinsic black-blood contrast of SE-based sequences [41–43]. It consists of a global inversion pulse followed by a re-inversion pulse selective only to the tissue in the desired image slice. After a suitable inversion time (TI), the re-inverted blood in the selected slice will be replaced by inverted blood from outside the slice. The signal of the inverted blood during relaxation is dependent on TI which can be adjusted to null the blood signal during image acquisition. To eliminate respiratory motion, the acquisition of one slice is typically performed during a breath-hold. In order to minimize cardiac motion, data collection is limited to an imaging period of about 200 ms in diastole.

For the acquisition of an image of a spatial resolution of 2 mm^2 and a FoV of 256 mm^2 (128 phase encoding steps), a TSE sequence with a turbo factor of 16 would require 8 shots to be applied and could be performed in a breath-hold of eight heartbeats with a TR of one R-R interval. A short effective TE can be combined with a short repetition time of one R-R interval to achieve T_1 -weighting. Conversely, an image with T_2 -weighting can be obtained using a long effective TE as well as a long repetition time, which is typically achieved by only triggering the sequence every two to three heartbeats. A clinical example of a morphological black-blood TSE image acquired at 3 T (bSSFP sequence, TR = 2 heartbeats, TE = 70 ms, A: #PE = 208, #RO=256, FoV = $292 \times 360 \text{ mm}^2$) is shown in Fig. 5.14. In addition to the segmentation, this dataset was accelerated using a rectangular FoV and parallel imaging with R=2 and a GRAPPA reconstruction. In conjunction with these rapid imaging techniques, 14 ECG trigger pulses were needed in this acquisition to acquire a single slice. The acquisition was triggered only every second ECG pulse to ensure a sufficient relaxation between the two inversion pulses.

Functional Imaging

Another important application for fast imaging sequences in clinical MRI is functional imaging of the heart including the dynamic study of cardiac motion and cardiac contractile function. The usual approach is to monitor the cardiac dynamics in a desired 2D slice of the heart over the entire cardiac cycle. This can be achieved by using a breath-held and ECG gated cine acquisition, which is based on a fast GRE sequence [44, 45]. As only one RF pulse is applied to generate the signal in gradient echo sequences, the spin washout effect of TSE sequences does not apply for GRE sequences. Instead, the signal from flowing blood is readily visible or even brighter than surrounding tissues, which is why these methods are often referred to as bright blood imaging. In combination with the lower signal of the tissue, this results in a high intrinsic contrast between blood and myocardium which is desirable for functional imaging.

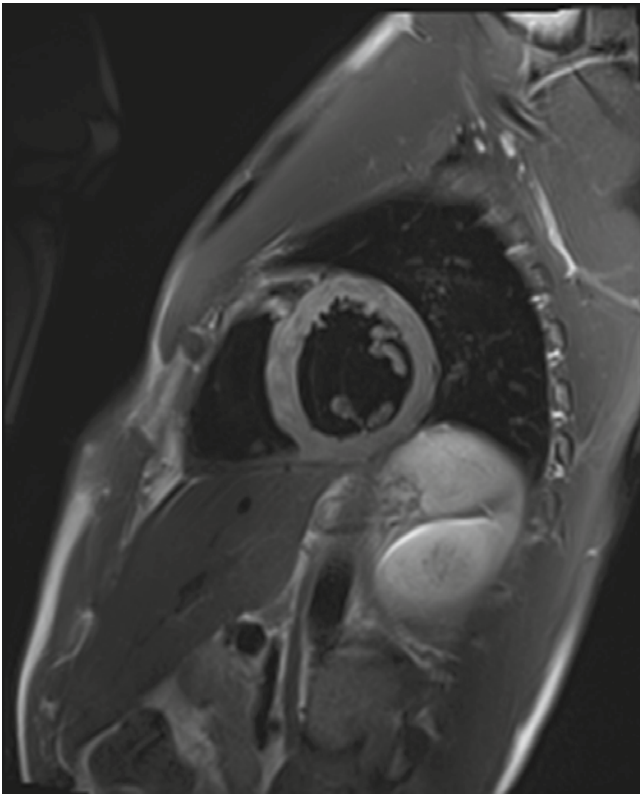


Fig. 5.14 Black-blood anatomical TSE imaging. A clinical example of a black-blood TSE sequence for morphological cardiac imaging is shown (TR = 2 heartbeats, TE = 70 ms, #PE = 208, #RO = 256, FoV = 292×360 mm²). The dataset was accelerated using a rectangular FoV, a segmented TSE sequence with a turbo factor of 17, and parallel imaging with R=2 and a GRAPPA reconstruction. In conjunction with these rapid imaging techniques, 14 heartbeats were needed to acquire a single slice. The acquisition was triggered only every second ECG pulse to ensure a sufficient relaxation between consecutive inversion pulses

Figure 5.15 depicts two clinical examples of retrospectively gated bSSFP cine acquisitions obtained at 3 T with identical parameters (25 cine frames, #PE = 216, #RO = 256, TR = 3.0 ms, TE = 1.5 ms, FoV = 286×340 mm², flip angle = 45°, R = 3). In addition to an acceleration with a rectangular FoV and parallel imaging with R=3, the acquisition was segmented by collecting only a group of 13 lines of k-space for each of the 25 cardiac phases in every heartbeat. With these rapid imaging techniques, one slice can be acquired within six heartbeats.

Myocardial Perfusion Imaging

One important application for fast imaging sequences is dynamic contrast-enhanced MRI (DCE-MRI). In DCE-MRI, the bolus passage of a signal enhancing contrast agent (CA) through the tissue to be investigated is imaged [46, 47]. After the intravenous injection of the usually gadolinium-based CA, a series of images of the desired anatomical

slice is acquired over multiple successive heartbeats. In order to minimize respiratory motion artifacts, the whole acquisition is performed in a breath-hold if possible. Additionally, an ECG trigger is used to ensure that the entire set of images is acquired at the same cardiac phase, freezing any cardiac motion. Typically, saturation magnetization preparation is used after every ECG trigger to obtain the same T₁-weighted contrast for every heartbeat. As the CA carried by the inflowing blood alters the signal intensity of perfused tissue, generating a movie from all images acquired after the CA administration enables the detection of regions with reduced perfusion. However, the first pass of a CA through the myocardium is very rapid (usually about 10 s), leading to extremely demanding imaging requirements in cardiac DCE-MRI. Ideally, the measurement should yield a dynamic series of at least three motion-free short axis views, plus one long axis view, of a sufficiently high spatial and temporal resolution which show the signal intensity increasing and then decreasing as the bolus of CA passes through the myocardial tissue. In order to achieve these minimal requirements, a compromise between temporal and spatial resolution has to be made, even though the fastest available imaging sequences such as FLASH or bSSFP with the shortest achievable repetition times in combination with partial Fourier and parallel imaging acceleration are typically used. Moreover, a compromise between the number of slices to be acquired in each heartbeat and the spatial resolution for each of these slices has to be found. In some cases, either the number of slices or the spatial resolution can be increased by stretching the acquisition over two successive heartbeats, thereby decreasing the temporal sampling of the bolus passage in each of these slices.

Given a patient with a relatively fast heart rate of 100 beats per minute, the available acquisition window within each heartbeat would be about 450 ms with a sufficiently large arrhythmia rejection period. After a saturation pulse and a trigger delay of about 100 ms for sufficient T₁-weighting, the use of a bSSFP sequence with a TR of 2.5 ms would allow the acquisition of three slices at a spatial resolution of 2 mm² and a FoV of 256 mm² including a parallel imaging acceleration of R=3 (corresponding to the acquisition of 43 phase encoding steps per slice resulting in 128 phase encoding steps after the parallel imaging reconstruction). This acquisition is typically repeated over 20–40 heartbeats, depending on the patient's heart rate. Although the fastest imaging sequences in conjunction with parallel imaging are used in this example, the coverage of only three slices per heartbeat illustrates the extremely high requirements in myocardial DCE-MRI. An example of a clinical first-pass perfusion measurement (bSSFP sequence, 60 frames, 3 slices, #PE = 174, #RO = 192, TR = 2.8 ms, TE = 1.4 ms, FoV = 344×379 mm², flip angle = 35°)

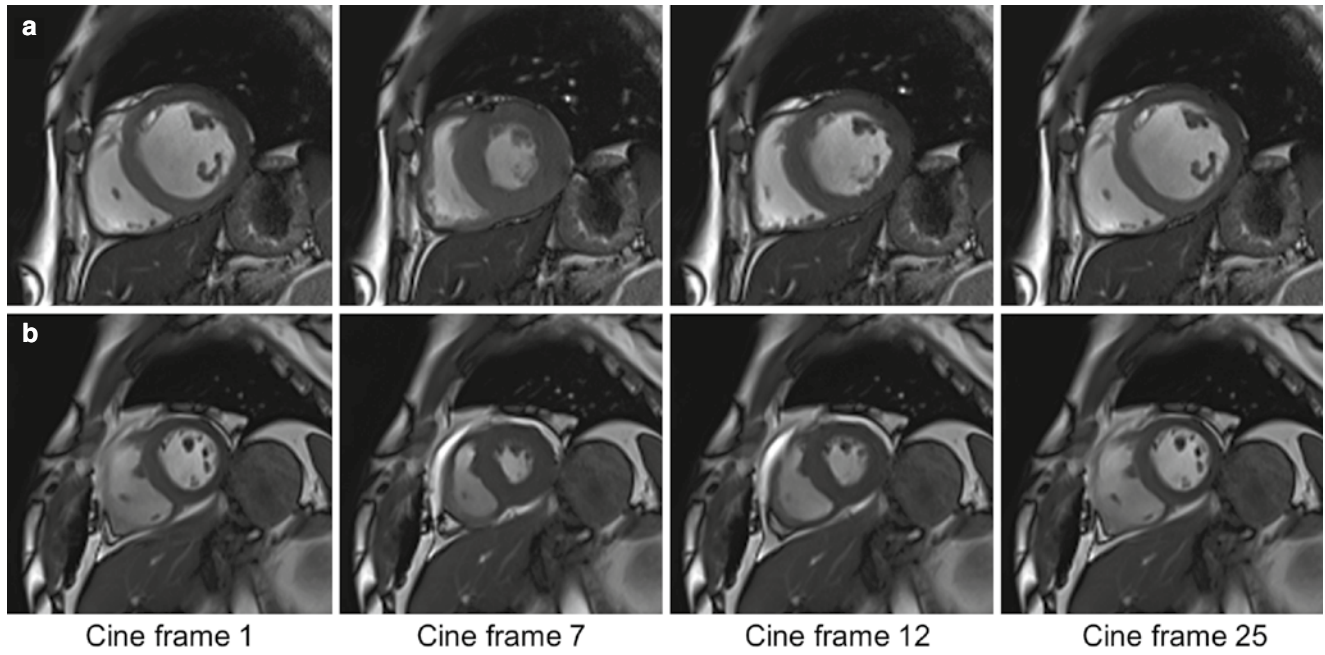


Fig. 5.15 Cine imaging. Two clinical examples both acquired with retrospectively gated bSSFP cine acquisition and identical parameters (25 cine frames, #PE = 216, #RO = 256, TR = 3.0 ms, TE = 1.5 ms, FoV = 286×340 mm², flip angle = 45°, R = 3). Both patients suffer from anterior transmural myocardial infarction, which is not as readily visible as in a morphological contrast-enhanced sequence (compared viability

images of patient a in Fig. 5.17a). In addition to a rectangular FoV, the acquisition was segmented by collecting only a group of 13 lines of k-space for each of the 25 cardiac phases in every heartbeat, and parallel imaging with R=3 was used for acceleration. With these rapid imaging techniques, one slice can be acquired within six heartbeats

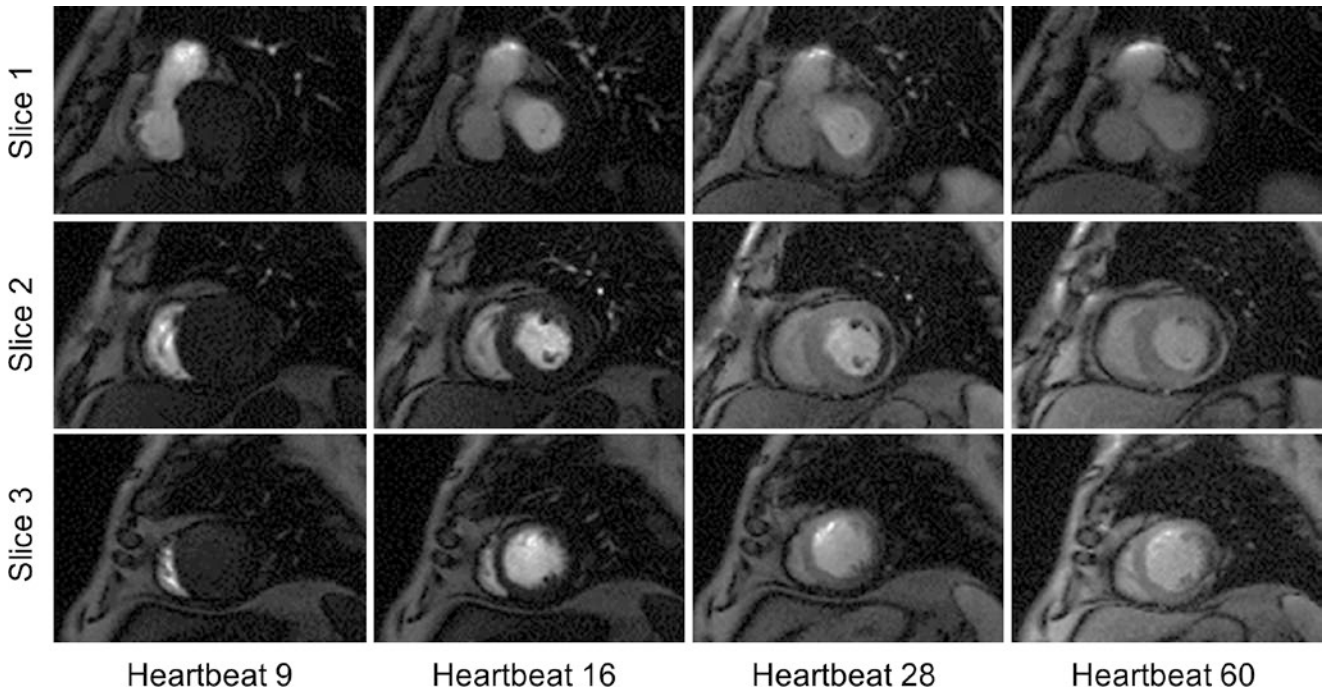


Fig. 5.16 First-pass perfusion. Clinical example of three slices collected in a contrast-enhanced first-pass perfusion study. The patient suffers from a posterior transmural myocardial infarction (areas with reduced contrast-enhancement). To obtain these snapshots of the contrast changes for 60 consecutive heartbeats without cardiac motion artifacts, a prospectively triggered bSSFP sequence (60 frames, #PE =174, #RO = 192, TR = 2.8 ms, TE = 1.4 ms, FoV = 344×379 mm², flip angle

= 35°) was accelerated with parallel imaging of R=3, leading to only 58 k-space lines for every image (or an acquisition window of ~162 ms per image and ~486 ms for 3 consecutive images). Note that a reduced FoV was used, resulting in fold-over artifacts at the corners of the full FoV images which do not obscure relevant anatomical information and are therefore acceptable in order to save acquisition time

obtained at 3 T is given in Fig. 5.16. To reduce cardiac motion artifacts, the acquisition window was kept to less than 200 ms by a $R=3$ parallel imaging acceleration, leading to only 58 k-space lines for every image (174 k-space lines per image divided by $R=3$). This resulted in an acquisition time of ~ 162 ms per slice, and three slices were consecutively acquired within ~ 486 ms, allowing data collection during diastole.

Viability Imaging

As seen in the previous section, the application of a contrast agent selectively alters the native tissue relaxation times in proportion to local tissue concentration. While this effect is used in myocardial DCE-MRI to image hypoperfusion, it can be used for the identification of scarred myocardial tissue in patients with acute or chronic myocardial infarction [48]. This measurement is also known as myocardial viability imaging. Delayed hyper-enhancement of myocardial tissue is exclusively related to irreversible injury [49]. Therefore, Late Gadolinium Enhanced (LGE) images of the myocardium are usually obtained several minutes after peripheral administration of a contrast agent (gadolinium chelate). At this time, the concentration of contrast agent changes relatively slowly and data collection can be performed over several heartbeats. To reduce motion artifacts, the acquisition is performed in breath-hold. After the ECG trigger, an inversion recovery prepared segmented turbo GRE sequence is applied. The inversion time, TI, between the inversion pulse and the start of the imaging sequence is chosen to approximately null the signal in the myocardium at the time of data collection. At this time point, regions of myocardial infarction appear hyper-enhanced and become clearly visible. Due to cardiac motion and the limited time window for the zero-crossing of the myocardial signal after global spin inversion, fast imaging sequences have to be used. To minimize any cardiac motion artifacts, an additional trigger delay between the ECG trigger and the inversion pulse is used in order to achieve an image acquisition in late-diastole, and the acquisition window for one group of k-space lines is limited to about 200 ms. For a regular heart rate, this sequence should be repeated every second heartbeat to ensure a sufficient relaxation between two inversions. As the total acquisition time is limited by the patient's breath-hold, a typical acquisition would therefore involve 8–10 inversion pulses within 16–20 R-R intervals.

As an example, a breath-hold of 10 s at a heart rate of 100 beats per minute would allow 16 heartbeats for image acquisition. If inversions are performed every second heartbeat, eight inversion pulses could be applied, each followed by a

data collection window of less than 200 ms. For the example, using a spoiled gradient echo readout with a TR of 7.5 ms and a spatial resolution of 2 mm^2 and a FoV of 256 mm^2 (corresponding to a 128 phase encoding steps), the image data can be acquired within the ten second breath-hold without applying any additional acceleration. Balanced SSFP can also be used to accelerate the readout. Two clinical LGE examples obtained with an inversion-recovery bSSFP sequence at 3 T are depicted in Fig. 5.17. It shows a short heart axis (patient A, #PE = 176, #RO = 256, TR = 2.4 ms, TE = 1.2 ms, FoV = $240 \times 350 \text{ mm}^2$, flip angle = 40°) and a four chamber view (patient B, #PE = 216, #RO = 256, TR = 2.4 ms, TE = 1.2 ms, FoV = $286 \times 340 \text{ mm}^2$, flip angle = 40°). Due to the very short time available for imaging, only 65 k-space lines of a bSSFP sequence are acquired in each heartbeat. As the acquisition is triggered only every second ECG pulse to ensure sufficient relaxation between the two inversion pulses, this leads to an acquisition time of six (patient A) and eight (patient B) heartbeats for the respective datasets.

Vascular Imaging

Imaging of blood vessels using magnetic resonance angiography (MRA) is another application which requires the use of fast imaging techniques. Similar to DCE-MRI, contrast-enhanced MRA (CE-MRA) monitors the first pass of an intravenously injected CA through the vessels of interest in areas of the body including the coronary arteries, the head and neck, abdomen, and extremities [50–52]. By using rapid T_1 -weighted imaging sequences, the presence of CA leads to enhancement of the blood signal in the vessels of interest, enabling the assessment of vascular abnormalities such as stenoses, occlusions or aneurysms. The small diameter of many vessels, often on the range of millimeters, in conjunction with the need to visualize contrast during the arterial phase without venous contamination, leads to challenging imaging requirements in terms of the spatiotemporal resolution. Spoiled gradient echo sequences with their extremely short repetition times are typically used in order to achieve both the necessary imaging speed and T_1 -weighting. High flip angles are used to improve the saturation of background tissue and hence maximize the contrast to the vessels. For a better spatial resolution in the slice selection direction, and to enable the complete coverage of the selected volume, 3D sequences with their better SNR properties are used. Additionally, other acceleration techniques such as parallel imaging or partial Fourier acquisitions are usually applied in one or both phase encoding directions to obtain a clinically relevant spatial and temporal resolution.

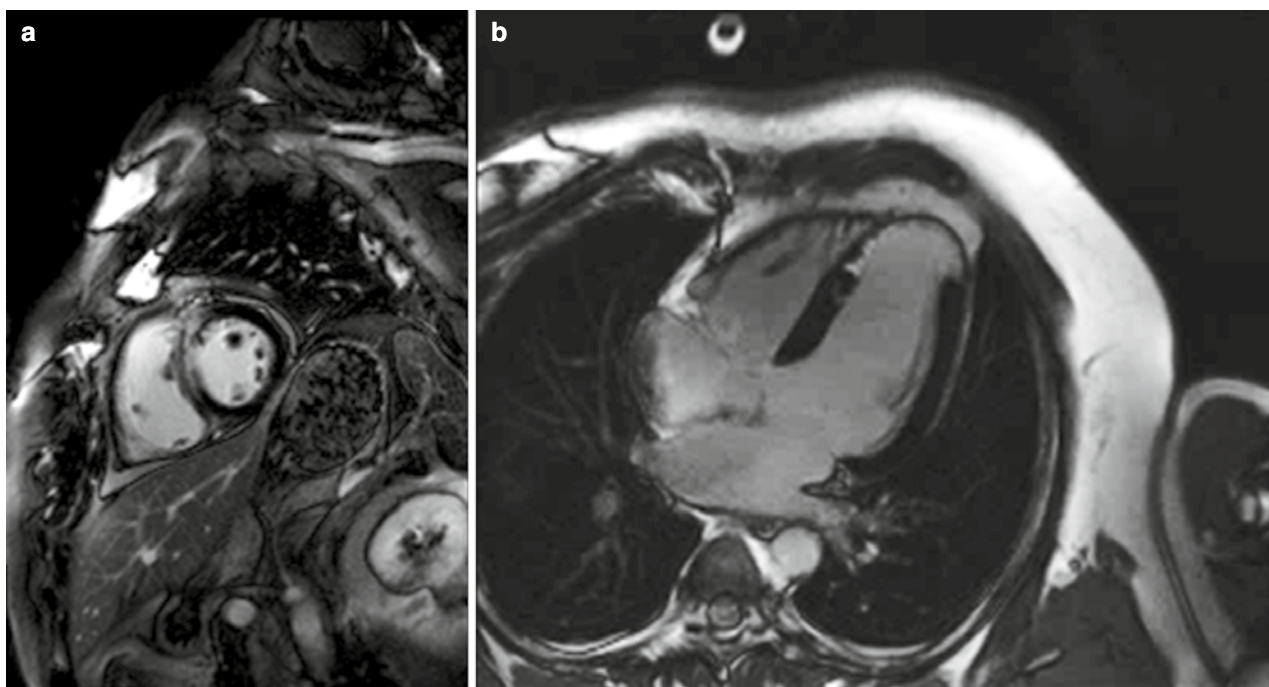


Fig. 5.17 Delayed gadolinium enhancement. Examples of a clinical contrast-enhanced delayed gadolinium enhancement measurement. (a) Short axis view of a patient suffering from an anteroseptal transmural myocardial infarction (bSSFP sequence, #PE = 176, #RO = 256, TR = 2.4 ms, TE = 1.2 ms, FoV = 240×350 mm², flip angle = 40°). (b) Four chamber view from a patient with apical infarction (bSSFP sequence, #PE = 216, #RO = 256, TR = 2.4 ms, TE = 1.2 ms, FoV = 286×340 mm², flip angle = 40°). The delay between inversion pulse and the start of the

imaging sequence is chosen to approximately null the signal in the healthy myocardial tissue. As this period is very short, only part of the diastole can be used for data collection, and only 65 k-space lines of a bSSFP sequence can be acquired in each heartbeat. The acquisition is triggered only every second ECG pulse to ensure sufficient relaxation between consecutive inversion pulses, leading to an acquisition time of six (patient A) and eight (patient B) heartbeats for the respective datasets

References

- Zur Y, Wood ML, Neuringer LJ. Spoiling of transverse magnetization in steady-state sequences. *Magn Reson Med.* 1991;21(2):251–63.
- van der Meulen P, Groen JP, Cuppen JJ. Very fast MR imaging by field echoes and small angle excitation. *Magn Reson Imaging.* 1985;3(3):297–9.
- Haase A, Frahm J, Matthaei D, Hancic W, Merboldt KD. FLASH imaging – rapid NMR imaging using low flip-angle pulses. *J Magn Reson.* 1986;67(2):258–66.
- Scheffler K, Lehnardt S. Principles and applications of balanced SSFP techniques. *Eur Radiol.* 2003;13(11):2409–18.
- Hennig J, Nauwerth A, Friedburg H. RARE imaging: a fast imaging method for clinical MR. *Magn Reson Med.* 1986;3(6):823–33.
- Listerud J, Einstein S, Outwater E, Kressel HY. First principles of fast spin echo. *Magn Reson Q.* 1992;8(4):199–244.
- Rzedzian R, Chapman B, Mansfield P, Coupland RE, Doyle M, Chrispin A, Guilfoyle D, Small P. Real-time nuclear magnetic resonance clinical imaging in paediatrics. *Lancet.* 1983;2(8362):1281–2.
- Poustchi-Amin M, Mirowitz SA, Brown JJ, McKinstry RC, Li T. Principles and applications of echo-planar imaging: a review for the general radiologist. *Radiographics Rev Publ Radiol Soc N Am Inc.* 2001;21(3):767–79.
- Lenz GW, Haacke EM, White RD. Retrospective cardiac gating: a review of technical aspects and future directions. *Magn Reson Imaging.* 1989;7(5):445–55.
- McGibney G, Smith MR, Nichols ST, Crawley A. Quantitative evaluation of several partial Fourier reconstruction algorithms used in MRI. *Magn Reson Med.* 1993;30(1):51–9.
- Noll DC, Nishimura DG, Macovski A. Homodyne detection in magnetic resonance imaging. *IEEE Trans Med Imaging.* 1991;10(2):154–63.
- Haacke EM, Lindsokj ED, Lin W. A fast, iterative, partial-fourier technique capable of local phase recovery. *J Magn Reson (1969).* 1991;92(1):126–45.
- Patel MR, Klufas RA, Alberico RA, Edelman RR. Half-fourier acquisition single-shot turbo spin-echo (HASTE) MR: comparison with fast spin-echo MR in diseases of the brain. *AJNR Am J Neuroradiol.* 1997;18(9):1635–40.
- van Vaals JJ, Brummer ME, Dixon WT, Tuithof HH, Engels H, Nelson RC, Gerety BM, Chezmar JL, den Boer JA. “Keyhole” method for accelerating imaging of contrast agent uptake. *J Magn Reson Imaging JMRI.* 1993;3(4):671–5.
- Jones RA, Haraldseth O, Muller TB, Rinck PA, Oksendal AN. K-space substitution: a novel dynamic imaging technique. *Magn Reson Med.* 1993;29(6):830–4.
- Haider CR, Glockner JF, Stanson AW, Riederer SJ. Peripheral vasculature: high-temporal- and high-spatial-resolution three-dimensional contrast-enhanced MR angiography. *Radiology.* 2009;253(3):831–43.
- Song T, Laine AF, Chen Q, Rusinek H, Bokacheva L, Lim RP, Laub G, Kroeker R, Lee VS. Optimal k-space sampling for dynamic contrast-enhanced MRI with an application to MR renography. *Magn Reson Med.* 2009;61(5):1242–8.

18. Griswold MA, Jakob PM, Nittka M, Goldfarb JW, Haase A. Partially parallel imaging with localized sensitivities (PILS). *Magn Reson Med.* 2000;44(4):602–9.
19. Pruessmann KP, Weiger M, Scheidegger MB, Boesiger P. SENSE: sensitivity encoding for fast MRI. *Magn Reson Med.* 1999;42(5):952–62.
20. Kellman P, Epstein FH, McVeigh ER. Adaptive sensitivity encoding incorporating temporal filtering (TSENSE). *Magn Reson Med.* 2001;45(5):846–52.
21. Köstler H, Sandstede JJ, Lipke C, Landschütz W, Beer M, Hahn D. Auto-SENSE perfusion imaging of the whole human heart. *J Magn Reson Imaging.* 2003;18(6):702–8.
22. Griswold MA, Jakob PM, Heidemann RM, Nittka M, Jellus V, Wang J, Kiefer B, Haase A. Generalized autocalibrating partially parallel acquisitions (GRAPPA). *Magn Reson Med.* 2002;47(6):1202–10.
23. Breuer FA, Kellman P, Griswold MA, Jakob PM. Dynamic autocalibrated parallel imaging using temporal GRAPPA (TGRAPPA). *Magn Reson Med.* 2005;53(4):981–5.
24. Glover GH, Pauly JM. Projection reconstruction techniques for reduction of motion effects in MRI. *Magn Reson Med.* 1992;28(2):275–89.
25. Meyer CH, Hu BS, Nishimura DG, Macovski A. Fast spiral coronary artery imaging. *Magn Reson Med.* 1992;28(2):202–13.
26. Jackson JI, Meyer CH, Nishimura DG, Macovski A. Selection of a convolution function for Fourier inversion using gridding [computerised tomography application]. *IEEE Trans Med Imaging.* 1991;10(3):473–8.
27. Peters DC, Derbyshire JA, McVeigh ER. Centering the projection reconstruction trajectory: reducing gradient delay errors. *Magn Reson Med.* 2003;50(1):1–6.
28. Pruessmann KP, Weiger M, Bornert P, Boesiger P. Advances in sensitivity encoding with arbitrary k-space trajectories. *Magn Reson Med.* 2001;46(4):638–51.
29. Lustig M, Pauly JM. SPiRiT: iterative self-consistent parallel imaging reconstruction from arbitrary k-space. *Magn Reson Med.* 2010;64(2):457–71.
30. Heidemann RM, Griswold MA, Seiberlich N, Kruger G, Kannengiesser SA, Kiefer B, Wiggins G, Wald LL, Jakob PM. Direct parallel image reconstructions for spiral trajectories using GRAPPA. *Magn Reson Med.* 2006;56(2):317–26.
31. Seiberlich N, Ehses P, Duerk J, Gilkeson R, Griswold M. Improved radial GRAPPA calibration for real-time free-breathing cardiac imaging. *Magn Reson Med.* 2011;65(2):492–505.
32. Barger AV, Block WF, Toropov Y, Grist TM, Mistretta CA. Time-resolved contrast-enhanced imaging with isotropic resolution and broad coverage using an undersampled 3D projection trajectory. *Magn Reson Med.* 2002;48(2):297–305.
33. Mistretta CA, Wieben O, Velikina J, Block W, Perry J, Wu Y, Johnson K, Wu Y. Highly constrained backprojection for time-resolved MRI. *Magn Reson Med.* 2006;55(1):30–40.
34. Tsao J, Boesiger P, Pruessmann KP. k-t BLAST and k-t SENSE: dynamic MRI with high frame rate exploiting spatiotemporal correlations. *Magn Reson Med.* 2003;50(5):1031–42.
35. Pedersen H, Kozerke S, Ringgaard S, Nehrke K, Kim WY. k-t PCA: temporally constrained k-t BLAST reconstruction using principal component analysis. *Magn Reson Med.* 2009;62(3):706–16.
36. Kim D, Dyvorne HA, Otazo R, Feng L, Sodickson DK, Lee VS. Accelerated phase-contrast cine MRI using k-t SPARSE-SENSE. *Magn Reson Med.* 2012;67(4):1054–64.
37. Candes EJ, Romberg J, Tao T. Robust uncertainty principles: exact signal reconstruction from highly incomplete frequency information. *IEEE T Inform Theory.* 2006;52(2):489–509.
38. Donoho DL. Compressed sensing. *IEEE T Inform Theory.* 2006;52(4):1289–306.
39. Lustig M, Donoho D, Pauly JM. Sparse MRI: the application of compressed sensing for rapid MR imaging. *Magn Reson Med.* 2007;58(6):1182–95.
40. Otazo R, Kim D, Axel L, Sodickson DK. Combination of compressed sensing and parallel imaging for highly accelerated first-pass cardiac perfusion MRI. *Magn Reson Med.* 2010;64(3):767–76.
41. Herfkens RJ, Higgins CB, Hricak H, Lipton MJ, Crooks LE, Lanzer P, Botvinick E, Brundage B, Sheldon PE, Kaufman L. Nuclear magnetic resonance imaging of the cardiovascular system: normal and pathologic findings. *Radiology.* 1983;147(3):749–59.
42. Simonetti OP, Finn JP, White RD, Laub G, Henry DA. “Black blood” T₂-weighted inversion-recovery MR imaging of the heart. *Radiology.* 1996;199(1):49–57.
43. Edelman RR, Chien D, Kim D. Fast selective black blood MR imaging. *Radiology.* 1991;181(3):655–60.
44. Sakuma H, Fujita N, Foo TK, Caputo GR, Nelson SJ, Hartiala J, Shimakawa A, Higgins CB. Evaluation of left ventricular volume and mass with breath-hold cine MR imaging. *Radiology.* 1993;188(2):377–80.
45. Atkinson DJ, Edelman RR. Cineangiography of the heart in a single breath hold with a segmented turboFLASH sequence. *Radiology.* 1991;178(2):357–60.
46. Atkinson DJ, Burstein D, Edelman RR. First-pass cardiac perfusion: evaluation with ultrafast MR imaging. *Radiology.* 1990;174(3 Pt 1):757–62.
47. Gerber BL, Raman SV, Nayak K, Epstein FH, Ferreira P, Axel L, Kraitman DL. Myocardial first-pass perfusion cardiovascular magnetic resonance: history, theory, and current state of the art. *J Cardiovasc Magn Reson.* 2008;10:18.
48. Kellman P, Arai AE, McVeigh ER, Aletras AH. Phase-sensitive inversion recovery for detecting myocardial infarction using gadolinium-delayed hyperenhancement. *Magn Reson Med.* 2002;47(2):372–83.
49. Kim RJ, Wu E, Rafael A, Chen EL, Parker MA, Simonetti O, Klocke FJ, Bonow RO, Judd RM. The use of contrast-enhanced magnetic resonance imaging to identify reversible myocardial dysfunction. *N Engl J Med.* 2000;343(20):1445–53.
50. Sivanathan UM, Ridgway JP, Bann K, Verma SP, Cullingworth J, Ward J, Rees MR. Fast magnetic resonance angiography using turbo-FLASH sequences in advanced aortoiliac disease. *Br J Radiol.* 1993;66(792):1103–10.
51. Prince MR, Yucel EK, Kaufman JA, Harrison DC, Geller SC. Dynamic gadolinium-enhanced three-dimensional abdominal MR arteriography. *J Magn Reson Imaging JMRI.* 1993;3(6):877–81.
52. Biglands JD, Radjenovic A, Ridgway JP. Cardiovascular magnetic resonance physics for clinicians: Part II. *J Cardiovasc Magn Reson.* 2012;14:66.

Yiu-Cho Chung

Abstract

High field MRI offers the high signal to noise ratio (SNR) that is much needed in CMR. SNR can be traded for speed using parallel imaging, improving the quality of fast imaging applications such as real time cine. SNR also allows for improved spatial resolution, making coronary MRA and vessel wall imaging feasible. The T_1 of tissues increases at high field. CMR imaging techniques that exploit T_1 differences between tissues such as LGE, first pass perfusion imaging, tagging, and contrast enhanced MR angiography have better T_1 contrast at high field. The improved spectral resolution at high field is also potentially advantageous to MR spectroscopy. However, high field MRI also poses certain challenges to CMR applications. Banding artifact in bSSFP and off-resonance artifact in non-Cartesian trajectories get worse at high field due to increased field inhomogeneity. Fat suppression becomes less robust. At 3 T and above, transmit field inhomogeneity can lead to signal inhomogeneity and even local heating. The safety issues related to the concomitant increase in projectile force and SAR need to be considered. Increased sensitivity to susceptibility is unfavorable to EPI imaging. Technical advances such as better shimming, improved RF pulse design and parallel RF transmission systems have helped to alleviate some of the challenges and make high field MRI a practical technology for clinical CMR applications. More research is needed before novel CMR applications such as ASL, BOLD and MR spectroscopy will benefit fully from high field MRI.

Keywords

High field MRI • Cardiovascular MR • B_0 field inhomogeneity • B_1^+ field inhomogeneity • Balanced SSFP

Introduction

Technological advances in the last two decades have brought high field imaging from research laboratories to clinics and hospitals. In the 1990s, 1.5 Tesla was the typical field strength for most whole body MR scanners in clinical use. Driven by

the need for ever higher signal to noise ratio (SNR), academic institutions, research laboratories and MRI systems manufacturers explored the feasibility of high field imaging of the brain starting in the 1990s [1]. Since the FDA approved the use of 3 T scanners for whole body clinical applications in 2002, 3 T whole body MRI systems have gained popularity in hospitals and imaging centers. Magnetic field strength up to 9.4 T for human imaging (not yet approved by the FDA) has also been found to have no effect on vital signs or cognitive ability [2]. Cardiovascular imaging, which has always demanded higher SNR and shorter acquisition times, is one application that many believe would benefit from high field MRI.

Y.-C. Chung, PhD
Paul C. Lauterbur Research Center for Biomedical Imaging,
Shenzhen Institutes of Advanced Technology,
Chinese Academy of Sciences, Shenzhen, China
e-mail: yc.chung@siat.ac.cn

Advantages of High Field MRI

The most obvious advantage of high field imaging is the SNR increase. In MRI, the signal is proportional to the square of the main magnetic field B_0 , while noise is linearly proportional to it. SNR therefore increases linearly with B_0 [3], and imaging at 3 T enjoys a $2\times$ SNR increase compared to 1.5 T. Note that this theoretical advantage is relevant only to proton density weighted images, and may not be fully realized in practice due to the concomitant change of T_1 and other MR parameters at high field.

Increased SNR can be used to improve spatial resolution. In theory, an image acquired at 1.5 T with a specific FOV using a matrix of 256×256 pixels at 1.5 T may be increased to 320×320 pixels with a 28 % SNR increase when imaging at 3 T. The higher SNR may also be traded for reduced image acquisition time. For instance, in parallel imaging [4]:

$$SNR_p = \frac{SNR_o}{g \cdot \sqrt{R}} \quad (6.1)$$

where SNR_p is the SNR when parallel imaging rate R is used, SNR_o is the original SNR without parallel imaging, and g is the so-called g -factor of the coil, which is related to its design and geometry. By going from 1.5 to 3 T, the $2\times$ SNR gain may be traded for a $4\times$ scan time reduction. In practice, the g -factor of the coils (which increases with acceleration factor) would limit these theoretical gains.

The spin-spin relaxation time, T_2 , is relatively insensitive to B_0 , while the T_1 (the spin-lattice relaxation time) increases with field strength [5]. This can be another advantage of high field imaging in some CMR applications, especially when T_1 -shortening contrast agents are used. The longer T_1 values at high field lead to larger T_1 differences between tissues, and this translates into improved T_1 contrast. Tissue suppression is improved at high field because tissues driven to saturation take longer to recover longitudinal magnetization. Table 6.1 shows the T_1 values of blood and myocardium at 1.5 and 3 T.

Experiments have shown that the relaxivities of Gd-DTPA at 1.5 T and 3 T were similar (4.79 ± 0.08 /mM/s and 4.5 ± 0.05 /mM/s respectively) for concentrations between 0.1 and 5 mM [8]. Since the T_1 times of unenhanced tissues

Table 6.1 The T_1 values of the myocardium and blood at two different field strengths from one study (cf. [6])

	1.5 T	3 T
Myocardium	1030 ± 34 ms	1471 ± 31 ms
Blood	1441 ± 120 ms	1932 ± 85 ms

Note that (1) the T_1 of blood also depends on other factors such as hematocrit and oxygen saturation; (2) these values vary among different studies. For instance, Sharma et al. [7] reported different T_1 values for blood and myocardium at 3 T

at 3 T are longer than those at 1.5 T, the same dose of gadolinium based contrast agent often produces a stronger signal change in contrast studies at 3 T. This means that to achieve the same contrast change at 3 T, gadolinium contrast dosage may be reduced.

Hydrocarbons such as lipids can have complex chemical structures and the Larmor frequency of hydrogen nuclei in these molecules is close to but often not equal to that of water protons. This is known as “chemical shift”, described in ppm (parts per million) of the Larmor frequency, and is intrinsic to a specific chemical species. The absolute value of the chemical shift increases with B_0 . For instance, lipid has a chemical shift of -3.5 ppm. At 1.5 T, this translates into a resonance frequency for lipid that is 220 Hz lower than that of water protons; this frequency difference increases to 440 Hz at 3 T. Metabolites in the body with different chemical shifts therefore have increased frequency separation at high field. Together with higher SNR, higher field strength benefits MR spectroscopy as it allows better distinction of spectral peaks of various metabolites.

Susceptibility is the degree to which a material is magnetized in response to an applied B_0 . In the body, oxygenated blood is diamagnetic while deoxygenated blood is paramagnetic; when the oxygen concentration in blood changes, its susceptibility changes, and its MR signal changes as well. This contrast mechanism is called BOLD (blood oxygenation level dependent contrast). As the absolute susceptibility change increases with B_0 , CMR techniques based on BOLD can benefit from high B_0 .

Challenges of High Field MRI

One major challenge of diagnostic imaging at high field is patient safety. When B_0 increases, the risk to patients with implanted cardio defibrillators (ICDs) or other implants increases accordingly. Currently, safety studies on implantable devices have mostly been performed using 1.5 T systems. Only a few studies have looked into the risks of implantable devices at 3 T [9–11], and there have been no similar published investigations yet at 7 T. Whether the risks to patients with implants can be justified for the benefits of imaging at 3 T and beyond remains an open question.

Another safety concern is the increased energy deposition at high field. When RF pulses are applied during imaging, energy is deposited into the body. Such RF energy is absorbed by the body and results in tissue heating. Energy deposition to the body is described by the Specific Absorption Ratio (SAR) and it is proportional to the square of the Larmor frequency (and hence B_0). As such, SAR will be increased four times when the same imaging sequence applied at 1.5 T is used in 3 T. SAR may be reduced through special RF pulse design such as VERSE [12], but it remains an important

limiting factor for RF intensive sequences like FSE, HASTE, and balanced SSFP.

Robust ECG triggering is more difficult at high B_0 . When a person lies in the scanner, the static B_0 field interacts with the ions in the flowing blood and induces voltage (due to the magnetodynamic effect) that can contaminate the ECG signal detected at the body surface [13]. Due to the timing of peak blood flow in the aorta, the T wave in the ECG appears to be elevated, and can be mistaken for the QRS wave. At 1.5 T, vectorcardiography can be used to detect QRS complexes reliably. At higher B_0 , the magnetodynamic effect becomes more pronounced and robust detection of QRS complexes becomes difficult. Special techniques may be needed at high field to ensure reliable ECG triggering [14].

Magnetic field inhomogeneity is usually described in terms of ppm (parts per million) relative to B_0 ; thus 1 ppm at 1.5 T (Larmor frequency = 64 MHz) is equivalent to a 64 Hz frequency offset, while 1 ppm at 3.0 T is equivalent to a 128 Hz offset. This means that field inhomogeneity in absolute terms over a specific volume at 1.5 T would be two times worse at 3 T within the same volume. Off-resonance effects on image quality are typically more severe at high field. Balanced SSFP (bSSFP, aka trueFISP), a workhorse pulse sequence for CMR at 1.5 T, is more prone to banding artifacts due to the increased field inhomogeneity at 3.0 T. Flow artifacts also appear more often in balanced SSFP images (see Fig. 6.1) at high field. Certain k-space traversal schemes such as the spiral trajectory that is more sensitive to off-resonance can suffer from increased artifacts as well.

To achieve a homogeneous B_0 field at 3 T, shimming is critically important.

Transmit field inhomogeneity, or B_1^+ field inhomogeneity, is another major challenge for CMR at high field. When an RF excitation pulse is applied, an electromagnetic wave at the Larmor frequency is transmitted to the body that tips the water protons into the transverse plane. This wave travels in the body at a speed determined by tissue conductivity. The frequency, f , of this electromagnetic wave increases with B_0 . As B_0 increases, the dielectric constants of tissues decrease, which leads to a decrease in the velocity, v , of the electromagnetic wave travelling inside the body [15]. The net result is that the wavelength of the RF field, λ , decreases (since $v = f\lambda$). At 3 T and above, λ becomes comparable in length to the size of the organs being imaged. Constructive or destructive interference can occur when such electromagnetic waves propagate through the different organs of the body (similar to light refraction). As a result, the flip angle produced by an RF pulse will vary spatially as spins at different locations are tipped differently, and images suffer from signal inhomogeneity [16] (see Fig. 6.2). The uneven distribution of energy throughout the body may also result in local heating. RF shimming and parallel transmit technology have been proposed to address these problems. Recent studies show that using two independent transmit channels, B_1^+ field inhomogeneity can be reduced and image quality is improved in CMR applications at 3 T [17].

Frequency dispersion at tissue interfaces due to tissue susceptibility differences increases with field strength and results in more signal loss (and distortion in the case of EPI)

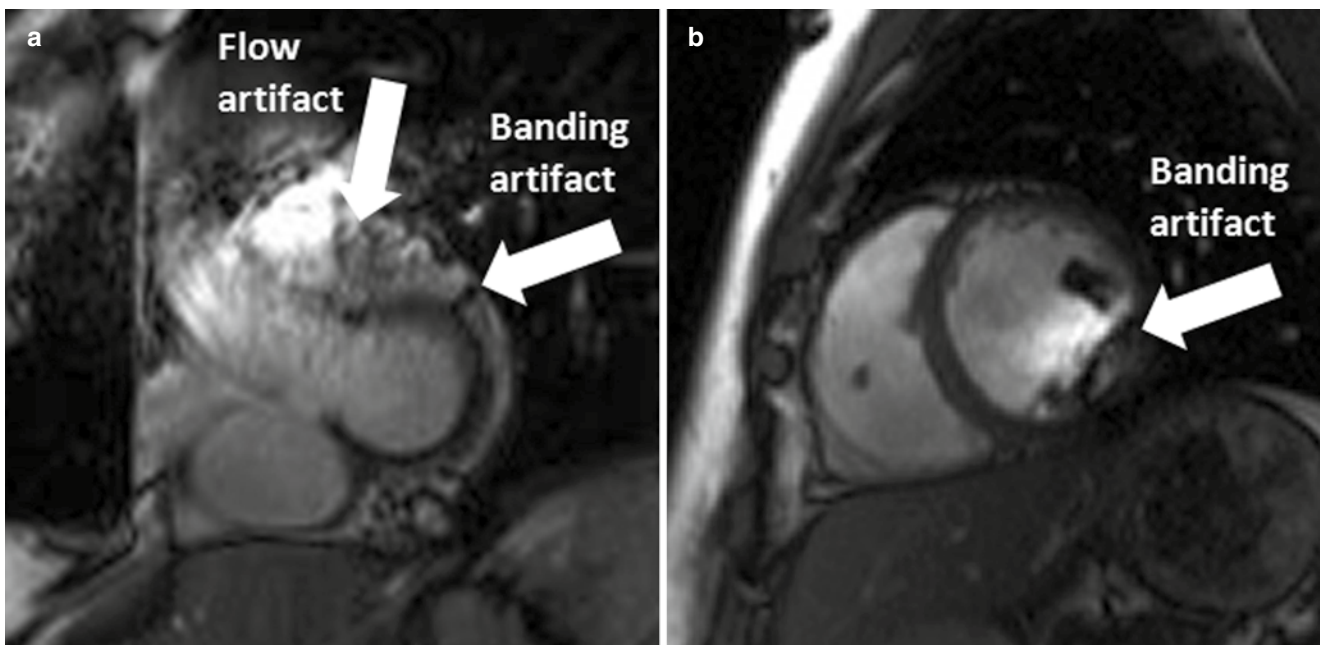


Fig. 6.1 Balanced SSFP artifacts at 3 T. (a) The flow artifact at the outflow tract and the banding artifact at the myocardium. (b) Typical banding artifact in the short axis cine of a mid-ventricular slice

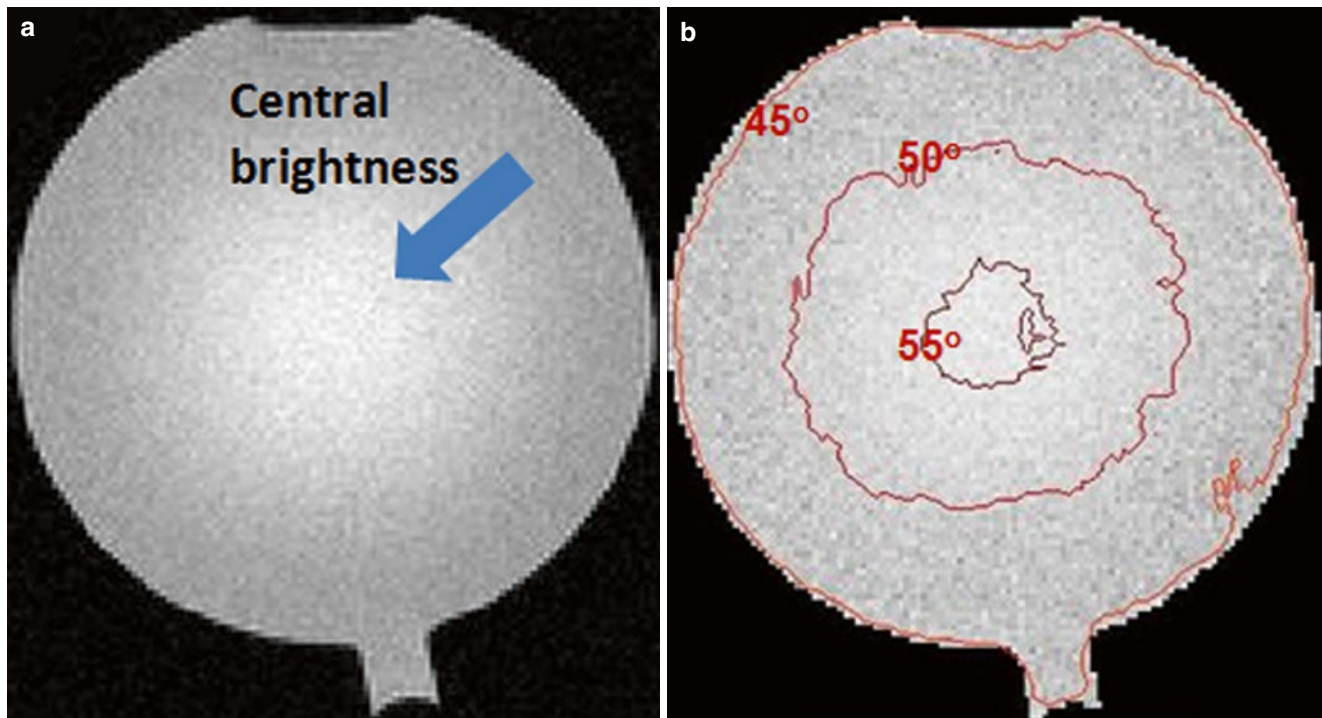


Fig. 6.2 RF field inhomogeneity at 3 T. (a) A phantom image acquired on a 3 T system using the body coil for both transmission and reception. This is a gradient echo image acquired with a flip angle of 45° . The image has non-uniform signal distribution. (b) The actual flip angle

distribution in the experiment. The signal non-uniformity is caused by B_1^+ field inhomogeneity. Here, the flip angle distribution was obtained using DAM (double angle method) and median filtered. At the image center, the effective flip angle exceeds 55°

because of increased signal dephasing. This is particularly problematic at the heart-lung interface [19]. This signal loss is commonly observed in bSSFP images (see Fig. 6.1), and in first pass perfusion images using EPI.

Local field inhomogeneity increases at high field. As a result, the T_2^* values of tissues at 3 T are lower than those at 1.5 T. Storey et al. [18] showed that changes in $1/T_2^*$ ($=R_2^*$) values of the heart and liver caused by iron burden are linearly related to field strength.

The increased T_1 at 3 T also has its downside in some cases. In gradient echo imaging, signal is approximately proportional to $\sqrt{(TR/T_1)}$ at the Ernst angle [20]. In bSSFP, the signal varies with $\sqrt{(T_2/T_1)}$. In both cases, longer T_1 reduces the MR signal and hence the overall SNR gain achievable at 3 T. In spin-echo based sequences, TR must be increased for good T_2 /PD contrast at high field, resulting in increased scan times. In most cases, optimal imaging parameters for 1.5 T and for 3 T are different due to differences in T_1 , field homogeneity, SAR, and SNR.

Despite the increased frequency separation between fat and water protons, fat saturation is more challenging at high field due to increased B_0 inhomogeneity. In the case of selective water excitation (composite) pulses, the higher fat-water difference in frequency at high field reduces the time interval between two RF pulses at which water and lipid protons go out-of-phase. Selective pulses with shorter duration are needed and may compromise slice profile and increase the SAR values.

The faster precession frequency at high B_0 also means that the TEs for in-phase and out-of-phase images in gradient echo based techniques are closer. Multipoint Dixon methods used for fat-water separation (such as [21]) require different choices of TEs if multiple echoes are acquired in one TR period.

CMR Applications at High Field

When going from 1.5 T to 3 T or higher field strength, the changes in MR properties of body tissues, and changes in other physical parameters, may benefit some CMR applications while making other CMR techniques challenging.

The main advantage that high field MR systems offer is higher SNR. This SNR advantage allows for higher readout bandwidth, reducing echo spacing, and hence shorter acquisition time.

Another way to exploit the SNR advantage at 3 T is by parallel imaging [22, 23] – see Eq. 6.1. This advantage applies to most CMR applications. For instance, when using single-shot FSE (aka HASTE) at 3 T, parallel imaging reduces the number of echoes and thus the SAR of the sequence. It also improves image sharpness.

Balanced SSFP (or trueFISP) provides exceptional contrast between blood and myocardium in cine imaging [24] and has been the workhorse of CMR at 1.5 T. Combined with

parallel imaging, patient breathhold time can be reduced. However, the technique is sensitive to field inhomogeneity, particularly at the heart-liver-lung interface [25]; the situation is worse at 3 T [26]. Quite some effort has been made to address the above issues in the past several years. Improved shimming becomes a necessity for bSSFP to work robustly at 3 T. A frequency scout technique has also been proposed to address this issue [27]. In this method, single-shot bSSFP images are acquired over multiple heartbeats, each using a resonance frequency slightly shifted (e.g., 50 Hz, 100 Hz, and so on) from the center frequency. The frequency offset that corresponds to the image with the best image quality will be the off-resonance frequency adjustment that needs to be applied to subsequent bSSFP acquisitions (Fig. 6.3).

Balanced SSFP for cines that have reduced sensitivity to B_0 inhomogeneity (and reduced sampling efficiency) have

also been proposed [28]. Alternatively, sensitivity to B_0 inhomogeneity may be minimized by reducing TR by reducing spatial resolution and increasing receiver bandwidth.

Real time cine with adequate image quality has been challenging to achieve at 1.5 T due to the SNR impact from the use of fast imaging. The SNR increase at 3 T makes real time imaging more practical. Equation 6.1 shows theoretically that parallel imaging with acceleration rate 4 at 3 T is possible if the g-factor is small. Matched with appropriate coils, appropriate k-space trajectories, and advanced reconstruction algorithms, the g-factor and the SNR penalty due to high acceleration factors can be kept small. Recent work has shown that real time cine at 3 T can achieve a temporal resolution as high as 20 ms at a spatial resolution of $2 \times 2 \times 8$ mm [29].

Readout using balanced SSFP is both time and SNR efficient compared to turboFLASH, and it is commonly used

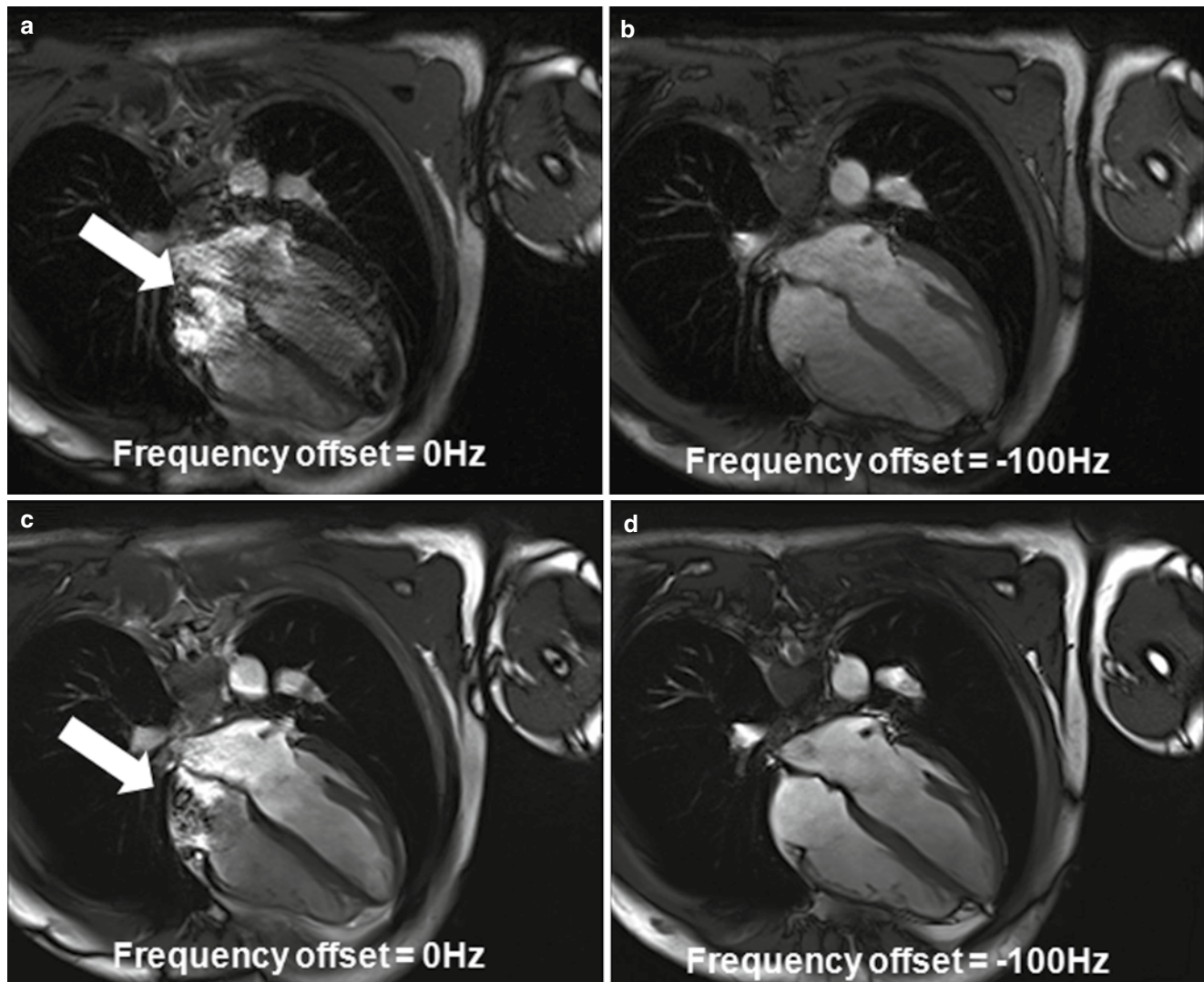


Fig. 6.3 The use of frequency scout to reduce the effects of B_0 field inhomogeneity at 3 T. The frequency scout images in (a, b) show the effect of varying the frequency offset on bSSFP image quality. (c, d) The bSSFP cine images acquired using the corresponding frequency

offsets. Note that the image contrast in (a, b), acquired using a single shot technique, is not the same as (c), which was acquired under steady state

with parallel imaging in single-shot techniques at 1.5 T. At 3 T, the use of bSSFP for readout is limited by its increased sensitivity to B_0 inhomogeneity, therefore a FLASH readout is often preferred. At high magnetic field, short TR and high bandwidth can be used with FLASH readout while maintaining adequate SNR.

Flow imaging is another application that benefits from the higher SNR at 3 T in a direct way, and parallel imaging can be used in the same way as in cine imaging to reduce scan time.

Late gadolinium enhancement (LGE) for infarct imaging using inversion recovery turboFLASH also benefits directly from the higher SNR at 3 T. Breath-hold time can be reduced. Single-shot infarct imaging with turboFLASH can be used in patients with arrhythmia. Uniform inversion of longitudinal magnetization can be problematic at 3.0 T, however, due to B_1^+ inhomogeneity.

Another important CMR application that benefits from higher field strength is first pass myocardial perfusion imaging. Higher field strength provides a boost to the much needed SNR and CNR in this application. The T_1 of tissue at 3 T is longer and so tissue saturation persists longer. The contrast between perfused, under-perfused, and non-perfused myocardial tissues therefore increases. SNR increase can also be traded for higher acquisition speed and improved coverage. 3D high resolution first pass perfusion imaging has been shown feasible at 3 T using appropriate parallel imaging techniques [30]. B_1^+ field inhomogeneity at 3 T, however, may affect the performance of this application as imperfect saturation pulses give rise to non-uniform tissue saturation over the heart, making the distinction between normal and ischemic myocardium challenging. Specially designed RF pulses are needed, but they often require increased SAR [31].

3 T imaging also benefits myocardial tagging. The tag lines that fade towards the end of the cardiac cycle at 1.5 T last longer through diastole at 3 T due to the longer inherent T_1 of the

myocardium. The contrast of the tags may be further improved by combining CSPAMM (which doubles the scan time) and parallel imaging (to speed up the acquisition).

Coronary MR angiography (coronary MRA) performed using T_2 -prepared balanced SSFP is challenging at 3 T for two reasons. First, high resolution imaging using bSSFP requires longer TR making it more susceptible to banding artifacts due to B_0 field inhomogeneity. Second, the classic T_2 -preparation technique is not as robust at 3 T as at 1.5 T due to its intrinsic sensitivity to B_0 and B_1^+ field inhomogeneity. New designs for T_2 -prep pulses have been proposed to combine with turboFLASH readout for coronary MRA at 3 T [32, 33]. Alternatively, contrast enhanced coronary MRA has been proposed [34]. By using an inversion pulse and choice of appropriate TI to null the normal myocardium during a slow infusion of Gd-based contrast, the technique demonstrated better depiction of coronary segments compared to bSSFP at 1.5 T [35]. In patients, this technique has been shown to detect coronary artery stenosis with a high diagnostic accuracy and reduced imaging time [36]. Figure 6.4 shows a clinical case where contrast enhanced coronary MRA matches well with DSA images. One limitation of the technique is that it cannot be repeated, which can be problematic if the final images are found to be contaminated by respiratory artifacts.

Both long native T_1 and high SNR at 3 T benefit contrast enhanced MR angiography (ceMRA) directly [37, 38]. The background tissues driven into saturation take longer to recover. Meanwhile the SNR of the blood signal increases with field strength. These effects work together and improve both spatial resolution and image contrast. A lower dose of gadolinium-based contrast agent can be used without compromising image quality.

TSE for myocardial tissue characterization at 3 T uses parallel imaging to shorten breath-hold time, and to reduce SAR by reducing the number of refocussing pulses. A flip

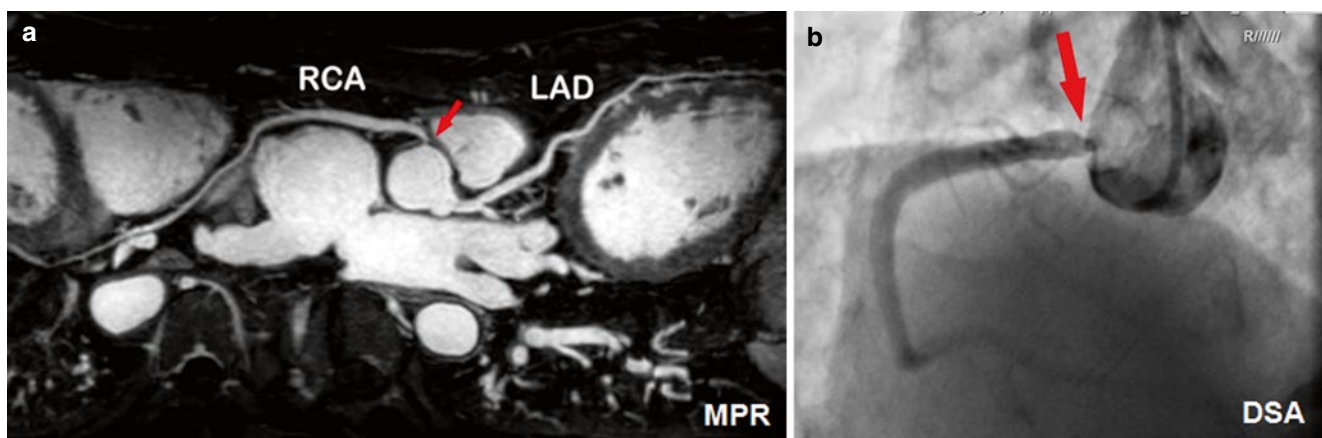


Fig. 6.4 Contrast enhanced coronary MRA at 3 T. A 65-year-old man with significant stenosis at the original of RCA (a) as shown in the coronary MR angiography (the MPR image); and (b) matched by digi-

tal subtraction angiography. The imaging time for the MR angiogram was 5 min (Courtesy of Dr. Qi Yang from Beijing Xuanwu Hospital. Reproduced with permission)

angle less than 180° can be used for the refocussing pulses to further reduce SAR. Due to the long T_1 of tissues at 3 T, a longer TR (in units of RR intervals) may be needed for TSE imaging in patients with fast heart rates.

Vessel wall imaging requires high SNR and high spatial resolution. 3 T MRI is therefore directly relevant to this application. In going from 1.5 to 3 T, a significant increase in SNR and CNR with gains in the range of 1.5–1.8 have been reported in carotid plaque imaging [39]. The improved SNR can be traded for better spatial resolution or shorter scan time. Using SPACE, a variant of TSE designed for efficient 3D imaging with low SAR [40], isotropic spatial resolution of 0.7 mm can be achieved for carotid vessel wall imaging at 3 T [41]. It has also been shown that higher isotropic spatial resolution of around 0.5 mm is possible for intracranial artery plaque imaging at 3 T [42, 43]. This is one application that benefits directly from the high field strength with little downside.

Table 6.2 summarizes how high field MRI benefits common CMR techniques.

Novel CMR Techniques at High Field

Much research has been done to adapt CMR applications commonly used at 1.5 T for use at 3 T so that routine clinical application can benefit from the advantages and circumvent the technical limitations of high field MRI. However, the real potential of high field MRI may lie in its ability to bring new techniques that are challenging or impractical at 1.5 T into routine clinical application.

It has been shown that myocardial ischemia can be detected using arterial spin labeling (ASL) [44, 45]. This application detects a signal change in the range of 1–8 % and would benefit directly from the $2\times$ SNR increase at 3 T [46]. The T_1 increase of tissues at 3 T also increases the signal dif-

Table 6.2 Summary of advantages and disadvantages of high field for CMR applications

	Advantages	Disadvantages	Remedies/alternatives
Safety		Stronger projectile force More severe metallic artifact High/localized SAR	Careful patient screening Avoid patients with stents and implants Use parallel imaging
ECG triggering		Magneto-hydrodynamic effect gets worse	Change electrode positions Use improved QRS detection method such as ACT [14]
bSSFP Cine	Faster Higher SNR	High SAR Banding artifact due to B_0 field inhomogeneity	Parallel imaging
Real time cine	Higher SNR Higher temporal resolution	High SAR	Parallel imaging
bSSFP readout	–	Banding artifact due to B_0 field inhomogeneity	turboFLASH readout
Flow imaging	Faster Higher SNR		
Tagging	Faster Higher SNR Better contrast		
LGE	Better contrast	Banding artifact with singleshot bSSFP due to B_0 field inhomogeneity	turboFLASH readout for singleshot imaging
First pass perfusion	Faster Higher SNR Better contrast	Signal inhomogeneity in images due to effect of B_1^+ field inhomogeneity on saturation recovery pulse	New SR pulse [31] (higher SAR)
Coronary MRA	Higher SNR	Banding artifact due to B_0 field inhomogeneity when using bSSFP Signal inhomogeneity in images due to effect of B_1^+ field inhomogeneity on T_2 -prep pulse	Use special T_2 -prep pulse and turboFLASH readout Use Gd and inversion recovery turboflash, can combine with 3D LGE
Tissue characterization by TSE	Higher SNR	High SAR Signal inhomogeneity in images due to effect of B_1^+ field inhomogeneity	Reduce refocusing flip angle System with parallel transmit
ceMRA	Better contrast Lower Gd dosage		
Plaque imaging	Higher SNR Higher spatial resolution	High SAR	Use SPACE for 3D imaging

ference between tagged and untagged blood. Zun showed that despite the use of higher field strength, the technique is still signal starved. Physiological noise remains one limiting factor [47]. Results from a preliminary clinical study show promise [48], but measurement variability, spatial resolution, and other issues remain to be addressed [49].

Improved BOLD effect in brain imaging was the initial driving force for high field MRI [1]. Studies found that the BOLD effect could also be observed in the myocardium using T_2 prepared gradient echo [50] or bSSFP [51] readouts at 1.5 T. Steady state bSSFP can also be used alone to detect the BOLD effect in the myocardium [52]. As field strength increases, both SNR and the susceptibility difference between oxygenated and deoxygenated blood increase, both of which benefit the detection of the BOLD effect [53]. However, the increased sensitivity to the BOLD effect is countered by the lack of robustness of the T_2 prep pulse, and B_0 field inhomogeneity at high field (affecting the bSSFP images). BOLD imaging of the myocardium remains a technical challenge at high field.

Frequency resolution and SNR are both doubled as compared to 1.5 T when MR spectroscopy is performed at 3 T. In in-vivo proton MR spectroscopy of myocardial lipid deposition, SNR at 3 T was increased by $76 \pm 72\%$ compared to 1.5 T [54]. However, one of the most physiologically relevant nuclei that is less abundant in the body than hydrogen is phosphorus. A preliminary study found that MRS of ^{31}P of the heart at 3 T provides an SNR of $206 \pm 94\%$ compared to 1.5 T [55]. A clinical study showed that the myocardial phosphocreatine/adenosine triphosphate (PCr/ATP) ratio measured at 3 T was lower in HCM patients compared to normal volunteers [56]. ^{31}P MRS has proven to be an outstanding research tool, but the spatial resolution of MRS attainable even at 3 T is still too low to provide segmental myocardial results using the standard 17-segment model, which requires a voxel volume of about 8 ml [57]. For now, the technique remains as a research tool.

Conclusions

Once perceived as challenging for CMR, technical advances over the past years have made CMR at 3 T a clinical reality. Various comparison studies have reported favorable SNR or shorter scan times with high field MRI. However, two issues still make CMR at 3 T a bit more challenging than CMR at 1.5 T. The need for good B_0 shimming to avoid banding and flow artifacts in bSSFP is an obvious issue that affects the workflow of CMR at 3 T. Another issue is the B_1^+ field inhomogeneity that can cause spatially varying signal, especially in sequences using saturation or inversion recovery preparation pulses. Parallel transmit technologies have been proposed and vendors have begun to support the required hardware on

the latest platforms. A recent study demonstrated the improvement in image quality of a 3 T system equipped with a 2-channel transmit system [17].

Over the last decade, multiple studies have demonstrated the SNR and CNR advantages of 3 T over 1.5 T for specific applications in CMR. Research and development efforts have successfully improved the reliability of CMR techniques at 3 T. More hospitals and clinics are using 3 T systems as their only system for CMR; however, there is not yet a common consensus regarding the superiority of 3 T over 1.5 T in terms of diagnostic accuracy in routine clinical use. Progress continues to address the various challenges in high field MRI. It is hoped that technological advances will address the remaining challenges of high field CMR so that its advantages can benefit routine clinical imaging in the near future.

References

1. Ugurbil K. The road to functional imaging and ultrahigh fields. *Neuroimage*. 2012;62(2):726–35. Epub 2012 Feb 8.
2. Atkinson IC, et al. Safety of human MRI at static fields above the FDA 8 T guideline: sodium imaging at 9.4 T does not affect vital signs or cognitive ability. *J Magn Reson Imaging*. 2007;26(5):1222–7.
3. Edelstein WA, et al. The intrinsic signal-to-noise ratio in NMR imaging. *Magn Reson Med*. 1986;3(4):604–18.
4. Pruessmann KP, et al. SENSE: sensitivity encoding for fast MRI. *Magn Reson Med*. 1999;42(5):952–62.
5. Bottomley PA, et al. A review of normal tissue hydrogen NMR relaxation times and relaxation mechanisms from 1–100 MHz: dependence on tissue type, NMR frequency, temperature, species, excision, and age. *Med Phys*. 1984;11(4):425–48.
6. Stanisz GJ, et al. T1, T2 relaxation and magnetization transfer in tissue at 3T. *Magn Reson Med*. 2005;54(3):507–12.
7. Sharma P, et al. Effect of Gd-DTPA-BMA on blood and myocardial T1 at 1.5T and 3T in humans. *J Magn Reson Imaging*. 2006;23(3):323–30.
8. Sasaki M, et al. Enhancement effects and relaxivities of gadolinium-DTPA at 1.5 versus 3 Tesla: a phantom study. *Magn Reson Med Sci*. 2005;4(3):145–9.
9. Nijveldt R, et al. 3.0 T cardiovascular magnetic resonance in patients treated with coronary stenting for myocardial infarction: evaluation of short term safety and image quality. *Int J Cardiovasc Imaging*. 2008;24(3):283–91.
10. Gimbel JR. Magnetic resonance imaging of implantable cardiac rhythm devices at 3.0 tesla. *Pacing Clin Electrophysiol*. 2008;31(7):795–801.
11. Zikria JF, et al. MRI of patients with cardiac pacemakers: a review of the medical literature. *AJR Am J Roentgenol*. 2011;196(2):390–401.
12. Conolly S, et al. A reduced power selective adiabatic spin-echo pulse sequence. *Magn Reson Med*. 1991;18(1):28–38.
13. Fischer SE, Wickline SA, Lorenz CH. Novel real-time R-wave detection algorithm based on the vectorcardiogram for accurate gated magnetic resonance acquisitions. *Magn Reson Med*. 1999;42(2):361–70.
14. Frauenrath T, et al. Feasibility of cardiac gating free of interference with electro-magnetic fields at 1.5 Tesla, 3.0 Tesla and 7.0 Tesla using an MR-stethoscope. *Invest Radiol*. 2009;44(9):539–47.

15. Bernstein MA, Huston 3rd J, Ward HA. Imaging artifacts at 3.0T. *J Magn Reson Imaging*. 2006;24(4):735–46.
16. Merkle EM, Dale BM. Abdominal MRI at 3.0 T: the basics revisited. *AJR Am J Roentgenol*. 2006;186(6):1524–32.
17. Krishnamurthy R, et al. Evaluation of a subject specific dual-transmit approach for improving B1 field homogeneity in cardiovascular magnetic resonance at 3T. *J Cardiovasc Magn Reson*. 2013;15(1):68.
18. Storey P, et al. R2* imaging of transfusional iron burden at 3T and comparison with 1.5T. *J Magn Reson Imaging*. 2007;25(3):540–7.
19. Atalay MK, et al. Cardiac susceptibility artifacts arising from the heart-lung interface. *Magn Reson Med*. 2001;45(2):341–5.
20. Haacke EM, et al. *Magnetic resonance imaging: physical principles and sequence design*. 1st ed. New York: Wiley; 1999.
21. Kellman P, et al. Multiecho Dixon fat and water separation method for detecting fibrofatty infiltration in the myocardium. *Magn Reson Med*. 2009;61(1):215–21.
22. Theisen D, et al. High-resolution cine MRI with TGRAPPA for fast assessment of left ventricular function at 3 Tesla. *Eur J Radiol*. 2013;82(5):e219–24.
23. Pruessmann KP. Parallel imaging at high field strength: synergies and joint potential. *Top Magn Reson Imaging*. 2004;15(4):237–44.
24. Carr JC, et al. Cine MR angiography of the heart with segmented true fast imaging with steady-state precession. *Radiology*. 2001;219(3):828–34.
25. Reeder SB, et al. In vivo measurement of T2 and field inhomogeneity maps in the human heart at 1.5 T. *Magn Reson Med*. 1998;39(6):988–98.
26. Noeske R, et al. Human cardiac imaging at 3 T using phased array coils. *Magn Reson Med*. 2000;44(6):978–82.
27. Deshpande VS, Shea SM, Li D. Artifact reduction in true-FISP imaging of the coronary arteries by adjusting imaging frequency. *Magn Reson Med*. 2003;49(5):803–9.
28. Nayak KS, et al. Wideband SSFP: alternating repetition time balanced steady state free precession with increased band spacing. *Magn Reson Med*. 2007;58(5):931–8.
29. Zhang S, et al. Real-time cardiovascular magnetic resonance at high temporal resolution: radial FLASH with nonlinear inverse reconstruction. *J Cardiovasc Magn Reson*. 2010;12:39.
30. Shin T, et al. Three dimensional first-pass myocardial perfusion imaging at 3T: feasibility study. *J Cardiovasc Magn Reson*. 2008;10:57.
31. Kim D, et al. Comparison of the effectiveness of saturation pulses in the heart at 3T. *Magn Reson Med*. 2008;59(1):209–15.
32. Nezafat R, et al. Spectrally selective B1-insensitive T2 magnetization preparation sequence. *Magn Reson Med*. 2009;61(6):1326–35.
33. Jenista ER, et al. Motion and flow insensitive adiabatic T(2)-preparation module for cardiac MR imaging at 3 tesla. *Magn Reson Med*. 2013;70(4):1360–8.
34. Bi X, Carr JC, Li D. Whole-heart coronary magnetic resonance angiography at 3 Tesla in 5 minutes with slow infusion of Gd-BOPTA, a high-relaxivity clinical contrast agent. *Magn Reson Med*. 2007;58(1):1–7.
35. Liu X, et al. Contrast-enhanced whole-heart coronary magnetic resonance angiography at 3.0 T: comparison with steady-state free precession technique at 1.5 T. *Invest Radiol*. 2008;43(9):663–8.
36. Yang Q, et al. 3.0T whole-heart coronary magnetic resonance angiography performed with 32-channel cardiac coils: a single-center experience. *Circ Cardiovasc Imaging*. 2012;5(5):573–9.
37. Finn JP, et al. Thorax: low-dose contrast-enhanced three-dimensional MR angiography with subsecond temporal resolution – initial results. *Radiology*. 2002;224(3):896–904.
38. Habibi R, et al. High-spatial-resolution lower extremity MR angiography at 3.0 T: contrast agent dose comparison study. *Radiology*. 2008;248(2):680–92. Epub 2008 Jun 23.
39. Yarnykh VL, et al. Multicontrast black-blood MRI of carotid arteries: comparison between 1.5 and 3 tesla magnetic field strengths. *J Magn Reson Imaging*. 2006;23(5):691–8.
40. Mugler JPI, Brookeman JR. Efficient spatially-selective single-slab 3D turbo-spin-echo imaging. In: *Proc. 11th ISMRM annual meeting*. 2004; p. 695.
41. Mihai G, et al. Assessment of carotid stenosis using three-dimensional T2-weighted dark blood imaging: initial experience. *J Magn Reson Imaging*. 2012;35(2):449–55. Epub 2011 Dec 6.
42. Chung YC, et al. High resolution 3D intracranial imaging at 3.0 T. In: *Proc. 18th ISMRM annual meeting*. 2010; p. 2255.
43. Qiao Y, et al. Intracranial arterial wall imaging using three-dimensional high isotropic resolution black blood MRI at 3.0 Tesla. *J Magn Reson Imaging*. 2011;34(1):22–30.
44. Troalen T, et al. Cine-ASL: a steady-pulsed arterial spin labeling method for myocardial perfusion mapping in mice. Part I. Experimental study. *Magn Reson Med*. 2013;70(5):1389–98.
45. Capron T, et al. Cine-ASL: a steady-pulsed arterial spin labeling method for myocardial perfusion mapping in mice. Part II. Theoretical model and sensitivity optimization. *Magn Reson Med*. 2013;70(5):1399–408.
46. An J, Voorhees A, Chen Q. SSFP arterial spin labeling myocardial perfusion imaging at 3 Tesla. In: *Proc. 13th ISMRM Annu Meet*. 2005; p. 253.
47. Zun Z, Wong EC, Nayak KS. Assessment of myocardial blood flow (MBF) in humans using arterial spin labeling (ASL): feasibility and noise analysis. *Magn Reson Med*. 2009;62(4):975–83.
48. Zun Z, et al. Arterial spin labeled CMR detects clinically relevant increase in myocardial blood flow with vasodilation. *JACC Cardiovasc Imaging*. 2011;4(12):1253–61.
49. Epstein FH, Meyer CH. Myocardial perfusion using arterial spin labeling CMR: promise and challenges. *JACC Cardiovasc Imaging*. 2011;4(12):1262–4.
50. Wright KB, et al. Assessment of regional differences in myocardial blood flow using T2-weighted 3D BOLD imaging. *Magn Reson Med*. 2001;46(3):573–8.
51. Shea SM, et al. T2-prepared steady-state free precession blood oxygen level-dependent MR imaging of myocardial perfusion in a dog stenosis model. *Radiology*. 2005;236(2):503–9.
52. Dharmakumar R, et al. Assessment of regional myocardial oxygenation changes in the presence of coronary artery stenosis with balanced SSFP imaging at 3.0 T: theory and experimental evaluation in canines. *J Magn Reson Imaging*. 2008;27(5):1037–45.
53. Arumana JM, Li D, Dharmakumar R. Deriving blood-oxygen-level-dependent contrast in MRI with T2-weighted, T2-prepared and phase-cycled SSFP methods: theory and experiment. *Magn Reson Med*. 2008;59(3):561–70.
54. Venkatesh BA, et al. MR proton spectroscopy for myocardial lipid deposition quantification: a quantitative comparison between 1.5T and 3T. *J Magn Reson Imaging*. 2012;36(5):1222–30.
55. Tyler DJ, et al. A comparison of cardiac (31)P MRS at 1.5 and 3 T. *NMR Biomed*. 2008;21(8):793–8.
56. Shivu GN, et al. (31)P magnetic resonance spectroscopy to measure in vivo cardiac energetics in normal myocardium and hypertrophic cardiomyopathy: experiences at 3T. *Eur J Radiol*. 2010;73(2):255–9.
57. Hudsmith LE, Neubauer S. Magnetic resonance spectroscopy in myocardial disease. *JACC Cardiovasc Imaging*. 2009;2(1):87–96.

Pedro Filipe Ferreira, Peter D. Gatehouse,
Raad H. Mohiaddin, and David N. Firmin

Abstract

Cardiovascular MR offers a large range of applications. Many of these are still currently under active development by the research community, for improved accuracy and reliability.

The complex nature of the cardiovascular system offers many challenges to clinicians. Its unique mixture of respiratory and cardiac motion; fast flowing blood; and the tissue-air interface between the heart and the lungs, are just some of the difficulties faced. Many of these challenges can result in imaging artifacts and measurement errors, which may limit the diagnostic potential of the scan or even contribute to misinterpretation. A good understanding of the physical principles behind the formation of such artifacts is imperative to identifying and minimising them.

This chapter summarises, in a language accessible for a clinical readership, the most problematic artifacts specific to cardiovascular MR, with particular regard to their physical basis, and implications for the different sequences and applications. It includes motion (respiratory, cardiac and blood flow); Gibbs ringing; aliasing; chemical-shift; and B_0 -inhomogeneities.

Keywords

Artifacts • Respiratory motion • Cardiac motion • Blood flow • Gibbs • Aliasing • Chemical-shift • Field distortion • Ghosting

Electronic supplementary material The online version of this chapter (doi:[10.1007/978-3-319-22141-0_7](https://doi.org/10.1007/978-3-319-22141-0_7)) contains supplementary material, which is available to authorized users.

P.F. Ferreira, PhD (✉)
NIHR Cardiovascular Biomedical Research Unit, Royal Brompton Hospital, Sydney Wing, Sydney Street, London SW3 6NP, UK

National Heart and Lung Institute, Imperial College London, London, UK
e-mail: p.ferreira@rbht.nhs.uk

P.D. Gatehouse, PhD • D.N. Firmin
NIHR Cardiovascular Biomedical Research Unit, Royal Brompton Hospital, Sydney Wing, Sydney Street, London SW3 6NP, UK

Department of Cardiac MRI, Royal Brompton Hospital, London, UK

National Heart and Lung Institute, Imperial College London, London, UK
e-mail: p.gatehouse@rbht.nhs.uk; d.firmin@rbht.nhs.uk

Introduction

The anatomical complexity of the chest in addition to the unique cardiac and respiratory motion and fast flowing blood, can lead to *artifacts* which can obscure or easily be misinterpreted as pathology. In this chapter we attempt to summarise some of the most common artifacts found in the wide range of different Cardiovascular Magnetic Resonance (CMR) applications along with possible solutions.

R.H. Mohiaddin, MD, FRCR, FRCP, FESC, PhD
NIHR Cardiovascular Biomedical Research Unit, Royal Brompton Hospital, Sydney Wing, Sydney Street, London SW3 6NP, UK

Department of Cardiology and Imaging, National Heart and Lung Institute, Imperial College, London, UK
e-mail: r.mohiaddin@imperial.ac.uk

An artifact can be defined as something that is visible in an image but it is artificial, and is often detrimental to diagnosis. For this reason it is important to have an understanding of the physical principles behind the formation of such artifacts so that they can be identified and possibly avoided. This chapter focuses on the most problematic artifacts specific to cardiovascular imaging. The causes of these include motion (respiratory, cardiac, and blood flow); Gibbs ringing; aliasing; chemical-shift; and B_0 -inhomogeneities. Different artifact sources will be discussed with particular regard to their physical basis and implications for the different sequences and applications.

Motion

The overall motion of the heart is a complex mixture of *cardiac motion* associated with its cyclic pumping and *respiratory motion* that results in an additional twisting and volumetric distortion.

Cardiac motion has been reasonably well controlled over the years by detecting the QRS complex of the ECG and *triggering* the acquisition at a certain delay following this. Evidently ECG triggering works best when there is low variation between beats; arrhythmias and ectopic heart-beats will therefore potentially cause artifacts.

Respiratory motion is relatively unpredictable and can vary considerably from person to person and from time to time. Acquiring the data over the period of a *breath-hold* has in recent years largely controlled it, although this can translate into a long acquisition window within the cardiac cycle, thus potentially including periods of more rapid cardiac motion. Restricting the acquisition to a period of mid diastole where the heart is reasonably still is sometimes not feasible during a breath-hold, especially for patients that have considerable problems in holding their breath longer than a few seconds. For patients with very rapid heart-rates it can also be difficult to find a “motion free” acquisition window. End-expiratory breath-holding is more reproducible but more difficult than end-inspiratory.

Respiratory gating is another technique that allows the removal of gross respiratory motion artifacts by restricting data acquisition to the expiratory pause, thus enabling longer scans with shorter acquisition windows within the cardiac cycle, which in turn reduces cardiac motion problems. Respiratory gating is most commonly used in 3D imaging, in particular in imaging of the coronary arteries due to the high spatial-resolution and coverage required, where breath-hold imaging is impracticable.

A moving object will change both the phase and magnitude of its k-space. Motion during image acquisition will therefore introduce artifacts, and these can be divided into two categories: *intra-view* motion during the acquisition

of one phase-encode line, and *inter-view* motion between different phase-encode lines. For most sequences intra-view motion at typical myocardial and respiratory speeds can be ignored, although rapid blood flow in major vessels can be an issue. Inter-view motion artifacts can be caused by cardiac motion and/or breathing motion and are very dependent on the nature of the motion in relation to the k-space coverage.

Motion artifacts can also be created by movement between different components of the sequence, for example between the timing of preparation pulses and image acquisition for a black-blood sequence. The next subsections describe the basics of motion artifacts introduced in cardiac studies and are divided by breathing motion, cardiac motion, and blood flow.

Breathing Motion

Most cardiac sequences are *segmented*, i.e. the acquisition of one image is divided into multiple heartbeats and the acquisition window in each heartbeat is restricted, in order to reduce cardiac motion artifacts and *blurring*. On the other hand, if breath-holding is deficient, respiratory motion will introduce k-space inconsistencies between different segments.

Breathing artifacts will depend on the phase-encoding order used, and the timing of the motion. If, for example, motion only occurred when sampling the edges of k-space, then motion artifacts would result in blurring of the edges of the moving object in the phase encoding direction. If, on the other hand, the central regions of k-space were affected then this would result in a more significant *ghosting* and image degradation (Fig. 7.1). If breathing motion is periodic along the phase-encode direction of k-space, it results in a number of defined “ghost” artifacts distributed in that direction on the image. As can be seen from Fig. 7.1, for acquisition sequences that employ an interleaved segmented coverage of k-space then a single movement or drift in the respiratory position will result in ghosting. On the other hand for sequences that acquire k-space in a block sequential manner a single movement, as long as it doesn’t coincide with the acquisition of the centre of k-space, or similarly a drift in position, will cause some blurring but will generally cause less impact through ghosting.

Different segmented sequences have different optimal phase-encoding orders, and therefore will be affected by respiratory motion differently. Generally, to avoid sudden signal amplitude and or phase discontinuities through k-space, which would lead to other artifacts, the Turbo-Spin-Echo (TSE) and conventional gradient echo sequences acquire the data with an interleaved manner, whereas for other reasons the balanced Steady-State Free Precession (SSFP) cine sequences acquire in a block sequential manner. However, it should be noted that the exact acquisition

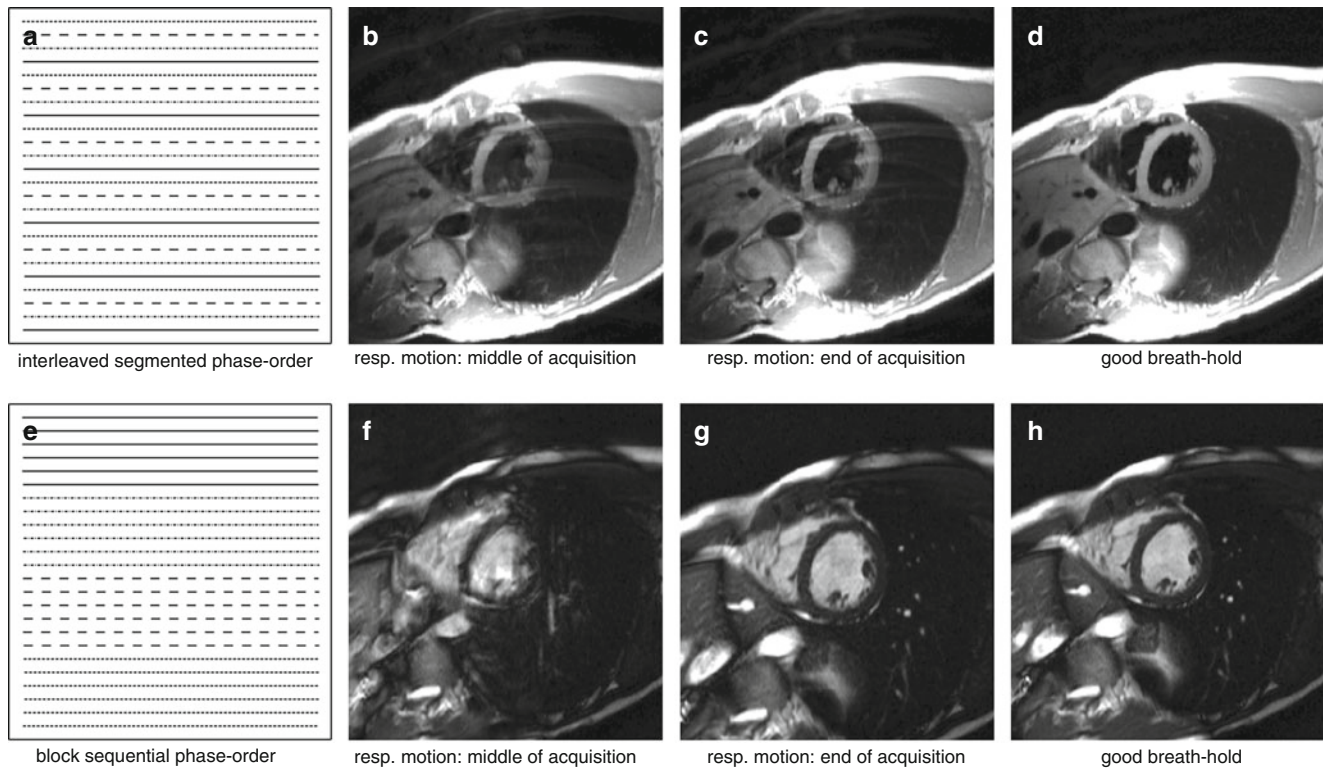


Fig. 7.1 Breathing motion artifacts with two different phase-orders. This figure shows the artifacts caused by changes in respiratory position at different times during a breath-hold acquisition for an interleaved (*top*) and sequential (*bottom*) phase-order. (a) Shows an interleaved segmented phase-order (as used in a black blood TSE sequence but reduced to only 24 phase-encode lines for illustration), with 4 segments each with 6 phase-encode lines. Each line-type represents a different cardiac-cycle of data. (b) The effects of a respiratory movement in the middle of the acquisition. (c) The effects of a respiratory movement at the end of the acquisition. (d) A good breath-hold. With interleaved acquisition, respiratory motion at any time during the scan is liable to

cause ghosting across the entire phase-encode FOV. (e) Shows a block sequential phase-order case (as used in a cine bSSFP sequence and again only 24 phase-encodes for illustration), with 4 segments each with 6 phase-encode lines. Each line-type represents a different cardiac-cycle of data. (f) The effects of a respiratory movement in the middle of the acquisition. (g) The effects of a respiratory movement at the end of the acquisition. (h) A good breath-hold. With a block sequential phase order the central region of k-space is acquired during a certain well defined period, and not spread throughout the whole acquisition window, therefore if no respiratory motion happens during this period, the artifacts are less conspicuous

methods might vary between manufacturers and even for the same manufacturer over time.

To avoid breathing motion artifacts, the total imaging time is kept short, and suitable for a breath-hold. If the patient is unable to hold their breath, the total imaging time needs to be reduced. Possible solutions include end-inspiratory breath-holds risking greater variability, or the use of parallel imaging, although the reduction of SNR in some applications such as Late-Gadolinium Enhancement (LGE) imaging may prohibit this; or the reduction of overall k-space lines acquired, thus reducing phase-encode spatial-resolution. Another solution that may be available is to reduce the temporal-resolution, by increasing the data lines per cardiac cycle and the imaging window of each cardiac-phase. This may have the cost of increasing cardiac motion problems, especially if imaging during rapid cardiac motion stages.

Breathing motion is one of the biggest challenges of MR coronary angiography. During cardiac motion, the coronaries have been shown to shift position from 5 to 20 mm [1],

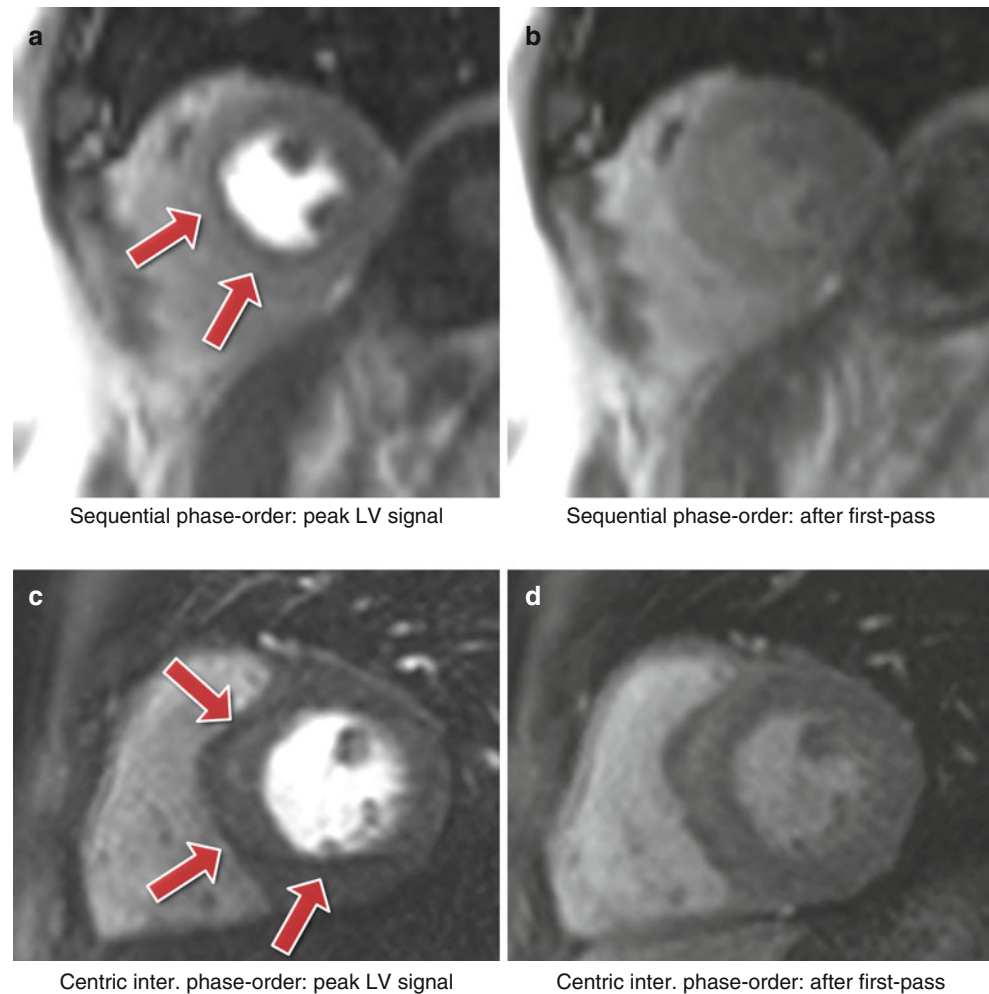
therefore the imaging window is limited to mid-diastole when the heart is relatively still. 3D coronary angiography imaging is performed during free-breathing and uses navigator echo techniques to monitor respiratory motion.

In general if imaging during a breath-hold, a *saturation band* can be positioned over the anterior chest wall to suppress any motion induced ghosting from it, if the breath-hold is imperfect.

Cardiac Motion

Cardiac motion is another source of inter-view motion artifacts. Cardiac motion is mainly a problem in sequences where the data acquisition window includes periods of rapid cardiac motion. This is commonly an issue for first-pass myocardial perfusion imaging, where several images are fully acquired during each heartbeat; therefore image acquisition windows are long and spread across the whole of

Fig. 7.2 Myocardial perfusion and cardiac motion artifacts for sequential and centric interleaved phase-orders. **(a)** In vivo short-axis image of a perfusion scan with a bSSFP sequence with a sequential phase-order acquisition. A subendocardial dark rim artifact is visible likely to be a superposition of motion and Gibbs ringing artifacts (arrows). **(b)** Same as *a* but after first-pass; the contrast between the LV and myocardial signal is reduced and the dark rim artifact is no longer visible. **(c)** In vivo short-axis image of a perfusion scan with an h-EPI sequence with a centric-interleaved phase-order acquisition. A typical motion artifact is visible in the septal wall. This is no longer a subendocardial dark rim as shown in *a*, but ghosting from the endocardial border offset along the phase-encode direction (arrows). **(d)** As in *b*, motion artifacts are no longer visible after first-pass due to the reduction of signal contrast between the LV and myocardium (Video 7.1)



the cardiac cycle, including rapid cardiac motion stages. The heart will go through contraction and expansion as different phase-encode lines are acquired; motion happens both in-plane and through-plane, resulting in artifacts. Acquisition windows for one perfusion image at typical in-plane resolution around 2.5 mm are approximately 100 ms for Gradient-Recalled Echo (GRE) and bSSFP sequences and 70 ms for h-EPI, with parallel imaging with an acceleration factor of 2.

For a Cartesian sequential phase-order, as typically employed in GRE and bSSFP sequences, a continuous motion results in banding artifacts next to sharp edges [2], shown in Fig. 7.2a, b. The appearance of these artifacts is similar to *Gibbs ringing* artifacts (described later). Alternatively the hybrid Echo-Planar Imaging (h-EPI) perfusion sequence is commonly used with a centric interleaved phase-order tailored for perfusion, minimising the effective TE, resulting in a dark ghosting of the endocardial border along the phase-encode direction (Fig. 7.2c, d).

For the GRE and bSSFP sequences with a sequential phase-order, motion induced ringing artifacts can be superimposed with Gibbs ringing and possibly mimic real subendocardial perfusion defects during first-pass. The h-EPI

sequence is more robust to motion artifacts, not only because it is the fastest of the three sequences, but also because of its different phase-order (centric interleaved); cardiac motion artifacts do not result in subendocardial dark rim artifacts. Whilst the h-EPI sequence is therefore useful to differentiate cardiac motion artifacts this also makes it very sensitive to frequency-offsets as described below.

As the motion ringing magnitude is dependent on the signal difference across the edges, motion artifacts are expected to be problematic during first-pass when there is a large contrast between the LV blood pool and the myocardium.

In general, whatever the k-space acquisition scheme, in order to minimise cardiac motion artifacts it is important to keep the image acquisition time as short as possible in each heartbeat and if possible aim for timings of the heart cycle where the heart is relatively still. Additional approaches include using a fast EPI readout, and/or parallel imaging.

The inversion pulse preparations used in dark-blood imaging or LGE are particularly sensitive to cardiac motion and arrhythmias. For the multiple inversion pulse preparation used in dark-blood imaging, a correct cardiac cycle synchronisation with the readout is important. If during image

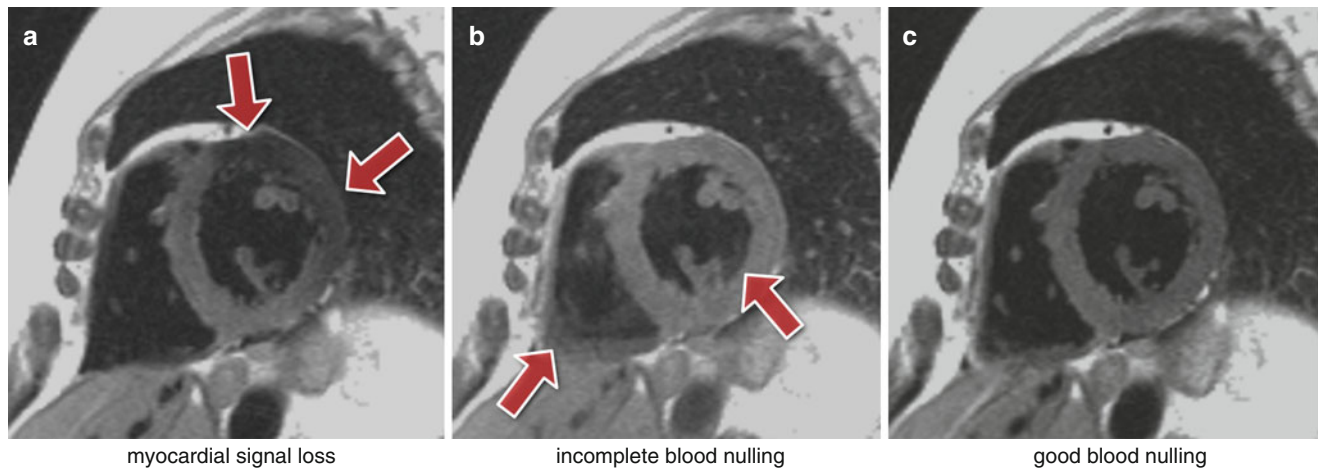
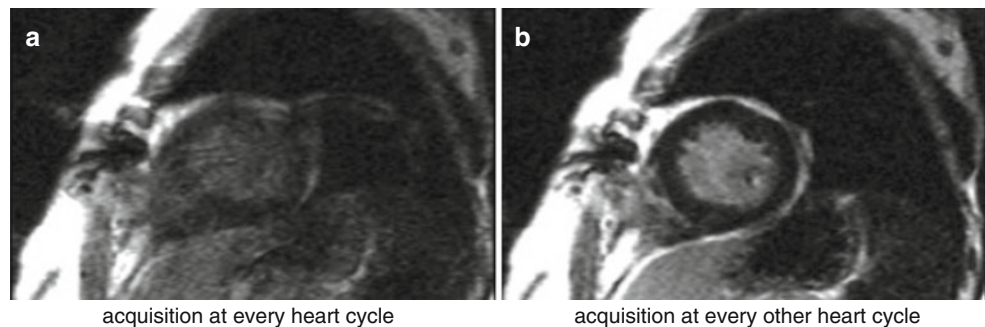


Fig. 7.3 Dark-blood imaging with cardiac motion artifacts. (a) Myocardial signal loss (*arrows*) due to incomplete re-inversion of the myocardial magnetisation. (b) Partial blood signal (*arrows*) due to incorrect inversion-recovery timing not coinciding exactly with the “null” time of the blood magnetisation. (c) Good blood signal nulling, without loss of myocardial signal. In this last example the inversion pulse thickness and timing were optimal for darkening the blood signal

Fig. 7.4 Arrhythmia artifacts in LGE. LGE short-axis image, in a patient with arrhythmia. (a) Image acquisition for every heart-cycle. (b) Image acquisition for every other heart-cycle. Image quality is improved in *b* by acquiring data at every other heart-cycle only, reducing the contrast inconsistencies between different k-space segments that were created by the irregular heart-rate



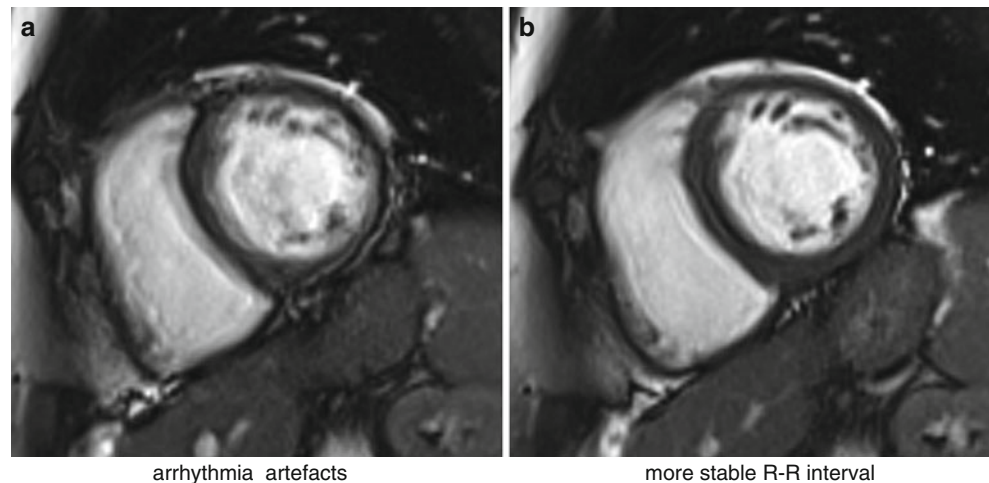
acquisition, the heart is not in the same position as when the double-inversion pulses were applied, then the myocardial signal can be affected resulting in myocardial signal loss (Fig. 7.3a). To reduce the potential for this the spatially selective inversion pulse thickness is commonly larger than the image-slice thickness by a factor of 2 or 3. The trade-off is the re-inversion of blood outside the image-slice potentially reducing the blood signal nulling efficiency for slow flow, which may be a factor for patients with an abnormally low cardiac function. Another reason for reduced blood signal nulling efficiency would be an inversion time that was either too long or too short (Fig. 7.3b). Although it is not always possible to change all the parameters required, it is normally possible to adjust the trigger delay and inversion time to change the timings of the preparation and imaging. It should be noted that the terminologies for these timing parameters vary between manufacturers.

Arrhythmias in LGE can lead to poor image quality due to contrast inconsistencies between different k-space segments, due to variations in the TR for the inversion recovery sequence. This leads to different amounts of recovery and therefore different levels of magnetisation before and after

the inversion pulse. For this reason data is usually acquired for every other heart-beat, reducing dependency on a regular heart cycle but increasing imaging time (Fig. 7.4). For patients with very fast heart-rates it might be required to trigger every three heart-cycles in order to guarantee good image quality.

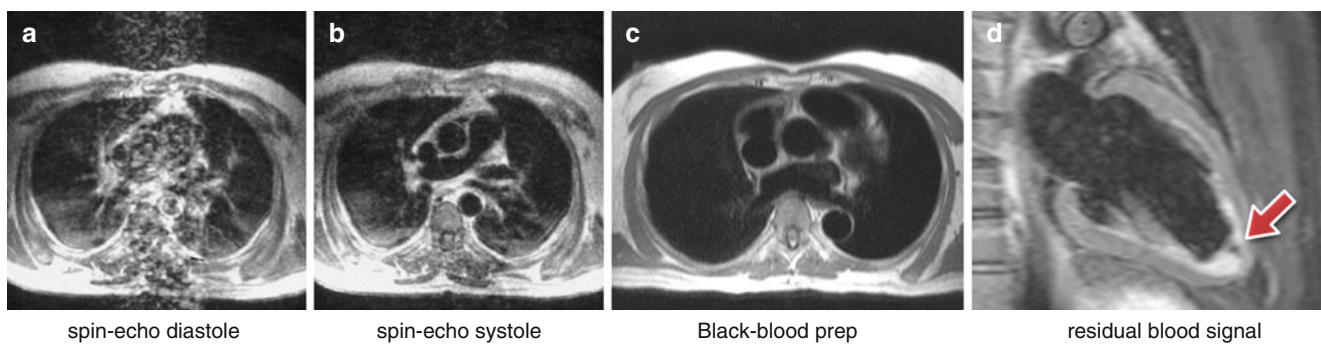
Poor cardiac triggering can also result in motion artifacts. Most cardiac imaging techniques require the acquisition of full images or k-space segments at specific cardiac phases, i.e. at specific times after the R-wave. Poor triggering due to patients with arrhythmias or weak ECG signal, or due to magneto-hydrodynamic [3] (generation of an electric field due to ions in blood flowing across the main magnetic field) and/or gradient pulse distortion, can cause effects varying from minor inconsistencies to conspicuous artifacts. For example, poor triggering in myocardial perfusion imaging typically results in slices at different cardiac phases per cycle of the perfusion first-pass series; this may not degrade the image quality of each individual image but it affects the clinical interpretation of first-pass and severely complicates segmentation in quantitative analysis. Triggering problems in cine imaging tend to result in more severe artifacts because each image frame's k-space is segmented across multiple

Fig. 7.5 bSSFP cine and arrhythmia. Short-axis bSSFP cine frame imaged twice: (a) with significant arrhythmia artifacts and (b) with reduced artifacts due to a more stable RR-interval (Video 7.2)



arrhythmia artefacts

more stable R-R interval



spin-echo diastole

spin-echo systole

Black-blood prep

residual blood signal

Fig. 7.6 Spin-echo blood flow artifacts. (a, b) An old example of blood flow artifacts on a conventional spin-echo sequence of a transverse slice through the great vessels above the heart: (a) image acquired in diastole, (b) image acquired in systole showing reduced flow artifacts due to increased intra-voxel dephasing and time of flight effects. (c) Similar transverse plane to a-b, acquired with a HASTE sequence in diastole. The introduction of faster segmented acquisitions with black blood

preparation avoids flow artifacts in diastole; multiple spin-echo sequences (HASTE, FSE) are generally reliable only in diastasis. (d) Dark-blood prepared FSE image (with STIR fat suppression) shows residual slowly moving blood signal (arrow) that was re-inverted by the double inversion preparation pulse and did not wash out between preparation and imaging

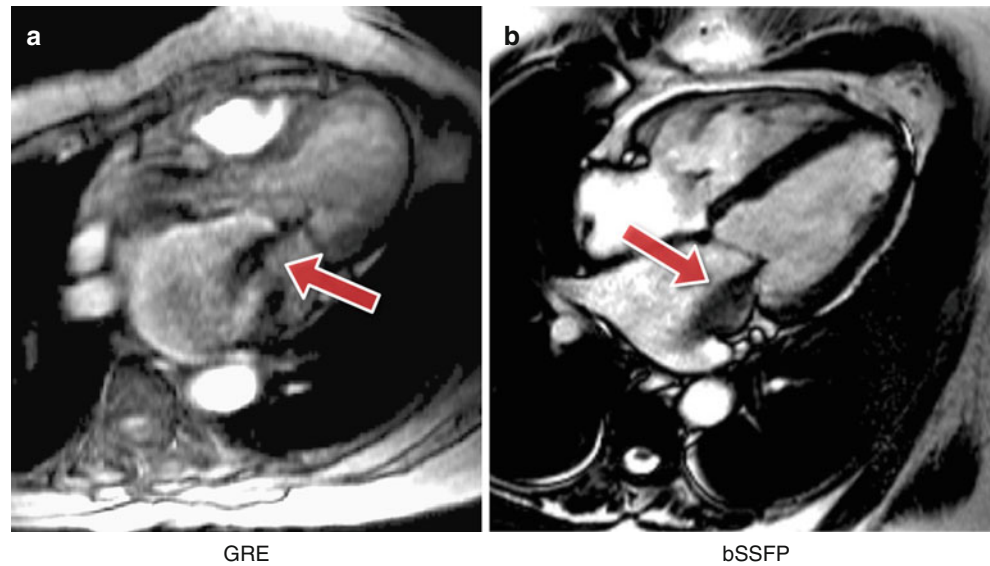
heart-cycles. Mis-triggers causing jumps in TR and or heart-cycle variations will create inconsistencies between k-space segments, thus leading to noticeable cardiac motion artifacts (Fig. 7.5). If ECG triggering quality is low, alternatives can be used such as pulse oximeters, although care must be taken with the fact that the pulse cycle is delayed relative to the heart-cycle and not as well defined, thus reducing timing precision. More recently real-time imaging strategies have been developed where the requirement of ECG triggering and/or breath-holding are relaxed [4].

Blood Flow

Flowing blood has historically been a source of artifacts on CMR images. For conventional sequences the movement of blood results in a signal phase shift related to the velocity of the blood flow. This would not cause a major problem if the blood flow was exactly the same on each successive cardiac

cycle of the scan; however, this is not usually the case and the result is that this changing velocity related phase shift will add to and corrupt the spatial phase encoding in such a way that the Fourier transformation will interpret the blood signal as coming from a range of locations spread across the image along the phase-encode direction. To avoid this problem in the early days of CMR for spin-echo acquisitions the images were often acquired in systole, when two factors combined to cause a loss of blood signal. Firstly, the blood flow was fast causing increased phase shifts leading to a broad phase distribution at a voxel scale known as intra-voxel phase dispersion, and secondly time-of-flight effects meant that the same blood was not excited by both the slice selective 90° and 180° pulses (Fig. 7.6a, b). With the introduction of faster segmented acquisitions of spin-echo images with double inversion blood signal nulling, this problem was largely removed (Fig. 7.6c), although residual static blood at ventricular trabeculations is commonly visible as a white layer in the left ventricle (Fig. 7.6d).

Fig. 7.7 Complex flow signal loss. Two examples of a systolic frame of an horizontal long axis cine acquisition from two different patients with insufficient mitral valves: (a) GRE, (b) bSSFP. The jet of signal loss caused by complex flows in the left atrium suggests mitral valve regurgitation (arrows)



For gradient-echo acquisitions in the early days the problem was largely removed by the introduction of velocity or flow compensation to null velocity related phase shifts. With the introduction of faster gradient performance and shorter TE's and consequently greatly reduced velocity related phase shifts, the potential for these artifacts has been reduced. Nonetheless velocity compensation remains an option to minimise the problem. However, as a consequence of some cardiovascular diseases, the blood flow often becomes much more complex and turbulent and contains higher orders of motion than simple velocity, (acceleration, jerk, etc.). These higher orders of flow motion can introduce phase shifts even to a velocity compensated sequence and the spatial scale of this motion is such that this can also lead to significant phase dispersion. This intra-voxel phase dispersion effect is dependent on the TE. Although this signal loss artifact has been found useful by some to assess the severity and form of defective heart valves (Fig. 7.7) it should be used with caution as the area of signal loss may not be directly related to the severity of the valve stenosis.

Gibbs Ringing

Gibbs ringing, also known as a truncation artifact, is present in every unfiltered MRI image and results from the fact that there is only enough time to acquire a finite region of k-space for each image. When the sampled signal is truncated at the k-space edge and then this k-space is inverse Fourier transformed into the image, ringing will unavoidably be present at high-contrast sharp edges of structures on the image. The ringing is a known mathematical limitation of the Fourier transform.

The 2 pixels both sides of and closest to the edge will show a maximal undershoot and overshoot of the true signal.

The magnitude of the under/overshoot can be shown mathematically to be approximately 9 % of the edge signal difference; the ringing magnitude is thus dependent on the signal difference at the edge, the higher the signal discontinuity the higher the under/overshoot (Fig. 7.8a, b). Gibbs ringing also scales with pixel size, i.e. the higher the spatial-resolution the thinner the ringing, but the under/overshoot magnitude does not change with spatial-resolution. The ringing visibility is also dependent on the edge position inside the pixel [5] (unless zero-filling is applied in k-space for interpolation, making Gibbs more consistent).

Gibbs ringing is present in all unfiltered MRI images, but it is especially problematic in certain applications such as myocardial first-pass perfusion studies where the spatial-resolution is low to reduce acquisition time. Gibbs ringing can mimic a real subendocardial perfusion defect during first-pass due to the large signal discontinuity between the bright LV blood pool and the darker myocardium [6].

One way of reducing Gibbs artifacts is by filtering the k-space data of the image, a process usually known as apodization. Hamming and Hann filters are commonly used in image and signal processing to reduce Gibbs ringing artifacts, although at the penalty of reducing spatial-resolution. Due to the image constraints of most cardiac imaging protocols, any further loss in spatial-resolution may affect diagnostic confidence and is therefore seldom used. It is then perhaps better for clinical diagnosis and image interpretation to be performed with some understanding of the characteristics of these artifacts and can discriminate between them and true perfusion defects (which is sometimes ambiguous, especially for mild perfusion defects). The access to k-space filtering options in the scanner's protocol may vary for different manufacturers.

Increasing spatial-resolution does not reduce the Gibbs ringing magnitude but it will make it less conspicuous due its

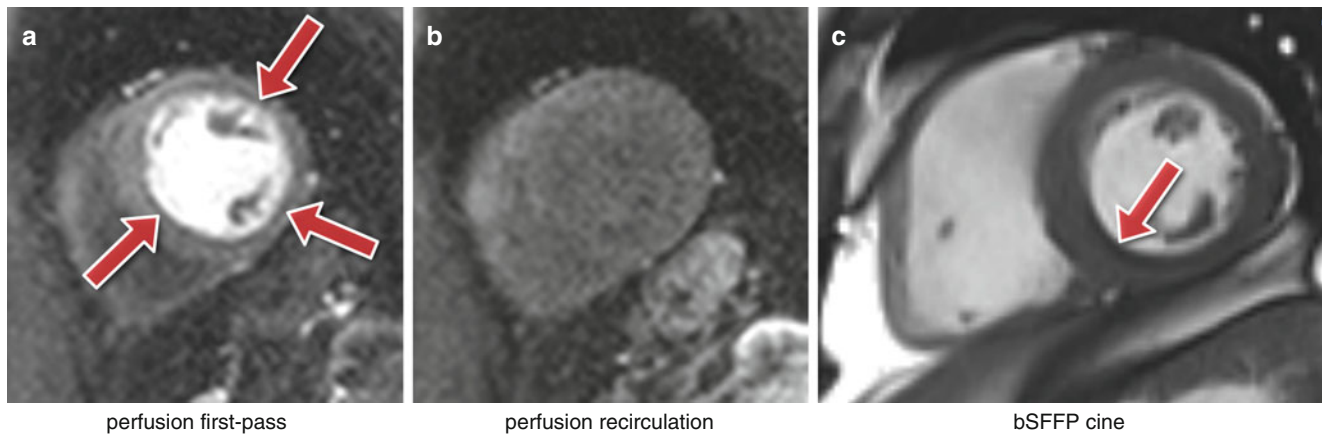


Fig. 7.8 Gibbs ringing. (a, b) In vivo short-axis first-pass perfusion example: (a) circumferential Gibbs ringing during the first-pass of contrast (arrows); (b) the same short-axis plane after the first-pass when

Gibbs ringing is no longer noticeable. (c) Example of Gibbs ringing in a short-axis frame of a bSSFP cine (arrow)

property of scaling with pixel size. Unfortunately in many cases it is not possible to increase the resolution as this would require increased time, which might not be available. Additionally, other sources of artifacts such as cardiac motion could be worsened. However, as techniques such as parallel imaging and other image acceleration methods improve they can be used to increase spatial-resolution without increasing imaging time [7–9], provided that loss of SNR and other consequences of acceleration are acceptable.

Even though this section focused on myocardial perfusion, Gibbs ringing is visible at any sharp edge, and therefore it could affect many other cardiac applications. For example, Fig. 7.8c shows an example of suspected Gibbs ringing in a short-axis frame of a bSSFP cine.

Aliasing or Wraparound Artifacts

One of the most basic artifacts commonly seen in MRI is the phase-encode field-of-view (FOV) *wraparound* artifact also known as *aliasing*. This artifact occurs whenever the size of the object being imaged exceeds the FOV in the phase-encode direction; the outside regions are wrapped into the opposite edge of the FOV. This is due to the failing of the Nyquist sampling requirements of the k-space signal for parts of the object outside the FOV. Aliasing is prevented along the frequency-encode direction either by filtering the frequencies above a limit determined by the Nyquist sampling requirement; or by signal oversampling, i.e. sampling more points in k-space than the ones prescribed by the protocol such that the FOV along the frequency-encode direction is bigger than that actually displayed on the image. The same technique cannot be used along the phase-encode direction without increasing the time of imaging. Therefore this type of artifact is common along the phase-encode direction and

also along the slice direction in a 3D acquisition. Figure 7.9b illustrates the chemical shift effect described below but also very nicely illustrates aliasing of patient’s arms into his chest.

Due to the need of large FOVs to cover the chest, aliasing is a common problem. If the region of interest is small, for example the heart only, then some wraparound can be acceptable as long as it does not superimpose on the heart. This keeps imaging time short without sacrificing diagnosis and experienced technologists commonly make careful use of this approach. Saturation bands can also be used to suppress the signal of the regions outside the FOV in sequences where the signal used for the acquisition is excited only once and immediately after the saturation, such as in the 90° excitation of a multiple spin-echo (FSE or TSE) sequence.

We have discussed aliasing artifacts in this section for Cartesian sampling only. Aliasing and undersampling artifacts are discussed further in section “[Artifacts specific to advanced cardiac imaging methods](#)”, particularly regarding non-Cartesian trajectories and parallel imaging.

Chemical Shift

The resonance frequency of water and fat differs by approximately 210 Hz at 1.5 T (420 Hz at 3 T), which causes a number of effects. Firstly it causes a *misregistration* between fat and water based tissues along the frequency-encode direction and more so along the perpendicular phase blip direction for EPI sequences. Secondly, it will result in a slice excitation offset between water and fat. Finally, for gradient-echo sequences only, a possible pixel cancellation effect at water-fat boundaries can occur.

The misregistration in pixels along the frequency direction results from the fact that fat and water that are

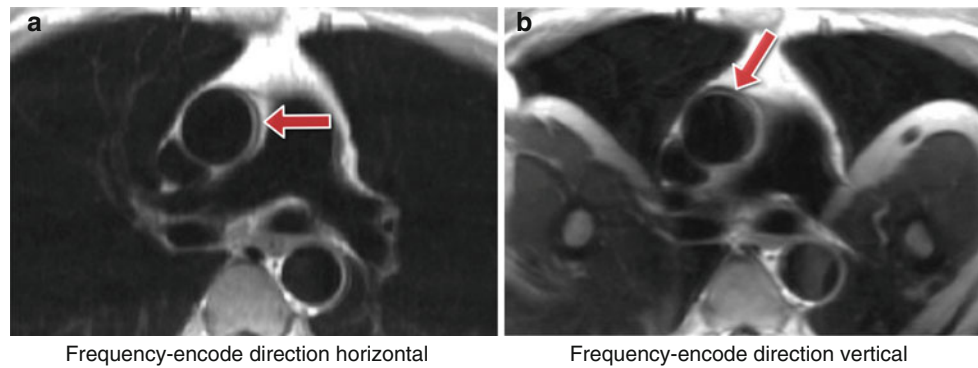
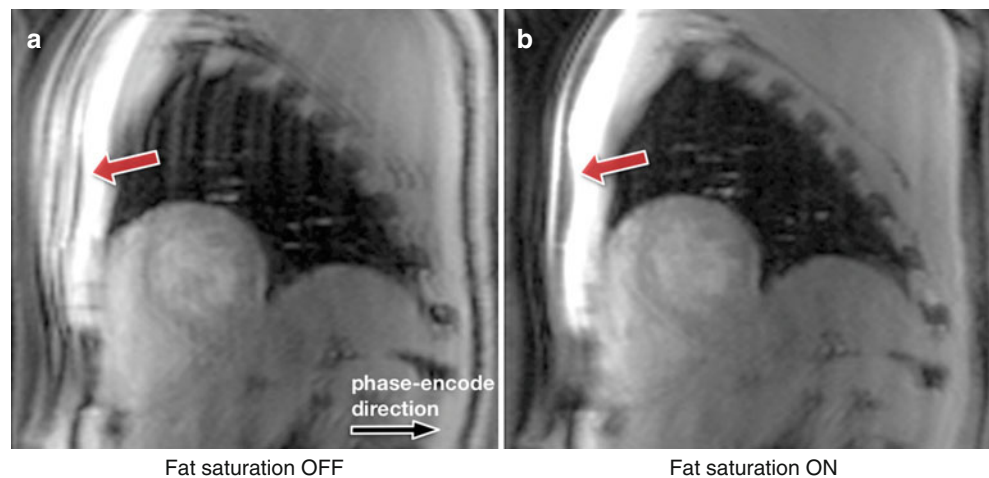


Fig. 7.9 TSE chemical shift artifacts. (a, b) TSE image of a transverse plane through the great vessels above the heart, illustrating chemical shift artifacts between the aortic wall and surrounding fat: (a) horizontal frequency-encode, (b) vertical frequency-encode. Artifacts are visible

in the aortic wall along the frequency-encode direction (arrows). This artifact can potentially be misdiagnosed as an aortic dissection in some cases. On image b with the frequency-encode direction swapped from a, wraparound artifacts of the patient's arms into the chest are also visible

Fig. 7.10 h-EPI chemical shift artifact. Short-axis images acquired with a centric interleaved h-EPI sequence with fat-saturation preparation turned off (a) and on (b). When there is no fat-saturation preparation, the fat signal in the chest wall is visible, displaced approximately 4 pixels in both directions (arrows). When fat saturation pulses are used, the fat signal in the chest wall is efficiently suppressed (arrow)



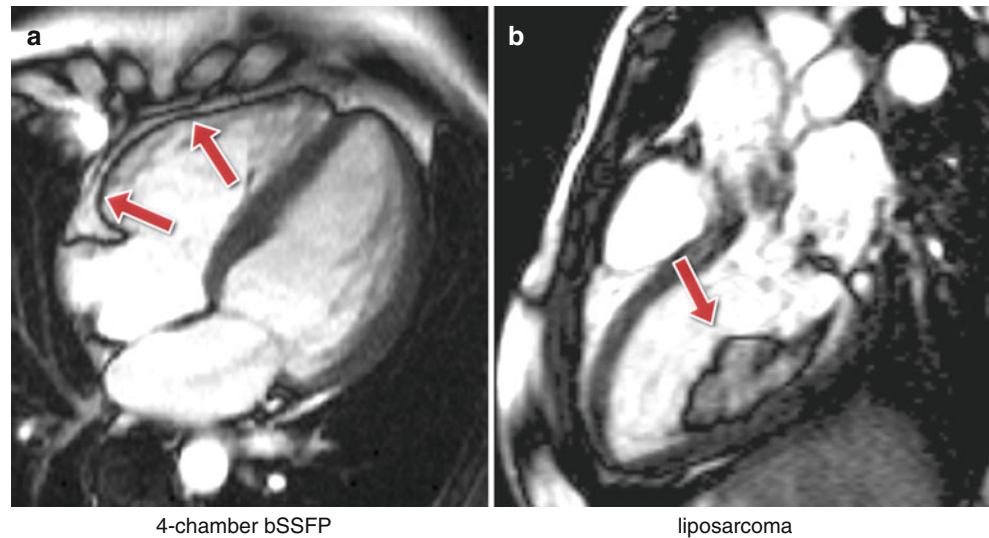
physically in the same position have different resonance frequencies, which will result in the frequency encoding process separating them on the reconstructed image. The distance of separation will depend on the receiver bandwidth. For example, if the bandwidth was 105 Hz/pixel then at 1.5 T their separation of 210 Hz would equate to 2 pixels on the reconstructed image. If the bandwidth was doubled to 210 Hz/pixel then the separation would be halved to 1 pixel. Increasing the bandwidth thus reduces the chemical shift effect; however, this has to be balanced against the loss of SNR. For most cardiac applications, the need of rapid sampling requires large bandwidths, so misregistration along the frequency-encode direction is relatively negligible. However, for TSE sequences where longer readouts with lower bandwidths can be used, it is possible to see the effect (Fig. 7.9).

As mentioned above, for an EPI readout misregistration can be a problem and can cause a considerable shift of the fat signal along the phase-encode direction relative to the water signal. For a single shot EPI acquisition, the shift can be several pixels and for a typical perfusion h-EPI sequence a

chemical shift of a pixel or two is typical. Where centric phase encoding is used, as is often the case, the shift is doubled and split into two opposite directions producing a complicated artifact when fat saturation is not applied correctly (Fig. 7.10). Using a small number of echoes per readout train or fat saturation pulses are common techniques to reduce chemical shift artifacts in EPI.

Another important artifact resulting from the chemical shift and sometimes referred to as the *Indian ink* artifact, is the pixel cancellation at boundaries between fat and water based tissues. This occurs with gradient-echo sequences and is TE dependent such that the maximum cancellation occurs when fat-water signals are completely out of phase, which first occurs at a TE of approximately 2.4 ms for 1.5 T. This is often prominent on bSSFP images where the TR has to be kept short enough to minimise the sensitivity of the sequence to field inhomogeneities and this generally leads to a TE in the order of 2 ms (Fig. 7.11). When imaging the coronaries, the signal cancellation artifacts can reduce the apparent diameter of the coronary arteries if fat signal is not properly suppressed.

Fig. 7.11 b-SSFP Fat-water signal cancellation. At TEs of approximately 2.4 ms at 1.5 T (1.2 ms at 3 T), the fat and water spins are out of phase and the resulting signal is reduced. (a) Fat water cancellation artifact around the right ventricular wall (arrows) on a long-axis cine. (b) The same artifact around a liposarcoma in the left ventricle (arrow)



B₀-Field Inhomogeneities

The magnetic field is never completely homogeneous over the volume of the heart. It is possible to correct low spatial-order variations by obtaining 3D field plots and calculating the required shim currents usually to second order; however, more localised (high-order) field variations will remain due to the magnetic field susceptibility variations around the heart.

Most tissues are *diamagnetic*, i.e. create a magnetic field that slightly opposes the applied magnetic field. It is important to understand that this arises from their electronic (“Lenz”) diamagnetism, which is much larger than the nuclear magnetisation we employ for MRI. The differences in diamagnetism cause distortion of the main field at interfaces between tissues, and particularly those between tissue and air such as between the heart and lungs. These B₀ field inhomogeneities cause resonance frequency offsets, where the local resonance frequency deviates from the scanner’s reference frequency, leading to off-resonance effects. Depending on the local geometry, and the sequence being used, this field distortion may sometimes be more intense causing artifacts such as signal loss or spatial distortion.

In CMR the sequences with the highest sensitivity to magnetic field inhomogeneities are the bSSFP sequence and sequences that employ rapid k-space acquisition techniques such as EPI and Spiral. The spin-echo sequence is relatively insensitive whilst the conventional gradient-echo sequence sensitivity increases largely with its TE parameter. Figure 7.12 illustrates the difference between a TE of 2 and 10 ms for distortion, signal loss, and phase shift caused by susceptibility variations around a pulmonary vessel and around the apex of the right ventricle on a GRE sequence.

Figure 7.13 illustrates an example where a patient with an insertable cardiac monitor has been scanned with both bSSFP and HASTE sequences. The bSSFP image shows signal loss and banding artifacts in the region proximal to the device due to magnetic field distortions, while the HASTE sequence is less sensitive. Many other medical devices are also a source of susceptibility artifacts by distorting the magnetic field (Fig. 7.14). Figure 7.15 shows an example of a patient with an aortic stent. When imaged with GRE 3D or bSSFP sequences, the stent causes not only localised main field inhomogeneities and signal loss but also an RF shielding effect within the stent, as elucidated by Fig. 7.15b.

B₀ inhomogeneity artifacts are very distinct and can be very severe for the bSSFP sequence [10]. The steady-state signal response to B₀ inhomogeneity remains approximately constant for small frequency-offsets, but drops down to near zero to form dark bands at regularly-spaced frequency offsets. The more inhomogeneous the magnetic field, the larger the frequency distribution in the image volume and the more black bands will appear. The frequency separation between regions with no signal is inversely proportional to the TR of the sequence; thus, reducing the TR reduces the number of artifacts observed.

Localised field inhomogeneities due to susceptibility differences in the locality of the cardiac veins [11]; and at tissue-air interfaces such as the heart-lung interface [12], or adjacent to air pockets [13] (in the bowel, stomach, and colon for example), introduce banding type artifacts on bSSFP images that can confuse the image interpretation. These signal loss artifacts should not be confused with intravoxel dephasing which is caused very differently. In this sequence, blood flow can also create artifacts in the presence of field inhomogeneities. Moving spins can exhibit signal variations and loss due to the breakdown of the steady-state signal

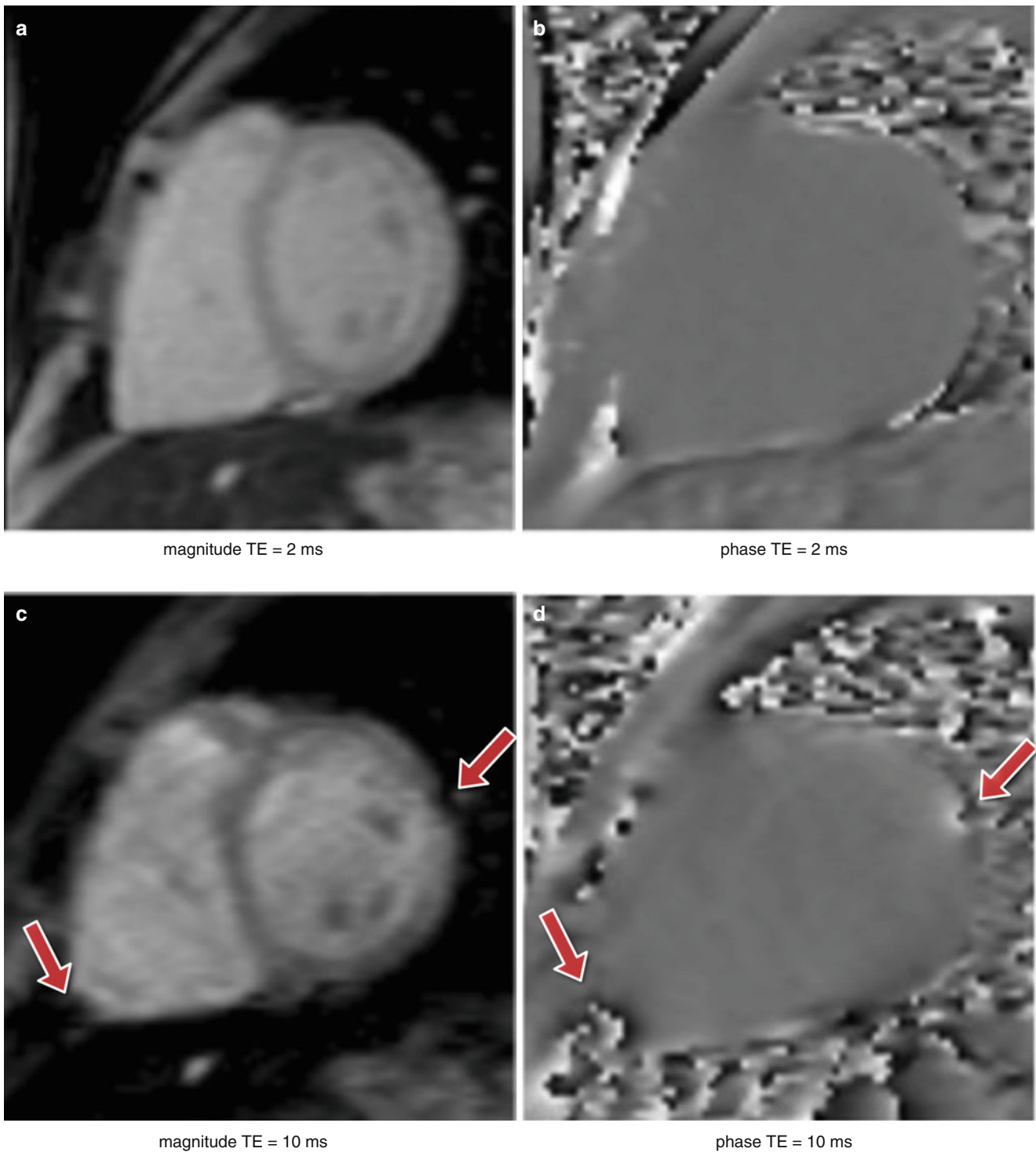


Fig. 7.12 GRE B_0 inhomogeneities at different TEs. Short-axis images acquired with a GRE sequence at two different TEs (**a, b**) 2 ms and (**c, d**) 10 ms. Both magnitude and phase images are shown. The *arrows*

point at two local field distortions (RV apex of the heart and in the proximity of a pulmonary vessel) that generate signal loss in the surrounding region as TE becomes larger

[14, 15]. These can occur due to in-plane flow moving through an off-resonance region, but also for through-plane flow leaving the image plane into such a region. Dark bands and signal variation artifacts are shown in Fig. 7.16. If such

artifacts affect an image then it is possible to move and/or suppress these by reacquiring with a slight frequency offset (≈ 50 Hz) of the scanner reference-frequency. It should be recognised, however, that as one black band moves out of the

Fig. 7.13 B_0 inhomogeneities and medical devices. Artifacts caused by an insertable cardiac monitor in a transverse plane through the great vessels above the heart: (a) image acquired with a bSSFP sequence with visible signal loss and banding artifacts (arrow), (b) image acquired with a HASTE sequence with less pronounced artifacts (arrow)

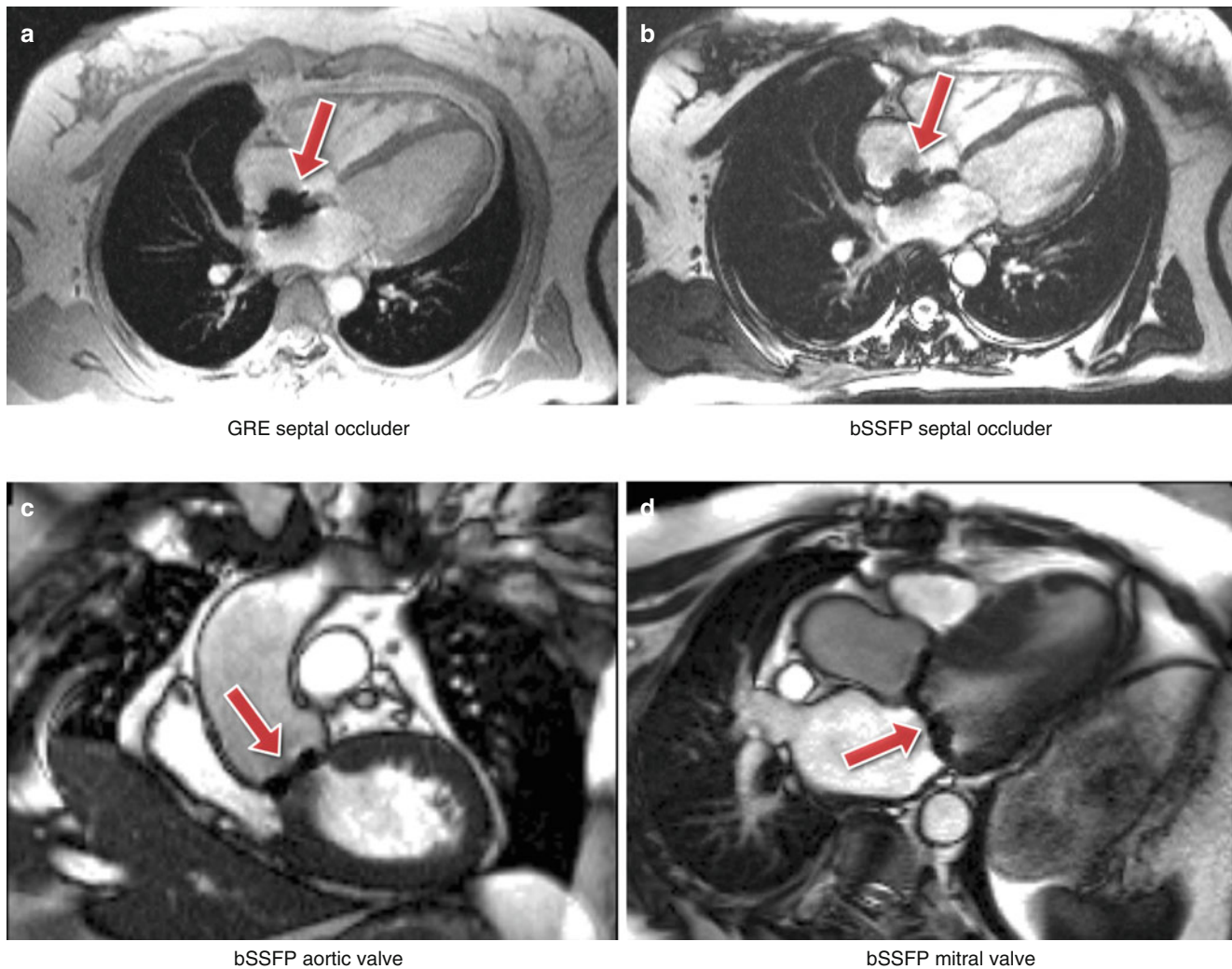
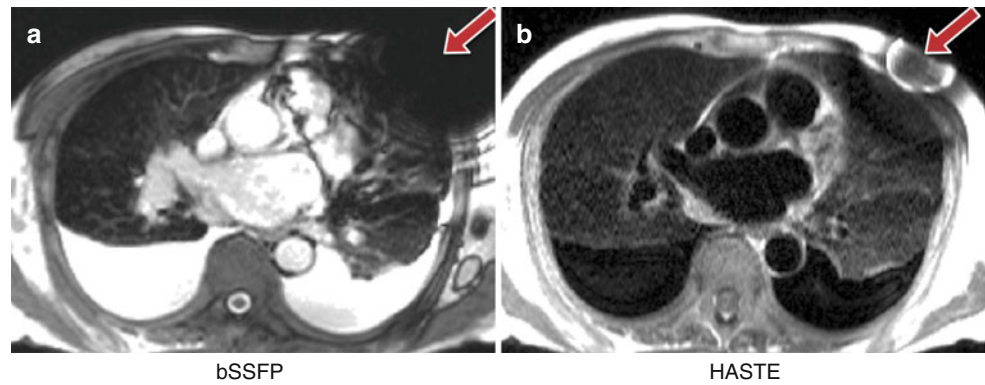


Fig. 7.14 B_0 inhomogeneities and medical devices II. (a, b) Four-chamber view acquired with GRE and bSSFP sequences respectively. The arrows point to signal loss caused by a septal occluder. (c, d)

bSSFP image planes containing localised signal loss (arrows) caused by bileaflet aortic and mitral valve replacements respectively

heart then another may be moving in from the other side (Fig. 7.16d). It is also sometimes crucial with such localised adjustments to understand that they should not be confined to the slice thickness. In the situation where through-plane flow or motion is large, then the shim adjustment should include sufficient distance perpendicular to the slice-plane.

Field inhomogeneities are also an important source of artifacts for the less widely-used EPI sequences. Sequences with an EPI readout tend to be used in a hybrid approach (h-EPI), in order to keep the readout train reasonably short, thus minimising blurring, ghosting, image distortion, and chemical shift artifacts. h-EPI sequences are commonly used

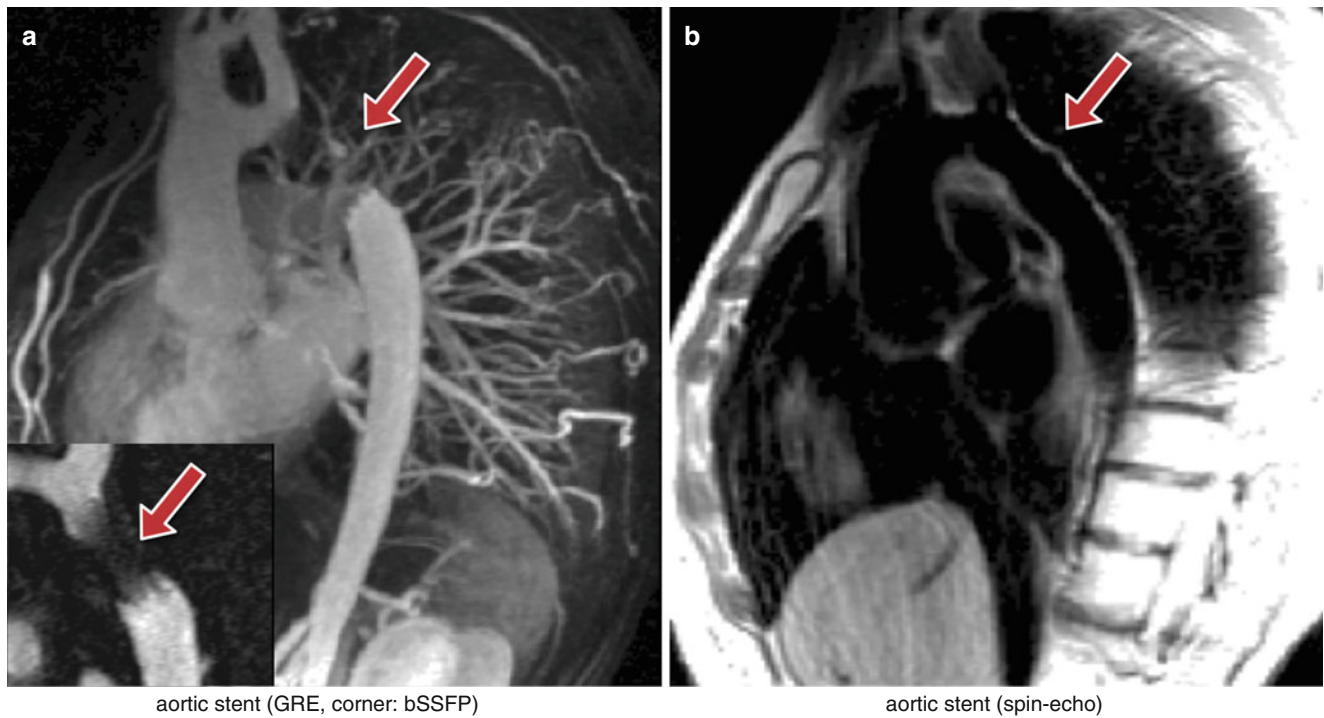


Fig. 7.15 B_0 inhomogeneities and medical devices III. (a) 3D GRE contrast-angiography maximum intensity projection reconstruction image showing signal loss in the descending aorta due to an aortic stent (arrow); the bottom left corner shows a bSSFP image plane containing the aortic stent also showing signal loss in the same region (arrow). The

signal void inside the stent is likely to be due to lack of RF penetration through the stent wall. (b) Spin-echo black-blood image also in a plane containing the aortic stent. The aortic wall outside the stent is clearly seen (arrow)

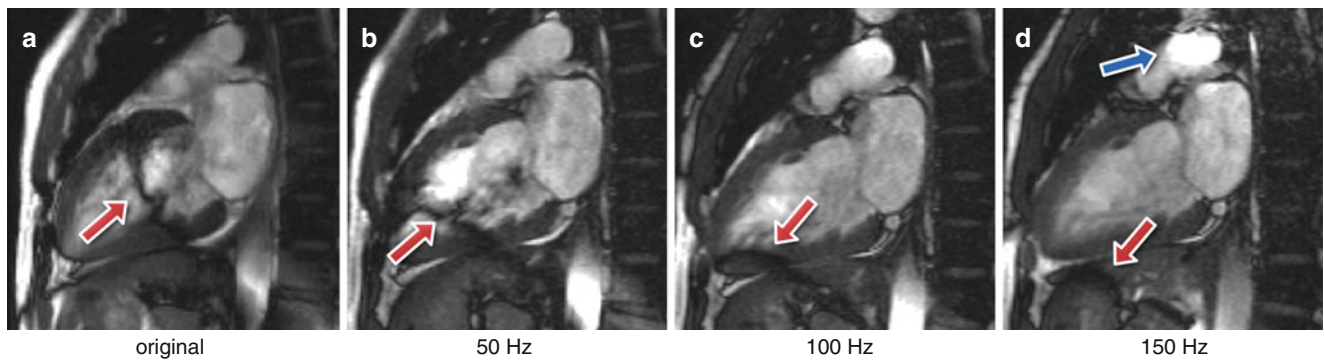


Fig. 7.16 bSSFP and B_0 inhomogeneities: reference frequency. (a–d) Series of vertical long axis bSSFP images acquired with different reference frequency offsets: original (0 Hz), 50 Hz, 100 Hz, and 150 Hz. Black band and flow artifacts through the ventricle are shown (arrows).

As the frequency is adjusted, the artifacts are shifted away from the heart. Image d shows a new flow artifact approaching the heart from the top (blue arrow). The approaching frequency-offset causes the blood signal to be hyperintense in the region

with an interleaved phase-order, where frequency offsets will introduce phase variations in a stepwise fashion, which can lead to artifacts such as blurring and ghosting. Magnetic field inhomogeneities caused by the arrival of a strong paramagnetic susceptibility contrast agent in the heart are commonly attributed as a possible mechanism for dark rim artifacts in myocardial perfusion imaging. The frequency offsets introduced in the myocardium by the first-pass of a Gadolinium-based contrast agent have been measured

at rest and shown to be insignificant for intra-voxel signal dephasing in the myocardium at 1.5 T [16], although when combined with other sources of field inhomogeneities or reference frequency-offsets it might produce artifacts such as signal loss or image degradation. The perfusion tailored h-EPI sequence has a centric interleaved phase-order, which makes it very sensitive to frequency-offsets [17], resulting in ghosting and splitting of the image along the phase-encode direction due to its centric sampling trajectory (Fig. 7.17).

In general to minimise B_0 -inhomogeneities careful shimming and especially localised scanner frequency adjustments are advised prior to imaging.

Inversion Pulse Ghosting

One artifact that affects any segmented acquisition with an inversion pulse, such as LGE imaging and STIR sequences, is the ghosting of fluids with a long T_1 . The long T_1 produces

a signal oscillation during its approach to the steady-state, with the signal inverting the magnetisation sign in alternate cycles of the acquired data, resulting in ghosts along the phase-encode direction.

Ghosting of the cerebrospinal fluid (CSF), which has a very long T_1 , is common in LGE and STIR black-blood studies. This is usually suppressed by applying a spatial saturation band (Fig. 7.18a–d). A possible example of the same ghosting mechanism of a pleural effusion in a STIR sequence is also shown in Fig. 7.18e.

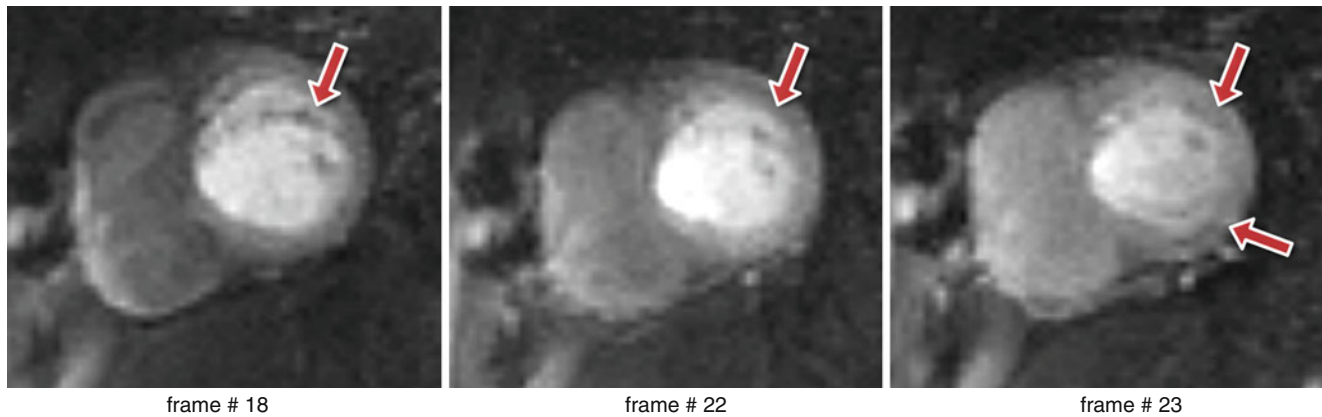


Fig. 7.17 h-EPI perfusion and B_0 inhomogeneities. Three frames during contrast first-pass perfusion imaging in a basal short-axis plane acquired with an h-EPI sequence. This example shows severe frequency-offsets which result in blurring and ghosting (arrows) along the phase

encode direction (*vertical*) with this sequence. This example is extreme and uncommon, although blurring of the myocardial wall along the phase-encode direction is believed to be a more common event in first-pass perfusion with this particular sequence

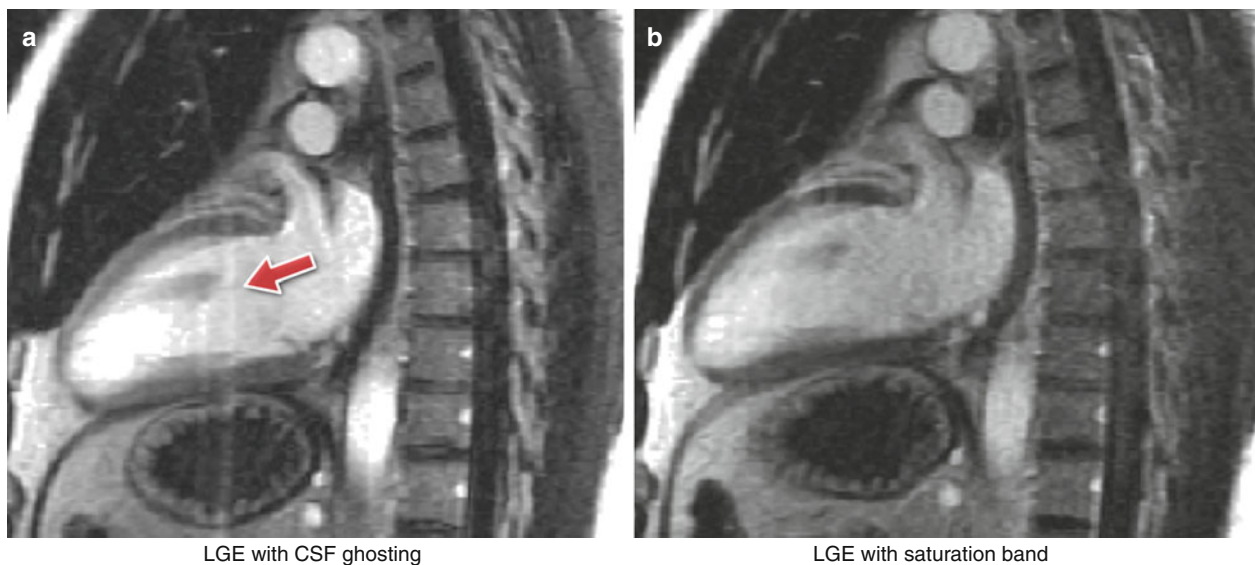


Fig. 7.18 CSF and pleural effusion ghosting. (a, b) Long-axis LGE image: (a) CSF ghosting is visible in the heart (arrow), (b) CSF ghosting suppressed by a saturation band placed over the spinal canal. In this example the spatial location of the saturation is not very clear, this is presumably because of the timing of the spatial saturation that cannot immediately precede the imaging k-space centre, and the M_z recovery of other tissues due to gadolinium shortened T_1 . However, the T_1 of CSF

remains very long, which means that this stays well saturated. (c, d) dark-blood (double-inversion-prepared) and STIR transverse TSE image: (c) CSF ghost visible in the RV (arrows), (d) CSF ghosting suppressed by saturation band placed over the spine (arrow). (e) Ghosting of the fluid in the pleural layers (pleural effusion) (arrows) in part due to its long T_1 . Pulsatility effects may also be present, contributing to the ghosting

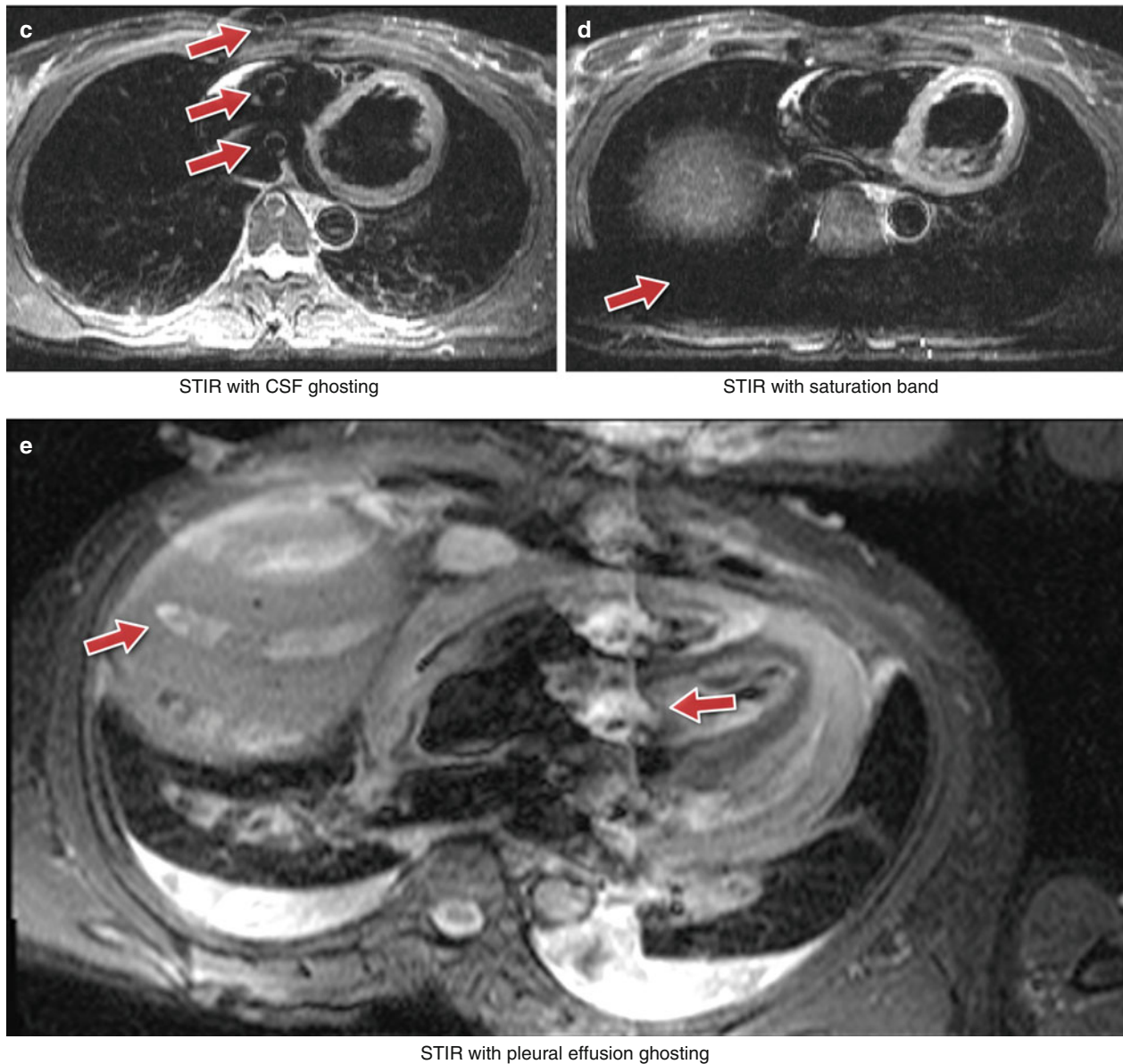


Fig. 7.18 (continued)

Artifacts Specific to Advanced Cardiac Imaging Methods

Methods of more efficiently acquiring the MR data are of particular interest to CMR because of the compromises that have to be made to acquire image data in a short time, often restricted to a fraction of one cardiac cycle or fractions of multiple cardiac cycles within a breath-hold. Methods such as non-Cartesian sampling, parallel imaging, and partial-Fourier have been introduced to accelerate the acquisition. Although each of these methods may work well a proportion of the time and in particular if extra care is taken to set up the scan, they

all tend to reduce the imaging robustness and tend to produce artifacts on images and or produce artifactual measurements.

Parallel imaging accelerates image acquisition which has the potential to reduce some problems. For example, although parallel imaging introduces an SNR penalty, it may also be employed to shorten the readout time of an EPI sequence reducing distortions caused by field inhomogeneities, decreasing blurring due to T_2^* and or T_2 decay and reducing sensitivity to motion. However, parallel imaging artifacts may appear if inaccurate coil sensitivity maps are acquired, for example due to respiratory motion, where errors will result in reconstruction artifacts (Fig. 7.19).

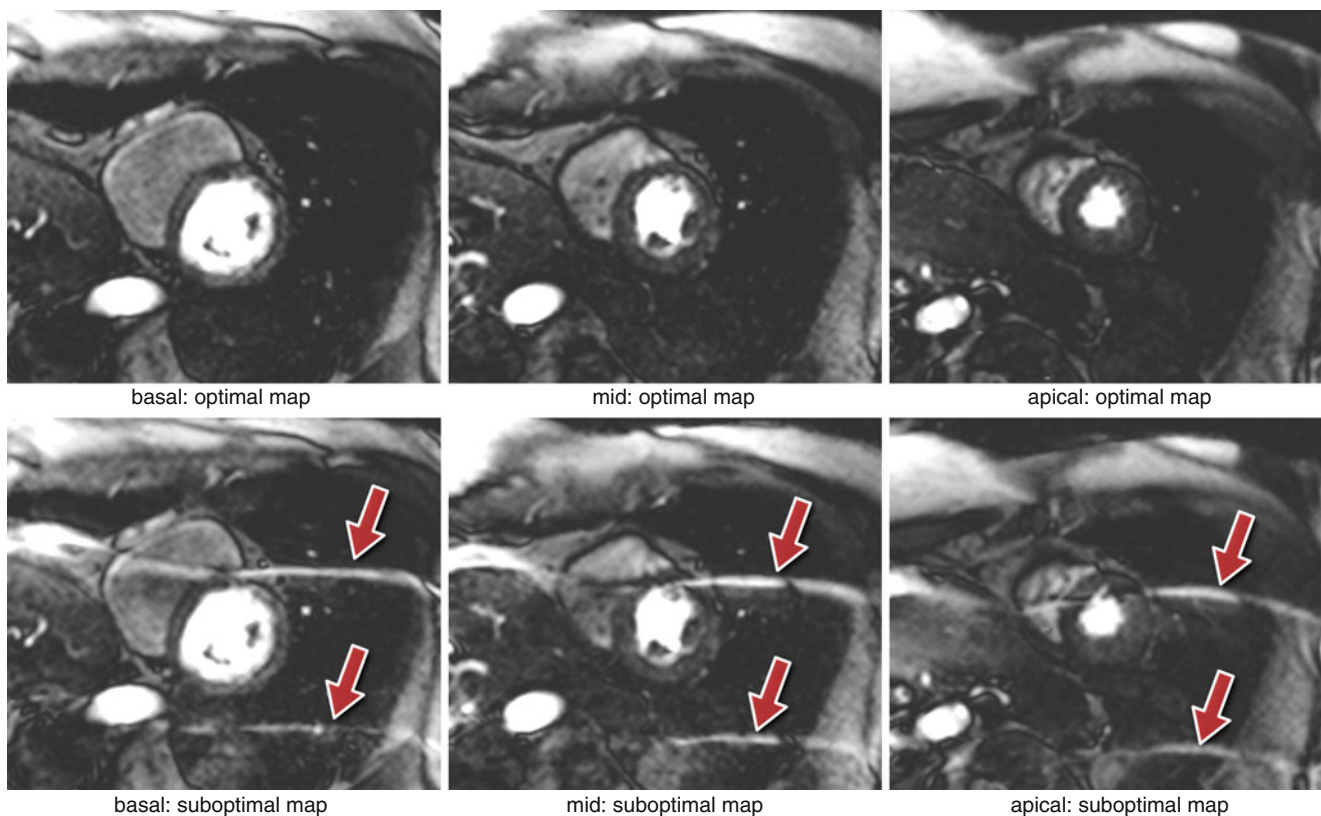


Fig. 7.19 SENSE with aliasing artifact due to respiratory motion. Three short-axis slices during first-pass perfusion, reconstructed with two different coil sensitivity maps (acquisition with a bSSFP sequence and SENSE with an acceleration factor of 4; zoomed images are shown). The three slices on *top* were reconstructed with the optimal coil sensitivity map, i.e. the coil sensitivity map acquired in the same respi-

ratory position as the perfusion images. On the *bottom* the same perfusion images were reconstructed with a coil sensitivity map that was acquired in a different respiratory stage from the perfusion images. The reconstruction is corrupted with aliasing artifacts (*arrows*) due to inconsistencies between the coil sensitivity map and the undersampled perfusion data (Video 7.3)

Sequences with non-Cartesian forms of k-space coverage such as radial and spiral have also been used to image the heart [18–20]. Artifacts discussed earlier can have very different characteristics when compared to the more conventional Cartesian methods.

Radial and spiral k-space acquisitions are generally thought of as being less sensitive to motion. Radial sequences tend to oversample the centre of k-space and this tends to reduce the visibility of breathing artifacts [21]. For a radial acquisition instead of ghosting in the phase-encode direction as seen with Cartesian sampling, respiratory motion results in streaking artifacts propagating from the moving object, perpendicular to the motion direction. For spiral sequences, motion artifacts tend to take the form of swirls and depending on the imaging region of interest these can be less of a problem than phase-encode ghosts.

Non-Cartesian approaches with long (>15 ms at 1.5 T) acquisitions after each RF pulse are highly sensitive to field inhomogeneities, where generally off-resonance and chemical shift translates into image blurring in all directions and signal loss. Due to the 2D readout gradients in these trajectories, aliasing artifacts happen from all directions resulting in additional streaks and swirls, therefore the FOV has to be

chosen with attention to aliasing in all directions. Commonly mild undersampling artifacts are tolerated in order to reduce imaging time.

The readout of an EPI echo train also introduces a specific artifact related to the alternating sampling gradients. This artifact is commonly known as *Nyquist ghost* or *N/2 artifact* and it is created by a mixture of gradient imperfections, eddy currents, concomitant fields, receiver filter asymmetry or susceptibility. All these factors will cause mismatches between odd and even echoes resulting in some signal being displaced, in single-shot EPI by half the field of view across the image along the phase-encode direction. Measuring the mismatches and post-processing the acquired data usually correct this artifact. When using h-EPI techniques with multiple excitations per acquisition, then the phase discrepancy between odd and even lines may lead to multiple ghosts at smaller fractions of the phase-encode FOV.

1.5 T vs 3 T

Cardiac imaging at 3 T is becoming increasingly popular due to the potentially higher SNR and CNR (Contrast to Noise Ratio). At higher fields, some of the above mentioned

artifacts become even more problematic such as those caused by B_0 and B_1 field inhomogeneities or chemical shift. The potential increase in SNR, however, can be traded for example for higher parallel imaging accelerations resulting in quicker imaging acquisitions, which can potentially reduce motion artifacts; or enable higher spatial-resolutions which can for example make Gibbs artifacts less prominent.

Together with an increase of approximately twofold in SNR, there is also a quadruple increase in RF power absorption. Some sequences, such as bSSFP, may have to be used with a reduced flip-angle and higher TR than at 1.5 T, which increases B_0 inhomogeneity sensitivity and reduces contrast. Although T_2 relaxation times of tissues remain approximately unchanged from those at 1.5 T, T_1 relaxation times are noticeably longer at 3 T. This requires many protocols to be adapted for use at 3 T. For example the optimal inversion times for black blood imaging and late-Gd-enhancement may need to be increased. The same changes in relaxation time can also be used to reduce the dose of Gd contrast agent in first-pass perfusion and LGE studies decreasing possible susceptibility problems.

Cardiac gating can also be more challenging at 3 T. The higher field strength creates more magnetohydrodynamic distortion of the ECG signal, which can prevent the scanner from gating properly leading to additional artifacts.

Summary

Cardiovascular imaging is complicated primarily by the complex nature of the cardiac motion. Many of the cardiac imaging artifacts are directly related to motion or indirectly introduced by the requirement to shorten the acquisition time to remove motion. The complex cardiac structure with mixtures of fat and water based tissues containing complex and varying blood flows, and the large chest region with many organs and tissue-air interfaces also open the door to additional artifacts and measurement errors.

If we understand the physical principles behind the formation of artifacts, we should be in a position to identify and possibly avoid them, increasing image quality and reliability of interpretation.

References

- Al-Kwif O, Stainsby J, Foltz WD, Sussman MS, Huang Y, Wright G. Characterizing coronary motion and its effect on MR coronary angiography-initial experience. *J Magn Reson Imaging*. 2006;24(4):842–50.
- Storey P, Chen Q, Li W, Edelman RR, Prasad PV. Band artifacts due to bulk motion. *Magn Reson Med*. 2002;48(6):1028–36.
- Togawa T, Okai O, Oshima M. Observation of blood flow E.M.F. in externally applied strong magnetic field by surface electrodes. *Med Biol Eng*. 1967;5(2):169–70.
- Setser RM, Fischer SE, Lorenz CH. Quantification of left ventricular function with magnetic resonance images acquired in real time. *J Magn Reson Imaging*. 2000;12(3):430–8.
- Ferreira P, Gatehouse P, Kellman P, Bucciarelli-Ducci C, Firmin D. Variability of myocardial perfusion dark rim Gibbs artifacts due to sub-pixel shifts. *J Cardiovasc Magn Reson*. 2009;11:17.
- Di Bella EVR, Parker DL, Sinusas AJ. On the dark rim artifact in dynamic contrast-enhanced MRI myocardial perfusion studies. *Magn Reson Med*. 2005;54(5):1295–9.
- Tsao J, Boesiger P, Pruessmann KP. k-t BLAST and k-t SENSE: dynamic MRI with high frame rate exploiting spatiotemporal correlations. *Magn Reson Med*. 2003;50(5):1031–42.
- Plein S, Ryf S, Schwitter J, Radjenovic A, Boesiger P, Kozerke S. Dynamic contrast-enhanced myocardial perfusion MRI accelerated with k-t sense. *Magn Reson Med*. 2007;58(4):777–85.
- Otazo R, Kim D, Axel L, Sodickson DK. Combination of compressed sensing and parallel imaging for highly accelerated first-pass cardiac perfusion MRI. *Magn Reson Med*. 2010;64(3):767–76.
- Scheffler K, Lehnhardt S. Principles and applications of balanced SSFP techniques. *Eur Radiol*. 2003;13(11):2409–18.
- Reeder SB, Faranesh AZ, Boxerman JL, McVeigh ER. In vivo measurement of T_2^* and field inhomogeneity maps in the human heart at 1.5 T. *Magn Reson Med*. 1998;39(6):988–98.
- Atalay MK, Poncelet BP, Kantor HL, Brady TJ, Weisskoff RM. Cardiac susceptibility artifacts arising from the heart-lung interface. *Magn Reson Med*. 2001;45(2):341–5.
- Sorrell VL, Anderson JL, Gatehouse PD, Mohiaddin RH. Off-frequency tuning error artifact in steady-state free precession cine imaging due to adjacent air-filled bowel. *J Cardiovasc Magn Reson*. 2004;6(3):709–16.
- Markl M, Alley MT, Elkins CJ, Pelc NJ. Flow effects in balanced steady state free precession imaging. *Magn Reson Med*. 2003;50(5):892–903.
- Storey P, Li W, Chen Q, Edelman RR. Flow artifacts in steady-state free precession cine imaging. *Magn Reson Med*. 2004;51(1):115–22.
- Ferreira P, Gatehouse P, Bucciarelli-Ducci C, Wage R, Firmin D. Measurement of myocardial frequency offsets during first pass of a gadolinium-based contrast agent in perfusion studies. *Magn Reson Med*. 2008;60(4):860–70.
- Ferreira PF, Gatehouse PD, Firmin DN. Myocardial first-pass perfusion imaging with hybrid-EPI: frequency-offsets and potential artefacts. *J Cardiovasc Magn Reson*. 2012;14:44.
- Liao JR, Pauly JM, Brosnan TJ, Pelc NJ. Reduction of motion artifacts in cine MRI using variable-density spiral trajectories. *Magn Reson Med*. 1997;37(4):569–75.
- Gatehouse PD, Firmin DN, Collins S, Longmore DB. Real time blood flow imaging by spiral scan phase velocity mapping. *Magn Reson Med*. 1994;31(5):504–12.
- Rasche V, Holz D, Schepper W. Radial turbo spin echo imaging. *Magn Reson Med*. 1994;32(5):629–38.
- Glover GH, Pauly JM. Projection reconstruction techniques for reduction of motion effects in MRI. *Magn Reson Med*. 1992;28(2):275–89.

Anja C.S. Brau, Christopher J. Hardy, and John F. Schenck

Abstract

MRI has been in widespread clinical use since the mid-1980s and its use continues to grow due in large part to the excellent soft-tissue image contrast MRI generates from its unique manipulation of atomic nuclei. MRI exposes the subject under study to a very strong static magnetic field, as well as radiofrequency (RF) fields and magnetic field gradients, to generate and detect the weak electromagnetic signals that can be sampled and processed to generate an image. This chapter presents the general patient safety considerations posed by MRI equipment and the MR image formation process. Particular emphasis is placed on those safety considerations specific to cardiac MRI exams, including imaging of patients with implanted cardiovascular devices. While a high record of MR patient safety has been achieved to date, continual vigilance is required to assure patient safety, especially with the introduction of newer MR hardware capabilities and increased prevalence of implantable devices.

Keywords

MRI safety • Cardiac MRI safety • RF heating • PNS • Acoustics • Cardiovascular devices • Implants

Introduction to MRI Safety

Magnetic resonance imaging (MRI) is a medical imaging technology capable of producing noninvasive images of the internal human anatomy. It is based on the phenomenon of nuclear magnetic resonance (NMR), which was demonstrated in bulk materials for the first time in 1946 by applying technologies developed during World War II. NMR exposes a sample under study to a very strong static magnetic field and also to a strong radiofrequency (RF) field. NMR can be

used to generate and detect weak electromagnetic fields produced by the precessional motion of the magnetic dipole moments possessed by many atomic nuclei. In addition to the static and RF magnetic fields, MRI utilizes strong gradient magnetic fields. These gradient fields produce a position-dependent aspect of the NMR signal that can be used to create an image based on the variation of the signal properties from one body region to another. MRI as well as NMR can be used to study the nuclei of many different chemical elements; however, in most clinical studies MRI is used to derive medically useful information that originates from the protons (nuclei of the element hydrogen) that are present for the most part in water molecules located in the tissues of the patient being imaged.

During the 1950s and 1960s NMR came into widespread use as a basic technology for chemical analysis. The concept of extending NMR to study human subjects was introduced in the early 1970s. The challenge to the engineers and scientists

A.C.S. Brau, PhD (✉)
GE Healthcare, Cardiac Center of Excellence, GE Global Research
Center, Freisinger Landstrasse 50, Munich 85748, Germany
e-mail: Anja.Brau@ge.com

C.J. Hardy, PhD • J.F. Schenck, MD, PhD
GE Global Research,
One Research Circle, Niskayuna, NY 12309, USA
e-mail: hardycj@ge.com; John.Schenck@ge.com

working on the transition from NMR to MRI involved the design and incorporation of gradient coils as well as the process of scaling from instruments designed to study test-tube-sized chemical samples to scanners capable of studying an entire human body. Successful imaging of humans was achieved in the late 1970s but the resistive whole-body magnets available at that time could not produce magnetic fields much stronger than 0.3 tesla (T) and such low fields were severely limited in the signal-to-noise ratio and image resolution that they could achieve. In 1982 MRI was demonstrated in a whole-body superconducting magnet operating at 1.5 T. The era of widespread clinical use of MRI began in the mid-1980s. Since that time the majority of clinical MRI studies have been conducted using superconducting whole-body magnets operating at field strengths of 1.5 T or higher.

From this standing start MRI was rapidly adopted into clinical practice and the total number of patient studies/year increased rapidly. There is no formal repository for such information, however, an informed estimate in 2015 would be that there are now approximately 80,000,000 MRI studies performed worldwide per year and, since the mid-1980s, there have been more than 700,000,000 clinical studies performed. During most of that time, 1.5 T scanners served as the standard platform for high-performance MRI. Since approximately the year 2000, whole-body scanners operating at 3 T have provided certain performance advantages and have become more prevalent in clinical practice.

It is also estimated that, as of 2012, there were approximately 24,000 whole-body superconducting scanners in clinical service worldwide and of these approximately 22,000 operated at 1.5 T and 2,000 at 3 T. There were also approximately 50 whole-body superconducting research scanners operating at field strengths of 7 T or higher. At this time 1.5 T scanners still represent approximately three out of four new installations. It should be kept in mind that, although the cylindrical whole-body magnets operating at 1.5 and 3 T dominate the field of clinical MRI, a wide variety of alternative designs based on permanent magnets, electromagnets and hybrid structures, mainly operating at substantially lower field strengths, are also in clinical use.

As implied by the large number of scans being performed, the impact of MRI on medical practice has been dramatic. An impressive measure of this impact was reported in 2001 [24]. A group of 225 general internists was asked to rank the importance of 30 medical innovations of the previous 25 years. Despite the fact that these 25 years had seen the introduction of many revolutionary medical technologies – coronary artery bypass grafts, medical therapies for depression, diabetes, joint diseases, etc. – these clinicians selected MRI, along with computed tomography, as the most important medical innovation in terms of advancing patient care during this period.

In the following sections, we present the general patient safety considerations posed by the use of MRI, with particular

emphasis placed on those considerations specific to cardiac MRI, such as imaging of patients with implanted cardiovascular devices. The topic of pharmacological MR contrast agent safety is addressed in a separate chapter.

Safety Issues and Regulations

From the beginning of MRI it was realized that this new imaging modality required the exposure of human patients to magnetic field strengths for which there was little or no prior experience, and given this lack of experience the issue of patient safety was a major concern [11]. As discussed below, the high record of patient safety that has been achieved for the hundreds of millions of patients who have been placed in these initially unfamiliar circumstances is a testament to the care and vigilance of the device manufacturers and of the clinicians and technologists involved in the patient studies. However, as also discussed below, the potential for the rapid development of life-threatening circumstances during scanning requires continual vigilance to assure patient safety.

In the United States (US), the federal regulation of drugs used in treating human diseases was instituted by passage of the Food, Drug and Cosmetic Act of 1938. Subsequently, the US Congress amended this Act to produce the Medical Devices Amendments of 1977 [49]. The goal of these amendments was to protect human subjects during the development and use of medical devices. In response to these congressional acts, the US Food and Drug Administration (FDA) issued regulations in 1980 that applied to manufacturers of new medical devices and to researchers studying these devices. These regulations were patterned on those already governing the introduction of new drugs. They required the submission of data regarding the safety and efficacy of new devices prior to obtaining permission to market them. Computed x-ray tomography (CT scanning) was introduced prior to 1980. Thus MRI was the first imaging modality in the US subjected to the device regulations. The FDA published initial guidelines governing MRI in 1982 [56]. Because of the limited experience with human exposure to strong magnetic fields, the original guidelines were rather conservative, and, if they had remained in effect indefinitely, they would have greatly hampered the capabilities of modern MRI. However, as experience accumulated, the FDA and other regulatory agencies have permitted the use of increasing magnetic field strengths and gradient field switching rates [6, 19, 85]. This has permitted significant advances in the clinical utility of MRI scanners.

In the United Kingdom (UK) the initial regulation of MRI was carried out by the National Radiological Protection Board (NRPB), which had been established by the Radiological Protection Act of 1970 [60]. In 2005 the NRPB became the Radiation Protection Division of the Health

Protection Agency (HPA). In Europe further MRI regulatory activity has been provided by the International Electrotechnical Commission (IEC) [37]; by the International Commission on Non-Ionizing Radiation Protection (ICNIRP) [33–36]; and by the World Health Organization (WHO) [82]. Guidelines for MRI safety have also been provided by the American College of Radiology (ACR) [38]. In the US, the FDA by its charter is concerned with regulating the safety and efficacy of a device in terms of its interaction with the patient only. The ICNIRP has a wider scope with regulations designed to protect staff members, cleaning personnel, magnet technicians and other workers as well as patients being imaged. The American Society for Testing Materials (ASTM) [3] has developed a number of FDA-sanctioned standards for demonstrating the MR safety and compatibility for various devices and implants [20]. These standard protocols can be found at the ASTM web site by searching the standards for “MRI Safety.” An extensive literature has developed describing these regulations and guidelines [25, 72, 73, 84, 85].

The regulations and guidelines put forward by various agencies differ in detail but efforts at coordination have been made, and the overall character of the regulations proposed by the different bodies is generally similar. In an attempt to protect non-imaging industrial workers and other personnel exposed to magnetic fields in their workplaces, the European Union has been considering stringent regulations – European Directive 2004/40/EC [16] – that would substantially limit any person’s daily exposure to these fields. This would greatly curtail the use of MRI for patient and research studies and the activities of MRI staff members. These limitations were viewed as unwarranted by most MR researchers and practitioners and were viewed as a threat to the future of clinical MRI and of MRI research in Europe. Consequently, these groups mounted a campaign to modify the Directive [31, 39, 50]. As an initial response to these efforts, the implementation of the Directive was postponed from April 2008 to April 2012. The efforts of the MRI community were eventually successful in modifying the impact of the proposed regulations on MRI [27] and, on June 29, 2013, the European Commission repealed Directive 2004/40/EC and published Directive 2013/35/EU [17]. The new Directive specifies that, if the magnetic field exposure is related to the installation, testing, use, development, maintenance of or research related to MRI, it may exceed the otherwise enforced exposure limits. Member states have until July 1, 2016, to transpose the Directive into national law.

Beginning in 1987, the FDA has issued guidelines for magnetic field strengths that can be considered as non-significant risk (NSR) and, as indicated in Table 8.1, this level has been increased over time as experience and confidence have accumulated. It is of interest to note that, while, in general, regulatory limits become tighter as time goes on,

Table 8.1 Evolution of FDA guidance for magnetic field strengths considered as nonsignificant risk (NSR) for whole body exposure to static magnetic fields

Year	1982	1987	1997	2003
NSR field strength	2 T	2 T	4 T	8 T ^a

^a4 T for infants less than 1 month of age

the limits on magnetic field strengths have increased substantially over time. Although magnetic fields above 8 T cannot be considered as NSR in the US at the present time, there are several whole body research scanners now operating or planned at still higher field strengths. Scanners operating above 8 T generally require additional levels of approval for human studies [7, 14, 67].

MR Injuries and Deaths

MRI is now a common procedure and is practiced on a worldwide basis. As a result there is no certain way to enumerate the number of deaths possibly related to MRI scanning. However, the known instances are extremely rare. As MRI is almost always performed in technically advanced locations with good access to communication networks it seems unlikely that there would be large numbers of unreported cases. A brief literature review in 1998 found reports of seven deaths attributed, at least in part, to MR scanning [62, 29], though in the absence of thorough clinical histories, autopsy results and details of scanning procedures in what were often gravely ill patients, it is uncertain whether MRI played a dominant role in any of these fatal outcomes.

However, two cases have been described in some detail and are worth careful study for the insight they provide regarding the type of circumstances that can rapidly lead to catastrophic outcomes. One is an example of magnetic foreign bodies and the other is an example of the missile effect.

In 1992 a 74-year old woman was referred to a major medical center in San Antonio, Texas for an MRI study [41]. The screening questionnaire disclosed that she had received an intracranial aneurysm clip at another institution in 1978. As a result the scan was not performed. However, the patient and her family returned in a few days and indicated they had contacted the operating neurosurgeon at the previous institution and had obtained the details of the implanted clip. This clip was identified as non-magnetic in published lists of medical devices and the MRI study was rescheduled. At the time of scanning, when approximately four feet from the 1.5 T magnet the patient complained of severe headache and her condition rapidly deteriorated. The patient was intubated and an emergency computed tomography study showed a large hematoma with subarachnoid hemorrhage. The patient died on the next day. Autopsy disclosed the clip and an

arterial tear at the site of the clip placement. Study of the clip showed that it was not of the type that had been indicated. Instead, the actual clip was listed as magnetic and this was verified by testing in the 1.5 T magnet.

In July 2001 a 6-year-old boy was operated on for a benign brain tumor at a large medical center near New York City. After the procedure he was taken to the MRI facility for post-operative imaging. He developed respiratory difficulty while in the scanner. The two technologists performing the scan were temporarily distracted because of difficulties with a built-in oxygen supply. As an emergency measure another hospital employee brought a ferromagnetic portable oxygen tank into the room. The tank was drawn rapidly into the magnet striking in boy in the head and fracturing his skull. The boy died 2 days later [2, 47]. This case provoked much discussion about how to further improve the safety of MR imaging with a focus on staff training, architectural design of imaging suites to give technologists better control over people and items entering the scan room, and the advantages and disadvantages of ferromagnetic detectors at scan room entrances.

As mentioned above, well over one-half billion MRI scans have been completed safely since the introduction of the technique. However, these two tragedies indicate the need for continual vigilance and improvements in operating procedures, training, and site design. They also emphasize how rapidly the interaction between powerful magnetic fields and ferromagnetic materials can produce a catastrophe.

Static Magnetic Fields

The essence of an MRI scanner is a large, powerful magnet used to partially align the magnetic moments of the protons within the patient's body against the forces of thermal randomization and to drive their precessional motion. These magnets can be constructed using various techniques, but the majority of clinical MRI scanners are built using a series of four to eight circular coils of wire on a common axis. This gives the scanner the form of an open circular cylinder that must be large enough to completely and comfortably surround the patient being imaged. These coils have a diameter of approximately 1.0 m. Depending on the desired field strength, a scanner may use a total of between 2 and 400 km of wire conductor. In addition to the requirement for an intense strength, it is necessary that the magnetic field be very uniform over the imaging volume – on the order of 1.0 part-per-million (ppm) – and very stable – on the order of 0.1 ppm/h – over the time of the imaging process. In order to achieve this high level of field homogeneity the coils must be wound and positioned to a very high level of accuracy. The main-field magnet constitutes most of the weight and cost of the scanner.

In the late 1970s the earliest whole-body MRI magnets used aluminum or copper wire as the conducting material. These resistive materials heat up substantially when carrying the large electric currents required to achieve strong magnetic fields. Consequently, these resistive magnets were limited to producing imaging fields on the order of 0.05–0.3 T. In the early 1980s the introduction of whole-body superconducting magnets using niobium-titanium alloy wire permitted much higher field strengths, most commonly 1.5 T, and consequently much improved imaging performance. In order to maintain the superconducting state it is necessary to maintain the coils at a temperature close to absolute zero, typically 4.2 K. This necessitates enclosing the coils in a vacuum-walled cryostat that contains a bath of liquid helium.

Gradient Fields

Specially designed coils are used to produce gradients in the magnetic field strength across the region of imaging. There are generally three separate coils – one for each of the Cartesian spatial coordinates, x , y and z . The strength of each of these gradient fields is switched between various levels during the imaging process. Each of these coils generally consists of a layer of a specific conductor pattern mounted on a cylindrical coil form. The completed cylindrical gradient package is located between the patient being imaged and coils of the main magnet. A shield gradient coil is usually placed between the primary gradient coils and the static-field magnet in order to minimize the interaction of this magnet with the gradient coils and to limit the spurious gradient fields produced by eddy currents induced in the electrically conducting components of the scanner.

The strength of the gradient fields determines the spatial resolving power of the scanner and its ability to measure diffusion of water molecules in the patient's tissues. Currently available MRI scanners generally are capable of producing gradient strengths on the order of 10–100 mT/m. An important capability of the gradient system is the slew rate (SR), which is a measure of the time required to switch the gradient strength from one level to another. The SR is determined both by the properties of the gradient coil and of the power supply used to drive it. The SR in clinical MRI scanners can range up to approximately 200 mT/m/ms in whole-body systems and can be several times higher than this in systems using small local gradient coils used to image a specific region of the body.

Peripheral Nerve Stimulation (PNS)

The magnetic fields produced by the gradient coils are much weaker than the main static field and create no additional safety issues. However, the electric fields produced when the

gradient currents are time-dependent can interact with the nervous system to produce sensations that may, in some cases, be unpleasant. These sensations are usually viewed as the result of a cascade of phenomena: the time-dependent coil currents produce electric fields which induce electric current densities in the tissues; if the amplitude is sufficient and the direction of the induced currents are parallel to relevant peripheral nerve cells they will depolarize the axons of those cells, leading to action potentials propagating into the central nervous system (CNS). Here they will be perceived as some form of sensation arising at the location of the depolarization [10]. Qualitatively, the production of sensations by coil current pulses is quite straightforward. However, attempts to treat the phenomenon quantitatively in a practical imaging situation require complex models involving the details of the coil geometry, the pulse sequences and switching parameters being used, the geometry and electrical properties of the involved body region and the nerve networks in this region. Several models based on the cable theory of nerve excitation have been developed for specific aspects of this process [13, 57, 86]. These models can provide qualitative guidelines for designing coils and pulse sequences to minimize the effects of PNS, but experimental investigation is necessary to achieve quantitative understanding.

It does not appear that a single depolarization pulse is ordinarily sufficient to create a perceived sensation in the CNS; instead, a sequence of several closely spaced pulses is usually required. For example, in one study, PNS thresholds were studied by use of a sequence consisting of 256 trapezoidal current pulses each approximately 1.3 ms long with the sequence repeated once every second [22]. Thresholds for excitation by a single pulse would be expected to be very much higher. Currents flowing parallel to nerve axons are much more effective in creating PNS than those flowing perpendicular to them.

The initial approach to regulation of gradient switching attempted to put a quantitative limit on the amplitude and duration of the magnetic fields produced by gradient coils. For example an early FDA regulation put an upper limit of 20 T/s for switching pulses lasting more than 0.12 ms [5]. This approach proved unwieldy and quite restrictive on scanner performance. Later it was recognized that nerve excitation per se is not harmful and it is only necessary to assure that PNS does not lead to painful sensations. For that reason the current FDA guidelines use a pragmatic criterion, requiring that the threshold for significant risk is “any time rate of change of gradient fields (dB/dt) sufficient to produce severe discomfort or painful nerve stimulation”.

It is important to note that although PNS is often cited as a serious hazard of MRI, the same process of using coils carrying time-dependent currents to depolarize cells in the nervous system is used in procedures such as transcranial magnetic stimulation (TMS) [8], which are generally not considered hazardous and potentially therapeutic. In TMS

the induced electric currents in the body are orders of magnitude larger than those produced in any MRI situation. TMS is being explored as a treatment for depression and motor disorders of the CNS [1, 15]. Thus, it appears that PNS is unlikely to produce serious injury in MRI. It can be ameliorated when necessary by reducing the number and amplitude of the gradient switching events in the pulse sequence.

Acoustics

Because the gradient coils are located within the strong static magnetic field of the main magnet, the pulsing of current through these coils during the MRI exam causes time-dependent Lorentz forces, resulting in sometimes-high acoustic noise levels. Indeed, the magnet/gradient system is in many respects similar to a dynamic loudspeaker system, which uses much smaller magnets and coils to convert electrical signals into sound. Sound pressure levels can reach 118 dBA or higher during an MRI exam [55], depending on the main magnetic field strength and the specific imaging pulse sequence.

The acoustic noise generated during the MRI exam can cause a variety of problems for patients and healthcare workers, ranging from increased anxiety and difficulties in communication to temporary or even permanent hearing loss. For this reason, hearing protection in the form of headphones or disposable earplugs is required. These measures can reduce the sound pressure levels experienced by the patient by up to roughly 30 dB [70]. Various government agencies have developed limits for sound level exposure for patients and workers, above which hearing protection should be worn. In the UK, the Medical Device Agency (MDA) recommends limits of 85 dBA averaged over 8 h for patients, or 100 dBA averaged over 15 min [55]. In the US, the FDA considers MRI studies to have significant risk if peak unweighted sound pressure levels reach 140 dB or A-weighted levels exceed 99 dBA with hearing protection in place [19]. The Occupational Safety and Health Administration (OSHA) workplace noise regulations limit noise exposures to 90 dBA averaged over an 8-h day, or 110 dBA over 30 min [52].

Radiofrequency Heating

The radiofrequency (RF) B_1 field used to manipulate the axis of spin rotation is inevitably accompanied by an electric field E , and this field, in turn, produces a current density J , within the patient's tissues. Using complex number notation, J can be written as the sum of a real component, $J_r = \sigma E$, in phase with E and an imaginary component, J_i , 90° out-of-phase with E . Here σ is the conductivity of the patient's tissues at the Larmor frequency.

The induced current density in the patient increases strongly with field strength and frequency and has profound implications for high-field MRI. In particular, the in-phase component of J , acting through the Joule heating effect, produces an energy deposition in the tissues given by $\frac{1}{2}\sigma E_r^2$. This energy deposition tends to heat the tissues and is measured by the specific absorption rate (SAR). During most pulse sequences, the RF energy is supplied in a series of short bursts and therefore the RF energy is not deposited continually during imaging but as a series of short pulses. The total heating effect of an imaging sequence depends on the strength, E , and frequency of the applied electric field and the duty cycle (fraction of the time the transmitter field is on). The FDA provides guidance [19] as to whether patient heating from a given sequence should be considered as a significant risk when the whole-body SAR averaged over a 15-min examination is greater than 4 W/kg. Similarly, the local SAR in the head is considered as significant risk if it larger than 8 W/kg when averaged over an 8 min examination.

In addition to the above global heating effects associated with the B_1 field, a number of other potential safety issues are associated with the RF transmitter fields. For example, the transmitter and receiver coils used in MRI contain tuning capacitors in series with the conducting loops of the coils. During RF transmission these capacitors may develop a large RF voltage in their immediate vicinity. These local voltages have the potential to produce local RF burns if the patient's skin is too close to them. For this reason, RF coils, particularly surface RF coils, are constructed with insulating coverings to prevent close contact of these capacitors with the patient's skin. Care should be taken to prevent accidental contact during the scanning procedure.

There may be a risk of RF heating from any external conducting devices that are in proximity to the patient [72]. All non-essential electrically conductive materials should be removed from the MR system before scanning. Care must be taken with the use of any ECG gating systems. Conventional ECG electrodes and leads are not classified as MR safe because of their incorporation of low-impedance conductors and/or ferromagnetic components, which can cause skin heating or burns. Only MR-safe electrodes and leads should be used; these can be found in the MR vendors' accessories catalogues. Care should also be taken with placement of ECG electrodes and leads. Leads should not be allowed to form loops, and should not be positioned along the sides of the scanner bore or close to the body RF coil or any other RF transmit coil [72].

Local edema and tissue swelling as well as localized image artifacts have been noted during MRI of patients with tattooing or permanently implanted eye shadow. This effect has been attributed to an interaction of the radiofrequency

field with electrically conducting components of the implanted pigments [46, 64, 81]. Also, medication patches containing metallic fibers or backing [21] are potential sources of RF-induced patient injury.

Patient Monitoring

While ECGs are used routinely for pulse sequence gating or triggering in cardiovascular MRI exams, their use for patient monitoring in this setting is problematic, in part because of the magneto-hydrodynamic (MHD) effect. This effect occurs when charged ions in flowing blood move through the magnetic field, inducing a voltage that can distort the ECG trace, especially in scanners with higher magnetic field strengths. This effect is especially prominent during the ST segment of the ECG during systolic ejection of blood, and thus can mask ST depression or elevation related to myocardial ischemia. In fact, the T wave can be elevated to a higher level than the R wave, possibly interfering with MRI gating. Figure 8.1 compares the ECG waveform recorded from a subject outside vs. inside the bore at 3.0 T, with elevated T-wave inside the bore due to the MHD effect. Fortunately, modern scanners equipped with vectorcardiogram (VCG) gating can offer more reliable detection of the R wave compared to conventional ECG gating by exploiting spatial information in the VCG. Additional distortion of the ECG waveform can be induced by radiofrequency pulses and gradient switching during MRI. Therefore, the ECG waveform acquired during MRI should only be regarded as a general representation rather than an exact depiction of the patient's cardiac electrical activity and should not be used for diagnostic purposes.

Physiological and Sensory Effects

Since high-field MRI magnets first became available, some patients undergoing MRI have reported a low level of specific physiological and sensory effects. These effects ordinarily do not represent true safety hazards but in some cases may be somewhat uncomfortable. They are generally associated with motion in the magnetic field or exposure to time-dependent magnetic fields – processes that are associated with low level induced electric fields within the tissues. These effects include metallic tastes, magnetophosphenes, balance disturbance, dizziness, vertigo and nausea [61, 63]. Importantly, these symptoms generally cease immediately or shortly after the subjects leave the vicinity of the magnet and are reported only by a minority of the subjects studied. Frank vomiting and incapacitating disturbances of gait or balance disturbances are rarely, if ever, reported. There is

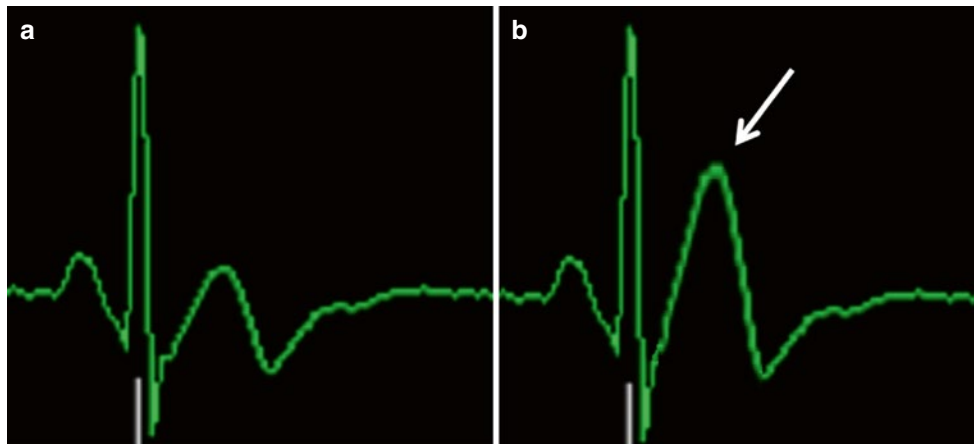


Fig. 8.1 ECG waveforms recorded from the same subject lying outside (a) vs. inside (b) a 3.0 T scanner bore. Note the T wave elevation in (b) (arrow) caused by the magneto-hydrodynamic effect

an impression that there are some individuals who are much more sensitive to these effects than is the norm, although this possibility has apparently not been studied quantitatively.

As one example, sensations of metallic taste have been reported with head motions in high field scanners [61]. One study [12] has measured the thresholds for the necessary rate of head motion and has found that the effect does not require the presence of dental fillings. It is likely that these metallic tastes result from motion-induced electric currents acting to depolarize sensory cells or their associated nerve cells.

Phosphenes are defined as visual sensations that occur even with no light entering the eye. When produced by an electric circuit with leads attached to the head in the vicinity of the eye they are called electrophosphenes; when produced by oscillating currents in a non-contacting electric coil they are called magnetophosphenes [26, 44, 45]. In high field MRI scanners in darkened rooms, brief sensations of faint light flashes are often reported when the direction of gaze is rapidly changed [61] and it has also recently been reported when subjects are exposed to very strong, rapidly switched gradient fields [68]. Magnetophosphenes are attributed to nerve or sensory cell depolarization in the optic nerve or retina or caused by electric currents induced by head or eye motion of in the applied magnetic field. Magnetophosphenes thus appear to be analogous to the sensations associated with PNS but the depolarized electrically excitable tissue here is in the visual apparatus rather than the peripheral nervous system.

Low grade and transient balance disturbances, dizziness, vertigo and nausea sometimes reported during and immediately following exposure to high field magnets has generally been attributed to magnetic field interactions with the

vestibular system and semicircular canals of the inner ear [61, 66]. A significant advance in the understanding of this effect resulted from a report that in high-field systems (3 and 7 T) in darkened rooms, a robust, spontaneous nystagmus develops in patients when lying still within the magnet [58, 77]. Infrared video cameras were used to observe this effect and demonstrated that it persists throughout the field exposure and does not require head or other motion. This nystagmus is attributed to a steady excitation of the vestibular portion of the eighth cranial nerve produced by a Lorentz force between the applied magnetic field and a constant electric current in the endolymphatic fluid within the inner ear. The reported vertigo, nausea and balance disturbances are all low level effects and do not represent a patient safety issue. They are most likely explained by the conflict hypothesis, wherein the brain is presented with incompatible positional information from the visual and vestibular systems resulting in the symptoms of motion sickness [51, 79].

As imaging systems operating at 7 T or higher (research only) have become more common over the last decade, reports both anecdotal and in the literature have indicated that a fraction of subjects and system operators exposed to them have reported a significant level of discomfort [30, 80]. The symptoms are similar, but generally milder, than those of car sickness, sea sickness, air sickness and space sickness, i.e., the symptoms of motion sickness, which are also explained by the conflict hypothesis. It has been suggested that the term ‘magnet sickness’ be used for the magnetic field-induced symptoms [65]. It is important to emphasize that, at present-day MRI field strengths, these symptoms are quite mild, are experienced by only a minority of subjects, and do not significantly limit the utility of these scanners. However, at still higher field strengths the symptoms may

become stronger and affect a larger fraction of the population. This explains the widespread practice of moving subjects slowly in high field magnets and it also raises the possibility that subjects prone to this discomfort might benefit from the use of medications used in the treatment of motion sickness including dimenhydrinate (Dramamine), meclizine (Antivert) and ginger root.

Lymphocyte Studies

It has recently been reported that blood lymphocytes from human venous samples taken before and after 1.5 T cardiac MRI demonstrated significant but transient increases of micronuclei [75] and increases in double-strand DNA breaks after MRI [23]. However, the significance of these studies for human exposure to cardiac MRI is uncertain and it has been noted that the lymphocyte DNA studies are subject to a variety of confounding factors [54].

Cardiac MR in Patients with Cardiovascular Devices

Patient Screening



In patients being referred for cardiac MR (CMR) examination, there is increasing prevalence of implants of various kinds, including passive and active cardiovascular devices [42]. Therefore it is especially important that every patient receive thorough screening before undergoing MR

examination. This should include an interview with a licensed technologist trained in MR safety, supervised by a physician knowledgeable in CMR, and completion of a standardized MR screening form. Examples of these forms can be downloaded from a number of websites (MRI Safety Web Site, Expert Panel on MR Safety 2013 – Appendix 2). Whenever possible, the specific type of any implanted device should be confirmed by use of wallet cards that may have been issued to the patient, or by procedure notes in the patient’s records. If an unfamiliar device is identified, experts in CMR safety should be consulted prior to scanning. If the type of device cannot be determined, alternatives to CMR should be considered, and the potential risks of patient injury weighed against benefits before proceeding. In addition, inpatients should be examined prior to scanning for the presence of temporary devices such as catheters or temporary pacing leads. If an unreported metallic object is discovered during scanning, the scan should be stopped and the patient questioned further until the object is identified.

Safety Terminology and Labeling

Terminology regarding implants and devices in the MR environment [73] has evolved over time, as outlined in Table 8.2. In 1997, the FDA Center for Devices and Radiological Health (CDRH) proposed the terms “MR safe” and “MR compatible” (Table 8.2, Older terminology) for labeling MR information relating to medical devices [18]. Testing for MR safety involved assessing the effects on the device of the “MR environment”, including the static, time-varying

Table 8.2 Terminology used for labeling implanted devices

<i>Older terminology</i>	
MR safe ^a :	The device, when used in the MR environment, has been demonstrated to present no additional risk to the patient, but may affect the quality of the diagnostic information
MR compatible ^a :	The device, when used in the MR environment, is MR safe and has been demonstrated to neither significantly affect the quality of the diagnostic information nor have its operations affected by the MR device
<i>Newer terminology</i>	
MR conditional 	An item with demonstrated safety in the MR environment within defined conditions. At a minimum, address the conditions of the static magnetic field, the switched gradient magnetic field and the RF fields. Additional conditions, including specific configurations of the item, may be required
MR safe	An item that poses no known hazards resulting from exposure to any MR environment. MR Safe items are composed of materials that are electrically nonconductive, nonmetallic, and nonmagnetic
MR unsafe 	An item that poses unacceptable risks to the patient, medical staff or other persons within the MR environment

^aThe use of the terms, “MR safe” or “MR compatible” without specification of the MR environment to which the device was tested should be avoided since interpretation of these claims may vary and are difficult to substantiate rigorously

gradient and RF electromagnetic fields produced by the MR system. Testing for MR compatibility involved safety testing plus characterization of any image artifacts produced by the device.

It became evident over time that this older terminology was confusing, with terms often used interchangeably or incorrectly [20, 71]. Sometimes, for example, the terms were used without specifying the conditions under which the device was demonstrated to be safe. Therefore, in 2005 (latest update 2013) the American Society for Testing and Materials International developed standard ASTM F2503 [4], which includes new MR labeling terms and icons (Table 8.2, Newer terminology). In particular, a label of “MR conditional” comprises a list of those conditions under which safety has been demonstrated, including static magnetic field strength, maximum spatial gradient field (a term relating to the static magnetic field, not the time varying gradients), time rate of change of the magnetic field, and RF specific absorption rate. Additional requirements may include specifying the approved position of the device or routing of leads. It is important to note that this new terminology has not been applied retrospectively to implants and devices that had previously received FDA approved labeling using the older terminology, so older devices may be encountered which are still labeled with the old definitions of MR compatible or MR safe. Labeling information for many devices and implants is available online [69].

CMR After Device Implantation

There are a variety of reasons why implanted devices may sometimes pose safety concerns for patients undergoing CMR. The static magnetic field of the MR scanner can potentially cause any implanted ferromagnetic objects to rotate and/or translate within the patient, an especially acute problem near regions of high spatial gradient in the static field. In addition to the static field, time-varying gradients generated during scanning can produce electric currents in leads, possibly interfering with proper functioning of active devices. RF electromagnetic fields generated during scanning can cause heating at the tips of implanted wires and electrodes, and can also potentially interfere with active devices, e.g. by activating or inhibiting pacing. Aside from safety concerns, implanted cardiac devices can also lead to MR image artifacts, including local signal loss and distortion due to susceptibility variations, which could impair visualization of surrounding tissues. In some cases, it may be necessary to modify pulse sequence selection or parameters to minimize artifacts induced by implants.

The presence of strongly ferromagnetic implants is a contraindication for MRI. However, most implanted devices are either nonferromagnetic or only weakly ferromagnetic [42].

Devices manufactured from nonferromagnetic materials (such as titanium, titanium alloy, or nitinol) that have no electrical components and that do not exhibit heating during CMR may undergo scanning even immediately after implantation [42]. Weakly ferromagnetic implants present a more complex problem. In theory such devices, if recently implanted, could be dislodged by the CMR scanner. But many of these implants, such as stents or artificial heart valves, are anchored to a vessel wall or adjacent tissues, and already undergo forces from the beating heart and blood flow that are stronger than those arising from any magnetic interactions. It is generally believed that tissue healing post implantation may provide additional anchoring, and therefore a wait of ~6 weeks after implantation before CMR has been recommended for some devices [32, 42]. Some weakly ferromagnetic implants have been more extensively studied than others, and have sufficient data to support scanning any time after implantation. For other less well-studied devices, the AHA Committee on Diagnostic and Interventional Cardiac Catheterization has recommended a case-by-case risk-benefit analysis, where patients with a clear potential benefit to immediate scanning should generally undergo MR examination, and those with less urgent need for scanning (e.g. those with chronic back pain), should defer scanning until 6 weeks post implantation [42].

Passive Implants

Most coronary artery or peripheral vascular stents that have been tested (including drug-eluting stents) are either nonferromagnetic or weakly ferromagnetic, with the majority composed of 316 L stainless steel or nitinol. Most of these have been labeled as MR safe, with the remainder labeled MR conditional [69]. For example, a recent study [78] showed that CMR at 1.5 T could be safely performed in stable patients within 1–7 days of bare-metal coronary stent implantation. Other ex vivo studies of coronary artery and peripheral vascular stents have concluded that MR imaging of patients at 3 T with these stents should be safe, with the exception of a stainless steel Zenith-Cook iliac stent, which was ferromagnetic [76]. And a retrospective review of patients with myocardial infarction who had undergone CMR at 1.5 T within 2 weeks of coronary stent implantation found no increase in adverse events relative to those who did not undergo MR imaging [53]. Most aortic stent grafts that have been tested have been labeled MR safe, with the exception of the Zenith AAA endovascular graft, labeled MR unsafe [69] because of significant deflection and torque even at fields below 3 T. Three aortic stents, including the Zenith AAA, were also found to create significant susceptibility artifacts in the MR images, making visualization of the endostent lumen and surrounding tissues difficult [42].

Most prosthetic heart valves and annuloplasty rings have been labeled as MR safe, with the remainder labeled as MR conditional [69]. Generally the magnetic forces acting on heart valves and annuloplasty rings are significantly less than those exerted by the beating heart and blood flow, and heating of such devices from MR imaging has been found to be less than 1 °C in ex vivo studies [32]. Most cardiac closure (e.g. Fig. 8.2) and left atrial appendage occluder devices that have been tested have been labeled as MR safe, with some others labeled as MR conditional [69]. CMR may be performed at any time after implantation if the devices are non-ferromagnetic. For weakly ferromagnetic devices, decisions about timing of CMR should be weighed on a case-by-case basis [42]. CMR is generally considered to be safe at fields of 3 T and lower in patients with sternal suture wires from cardiac surgery [28, 42], as seen in Fig. 8.3.

Most inferior vena cava filters that have been tested have been labeled as MR safe, with the remainder labeled as MR conditional [69]. Patients implanted with nonferromagnetic IVC filters may undergo CMR at any time after implantation. IVC filters are attached to the vessel wall with hooks, and it is generally believed that they become securely incorporated into the wall after ~6 weeks of healing. Therefore it is recommended that patients treated with weakly ferromagnetic IVC filters in most cases wait at least this period of time after implantation before undergoing CMR [42]. Most embolization coils that have been tested have been labeled as MR safe, with the remainder labeled as MR conditional [69]. For weakly ferromagnetic embolization coils, risks of performing CMR prior to 6 weeks after coil placement should be evaluated on a case-by-case basis. In addition, some stainless steel embolization coils can create severe artifacts in the MR images, making large zones of anatomy uninterpretable [40].

Active Implants

Because of the prevalence of cardiovascular diseases, a significant proportion of patients referred for MRI will have permanent cardiac pacemakers or implantable cardioverter defibrillators (ICDs). These contain metal with various ferromagnetic properties, include complex electrical circuits, and utilize one or more leads implanted into the myocardium. There is potential during the MR exam for movement or damage of the device, inhibition of pacing output, activation of tachyarrhythmia therapy, or heating of the electrodes. These effects can potentially lead to clinical sequelae such as changes in pacing or defibrillation thresholds, cardiac arrhythmia, or death [42]. For this reason, most pacemakers and ICDs have been labeled MR unsafe and presence of such a device was considered a contra-indication to MRI. However, there is evidence that pacemakers developed after 2000 have better performance in the MRI

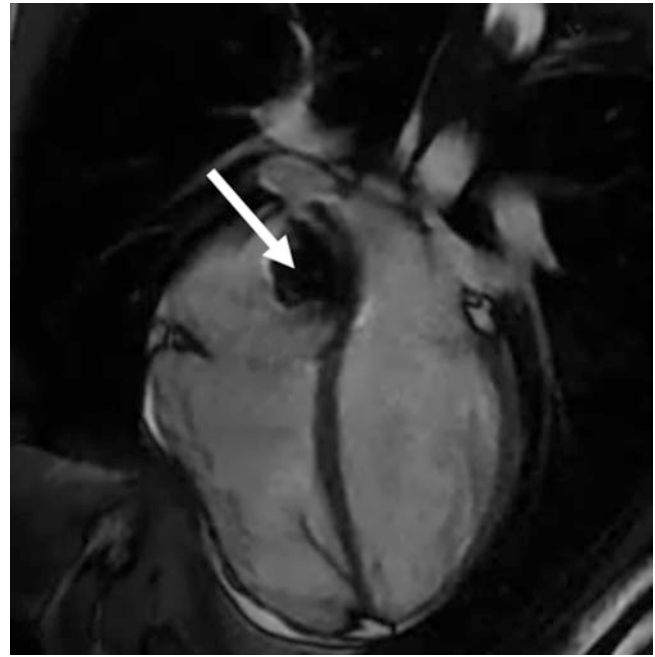


Fig. 8.2 4-chamber cardiac MR image from a patient with an atrial septal repair implant (*arrow*) imaged at 1.5 T (Courtesy of Dr. Gianluca Pontone, Centro Cardiologico Monzino)

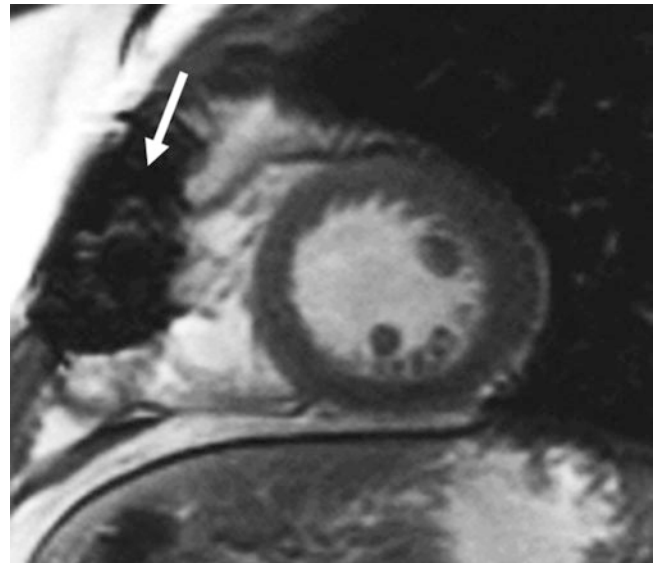


Fig. 8.3 Typical sternal wire image artifact (*arrow*) seen in a short-axis cardiac MR scan performed at 1.5 T appears as local signal loss near the sternal closure site and extending into the right ventricle (Courtesy of Dr. Christopher Francois, University of Wisconsin Madison)

environment [59]. The US FDA and the European EMA have recently approved the first MR conditional pacemakers and ICDs designed for use under very specific conditions, including device programming, monitoring, imaging protocols and MRI field strength [43, 74, 83]. These conditions also included patient positioning constraints that have

precluded CMR, but a recent study has demonstrated successful off-isocenter CMR in a patient with an MR conditional pacemaker [9], and more recently, the restrictions on patient positioning have been lifted for some pacemaker types. At the time of writing, regulatory approvals for MR-conditional pacemakers and ICDs varied by device manufacturer and by region. The landscape of MR conditional devices is anticipated to continue to change as several large ongoing patient studies reach their conclusion and device manufacturers apply for additional regulatory approvals. It is strongly recommended to follow vigilant patient screening procedures and consult the device manufacturer's imaging guidelines for a particular device.

Active devices incorporating cardiovascular catheters, such as pulmonary artery hemodynamic monitoring/thermodilution catheters, and temporary transvenous cardiac pacing devices, as a rule contain nonferromagnetic components but may include electrically conductive leads. There have been few studies of MR compatibility of these devices, but there have been reports of heating, and those devices that have been tested have generally been labeled as "MR unsafe" [42]. Retained temporary epicardial leads, on the other hand, tend to be short in length, and so pose relatively little risk, and there have been no reports of complications relating to MR scanning of patients with such leads [32]. CMR of patients with temporary pacemaker external pulse generators is not recommended because this can change the pulse generator's operation or damage it, or make pacing unreliable.

The 9526 Reveal Plus (Medtronic) [48] insertable loop recorder is a single-use implanted device with surface electrodes used to continuously record the patient's ECG. This device contains no lead wires and has been labeled "MR conditional." ECG data acquired during MR scanning, however, should be considered unreliable, and any stored ECG data should be downloaded before the MR exam [42]. An example cardiac MR image of a patient with a loop recorder is shown in Fig. 8.4.

Hemodynamic support devices such as ventricular assist devices and intra-aortic balloon pumps are complex electromagnetic devices containing ferromagnetic materials, which have not been CMR tested. It is believed that these devices are contraindicated for CMR.

Summary

Work to date has established cardiovascular MRI as a very safe imaging modality. However, because of increased magnetic field and gradient strengths, increased prevalence of implants of various kinds, and further technical advances, there is a need for continued vigilance in the important area of cardiac MR safety.

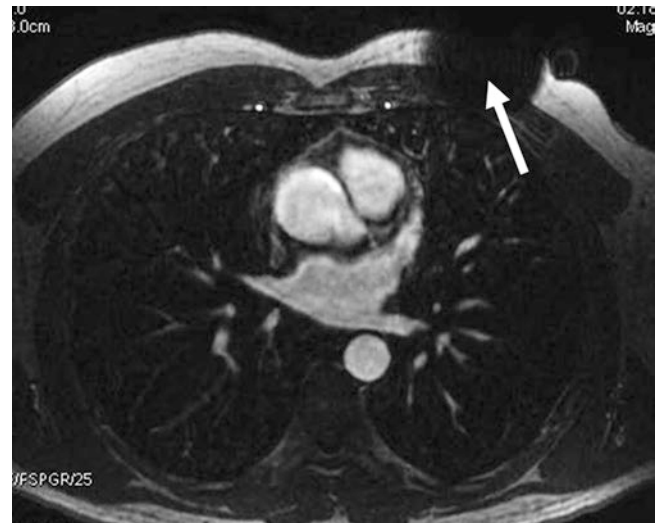


Fig. 8.4 Axial MR image of a patient with a loop recorder imaged at 1.5 T. A local area of signal loss is visible near the area of subcutaneous implantation (*arrow*) (Courtesy of Dr. Gianluca Pontone, Centro Cardiologico Monzino)

Acknowledgement The authors would like to thank Dr. Massimo Lombardi for carefully reading the manuscript and providing useful suggestions.

This chapter is reprinted in part from Schenck [65] (with modifications and permission).

References

- Allan CL, Herrmann LL, Ebmeier KP. Transcranial magnetic stimulation in the management of mood disorders. *Neuropsychobiology*. 2011;64:163–9.
- Archibold RC. Hospital details failures leading to M.R.I. fatality. 2001. *New York Times*, 22 August 2001.
- ASTM. ASTM standards worldwide. 1996. www.astm.org. Accessed 18 May 2014.
- ASTM. Designation: F2503-13, standard practice for marking medical devices and other items for safety in the magnetic resonance environment. West Conshohocken: American Society for Testing and Materials International; 2013.
- Athey TW. Current FDA guidance for MR patient exposure and considerations for the future. *Ann N Y Acad Sci*. 1992;649:242–57.
- Athey TW. FDA regulation of the safety of MR devices: past, present and future. *Magn Reson Imaging Clin N Am*. 1998;6:791–800.
- Atkinson IC, Renteria L, Burd H, et al. Safety of human MRI at static fields above the FDA 8 T guideline: sodium imaging at 9.4 T does not affect vital signs or cognitive ability. *J Magn Reson Imaging*. 2007;26:1222–7.
- Barker AT, Jalinous R, Freeston IL. Non-invasive magnetic stimulation of human motor cortex. *Lancet*. 1985;1(8437):1106–7.
- Bhandiwad AR, Cummings KW, Crowley M, et al. Cardiovascular magnetic resonance with an MR compatible pacemaker. *J Cardiovasc Magn Reson*. 2013;15:18–21.
- Brinley Jr FJ. Excitation and conduction in nerve fibers. In: Mountcastle VB, editor. *Medical physiology*. 13th ed. Saint Louis: Mosby; 1974. p. 34–76.
- Budinger TF. Nuclear magnetic resonance (NMR) in vivo studies: known thresholds for health effects. *J Comput Assist Tomogr*. 1981;5:800–11.

12. Cavin ID, Glover PM, Bowtell RW, et al. Thresholds for perceiving metallic taste at high magnetic field. *J Magn Reson Imaging*. 2007;26:1357–61.
13. Chronik BA, Rutt BK. Simple linear formulation for magneto-stimulation specific to MRI gradient coils. *Magn Reson Med*. 2001;45:916–9.
14. de Vocht F, Kromhout H. Human MRI above the FDA 8 T guideline: can we conclude that it is safe? *J Magn Reson Imaging*. 2008;27:938–9, author reply 939.
15. Edwards MJ, Talelli P, Rothwell JC. Clinical applications of transcranial magnetic stimulation in patients with movement disorders. *Lancet Neurol*. 2008;7:827–40.
16. EUR-Lex. Document 02004L0040-20081211. 2004. <http://eur-lex.europa.eu/legal-content/EN/ALL/?uri=CELEX:02004L0040-20081211>. Accessed 29 May 2014.
17. EUR-Lex. Document 32013L0035. 2013. <http://eur-lex.europa.eu/legal-content/EN/ALL/?uri=CELEX:32013L0035>. Accessed 15 May 2014.
18. FDA. A primer on medical device interactions with magnetic resonance imaging systems. U.S. Food and Drug Administration, Center for Devices and Radiological Health Web site. 1997. <http://www.fda.gov/MedicalDevices/DeviceRegulationandGuidance/GuidanceDocuments/ucm107721.htm>.
19. FDA. Guidance for industry and FDA staff: criteria for significant risk investigations of magnetic resonance diagnostic devices. 2003. <http://www.fda.gov/downloads/MedicalDevices/DeviceRegulationandGuidance/GuidanceDocuments/UCM072688.pdf>. Accessed 16 May 2014.
20. FDA. Guidance for industry and FDA staff: establishing safety and compatibility of passive implants in the magnetic resonance (MR) environment. Published August 21, 2008. 2008. <http://www.fda.gov/downloads/MedicalDevices/DeviceRegulationandGuidance/GuidanceDocuments/UCM107708.pdf>. Accessed 18 May 2014.
21. FDA. Public health advisory: risk of burns during MRI scans from transdermal drug patches with metallic backings. 2009. <http://www.fda.gov/drugs/drugsafety/postmarketdrugsafetyinformationforpatientsandproviders/drugsafetyinformationforhealthcareprofessionals/publichealthadvisories/ucm111313.htm>. Accessed 19 June 2014.
22. Feldman RE, Hardy CJ, Aksel B, et al. Experimental determination of human peripheral nerve stimulation thresholds in a 3-axis planar gradient system. *Magn Reson Med*. 2009;62:763–70.
23. Fiechter F, Stehli J, Fuchs TA, et al. Impact of cardiac magnetic resonance imaging on human lymphocyte DNA integrity. *Eur Heart J*. 2013;34:2340–5. doi:10.1093/eurheartj/eh184.
24. Fuchs VR, Sox Jr HC. Physicians' views of the relative importance of thirty medical innovations. *Health Aff (Millwood)*. 2001;20:30–42.
25. Gangarosa RE, Minnis JE, Nobbe J, et al. Operational safety issues in MRI. *Magn Reson Imaging*. 1987;5:287–92.
26. Geddes LA, Baker LE. Principles of applied biomedical instrumentation. 3rd ed. New York: Wiley; 1989.
27. Gethins M. Cautious optimism for proposed European MRI exposure limit exemption. *J Natl Cancer Inst*. 2011;103:1495–7.
28. Gill A, Shellock FG. Assessment of MRI issues at 3-Tesla for metallic surgical implants: findings applied to 61 additional skin closure staples and vessel ligation clips. *J Cardiovasc Magn Reson*. 2012;14:3–9.
29. Gimbel JR, Johnson D, Levine PA, et al. Safe performance of magnetic resonance imaging on five patients with permanent cardiac pacemakers. *Pacing Clin Electrophysiol*. 1996;19:913–9.
30. Heilmaier C, Theysohn JM, Maderwald S, et al. A large-scale study on subjective perception of discomfort during 7 and 1.5 T MRI examinations. *Bioelectromagnetics*. 2011;32:610–9.
31. Hill DL, McLeish K, Keevil SF. Impact of electromagnetic field exposure limits in Europe: is the future of interventional MRI safe? *Acad Radiol*. 2005;12:1135–42.
32. Hundley WG, Bluemke DA, Finn JP, et al. ACCF/ACR/AHA/NASCI/SCMR 2010 expert consensus document on cardiovascular magnetic resonance: a report of the American College of Cardiology Foundation task force on expert consensus documents. *Circulation*. 2010;121:2462–508.
33. ICNIRP. Guidelines on limits of exposure to static magnetic fields. *Health Phys*. 1994;66:100–6.
34. ICNIRP. Medical magnetic resonance (MR) procedures: protection of patients. *Health Phys*. 2004;87:197–216.
35. ICNIRP. Amendment to the ICNIRP “Statement on medical magnetic resonance (MR) procedures: protection of patients”. *Health Phys*. 2009;97:259–61.
36. ICNIRP. Guidelines on limits of exposure to static magnetic fields. *Health Phys*. 2009;96:504–14.
37. IEC. 60601-2-33: medical electrical equipment – part 2–33: particular requirements for the basic safety and essential performance of magnetic resonance equipment for medical diagnosis. 3rd ed. Geneva: International Electrotechnical Commission; 2010.
38. Kanal E, Barkovich AJ, Bell C, et al. ACR guidance document on MR safe practices: 2013. *J Magn Reson Imaging*. 2013;37:501–30.
39. Keevil SF, Gedroyc W, Gowland P, et al. Electromagnetic field exposure limitation and the future of MRI. *Br J Radiol*. 2005;78:973.
40. Khan SN, Rapacchi S, Levi DS, et al. Pediatric cardiovascular interventional devices: effect on CMR images at 1.5 and 3 Tesla. *J Cardiovasc Magn Reson*. 2013;15:54–67.
41. Klucznik RP, Carrier DA, Pyka R, et al. Placement of a ferromagnetic intracerebral aneurysm clip in a magnetic field with a fatal outcome. *Radiology*. 1993;187:855–6.
42. Levine GN, Gomes AS, Arai AE, et al. Safety of magnetic resonance imaging in patients with cardiovascular devices: an American Heart Association scientific statement from the Committee on Diagnostic and Interventional Cardiac Catheterization, Council on Clinical Cardiology, and the Council on Cardiovascular Radiology and Intervention: endorsed by the American College of Cardiology Foundation, the North American Society for Cardiac Imaging, and the Society for Cardiovascular Magnetic Resonance. *Circulation*. 2007;116:2878–91.
43. Lobodzinski SS. Recent innovations in the development of magnetic resonance imaging conditional pacemakers and implantable cardioverter-defibrillators. *Cardiol J*. 2012;19:98–104.
44. Lovsund P, Oberg PA, Nilsson SE. Magneto- and electrophosphenes: a comparative study. *Med Biol Eng Comput*. 1980;18:758–64.
45. Lovsund P, Oberg PA, Nilsson SE, et al. Magnetophosphenes: a quantitative analysis of thresholds. *Med Biol Eng Comput*. 1980;18:326–34.
46. Lund G, Nelson JD, et al. Tattooing of eyelids: magnetic resonance imaging artifacts. *Ophthalmic Surg*. 1986;17:550–3.
47. McNeil Jr DG. M.R.I.'s strong magnets cited in accidents. 2005. *New York Times*, 19 August 2005.
48. Medtronic. Medtronic SureScan® pacing systems first to be approved for full body MRI scans without positioning restrictions. Medtronic Web site. 2014. <http://newsroom.medtronic.com/phoenix.zhtml?c=251324&p=irol-newsArticle&ID=1892624&highlight>. Published 22 Jan 2014.
49. Merrill RA. Regulation of drugs and devices: an evolution. *Health Aff (Millwood)*. 1994;13:47–69.
50. Moratal D, Marti-Bonmati L, Gili J. European Directive 2004/40/EC on workers' exposure to electromagnetic fields from MRI. *Radiologia*. 2009;51:30–7 (in Spanish).

51. Oman CM. Motion sickness: a synthesis and evaluation of the sensory conflict theory. *Can J Physiol Pharmacol*. 1990;68:294–303.
52. OSHA standard number 1910.95. Occupational noise exposure. Occupational safety and health administration. https://www.osha.gov/pls/oshaweb/owadisp.show_document?p_table=standards&p_id=9735. Accessed 18 May 2014.
53. Patel MR, Albert TS, Kandzari DE, et al. Acute myocardial infarction: safety of cardiac MR imaging after percutaneous revascularization with stents. *Radiology*. 2006;240:674–80.
54. Pennell DJ, Neubauer S, Cook SA, et al. No evidence that MR causes dsDNA damage. *European Heart Journal eLetter*, published online July 22, 2013. http://eurheartj.oxfordjournals.org/eletters?page=14&pager_limit=10&days=
55. Price DL, De Wilde JP, Papadaki AM, et al. Investigation of acoustic noise on 15 MRI scanners from 0.2 T to 3 T. *J Magn Reson Imaging*. 2001;13:288–93.
56. Randolph W. Guidelines for evaluating electromagnetic exposure risk for trials of clinical NMR systems; availability. *Fed Regist*. 1982;47:11972–3.
57. Reilly JP. Peripheral nerve stimulation by induced electric currents: exposure to time-varying magnetic fields. *Med Biol Eng Comput*. 1989;27:101–10.
58. Roberts DC, Marcelli V, Gillen JS, Carey JP, et al. MRI magnetic field stimulates rotational sensors of the brain. *Curr Biol*. 2011;21:1635–40.
59. Roguin A, Zviman MM, Meininger GR, et al. Modern pacemaker and implantable cardioverter/defibrillator systems can be magnetic resonance imaging safe: in vitro and in vivo assessment of safety and function at 1.5 T. *Circulation*. 2004;110:475–82.
60. Saunders RD, Smith H. Safety aspects of NMR clinical imaging. *Br Med Bull*. 1984;40:148–54.
61. Schenck JF. Health and physiological effects of human exposure to whole-body four-tesla magnetic fields during MRI. *Ann NY Acad Sci*. 1992;649:285–301.
62. Schenck JF. Safety issues in the MR environment. In: Debatin JF, Adam G, editors. *Interventional magnetic resonance imaging*. Heidelberg: Springer; 1998. p. 95–103.
63. Schenck JF. Physical interactions of static magnetic fields with living tissues. *Prog Biophys Mol Biol*. 2005;87:185–204.
64. Schenck JF. Safety of strong, static magnetic fields. *J Magn Reson Imaging*. 2000;12:2–19.
65. Schenck JF. Safety and sensory aspects of main and gradient fields in MRI. *eMagRes*. 2013;2:55–66. doi:10.1002/9780470034590.emrstm1324. John Wiley & Sons, Chichester.
66. Schenck JF, Dumoulin CL, Redington RW, et al. Human exposure to 4.0-Tesla magnetic fields in a whole-body scanner. *Med Phys*. 1992;19:1089–98.
67. Schild T, Maksoud WA, Aubert G, et al. The Iseult/Inumac whole body 11.7 T MR magnet R&D program. *IEEE Trans Appl Supercond*. 2010;20:702–5.
68. Setsompop K, Kimmlingen R, Eberlein E, et al. Pushing the limits of in vivo diffusion MRI for the human connectome project. *NeuroImage*. 2013;80:220–33.
69. Shellock FG. MRI safety web site. <http://www.MRIsafety.com/>. Accessed 18 May 2014.
70. Shellock FG, Ziarati M, Atkinson D, et al. Determination of gradient magnetic field-induced acoustic noise associated with the use of echo-planar and three-dimensional fast spin echo techniques. *J Magn Reson Imaging*. 1998;8:1154–7.
71. Shellock FG, Crues 3rd JV. MR safety and the American College of Radiology white paper. *Am J Roentgenol*. 2002;178:1349–52.
72. Shellock FG, Crues 3rd JV. MR procedures: biologic effects, safety, and patient care. *Radiology*. 2004;232:635–52.
73. Shellock FG, Woods TO, Crues 3rd JV. MR labeling information for implants and devices: explanation of terminology. *Radiology*. 2009;253:26–30.
74. Shinbane JS, Colletti PM, Shellock FG. Magnetic resonance imaging in patients with cardiac pacemakers: era of “MR Conditional” designs. *J Cardiovasc Magn Reson*. 2011;13:63–75.
75. Simi S, Ballardini M, Casella M, et al. Is the genotoxic effect of magnetic resonance negligible? Low persistence of micronucleus frequency in lymphocytes of individuals after cardiac scan. *Mutat Res*. 2008;645(1–2):39–43.
76. Sommer T, Maintz D, Schmiedel A, et al. High field MR imaging: magnetic field interactions of aneurysm clips, coronary artery stents, and iliac artery stents with a 3.0 Tesla MR system. *Röfo*. 2004;176:731–8.
77. Straumann D, Bockisch CJ. Neurophysiology: vertigo in MRI machines. *Curr Biol*. 2011;21:R806–7.
78. Syed MA, Carlson K, Murphy M, et al. Long-term safety of cardiac magnetic resonance imaging performed in the first few days after bare-metal stent implantation. *J Magn Reson Imaging*. 2006;24:1056–61.
79. Takeda N, Morita M, Horii A, et al. Neural mechanisms of motion sickness. *J Med Invest*. 2001;48:44–59.
80. Theysohn JM, Maderwald S, Kraff O, et al. Subjective acceptance of 7 Tesla MRI for human imaging. *Magn Reson Mater Phys*. 2008;21:63–72.
81. Wagle WA, Smith M. Tattoo-induced skin burns during MR imaging. *AJR Am J Roentgenol*. 2000;174:1795.
82. WHO. Environmental health criteria 232: static fields. Geneva: World Health Organization; 2006.
83. Wilkoff BL, Bello D, Taborsky M, et al. Magnetic resonance imaging in patients with a pacemaker system designed for the magnetic resonance environment. *Heart Rhythm*. 2011;8:65–73.
84. Yamaguchi-Sekino S, Sekino M, Ueno S. Biological effects of electromagnetic fields and recently updated safety guidelines for strong static magnetic fields. *Magn Reson Med Sci*. 2011;10:1–10.
85. Zaremba LA. FDA guidelines for magnetic resonance system safety and patient exposures: current status and future considerations. In: Shellock FG, editor. *Magnetic resonance procedures: health effects and safety*. Boca Raton: CRC Press; 2001. p. 183–96.
86. Zhao H, Crozier S, Liu F. Finite difference time domain (FDTD) method for modeling the effect of switched gradients on the human body in MRI. *Magn Reson Med*. 2002;48:1037–42.

Part II

Cardiovascular Magnetic Resonance Techniques

David Lopez and Michael Salerno

Abstract

The constant motion of the heart imposes particular challenges on cardiac magnetic resonance (CMR) as compared to magnetic resonance imaging (MRI) of other organs. Thus, imaging the heart requires synchronization of data acquisition to the cardiac cycle, typically using an electrocardiographic recording of the heart's electrical activity. This technique is known as electrocardiographic (ECG)-gating. Depending on the specific anatomical or functional information desired, data acquisition may need to occur throughout the cardiac cycle, or may need to be synchronized to a particular phase of the cardiac cycle. This chapter will review basic ECG concepts, ECG-gating modes, common problems and suggestions for troubleshooting these issues.

Keywords

Cardiovascular magnetic resonance • Electrocardiographic gating • Magnetic resonance imaging • Cardiovascular imaging

Introduction

CMR is a particularly challenging and demanding application of magnetic resonance imaging (MRI) because, as compared to other organs, the heart is in constant motion. As such, optimal image quality requires synchronization of data acquisition to the cardiac cycle. The surface electrocardiogram (ECG) is a non-invasive recording of the heart's electrical activity and provides an ideal reference to accurately match the acquired images to the corresponding phase of the cardiac cycle, a technique known as **ECG-gating**. Depending on what information is desired, different gating

strategies are utilized. While imaging cardiac anatomy often requires collecting data during the quiescent period of diastole, evaluation of cardiac function necessitates imaging throughout the cardiac cycle. In this chapter we discuss basic ECG concepts, ECG-gating modes, common problems, and troubleshooting recommendations.

The ECG and the Cardiac Cycle

Every cardiac event is triggered by an electrical stimulus which precedes the heart's mechanical activity by 40–60 ms [1]. The surface ECG is a recording of this electrical activity (Fig. 9.1). The P wave represents atrial depolarization and precedes atrial contraction. The QRS complex depicts ventricular depolarization preceding ventricular contraction. The T wave marks ventricular repolarization and the onset of diastole. The T-P segment is the isoelectric portion of the tracing flanked by the T and P waves. It typically coincides with diastasis (Fig. 9.1), the end of passive ventricular filling just before atrial contraction and the time of minimum cardiac

Electronic supplementary material The online version of this chapter (doi:10.1007/978-3-319-22141-0_9) contains supplementary material, which is available to authorized users.

D. Lopez, MD • M. Salerno, PhD, MD (✉)
Cardiovascular Division, Department of Medicine,
University of Virginia Health System, Charlottesville, VA, USA
e-mail: msalerno@virginia.edu

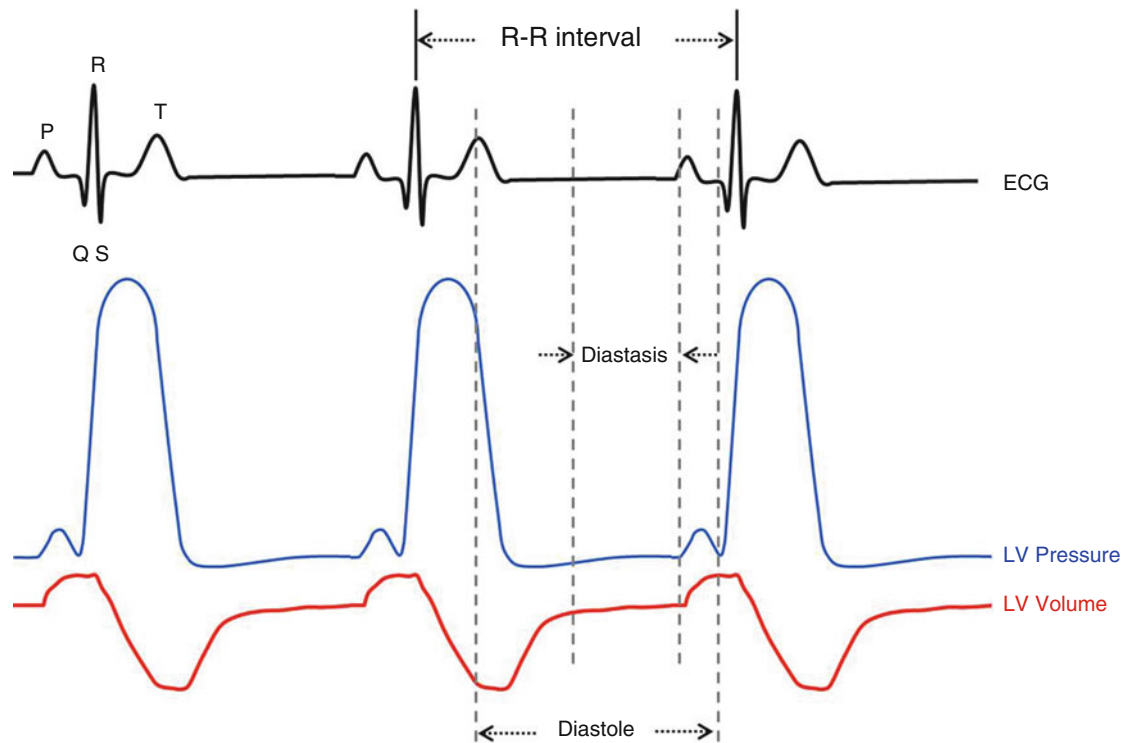


Fig. 9.1 Simultaneous ECG (black), left ventricular pressure (blue) and volume (red) waveforms illustrate the electromechanical relationship of a cardiac cycle. The P wave represents atrial depolarization and occurs at the end of ventricular diastole. The QRS complex signifies

ventricular depolarization and precedes ventricular contraction. The T wave heralds ventricular relaxation and the beginning of diastole. Diastasis is the period of ventricular standstill and the ideal phase for anatomic imaging

motion. Hence, the T-P interval may be an optimal phase of the cardiac cycle for static or anatomic image acquisition.

ECG Setup

First and foremost, MR-safe electrodes must be used in the MR-environment in order to avoid skin burns. ECG wires should be draped in a straight line over the patient avoiding loops or coil patterns. Most MR systems will use a three or four lead telemetry system to transmit the ECG signal. Electrodes are placed in the left chest area forming a triangle or square around the heart (Fig. 9.2). In women the “left leg” electrode should be placed just below the left breast fold and not on the breast tissue itself. A closer electrode configuration tends to yield higher amplitude signals. Signal amplitude is also increased by ensuring good electrode contact with the skin, facilitated by shaving hirsute patients and the use of coupling gel in all patients.

In order to ensure proper ECG-gating, the ideal tracing should have predominant R-wave with minimum T wave amplitude. In some individuals the T wave amplitude can exceed the R-wave, which may cause the scanner to inappropriately trigger off of the T wave. While this is not absolutely detrimental to image quality, it can lead to improper

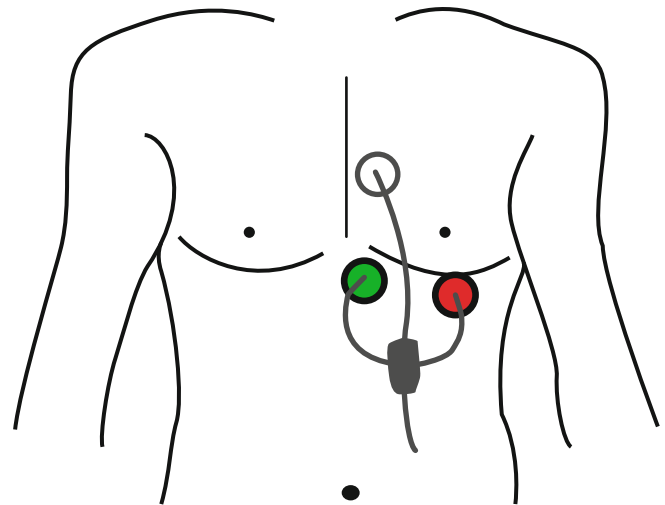


Fig. 9.2 Typical ECG lead placement configuration

placement of the acquisition window during prospective gating and errors in quantitative analysis. Thus, it is best to make adjustments to allow triggering off the R-wave. The ECG tracing profile can be changed by selecting different lead polarities (Lead I, aVF, etc.) at the MR console, however manual electrode adjustments may be necessary. Modern scanners are typically equipped with vectorcardiography

Table 9.1 Heart rate in beats per minute and the corresponding R-R interval as calculated from Eq. 9.1

HR (bpm)	R-R interval (ms)
50	1200
60	1000
70	857
80	750
90	667
100	600
110	545
120	500

HR heart rate, bpm beats per minute, ms milliseconds

(VCG), which can mitigate magnetohydrodynamic (MHD) artifacts as discussed later in the chapter.

Interpreting the ECG Tracing

The ECG tracing can reveal the origin of the electrical activity, rhythm, rate, conduction abnormalities and even give clues about cardiac ischemia or prior myocardial infarctions. For the purpose of cardiac imaging, we are most concerned about the heart rate and rhythm pattern. Heart rate (HR) can be expressed in beats per minute (bpm) as determined by the number of QRS complexes per minute. Cardiac activity is also described by the **R-R interval**, the cardiac cycle duration between R waves in milliseconds (ms). Heart rate and R-R intervals are related by Eq. 9.1. Table 9.1 lists typical heart rates with the corresponding R-R intervals.

$$R - R \text{ interval (ms)} = \frac{60,000(\text{ms} / \text{min})}{HR(\text{bpm})} \quad (9.1)$$

Heart rhythm is defined by the origin of each electrical impulse and the regularity of the stimuli. Rhythm regularity is most important during CMR and it is easily determined by observing the R-R interval variability. The normal sinus rhythm is regular and usually between 60 and 100 bpm corresponding to R-R intervals of 1000–600 ms. However, individuals referred for CMR may often have slow (bradycardia; <60 bpm), fast (tachycardia; >100 bpm) or irregular heart rhythms (arrhythmias). The most common irregular rhythms seen in typical patients with cardiac disease referred for CMR examination are atrial fibrillation, premature atrial or ventricular contractions, and non-sustained ventricular tachycardia. Prompt recognition of these abnormalities allows the imager to adjust the acquisition technique to achieve optimal image quality and make sure that the exam is completed safely or terminated early if needed to facilitate rhythm management. Later in the chapter we will discuss how to tailor the exam in the setting of cardiac arrhythmias.

ECG-Gating and Data Acquisition

Basic Concepts

The goal of ECG-gating is to synchronize data acquisition to the cardiac cycle, which reduces cardiac motion-induced artifacts and optimizes image quality. The R-wave is the most prominent and easily detected feature on the ECG and serves as a temporal reference point within the cardiac cycle. Thus, it is the preferred marker to gate and trigger data acquisition. Although the terms often used interchangeably, ECG-triggering and ECG-gating are not synonymous. **ECG-triggering** specifically refers to the initiation of the MRI pulse sequence after detection of an R-wave, whereas **ECG-gating** refers to the process of matching the acquired data to the corresponding temporal phase within the RR-interval.

Two primary ECG gating modes are commonly used in CMR: **prospective** and **retrospective**. In prospective gating, detection of an R wave triggers the MR pulse sequence to acquire a fixed number of data lines at a given timepoint within the R-R interval. Thus, data is prospectively collected at a particular time in the cardiac cycle with respect to the R-wave detection. In retrospective mode, data is collected continuously over several heart beats and retrospectively binned into a fixed number of reconstructed cardiac phases using the detected R-waves as reference points.

These ECG gating modes are combined with two data collection strategies: **single-shot** or **segmented** acquisitions. Single-shot pulse sequences are typically prospectively gated and all the data needed to make an image is acquired during a single heart beat. Alternatively, during segmented acquisitions, a fraction of the total number of data lines is acquired with each heartbeat, and the data needed to reconstruct a single image is obtained over multiple R-R intervals. In the next sections we will describe in detail the various ECG-gating and acquisition strategy combinations that are used in a cardiac exam. Table 9.2 summarizes typical ECG-gating and acquisition mode combinations, their respective applications, and their advantages and limitations.

Prospectively Gated Single-Shot Acquisition

Single-heartbeat (also termed ‘single-shot’) pulse sequences are typically prospectively gated and all the data needed to make an image is acquired during a single cardiac cycle (Fig. 9.3). During a prospectively gated acquisition, data is acquired after a programmed delay, or **trigger delay (TD)**, from the R-wave. Data is then collected for a period called the **acquisition window (AW)**, which typically ends several milliseconds prior to the next heartbeat. This gap, or **trigger window (TW)**, allows the scanner to detect the next R-wave. As a result, data is not sampled during this end-diastolic

Table 9.2 Common k-space filling strategies and ECG-gating mode combinations, sequences, advantages and limitations

Acquisition mode	ECG-gating mode	Sequence	Advantages and limitations
Single heartbeat	Prospective	Scouts (SSFP or TSE)	Robust to arrhythmias and breathing artifacts
		Perfusion	Fast acquisition
		LGE	Low spatial resolution
	Non-ECG-gated	Real time	Insensitive to rhythm or breathing variations Free breathing acquisition Low spatial and temporal resolution
Segmented	Prospective	T ₁ -weighted	High temporal and spatial resolution
		T ₂ -weighted	Longer acquisition/ breath hold
		Cine SSFP	
		Cine VENC	Sensitive to arrhythmias and breathing artifacts
		Cine Grid-tagging	Incomplete interrogation of the cardiac cycle for cine and grid-tagging images
		LGE	
	Retrospective	Cine SSFP	High temporal and spatial resolution
		Cine VENC	Complete acquisition of the cardiac cycle
		Cine Grid-tagging	Sensitive to arrhythmias and breathing artifacts Longer acquisition time

SSFP steady-state free precession, TSE turbo spin echo, LGE phase sensitive inversion recovery, VENC velocity encoded or phase contrast

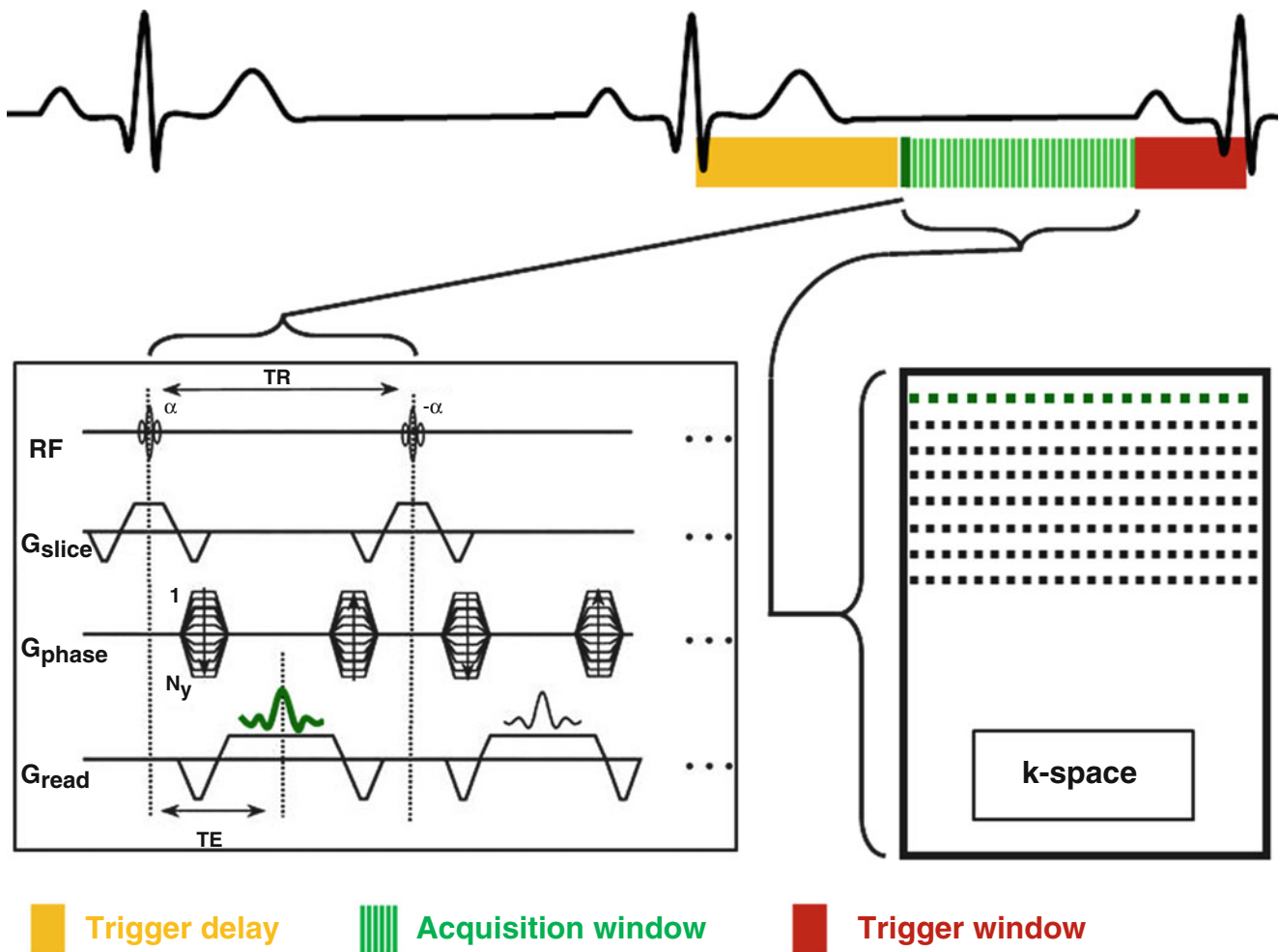


Fig. 9.3 Schematic of a single-shot prospectively-gated sequence. The AW (green bars) is positioned during the diastasis period. It is preceded by a TD (yellow rectangle) and ends at the beginning of the P wave, leaving a TW (red rectangle) to allow detection of the following

R-wave. In this case all the data needed to make an image is acquired during a single heart beat. One or multiple slices can be acquired during a breath-hold. AW acquisition window, TD trigger delay, TW trigger delay

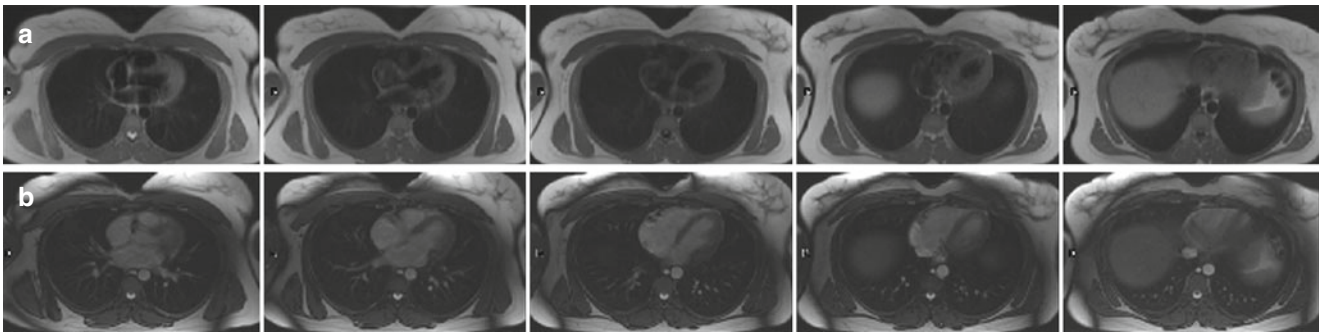


Fig. 9.4 Single-shot HASTE (a) and SSFP (b) axial anatomic images. Multiple slices can be acquired during a single breath-hold. *HASTE* half-Fourier turbo spin echo, *SSFP* steady-state free precession

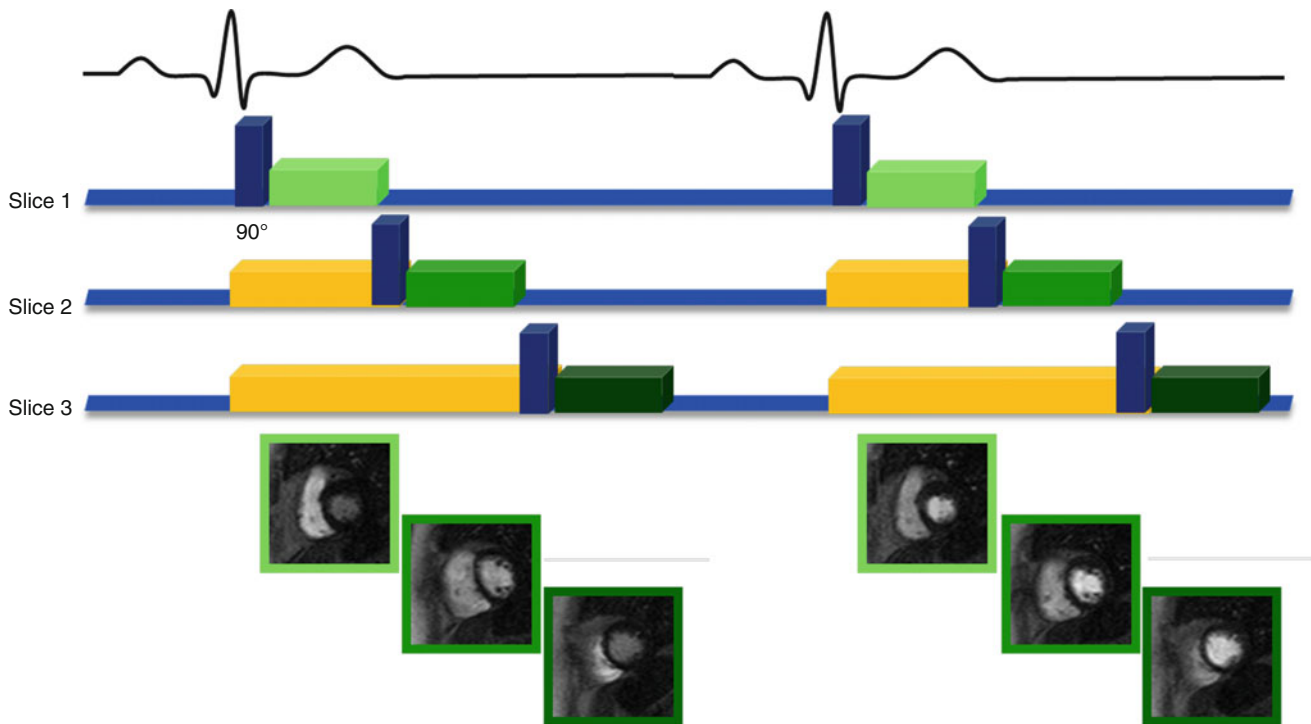


Fig. 9.5 Myocardial perfusion imaging is a special form of a prospectively gated single-shot sequence. Usually three slices are acquired sequentially during each R-R interval. Variable trigger delays (yellow)

are used for each slice position. Myocardial perfusion can be assessed at rest or during stress by obtaining multiple measurements of the same slice location while rapidly infusing gadolinium-based contrast

period of the cardiac cycle. For still frames or anatomic images, the TD and AW are adjusted to allow data collection during diastasis which coincides with the T-P segment (Fig. 9.1). One or multiple slice locations can be acquired during each breath hold.

Prospectively gated single-shot sequences are used for anatomic or static imaging. Examples include dark-blood half-Fourier turbo spin echo (HASTE) and bright-blood steady-state free precession (SSFP) images which are used as scouts during the initial survey of cardiac exams or to image cardiac anatomy (Fig. 9.4). Single-shot sequences may be

used instead of segmented acquisitions for applications such as late gadolinium enhanced imaging (LGE) in patients with arrhythmias or in subjects who cannot perform adequate breath holding to acquire diagnostic segmented images.

Perfusion imaging is a special form of single-shot imaging. Myocardial perfusion is assessed by acquiring several prospectively triggered single-shot images in each heart beat at a given slice location during the first-pass of a gadolinium DTPA contrast agent (Fig. 9.5). Multiple slice locations can be interrogated per heart beat by using variable TD for each location (i.e. $TD_1=0$; $TD_2=AW \times 1$; $TD_n=AW \times n-1$)

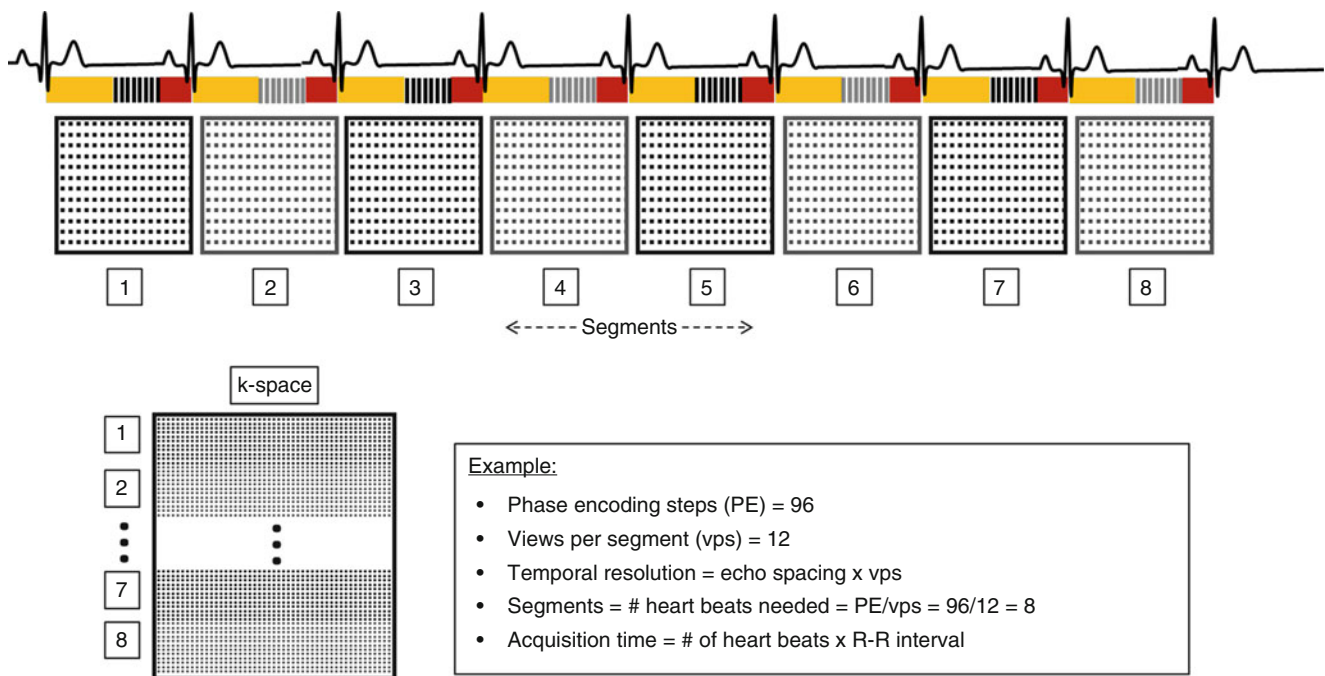


Fig. 9.6 Prospectively gated segmented acquisitions enable better temporal and spatial resolution and improved signal to noise ratio. In this example 12 lines of data (views per segment) are acquired per heart beat to fill a matrix of 98 phase encoding steps. Eight heart beats are thus

needed to collect all the data. The temporal resolution is equal to the acquisition window and is given by the product of the echo spacing and the views per segment. The total acquisition duration is determined by the number of heart beats or segments times the R-R interval

(Fig. 9.5). The maximum number of slices that can be sampled per heart beat is equal to the R-R interval divided by the AW for each image.

Single-heartbeat sequences allow fast data acquisition, making them robust to ECG gating and breath-hold variability at the expense of lower signal to noise ratio (SNR) and reduced temporal and spatial resolution.

Prospectively Gated Segmented Acquisition

In a prospectively gated segmented acquisition a fixed subset of the data lines are acquired over multiple R-R intervals to form a complete image (Fig. 9.6). For example, if a matrix has 96 phase encoding (PE) steps, 12 lines of data can be acquired per heart beat to fill eight segments of the data matrix over an eight heart beat acquisition. This segmented approach allows for shorter AWs per heart beat, resulting in higher spatial and temporal resolution at the expense of increased sensitivity to ECG-gating and breath-hold variations.

The number of lines per segment is referred to as views per segment (vps) and determines the temporal resolution as indicated in Eq. 9.2:

$$\text{Temporal resolution} = \text{Echo spacing} \times \text{vps} \quad (9.2)$$

The echo spacing represents the time between radiofrequency pulses, which is also referred to as the repetition time (TR). Segmented data acquisition can be used for static anatomical or cine imaging. The number of heart beats needed to acquire a complete dataset is equal to the number of matrix segments and is determined by the total number PE lines divided the vps (Eq. 9.3).

$$\# \text{ of heart beats} = \frac{PE}{vps} \quad (9.3)$$

The acquisition time, which represents the breath hold duration, can be calculated by multiplying the # of heart beats by the R-R interval (Eq. 9.4).

$$\text{Acquisition time} = \# \text{ heart beats} \times \text{RR interval} \quad (9.4)$$

Using the previous example, the acquisition time for a patient with a HR of 60 bpm (R-R interval=1000 ms) would be 8 s (s). This same scan in a patient with a HR of 100 bpm (R-R interval=600 ms) would take 4.8 s. Later in the chapter we will discuss strategies to optimize segmented imaging parameters in the setting of various rhythm abnormalities.

Prospectively gated segmented acquisitions are routinely used for T₁-weighted (T₁w), T₂-weighted (T₂w) and LGE imaging (Fig. 9.7).

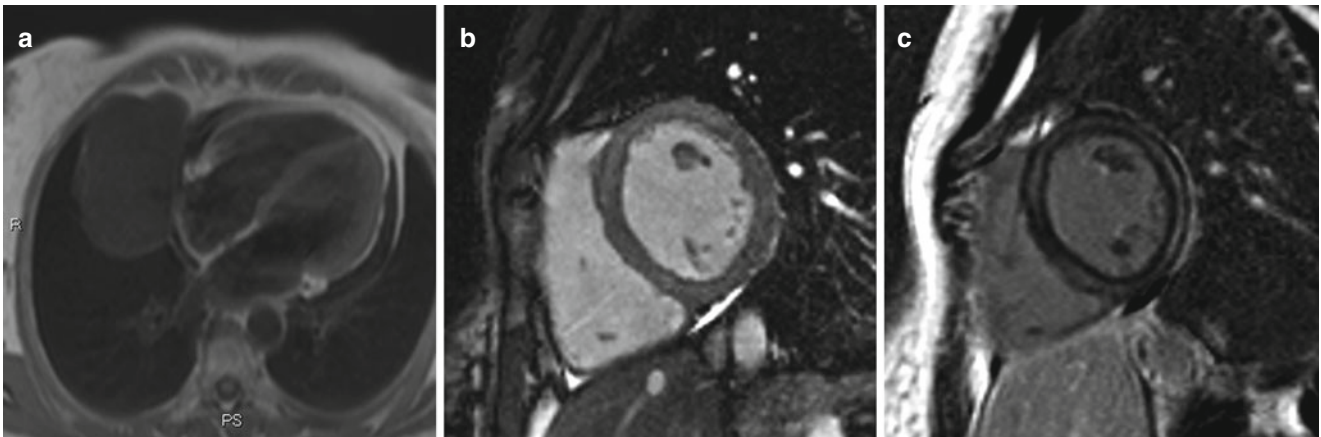


Fig. 9.7 Prospectively gated segmented acquisition modes are used for T_1w (a), T_2w (b), and LGE images (c). T_1w T_1 -weighted, T_2w T_2 -weighted, *LGE* inversion recovery late gadolinium enhanced

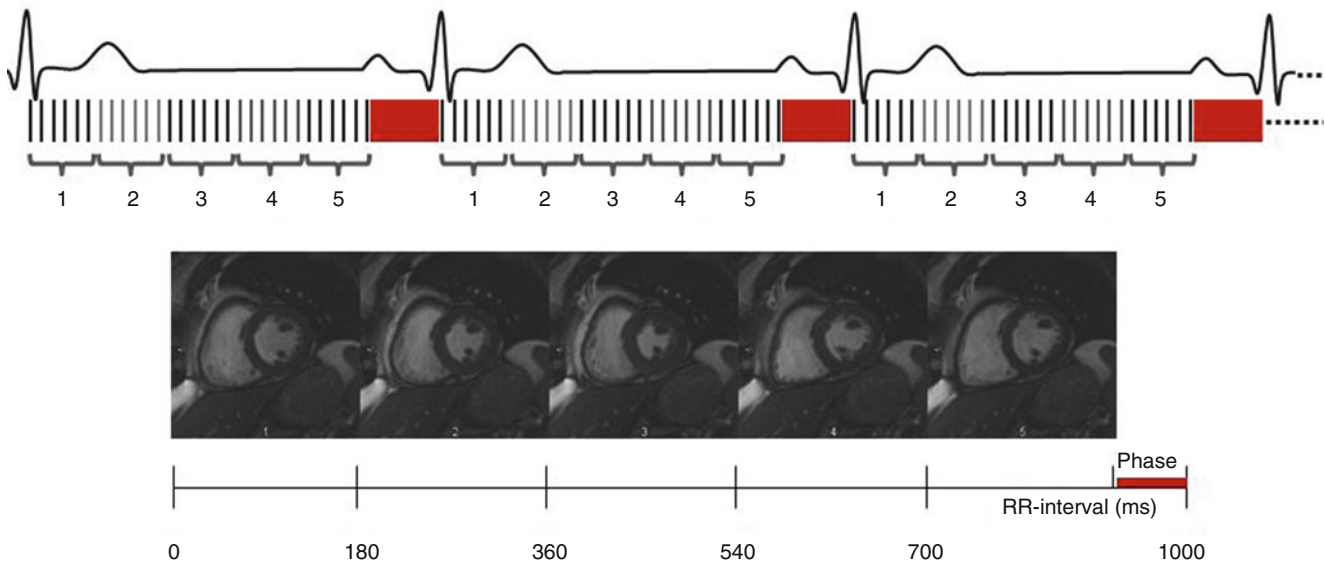


Fig. 9.8 Prospectively gated segmented cine acquisition. Note that data is not acquired during the trigger window (red)

Prospectively Gated Segmented-Cine Acquisition

In prospectively gated segmented cine acquisition, multiple segmented images are formed at different phases of the cardiac cycle. Data acquisition is triggered by R-wave detection and prospectively acquired relative to the triggering R-wave (Fig. 9.8). The temporal resolution of each phase, the total number of required heart beats, and the total imaging time are determined similar to prospectively gated segmented anatomic acquisitions described above. In a prospective segmented cine acquisition, the TD is set to zero, and a fixed number of cardiac phases are acquired over an AW that

typically ends about 100 ms before the next R-wave (Fig. 9.8). The number of cardiac phases is given by Eq. 9.5.

$$\# \text{ of phases} = \frac{\text{Acquisition window}}{\text{Temporal resolution}} \quad (9.5)$$

The presence of a TW means that the complete cardiac cycle is not imaged using this acquisition mode. As a result, cardiac motion corresponding to the P wave and early QRS complex is not displayed (Video 9.1), and can lead to underestimation of the end-diastolic volume. However, with the inherent 40–60 ms electromechanical delay between the R-wave and ventricular contraction, end-diastole (ED) is often

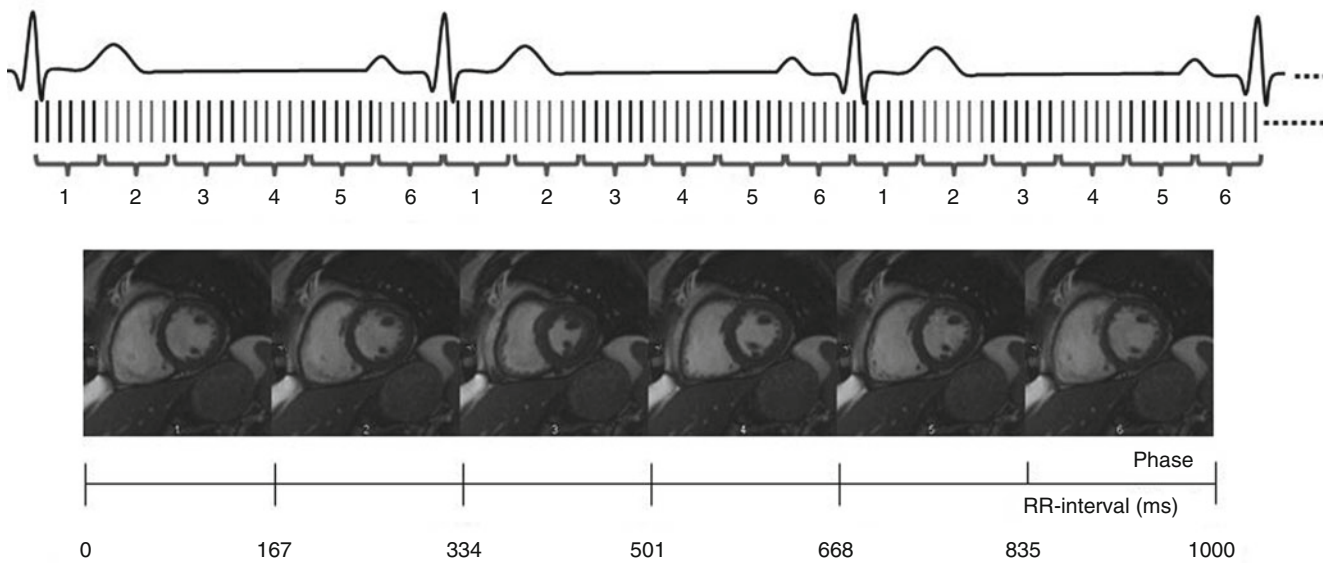


Fig. 9.9 Retrospectively gated segmented cine acquisition. If all parameters are kept unchanged, this mode provides similar spatial and temporal resolution. However, complete imaging of the cardiac cycle is now possible with the elimination of the trigger window

captured as the first frame of the cine movie when triggering off the R wave. Nevertheless, some have reported volume underestimation of up to 10 % using prospective vs. retrospective gated cine acquisitions [2]. As we will discuss later, the ability to adjust the AW can be a very useful in the presence of arrhythmias which cause variation in the R-R intervals.

Retrospectively Gated Segmented-Cine Acquisition

Retrospective ECG-gating allows imaging of the entire cardiac cycle and has been shown to yield higher ED volumes than prospectively gated cine imaging [2]. In this mode, data is acquired continuously over several R-R intervals enabling interrogation of the entire cardiac cycle (Fig. 9.9; Video 9.2). This results in variable number of k-space lines per R-R interval due to beat-to-beat variability. Using interpolation algorithms based on the detected R waves, the computer retrospectively determines the corresponding cardiac phase for each line of data acquired. This is done by dividing the cardiac cycle into a user defined fixed number of reconstructed cardiac phases. Each phase represents a certain percentage of the R-R interval.

The **apparent temporal resolution** ($TR_{apparent}$) is the average R-R interval divided by the number of reconstructed phases. Increasing the reconstructed phases yields a smooth cine loop with higher $TR_{apparent}$. However, to accurately depict ventricular function, the number of reconstructed phases should be set so that the $TR_{apparent}$ is equal or greater to the true temporal resolution (TR_{true}). This can be determined by dividing the average R-R interval by the TR_{true} . Table 9.3 lists common R-R intervals, the corresponding $TR_{apparent}$ for a typical cine of 25 reconstructed

phases and the number of reconstructed phases needed to match typical TR_{true} for any given HR. The gray zone indicates cases in which 25 reconstructed phases would overestimate TR_{true} . However, it should be noted that in most circumstances differences between $TR_{apparent}$ and TR_{true} are not clinically relevant and frequent adjustment of the reconstructed phases is not necessary. In practice for most clinical situations a temporal resolution of 35–50 ms is adequate for most applications.

Common Challenges and Troubleshooting Suggestions

Implementation of ECG-gating is often challenged by various sources of artifacts. In this section we will discuss common problems, and provide troubleshooting recommendations for a successful exam.

Poor ECG Signal

An easily corrected source of artifact is a faulty ECG signal that leads to inconsistent R wave detection. This is usually the result of poor lead contact and can be prevented by proper skin preparation which involves wiping dry any perspiration and shaving the area. Reinforcement with adhesive tape may be needed in some cases. Other reasons for low amplitude signal include obesity, obstructive lung disease and pericardial effusions. In patients with hyperinflated lungs, the heart may be displaced closer to the midline with a vertical orientation. Shifting the electrode placement toward the xyphoid process may provide improved signal amplitude.

Table 9.3 Relationship between HR, the number of reconstructed phases, $TR_{apparent}$ and TR_{true} .

HR (bpm)	RR Interval (ms)	$TR_{apparent}$ for 25 phases (ms)	# of reconstructed phases needed to match the TR_{true}			
			TR_{true} 35 ms	TR_{true} 45 ms	TR_{true} 55 ms	TR_{true} 65 ms
30	2000	80	57	44	36	31
40	1500	60	43	33	27	23
50	1200	48	34	27	22	18
60	1000	40	29	22	18	15
70	857	34	24	19	16	13
80	750	30	21	17	14	12
90	667	27	19	15	12	10
100	600	24	17	13	11	9
110	545	22	16	12	10	8
120	500	20	14	11	9	8

The grey zone indicates instances in which reconstruction of 25 phases would depict a faster temporal resolution than the TR_{true} . However, if TR_{true} is optimized these differences are small and of little clinical relevance. Hence, it is not necessary to adjust the reconstructed phases on a regular basis
HR heart rate, *bpm* beats per minute, *ms* milliseconds, $TR_{apparent}$ apparent temporal resolution, TR_{true} true temporal resolution

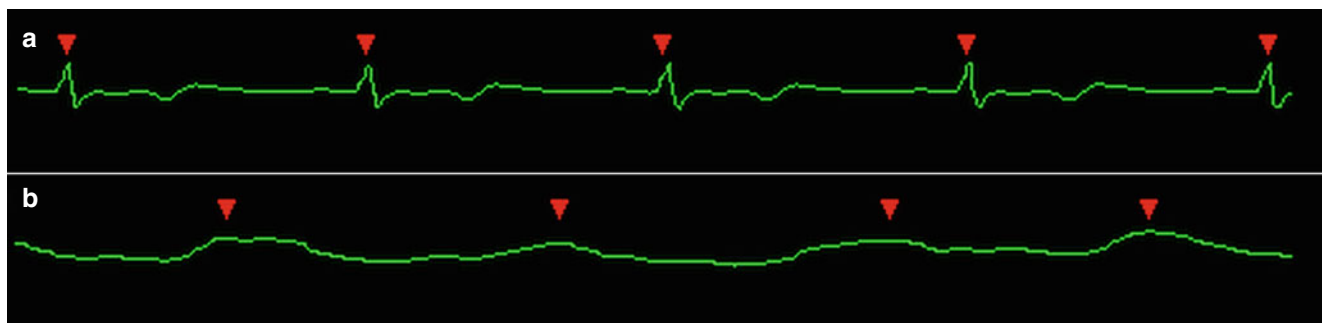


Fig. 9.10 In rare cases when ECG-gating fails, pulse oximetry-gating can be used (b). In this case triggering and gating occurs at end systole or early diastole since the peak of the waveform coincides with the

pulse wave. Note the temporal relationship between the R wave on the ECG and the pulse wave (b)

In rare cases, pulse oximetry can be used to trigger and gate data acquisition. The positive deflection of the sinusoidal pulse waveform is used for triggering and gating. As illustrated in the simultaneous ECG and pulse oximetry tracings shown in Fig. 9.10, triggering with the pulse waveform occurs during end-systole or early diastole. Thus, the AW for anatomic images should be moved toward the first half of the pulse wave interval so that imaging occurs during diastasis.

Magnetohydrodynamic (MHD) Effect

After obtaining a consistent ECG with high R-wave amplitude we can put the patient into the scanner. However, the ECG tracing inside the magnet can be very different from the

tracing outside (Fig. 9.11). This is mainly the result of MHD effects. As a patient enters the scanner, charged particles flowing in blood perpendicular to the main magnetic field, B_0 , experience a force which is oppositely directed for positive and negative charges. This charge separation generates transient voltages that shift the QRS complex and T wave axis. Since flow of charged particles is required, these artifacts are most prominent during systole causing alterations in the ST segment and T wave. This can cause inconsistent R-wave detection or consistent detection of an amplified T wave leading to inappropriate gating (Fig. 9.11). This artifact is more prominent at higher magnetic field strengths. It can sometimes be reduced by selecting different lead polarities (i.e. Lead I vs. aVF) at the MR console, using various filters, or changing the electrode placement. VCG has emerged as a routine approach to overcome this gating issue.

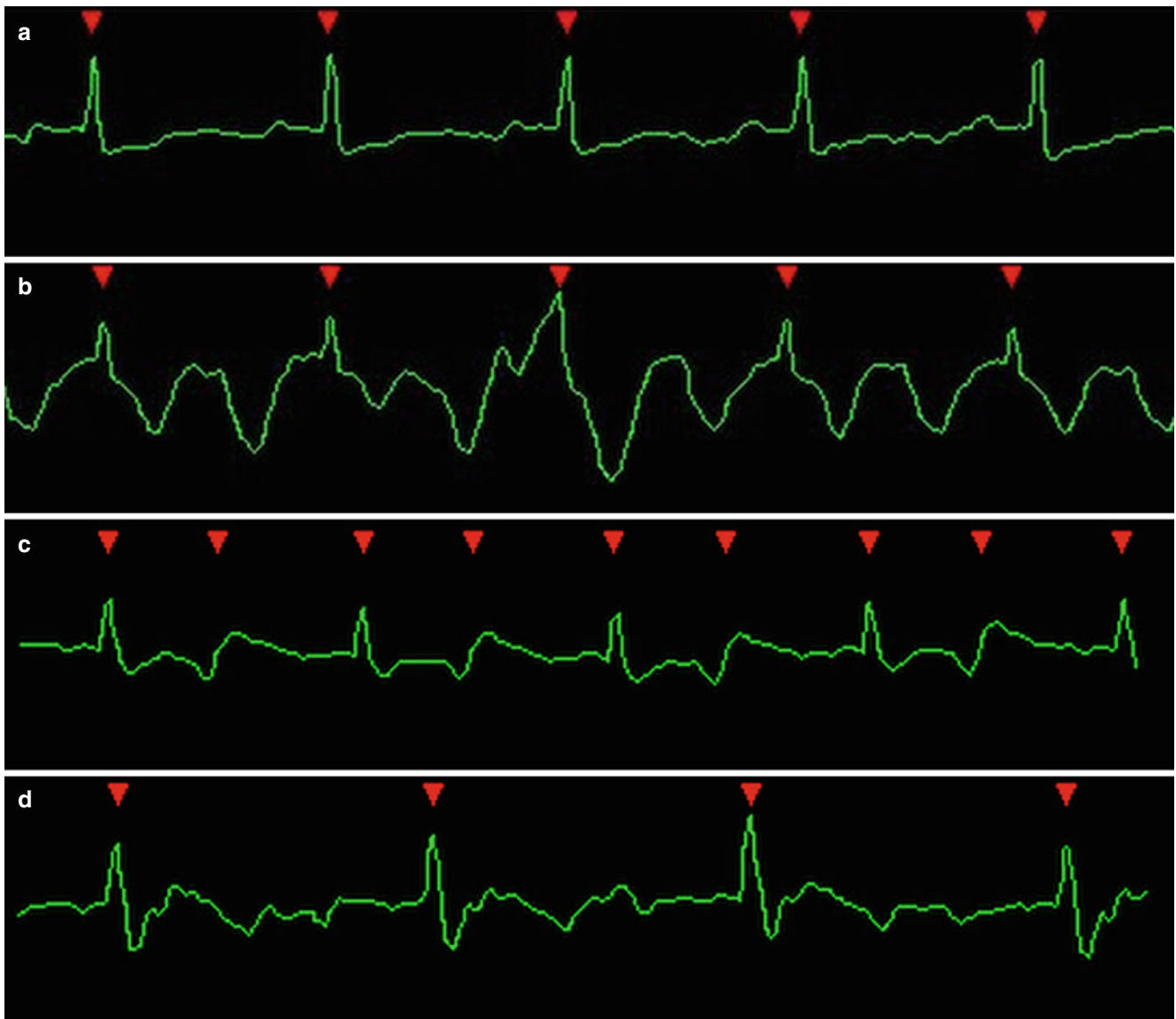


Fig. 9.11 Magneto-hydrodynamic effects can cause significant ECG signal alterations. (a) The ECG tracing from a subject outside the MRI bore demonstrates normal EKG wave morphology. (b) When the subject is placed inside the MRI bore, there is significant alteration of the ST segments and accentuation of the T wave due to the

Magneto-hydrodynamic effect. Accurate R-wave detection was achieved using VCG gating. (c) In another case, a T wave was incorrectly identified as an R-wave leading to two detected events per RR interval. (d) In this case, manual repositioning of the ECG leads corrected the issue

Vectorcardiography

VCG is a method of displaying the temporal evolution of cardiac electrical activity as a vector in three-dimensional space. The result is a time loop with varying distance of this vector to the x, y and z axes, where z is parallel to B_0 (Fig. 9.12). Exploiting the differences between the R-wave VCG loop, as determined outside the magnet, and MHD induced voltages, modern MR scanners are generally capable of filtering out the artifactual signal. This method has

been an important improvement to cardiac MRI. However, it is less effective at higher field strengths [3].

Induced Currents

Radiofrequency pulses (RF) and magnetic gradients used during imaging can induce currents on the ECG wires and cause artifacts on the ECG tracing. In some cases these artifacts can interrupt proper R-wave detection. For this reason,

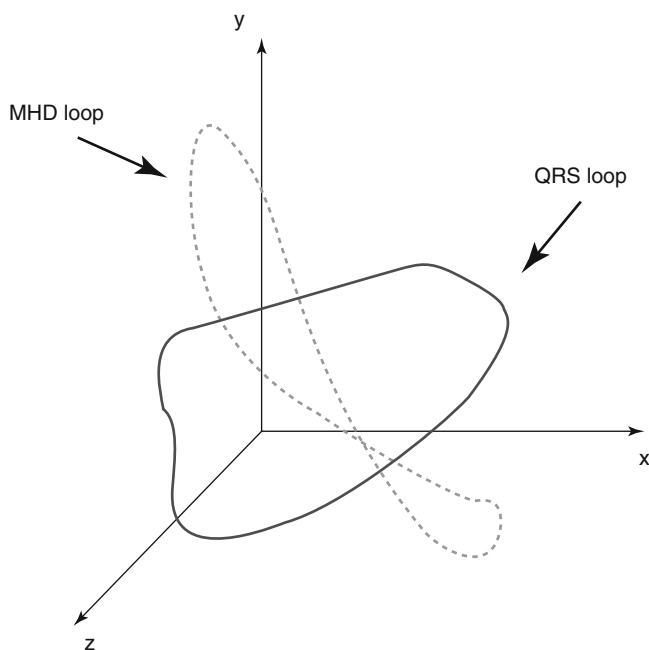


Fig. 9.12 A Prototypical vectorcardiogram loops illustrate how voltages from the heart electrical activity can be differentiated from MHD voltages based on their respective temporal-spatial trajectories. *MHD* magnetohydrodynamic

the length of ECG leads used in CMR is short to minimize sensitivity to interference. When the CMR pulse sequence interferes with the ECG, gradient and RF pulse modes can usually be adjusted to mitigate this gating issue.

Arrhythmias

Arrhythmias present a significant challenge for segmented CMR imaging. These include slow (bradycardia), fast (tachycardia) and irregular (dysrhythmias) rhythms. Recognition of these abnormalities enables the imager to make adjustments to the pulse sequence parameters to obtain accurate and diagnostic quality images.

Bradycardia is defined as a HR of <60 bpm or an R-R interval >1000 ms. Although, not an ECG gating problem per se, it leads to prolonged acquisition/breath hold duration (Eq. 9.4) (Video 9.3) that can result in respiratory motion artifacts. In this case the acquisition time can often be shortened by reducing temporal and/or spatial resolution without a significant impact on image quality. Most individuals undergoing a cardiac examination can hold their breath comfortably for 10–12 s, which in this case would represent 10–12 heart beats or less. One initial approach that does not affect temporal or spatial resolution is to minimize the required number of phase encoding steps by utilizing a rectangular field of

view (FOV) which is shorter in the phase encoding direction. This directly reduces the number of heart beats needed to make an image (Eq. 9.3). Secondly, the number of vps can be increased. This change will result in a lower temporal resolution, which is usually acceptable given the slow heart rate. Lastly, the phase encoding steps can be decreased by reducing the matrix size (and hence resolution) in the phase encoding direction.

Tachycardia is defined as a HR of >100 bpm or an R-R interval <600 ms. Assuming equal sequence parameters, total acquisition time decreases as HR increases because the number of heart beats is fixed but the R-R interval is decreasing (Eq. 9.4). However, a higher temporal resolution is needed to accurately depict cardiac events such as end-systole or end-diastole. The temporal resolution is optimized by reducing the number of vps at the expense of increasing the number of heart beats required to obtain each image. As the R-R interval is shorter in patients with tachycardia, increasing the temporal resolution results in similar breath-hold duration as that of patients with a normal heart rate.

The most challenging rhythm abnormalities for CMR are arrhythmias such as atrial fibrillation, non-sustained ventricular tachycardia and frequent atrial or ventricular ectopy. This is particularly challenging when the rates are fast with very short and irregular R-R intervals. In the setting of irregular rhythms, retrospective gating does not work well since the duration of the cardiac cycle changes for each heart beat, resulting in a mismatch of the reconstructed phases to the events of the cardiac cycle. The result is a blurry, non-diagnostic image with ghosting artifacts (Video 9.4). The initial approach to this problem is to switch to prospectively gated cine acquisition. The AW duration is then set to be shorter than the shortest RR-interval identified to allow a reasonable TW. If the shortest RR-interval is extremely short, the required AW may be too short to depict end-systole and ejection fraction would be underestimated. The resulting image may not be diagnostic (Video 9.5). In these cases, real time, non-gated sequences may be used. We will discuss real-time imaging and other gating techniques in the next section.

Advanced Topics

Real-Time Imaging

Real-time imaging is routinely used in the evaluation of pericardial disease to assess for the presence of ventricular interdependence. Otherwise, it is useful to study patients with extreme arrhythmias, inability to perform breath-hold maneuvers, or in cases with persistently poor ECG signal despite efforts to obtain a reliable tracing. Real-time imaging is a

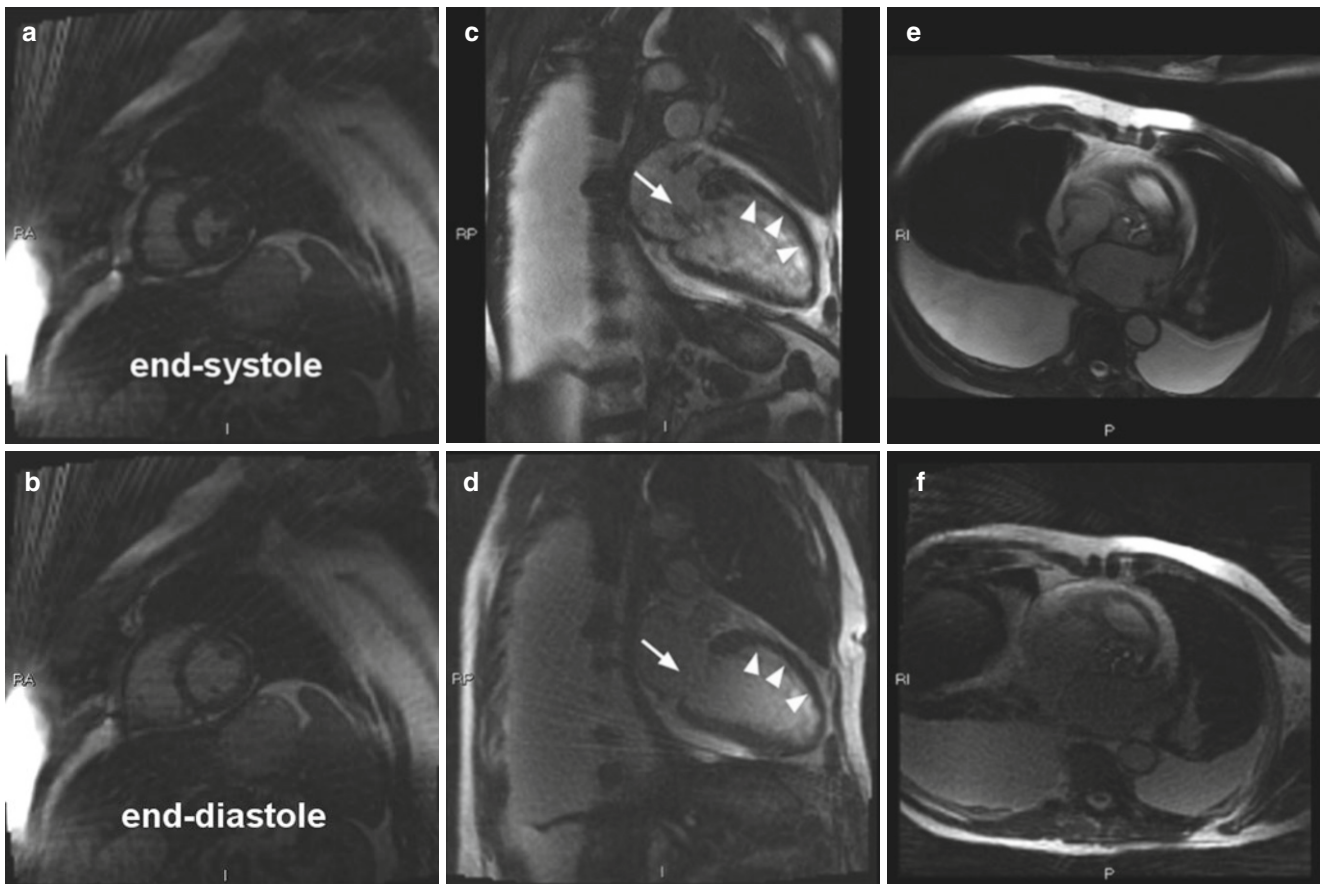


Fig. 9.13 Radial real-time images from a patient with slow atrial fibrillation and large pleural effusions allowed accurate assessment of ventricular function (a, b). Note the lower SNR and radial streaking artifact (a, b, d, f). Even in these cases, segmented imaging (c, e) should be

attempted for valve assessment because of greater spatial and temporal resolution. Note that mitral valve regurgitation is better seen with the segmented (c) acquisition compared to real-time (d)

non-gated single-shot sequence. A train of single-shot images is acquired sequentially to yield a series of images over multiple R-R intervals. Some versions, may be triggered by the first detected R-wave so that all images start at the same point, but the data is not gated or sorted to the cardiac cycle. Given the R-R variability across slice locations, cardiac events are not always on the same frame of the cine images. Thus 3D quantitative analysis is not readily possible with currently available software. Quantitative methods that use geometric assumptions such as Simpson's biplane method of discs could be applied with this technique. However, software packages to make such measurements are not readily available for CMR.

As a single-shot-based technique, real-time images have lower SNR, and lower spatial and temporal resolutions (Fig. 9.13; Video 9.6). A typical minimal temporal resolution is in the order of 50–60 ms, which is sufficient in the case of bradyarrhythmias, but may underestimate ventricular events during tachyarrhythmias. The total acquisition time should be adjusted to allow visualization of three to four heart beats for optimal visual assessment of cardiac function. The limited temporal and spatial resolution hinders accurate evaluation of valvular structure and function. Breath-holds

are not absolutely necessary, but help minimize respiratory motion and provide reproducible slice location.

Cardiac Self-Gating

Over the past 10–20 years there has been increasing motivation to develop ECG-free, non-breath-hold self-gating techniques. These methods are most valuable at high field strengths when MHD effects are most intrusive, but have the potential to significantly streamline daily clinical CMR workflow. There are multiple proposed methods for cardiac self-gating, and an advance discussion of this topic is beyond the scope of this chapter. Typically radial acquisition schemes are preferentially utilized because the gating information can be extracted from the imaging data without the addition of navigators [4]. A center point of the k-space can be tracked over time to plot a kymogram of the cardiac and respiratory cycles, which are then used to trigger the acquisition and sort the data (Fig. 9.14). Two and three-dimensional approaches have been used for self-gating [5]. Once the gating signal is obtained, image reconstruction follows similar principles as

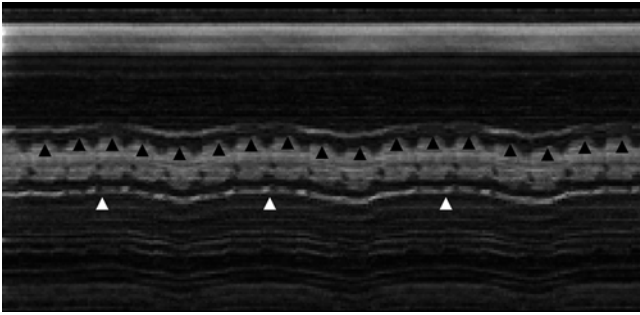


Fig. 9.14 The kymogram above illustrates how the cardiac (*black arrowheads*) and respiratory cycles (*white arrowheads*) are identified from the imaging data during a free-breathing acquisition

that of retrospective segmented sequences. However, this approach is potentially more robust to R-R variability. Free-breathing self-gated techniques eliminate the need for breath-holding, enabling longer data acquisition; hence more heart beats are sampled. R-R intervals outside a predetermined acceptance window are rejected and only data from cycles of similar duration are used to reconstruct the images. Currently, self-gating techniques remain a research tool, and are not widely available in a clinical setting.

Summary

Accurate ECG-gating is an essential component of every successful CMR study. Gating the image data to the cardiac cycle provides maximal accuracy of visual and quantitative

analysis of cardiac structure, contractile function and physiology. The concepts and troubleshooting recommendations discussed in this chapter, will allow the reader to tackle common technical and patient related factors that hinder ECG-gating. While real-time CMR allows diagnostic visual assessment of cardiac structure and function, it should be used with caution with an understanding of its limitations. Emerging self-gating techniques may ultimately eliminate the need for ECG-gating and permit free-breathing acquisitions.

References

1. Cordeiro JM, Greene L, Heilmann C, Antzelevitch D, Antzelevitch C. Transmural heterogeneity of calcium activity and mechanical function in the canine left ventricle. *Am J Physiol Heart Circ Physiol.* 2004;286:H1471–9.
2. Sievers B, Addo M, Kirchberg S, et al. Impact of the ECG gating method on ventricular volumes and ejection fractions assessed by cardiovascular magnetic resonance imaging. *J Cardiovasc Magn Reson.* 2005;7:441–6.
3. Fischer SE, Wickline SA, Lorenz CH. Novel real-time R-wave detection algorithm based on the vectorcardiogram for accurate gated magnetic resonance acquisitions. *Magn Reson Med.* 1999;42:361–70.
4. Paul J, Divkovic E, Wundrak S, et al. High-resolution respiratory self-gated golden angle cardiac MRI: comparison of self-gating methods in combination with k-t SPARSE SENSE. *Magn Reson Med.* 2014;73(1):292–298.
5. Liu J, Spincemaille P, Codella NC, Nguyen TD, Prince MR, Wang Y. Respiratory and cardiac self-gated free-breathing cardiac CINE imaging with multiecho 3D hybrid radial SSFP acquisition. *Magn Reson Med.* 2010;63:1230–7.

David C. Wendell and Robert M. Judd

Abstract

Cine cardiac imaging is the primary technique by which cardiovascular magnetic resonance (CMR) imaging characterizes regional and global contractile function of the heart and resulting blood flow through the great vessels. As such, cine imaging is of fundamental importance to clinical and research applications of CMR. The underlying technical challenge is to acquire high-quality images fast enough to characterize cardiac motion. A number of strategies have been developed to overcome this intrinsic challenge for MR-based imaging compared to real-time x-ray or ultrasound-based imaging. In general these strategies are highly successful, but typically involve trade-offs that vary somewhat depending on the health of the patient and the specific clinical question. In this chapter we review the fundamental principles of cine imaging, discuss the trade-offs associated with different strategies, and summarize these in the context of a typical CMR clinical service.

Keywords

Cine imaging • Contractile function • Cardiac magnetic resonance • Segmented k-space • Gradient echo imaging • Steady state free precession • Magnetic resonance imaging

Introduction

In general, magnetic resonance imaging can be divided into spin echo and gradient echo approaches. Compared to gradient echo imaging, spin echo imaging requires the use of a second, relatively time-consuming radiofrequency (RF)

pulse. Due to the need to image as fast as possible to characterize cardiac contraction, spin echo imaging is rarely used for cine cardiac imaging. Accordingly, spin echo imaging will not be described in this chapter.

Gradient echo imaging can be broadly divided into two categories, namely spoiled and refocused. In spoiled gradient echo imaging, the CMR signal derived from each radiofrequency excitation is independent of the CMR signal associated with previous RF excitations. From a technical perspective, a number of different strategies can be used to spoil or “erase” this historical dependence of the CMR signal. In refocused gradient echo imaging, conversely, an active attempt is made to preserve the CMR signal from RF pulse to RF pulse. This refocused state is relatively difficult for the CMR scanner hardware to achieve, but yields a significant increase in signal-to-noise ratio resulting in improved image quality. Both spoiled and refocused gradient echo imaging play an important role in CMR, and both are described in detail here following a brief introduction to the basic principles common to both.

Electronic supplementary material The online version of this chapter (doi:[10.1007/978-3-319-22141-0_10](https://doi.org/10.1007/978-3-319-22141-0_10)) contains supplementary material, which is available to authorized users.

D.C. Wendell, PhD
Department of Medicine/Cardiology, Duke Cardiovascular
Magnetic Resonance Center, Duke University Medical Center,
Durham, NC, USA
e-mail: david.wendell@duke.edu

R.M. Judd, PhD (✉)
Department of Medicine, Duke Cardiovascular Magnetic
Resonance Center, Duke University Medical Center,
Durham, NC, USA
e-mail: Robert.judd@duke.edu

Gradient Echo Imaging

Gradient echo imaging is a method of creating an MR image by imposing a magnetic field gradient across the desired imaging volume, and measuring resultant frequencies to encode frequency components from a given region. The pulse sequence is designed such that the readout gradient dephases the transverse magnetization, and then re-phases the magnetization to create an echo. The components of the gradient echo pulse sequence are outlined in Fig. 10.1, including RF pulse, slice, phase, and read encoding gradients.

What Is the FID?

Once the externally-applied RF signal has ended, H^1 spins will realign such that the net magnetic moment (M) is parallel to B_0 . During relaxation these H^1 spins lose energy by emitting their own RF signal, which is referred to as the free-induction decay (FID) response signal. These FIDs are measured by the receive coils placed around the body. The strength of the FID is dependent on the proton density of the tissue being imaged, the longitudinal relaxation time (T_1), and the transverse relaxation time (T_2). In theory, T_2 can be measured directly as the mono-exponential decay rate of the signal in a perfectly homogeneous magnetic field. By purposely applying magnetic field gradients, for example by

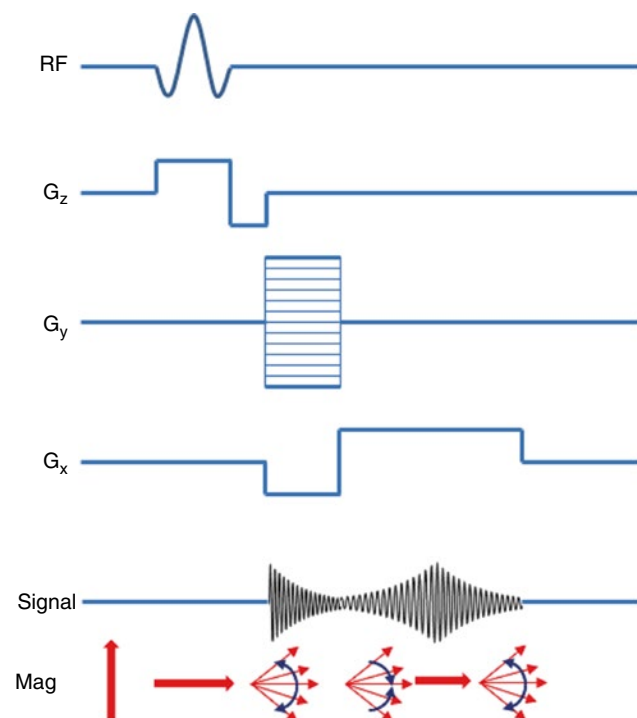


Fig. 10.1 GRE pulse sequence with resulting magnetization displayed at the *bottom*

slightly increasing the magnetic field experienced by the left side of the patient's body compared to the right side, the signal is forced to decay more quickly. Subsequent reversal of the gradient direction from left-right to right-left causes the formation of echoes (Fig. 10.1: Signal). The frequency components of these echoes contain information about spatial location, i.e. information regarding how much signal originated from the left versus right side of the patient's body, and therefore can be used to build an image.

What Are Echoes?

Unlike in a traditional spin-echo pulse sequence that uses 180° refocusing pulses, a gradient echo pulse sequence requires a bipolar readout gradient. This is achieved by first applying a dephasing gradient followed by the frequency-encoding readout gradient. The dephasing stage is inverse in sign and half the area of the frequency encoding gradient (see Fig. 10.1: G_x). This is designed such that the first half of the frequency-encoding gradient inverts the dephasing created by the negative lobe, and the peak of the echo occurs at the middle of the readout gradient (i.e. echo time (TE), Fig. 10.1: Signal).

Spoiled Gradient Echo Imaging (SPGR, FGRE, etc.)

The T_1 and T_2 times in the tissues involved in cardiac imaging are generally in the range of tens to hundreds of milliseconds. This means there is significant signal remaining in the transverse plane for repetition times normally used in cardiac imaging. In order to allow for fast cardiac imaging using GRE pulse sequences, the remaining magnetization should be 'spoiled' so it does not contaminate subsequent phase encoding steps. This can be accomplished either with gradient spoiling, which allows for shorter overall TR, or RF spoiling, which can facilitate T_1 weighting throughout the image acquisition.

Gradient Spoiling (Shortens TR)

Gradient spoiling is commonly used in cardiac imaging to destroy the residual transverse magnetization following each readout (Fig. 10.2). This is necessary to prevent transverse magnetization from previous RF pulses from contaminating subsequent readouts (known as stimulated echoes). The downside of gradient spoiling is the dephased spins no longer contribute to subsequent MR signals. Since the T_1 and T_2 of myocardium and blood are long, and TR is short, low flip angles are necessary to prevent loss of signal due to gradient spoiling [1].

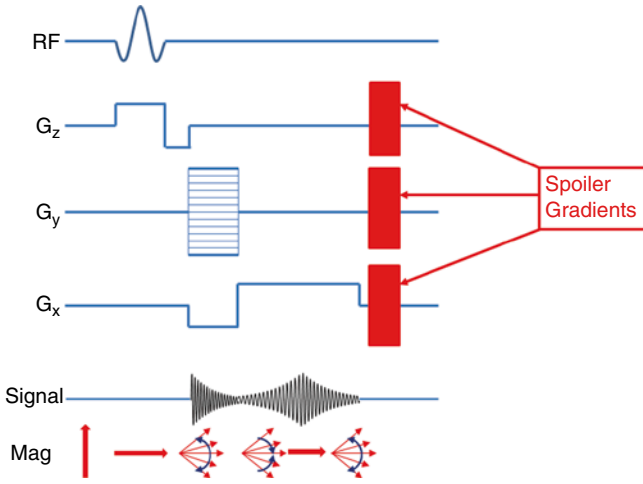


Fig. 10.2 Spoiled GRE pulse sequence showing spoiler gradients added at the end of each RF pulse

RF Spoiling

RF spoiling can also be referred to as RF pulse phase cycling. This takes advantage of the fact that the RF pulse can be played at any phase (i.e. direction in the x-y plane) and the refocusing occurs at that phase location. Therefore, if the RF pulse is played at a random phase, the likelihood that a stimulated echo will rephase at the same location is greatly reduced. In most practical applications the RF pulses played in a series of TRs are pseudo-random, incrementing phase quadratically to provide better spatially and temporally invariant spoiling than either gradient spoiling or completely random RF spoiling [2].

Signal Equation

The signal for a spoiled-GRE sequence depends on sequence-selectable variables (TR, TE, and flip angle (α)), along with three variables intrinsic to the tissue being imaged (T_1 , T_2^* , and spin density [H]). We have introduced a new term, T_2^* , rather than T_2 since the spoiled-GRE sequence does not account for field inhomogeneities as a spin-echo sequence would. Assuming we have reached a steady-state (see below) and have achieved perfect spoiling, the signal (S) of a spoiled-GRE sequence is given in Eq. 10.1

$$S = k[H] \frac{\sin \alpha (1 - e^{-TR/T_1})}{(1 - (\cos \alpha) e^{-TR/T_1})} e^{-TE/T_2^*} \quad (10.1)$$

where k is a scaling factor. The first term ($k[H]$) accounts for spin-density effects, the second term contributes to the T_1 weighting of the image, and the third term contributes to T_2^* weighting. From this, it is clear to see how α , TR, and TE contribute to T_1 and T_2^* weighting in spoiled-GRE sequences.

As α decreases, the T_1 effect is reduced ($1 - e^{-TR/T_1}$ term cancels), and we are left with [H] and T_2^* . If TR is long and TE is minimized, we are left with a proton-density weighted image. As the TE is increased, the amount of T_2^* weighting is increased. Conversely, as TR is decreased the amount of T_1 weighting actually increases (e^{-TR/T_1} term becomes large). Finally, if the TE is kept short (minimize T_2^*) and TR is short as well, α can be used to increase T_1 weighting as is given below [3].

To obtain the maximum signal, the optimal flip angle, called the Ernst angle (α_E), can be calculated by setting $dS/d\alpha = 0$ above.

$$\alpha_E = \arccos(e^{-TR/T_1}) \quad (10.2)$$

Saturation and In-Flow Effects

Using the explanation of spoiled-GRE signal and optimal flip angle above, it is easy to see how an aggressively high flip angle would tend to saturate the resulting spoiled-GRE signal. This saturation is more noticeable with shorter repetition times as are used for cardiac imaging. Basically, the acquisition is not allowing enough T_1 recovery between high flip angle RF pulses, so the majority of the MR signal is being spoiled, thus no longer contributing to subsequent MR signals.

The preceding derivation assumes everything within the imaging space has reached a steady-state. A more detailed description of steady-state imaging is provided below. For the discussion on inflow effects let's assume we are operating in a steady-state regime, which means the M_z signal returns to a consistent level between RF pulses. Now, assume there is inflowing blood from another part of the body, which has not been exposed to these RF pulses, and thus enters the imaging plane with a higher starting M_z than in-slice tissue. This results in a portion of the imaging plane not being in steady-state which manifests itself as signal inhomogeneities throughout the image (see blood pool in Fig. 10.3). The severity of this artifact is related to the tissue characteristics and imaging parameters chosen. The more saturated the steady-state signal (increased α , decreased TR), the larger the difference in M_z between steady-state and inflowing tissue, the more heterogeneous the signal appears [4].

Time to Steady State and the Role of Dummy Heartbeats

Performing spoiled GRE imaging requires the transverse and longitudinal magnetization to have achieved a steady state. This limits the fluctuation in magnetization from one RF

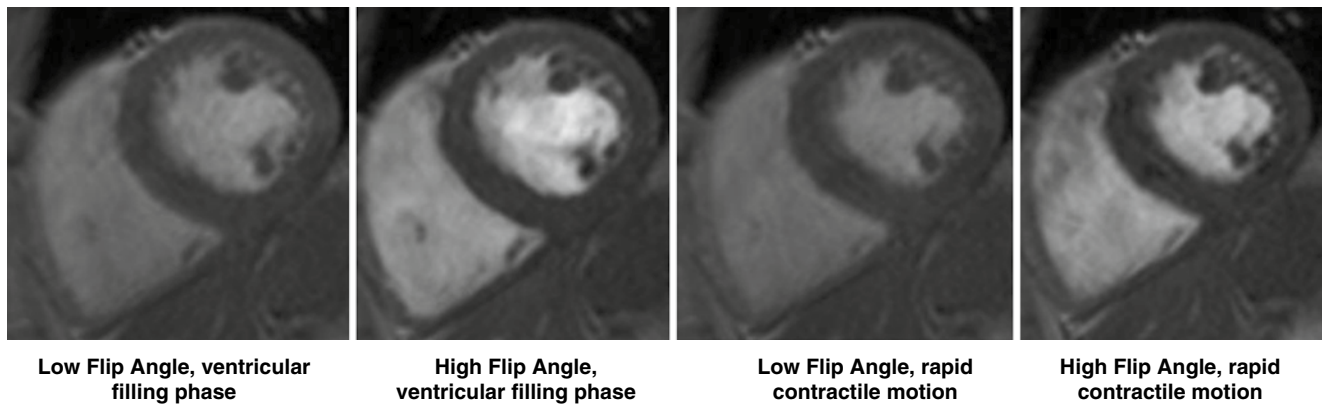


Fig. 10.3 Effects of high flip angle on spoiled GRE cine imaging. Note the heterogeneous blood signal during ventricular filling phase (*left*) due to inflowing spins. *Right*: myocardial heterogeneity due to rapid cardiac motion during relaxation

pulse to the next. The time it takes to reach a steady state depends on the MR parameters chosen (TR and flip angle) and inherent tissue properties such as T_1 .

To determine how many dummy RF pulses are required to reach steady-state, an experiment of repeated measures (RF pulses) can be performed empirically for a given set of tissue parameters. For example, the number of RF pulses required to reach 95 % of steady-state spoiled GRE signal for myocardium ($T_1 = 1,000$ ms, $T_2 = 45$ ms), with a TR/TE/flip angle of 10/2/15°, is 87 RF pulses (87×10 ms = 870 ms). For a patient with normal sinus rhythm (60–70 bpm), this would be one heartbeat worth of dummy pulses [5].

Dummy heartbeats can be included at the start of an acquisition to drive the spoiled GRE signal to steady-state prior to data acquisition. This is realized in the example described above. In this case a single heartbeat of dummy RF pulses would be sufficient to reach 95 % of the steady state signal. The number of dummy heartbeats can be adjusted as well due to differences in tissue T_1 , flip angle, TR, and patient heart rate. The accepted steady state tolerance may be decreased (from 95 % above, to 85 %), to prevent increasing overall scan time.

SNR Considerations for Rapid Imaging

Some compromises become necessary to perform rapid clinical cardiac MRI, for example, sacrifices in SNR in order to acquire the necessary data in a timely manner. Most of the acceleration techniques have a similar goal: to decrease the number of phase-encoding lines (and hence, RF pulses) required to reliably reconstruct an image. Non-symmetric fields of view or matrix dimensions can reduce the number of phase encoding steps required with no inherent loss in SNR. However, acquiring only a portion of k-space, either through partial Fourier acquisition, or acceleration techniques

such as GRAPPA or mSENSE, inherently alters the noise signature throughout the image and reduces SNR. Both of these techniques undersample the phase-encoding data during acquisition, and estimate the missing data during reconstruction. The resulting post-processed lines are created using these acquired lines. Therefore, the fewer true k-space lines acquired, the lower the overall SNR (reduced signal and increased noise).

Effect of Chemical Shift and Off-Resonance Effects

The Larmor frequency of a given H^1 spin can be calculated empirically from the gyromagnetic ratio (γ) and the B_0 field strength. However, H^1 spins behave differently depending on their chemical environment. For example, the Larmor frequency commonly associated with H^1 spins is calculated from water molecules. Chains of fatty acids have a different chemical environment, and hence a slightly different gyromagnetic ratio. This causes H^1 spins in fat to resonate at a slightly different frequency from water (220 Hz at 1.5 T, 440 Hz at 3.0 T).

This can be imagined as two wheels spinning at slightly different rates. The signal received by the scanner is combined of spins in fat and in water, but the scanner expects to receive a signal at the water H^1 Larmor frequency. Recall, frequency encoding gradient is used to record the excited spins from the imaged volume. If the H^1 spins in fat are precessing at a slightly different frequency, they will be localized to a slightly different position, or “shifted” along the frequency-encoding direction (Fig. 10.4).

Obviously the mis-localization of fat can be problematic if it obscures anatomy, or worse, is confused with pathology (i.e. fat within the myocardium). Therefore, adjustments in receiver bandwidth can reduce the amount of chemical shift

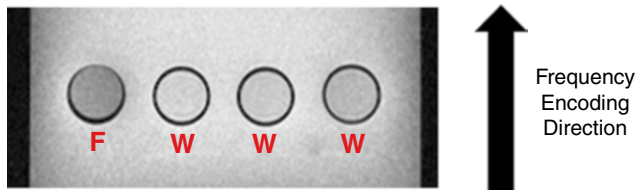


Fig. 10.4 MRI phantom showing chemical shift artifact (*F* fat, *W* water). With the frequency encoding direction from bottom to top, the fat tube (*F*) appears to be shifted 1–2 pixels higher than the water tubes. In reality, all tubes are in line

that occurs in an image. As an example, assume 1.5 T and a fat/water difference of 220 Hz. If our readout bandwidth is 220 Hz/pixel, then the fat will shift a full pixel in the frequency encoded direction, potentially confounding image interpretation. If the bandwidth were increased to 440 Hz, this shift would only be 0.5 pixels and the effect on image interpretation can be reduced [6].

Along the same lines as chemical shift artifacts, off-resonance effects can cause similar artifacts. In fact, chemical shift artifacts can be considered one specific type of off-resonance effect. In general, anything which causes a spin to precess at a resonant frequency which is different from its Larmor frequency can cause an off-resonance artifact. Off-resonance effects occur wherever a magnetic field gradient is present within the body. This could either be from intrinsic properties in the body (i.e. the “magnetizability” of tissue), or extrinsic sources such as eddy currents (produced from switching gradient coils on/off) or concomitant gradients (magnetic field changes orthogonal to applied magnetic field gradients). Overall, these effects result in a loss of signal in certain areas of the image due to a majority of H^1 spins no longer precessing at the expected frequency. These can manifest themselves as spatial distortion (images appear warped), signal loss (at interfaces between tissue and lung), blurring, or overall signal heterogeneity (similar tissue appears bright or dark throughout the image) [7].

Parameter Selection (BW, FA/Ernst Angle, TE, TR, Scan Time, etc.)

When setting up a clinical cine CMR study, certain trade-offs come into play when optimizing spatial and temporal resolution, SNR, scan time, breath-hold capability, and overall image quality. As described below, the top requirement of cine MRI would be to capture the fastest phases of cardiac motion during contraction and relaxation of the ventricle. This requires high temporal resolution on the order of about 20 cine frames per cardiac cycle. If the temporal resolution is too low the tradeoff is missing peak systole causing an overall underestimation of ejection fraction, blurring of

myocardium during cardiac motion, and inability to visualize wall motion abnormalities.

The required temporal resolution can be calculated by taking the patient’s average R-R interval, divide by 20 cine frames, and this produces the required temporal resolution. For example, a heart rate of 75 bpm is ~850 ms interval, if 20 cine frames are required, then the temporal resolution should be at least 42.5 ms. More details on setting optimal temporal resolution are included below.

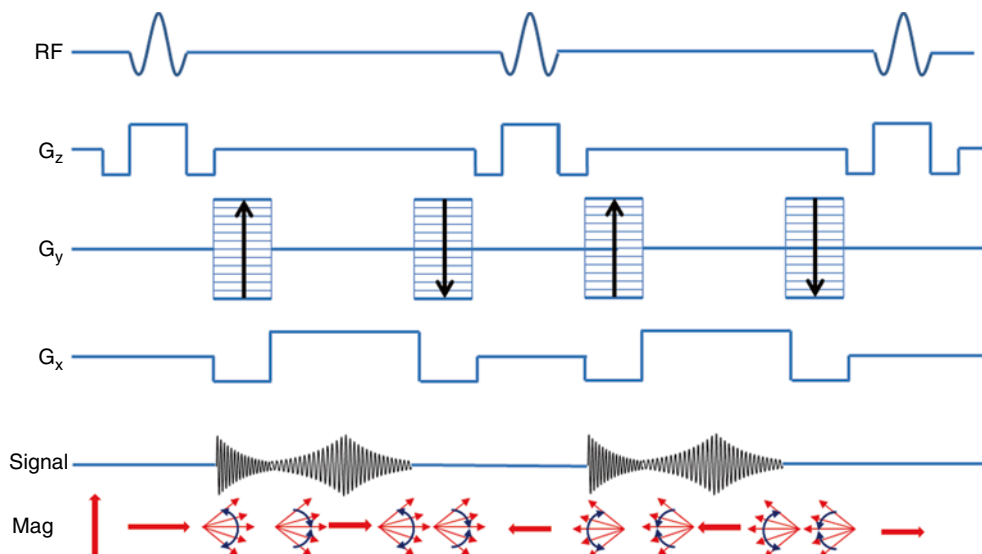
Another way to optimize signal in a spoiled GRE image are to calculate the Ernst angle, which was described in Eq. 10.2 above. TE and TR need to be minimized in order to allow for increased imaging speed and reduction in breath-hold duration. Increasing the bandwidth can reduce the chemical shift artifact. The trade-off of increasing the bandwidth is a decrease in SNR. Finally, spatial resolution needs to be of a level where one can reliably delineate the border between the blood pool and myocardium, and the myocardial wall itself. Sacrificing spatial resolution for reduced scan time may limit the number of imaging voxels present across the myocardium, which may cause blurring of the myocardium during the most vigorous cardiac motion.

Balanced Steady-State Free Precession (bSSFP)

One method to overcome the limitations of spoiled GRE imaging is, instead of destroying transverse magnetization after each RF pulse, the magnetization can be “recycled” to increase SNR and image contrast between blood and myocardium. The approach, referred to as balanced steady state free precession (bSSFP) imaging, can be thought of as a hybrid of a GRE image and a spin-echo image. The RF pulses are played at a flip angle which oscillates from pulse to pulse, the spacing between RF pulses is double the echo time, and imaging gradients are perfectly matched between RF pulses. This results in magnetization that perfectly refocuses at each TE and eliminates the loss of signal seen in spoiled GRE imaging (Fig. 10.5) [8].

bSSFP imaging has become the predominant cine imaging technique in most patients due to its high SNR, fast imaging speed, reduced flow dependency, and excellent blood to myocardium contrast. There are some caveats to these advantages. High flow velocity, metallic structures, and B_0 inhomogeneities can cause severe artifacts in bSSFP imaging. Because the magnetization is refocused there is a “history” present with the H^1 spins. Specifically, since spins are continually being refocused, if a spin is out of phase with other spins, the refocusing occurs at an arbitrary orientation, leading to signal loss. This is why artifacts from high velocity blood or metal implants are propagated through the image (see Video 10.1).

Fig. 10.5 bSSFP pulse sequence showing RF pulses, balanced gradients for slice encoding (G_z), phase encoding (G_y), and frequency encoding (G_x). Relative signal during each readout event (Signal), and resulting magnetization from each pulse sequence component (Mag)



Signal Equation

The signal for a bSSFP sequence depends on sequence-selectable variables (TR, TE, and flip angle (α)), along with three variables intrinsic to the tissue being imaged (T_1 , T_2 , and M_0). The steady-state equation for bSSFP signal is given in Eq. 10.3 below.

$$M_{ss} = M_0 \frac{\sqrt{\sin \alpha (e^{-TR/T_2}) (1 - e^{-TR/T_1})}}{1 - (e^{-TR/T_1} - e^{-TR/T_2}) \cos \alpha - (e^{-TR/T_1} e^{-TR/T_2})} \quad (10.3)$$

For short TR ($TR \ll T_1$ or T_2), which is the case for cardiac imaging, the exponentials in Eq. 10.3 can be approximated to $1 - TR/T_1$ and $1 - TR/T_2$, respectively. So Eq. 10.3 reduces down to:

$$M_{ss} = M_0 \frac{\sin \alpha}{\left(\frac{T_1}{T_2} + 1\right) - \cos \alpha \cdot \left(\frac{T_1}{T_2} - 1\right)} \quad (10.4)$$

It can be seen from Eq. 10.4, that the signal generated from a bSSFP image relies solely on flip angle (α) [8]. Therefore, to optimize signal from tissues, the Ernst angle (α_E) can be calculated as follows:

$$\alpha_E = \arccos \left(\frac{T_1 - T_2}{T_1 + T_2} \right) \quad (10.5)$$

SNR is increased by the re-wound gradients seen in Fig. 10.5 and in tissues with a T_2/T_1 ratio close to 1 (i.e. blood has a T_2/T_1 of 0.15 v. myocardium which is 0.0375).

Saturation and Inflow Effects

Fortunately, since the “recycling” feature of bSSFP imaging retains some of the magnetization, a high flip angle does not

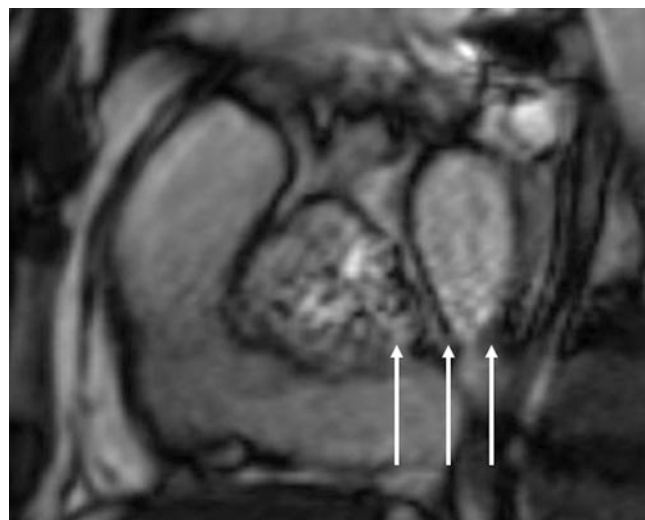


Fig. 10.6 Ringing in the frequency-encoding direction (arrows) due to high, fully relaxed blood signal entering the imaging plane in bSSFP imaging

have the saturation effect seen in spoiled GRE imaging. However, the likelihood of reaching specific absorption rate (SAR) limits, i.e. exposing the patient to excessive RF radiation, prohibits excessively high flip angles.

One common artifact seen in bSSFP imaging pertains to inflowing blood. Because by definition the MRI signal needs to be at steady-state, any spins entering the imaging plane which are not at steady state result in a larger starting M_0 than spins within the imaging slice. This discrepancy can cause ringing artifacts throughout the image in the phase-encoding direction (see Fig. 10.6). The main difference in inflow effects in bSSFP imaging compared to spoiled GRE imaging is the inherent “history” in the SSFP signal. Since magnetization is continually refocused, the discrepancy between incoming and steady state spins persists until the incoming spins reach steady state. The severity of this

artifact is related to the tissue characteristics and imaging parameters chosen. The higher the velocity of incoming blood the more discrepant the starting magnetization, and the more dramatic the artifact. Imaging parameters such as higher flip angles, or longer TR (and inherently TE since $TR=2 \times TE$ for bSSFP imaging), can exacerbate these artifacts as well [9].

Prep Pulses and Time to Steady State, Dummy Heartbeats

Similar to the discussion in the spoiled GRE section, bSSFP imaging requires the magnetization to have reached at steady state. The fluctuations in magnetization from one RF pulse to the next can have detrimental effects on image quality, especially since traveling spins tend to have a “memory” from previous RF pulses. As described above, the first RF pulse played is actually $\alpha/2$ followed by a series of α pulses which oscillate from $+x$ to $-x$ to establish a steady-state. The number of the pulses required to reach steady state depend on TR, flip angle, and tissue properties (T_1).

The method to determine the number of RF pulses required to reach steady state can be determined implicitly. For example, if we assume a threshold of 95 % of steady-state signal, the signal from myocardium ($T_1=1,000$ ms, $T_2=45$ ms), and a TR/TE/flip angle of 3/1.5/50°, then the number of RF pulses required to reach steady state is 76. However, most scanners will ramp up the beginning RF pulses to eliminate the high oscillations associated with these sequences. For example, 10 RF pulses at increasing flip angle may be used at the start of the sequence to more smoothly drive the signal to a steady state. Using this scheme, the number of leading RF pulses can be reduced to 46, well within a single dummy heartbeat [10].

SNR Efficiency/Fast Imaging

The bSSFP sequence itself is inherently faster than spoiled GRE imaging due to the shorter repetition time and higher bandwidth. High bandwidth imaging tends to reduce overall SNR, but the higher flip angle implemented within bSSFP imaging compensates for some of this loss. Similar acceleration techniques are still employed within cine cardiac imaging using bSSFP sequences to reduce imaging time and create reasonable breath hold durations. The overall goal in reducing imaging time is undersampling of k-space lines in the phase encoding direction. Accelerated imaging can be obtained by intuitively prescribing imaging planes, for example, orienting the phase-encoding direction along the narrower dimension of the image (anterior/posterior direction). This allows non-symmetric fields of view or matrix dimensions to reduce the number of phase encoding lines without the risk of image wrap obscuring anatomy. Other

techniques such as acquiring only a portion of k-space, either through partial Fourier acquisition, or acceleration techniques such as GRAPPA or mSENSE, inherently alters the noise signature throughout the image and reduces SNR. These techniques selectively undersample k-space data using an algorithm which allows the back-calculation of the missing k-space data to avoid image wrap. In brief, these techniques acquire a central core of k-space lines around $k_x = 0$ (24–36 lines), and then selectively undersample k-space lines moving outward towards higher k_y lines. The scheme can either sample every other line (referred to as GRAPPA 2), or the algorithm can sample only every third line (GRAPPA 3). Both techniques will reconstruct the imaging data by filling in the missing k-space lines using the data acquired from prior and subsequent k-space lines. However, the fewer acquired lines, and the more interpolated lines, the more the image will suffer from increased noise, decreased SNR, and imaging artifacts. Therefore, the fewer true k-space lines acquired, the lower the overall SNR (reduced signal and increased noise).

Effects of Chemical Shift and Off Resonance

Chemical shift artifacts and off resonance effects become more noticeable due to the tight timing constraints on bSSFP imaging, and the “memory” encoded into spins as they are imaged repeatedly using the bSSFP sequence. Chemical shift effects were discussed in the spoiled GRE section, but a different type of chemical shift is present in bSSFP imaging. Pass bands were described previously in relation to the appearance of stop-bands within bSSFP images. It turns out that, because of the bandwidth used in bSSFP imaging, the signal peaks from water and fat (440 Hz/pixel at 3 T) occur in opposite frequency lobes. This results in signal loss at the interfaces between fat and water. This “india ink” artifact is due to the presence of fat and water within the same voxel in the image. If we assume a 50/50 fat/water voxel in a bSSFP image, where fat and water are out of phase with each other, the sum of the vectors within this voxel adds up to zero (Fig. 10.7).

Off resonance effects have a large impact on bSSFP cine imaging. The timing between RF pulses in the “balanced” SSFP is set such that spins are refocused at each echo time. The off-resonance effects within the image cause changes in the magnetic field, which cause spins to precess at a different rates, thus inhibiting the refocusing that is essential to bSSFP imaging. These effects can be seen as dark bands throughout the image either near tissue interfaces, near metallic implants, or regions of high flow. Figure 10.8 shows dephasing artifacts in bSSFP imaging due to high flow through aortic regurgitant orifice (top) and aortic stenosis (bottom). Dephasing of spins near metallic implants propagate throughout the image in bSSFP imaging (Fig. 10.9), but are contained to the region surrounding the metallic implant in spoiled GRE imaging (Fig. 10.9, Video 10.1 and 10.2).

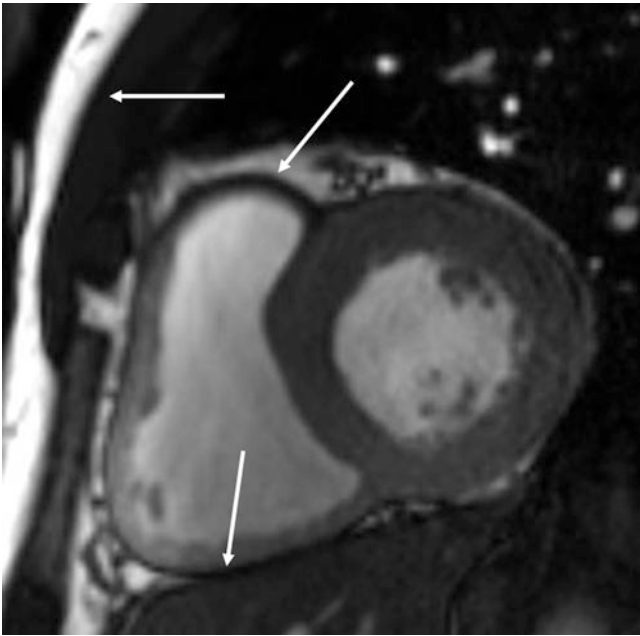


Fig. 10.7 bSSFP cine imaging showing chemical shift artifact (arrows) due to water and fat occupying the same voxel causing signal cancellation

The presence and location of artifacts from off-resonance effects can be reduced by creating a more homogeneous magnetic field through magnet shimming, decreasing the repetition time (which increases the spacing between stop bands), or applying a frequency shift which moves the stop bands out of the imaging area of interest [10].

Parameter Selection (BW, FA/Ernst Angle, TR, TE, Frequency Scout)

Overall, the goal of parameter selection for bSSFP imaging is rapid imaging, good myocardial/blood contrast, adequate spatial and temporal resolution, and high SNR. The high temporal resolution is achieved by reducing the TR (and TE, which is $1/2 \times TR$ for bSSFP) by increasing the bandwidth. The decrease in SNR due to the higher bandwidth in bSSFP imaging is counteracted by the high flip angles available due to spin “recycling.” The flip angle does have an upper limit, which is related to SAR.

Temporal and spatial resolutions need to be optimized similar to spoiled GRE imaging. High temporal resolution is necessary to accurately capture rapid systolic motion of the heart. To visualize small structures, high spatial resolution is required as well. The benefit of bSSFP over spoiled GRE is the short TR allows for better spatial and temporal resolution without extending imaging time and breath hold duration.

The overall benefits of bSSFP over spoiled GRE are high SNR, good conspicuity of myocardium and blood, and shorter breath hold imaging. However, susceptibility artifacts pose a larger challenge due to the “memory” inherent to

bSSFP imaging. Therefore, for most cine imaging studies, bSSFP is the desired imaging sequence, but in situations where metal artifacts, B_0 inhomogeneity, or inflow artifacts obscure the structures of interest, spoiled GRE imaging can be used. The drawbacks of lower myocardial/blood contrast and longer scan times may offset some of the difficulties associated with imaging artifacts. These effects may be more prominent at 3 T. The trade-offs with specific consideration to cardiac imaging will be discussed in the next section.

Cardiac Imaging

For both spoiled and refocused gradient echo imaging approaches, modern CMR scanner hardware can typically achieve a repetition time (TR) between RF excitations of roughly 3–8 ms. The number of excitations (k-space lines) needed to obtain reasonable image spatial resolution of the human heart is roughly 120–180. Even with a TR of 3 ms and only 120 k-space lines, total imaging time is 360 ms, yielding approximately three images per second. This temporal resolution is too slow to examine cardiac contraction.

The most widely used approach to address this limitation is segmented k-space data acquisition, first described by Edelman et al. in the late 1980s [11]. The underlying concept is similar to that used for gated SPECT. Specifically, the image data are acquired over several consecutive cardiac cycles, and then combined during image reconstruction to produce a composite movie loop depicting a single cardiac cycle. In practice the CMR data are typically acquired while the patient holds their breath in order to eliminate respiratory motion, and total acquisition time for a single movie loop is typically 8–12 s. Breath hold image acquisitions typically result in movie loops comprised of 16–24 movie frames across the entire cardiac cycle (systole and diastole).

Segmented k-Space

The basic principles of segmented k-space imaging are shown in Fig. 10.10. Note that k-space represents the raw data for the image, such that filling the lines of k-space is synonymous with acquiring the resulting image (the gray-scale image is obtained by performing a two dimensional Fourier transform on the k-space data).

In PANEL A of Fig. 10.10, the patient has just started holding their breath, and the first cardiac cycle has begun. At this time k-space lines 1, 2, 3, and 4 of the first movie frame are acquired. Rather than continuing to acquire k-space lines 5, 6, 7, etc. of the first movie frame, however, the CMR scanner is programmed to acquire lines 1, 2, 3, and 4 of the second movie frame (PANEL B of Fig. 10.10). This process continues until lines 1, 2, 3, and 4 of all movie frames have been acquired, which is timed to complete at the end of the first cardiac cycle.

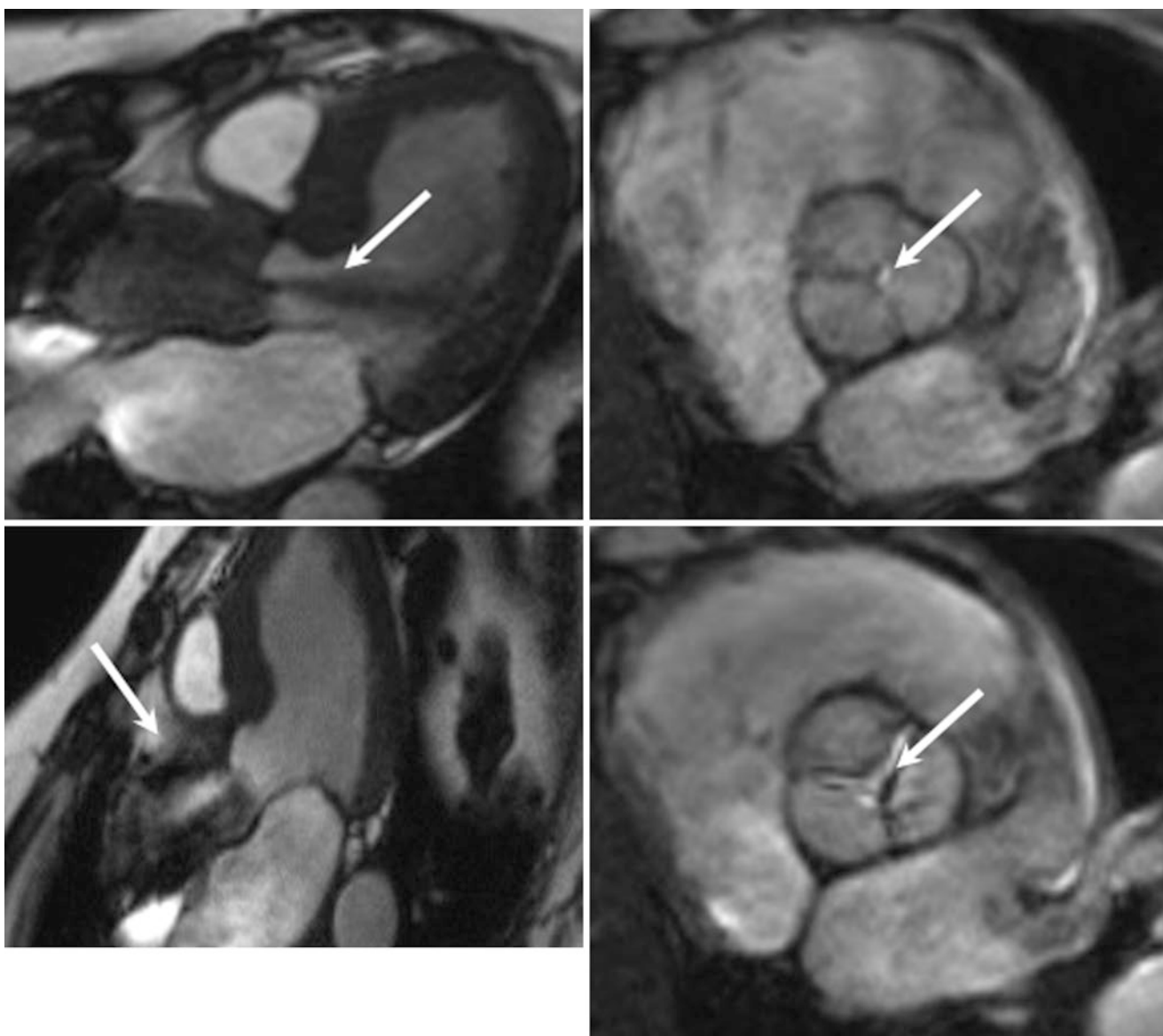


Fig. 10.8 bSSFP cine imaging showing dephasing of spins (*arrows*) due to high flow in a patient with aortic insufficiency (*top*) and a patient with aortic stenosis (*bottom*) (en face view of aortic valve shown at *right*)

At this point (end of first cardiac cycle) all movie frames have some k-space data (lines 1, 2, 3, and 4), but no movie frames have all k-space data (no lines 5 or greater).

In PANEL C of Fig. 10.10 the second cardiac cycle begins, and lines 5, 6, 7, and 8 of the first movie frame are acquired (lines 5–8 are white, lines 1–4 are red). In PANEL D of Fig. 10.10, lines 5, 6, 7, and 8 of the second movie frame are acquired. At the end of the second cardiac cycle all movie frames have 8 k-space lines (lines 1–8).

This process continues during subsequent cardiac cycles until all movie frames have all k-space lines, at which point the grayscale movie loop depicting cardiac contraction can be reconstructed by applying a two dimensional Fourier transform to the raw k-space data.

The basic equations used by the CMR scanner to segment k-space are:

$$\text{Heart Beats} = \frac{\text{Total Lines}}{\text{Segments}}$$

$$\text{Number of Movie Frames} = \frac{\text{Acquisition Window}}{(\text{Segments} \cdot \text{Time Per Line})}$$

Perhaps the most important variable in these equations is “segments”, which represent the number of k-space lines acquired for each movie frame in a single cardiac cycle. In the example of Fig. 10.10, segments = 4.

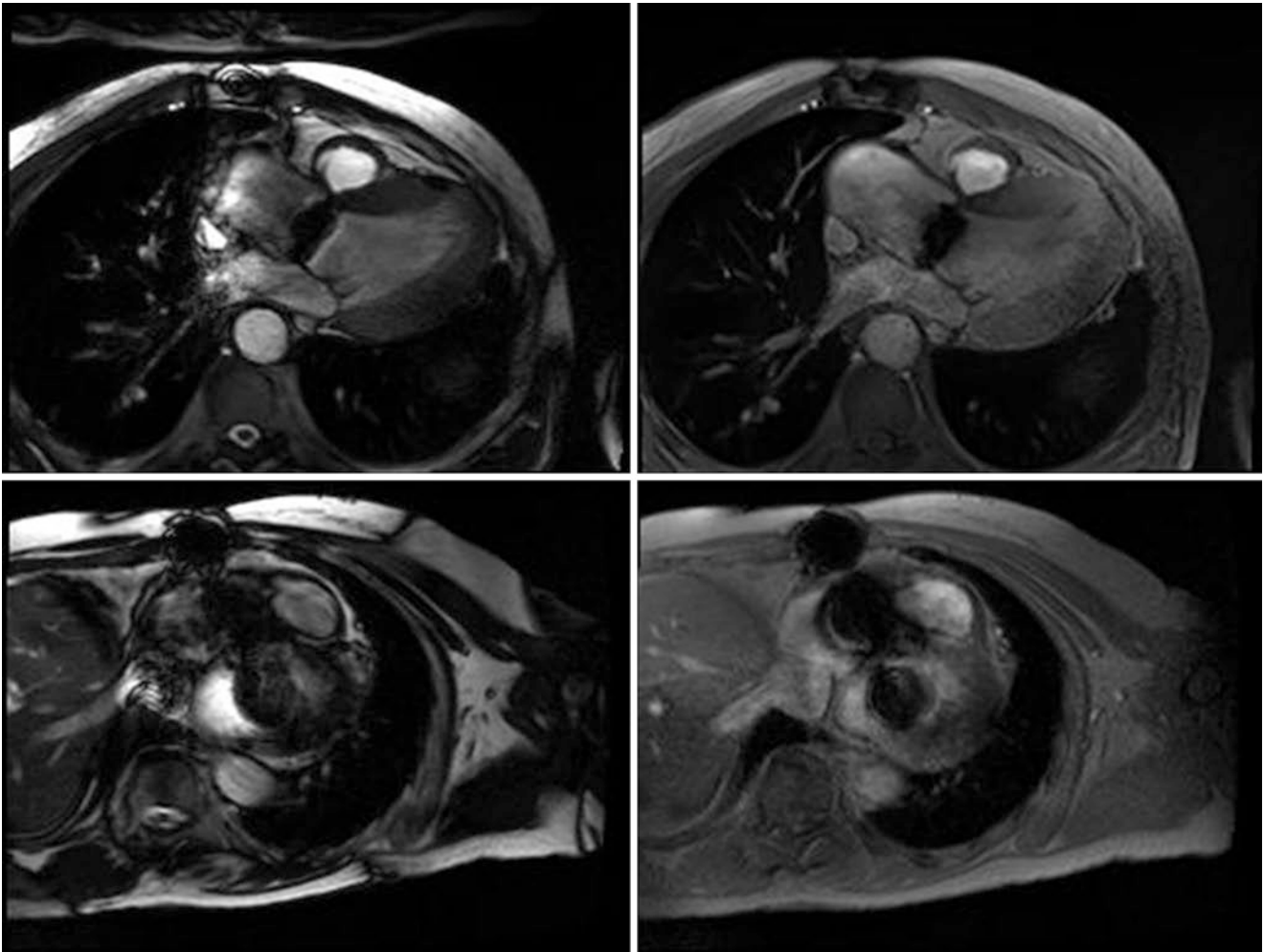


Fig. 10.9 bSSFP cine imaging showing dephasing of spins due to metallic implants (*top*: mechanical aortic valve, *bottom*: mechanical aortic and mitral valve). bSSFP show large artifacts obscuring most

heart structures, spoiled GRE (*right*) show localized artifacts with the majority of cardiac structures visible

Typical values for “total lines” and “segments” would be 192 and 14. Using the first equation with these values, breath hold duration would be 14 heart beats (192/14). Using the second equation, and assuming a typical value of 750 ms for the “acquisition window” (essentially the cardiac R-R interval) and a value of 3 ms for “time per line” (the TR for a bSSFP imaging pulse sequence), the number of movie frames would be 20 ($750 / \{14 \times 3\}$). In a clinical setting the CMR scanner operator would adjust these values based on the patient’s heart rate and the patient’s ability to repeatedly hold their breath in order to obtain the best image quality with the most movie frames.

Breath-Holding

Clinical imaging generally involves choosing the best trade-offs for the current patient. If the patient is relatively healthy

and can hold their breath for 15–20 s, more movie frames and/or images with better spatial resolution (more “total lines”) can be acquired. It’s important to recognize, however, that each movie requires a separate breath hold, and that the patient will need to hold their breath many times during the overall 30–60 min CMR procedure. In clinical practice we have found that even relatively ill cardiac patients can repeatedly hold their breath for 10 s, corresponding to roughly 18 movie frames and 2 mm spatial resolution for a typical modern CMR scanner.

For those patients that cannot hold their breath, and/or have irregular heart rates due for example to atrial fibrillation, segmented k-space image acquisition cannot be used. In these patients the only practical approaches involve sacrificing image quality. Perhaps the most common approach for patients that cannot breath hold is sacrificing image signal-to-noise and spatial resolution to the point where poor-quality images are acquired every 100 ms (ten images per

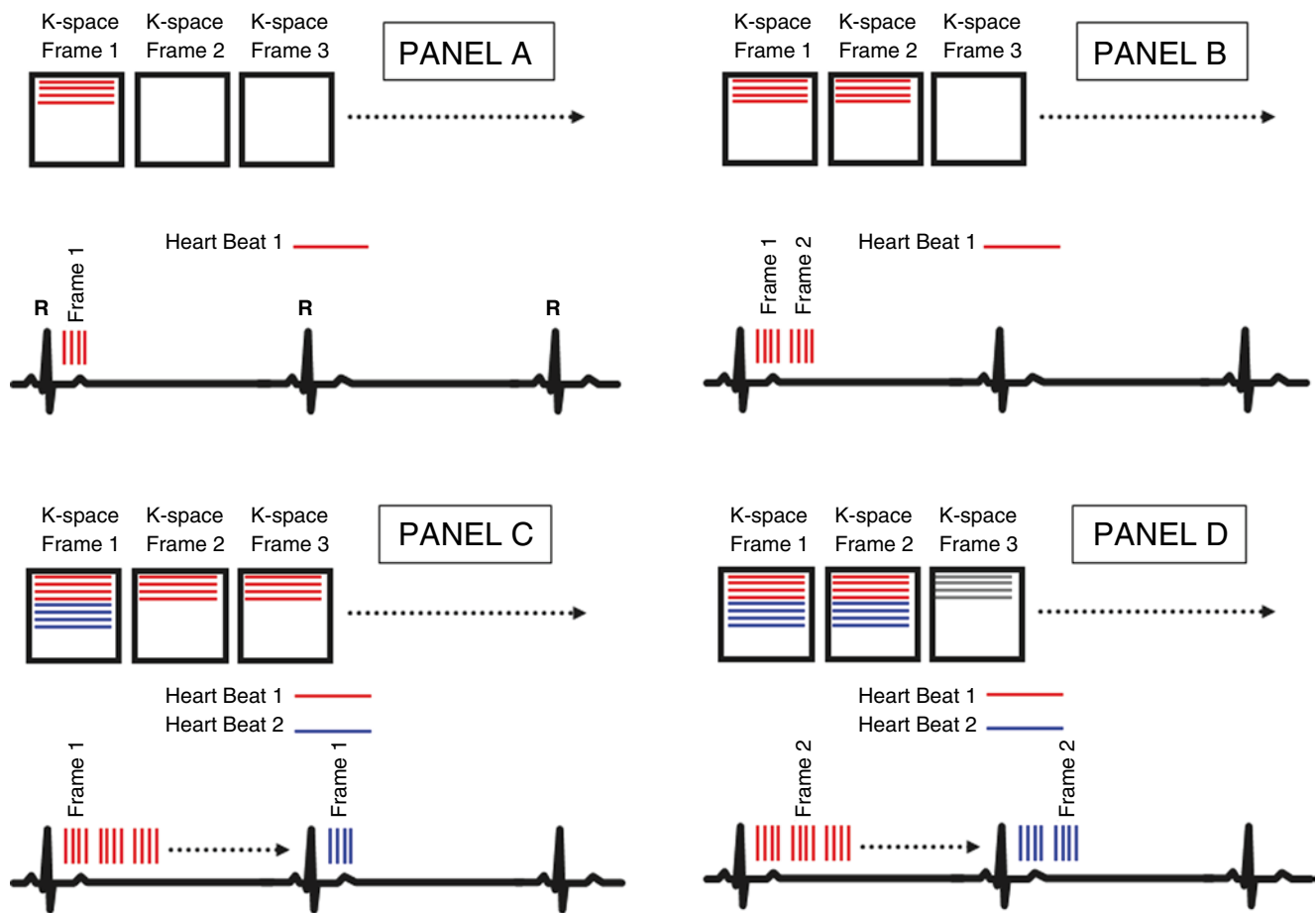


Fig. 10.10 Segmented k-space image acquisition. Within each cardiac cycle, some but not all data are acquired for each movie frame. No movie frames are complete until the last cardiac cycle, during which all

movie frames are completed. Panel A: First heart beat, first movie frame. Panel B: First heart beat, second movie frame. Panel C: Second heart beat, first movie frame. Panel D: Second heart beat, second movie frame

second), typically referred to as “real time” imaging. Other approaches have also been described, but regardless of the approach image quality is significantly reduced in patients that cannot repeatedly hold their breath, and/or have irregular heart rates.

Retrospective Gating

The preceding technique, where the MRI scanner hardware is triggered in synchrony with cardiac contraction, is referred to as prospective gating. Retrospective gating, conversely, involves acquiring not only the k-space lines but also the patient’s R wave (see Fig. 10.11). Relatively complex image reconstruction techniques are then applied after data acquisition (after the breath hold) to arrange the k-space lines across consecutive cardiac cycles in such a way that the resulting data are similar to prospective gating (Fig. 10.11). Until the early twenty-first century retrospective gating reconstruction algorithms were problematic, and most CMR imaging employed prospective gating. In recent years, however,

retrospect gating reconstruction algorithms have improved significantly, and the use of retrospective gating has become increasingly common in the clinical setting.

Retrospective gating has the advantage that the final 10–50 ms of the cardiac cycle is well characterized, whereas this time period is generally ignored with prospective gating due to the need for the CMR scanner to “listen” for the next R-wave. This difference is particularly important for velocity-encoded imaging, where the loss of flow data near the end of diastole can introduce significant errors (ca. 20 %) in estimates of arterial and venous flows.

View Sharing

View sharing essentially involves interpolating k-space data across movie frames in order to shorten breath hold times. As shown in Fig. 10.12, k-space lines in movie frame 1 and 3 are acquired by the scanner (solid lines), whereas the k-space lines for movie frame 2 are interpolated (dotted lines). View sharing typically involves the interpolation of some, but not

Fig. 10.11 Retrospective gating. Both the k-space data and the R-wave trigger are recorded. Specialized reconstruction software retrospectively distributes the k-space lines amongst the movie frames

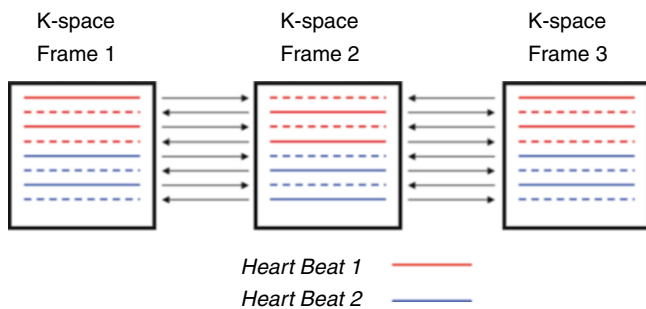
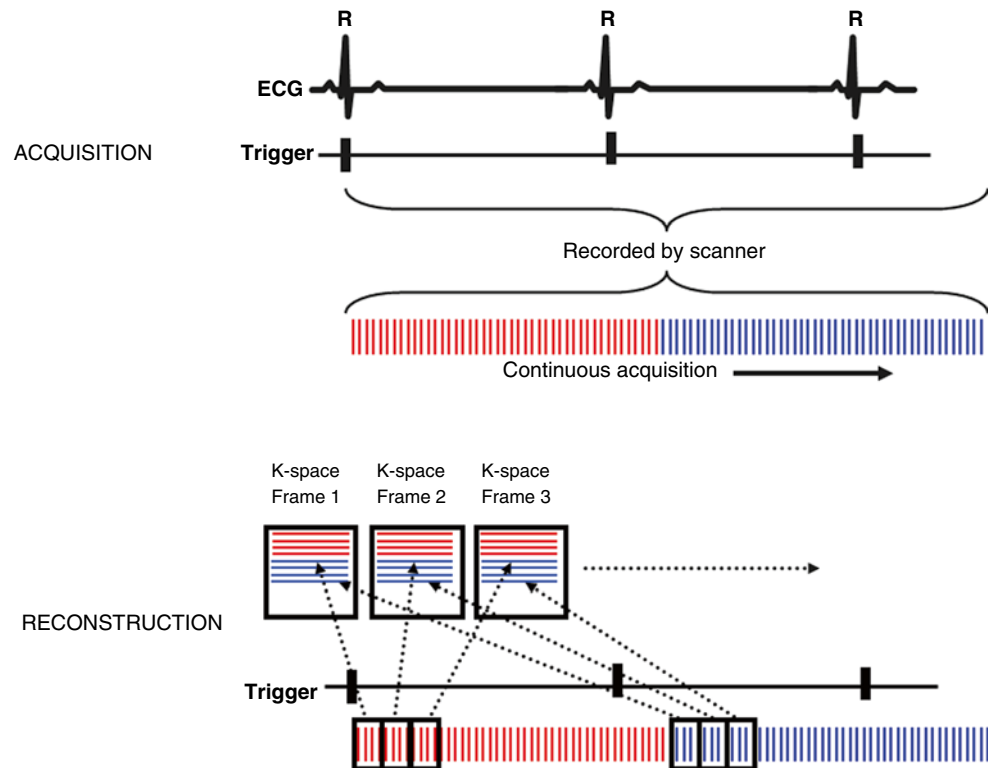


Fig. 10.12 View sharing. Solid k-space lines are acquired. To shorten overall movie acquisition time (breath hold time), dotted k-space lines are not actually acquired but rather are calculated as the average of the corresponding lines from the previous and next movie frames

all, k-space lines in order to minimize the negative effects of interpolation. The trade offs of view sharing are conceptually similar to those obtained by any other interpolation technique, namely some of the data is essentially fictitious. The use of view sharing in the clinical setting has in general become less common in recent years, perhaps in part because parallel imaging techniques offer similar reductions in breath hold duration with less loss of information.

Partial Fourier, Parallel Imaging

Parallel imaging techniques, such as GRAPPA and mSENSE, are based on a clever idea first described in the late 1990s

[12–14]. The underlying idea is that each of the multiple radiofrequency receiver coils placed around the patient's thoracic cavity contains differing spatial information, and that by incorporating this information during the image reconstruction process some k-space lines can be constructed without acquiring them directly.

Over the past decade a family of these techniques has developed and matured, each with characteristic advantages and disadvantages. For cardiovascular imaging, the primary advantage of all parallel imaging techniques is that they reduce patient breath hold durations. The primary disadvantage is a loss of signal-to-noise, but for a given reduction in breath hold duration the loss of signal is smaller than would occur with alternative approaches. Because of this, parallel imaging represents a major advance for cine cardiac imaging. The conceptual details of the various techniques themselves are complex, and beyond the scope of this chapter. From the perspective of the scanner operator, conversely, implementing these techniques is so simple that virtually all routine clinical CMR scans incorporate some form of parallel imaging.

Clinical Applications

When Is bSSFP Appropriate?

For both our inpatient and outpatient MRI scanners at Duke University Hospital, most patients have a steady heart rate and can repeatedly hold their breath for 10–12 s. In these

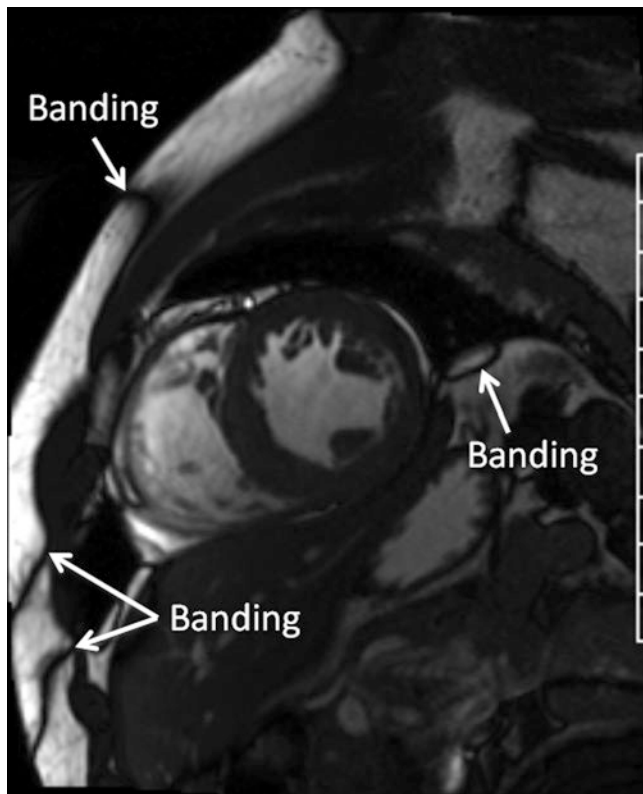


Fig. 10.13 bSSFP imaging at 3T. Overall image quality is excellent. Although banding artifacts are present, their position does not obscure the areas of diagnostic interest

patients, balanced SSFP cine imaging is arguably the clear choice and its use is often recommended in society guidelines [15, 16]. Image signal to noise is generally excellent, and the short TR allows more than adequate spatial and temporal resolution. The resulting movie loops are typically far more than adequate for careful inspection of regional and global wall motion, and often reveal subtle structures and blood flow patterns than are not available using any other CMR technique or other imaging modality.

At 1.5 T, artifacts for bSSFP are relatively infrequent. At 3 T artifacts are more frequent and, when present, typically appear in the chest wall and/or in the inferior portion of left ventricular free wall adjacent to the lung. In these regions the air/water interface causes local inhomogeneities in the static magnetic field, resulting in local destruction of the MRI signal and, therefore, dark bands. Perhaps the best way to address this issue is by applying 3D shimming techniques locally around the heart, rather than across the entire body, in order to improve homogeneity in the region of diagnostic interest (the heart). If shimming is not successful, the dark bands can be moved (but not eliminated) away from the heart and large vessels by small manual changes in transmitter frequency (eg. 50 Hz). Fig. 10.13 and Video 10.3 show 3 T bSSFP images with artifactual dark bands located away from the heart, i.e. away from the areas of diagnostic importance

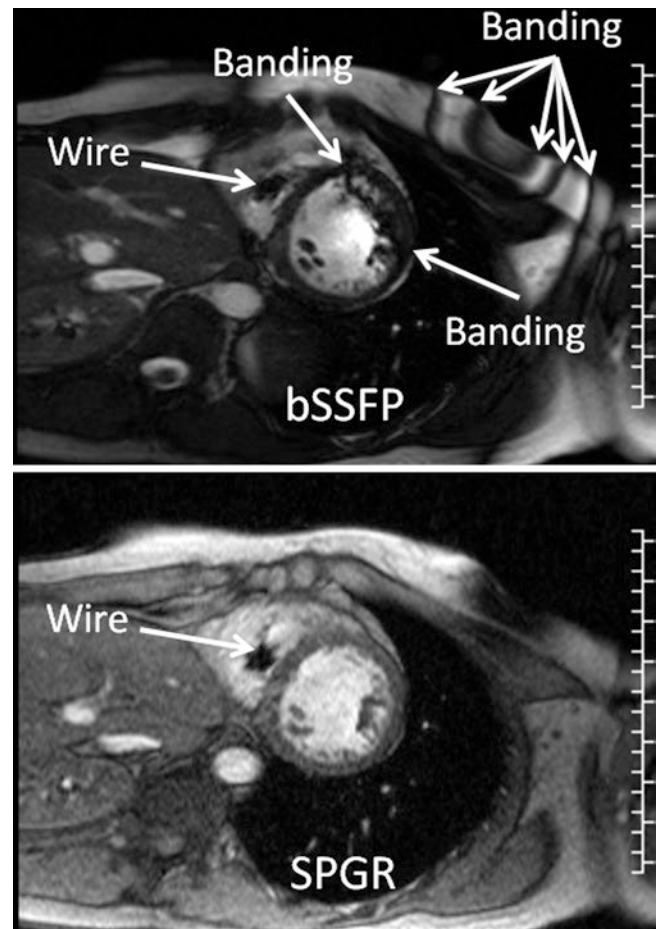


Fig. 10.14 Cine imaging in a patient with a pacemaker. bSSFP imaging exhibit severe artifacts (*top*) that can be avoided by using SPGR imaging instead (*bottom*)

to CMR. Note that the heart itself has excellent image quality, and even subtle structures like trabeculae can be visualized in detail. Occasionally, even the chordae connecting papillary muscles to the leaflets of the mitral and aortic valves can be visualized.

When Is SPGR Cine Appropriate?

In some patients, especially those with metallic implants or severe iron overload, the dark bands on bSSFP images cannot be successfully moved away from the heart, even by a combination of shimming and transmitter frequency shifting. In these patients the best strategy is to use spoiled GRE (SPGR) techniques instead. Figure 10.14 and Video 10.4 show an example of a patient with a pacemaker in whom bSSFP images resulted in a dark band through the LV free wall, precluding confident interpretation of wall motion in this area. The SPGR images (Video 10.5), conversely, are free of this artifact because SPGR imaging is much less dependent on magnetic field homogeneity. Because mag-

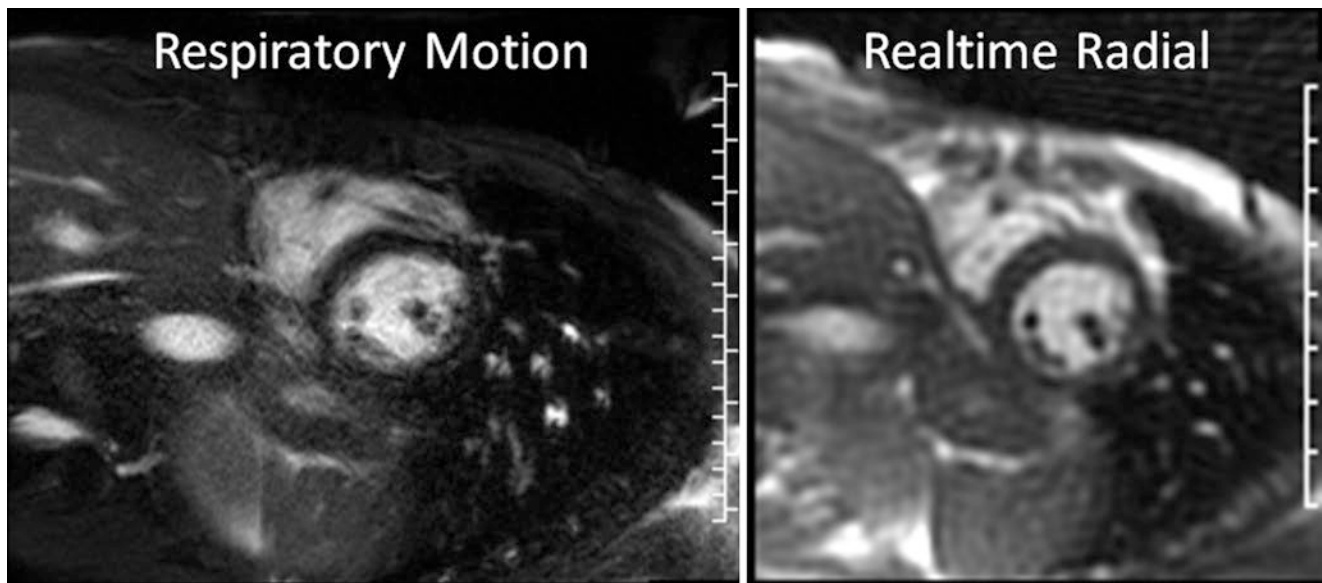


Fig. 10.15 ECG gated (*left*) and real-time (*right*) imaging in a patient that could not hold their breath

netic field inhomogeneities increase with field strength, the need to use SPGR instead of bSSFP is more common at 3 T compared to 1.5 T. An additional advantage of SPGR is that patient exposure to RF radiation is lower, typically reported by the scanner as specific absorption rate (SAR), due to the use of a lower imaging flip angle and a longer TR. In some circumstances the need to lower SAR alone may motivate the use of SPGR as opposed to bSSFP.

When Is Real-Time Cine Appropriate?

In patients with arrhythmia and/or an inability to hold their breath, ECG gating is typically not clinically practical. Cine imaging is still possible in these patients, but all current approaches result in poorer image quality. Real-time cine imaging may actually be preferred in some instances where beat-to-beat variation in wall motion helps make the diagnosis, such as the respiratory variation of septal motion in pericardial disease with constrictive physiology. Arguably the best choice in this circumstance is to use real-time cine imaging, which as previously described involves trading off spatial resolution and image quality to achieve image acquisition times of approximately 100 ms. At ten images per second the real-time CMR images begin to resemble images from echocardiography, i.e. the images are acquired and displayed during cardiac contraction. Figure 10.15 and Videos 10.6 (bSSFP) and 10.7 (SPGR) show an example of a patient that could not hold their breath. The gated images are of poor quality and arguably not clinically useful. The real-time images,

conversely, are at least clinically useful even though they are significantly worse than gated bSSFP or SPGR. Note that the real-time images portray several cardiac cycles, as with echocardiography, as opposed to one cycle played in a loop for bSSFP and SPGR. As described above, this is because the bSSFP and SPGR movie frames are reconstructed to represent a composite cardiac cycle (segmented k-space gating).

References

1. Wood ML, Silver M, Runge VM. Optimization of spoiler gradients in FLASH MRI. *Magn Reson Med.* 1987;5(6):455–63.
2. Crawley AP, Wood ML, Henkelman M. Elimination of transverse coherences in FLASH MRI. *Magn Reson Med.* 1988;8(3):248–60.
3. Buxton RB, Edelman RR, Rosen BR, et al. Contrast in rapid MR imaging: T1- and T2-weighted imaging. *J Comput Assist Tomogr.* 1987;11(1):7–16.
4. Han M, Hargreaves BA. Reduction of flow artifacts by using partial saturation in RF-spoiled gradient-echo imaging. *Magn Reson Med.* 2011;65(5):1326–34.
5. Busse RF, Riederer SJ. Steady-state preparation for spoiled gradient echo imaging. *Magn Reson Med.* 2001;45:653–61.
6. Smith RC, Lange RC, McCarthy SM. Chemical shift artifact: dependence on shape and orientation of the lipid-water interface. *Radiology.* 1991;181(1):225–9.
7. Ferreira PF, Gatehouse PD, Mohiaddin RH, et al. Cardiovascular magnetic resonance artefacts. *JCMR.* 2013;15:41–80.
8. Nayak KS, Lee HL, Hargreaves BA, et al. Wideband SSFP: alternating repetition time balanced steady state free precession with increased band spacing. *Magn Reson Med.* 2007;58(5):931–8.
9. Amano Y, Nozaki A, Takahama K, et al. Reduction in flow artifacts by using interleaved data acquisition in segmented balanced steady

- state free precession cardiac MRI. *Comput Med Imaging Graph.* 2005;29(6):441–5.
10. Scheffler K, Lehnhardt S. Principles and applications of balanced SSFP techniques. *Eur Radiol.* 2003;13:2409–18.
 11. Atkinson DJ, Edelman RR. Cineangiography of the heart in a single breath hold with a segmented turbo-FLASH sequence. *Radiology.* 1991;178:357–60.
 12. Sodickson DK, Manning WJ. Simultaneous acquisition of spatial harmonics (SMASH): fast imaging with radiofrequency coil arrays. *Magn Reson Med.* 1997;38:591–603.
 13. Pruessmann KP, Weiger M, Scheidegger MB, et al. SENSE: sensitivity encoding for fast MRI. *Magn Reson Med.* 1999;42:952–62.
 14. Griswold MA, Jakob PM, Heidemann RM, et al. Generalized auto-calibrating partially parallel acquisitions (GRAPPA). *Magn Reson Med.* 2002;47:1202–10.
 15. Kramer CM, Barkhausen J, Flamm SD, Kim RJ, Nage E. Society for cardiovascular magnetic resonance and board of trustees task force on standardized protocols: standardized cardiovascular magnetic resonance (CMR) protocols 2013 update. *J Cardiovasc Magn Reson.* 2013;15:91.
 16. Hundley WG, Bluemke DA, Finn JP, et al. ACCF/ACR/AHA/NASCI/SCMR 2010 Expert consensus document on cardiovascular magnetic resonance, a report of the American College of Cardiology Foundation Task Force on Expert Consensus Documents. *J Am Coll Cardiol.* 2010;55(23):2619.

Henrik Engblom, Christos G. Xanthis,
Sophie I. Mavrogeni, Suzanne M. Smart,
and Anthony H. Aletras

Abstract

Cardiac magnetic resonance is often used to provide detailed information on structures such as the myocardium, pericardium, pulmonary veins, and emanating great vessels. While blood travels throughout the heart and blood vessels, its signal may obscure the assessment of these structures depending on the clinical questions being addressed. Black blood imaging techniques seek to suppress the signal from blood and thereby improve delineation of cardiovascular anatomy. Fast spin echo-based sequences are in routine use for the suppression of blood flowing into the imaging plane. Such approaches have known limitations that may result in inadequate image quality or artifacts in the image. More recent advances have overcome some of these limitations, but it is incumbent upon the reader to recognize them as they occur. For instance, cardiac motion may lead to signal loss, and may be overcome by optimizing the cardiac phase during which data acquisition occurs. For those relying on black blood imaging to detect myocardial edema, caution must be exerted in recognizing spuriously bright areas of myocardium resulting from slow-flowing blood. While contemporary tissue mapping techniques overcome some of these limitations, black blood imaging will remain an important tool in the CMR armamentarium, particularly with increasing prevalence of implantable devices in patients with various forms of cardiovascular disease. Particularly with bright blood imaging, devices such as intravascular stents and implantable loop recorders can produce considerable susceptibility artifact obscuring visualization of the anatomy of interest; using black blood imaging can significantly reduce this artifact.

Keywords

Black blood • Magnetic resonance • Blood suppression • Cardiovascular • Inversion recovery

H. Engblom, MD, PhD
Department of Clinical Physiology and Nuclear Medicine, Lund
University Hospital, Lund, Sweden

C.G. Xanthis, PhD
Department of Computer Science and Biomedical Informatics,
University of Thessaly, Lamia, Greece

S.I. Mavrogeni, MD, FESC
Department of Cardiology, Onassis Cardiac Surgery Center,
Athens, Attiki, Greece

S.M. Smart, BS
Davis Heart and Lung Research Institute, Ohio State University
Wexner Medical Center, Columbus, OH, USA

A.H. Aletras, PhD (✉)
Department of Clinical Physiology and Nuclear Medicine, Lund
University Hospital, Lund, Sweden

Department of Medicine, Laboratory of Medical Informatics,
Aristotle University of Thessaloniki, Thessaloniki, Greece
e-mail: aletras@hotmail.com

Basic Physics for Obtaining Black-Blood Images

Magnetic resonance imaging can be used for diagnostic purposes in the heart when anatomical information is needed. In such cases, it is advantageous to exploit the versatility of MRI pulse sequence programming in order to produce images of a single cardiac phase where the blood pool appears “black” (Fig. 11.1). In this manner, it is possible to more easily detect, for example, tumors within the blood pool since the blood signal is zero. The clinical applications of black-blood imaging in cardiac magnetic resonance are numerous and have stood the test of time since the technique was first introduced by Simonetti and colleagues in 1996 [1]. Black-blood imaging is considered to be part of the first line of defense of pulse sequences for interrogating disease in the clinic. This so-called black-blood contrast can also be used in conjunction with other contrast mechanisms (e.g. T_1 -weighted, T_2 -weighted) so as to produce images for tissue characterization and intramyocardial edema detection or fat infiltration. It is most important to note that black-blood contrast in the image is created by suppressing (or by totally eliminating) the signal arising from the blood while preserving signals arising from tissues. Blood signal suppression is closely linked with how signal is generated and manipulated by the MRI pulse sequence. In the next section, the basic physics for creating black-blood contrast will be presented.

A simplified pulse sequence diagram for black-blood contrast CMR is seen in Fig. 11.2. This diagram describes the time sequence of radiofrequency (RF) and gradient pulses that results in suppressed blood signal within a single phase image of the heart. This sequence of events not only suppresses signal from the ventricular cavities but also preserves signal arising from the myocardium. The pulse sequence can be separated into two distinct parts (Fig. 11.2): the so-called “double inversion” spin preparation, which occurs right after the detection of the R-wave of the EKG, and the readout, which occurs during late diastole. There are three basic concepts contributing to blood suppression in this pulse sequence. First, the intrinsic property of the fast spin echo (FSE) (a.k.a. turbo spin echo, TSE) readout to dephase moving spins and therefore reduce signal. Second, the null signal point encountered during inversion recovery. Last, the exchange of blood within the slice of interest. These basic ideas will be described below in more detail.

The first contribution to black-blood contrast is due to the FSE readout itself. The FSE readout, which is used in black-blood contrast, consists of a 90° excitation RF pulse (Fig. 11.3), which brings the longitudinal magnetization from the z-axis to the transverse plane so that imaging and signal acquisition can be performed. The transverse magnetization is then rephased multiple times into multiple spin echoes by a series of consecutive equidistant 180° RF pulses. This recycles the magnetization and multiple phase encoding steps can be performed

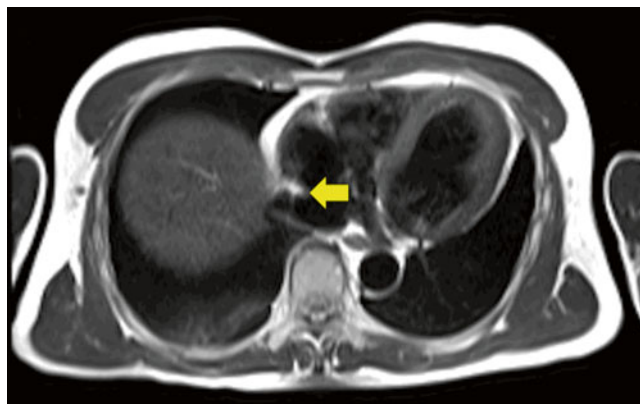


Fig. 11.1 Black blood imaging is shown in a patient referred for cardiac magnetic resonance. A right atrial mass seen by echocardiography corresponded to a prominent Eustachian valve (arrow)

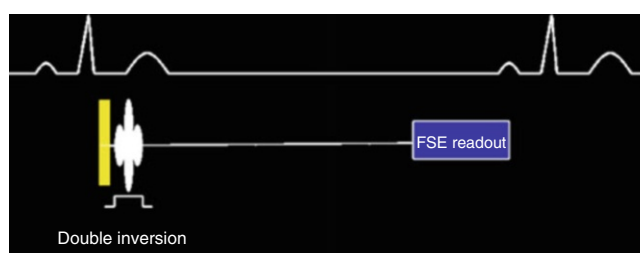


Fig. 11.2 Simplified black-blood pulse sequence

from a single excitation, thus speeding up image acquisition. In theory, a single train of 180° s could be used to acquire all phase encoding steps of an entire image. In practice, for cardiac imaging the length of the echo train is limited (to approximately 100–120 ms) by the T_2 decay and the time period available for imaging during the cardiac cycle, which by design coincides with diastasis so that cardiac motion and related artifacts are minimized. In practice, image acquisition is segmented and the image is collected over several cardiac cycles by using echo train lengths of 12–32. The spin echoes acquired with the 180° echo train exhibit different T_2 losses since the spins of the different echoes spend different amounts of time on the transverse plane. The later the echo is acquired, the more T_2 -weighting it carries. Carefully arranging the acquired echoes within the k-space acquisition matrix can yield proton density or T_2 -weighted images if the FSE readout is applied during every other heartbeat (2RR imaging). If the FSE readout is applied during every heartbeat (1RR imaging) then T_1 -weighted images can be obtained.

The FSE readout has the tendency to suppress signal from moving blood by means of through-plane motion and intravoxel dephasing. Spins excited by the 90° pulse that move outside of the imaging plane during the application of the 180° pulses will not contribute bright signal to the image. This helps create dark-blood contrast. Intravoxel dephasing occurs when the spins within a voxel of the image are not aligned and are at different angles (i.e. have different phases) with one another.

Fig. 11.3 The FSE readout used during diastasis

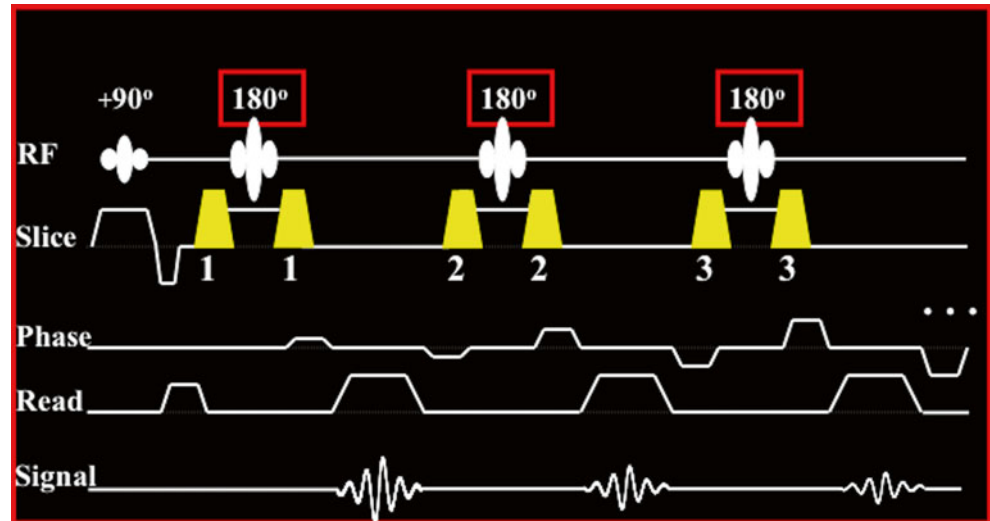
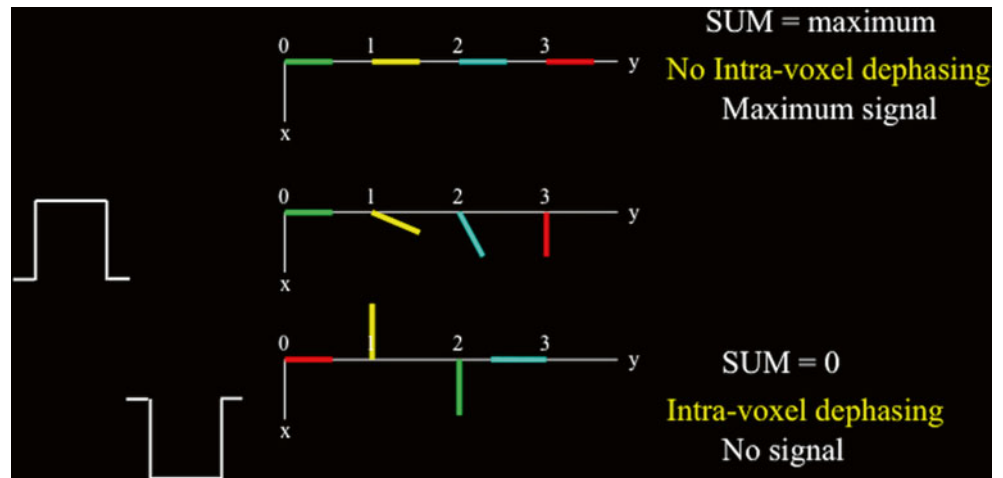


Fig. 11.4 Intra-voxel dephasing when blood spins mix (i.e. change position) during gradient pulse application



This causes reduction of the signal arising from that voxel. In the most extreme case of intravoxel dephasing the spins will have phases opposite to one another and as a result zero signal will be obtained from the voxel. One can think of this as a tug of war where nobody wins. The combination of strong gradient pulses and turbulent blood motion results in spin mixing within a voxel and therefore intravoxel dephasing exists.

Figure 11.4 shows a voxel that extends from 0 to 3 on the y-axis and the effect of two gradient pulses applied along the y-axis. These gradient pulses are the same except for their opposite signs. The positive gradient pulse imparts phase to the spins depending on where they sit on the y-axis: the further away from zero, the more phase the spins acquire. If the spins are stationary then the negative gradient pulse imparts an equal phase with opposite sign to each spin thus bringing the spins into alignment and therefore maximum signal from the voxel will be acquired. However, when turbulent motion is present, as is the case with blood, the spins are likely at a different y-axis location when the negative gradient pulse is applied. For example, in Fig. 11.4, the green spin moves from position

0 to position 2 on the y-axis. Therefore, the phases from the two gradients do not cancel out and a weaker signal is acquired. If the gradients are strong enough and the blood motion is sufficiently turbulent then the spins can point in opposite directions. Then full intravoxel dephasing can occur, therefore resulting in zeroing of the signal.

The FSE readout uses strong gradient pulse pairs that bracket the 180s (numbered gradient pulses in Fig. 11.3) so that the 180° RF pulses only refocus existing spins and do not cause new spin excitation. The details are beyond the scope of this chapter. The important concept is that moving blood spins experience these strong gradient pulse pairs during the FSE readout. Therefore, in FSE, intravoxel dephasing occurs and blood signal is suppressed to some extent. Unfortunately, blood signal suppression is not adequate and some of the moving spins can cause image flow artifacts.

The second and third contributions to black-blood contrast are due to the “null point” of the inversion recovery and due to blood motion. The so-called “double inversion” spin preparation in conjunction with through-slice blood motion

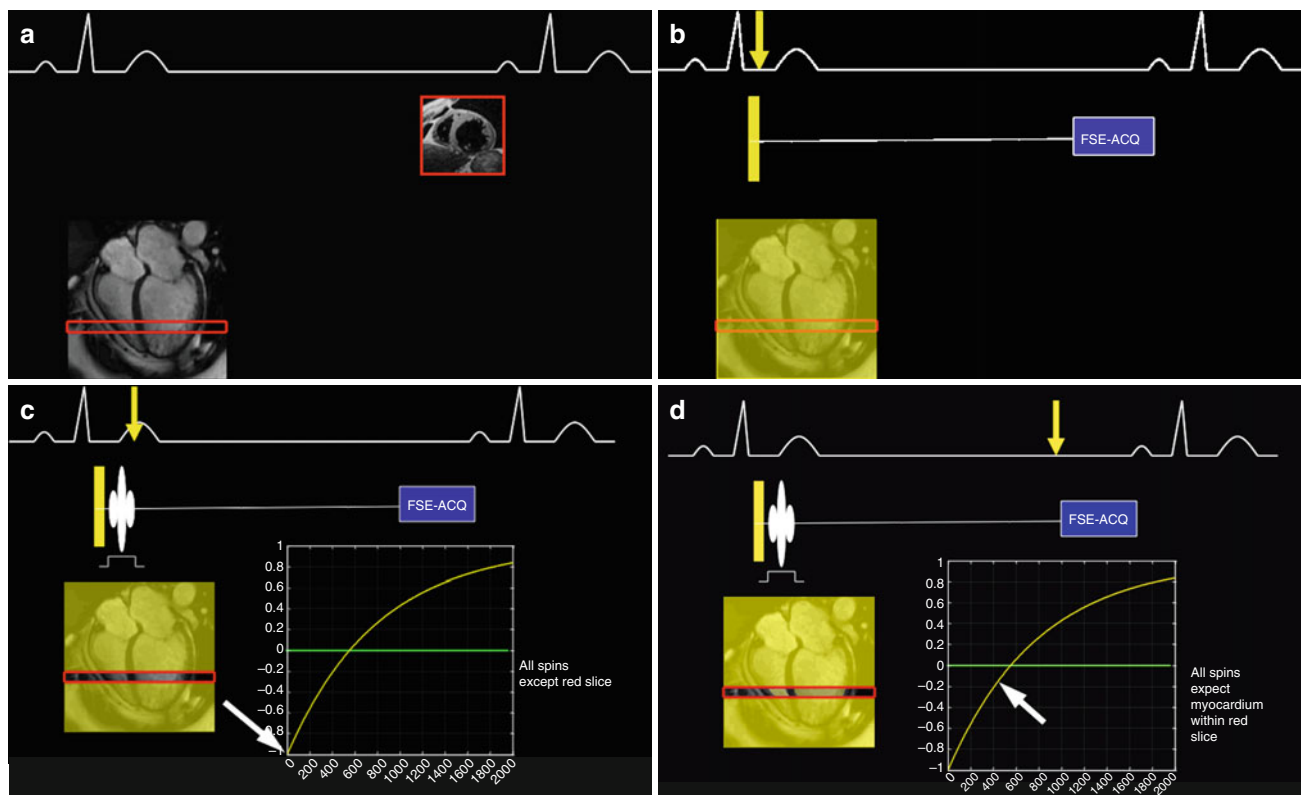


Fig. 11.5 (a) Short axis slice to be imaged during diastasis and its cross reference on the long axis. (b) After non-selective inversion pulse. (c) After selective inversion. (d) After contraction [FSE-ACQ: Fast spin echo acquisition]

further suppresses the moving blood signal in order to produce black-blood images of diagnostic quality. This preparation is applied as soon as the R-wave of the EKG is detected. Theoretically at least, it affects the exact same myocardial tissue that is imaged by the FSE readout during diastasis. This is because the spin preparation is applied prior to any cardiac contraction and because, at least theoretically, the myocardial tissue contracts and then returns to the same location in space during diastasis. This is certainly not true for the flowing blood within the cavities of the heart. It is this difference between tissue and blood that the spin preparation takes advantage of in order to preserve the signal from the myocardial tissue and suppress the signal from the blood. The actual sequence of events is described below.

Figure 11.5a shows an FSE short axis image being acquired during diastasis (albeit in practice this is done in a segmented manner) and a long axis image for reference purposes only. The spin preparation consists of a double inversion i.e. two consecutive 180° RF inversion pulses executed very fast before the onset of myocardial contraction. The first of the two inversion pulses is not slice selective and inverts the magnetization, bringing it along the $-z$ axis, within the entire heart (inverted spins are depicted as yellow in Fig. 11.5b). The subsequent second inversion pulse is a slice selective one (i.e. the RF is applied simultaneously with a gradient pulse). This second RF pulse cancels out the effects of the first inversion pulse;

however, this cancellation (Fig. 11.5c) only occurs within the slice that we are interested in imaging with the FSE readout during diastasis. The second 180° pulse cancels out the effects of the first 180° within the slice of interest since a re-inversion of the recently inverted magnetization brings spins within the slice back to $+z$. So, at the end of the double inversion prep, there are two distinct populations of spins: the first consists of spins (both blood spins and tissue spins) within the short axis slice of interest that are seemingly “untouched” by the two RF pulses and the second which consists of spins outside of the slice of interest that have been inverted and will undergo inversion recovery during systole (Fig. 11.5c, inverted spins in yellow). As the heart contracts, blood spins from outside the slice of interest undergoing inversion recovery begin to flow inside the slice of interest while at the same time “untouched” blood spins from within the slice of interest leave the imaging plane. Therefore, assuming that sufficient through-plane blood flow takes place, at the end of cardiac contraction blood spins within the slice of interest have been undergoing inversion recovery throughout systole. On the other hand, myocardial tissue spins within the slice of interest have not been undergoing inversion recovery since they were seemingly “untouched” by the RF pulses of the spin preparation (Fig. 11.5d, inverted spins in yellow; note that blood spins inside the slice are yellow). The signal from the blood spins will be close to crossing the inversion “null” point. This is the same mechanism that is

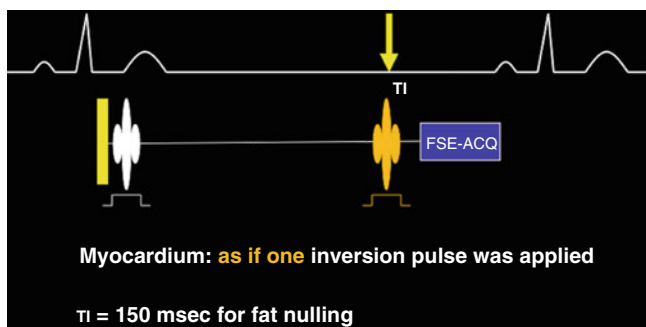


Fig. 11.6 STIR: a third inversion pulse for fat saturation

also observed with late gadolinium delayed enhancement viability imaging in normal tissue. However, with black-blood imaging there is no gadolinium to shorten the T_1 values and therefore, with a T_1 greater than 1000 ms, the inversion recovery of the blood signal does not quite reach the “null”. Nonetheless, the blood signal is close enough to the inversion recovery “null point” so that, in combination with the FSE readout’s intrinsic intravoxel dephasing, the blood signal is suppressed to yield black-blood contrast. The “untouched” myocardial signal yields myocardial T_1 or T_2 -weighted contrast depending on the FSE readout as described earlier.

In Short T_1 Inversion Recovery (STIR) imaging, a third 180 inversion RF pulse is used in combination with the double inversion spin preparation and the FSE readout in order to introduce fat signal suppression on top of the existing black-blood image contrast (Fig. 11.6). As is the case for myocardial signal where the double inversion spin preparation leaves myocardial spins “untouched”, the same holds true for adipose tissue spins, which also are left “untouched” by the double inversion preparation. Fat signal is suppressed by exploiting its markedly shorter T_1 compared to the long T_1 s of myocardium and blood. The third 180 inversion pulse is most commonly a slice selective pulse that is applied at the appropriate time (about 150 ms) prior to the FSE readout so that fat will be going through its inversion “null” point when the FSE readout starts (Fig. 11.6). This predictably results in T_1 contrast within the image and therefore causes signal loss from the myocardial tissue (greater than 25 %). For this reason, the benefits of fat suppression with triple inversion STIR imaging should be weighed on a case-by-case basis against the higher signal obtained with double inversion recovery alone.

Artifacts with Black-Blood Methods

The double inversion spin preparation in conjunction with the FSE readout during diastasis can yield high quality black-blood contrast diagnostic images. However, in some cases, it is also possible that it can lead to misdiagnosis as a result of image artifacts that are not easy for the less experienced reader to identify. For blood suppression to be effective it is important

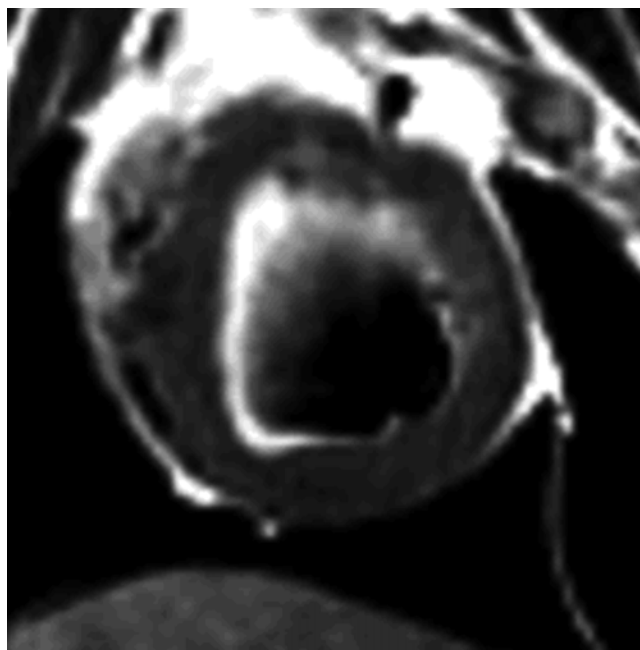


Fig. 11.7 Bright-blood near hypokinetic endocardium causes artifact with DIR-FSE

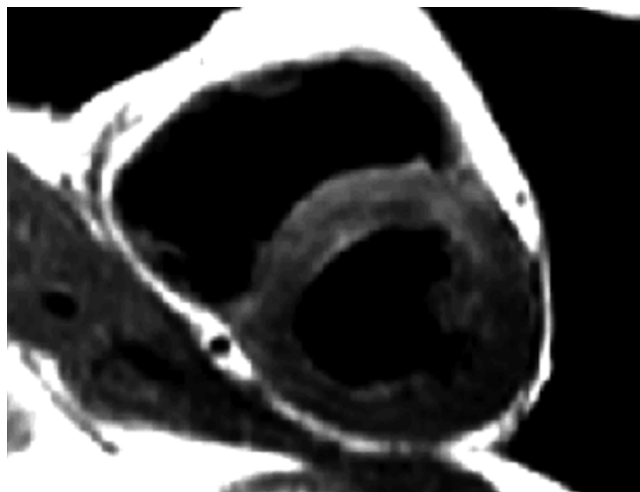


Fig. 11.8 Signal loss due to myocardium not returning to the same position during diastasis causes artifact with DIR-FSE

that within the short axis slice of interest the non-inverted blood spins are replaced by out-of-slice blood spins that are undergoing inversion recovery. In cases of reduced contractile function in the diseased heart, this is not always true. Regional hypokinesia and akinesia can result in insufficient blood replacement close to the endocardial wall within the slice of interest, which in turn results in localized bright blood signal arising from these areas (Fig. 11.7). Thus, these so called bright-blood artifacts are often localized near the endocardium of the diseased wall that one wishes to examine with CMR. This type of signal is sometimes difficult to distinguish from subendocardial edema on T_2 -weighted black-blood

images. With clinical experience it is possible to identify the artifact and avoid misdiagnosis.

Another common artifact with black-blood imaging is that of posterior myocardial signal loss. Figure 11.8 shows an example of this type of artifact with T₂-weighted double-inversion black-blood FSE imaging in a normal volunteer. The myocardial signal arising from the posterior wall is noticeably less than that of the septal wall. An inexperienced reader could interpret this signal gradient as signal elevation in the septum due to intramyocardial edema, which is not the case with this healthy heart. With double-inversion black-blood imaging the posterior wall signal loss artifact is caused by either a long FSE readout or by an inappropriately timed FSE readout or a combination of the two.

A too long FSE readout can cause myocardial signal losses. The FSE readout is based on a single RF pulse excitation and multiple echoes being read out. Myocardial tissue motion, for example due to the atrial kick, during the FSE readout can result in unexpected signal losses. The reason is that the FSE readout excites myocardial signal within a particular slice with the 90° RF pulse but this particular tissue moves out of the imaging slice and its signal cannot be rephased by the train of 180s. Similar problems for the same reason can also arise if the FSE echo train begins too early before diastolic filling has finished. In order to mitigate such signal losses it is common that the 180 RF pulses of the FSE readout refocus signal in a volume about 50–100 % thicker than the prescribed slice thickness that is excited by the 90° RF pulse. This allows for some myocardial through-plane motion during the FSE train. This is done usually without requiring user interaction.

Another problem can arise if, due to through-plane motion, the double-inversion preparation does not prepare the same spins that are going to be imaged by the FSE readout. Then signal losses will also occur for the aforementioned reasons. A third inversion RF pulse for fat suppression with STIR black-blood imaging further complicates the timing of this pulse sequence in practice and can lead to even total signal loss from the myocardium. This is most common in cases when the patient has a high heart rate and as a result very short periods of diastasis. To lessen these effects of through-plane motion, the slice thickness is increased to

200–300 % of that of the imaging slice both for the slice selective pulse in the double-inversion preparation as well as for the STIR third inversion pulse. However, doing so may result in inadequate blood suppression [2].

In the end, superior image quality becomes a matter of selecting appropriate imaging parameters on a patient-by-patient basis depending on expected findings, heart rate, and the ability to hold his/her breath during the image acquisition. An appropriate set of imaging parameters is dependent on the clinician's and technologist's experience. This is the main reason why some imaging sites routinely acquire quality images whereas newly established facilities do not do as well. Approaches to automate parameter selection have been introduced by the equipment manufacturers in order to improve image quality in routine clinical black-blood MRI scans. For further details on black-blood imaging, see references [3–7].

References

1. Simonetti O, Finn J, White R, Laub G, Henry D. "Black blood" T₂-weighted inversion-recovery MR imaging of the heart. *Radiology*. 1996;199:49–57.
2. Ferreira PF, Gatehouse PD, Mohiaddin RH, Firmin DN. Cardiovascular magnetic resonance artefacts. *J Cardiovasc Magn Reson*. 2013;15:41.
3. Edelman RR, Chien D, Kim D. Fast selective black blood MR imaging. *Radiology*. 1991;181:655–60.
4. Judd RM, Reeder SB, Atalar E, McVeigh ER, Zerhouni EA. A magnetization-driven gradient echo pulse sequence for the study of myocardial perfusion. *Magn Reson Med*. 1995;34:276–82.
5. Payne AR, Casey M, McClure J, McGeoch R, Murphy A, Woodward R, Saul A, Bi X, Zuehlsdorff S, Oldroyd KG, Tzemos N, Berry C. Bright-blood T₂-weighted MRI has higher diagnostic accuracy than dark-blood short tau inversion recovery MRI for detection of acute myocardial infarction and for assessment of the ischemic area at risk and myocardial salvage. *Circ Cardiovasc Imaging*. 2011;4:210–9.
6. Ridgway JP. Cardiovascular magnetic resonance physics for clinicians: part I. *J Cardiovasc Magn Reson*. 2010;12:71.
7. Sinha S, Mather R, Sinha U, Goldin J, Fonarow G, Yoon H-C. Estimation of the left ventricular ejection fraction using a novel multiphase, dark-blood, breath-hold MR imaging technique. *AJR Am J Roentgenol*. 1997;169:101–12.

Marcus Carlsson, Christos G. Xanthis, Suzanne Smart, Sebastian Bidhult, and Anthony H. Aletras

Abstract

Noninvasive characterization of tissue has long been the unique domain of magnetic resonance imaging (MRI) when compared to other imaging modalities. Techniques for such typically emphasize one or more MR-based relaxation parameters and the corresponding image contrast or weighting. With or without administration of an exogenous contrast agent, cardiac MRI affords detailed myocardial tissue characterization via various segmented as well as single heart beat approaches. The workhorse technique for myocardial characterization has been late gadolinium enhancement (LGE); LGE is routinely performed in MRI centers around the world as an integral part of nearly every cardiac MRI exam. While originally developed to characterize infarct scar, LGE has since become an important technique to delineate other features of myocardial disease such as fibrosis in nonischemic cardiomyopathy and infiltrates such as sarcoid granuloma and amyloid protein. LGE usually provides robust myocardial characterization, but has two major limitations. First, it requires administration of gadolinium-based contrast, which may not be suitable for individuals with known allergy to such agents or patients with advanced kidney disease. Second, it may be insensitive to more diffusely diseased myocardium where one loses the ability to 'null' normal tissue via this technique's key inversion time parameter. To overcome these limitations, as well as to characterize other myocardial features, imaging techniques that capture intrinsic contrast in T_1 , T_2 and other MR-based relaxation parameters are often incorporated into the cardiac MRI examination. Accumulating evidence suggests that quantitative approaches, also known as tissue mapping techniques, are helping to further advance MR-based myocardial characterization.

Keywords

Tissue characterization • Magnetic resonance • Gadolinium-based contrast agent • Myocardium • Cardiac • T_1 • T_2 • Mapping

M. Carlsson, MD, PhD • S. Bidhult, MSc
Department of Clinical Physiology and Nuclear Medicine, Lund
University Hospital, Lund, Sweden

C.G. Xanthis, PhD
Department of Computer Science and Biomedical Informatics,
University of Thessaly, Lamia, Greece

S. Smart, BS
Davis Heart and Lung Research Institute, Ohio State University
Wexner Medical Center, Columbus, OH, USA

A.H. Aletras, PhD (✉)
Department of Medicine, Laboratory of Medical Informatics,
Aristotle University of Thessaloniki, Thessaloniki, Greece

Department of Clinical Physiology and Nuclear Medicine, Lund
University Hospital, Lund, Sweden
e-mail: aletras@hotmail.com

Introduction

Clinical cardiac MRI has evolved since the late 1990s from a research tool to a valuable clinical imaging modality. The basic MRI clinical scan usually includes CINE function, myocardial perfusion under rest and/or stress and, last but not least, tissue viability imaging. For most clinical cases images are interpreted based on image contrast. However, during the last few years research has shown that there are advantages to collecting quantitative data rather than relying on image contrast [1]. For example, quantitative techniques have the advantage of providing absolute values for quantifying abnormalities. This is useful especially in diseases where the entire heart is affected and diagnosis cannot rely on localized tissue contrast [2]. Tissue parameter mapping is currently under intense evaluation and development so that it is now used as a routine clinical tool. In tissue mapping, every pixel of the image contains the value of a tissue relaxation parameter, such as T_1 , T_2 or T_2^* . While a variety of mapping techniques with increasing complexity are becoming available, the basic principles and basic techniques have similarities. These basic principles are the focus of this section.

Relaxation Along the z-Axis

Longitudinal, spin-lattice or T_1 relaxation describes how the nuclear spins dispose of energy, which they acquire by a radio frequency (RF) pulse during spin excitation. In the absence of contrast agents, energy is deposited by the spins to the surrounding magnetic environment i.e. to the lattice. In effect, longitudinal relaxation shows how magnetization recovers along the longitudinal z-axis. This recovery is

described by an exponential. More specifically, in saturation recovery, following a 90° RF excitation, which brings spins onto the transverse xy-plane, the spins recover over time T_{sat} as seen in Fig. 12.1. In this case, the magnetization starts from zero and over time recovers to 100 % along the +z axis. If instead the RF pulse inverts the magnetization by bringing it along the -z axis then the spins undergo inversion recovery as seen in Fig. 12.2. In this case, the magnetization on the z-axis starts from -100 %, goes through zero and recovers to +100 %. For both saturation and inversion recovery methods a readout imaging pulse sequence (denoted by ACQ [acquisition]) is used to collect an image “weighted” by either saturation or inversion recovery, respectively. It is important to note that while the equations describing the recovery processes are somewhat different (Figs. 12.1 and 12.2), the recovery in both cases is exponential and is governed by a common time constant, namely T_1 . T_1 can vary among tissues as well as between normal and diseased tissues. This so-called “native T_1 ” can be used for detecting edematous or infarcted myocardium. With the addition of gadolinium (Gd) based contrast agents, spins can also dispose of their energy onto the Gd-metal and therefore recover faster along the longitudinal z-axis. This is seen as shortening of the T_1 relaxation constant. Collecting T_1 -weighted images either with or without contrast agents can produce images that are clinically useful. The acquisition of T_1 -weighted images becomes more complicated in the presence of cardiac and respiratory motion. Also, images must be acquired within the limited amount of time a patient is inside the MRI scanner.

The most commonly used T_1 -weighted imaging sequence is the one used for evaluating myocardial viability with late gadolinium enhancement (LGE), which is T_1 weighted so as to depict normal myocardium dark and infarcted myocardium

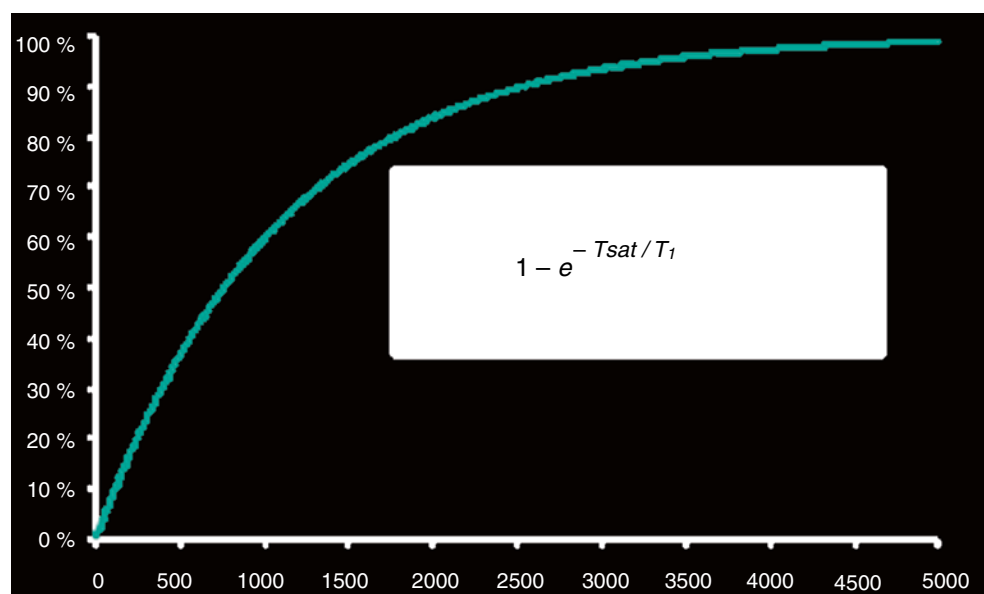


Fig. 12.1 Saturation recovery (90- T_{sat} -ACQ)

Fig. 12.2 Inversion recovery (180-TI-ACQ)

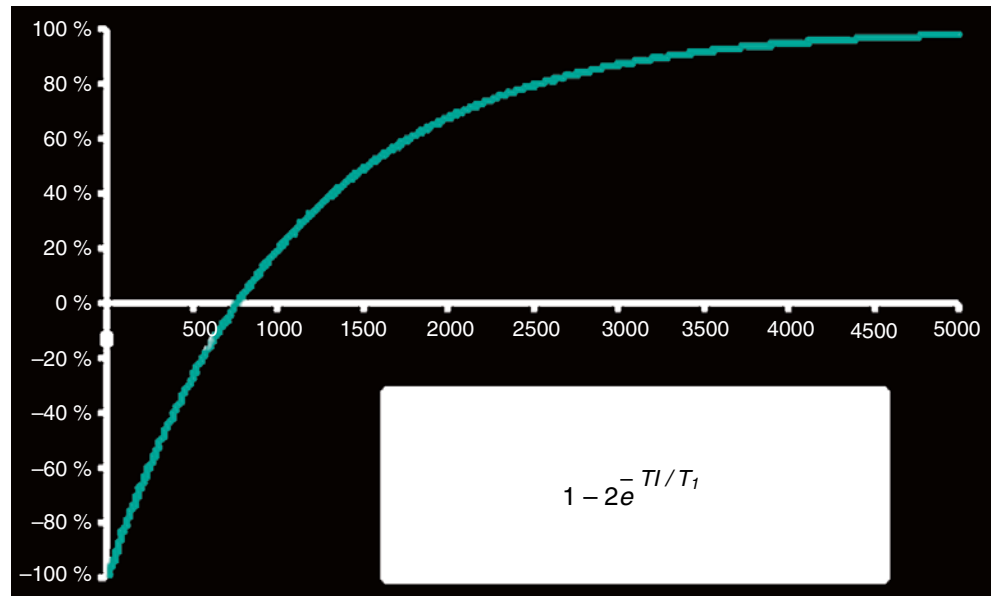


Fig. 12.3 Example of late Gd viability image. Normal myocardium is black while infarcted myocardium is bright

bright (Fig. 12.3). The contrast between normal and infarcted myocardium is based on the premise that 20 min after intravenous Gd-DTPA administration the contrast agent distributes not only in the extracellular but also in the intracellular space in acutely infarcted myocardium. In viable myocardium Gd-DTPA cannot cross the cellular membrane and, therefore, distributes only in the extracellular space [3]. Fibrosis replaces

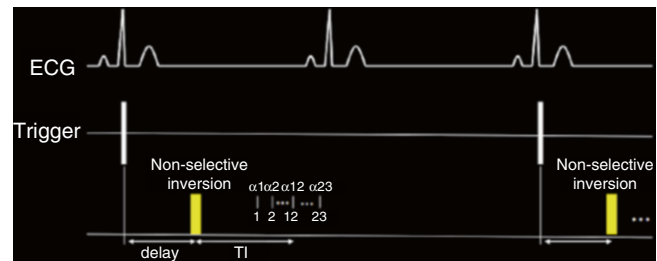


Fig. 12.4 ECG triggered segmented GRE inversion recovery

viable myocytes in chronic infarct, thus increasing the extracellular space. Therefore, both acute and chronic infarctions have increased extracellular space compared to viable myocardium. The pulse sequence for viability imaging was presented by Simonetti et al. [4] and was extensively validated by Kim and Judd [5]. The pulse sequence diagram can be seen in Fig. 12.4. This is an ECG triggered pulse sequence where signal acquisition is performed during diastasis in a segmented manner with gradient echoes over several cardiac cycles. This type of acquisition provides diagnostic quality gradient echo images that have been T₁-prepared by the inversion pulse. Approximately 20 k-lines are acquired following every inversion pulse within a given RR interval. A heartbeat is usually skipped to allow for T₁ recovery before another inversion pulse is applied. Given that the T₁ of normal myocardium in the presence of Gd-DTPA 20 min after injection is about 400–500 ms, the inversion time TI can be adjusted by the user to null normal myocardial signal (Fig. 12.5, magenta line) without much dependence on heart rate. This is because for heart rates slower than 80 bpm the 2xRR interval between inversion pulses is about 1.5 s, which corresponds to almost full T₁ recovery. For typical LGE images of 160 lines (with-

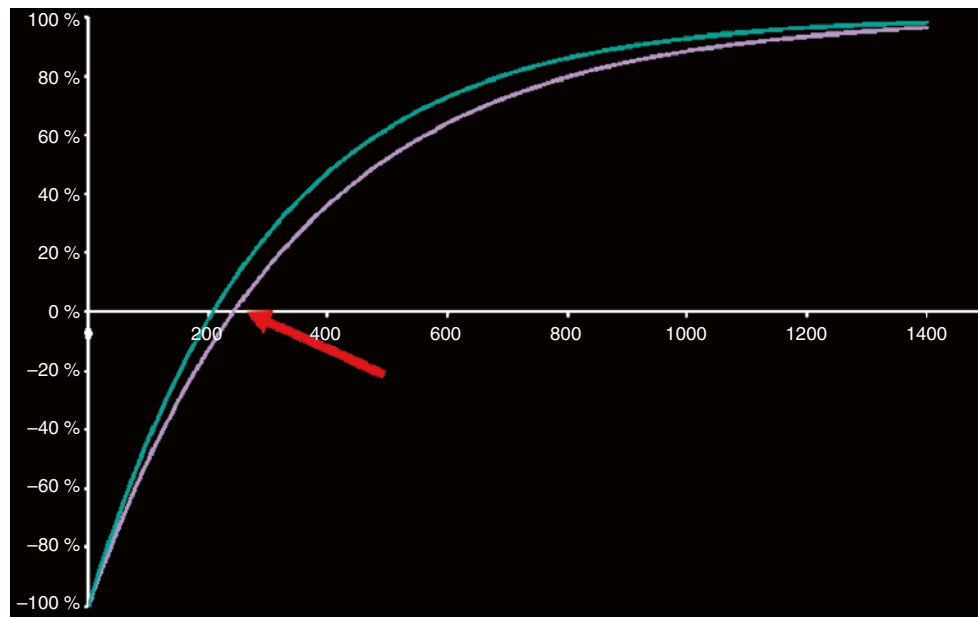


Fig. 12.5 LGE nulling of normal myocardium (*magenta*). The *red arrow* points to the time point of myocardial signal nulling. The infarct appears with positive signal, bright (*green*)

out applying any additional acceleration techniques) this results in a 16-heartbeat breath-hold.

A modification to the pulse sequence described above has been used in the absence of contrast agents for acquiring T_1 -weighted images that depict myocardial edema associated with acute myocardial infarction [6]. While this type of pulse sequence was initially used with contrast agents to estimate the appropriate inversion time TI for the LGE viability acquisition, Goldfarb and colleagues used it without gadolinium to evaluate intramyocardial edema. In this case, a CINE acquisition is performed immediately following a non-selective inversion pulse, which is applied upon detection of the R-wave. Aside from the inversion pulse, the acquisition is similar to the CINE used for myocardial function evaluation i.e. it is a segmented acquisition over several heartbeats with a Balanced Steady-State Free Precession (bSSFP) readout (also known as TrueFISP, FIESTA, b-FFE). Within the cardiac cycle, the later cardiac phases are more T_1 -weighted as a result of the increasing time from the inversion pulse.

Visualizing edema in the heart with T_1 tissue-contrast based methods such as the one described above has several drawbacks. First, this type of acquisition demands that two different types of tissue with different intensities are present at any time for contrast (i.e. signal difference) to emerge. This may not always be true for diffuse systemic diseases. Furthermore, the phased array coils used for receiving the MRI signal are not equidistant to all areas of interest within the heart. As a result, the signal is received with different intensities even when all tissue characteristics are the same. Such a surface coil intensity profile may create artificial contrast in otherwise normal tissue based solely on distance from the receiving coil.

In other cases, such as with dark-blood methods seen in Chap. 11, the artificial contrast may originate from sequence specific shortcomings. Therefore, rather than looking at signal intensities, it may be beneficial to quantify the intrinsic T_1 values within image pixels of the tissue. Such quantification, if performed correctly, has the advantage of providing numbers that depend less on the surface coil intensity profile. Such T_1 measurements can also provide an easy way to exchange data between different imaging centers and allow for defining thresholds between diseased and healthy myocardium. In order to quantify the T_1 values, an inversion recovery experiment needs to be performed multiple times so that several points along the Inversion Recovery curve can be acquired (Fig. 12.6). This is done by acquiring Inversion Recovery images with different inversion times TI and fitting with an exponential the resulting images on a pixel by pixel basis in order to yield color maps where the T_1 value of each pixel can be visualized (Fig. 12.6). While accurate and precise, using such multiple experiments to estimate the T_1 values takes a lot of time and is subject to artifacts due to patient motion.

In practice, a modified Look-Locker technique is most commonly used, which provides some accuracy and reasonable precision within a single breath-hold. This method is known as MOLLI [5]. The MOLLI pulse sequence diagram is depicted in Fig. 12.7. A non slice-selective inversion RF pulse inverts all the magnetization upon detecting the R-wave. Different time points of the inversion recovery curve (i.e. inversion times TI) are sampled over multiple cardiac cycles with single-shot bSSFP images, which last on the order of 200 ms each. Following a pause, so that the magnetization can recover (commonly a pause of three heartbeats is used for

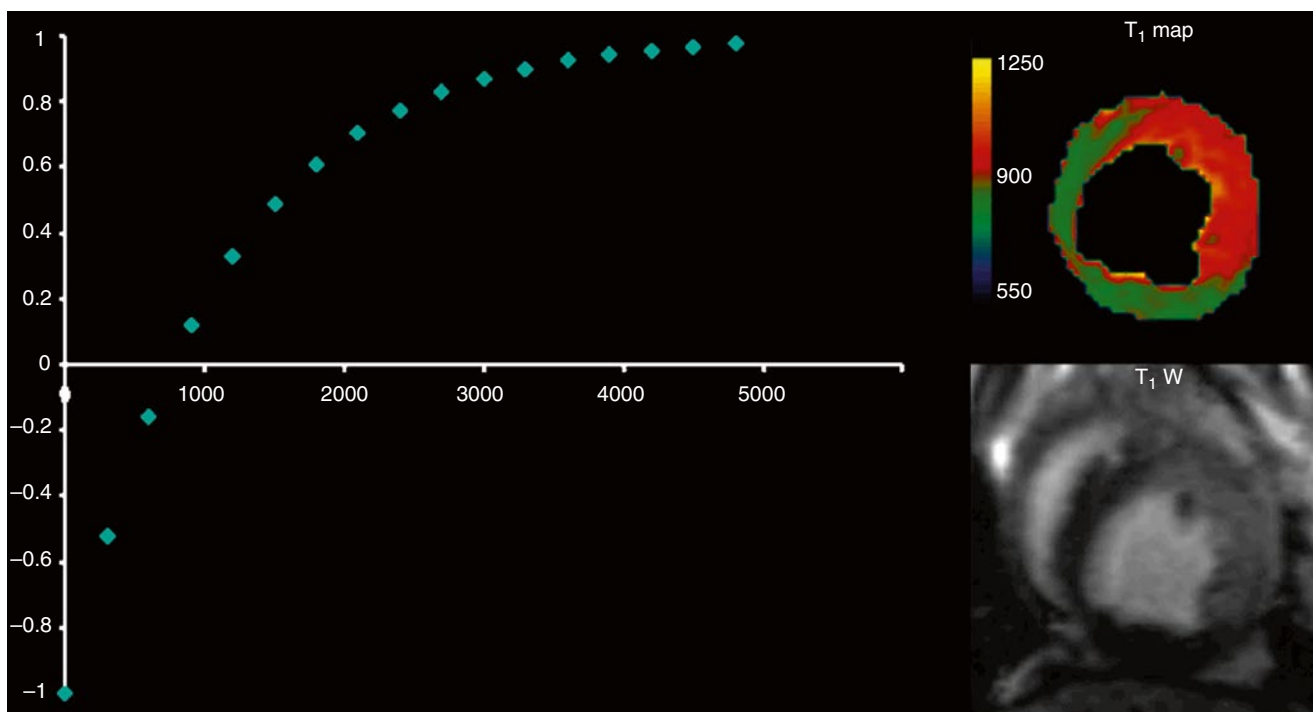


Fig. 12.6 To produce a T_1 map, the inversion time TI is varied in a number of inversion recovery experiments and multiple images at different TIs are collected. Each point on the T_1 recovery curve is derived from an

experiment. The inversion recovery equation (Fig. 12.2) is fit on a pixel-by-pixel basis to yield the T_1 value in each pixel (REF: Aletras et al, Program #2102, 11th SCMR Scientific Sessions, Los Angeles, CA, 2008)

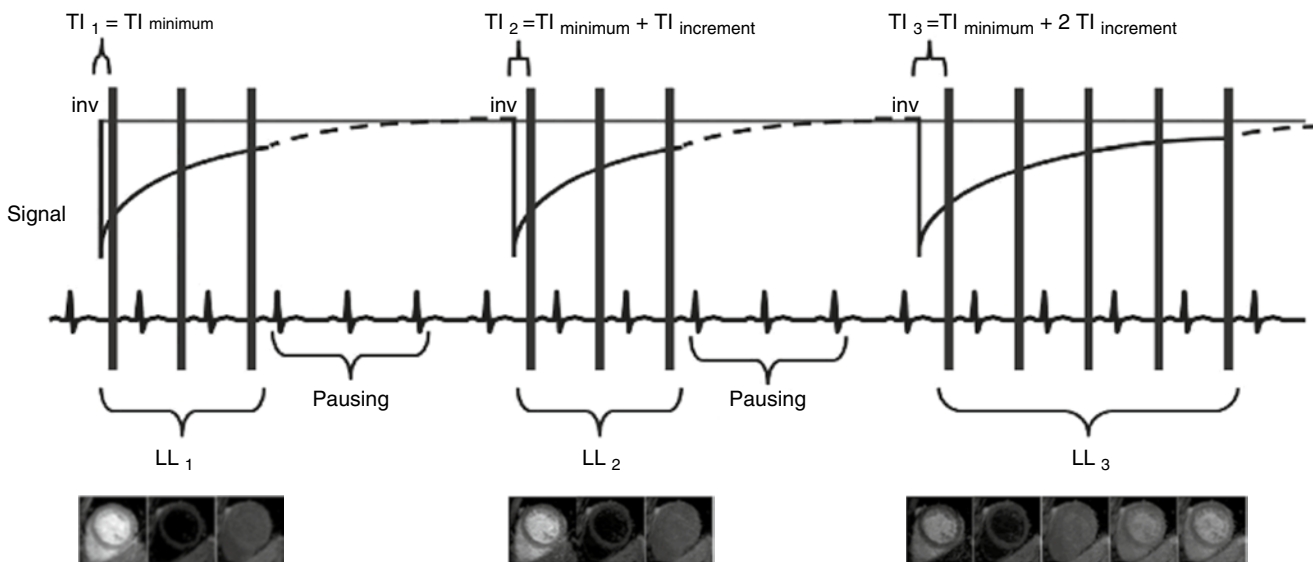


Fig. 12.7 The MOLLI approach: inversion recovery images are obtained with ECG-triggered single-shot bSSFP at different inversion times TI [5]

native T_1), the inversion is performed anew and single-shot bSSFP images are acquired at different inversion times TI so as to sample different time points on the curve. This is accomplished by adding a fixed increment to the TI. After a second pause (of three heartbeats), a third inversion pulse is applied and five images are acquired in a similar manner to that described above. Since this is the last inversion pulse, five images are acquired instead of three. Figure 12.7 shows the

three, three and five inversion recovery images obtained in this manner. One can appreciate the change in contrast with varying inversion time TI. Figure 12.8 shows how MOLLI images are post-processed. The images are listed according to their inversion time. Since these are magnitude images, negative signal intensity values have lost their negative sign and appear positive i.e. the absolute value (i.e. rectified value) of the signal is seen. The sign is recovered based on the shape of

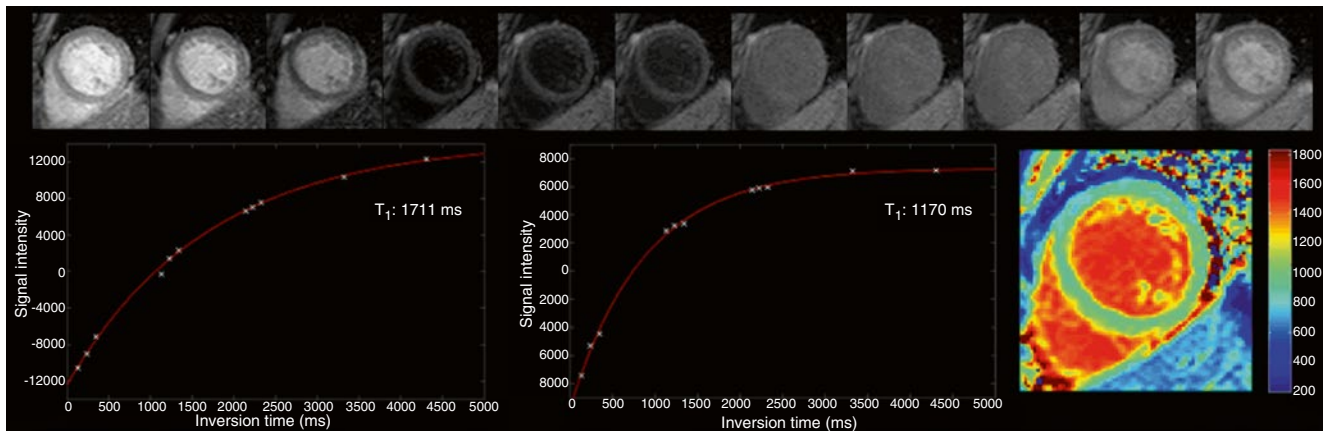


Fig. 12.8 MOLLI magnitude images are first listed according to their TI value. Sign recovery is performed and the Look-Locker correction is applied. Fitting produces the T_1 map where each pixel depicts the T_1 value

the rectified inversion recovery curve. Since each of the single-shot bSSFP images that sample the inversion recovery curve essentially modifies the inversion curve, a correction factor is applied when fitting the data with the exponential equation. This correction factor attempts to compensate for the successive imaging of the recovery curve so as to produce better estimates of the true T_1 values within each pixel. Fitting is done on a pixel-by-pixel basis to produce the T_1 map. In the resulting T_1 map the value of each pixel represents the T_1 value of the tissue within the pixel. Motion correction prior to fitting can improve the T_1 estimates since it is common to observe diaphragmatic motion throughout the MOLLI pulse sequence. Modifications to the MOLLI pulse sequence have been proposed during the last few years in order to further improve the T_1 estimates [7]. Also, newer methods to overcome MOLLI accuracy issues have been presented. For example, SASHA is based on multiple saturation recovery experiments rather than successive inversions [8]. Its advantage is higher accuracy since the signal recovers from zero and therefore the estimates are less vulnerable to heart rate variations. Prior to collecting patient data, each T_1 mapping technique should be thoroughly tested on-site with phantoms of known T_1 values so as to avoid surprises later on. These are complicated data acquisition methods where errors that can occur either during image acquisition or post-processing can be avoided with careful planning and testing.

Extracellular volume (ECV) imaging uses the MOLLI pulse sequence. ECV imaging provides estimates of the extracellular volume on a pixel-by-pixel basis and can provide a truly fresh look into diffuse myocardial diseases. ECV imaging is based on the fact that the MRI contrast agent Gd-DTPA does not cross the cellular membrane and that after injection remains primarily within the extracellular space. As such, Gd-DTPA becomes a probe for extracellular space. In general, the higher the concentration of Gd, the

lower the T_1 observed in the myocardium. If one defines R_1 as the inverse of T_1 (i.e. $R_1 = 1/T_1$) then the change observed in the native (i.e. pre-contrast) R_1 after the injection of Gd is proportional to the concentration of the contrast agent [Gd] [9], which distributes in the extracellular space. If one measures the change in R_1 both in myocardium and blood then

$$\frac{\Delta R_{1 \text{ myocardium}}}{\Delta R_{1 \text{ blood}}} = \frac{[\text{Gd}]_{\text{myocardium}}}{[\text{Gd}]_{\text{blood}}} = \frac{\text{ECV}_{\text{myocardium}}}{\text{ECV}_{\text{blood}}}$$

Furthermore, the hematocrit is the percent volume of red blood cells in blood. Since we have defined $\text{ECV}_{\text{blood}}$ as the percentage of extracellular volume in blood then $\text{ECV}_{\text{blood}} = 1 - \text{HCT}$. Therefore, the hematocrit provides a measurable quantity, obtained via a blood sample. The hematocrit can be used for converting the observed changes in R_1 values into an ECV measurement for the myocardium as follows:

$$\text{ECV}_{\text{myocardium}} = \frac{\Delta R_{1 \text{ myocardium}}}{\Delta R_{1 \text{ blood}}} (1 - \text{HCT})$$

A block diagram of the steps taken to produce color ECV maps by magnetic resonance is shown in Fig. 12.9 [10].

Relaxation on the Transverse Plane

Transverse, spin-spin or T_2 relaxation describes how the transverse plane magnetization, which is the source of the acquired MRI signal, is lost over time as a result of interactions between spins. Following a 90° RF excitation pulse, spins are brought onto the transverse plane together i.e. the spins are “in-phase” forming a single magnetization vector. However, over time, the spins on the transverse plane start to spin with ever so slightly different speeds thus acquiring dif-

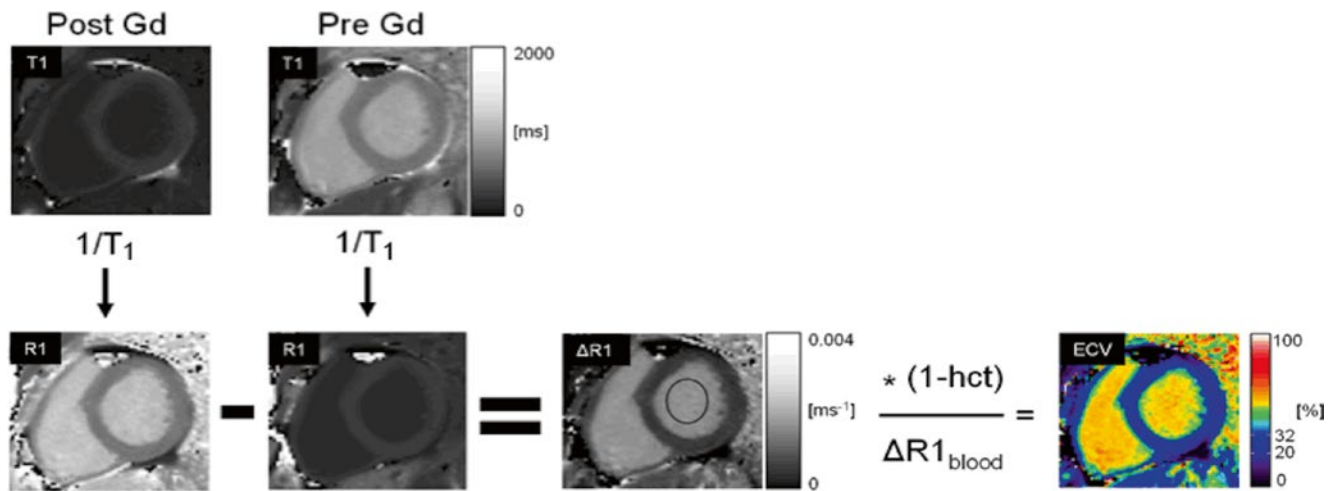


Fig. 12.9 Extracellular volume (ECV) is estimated by subtracting an R1 map obtained post Gd-DTPA administration from the native R1 map obtained prior to contrast administration. The R1 of the blood pool and

the hematocrit are used to convert R1 values in the myocardium into ECV estimates in the myocardium, as described in the text [10]

ferent phases from one another (this “dephasing” is equivalent to race cars starting from one particular point on a circular racing track and over time spreading out around the track). As a result, over time the spins add less and less constructively with one another thus resulting in less and less signal being observed. After some time, spins on the transverse plane have all possible orientations (i.e. phases) and therefore the observed signal is zero. This process is based on the fact that each spin experiences a slightly different magnetic field strength, which in turn makes it spin (i.e. precess) at a slightly different speed than others. This is a direct consequence of Larmor’s equation, which says that spins inside a magnetic field will spin with a speed (i.e. frequency) that linearly depends on the magnetic field strength.

There are two reasons why spins experience different magnetic field strengths. The first depends on inherent tissue properties and the second depends on how homogeneous the main magnetic field is. When considering tissue properties alone, the magnetic dipoles in tissue tumble either fast or slow depending on whether the water is free or restricted in its motion. At the local level, these spin dipoles perturb the magnetic field that the other neighboring spins are experiencing, thus changing the spinning speed (i.e. frequency) of neighboring spins. The magnetic dipoles of fast tumbling spins do not interact with one another as much as the magnetic fields of slower tumbling spins do between each other. Therefore, for free water fast tumbling spins the signal is preserved for a longer time when compared to the signal arising from water that is restricted in its motion (Fig. 12.10). The loss of signal on the transverse plane as a result of spin-spin interactions alone is described by an exponential decay with a decay constant T_2 . The longer the T_2 constant, the longer the MRI signal persists.

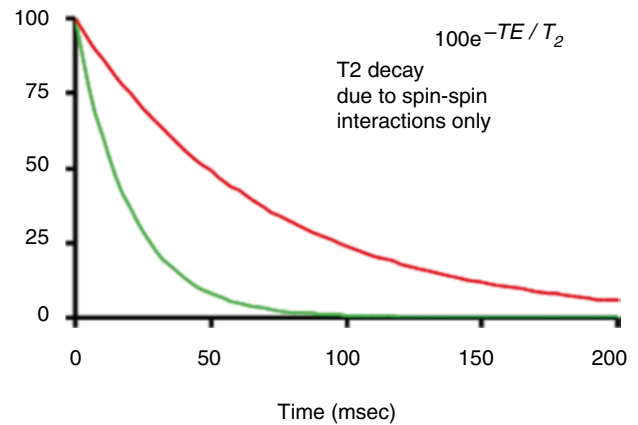


Fig. 12.10 Fast tumbling water molecules (e.g. free water) produce a signal (red) that decays slower than the signal (green) from water molecules with restricted motion that tumble slower. The exponential decay T_2 constant for fast tumbling spins is longer than that of slower tumbling spins

When considering the effects of main field inhomogeneity alone, the Larmor equation applies. This equation tells us that spins precess at a frequency that depends on the strength of the magnetic field. Our inability to create a perfectly homogeneous magnetic field throughout the body of the patient results in different spinning frequencies among spins and, therefore, signal loss over time due to dephasing. In this case, the dephasing and signal loss are the result of an external factor (main field inhomogeneity) rather than due to spin-spin interactions within the tissue. The combined effect of both spin-spin interactions and main magnetic field inhomogeneity is observed as an exponential decay of the MRI signal with a decay constant T_2^* . Because spin-spin interactions are part of the combined effect on signal decay, T_2 is always

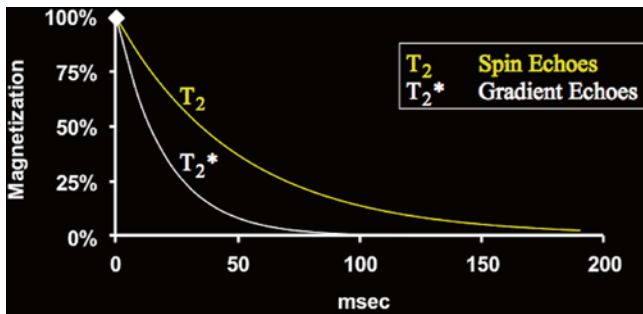


Fig. 12.11 The magnetization decays exponentially as a function of time spent on the transverse plane. Spin echo imaging depicts T_2 relaxation. Gradient echo imaging depicts T_2^* relaxation (The magnetization is plotted as a function of echo formation time, TE)

greater than (or in the case of a perfectly homogeneous field, equal to) T_2^* . The signal disappears faster when main field inhomogeneity is present. Spin echoes, which compensate for field inhomogeneity, can be used to visualize the signal decay on the transverse plane due to T_2 relaxation (Fig. 12.11, yellow decay). Gradient echoes can be used to visualize the decay due to T_2^* relaxation (Fig. 12.11, white decay).

A spin echo is created by a 180° radiofrequency pulse that refocuses any phase imparted onto the spins by static magnetic field inhomogeneity. The idea is that a spin will accumulate a certain amount of phase over a certain time due to field inhomogeneity. As can be derived from the Larmor equation, the larger the field inhomogeneity the more the accrued phase. Also, the longer the time under the influence of the inhomogeneity, the more the accrued phase. The peak of the spin echo forms when the spins have been on the transverse plane equal amounts of time before and after the 180° RF pulse. Simply explained, the 180° pulse acts as a “minus sign” so that phase accrued prior to the 180° RF due to field inhomogeneity is canceled out by the equal amount of phase accrued after the 180° pulse. Therefore, since field inhomogeneity effects are not visible, a spin echo reflects only T_2 signal losses.

A gradient echo is created by gradient pulses. These gradient pulses are designed in such a manner so as to impart a certain amount of phase to spins and then remove the exact same amount, thus forming an echo. This is accomplished with two otherwise identical gradient pulses except for their inverse polarity. This type of manipulation of the spins’ phase with gradient sign reversals is useful for creating images. However, gradient sign reversals are not capable of rephasing any accumulated phase due to static magnetic field inhomogeneity. This is easier to understand if one considers that a field inhomogeneity is itself a gradient, which is always on and cannot be reversed in terms of its sign. Therefore, it imparts phase to the spins that cannot be canceled out when forming a gradient echo. Therefore, gradient echoes reflect T_2^* since the signal experiences losses due to dephasing as a result of field inhomogeneity.

The pulse sequence commonly used in CMR for visualizing intramyocardial edema is based on a Turbo Spin Echo

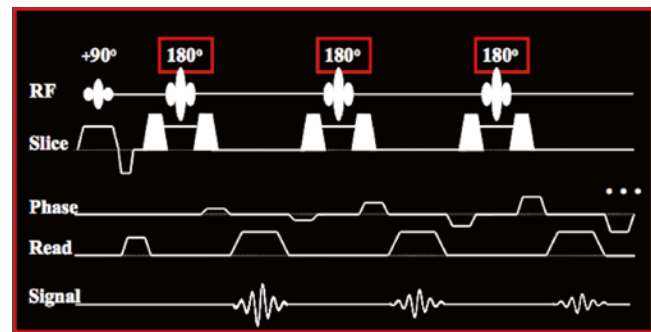


Fig. 12.12 With a turbo spin echo pulse sequence, multiple spin echoes are formed by a train of RF pulses, each 180° . While all spin echoes are immune to dephasing due to field inhomogeneity, subsequent spin echoes have more T_2 -weighting due to spin-spin relaxation

(TSE) or otherwise known as a Fast Spin Echo (FSE) (Fig. 12.12). Instead of creating only a single spin echo with a single 180° pulse, multiple spin echoes are created by a train of equidistantly spaced 180° pulses. Since all spin echoes are compensated for static magnetic field inhomogeneity, all spin echoes reflect T_2 signal losses. The closer the echo is to the 90° excitation RF pulse, the less the T_2 -weighting. Later echoes are more T_2 -weighted since the spins spend more time on the transverse plane and therefore lose more signal due to spin-spin interactions. Echoes forming with an echo time TE of about 60–100 ms are well suited for imaging edema in the myocardial wall. Usually, TSE T_2 -weighted imaging is segmented over several heartbeats. Imaging is performed with about 24–32 echoes during diastasis so that cardiac motion artifacts can be minimized. Between successive echo trains a heartbeat is left with no spin excitation (2RR imaging) so that T_1 effects can be mitigated. Dark-blood contrast is most commonly implemented with a set of preparation pulses so that images with suppressed blood signal can be obtained (see Chap. 11).

During the last several years Steady-State Precession (bSSFP) techniques have been proposed as an alternative to using TSE for T_2 -weighted imaging of edema in the heart. bSSFP provides bright-blood contrast (i.e. the blood appears bright in images) instead of the dark-blood contrast obtained with TSE. Bright-blood contrast has the advantage of more clearly delineating the endocardial surface near hypokinetic myocardium where dark-blood methods may lead to false positives [11]. bSSFP utilizes gradient moment nulling to avoid dephasing of spins so as to yield bright-blood contrast. With gradient moment nulling, all gradient pulses in bSSFP are canceling each other out (Fig. 12.13, yellow lines) so that the net phase imparted by the imaging gradients on the spins is zero. This approach results in “bright blood” since blood spins are not dephased. By means of appropriate RF pulses, the magnetization vector in bSSFP is tipped symmetrically about the z-axis by half the flip angle that the user prescribes (Fig. 12.14). This allows for a large component of the magnetization to be projected onto the transverse plane. As a

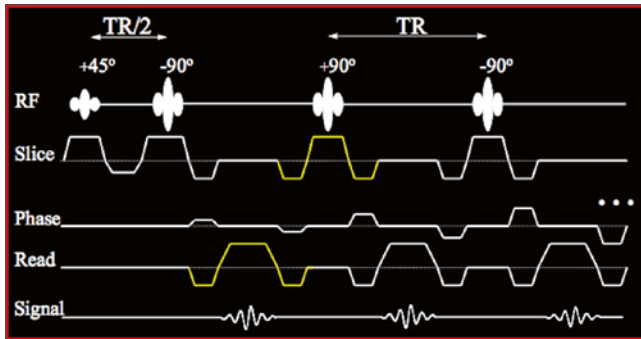


Fig. 12.13 bSSFP relies on refocusing phase imparted by the imaging gradient pulses. This is accomplished by compensating for each gradient pulse with additional pulses of opposite sign and equal area (yellow pulses)

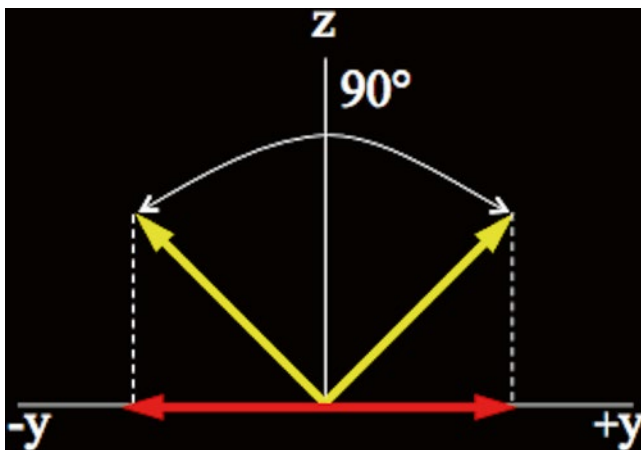


Fig. 12.14 With bSSFP, the magnetization (yellow) is tipped symmetrically about the z-axis. As a result of the large flip angles used (e.g. 90°), the transverse component of the magnetization, which we can receive, is also large (e.g. about 70 % of total). Thus quality images can be acquired

result, the bSSFP images are usually of higher quality (in terms of signal to noise ratio) when compared to gradient echo images. Furthermore, because the magnetization is tipped symmetrically about the z-axis, the transverse component of the magnetization behaves similar to the manner in which a spin echo would. As a result, the echoes obtained with bSSFP are compensated for field inhomogeneity and reflect T_2 relaxation (rather than T_2^*). Since the magnetization does not spend all its time on the transverse plane but also along the z-axis, there is also T_1 relaxation contrast in the image. With an RF pulse with a flip angle of 90° the bSSFP images have $\frac{T_2}{T_1}$ contrast.

For imaging myocardial edema with bSSFP, the T_2 contrast of the image can be improved considerably by incorporating a so-called “ T_2 -prep” prior to utilizing bSSFP for image readout. The T_2 -prep adds T_2 contrast by preparing the spins in a manner that depends on spin echoes (Fig. 12.15). The T_2 -prep consists of a non-selective 90°

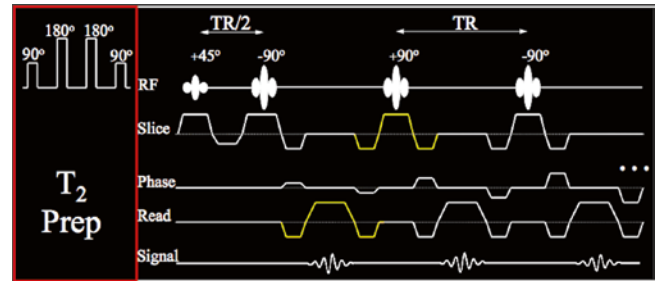


Fig. 12.15 When the bSSFP readout is preceded by a T_2 -preparation (red box), then good T_2 contrast can be obtained. The contrast depends on the time the spins spend on the transverse plane during the T_2 -prep

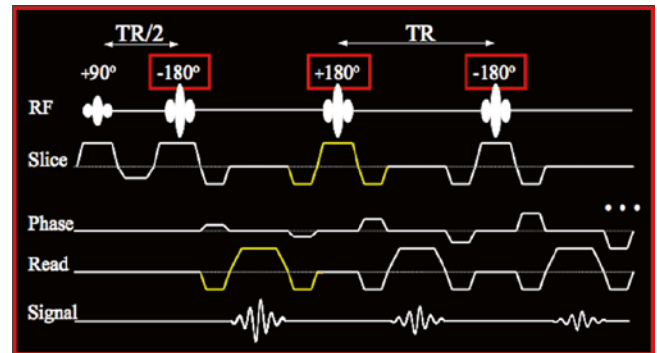


Fig. 12.16 When the bSSFP readout is played out with a flip angle of 180° , then spin echoes form in a similar manner as in the turbo spin echo readout. This gives the bSSFP readout inherent T_2 contrast. Bright-blood contrast is also obtained because gradients in bSSFP are balanced

excitation RF pulse, which excites the entire heart, and a small number of 180° pulses that create spin echoes. However, an image is not created directly by these spin echoes. Instead, the last spin echo, which reflects T_2 relaxation, is stored along the z-axis by means of a second 90° pulse (Fig. 12.15). Then, the stored magnetization is encoded in space by a single-shot bSSFP read out, which creates the image. Alternatively, the T_2 -weighted image can be acquired in a segmented manner over several heartbeats by repeating the T_2 preparation and the bSSFP readout multiple times; however, acquiring only a fraction of the raw data needed to form the image per heartbeat.

Another way to improve T_2 contrast in bSSFP images, without using a T_2 -prep scheme, is the ACUT2E (Acquisition for Cardiac Unified T_2 Edema) pulse sequence (Fig. 12.16) [12]. With ACUT2E it is only necessary to increase the flip angle to 180° and appropriately arrange how data are acquired during the image read out. No T_2 preparation of the magnetization with spin echoes is needed because the bSSFP train, with the 180° pulses, forms spin echoes, which have inherent T_2 contrast. The use of 180° pulses allows for the entire magnetization to be on the transverse plane, which results in higher quality images. Since the bSSFP is using balanced gradients to avoid dephasing the spins, the ACUT2E images possess bright-blood contrast as well. In many ways

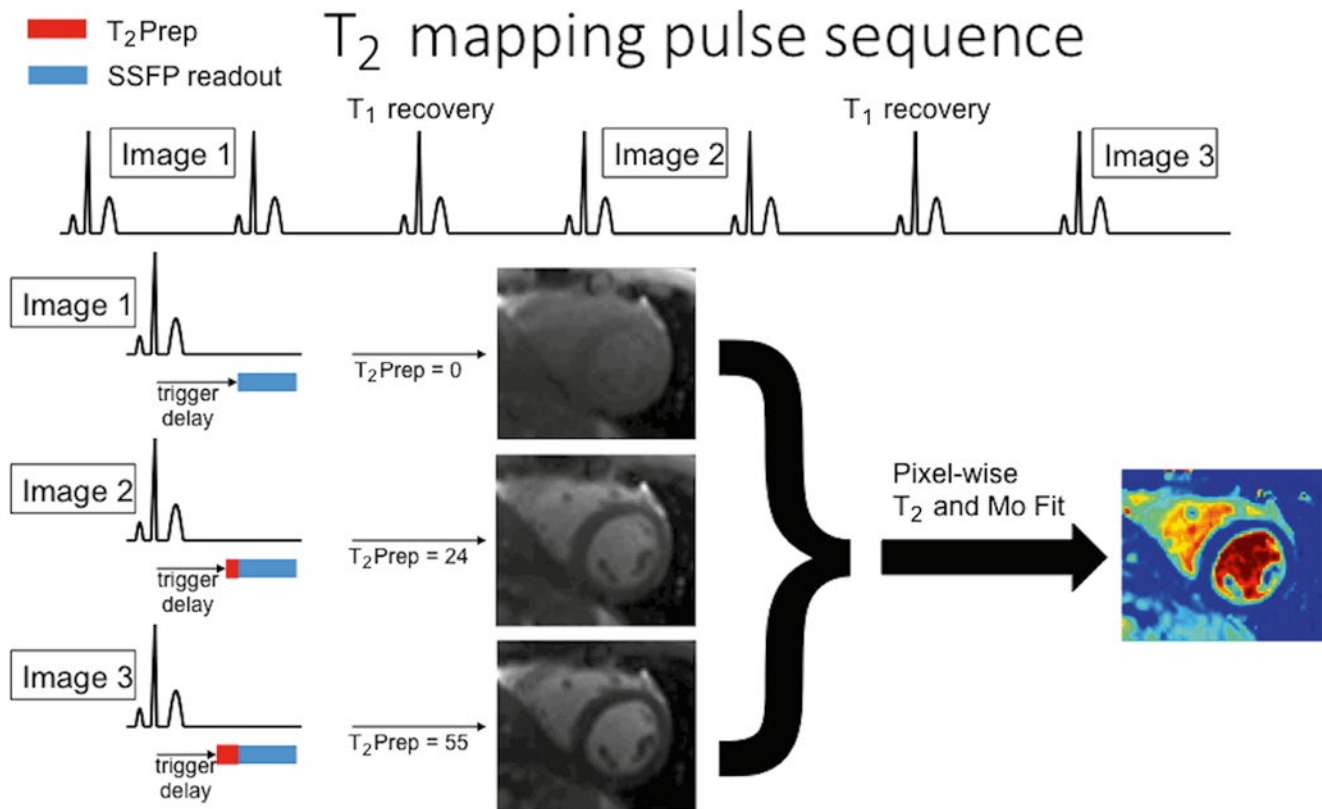


Fig. 12.17 The T₂ of the tissue can be estimated by collecting T₂-prep bSSFP images with different preparation times and combining the data with exponential fitting

the ACUT2E pulse sequence can be thought of as a TSE with balanced gradients [13]. Therefore, ACUT2E is a TSE-bSSFP hybrid.

Rapid T₂ mapping of myocardial tissue has been accomplished by means of the T₂-prep bSSFP methods in a single breath hold [14]. The idea is based on collecting three images with different preparation times so that three different points of the T₂ exponential decay can be measured (Fig. 12.17). The three measurements are then fitted with a two-parameter exponential decay in order to estimate the T₂ value on a pixel-by-pixel basis. In order to acquire the first data point of the exponential decay (i.e. at t=0) the T₂-prep is turned off. It is interesting to note that with T₂-prep bSSFP the signal does not become zero when the preparation time becomes very long. Therefore, a two-parameter model for fitting the data would not seem appropriate. However, within the physiological range of T₂ values in myocardium this methodology yields reasonable results.

T₂* contrast has been shown to provide insight in diseases that are associated with increased deposition of iron in the tissue such as thalassemia [15]. Such images are relatively easy to acquire by means of traditional gradient echo imaging with a long echo time (TE) and a long repetition time

(TR). However, it is T₂* mapping, where the actual values of the T₂* relaxation characteristics are known, that has revolutionized the manner by which patients with thalassemia are treated. Mapping the T₂* values in the myocardium and the liver allow for guiding the treatment. To obtain T₂* maps, gradient echoes have to be used since they depict local field inhomogeneity, which increases with increased iron deposition. In this case, multiple gradient echoes are acquired by rephasing the spins multiple times from a single excitation (Fig. 12.18). The rephasing of spins is done with gradient pulses. These pulses are designed so that their areas (and therefore the dephasing effect on the spins) add to zero at regular intervals, thus forming echoes. In Fig. 12.15 the readout gradients serve this purpose in order to form the train of gradient echoes. Every time there is a change in color (yellow/white) the area of the pulses adds to zero and an echo forms. Depending on how many of these echoes are grouped together in each image, images with successively longer echo times can be obtained (e.g. TE1 and TE2). Images with different echo times can be interrogated at the pixel level so as to produce T₂* maps by means of exponential fitting. Since the T₂* values in the heart and the liver are not the same, different imaging protocols are used for each tissue.

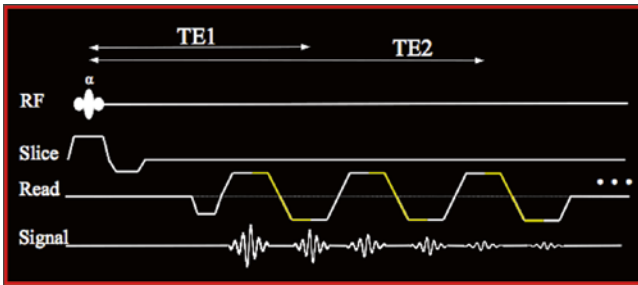


Fig. 12.18 A pulse sequence that collects multiple gradient echoes by rephasing the spins multiple times depends on balancing the gradient pulses. An echo is created every time the total area of a gradient pulse is canceled by an equal amount of area with the opposite sign (e.g. yellow line). The echoes are grouped in images with different echo times (e.g. TE1, TE2), which can be used to estimate T_2^*

Conclusions

Tissue characterization methods are developing rapidly. This arena is one that makes magnetic resonance imaging different from other imaging techniques and is likely one that will benefit future clinical applications the most. As the field evolves it is important, especially for mapping methods, that appropriate testing is done during development but also at the application site to verify that the values measured are correct. This will ensure that quality data are acquired for clinical purposes.

References

- van der Geest RJ, Reiber JHC. Quantification in cardiac MRI. *J Magn Reson Imaging*. 1999;10:602–8.
- Ferreira VM, Piechnik SK, Dall'Armellina E, Karamitsos TD, Francis JM, Ntusi N, Holloway C, Choudhury RP, Kardos A, Robson MD, Friedrich MG, Neubauer S. Native T_1 -mapping detects the location, extent and patterns of acute myocarditis without the need for gadolinium contrast agents. *J Cardiovasc Magn Reson*. 2014;16:36.
- Thornhill RE, Prato FS, Wisenberg G. The assessment of myocardial viability: a review of current diagnostic imaging approaches. *J Cardiovasc Magn Reson*. 2002;4:381–410.
- Simonetti OP, Kim RJ, Fieno DS, Hillenbrand HB, Wu E, Bundy JM, Finn JP, Judd RM. An improved MR imaging technique for the visualization of myocardial infarction. *Radiology*. 2001;218:215–23.
- Messroghli DR, Greiser A, Frohlich M, Dietz R, Schulz-Menger J. Optimization and validation of a fully-integrated pulse sequence for modified Look-Locker inversion-recovery (MOLLI) T_1 mapping of the heart. *J Magn Reson Imaging*. 2007;26:1081–6.
- Goldfarb JW, Arnold S, Han J. Recent myocardial infarction: assessment with unenhanced T_1 -weighted MR imaging. *Radiology*. 2007;245:245–50.
- Kellman P, Herzka DA, Hansen MS. Adiabatic inversion pulses for myocardial T_1 mapping. *Magn Reson Med*. 2014;71:1428–34.
- Chow K, Flewitt JA, Green JD, Pagano JJ, Friedrich MG, Thompson RB. Saturation recovery single-shot acquisition (SASHA) for myocardial T_1 mapping. *Magn Reson Med*. 2014;71:2082–95.
- Arheden H, Saeed M, Higgins CB, Gao D-W, Bremerich J, Wyttenbach R, Dae MW, Wendland MF. Measurement of the distribution volume of gadopentetate dimeglumine at echo-planar MR imaging to quantify myocardial infarction: comparison with ^{99m}Tc -DTPA autoradiography in rats. *Radiology*. 1999;211:698–708.
- Ugander M, Oki AJ, Hsu LY, Kellman P, Greiser A, Aletras AH, Sibley CT, Chen MY, Bandettini WP, Arai AE. Extracellular volume imaging by magnetic resonance imaging provides insights into overt and sub-clinical myocardial pathology. *Eur Heart J*. 2012;33:1268–78.
- Kellman P, Aletras AH, Mancini C, McVeigh ER, Arai AE. T_2 -prepared SSFP improves diagnostic confidence in edema imaging in acute myocardial infarction compared to turbo spin echo. *Magn Reson Med*. 2007;57:891–7.
- Aletras AH, Kellman P, Derbyshire JA, Arai AE. ACUT2E TSE-SSFP: a hybrid method for T_2 -weighted imaging of edema in the heart. *Magn Reson Med*. 2008;59:229–35.
- Hinks RS, Constable RT. Gradient moment nulling in fast spin echo. *Magn Reson Med*. 1994;32:698–706.
- Giri S, Chung YC, Merchant A, Mihai G, Rajagopalan S, Raman SV, Simonetti OP. T_2 quantification for improved detection of myocardial edema. *J Cardiovasc Magn Reson*. 2009;11:56.
- Anderson LJ, Holden S, Davis B, Prescott E, Charrier CC, Bunce NH, Firmin DN, Wonke B, Porter J, Walker JM, Pennell DJ. Cardiovascular T_2 -star (T_2^*) magnetic resonance for the early diagnosis of myocardial iron overload. *Eur Heart J*. 2001;22:2171–9.

Daniel C. Lee, Neil R. Chatterjee, and Timothy J. Carroll

Abstract

Myocardial perfusion is an important measurement in the diagnosis and management of coronary artery disease. While clinical measurement of myocardial perfusion has long been dominated by nuclear imaging, MRI has recently emerged as an alternative method with many significant advantages. Compared to single photon emission computed tomography (SPECT), MRI has much higher resolution, requires no radiation dose, and has the potential for more quantitative measurements. MR perfusion measurement can be complex, however, and when designing an MR perfusion experiment there are a variety of choices to consider. Unfortunately, there is no consensus MRI perfusion implementation that is best for all situations, and choosing the ideal parameters for a given scan requires a careful understanding of the pros and cons of each component of an MRI perfusion experiment. In this chapter, we discuss the different components of cardiac perfusion MRI including pulse sequences, image readout, acceleration techniques, and image analysis. In each section, we review the basic theory behind each technique and then discuss their relative advantages and disadvantages. We conclude with a brief discussion of emerging techniques that are currently being researched.

Keywords

MRI • CMR • Perfusion • Blood flow • Pulse sequences • Quantification

Introduction

Imaging myocardial perfusion, the amount of blood flow within heart muscle, plays a critical role in diagnosing coronary artery disease, making revascularization decisions, and

predicting a patient's future risk of a cardiac event. In addition to its role in coronary artery disease, abnormalities in myocardial perfusion have also been identified in other diseases such as cardiomyopathy [1], repaired coarctation of the aorta [2], and asymptomatic individuals with variable atherosclerosis risk factors [3].

D.C. Lee, MD (✉)
Division of Cardiology, Department of Medicine, Northwestern
University Feinberg School of Medicine, Chicago, IL, USA
e-mail: dlee@northwestern.edu

N.R. Chatterjee, BS
Northwestern University Feinberg School of Medicine,
Chicago, IL, USA
e-mail: neil-chatterjee@northwestern.edu

T.J. Carroll, PhD
Department of Radiology, Northwestern Memorial Hospital,
Chicago, IL, USA
e-mail: t-carroll@northwestern.edu

The clinical measurement of myocardial perfusion has long been dominated by nuclear imaging -principally single photon emission computed tomography (SPECT) [4]. More recently, MRI has emerged as an alternative way to measure cardiac perfusion. MRI has significant advantages over SPECT including much higher resolution (Fig. 13.1), no required radiation dose, and the potential for more quantitative measurements. MRI measurement of myocardial perfusion has been the subject of much research and has been described in a number of review articles [5–9].

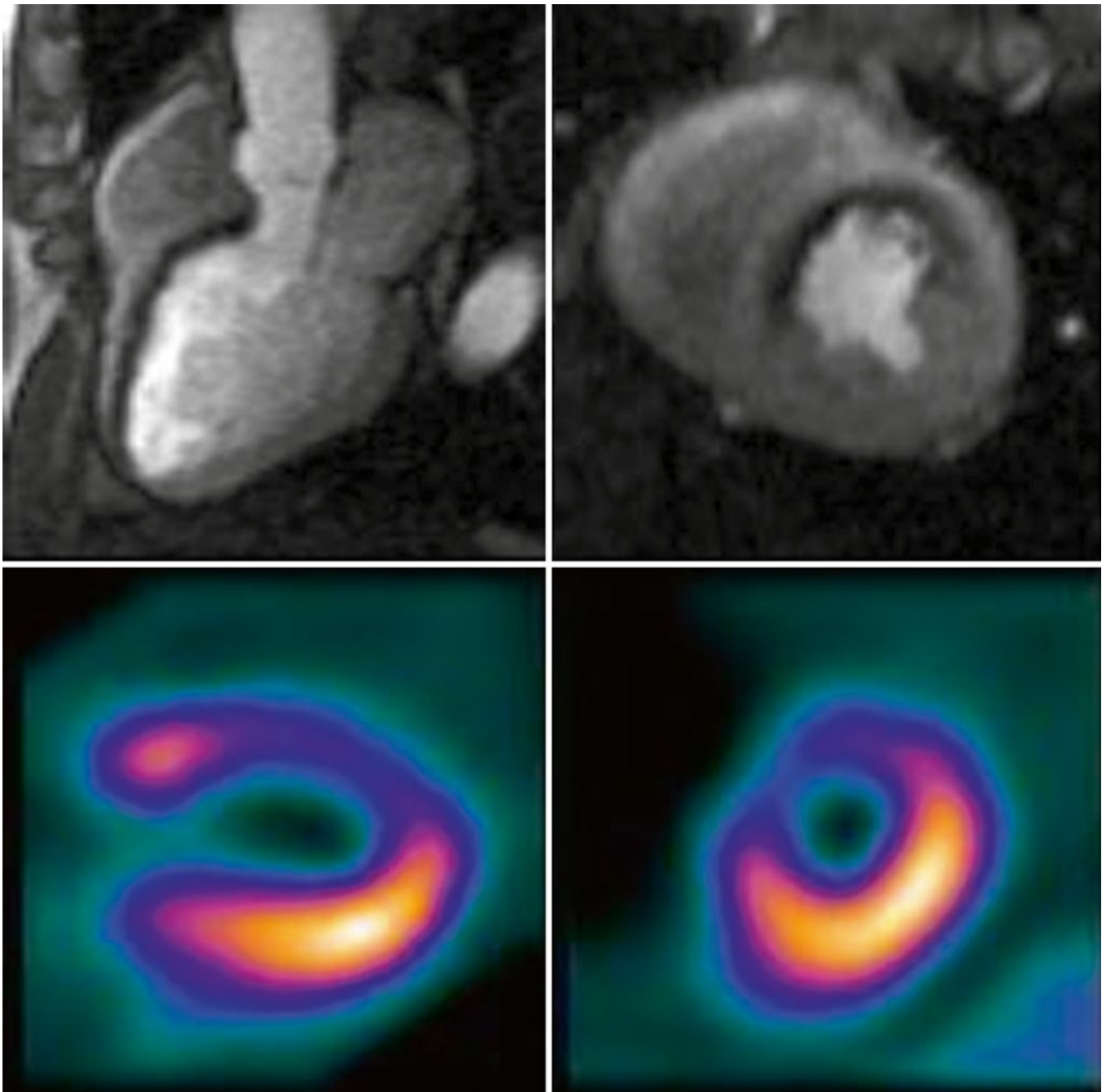


Fig. 13.1 Severe ischemia in the distribution of the left anterior descending coronary artery seen by MR perfusion (*top row*) and SPECT imaging (*bottom row*). A single frame from the first-pass MR perfusion series demonstrates severe ischemia of the anteroseptum from base to

apex in the three-chamber view (*top left*) and of the septal and anterior walls in the mid-chamber short axis view (*top right*). On SPECT imaging, a similar distribution of ischemia is seen on the vertical long axis (*bottom left*) and mid-chamber short axis view (*bottom right*)

The most common way to measure perfusion with CMR is via the “first pass” technique. A bolus of contrast is injected in a peripheral vein, and contrast enhancement is observed as the bolus passes through the myocardium. Mathematical analysis of the shape of the time-signal intensity curve measured in the myocardium is used to quantify the tissue perfusion in ml/g-min. There are other techniques for measuring perfusion with MRI, but they

have notable drawbacks. Arterial spin labeling (ASL) [10] is a promising technique that uses no exogenous contrast, but has less contrast to noise ratio (CNR) than traditional first pass methods. Blood Oxygen Level Dependent (BOLD) imaging [11] also uses no exogenous contrast, but its interpretation for quantitative perfusion can be complicated because it also depends on factors such as oxygen extraction fraction. Because first pass with a contrast bolus

makes up the overwhelming majority of cardiac perfusion scans, it will be the focus of this chapter.

Pulse Sequences

Constraints and Requirements

The choice of which pulse sequence to use is a key determinant of image contrast, spatial and temporal resolution, coverage, and degree of artifacts. These characteristics are usually at odds with one another – for example gains in contrast may come at the expense resolution or coverage – and selecting the optimal sequence requires weighing these competing gains and losses against each other. Consequently, when selecting a perfusion sequence, it is critical to consider the basic requirements for cardiac perfusion imaging. These are:

1. **Strong T_1 contrast.** The contrast agent used in MRI perfusion significantly alters the T_1 of the myocardium during first pass, therefore T_1 sensitive image contrast is desirable.
2. **Coverage of relevant myocardium.** Usually this includes at minimum one short axis slice each through the base, middle, and apex of the myocardium of the left ventricle (LV).
3. **Spatial Resolution.** At minimum, most sequences must be able to distinguish between subendocardial and transmural ischemia.
4. **Temporal Resolution.** To adequately sample flow at the myocardial level, images must be acquired every one to two heartbeats. For quantitative perfusion, there is the additional requirement of being able to adequately sample the input function within the blood pool of the LV. Because contrast passes much quicker through the LV than the myocardium, this usually requires sampling every heartbeat.
5. **Lack of Artifacts.** In particular, the dark rim artifact is a specific property of MRI perfusion images that can mimic perfusion defects resulting in potential for misinterpretation and should be minimized.

In meeting these requirements, perfusion imaging has a critical constraint that is absent in much of CMR: because characterizing the bolus passage requires acquiring a full image every one to two heart beats, segmented acquisition (as is used in Cine and Late Gadolinium Enhanced imaging) is limited or impossible. In order to achieve full heart coverage, typically three short axis images must be acquired within the time course of a single heartbeat. This limits perfusion imaging to very time-efficient pulse sequences that reduce the time to acquire an image to ~100 ms. The image

acquisition time is determined by the length of the cardiac cycle which is often shortened by vasodilator stress.

Preparation Pulses

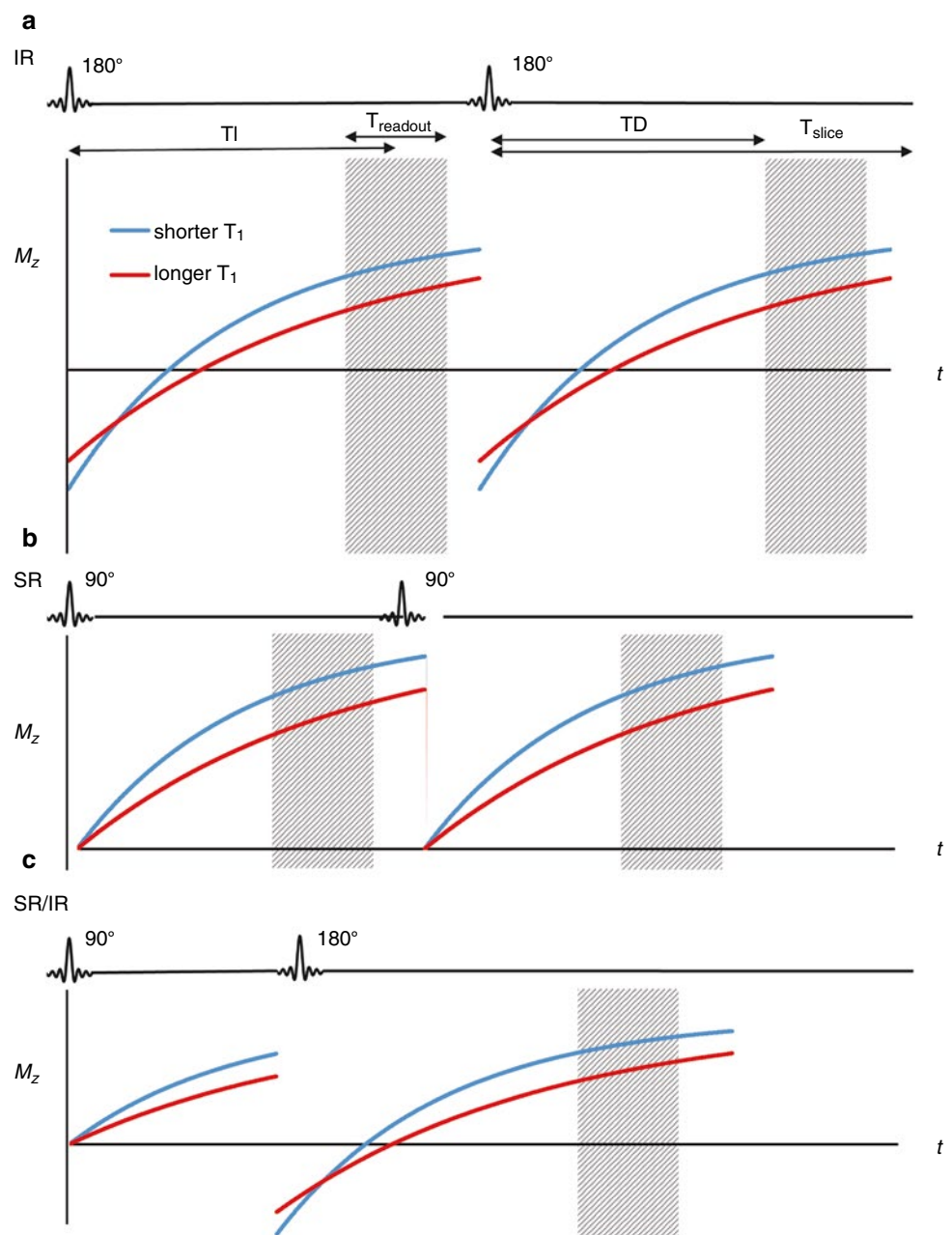
At the most basic level, a T_1 -weighted image is acquired by perturbing the longitudinal magnetization (M_z) away from equilibrium through the application of an RF pulse at the beginning of the pulse sequence and then acquiring images before the magnetization has a chance to return to normal. As a general rule, blood, fat, and myocardium with short T_1 will return to its unperturbed state faster, appearing bright in a T_1 -weighted images. There are two approaches to perturb M_z in cardiac perfusion imaging: with a 180° (i.e. an inversion) RF pulse in inversion recovery (IR) exams and a 90° RF pulse which completely eliminates or “saturates” MRI signal in a so-called saturation recovery (SR) exam. The SR and IR pulses are often referred to as magnetization preparation pulses and are separate from the RF pulses played during the image acquisition or image “readout”, both of which must be considered in the optimization of a cardiac perfusion exam.

Historically, IR was used for CMR perfusion. Because IR is a 180° pulse, it has the potential for the most dynamic range and hence most contrast (Fig. 13.2). However, M_z after the pulse is dependent on M_z immediately prior to the pulse (it will be the same magnitude but point in the opposite direction). This means that the length of the previous TR will affect the magnitude of M_z after inversion pulse. In a gated cardiac scan, the TR is roughly equal to the RR interval. This makes scans with IR preparation very sensitive to changes in heart rate and arrhythmias because the RR and TR change throughout the scan. The other disadvantage of IR is that it requires a longer readout because it takes longer for the magnetization to recover. Practically, this means that more time is required per slice, so fewer slices can be acquired, and there is a decrease in spatial coverage.

Currently, the majority of CMR perfusion scans are acquired using SR preparation. While there is less dynamic range and contrast because it is only a 90° pulse (see Fig. 13.2), SR does not have the other drawbacks of IR. Critically, SR pulses will always set M_z to zero regardless of the prior M_z , so the signal has no heart rate dependence. Additionally, because the readout is faster, more slices can be acquired allowing for greater spatial coverage.

Other pulse preparations are currently being developed. Some, like magnetization driven steady state, offer better linearity at the expense of CNR, which may be useful for some quantification applications. Others are a hybrid of SR and IR preparations. For example, an SR prep followed by an IR prep [12] will exhibit some characteristics of each. There will be no heart rate dependence, and CNR will be improved

Fig. 13.2 (a) Saturation recovery (SR), (b) inversion recovery (IR), and (c) hybrid SR-IR preparations for myocardial imaging. IR has a greater signal range but is slower and is susceptible to variations in heart rate (note that M_z after the inversion pulse is dependent on T_{slice}/T_1). For the hybrid SR-IR, the initial SR preparation removes any heart rate variability, and the following IR pulse increases signal range over an SR only prep. TD trigger delay, TI inversion time (time from preparation to center of k-space), T_{readout} total time for acquisition of all k-space data for a single slice, T_{slice} total time required for acquiring a single slice. Note that TI is TD plus half T_{readout}



over a simple SR prep, but readout would take even longer and coverage would decrease. This could be used in cases where good CNR is important but coverage is not (e.g. a diffuse process like systemic sclerosis).

For a 90° SR preparation, there are a few different choices for how to implement the RF pulse. A rectangular pulse is the simplest, however in the presence of any B_1 field inhomogeneity (common in cardiac imaging) a rectangular pulse will result in incomplete saturation. Other RF pulses have been designed that have improved performance in the presence of B_1 inhomogeneity. Two important ones are adiabatic pulses [13] and rectangular pulse trains [14]. Both of these show markedly improved saturation (Fig. 13.3) [6, 14].

However their drawbacks are longer pulse durations and higher SAR. The longer pulse duration is minor compared the image acquisition time (~8 ms compared to ~150–200 ms), but additional SAR can be problematic with large coverage at higher field strengths (3 T).

Image Readout: Snapshot FLASH, SSFP, GRE-EPI

Each type of magnetization preparation pulse can be combined with different types of image readout. The most common types are ultra fast gradient echo (e.g. TurboFLASH,

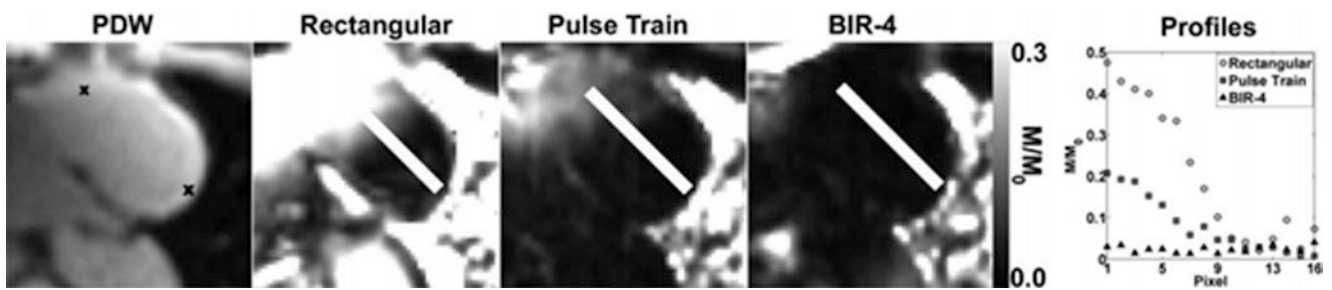


Fig. 13.3 Short axis images demonstrating saturation inhomogeneity with different types of SR preparation pulses. “x” marks on the PDW image mark the end points of the measured signal intensity. For complete homogeneous saturation, the signal should be zero across the

entire line. The pulse train shows improved homogeneity over a simple rectangular pulse, and the BIR-4 adiabatic pulse is even more homogeneous (Reproduced from Kim et al. [14], with permission of John Wiley & Sons)

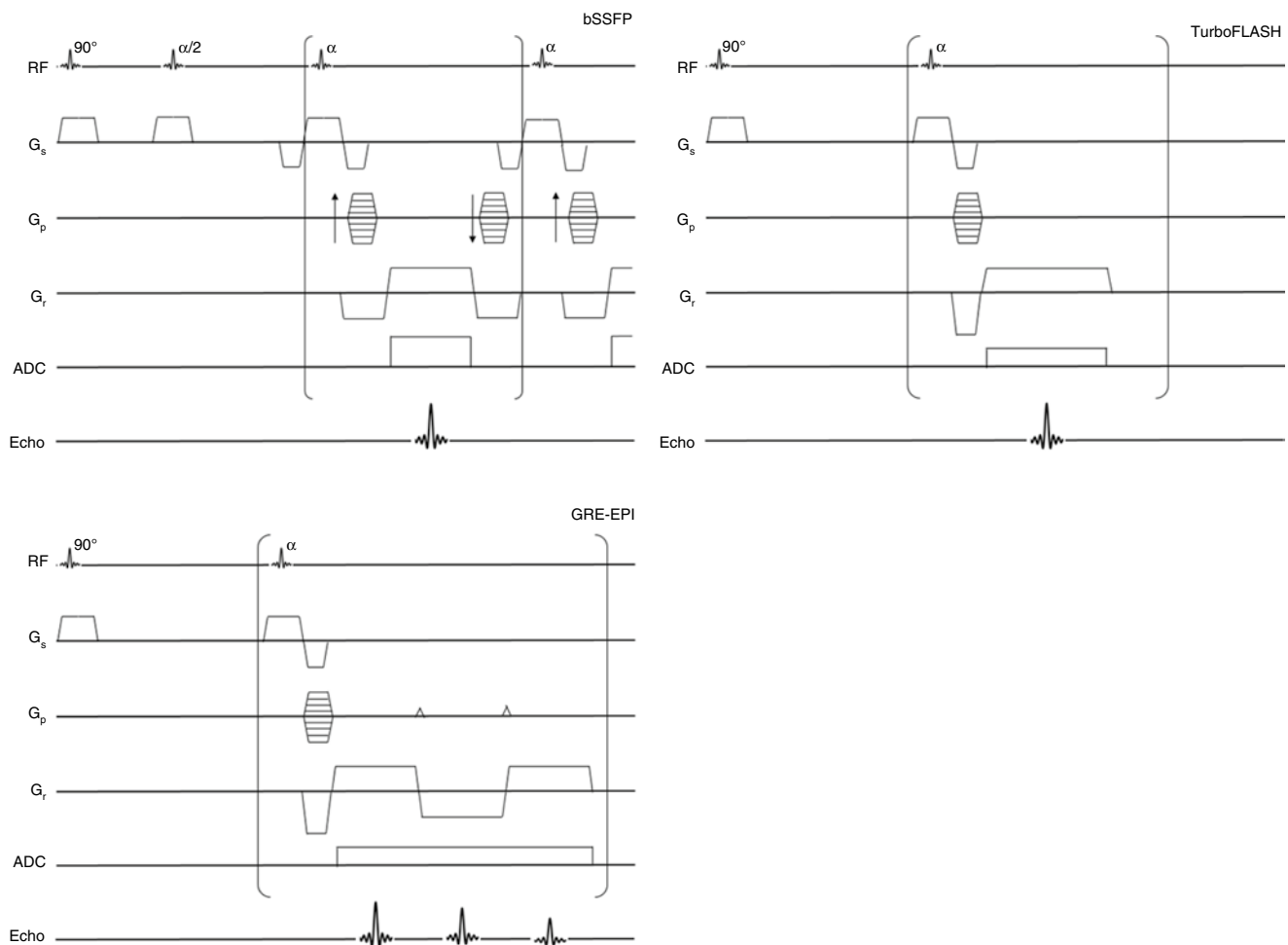


Fig. 13.4 Pulse sequence diagrams for bSSFP, FLASH, and GRE-EPI readouts

fast GRE, and Turbo Field Echo) [15], gradient echo with echo planar readout (GRE-EPI) [16], or steady state free precession (SSFP – termed TrueFISP, FIESTA, balanced FFE by various vendors) [17], and despite much debate, there is no clear consensus for which sequence is best for CMR perfusion and is usually determined based on the preference of the physician.

Fast Low Angle Shot (FLASH) was one of the first available rapid imaging sequences. With FLASH, each line in k-space is preceded by a low flip angle excitation and then any transverse magnetization at the end of the readout is spoiled before moving to the next line (Fig. 13.4). Since each line has its own excitation, the imaging time for the readout (not including preparation) will be $T_{\text{readout}} = TR * N_{\text{phase}}$. E.g.

for a 128×80 matrix at $TR = 2$ ms, the readout time would be 160 ms. (Note: TR here refers to time between excitations during the readout, it does not refer to the time between successive image acquisitions.) TurboFLASH is a variation on FLASH with very short TR and low flip angle. As a consequence, TurboFLASH is predominantly proton density weighted instead of having the typical T_1 FLASH weighting. However, with IR or SR prep a TurboFLASH sequence will have T_1 weighting.

GRE-EPI is similar to FLASH, except that instead of reading out one line of k -space per acquisition, multiple lines are read out. This means that fewer excitations are needed during readout, which makes GRE-EPI more efficient and hence faster than FLASH. The number of lines read per excitation is referred to as the echo train length (ETL). For GRE-EPI, the readout time will instead be $T_{\text{readout}} = TR * N_{\text{phase}} / \text{ETL}$. For example a 128×80 matrix at $TR = 6$ ms with an ETL of 4, the readout time would be $80 * 6 / 4 = 120$ ms. The imaging readout time is particularly important in CMR because motion artifacts are reduced with shorter readout times. This makes GRE-EPI less sensitive to motion than FLASH. Additionally, the faster readout time reduces the overall imaging time per slice, which means more slices can be acquired during each heartbeat. One drawback of GRE-EPI, however, is that magnetic field imperfections accumulate through the extended readout. The accumulation of error manifests itself as additional phase, which can mimic the intended phase used to localize signal within an image. The result is that EPI images can exhibit phase related “ghosting” artifacts.

Steady State Free Precession (SSFP) images are a variant of FLASH. Unlike in FLASH, in SSFP, transverse magnetization (M_{x-y}) is not eliminated before the next excitation. Rather than being destroyed (i.e. spoiled) by the application of phase-modulated RF pulses or large field gradients, the residual transverse magnetization is refocused and combined with newly excited transverse excitation to dramatically increase the magnetization used in the formation of an image (Fig. 13.4). This gives SSFP greater SNR than either FLASH or GRE-EPI. Also, because initial magnetization depends on both the longitudinal magnetization and the refocused transverse magnetization, SSFP will have some T_2 as well as T_1 contrast. This makes TE particularly important for SSFP readouts. Like FLASH, SSFP requires one excitation per readout line, and has comparable readout times. Some studies have found more dark rim artifacts with SSFP [18, 19]. Magnetic field inhomogeneity, which can be problematic in the chest where the lungs impart large local magnetic susceptibility changes, is also a problem in SSFP readouts, which has limited SSFP adoption at 3 T. It has also been reported that the excitations in SSFP can interfere with accurate ECG gating [17]. Still, in spite of these drawbacks, the gain in SNR has seen SSFP become increasingly popular in CMR perfusion.

Despite multiple studies comparing the above methods, there is no clear-cut consensus as to which is the best method, and each one offers advantages and disadvantages. In a review article, Kellman and Arai compared SSFP, FLASH, and GRE-EPI using state-of-the-art implementations in 2007 [6]. They found that GRE-EPI had the fastest acquisition, but that SSFP has 40 % higher CNR.

Acquiring Multiple Slices

Typically CMR perfusion scans require multiple slices for adequate coverage of the LV myocardium supplied by the coronary arteries. The most common method for acquiring multiple slices is to use multiple SR preps. The first slice is SR prepped and read out, then the second slice is SR prepped and read out, etc. until all the slices are completed. Another approach is to use a single SR prep and then read out multiple slices. This is faster than using multiple SR preps, so greater spatial coverage is possible. However, the time between the SR prep and readout will be different for each slice. This leads to a very important disadvantage: each slice will have a different TI, so each slice will have different CNR. A third possibility is to use a single SR prep but interleave the slice readouts. This keeps the same efficiency gains but equalizes the TIs, so there is no CNR variation between slices. However, the readout per slice is longer, which increases susceptibility to motion artifacts.

Acceleration Techniques

Due to the need for very fast image acquisition, cardiac perfusion sequences are almost always run with some sort of acceleration technique. Acceleration techniques include parallel imaging (e.g. SMASH [20], SENSE [21], and GRAPPA [22]), k -t Blast/ k -t SENSE [23], and HYPR [24, 25]. Much research has been focused on acceleration techniques in recent years, and a multitude of techniques have been developed and compared [26, 27]. In all of these techniques, image acquisition time is reduced by intentionally sampling only a subset of the data needed to create an MRI images. The uncollected or “missing” MRI data are mathematically synthesized using complimentary information collected from different receiver coils. In other words, most acceleration techniques use the spatial location of the acquired signal which is inherent in the receiver coil configuration to reduce the amount of imaging data that must be acquired for artifact free images. Since receiver coil information is acquired simultaneously, i.e. in parallel, the general approach to accelerate is referred to as “parallel imaging”. However, a major tradeoff in all cases is that faster acquisition results in lower SNR. A review of parallel imaging basics can be found by Deshmene et al. [28].

Sensitivity encoding (SENSE) and generalized autocalibrating partially parallel acquisition (GRAPPA) are two widely available methods of parallel imaging, and both have major advantages in that they rely on relatively simple theoretical underpinnings and make very few assumptions about the nature of the underlying images. With parallel imaging, reconstruction additionally incorporates information from multiple independent receiving coils. In essence, spatial information that would otherwise be obtained by spatial encoding via gradients is instead obtained by information in independent coils in the receiver coil array. With SENSE, coil sensitivity profiles are used to unwrap the aliased images in image space. With GRAPPA, the unsampled lines in k-space are calculated by combining information from neighboring lines in multiple coils, and the filled-in k-space is then reconstructed as usual. This eliminates the ghosting artifacts that would normally be seen by undersampling, and the more receiving channels that are used, the more k-space can be undersampled and acquisition speed increased.

Other techniques achieve even greater acceleration by incorporating temporal information. For most rapidly acquired image series of the heart, much of the image remains unchanged between images, and data is correlated in time. k-t BLAST and k-t SENSE are two well-known techniques that take advantage of this correlation by acquiring a training data set (acquired at low resolution and un-aliased) that is used to inform the reconstruction of the sparsely sampled and rapidly acquired data. k-t BLAST does not incorporate coil channel information in its reconstruction and can be used with single channel coils whereas k-t SENSE incorporates coil channel information as well. Compared to standard parallel imaging techniques, k-t BLAST and k-t SENSE are capable of faster imaging, but at the cost of increased noise and more assumptions in the model (e.g. that motion during the training data is representative of motion in the rest of the data).

Motion Correction

While many cardiac MRI scans rely on breath holds to ensure that there is minimal movement of the heart during the scan, the longer acquisition times of a cardiac perfusion scan (typically 45 s–1.5 min) can make breath holds impractical. As a result, there is usually considerable cardiac motion over the course of a perfusion scan. This is problematic when analyzing perfusion images. Generating signal intensity time curves requires segmenting along the epi- and endocardial borders, but this is an extremely time intensive process to do frame by frame, and automatic segmentation often does not trace the borders well. A more efficient process is to first register all of the images together, draw the contours on a single image,

and then propagate the contours throughout the series and make (relatively minor) adjustments as needed. As such, most cardiac perfusion scans will include some form of motion correction for image registration.

There are a multitude of motion corrections algorithms that have been proposed. Motion can be corrected prospectively using navigator pulses that track the motion of the diaphragm [29]. Motion can also be corrected retrospectively using a variety of methods [30–33]. In practice, many vendors will have some form of inline motion correction included in their cardiac sequences. A comprehensive review of cardiac motion correction can be found in the review by Scott et al. [34].

Artifacts

There are several artifacts seen in CMR perfusion imaging, and the most important one is the dark rim artifact (DRA) (Fig. 13.5). The DRA manifests as a dark rim that is sometimes seen in the subendocardial border of the ventricle. This ring can easily be mistaken for hypoperfusion and cause incorrect diagnoses, which is why DRA is regarded as the most concerning artifact in CMR. Much research has gone into determining the cause of the DRA, and some common hypotheses include Gibbs ringing, contrast associated susceptibility changes, motion artifacts, and partial volume effects [35]. However, no theory has been clearly identified as the sole cause of DRA, and its origins remain widely debated.

1.5 T vs 3 T

While the majority of clinical scanners use 1.5 T magnets, 3 T is becoming increasingly common, and the choice between the two has a significant effect on CMR perfusion. The higher magnetic field of the 3.0 T results in a doubling of the signal-to-noise ratio of images and a 30 % prolongation of T_1 values [36]. Importantly, Gadolinium-based contrast agents have less relaxivity at 3 T. However, since T_1 values are also higher in the blood and myocardium at 3 T than at 1.5 T there is a net increase in ΔT_1 and gain in CNR [37].

While 3 T offers CNR advantages, it has other disadvantages. Artifacts are more prominent at 3 T, though faster imaging and higher bandwidth can mitigate artifacts at the cost of SNR. Critically for SSFP sequences, there is more inhomogeneity at 3 T [38]. There is also greater energy deposition as quantified by the Specific Absorption Rate (SAR) at 3 T, which limits the TR and flip angles that can be used, and ECG signal is noisier at 3 T, which can influence any scan where accurate gating is critical.

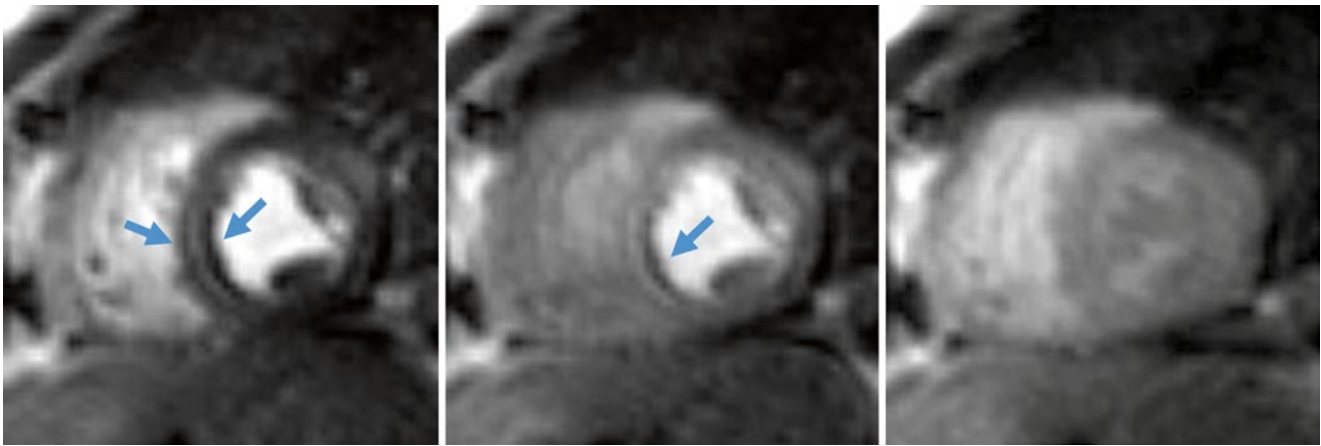


Fig. 13.5 Dark rim artifact (DRA). Note that the artifact is only apparent when there is contrast in the adjacent ventricle and does not persist after the first-pass

Summary

There are a multitude of choices available when creating a CMR perfusion sequence. Preparation can be IR, SR, or a hybrid, and there are multiple ways to implement the preparation. Readouts can be some variation of FLASH, GRE-EPI, or SSFP. There is no single best combination for all applications, and selection of the “best” sequence depends on the specific needs of a particular scan. For example, relative to ischemia, post infarction imaging involves more microvascular than macrovascular obstruction, so contrast washes out more slowly [8]. In this case, some temporal resolution could be sacrificed to gain greater spatial resolution to better delineate the size of injured myocardium. Conversely, for a diffuse process like microvascular dysfunction in Syndrome X, spatial coverage could be neglected in favor of having greater spatial resolution in fewer slices to evaluate subendocardial hypoperfusion.

Image Analysis

For any given image series, there are a multitude of different ways to process the data and provide an assessment of cardiac perfusion. Recent articles have reviewed and compared various methods [8, 9, 39], there is no clear consensus on the best approach. Broadly speaking, perfusion analysis can be categorized as qualitative, semi-quantitative, or absolute quantitative where parametric images present signal intensity in proportion to ml/-g-min of perfusion. Absolute quantification allows a more direct comparison in cross-sectional and longitudinal studies of perfusion changes within individual patients and in patient populations.

Qualitative

The simplest way of analyzing perfusion data is to simply visually inspect myocardial signal changes as the bolus of contrast agent passes, which is what is done in most clinical applications. A physician will cycle through the perfusion series and watch the myocardium as the contrast flushes through. Any areas that remain dark have less perfusion than the surrounding bright tissue. Comparison of stress, rest, and late gadolinium enhanced images allows defects to be attributed to ischemia, infarction, or artifact. Defects seen at stress but not at rest are interpreted as reversible ischemia. Matched defects seen at stress and rest with a corresponding area of late gadolinium enhancement are interpreted as infarction. Matched defects seen at stress and rest without any late gadolinium enhancement are interpreted as artifact. This algorithm improves the diagnostic accuracy over interpretation of the perfusion images alone [40].

While this approach is usually sufficient for most diagnostic purposes, it has limitations. First, because no actual numeric metric for perfusion is calculated, it is difficult to compare scans longitudinally over time or in a cross-section between different subjects. Second, because perfusion defects represent relative reductions in blood flow with respect to the best-perfused region of the myocardium, assessment of relative perfusion alone may result in either an over- or underestimation of myocardial perfusion, or a failure to recognize diffuse limitations in flow reserve, which can be seen in multi-vessel coronary artery disease or diffuse microvascular dysfunction. Lastly, without being able to use numeric thresholds, there is considerable subjectivity in determining what is normal vs abnormal perfusion, which can introduce bias into measurements. For these reasons, there has been a great deal of effort towards quantifying cardiac perfusion measurements.

Semi-quantitative

Broadly speaking, semi-quantitative approaches result in numeric indices of perfusion, but the units of the measurement are not synonymous with blood flow (i.e. not ml/min/g). For example, the qualitative approach described above could be modified by comparing the change in signal in diseased myocardium versus the change in signal in healthy myocardium in the same subject. While this ratio will give a numeric value, it will not be units of blood flow. In general, while semi-quantitative approaches do allow for some statistical comparisons to be made, they are still limited compared to a true quantitative approach. The measurements themselves often depend on non-flow related parameters such as contrast dose or coil sensitivity, so there can still be problems comparing across subjects and over time. Additionally, because units are not in ml/min/g, direct comparisons cannot be made to other imaging modalities that are truly quantitative. For example, blood flow measured by PET or microspheres would not be directly comparable to MRI signal ratios. In experimental models, semiquantitative perfusion indices have been shown to underestimate myocardial blood flow, especially in hyperemic zones [41].

Of the semi-quantitative approaches, one of the most common ones is measuring the upslope of the signal intensity

curve in the myocardium (Fig. 13.6). Because only the upslope is measured, this method is dependent wholly on the contrast wash-in and is insensitive to contrast wash-out. During the wash-in, changes in tissue relaxivity are due principally to incoming contrast agent from arterial blood, and the rate of incoming contrast will be proportional to blood flow. However, most contrast agents used in CMR are not intravascular and will leak into the extravascular space, and additionally there is significant spin exchange between intravascular and extravascular compartments. Both of these effects complicate interpretation of relaxivity changes during the wash-out period. By using only the wash-in period, upslope measurement largely avoids these concerns. Because upslope measurement does not give units of flow, it is not an absolute quantitative approach. However, upslope of the AIF is often used to normalize between scans, and a recent publication [42] has suggested that calibrating global upslope (measured across the entire LV) to global flow (measured at the coronary sinus) may allow for absolute quantification.

Absolute Quantification: Theory

Absolute quantification approaches aim to measure not just a perfusion related parameter but an exact measurement of

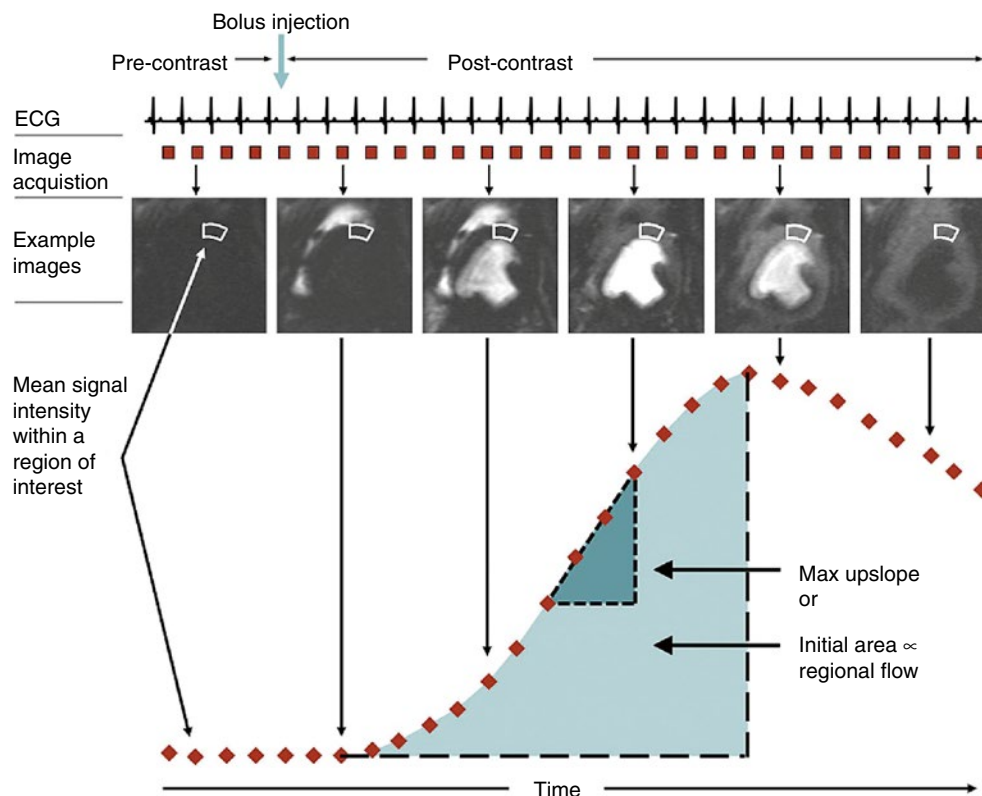


Fig. 13.6 Peak upslope or area under the curve are often used as semi-quantitative ways to measure perfusion (Reproduced from Lee and Johnson [39], with permission of Elsevier)

perfusion in ml of blood, per minute of time, per gram of myocardium (ml/min/g). These approaches all make use of kinetic modeling and input functions.

The fundamental model for quantitative perfusion imaging in any organ system is

$$C(t) = BF \cdot (AIF(t) \otimes R(t))$$

Where $C(t)$ is the contrast in the tissue, BF is the blood flow in the tissue, $AIF(t)$ is the arterial input function, and $R(t)$ is the residue function. $AIF(t)$ is the contrast in the feeding artery, so $BF \cdot AIF(t)$ describes the amount of contrast that is flowing into the tissue. In CMR perfusion, the AIF is typically sampled in the left ventricular blood pool. The residue function, $R(t)$, is a measure of contrast retention in the tissue. $R(t)$ can also be thought of as the tissue response to a short bolus of contrast directly in the feeding artery, and it is analogous to an impulse response function. \otimes is the convolution function, defined by

$$f(t) \otimes g(t) = \int_{-\infty}^{\infty} f(\tau) g(t - \tau) d\tau$$

The aim of absolute quantification is to solve the first equation for BF . However, only $C(t)$ and $AIF(t)$ can be measured directly. To find BF , $R(t)$ must be found by deconvolving $AIF(t)$ from $C(t)$. Once $BF \cdot R(t)$ is found, BF is measured as the maximum of the $BF \cdot R(t)$ curve ($R(t)$ is defined as having a max of 1, so the maximum of $BF \cdot R(t)$ will be BF) (Fig. 13.7).

There are a number of possible methods for deconvolving an AIF from a measured signal. With a model-dependent approach, there is an assumed general shape for $R(t)$ that is described by a few parameters (typically a Fermi function), and finding $R(t)$ essentially becomes a fitting problem to find the parameters for $R(t)$ that cause $AIF(t) \otimes R(t)$ to best fit the experimental data. Another popular variation on a model-dependent approach is to use compartment models. In compartment models, a system of differential equations that depends on blood flow is used to describe contrast flow between various compartments (e.g. intravascular, extracellular). With a model-independent approach, no assumptions whatsoever are made about the shape of $R(t)$, and finding

$R(t)$ is done mathematically via regularized inverse Fourier transformations or singular value decomposition (SVD). For cardiac perfusion, the most popular approaches are Fermi function and two compartment models.

Absolute Quantification: AIF Selection

Accurately deconvolving the AIF and finding the correct residue function requires an accurate sampling of the AIF. While it is easy to locate the AIF in CMR – it is easily sampled in the LV – it is difficult to accurately capture the correct shape of the AIF. First, the AIF peak is very sharp since the contrast passes through the LV so quickly, and most acquisition schemes will miss the exact top of the peak. To account for this, many processing algorithms assume the AIF is described by a gamma variate function [43] and will use the sampled AIF data to fit a continuous gamma variate that is then used in the rest of the algorithm. Second, because the concentration of contrast is so high in the LV during the first pass of the bolus, there are significant saturation and T_2^* effects, which manifest as flattening the measured AIF (Fig. 13.8). This problem is much more difficult to correct, and there have been a number of proposed methods to remedy it. One method which has gained much attention is the dual-bolus method.

In a dual bolus scheme, there are two separate injections of the contrast agent. The first dose is small and is used only for measuring the AIF. The second dose is larger (typically 4–10× larger) and is used to measure the contrast uptake in the tissue. Because the first dose is so small, many of the saturation and non-linear effects from high contrast concentration are avoided, so the sampled AIF better represents the true shape of the bolus passage through the LV. The AIF from the large bolus is then calculated from the measured AIF from the smaller bolus (Fig. 13.9). This constructed AIF is then used to deconvolve signal curves from the tissue during passage of the larger bolus. Because the second dose is so much larger, the effects on the tissue from any remaining contrast from the first dose can be ignored. Dual bolus has been validated against microspheres [41] but it can be difficult to implement. Without a second separate injector for the smaller bolus (which is not available in many imaging cen-

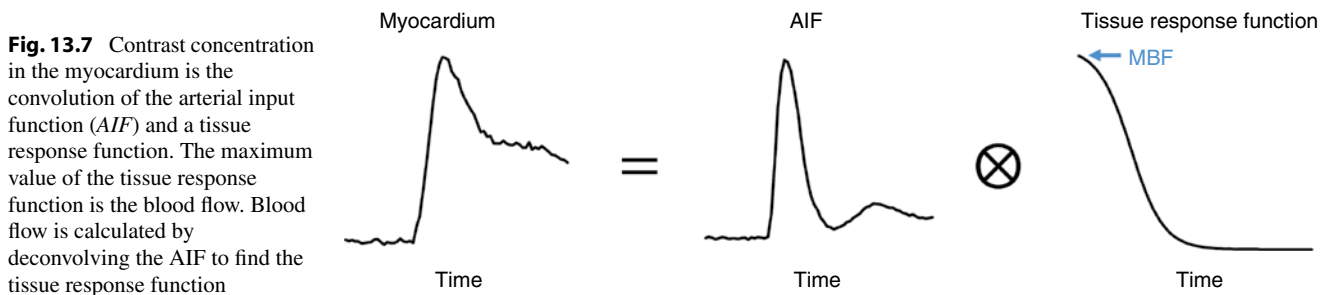


Fig. 13.8 Signal intensity of central k-space lines vs R_1 for a SR prepared FLASH sequence (signal equation can be derived similarly to the FLASH equation with no preparation. See any MRI sequence textbook, e.g. Haacke et al. for a FLASH signal derivation). For low doses of contrast, the signal response is linear, but at higher doses there is significant non-linearity

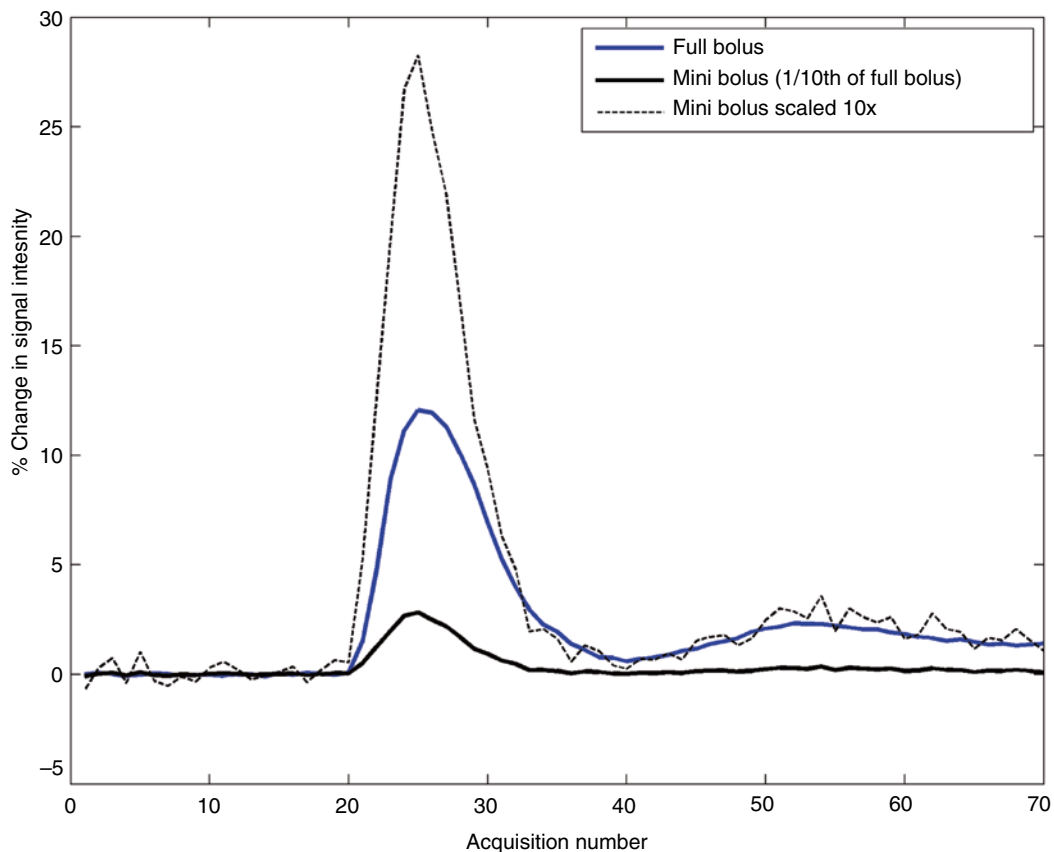
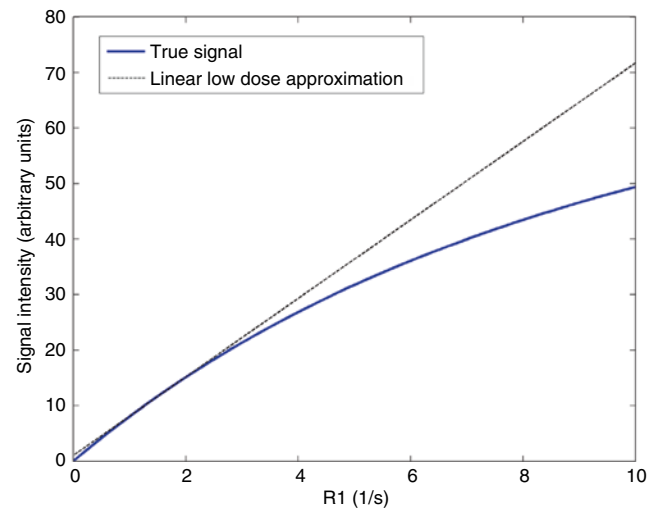


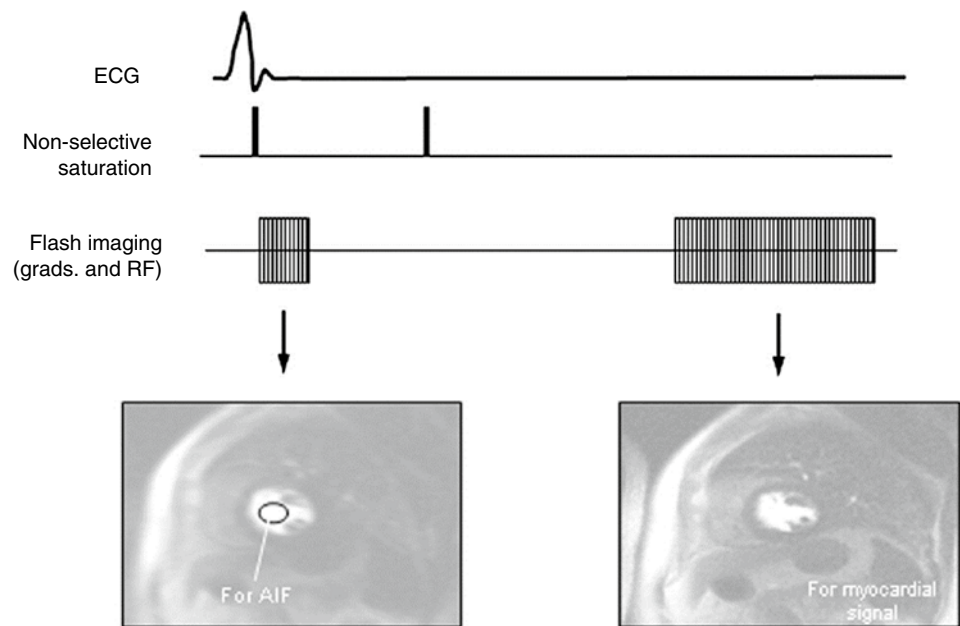
Fig. 13.9 AIF for a full bolus, a bolus diluted to one tenth full dose, and the one tenth dose scaled up 10x. Note that the full bolus has a significantly lower peak than the scaled mini-bolus

ters), using one injector to administer both boluses can be technically challenging.

Other approaches have been suggested that do not rely on separate contrast injections. Like dual bolus schemes, dual sequence [44] schemes also use the principle of measuring the AIF and tissue uptake separately. However, instead of

using a separate bolus to measure the AIF, with dual sequence there is a special slice selected during acquisition that is meant solely for measuring the AIF (Fig. 13.10). This slice is acquired with different imaging parameters (lower resolution, short TE, short TI) that minimize non-linearity and T_2^* effects. Another recently proposed method uses

Fig. 13.10 Dual sequence method for measuring AIF. One low resolution slice is imaged with short TE and TI and is intended solely for measuring the AIF (Reproduced from Gatehouse et al. [44], with permission of John Wiley & Sons)



constrained modeling to estimate the input function from the tissue curves and requires neither a separate bolus nor acquisition [45].

Future Directions

Cardiac perfusion MRI is a rapidly evolving field, and there are a number of emerging techniques. We conclude the chapter by briefly discussing just a few of them.

Myocardial Non-linearity

Considerable attention has been paid to the non-linearity of the arterial input function. However, less commonly investigated are the effects of non-linearity on the myocardial signal. It is sometimes assumed that there is no myocardial saturation because the total signal in a myocardial voxel is not saturated, but this is not true. While not all of the voxel is saturated, the part of the voxel composed of blood may be saturated, which would introduce non-linear effects into the myocardial signal even if the total signal intensity is much less than that of pure blood. Some models have been proposed for correcting myocardial saturation [46, 47], but research is still ongoing.

ASL

The vast majority of cardiac perfusion scans use a contrast bolus as described above. However, some groups have also used arterial spin labeling (ASL) as alternative to contrast

administration. In general, ASL has worse CNR than bolus first-pass, but because it does not use injected contrast agent the number of acquisitions is not limited by contrast dose, and concerns about nephrogenic systemic sclerosis are avoided. At this time, ASL remains mostly an experimental method for MR cardiac perfusion, but it has been used in both animals [48–51] and humans [52–54].

BOLD

Like ASL, blood oxygenation level dependent (BOLD) imaging is another experimental cardiac perfusion technique that requires no exogenous contrast and is minimally invasive. Used extensively in functional MRI (fMRI) neuroimaging, the BOLD effect relies on T_2 differences between oxygenated and deoxygenated hemoglobin. Unlike ASL or contrast imaging, BOLD signal is proportional to blood oxygenation, not blood flow. The two are often related, however, and changes in BOLD signal have been shown by some groups to be associated with coronary artery disease in both humans [55, 56] and animal models [11, 57–60].

Summary

Cardiac MRI is emerging as an alternative to SPECT for measuring cardiac perfusion that has many potentially important clinical applications. There are many options when designing a cardiac MRI sequence, including preparation, RF design, and image readout, and after collecting images there are still further options in how to analyze the data. For many of these choices there is no clear consensus

on which is best, and each decision has its own tradeoffs depending on the application. Cardiac perfusion MRI is the focus of much exciting research, and outside of the most commonly used contrast agent first-pass scans, there are a number of exciting newer techniques such as ASL, BOLD, and methods for absolute quantification that may improve how cardiac MRI is used in the clinic and lead to further advances in the diagnosis of cardiac disease.

References

1. Stirrat J, White JA. The prognostic role of late gadolinium enhancement magnetic resonance imaging in patients with cardiomyopathy. *Can J Cardiol*. 2013;29(3):329–36.
2. Cook SC, Ferketich AK, Raman SV. Myocardial ischemia in asymptomatic adults with repaired aortic coarctation. *Int J Cardiol*. 2009;133(1):95–101.
3. Wang L, et al. Coronary risk factors and myocardial perfusion in asymptomatic adults: the Multi-Ethnic Study of Atherosclerosis (MESA). *J Am Coll Cardiol*. 2006;47(3):565–72.
4. Klocke FJ, et al. ACC/AHA/ASNC guidelines for the clinical use of cardiac radionuclide imaging – executive summary: a report of the American College of Cardiology/American Heart Association Task Force on Practice Guidelines (ACC/AHA/ASNC Committee to Revise the 1995 Guidelines for the Clinical Use of Cardiac Radionuclide Imaging). *J Am Coll Cardiol*. 2003;42(7):1318–33.
5. Jerosch-Herold M. Quantification of myocardial perfusion by cardiovascular magnetic resonance. *J Cardiovasc Magn Reson*. 2010;12:57.
6. Kellman P, Arai AE. Imaging sequences for first pass perfusion – a review. *J Cardiovasc Magn Reson*. 2007;9(3):525–37.
7. Coelho-Filho OR, et al. MR myocardial perfusion imaging. *Radiology*. 2013;266(3):701–15.
8. Gerber BL, et al. Myocardial first-pass perfusion cardiovascular magnetic resonance: history, theory, and current state of the art. *J Cardiovasc Magn Reson*. 2008;10:18.
9. Jerosch-Herold M, et al. Analysis of myocardial perfusion MRI. *J Magn Reson Imaging*. 2004;19(6):758–70.
10. Zhang H, et al. Accurate myocardial T_1 measurements: toward quantification of myocardial blood flow with arterial spin labeling. *Magn Reson Med*. 2005;53(5):1135–42.
11. Wright KB, et al. Assessment of regional differences in myocardial blood flow using T_2 -weighted 3D BOLD imaging. *Magn Reson Med*. 2001;46(3):573–8.
12. Tsekos NV, et al. Fast anatomical imaging of the heart and assessment of myocardial perfusion with arrhythmia insensitive magnetization preparation. *Magn Reson Med*. 1995;34(4):530–6.
13. Kim D, Cernicanu A, Axel L. B(0) and B(1)-insensitive uniform T(1)-weighting for quantitative, first-pass myocardial perfusion magnetic resonance imaging. *Magn Reson Med*. 2005;54(6):1423–9.
14. Kim D, et al. Comparison of the effectiveness of saturation pulses in the heart at 3T. *Magn Reson Med*. 2008;59(1):209–15.
15. Haase A, et al. Inversion recovery snapshot FLASH MR imaging. *J Comput Assist Tomogr*. 1989;13(6):1036–40.
16. Ding S, Wolff SD, Epstein FH. Improved coverage in dynamic contrast-enhanced cardiac MRI using interleaved gradient-echo EPI. *Magn Reson Med*. 1998;39(4):514–9.
17. Schreiber WG, et al. Dynamic contrast-enhanced myocardial perfusion imaging using saturation-prepared TrueFISP. *J Magn Reson Imaging*. 2002;16(6):641–52.
18. Fenchel M, et al. Multislice first-pass myocardial perfusion imaging: comparison of saturation recovery (SR)-TrueFISP-two-dimensional (2D) and SR-TurboFLASH-2D pulse sequences. *J Magn Reson Imaging*. 2004;19(5):555–63.
19. Lyne JC, et al. Direct comparison of myocardial perfusion cardiovascular magnetic resonance sequences with parallel acquisition. *J Magn Reson Imaging*. 2007;26(6):1444–51.
20. Sodickson DK, Manning WJ. Simultaneous acquisition of spatial harmonics (SMASH): fast imaging with radiofrequency coil arrays. *Magn Reson Med*. 1997;38(4):591–603.
21. Pruessmann KP, et al. SENSE: sensitivity encoding for fast MRI. *Magn Reson Med*. 1999;42(5):952–62.
22. Griswold MA, et al. Generalized autocalibrating partially parallel acquisitions (GRAPPA). *Magn Reson Med*. 2002;47(6):1202–10.
23. Tsao J, Boesiger P, Pruessmann KP. k-t BLAST and k-t SENSE: dynamic MRI with high frame rate exploiting spatiotemporal correlations. *Magn Reson Med*. 2003;50(5):1031–42.
24. Mistretta CA, et al. Highly constrained backprojection for time-resolved MRI. *Magn Reson Med*. 2006;55(1):30–40.
25. Ge L, et al. Myocardial perfusion MRI with sliding-window conjugate-gradient HYPR. *Magn Reson Med*. 2009;62(4):835–9.
26. Kozerke S, Tsao J. Reduced data acquisition methods in cardiac imaging. *Top Magn Reson Imaging*. 2004;15(3):161–8.
27. Grist TM, et al. Time-resolved angiography: past, present, and future. *J Magn Reson Imaging*. 2012;36(6):1273–86.
28. Deshmane A, et al. Parallel MR imaging. *J Magn Reson Imaging*. 2012;36(1):55–72.
29. Pedersen H, et al. Quantification of myocardial perfusion using free-breathing MRI and prospective slice tracking. *Magn Reson Med*. 2009;61(3):734–8.
30. Milles J, et al. Fully automated motion correction in first-pass myocardial perfusion MR image sequences. *IEEE Trans Med Imaging*. 2008;27(11):1611–21.
31. Stegmann MB, Olafsdottir H, Larsson HB. Unsupervised motion-compensation of multi-slice cardiac perfusion MRI. *Med Image Anal*. 2005;9(4):394–410.
32. Bidaut LM, Vallee JP. Automated registration of dynamic MR images for the quantification of myocardial perfusion. *J Magn Reson Imaging*. 2001;13(4):648–55.
33. Yang GZ, et al. Motion and deformation tracking for short-axis echo-planar myocardial perfusion imaging. *Med Image Anal*. 1998;2(3):285–302.
34. Scott AD, Keegan J, Firmin DN. Motion in cardiovascular MR imaging. *Radiology*. 2009;250(2):331–51.
35. Di Bella EV, Parker DL, Sinusas AJ. On the dark rim artifact in dynamic contrast-enhanced MRI myocardial perfusion studies. *Magn Reson Med*. 2005;54(5):1295–9.
36. Sharma P, et al. Effect of Gd-DTPA-BMA on blood and myocardial T_1 at 1.5T and 3T in humans. *J Magn Reson Imaging*. 2006;23(3):323–30.
37. Kim D, Axel L. Multislice, dual-imaging sequence for increasing the dynamic range of the contrast-enhanced blood signal and CNR of myocardial enhancement at 3T. *J Magn Reson Imaging*. 2006;23(1):81–6.
38. Noeske R, et al. Human cardiac imaging at 3 T using phased array coils. *Magn Reson Med*. 2000;44(6):978–82.
39. Lee DC, Johnson NP. Quantification of absolute myocardial blood flow by magnetic resonance perfusion imaging. *JACC Cardiovasc Imaging*. 2009;2(6):761–70.
40. Klem I, et al. Improved detection of coronary artery disease by stress perfusion cardiovascular magnetic resonance with the use of delayed enhancement infarction imaging. *J Am Coll Cardiol*. 2006;47(8):1630–8.
41. Christian TF, et al. Absolute myocardial perfusion in canines measured by using dual-bolus first-pass MR imaging. *Radiology*. 2004;232(3):677–84.
42. Aquaro GD, et al. A fast and effective method of quantifying myocardial perfusion by magnetic resonance imaging. *Int J Cardiovasc Imaging*. 2013;29(6):1313–24.

43. Thompson Jr HK, et al. Indicator transit time considered as a gamma variate. *Circ Res.* 1964;14:502–15.
44. Gatehouse PD, et al. Accurate assessment of the arterial input function during high-dose myocardial perfusion cardiovascular magnetic resonance. *J Magn Reson Imaging.* 2004;20(1):39–45.
45. Fluckiger JU, et al. Absolute quantification of myocardial blood flow with constrained estimation of the arterial input function. *J Magn Reson Imaging.* 2013;38(3):603–9.
46. Cernicanu A, Axel L. Theory-based signal calibration with single-point T_1 measurements for first-pass quantitative perfusion MRI studies. *Acad Radiol.* 2006;13(6):686–93.
47. Hsu LY, Kellman P, Arai AE. Nonlinear myocardial signal intensity correction improves quantification of contrast-enhanced first-pass MR perfusion in humans. *J Magn Reson Imaging.* 2008;27(4):793–801.
48. Jacquier A, et al. Quantification of myocardial blood flow and flow reserve in rats using arterial spin labeling MRI: comparison with a fluorescent microsphere technique. *NMR Biomed.* 2011;24(9):1047–53.
49. Troalen T, et al. Cine-ASL: a steady-pulsed arterial spin labeling method for myocardial perfusion mapping in mice. Part I. Experimental study. *Magn Reson Med.* 2013;70(5):1389–98.
50. Abeykoon S, Sargent M, Wansapura JP. Quantitative myocardial perfusion in mice based on the signal intensity of flow sensitized CMR. *J Cardiovasc Magn Reson.* 2012;14:73.
51. McCommis KS, et al. Feasibility study of myocardial perfusion and oxygenation by noncontrast MRI: comparison with PET study in a canine model. *Magn Reson Imaging.* 2008;26(1):11–9.
52. Zun Z, Wong EC, Nayak KS. Assessment of myocardial blood flow (MBF) in humans using arterial spin labeling (ASL): feasibility and noise analysis. *Magn Reson Med.* 2009;62(4):975–83.
53. Northrup BE, et al. Resting myocardial perfusion quantification with CMR arterial spin labeling at 1.5 T and 3.0 T. *J Cardiovasc Magn Reson.* 2008;10:53.
54. Do HP, Jao TR, Nayak KS. Myocardial arterial spin labeling perfusion imaging with improved sensitivity. *J Cardiovasc Magn Reson.* 2014;16(1):15.
55. Walcher T, et al. Myocardial perfusion reserve assessed by T_2 -prepared steady-state free precession blood oxygen level-dependent magnetic resonance imaging in comparison to fractional flow reserve. *Circ Cardiovasc Imaging.* 2012;5(5):580–6.
56. Arnold JR, et al. Myocardial oxygenation in coronary artery disease: insights from blood oxygen level-dependent magnetic resonance imaging at 3 tesla. *J Am Coll Cardiol.* 2012;59(22):1954–64.
57. Shea SM, et al. T_2 -prepared steady-state free precession blood oxygen level-dependent MR imaging of myocardial perfusion in a dog stenosis model. *Radiology.* 2005;236(2):503–9.
58. Tsaftaris SA, et al. Ischemic extent as a biomarker for characterizing severity of coronary artery stenosis with blood oxygen-sensitive MRI. *J Magn Reson Imaging.* 2012;35(6):1338–48.
59. Ghugre NR, et al. Myocardial BOLD imaging at 3 T using quantitative T_2 : application in a myocardial infarct model. *Magn Reson Med.* 2011;66(6):1739–47.
60. Fieno DS, et al. Myocardial perfusion imaging based on the blood oxygen level-dependent effect using T_2 -prepared steady-state free-precession magnetic resonance imaging. *Circulation.* 2004;110(10):1284–90.

Amedeo Chiribiri, Islam Mahmoud, and Sven Plein

Abstract

Stress imaging has become a major application of cardiovascular MRI with recent practice guidelines recommending its use in different clinical scenarios. Current indications for stress CMR include imaging of patients with suspected coronary artery disease and patients with heart failure and cardiomyopathy. In current practice, the most commonly used stress method in CMR is vasodilator stress combined with dynamic first pass contrast enhanced perfusion imaging, although inotropic and physiological stress to detect either perfusion or wall motion abnormalities are also feasible. When performing stress CMR, additional safety considerations arise due to the potential to cause cardiac arrhythmias or induce ischemia. Particular challenges in pulse sequence design for stress CMR relate to the fast heart rates encountered and the need in dynamic first pass perfusion CMR to capture image data with high temporal and spatial resolution. Current trends in stress MRI include the development of higher spatial resolution and three-dimensional methods for myocardial perfusion CMR.

Keywords

Myocardial perfusion • Myocardial blood flow • Ischemia • Coronary artery disease • Contrast enhanced MRI • Cardiac magnetic resonance imaging

Introduction

The main indication for stress testing in cardiology practice is the detection of myocardial ischemia in patients with known or suspected coronary artery disease (CAD). Myocardial

blood flow (MBF) is controlled through autoregulation of myocardial resistance vessels, mainly the pre-arterioles and the precapillary arterioles. These mechanisms maintain a relatively constant MBF at rest and facilitate an up to fivefold increase of MBF in response to increased demand, for example during physical exercise. In the presence of significant epicardial coronary artery stenosis, resting MBF may be maintained through the autoregulatory mechanisms, but MBF reserve (the level to which MBF can be increased over the resting level) is reduced. This results in myocardial ischemia and the clinical symptom of angina if oxygen demand increases and a mismatch between myocardial oxygen demand and oxygen supply ensues [1]. It follows that the induction of stress is required to detect ischemia in diagnostic testing.

With CMR, stress testing can be performed using three principal stress modes; physical stress using either a scanner-mounted bicycle ergometer or treadmill near the scanner, pharmacological stress using positive inotropic agents such

A. Chiribiri, MD, PhD • I. Mahmoud, MD
Department of Cardiovascular Imaging, King's College London,
London, UK

Division of Imaging Sciences and Medical Engineering, The
Rayne Institute, St. Thomas' Hospital,
4th Floor Lambeth Wing, London SE1 7EH, UK
e-mail: amedeo.chiribiri@kcl.ac.uk; islamzakareya@gmail.com

S. Plein, MD, PhD (✉)
Division of Biomedical Imaging,
Leeds Institute for Cardiovascular and Metabolic Medicine,
LIGHT Laboratories, Clarendon Way, University of Leeds, Leeds
LS2 9JT, UK
e-mail: s.plein@leeds.ac.uk

as dobutamine, or vasodilator stress using agents such as adenosine, which ideally induce maximal hyperemia and indirectly demonstrate ischemia through reduced MBF reserve [2, 3]. The myocardial response to stress and the presence of ischemia can be assessed using either cine imaging to detect stress-induced wall motion abnormalities or myocardial perfusion imaging to detect impaired stress MBF or MBF reserve. By far the most commonly used method in clinical practice is vasodilator-stress first pass dynamic myocardial perfusion imaging.

Safety Considerations

Patient safety is paramount when stress imaging is performed in the MRI environment. The magneto-hydrodynamic effect precludes reliable detection of electrocardiogram (ECG)-based markers of myocardial ischemia such as ST segment depression while the patient is within or adjacent to the magnet bore. Close monitoring of the patient's symptoms is therefore mandatory, especially during ergometer or dobutamine stress. The magnetic environment also prevents the use of standard resuscitation equipment within the scanner room. Evacuation procedures from the magnet room therefore have to be established and rehearsed regularly to ensure rapid and safe transfer of patients who develop complications during stress testing in CMR. Contra-indications to the use of the various pharmacological stress agents should be observed (Table 14.1). Finally, blood pressure and heart rate monitoring is mandatory during stress CMR, and the presence of a physician trained in advanced cardiac life support is recommended during all CMR stress tests.

Stress Wall Motion Assessment

Stress wall motion assessment by CMR can be performed using pharmacological stressors (most commonly dobutamine) or physiological stress using bicycle or treadmill

ergometers. Pharmacological stress is the more commonly used approach while physiological stress remains a research application.

Stress Modes

Ergometer Stress

Ergometer stress can be performed with either a (supine) scanner mounted bicycle ergometer or a treadmill near or in the scanner room. With supine cycling, it can be challenging to achieve target physiological responses. Treadmills offer a more physiological exercise regime but require rapid transfer of patients onto the scanner for imaging. Recently, an MR compatible treadmill has been described, which can be located immediately adjacent to the scanner with shortened transfer times [3].

Dobutamine Stress CMR

Dobutamine directly stimulates β_1 and β_2 receptors in the heart, leading to a dose-related increase in heart rate, blood pressure and myocardial contractility.

Dobutamine stress CMR testing is performed using standard protocols in which the dose of intravenous dobutamine is determined by the patient's bodyweight. Dobutamine is administered in increments of 5–10 $\mu\text{g}/\text{kg}/\text{min}$ to a maximum of 40 $\mu\text{g}/\text{kg}/\text{min}$ until the target heart rate, calculated as $((220-\text{age}) \times 0.85)$, is reached. If required to achieve the target heart rate, intravenous atropine may be added up to a maximal dose of 2 mg.

Because of the inability to use the electrocardiogram for ischemia detection, close monitoring of the patient is mandatory: ischemia detection relies on patient symptoms, physical signs and imaging findings. At each dobutamine stress level, a series of cine images is acquired and reviewed by the examiner immediately after data acquisition. The presence of new or worsening wall motion abnormalities is

Table 14.1 Contraindications to drugs used in stress CMR

Dobutamine	Adenosine or regadenoson
Severe systemic arterial hypertension ($\geq 220/120$ mmHg)	2nd or 3rd degree atrioventricular (AV) block or sinus node dysfunction
Unstable angina pectoris	Systolic blood pressure less than 90 mmHg
Significant aortic valve stenosis (peak aortic valve gradient >50 mmHg or aortic valve area <1 cm^2)	Sinus bradycardia (heart rate <40 bpm)
Complex cardiac arrhythmias including uncontrolled atrial fibrillation	Active bronchoconstrictive or bronchospastic disease with regular use of inhalers
Hypertrophic obstructive cardiomyopathy	Known hypersensitivity to adenosine or regadenoson
Myocarditis, endocarditis, pericarditis	(Side effects are described as less significant with regadenoson than with adenosine, however, the half life of regadenoson is longer)
Uncontrolled congestive heart failure	
Atropine	
Narrow-angle glaucoma	
Myasthenia gravis	
Obstructive uropathy	
Obstructive gastrointestinal disorders	

From Kramer et al. JCMR 2013. <http://creativecommons.org/licenses/by/2.0/legalcode>

a termination criterion alongside other published criteria (Table 14.2) [4].

Vasodilator Stress

Vasodilator stress (see next section as well as the chapter on Perfusion for more details) can in principle be used for the induction of ischemic wall motion abnormalities, but has a significantly lower diagnostic accuracy for the detection of CAD [2]. The use of vasodilator stress to detect ischemic wall motion changes is not advised.

Pulse Sequences for Stress Wall Motion Assessment

Images are acquired in multiple planes (typically at least three short axis and two orthogonal long axis planes) at each stress level. See Fig. 14.1.

The CMR methods used for stress wall motion imaging are similar to those used for standard cine imaging. Typically retrospectively gated balanced steady state free precession (bSSFP) cine pulse sequences are used. Adjustments to the standard pulse sequences may be made to allow for higher heart rates and reduced breath-hold capacity during stress testing.

The aim of pulse sequence design is to achieve a breath hold duration of 4–6 s, a temporal resolution of >25 phases/cardiac cycle and in-plane spatial resolution of 1.5–2 × 1.5–2 mm with a slice thickness of 8–10 mm [5]. To achieve these requirements the following adjustments are often made:

- Use of (higher factor) parallel imaging (so that fewer lines of k-space need to be acquired, reducing acquisition time)
- Reduced temporal resolution (so that more lines of k-space can be acquired in each R-R interval for each cardiac phase)
- Reduced spatial resolution (use of a smaller matrix at similar field of view, resulting in fewer required lines of k-space)

Many other adjustments can be made and with a combination of these, real time cine acquisition and monitoring can be achieved [6].

Making Good Images: Practical Considerations

The main challenge in stress wall motion CMR is the acquisition of artifact-free images at the high heart rates

Table 14.2 Termination criteria for dobutamine and vasodilator stress CMR

Dobutamine stress CMR	Vasodilator stress CMR
Submaximal heart rate reached [(220–age) × 0.85]	Persistent or symptomatic AV block
Blood pressure decrease >20 mmHg systolic below baseline systolic blood pressure or decrease >40 mmHg from a previous level	Significant drop in systolic blood pressure (>20 mmHg)
Blood pressure increase >240/120 mmHg	Persistent or symptomatic hypotension
Intractable symptoms	Severe respiratory difficulty
New or worsening wall motion abnormalities in at least 2 adjacent left ventricular segments (out of 17)	
Complex cardiac arrhythmias	

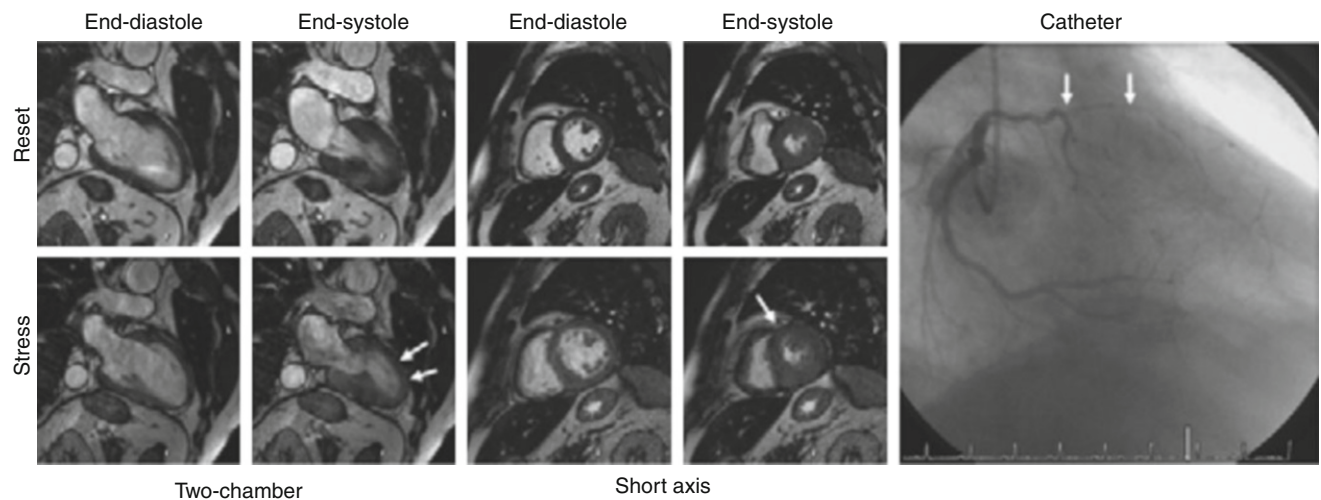


Fig. 14.1 Dobutamine-stress magnetic resonance in a patient with suspected CAD. At baseline: normal increase in systolic wall thickening shown in two-chamber and mid-short-axis views. During dobutamine stress, onset of hypokinesia in the anterior and antero-septal

segment. Catheterization showed double-vessel CAD with high-grade stenosis of the left anterior descending artery was found (white arrows) (From Kelle et al. [42])

encountered in patients that may be less able to breath-hold. As outlined above, pulse sequences used in stress cine imaging need to be set up to allow for these requirements.

Generally, fast gradient recalled echo (FGRE) imaging enables much faster data acquisition than spin echo imaging and is thus used in dobutamine stress protocols. However, in spoiled non-balanced FGRE acquisitions, the image contrast is heavily dependent on flow effects, with reduced signal and contrast between the wall and blood particularly in segments with impaired wall motion or globally in patients with heart failure. These limitations can impact image quality particularly at 3 T and at high heart rates achieved with medium and high dosages of dobutamine.

On current scanners, bSSFP sequences have therefore replaced FGRE cines. bSSFP provide a higher signal to noise ratio, do not suffer from flow related artifacts enabling a good contrast between the blood and the myocardium. The elevated signal to noise ratio typical for bSSFP allows the use of parallel imaging with higher acceleration factors, resulting in high speed and high contrast acquisitions and in a significant reduction of breathing artifacts, particularly if the images are acquired in the end-expiratory phase. These properties make bSSFP cine imaging particularly useful during stress testing. bSSFP sequences are however very sensitive to off-resonance artifacts in particular at higher field strength and with rapid blood flow, for example in the descending aorta, can result in image artifacts, particularly in the four chamber view. Pulsatile flow creates ghost artifacts of the vessel extending across the image in the phase-encoding direction. Modifying the phase-encoding direction and more accurate shimming can reduce significantly the occurrence and extent of these artifacts.

At high heart rates, VCG artifacts due to magneto-hydrodynamic effects are relatively common, leading to poorer image quality and sometimes resulting in non-diagnostic scans. Their occurrence can be minimized by careful preparation of the patient to ensure good electrical contact of the VCG electrodes. Moreover, different geometric schemes can be used for positioning the electrodes in order to maximize the signal.

In patients with MR conditional metallic implants, FGRE sequences sometimes enable superior image quality in comparison to bSSFP, which are more susceptible to inhomogeneities of the magnetic field.

The ideal cine approach for dobutamine stress CMR may be real-time techniques, considering the often unpleasant sensation of having a positive inotropic and chronotropic drug infused while laying still. Real-time cine imaging, while not necessarily the most suitable approach for ventricular function quantification, is more than adequate (and still usually superior to echocardiography-based cine imaging with dobutamine stress echo) for visual assessment of regional wall motion at rest and at each stage of dobutamine infusion. Real-time cine

vs. segmented cine imaging eliminates not only the need for breath-holding but also a regular cardiac rhythm, recognizing that ectopic heart beats are more likely to occur with higher doses of dobutamine in many cardiac patients.

Analysis

For image analysis of stress wall motion studies, the myocardium is divided into 17 segments as defined by the American Heart Association [7]. Each of these segments is visualized in two standard views (apical, mid and basal short axis view, four-chamber, two-chamber and three-chamber view). Images acquired at rest and at incremental dobutamine dose levels should be displayed simultaneously and their display should be synchronized. Worsening or lack of improving wall motion or systolic wall thickening is considered a sign of ischemia. Segmental wall motion can be graded on a four-point scale (normokinetic, hypokinetic, akinetic, dyskinetic) and an overall wall motion score generated as the sum of segmental scores divided by the number of analyzed segments. Newer methods such as feature tracking may have a role for more objective and partly automated wall motion analysis from cine images.

Safety of Dobutamine-Stress CMR

The induction of ischemia has inherent risks, most prominently the risk of inducing malignant tachyarrhythmias. However, if safety considerations are addressed, dobutamine stress CMR is a safe procedure. In a series of 1,000 consecutive patients undergoing dobutamine-stress CMR, one sustained ventricular tachycardia was encountered and no cases of death or myocardial infarction occurred [8]. These data are similar to dobutamine stress echocardiography.

Diagnostic Performance of Wall Motion-Stress CMR

Several single-center studies have reported on the diagnostic performance of wall motion-stress CMR in patients with suspected CAD. These were summarised in a meta-analysis that showed a sensitivity of 83 % with a specificity of 86 % for all stressors (dobutamine, exercise or dipyridamole) [9]. Multi-center evidence is not available. Several studies have also suggested that stress-CMR is superior to stress echocardiography due to better image quality and unlimited imaging windows, but most of these studies preceded the introduction of the current standard of second harmonic echocardiography and other improvements in echocardiographic image quality [10]. Diagnostic accuracy and prognostic value of

CMR stress wall motion testing may be improved by the use of strain imaging (e.g. SENC) or feature tracking [11, 12].

Prognostic Value of Dobutamine-Stress CMR

The prognostic value of dobutamine-stress CMR, but not that with other stressors, has been reported in several single center studies. All of these studies have shown a low cardiac event rate in patients with negative dobutamine-CMR testing of 1–2 % per year, with much higher event rates in patients with positive CMR studies. The largest cohort by Gebker et al. reported on 1,532 patients examined with dobutamine-CMR and found a 1.5 % death rate in patients with a negative test while patients with a positive test had a 6 % death rate [13].

Functional Assessment of Viable Myocardium

Dobutamine-CMR also allows an assessment of the functional reserve and thus viability of myocardium. In the context of chronic ischemia, myocardium may be hibernating, meaning that its metabolic and functional activity is down regulated. In the setting of acute myocardial infarction, ‘stunning’ can have similar effects, with reduced or absent contraction despite viable myocardium being present. With low-dose (5–10 mcg/kg/min) dobutamine stimulation, hibernating myocardium can be stimulated and shows an improvement of contractile function. With further increases

of dobutamine dose, the flow limitation of an upstream coronary stenosis leads to ischemia and a reduction in contractile function, provoking the typical “biphasic response” of resting a wall motion abnormality, improvement at low dose, and deterioration at high dose dobutamine. Such functional assessment may be complementary or even superior to LGE imaging [14]. Serial cine CMR with doses of dobutamine may be particularly appealing as an alternate approach to LGE to assess myocardial viability in circumstances such as advanced renal insufficiency where administration of gadolinium-based contrast is contraindicated.

Myocardial Perfusion CMR

Basic Principles

In myocardial perfusion CMR, a bolus of an MRI contrast agent is injected into a peripheral, usually antecubital vein with an automated power injector, followed by a flush of saline. A dynamic series of images is acquired (typically for 40–60 heart beats) to track the myocardial passage of the contrast agent bolus. Figure 14.2 illustrates this principle.

Image acquisition is generally performed at rest and during stress, most commonly applied as pharmacological vasodilator stress using adenosine, dipyridamole or regadenoson. All of these agents aim to induce maximal myocardial hyperemia through direct or indirect stimulation of the coronary adenosine receptors. Myocardium supplied by significantly stenosed

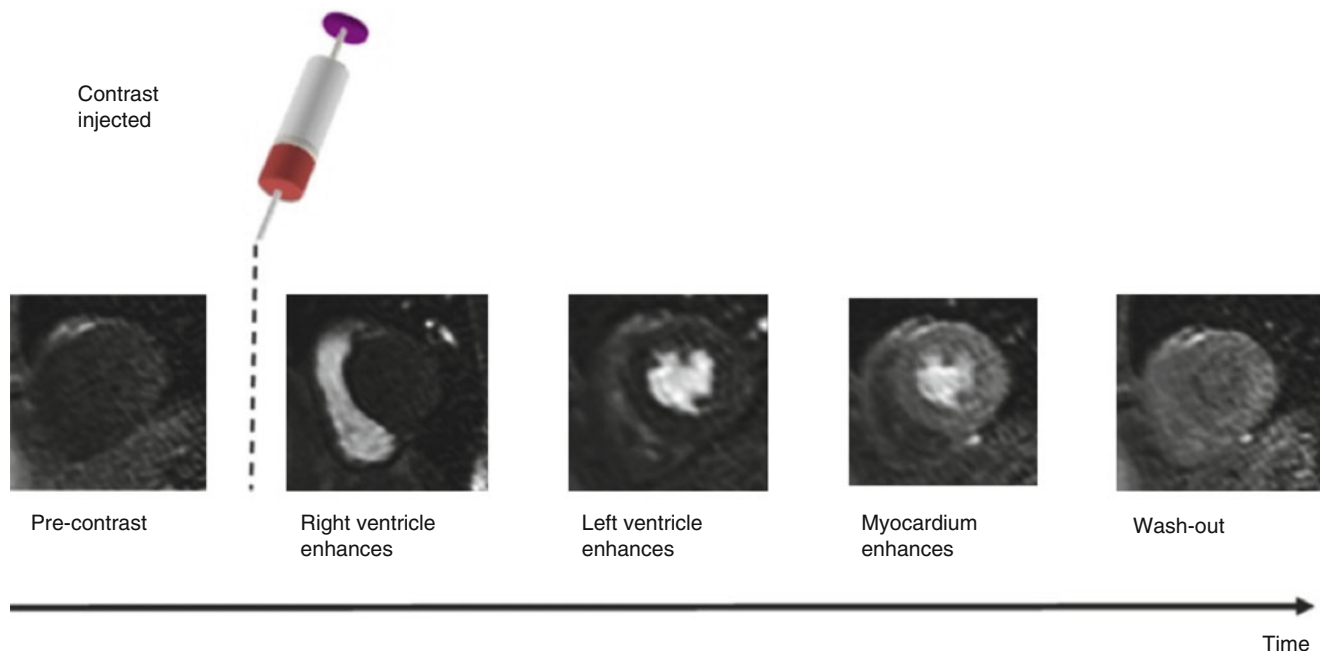


Fig. 14.2 Contrast agent is injected whilst the dynamic scan is in progress. Contrast agent can be seen as signal enhancement in the right ventricle (RV) followed by the left ventricle (LV) and more gradually in

the myocardium, before finally washing out (From Biglands et al. [15] <http://creativecommons.org/licenses/by/2.0/legalcode>)

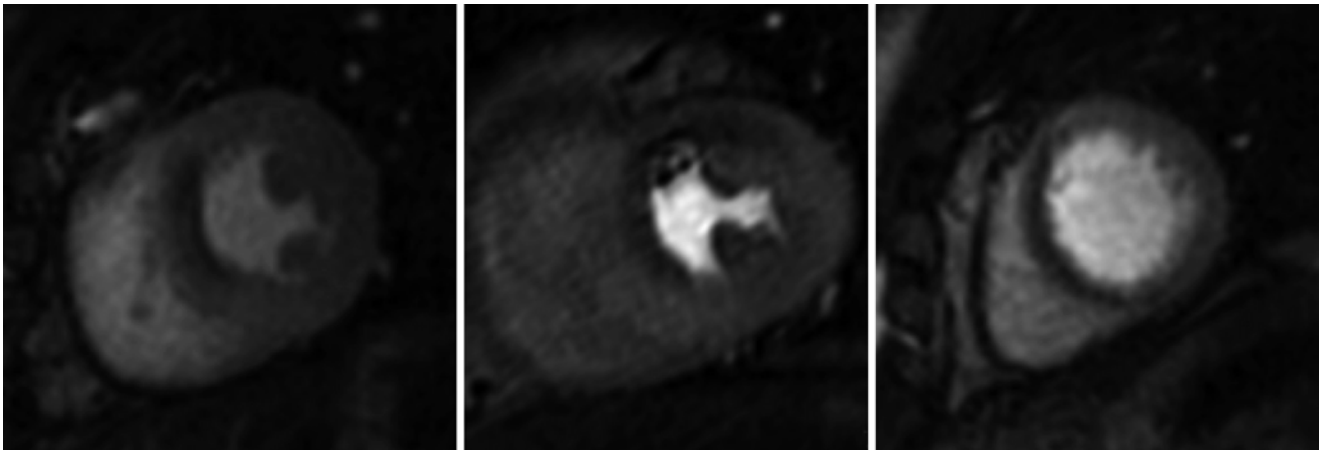


Fig. 14.3 Single dynamic image at peak myocardial contrast enhancement in a patient with a severe stenosis in the left anterior descending coronary artery. Inducible perfusion defect in the anterior and antero-septal segments (*arrows*). Note the lower signal intensity in these

coronary arteries has reduced perfusion reserve and thus takes up less contrast agent and appears darker compared with remote myocardium. Alternatively, inotropic or physiological stress can be applied as described in Sect. 3 and perfusion imaging performed at peak stress. In this case, the images depict myocardial ischemia directly rather than MBF reserve. Figure 14.3 shows an example of such an inducible perfusion defect.

Stress Agents

Adenosine, dipyridamole and regadenoson are the most widely available vasodilators for pharmacologic stress testing. All of these agents dilate coronary vessels and can increase myocardial blood flow in myocardium subtended by unobstructed coronary arteries by 3.5 to 4 fold. Tissue supplied by stenotic vessels has reduced coronary flow reserve and thus shows an attenuated hyperemic response to pharmacological vasodilatation. Consequently, a differential perfusion reserve is seen in normal versus abnormally perfused myocardium, with the difference dependent on stenosis severity, absolute MBF and coronary collateralization. Vasodilators do not usually induce ischemia as all vascular beds are dilated through the medication, but in certain physiological settings (collateral-dependent circulation), coronary steal phenomena may induce regional ischemia.

Adenosine

Adenosine induces direct coronary arteriolar vasodilation through activation of the A_{2A} receptor, but it also activates A₁, A_{2b}, and A₃ receptors, which leads to the side effects of adenosine infusion such as atrio-ventricular block, peripheral

regions compared to the rest of the myocardium. Note also that the high in plane spatial resolution allows an assessment of the transmural extent of the perfusion defect

vasodilation (causing flushing sensation) and bronchospasm (causing chest discomfort). A modest increase in heart rate and often a small drop in systemic blood pressure are also observed. Adenosine is administered as a continuous intravenous infusion at a standard dose of 140 mcg/kg/min. Maximal hyperemia is typically reached at 3 min of infusion and image acquisition can begin. In the absence of any of these signs and symptoms, many investigators now recommend increasing the adenosine dose to 170 or 210 mcg/kg/min to overcome an assumed failure of full adenosine effect. Such a failure may be mediated by caffeine, which is a competitive antagonist of the adenosine receptor, if patients have failed to adhere to the recommended scan preparation.

Dipyridamole

Dipyridamole is an indirect coronary vasodilator that increases intravascular adenosine levels through inhibition of intracellular reuptake and deamination of adenosine. It is administered intravenously at a dose of 0.56 mg/kg over a 4-min period and induces hyperemia for more than 15 min.

Regadenoson

The more recently approved regadenoson is a selective A_{2A} adenosine receptor agonist although it also has some effect on the A₁, A_{2B} and A₃ adenosine receptors. Regadenoson is injected as a rapid (10 s) intravenous bolus of 5 mL (0.4 mg), followed by a saline flush. Regadenoson reaches its maximal effect within 1–4 min. In CMR, regadenoson stress imaging therefore commences at approximately 2–4 min. A key advantage of regadenoson over adenosine is the upfront bolus injection, so that only one cannula is needed, and a better side effect profile through more selective A_{2A} receptor affinity. For example, first degree AV block occurs in 3 %

with regadenoson (7 % with adenosine) and second degree AV block in 0.1 % (1 % with adenosine). It does however lead to a higher increase in heart rate (more than 40 bpm in 5 % vs 3 % for adenosine), which in some cases may result in reduced image quality.

Dobutamine

Dobutamine increases regional myocardial blood flow in response to its positive inotropic and chronotropic stimulation, which lead to increased oxygen demand. Vascular beds supplied by significantly stenosed coronary arteries have a reduced perfusion reserve and when oxygen demand exceeds supply, hypoxia and ischemia ensues, demonstrated on perfusion imaging as an area of reduced contrast uptake. Perfusion CMR during dobutamine stress faces challenges of high heart rates and higher risk profile than vasodilator imaging.

Physiological Stress

Physiological stress with an ergometer or treadmill can in principle also be used in perfusion CMR, although remains a research application.

Pulse Sequences for Myocardial Perfusion CMR: Challenges and Requirements

The key challenges in designing a pulse sequence for myocardial perfusion CMR are:

1. Data must have strong T_1 weighting to be sensitive to the signal intensity change induced by the MRI contrast agent.
2. The dynamic contrast passage leads to different signal in each image, so that segmented multi-shot k-space filling is not feasible and single shot methods need to be used. Furthermore, at least three slices should be acquired at each heart beat with an in plane spatial resolution of at least 3 mm and at heart rates that may exceed 100 bpm during stress. Rapid data acquisition is therefore essential.

T_1 -Weighting

Signal enhancement of MRI contrast agents is predominantly the result of their effect on the T_1 relaxation times of their surrounding tissues. Myocardial perfusion CMR pulse sequences therefore need to be strongly T_1 -weighted. Given the short TR required for fast data acquisition, T_1 -weighting in perfusion CMR is most commonly achieved with saturation recovery methods, i.e. by applying a 90-degree preparation pulse prior to the read-out pulse sequence. Saturation recovery methods are robust to heart rate variation, which is the reason why they have replaced previously used inversion

recovery methods. The saturation time (TS) needs to be long enough to establish a high T_1 -contrast before the read-out sequence is employed and in most clinically used pulse sequences is around 100 ms. As for other MRI applications, the relationship between contrast agent concentration and signal is not linear, in particular at higher contrast doses and with longer TS. Shorter TS values and contrast agent doses may therefore be desirable if quantitative perfusion imaging analysis is planned – rarely the case in current clinical practice. Shorter TS also allows longer read out, usually allowing the acquisition of images with higher in-plane resolution, or acquisition of more slices within the constraints of each RR interval.

For signal readout, a wide variety of methods is in use, often vendor and institution specific. Most commonly, fast spoiled gradient echo methods (GRE), echo planar imaging (EPI), balanced Steady State Free Precession (bSSFP) pulse sequences or hybrids of these methods are used. Often, these readout schemes are combined with parallel acquisition techniques or image undersampling to shorten acquisition times and improve spatial resolution.

See Fig. 14.4 for typical myocardial perfusion CMR pulse sequences.

Fast Spoiled Gradient Echo (FGRE)

A fast gradient echo (FGRE) read-out sequence utilises a very short repetition time TR (<10 ms) and echo time TE (<5 ms), combined with a small flip angle of around 20–30°, resulting in a pulse sequence with predominant T_1 -weighting. A 90° preparation-pulse applied before the FGRE read-out increases image contrast. Since a very short TR is used, myocardial tissue or blood that stays in the slice becomes saturated (spoiling effect). Signal in FGRE therefore depends on the flow of blood to generate contrast. In clinical practice, FGRE pulse sequences are attractive because they are relatively robust to dark rim artifact.

Echo Planar Imaging (EPI)

This technique generates multiple gradient echoes following one rf pulse by quickly alternating the direction of frequency encoding gradients forming an echo train. The successive frequency gradients are interspersed by small phase encoding gradients to fill different lines of k-space within each heartbeat. However, T_2^* decay throughout the echo train causes image degradation with long echo trains. Thus a hybrid-EPI (also known as segmented EPI) technique is generally used in perfusion imaging where a number of shorter echo trains are acquired by applying multiple rf pulses. This reduces the destructive effect of T_2^* weighting, improving the image quality while maintaining part of the acceleration advantage provided by the EPI technique.

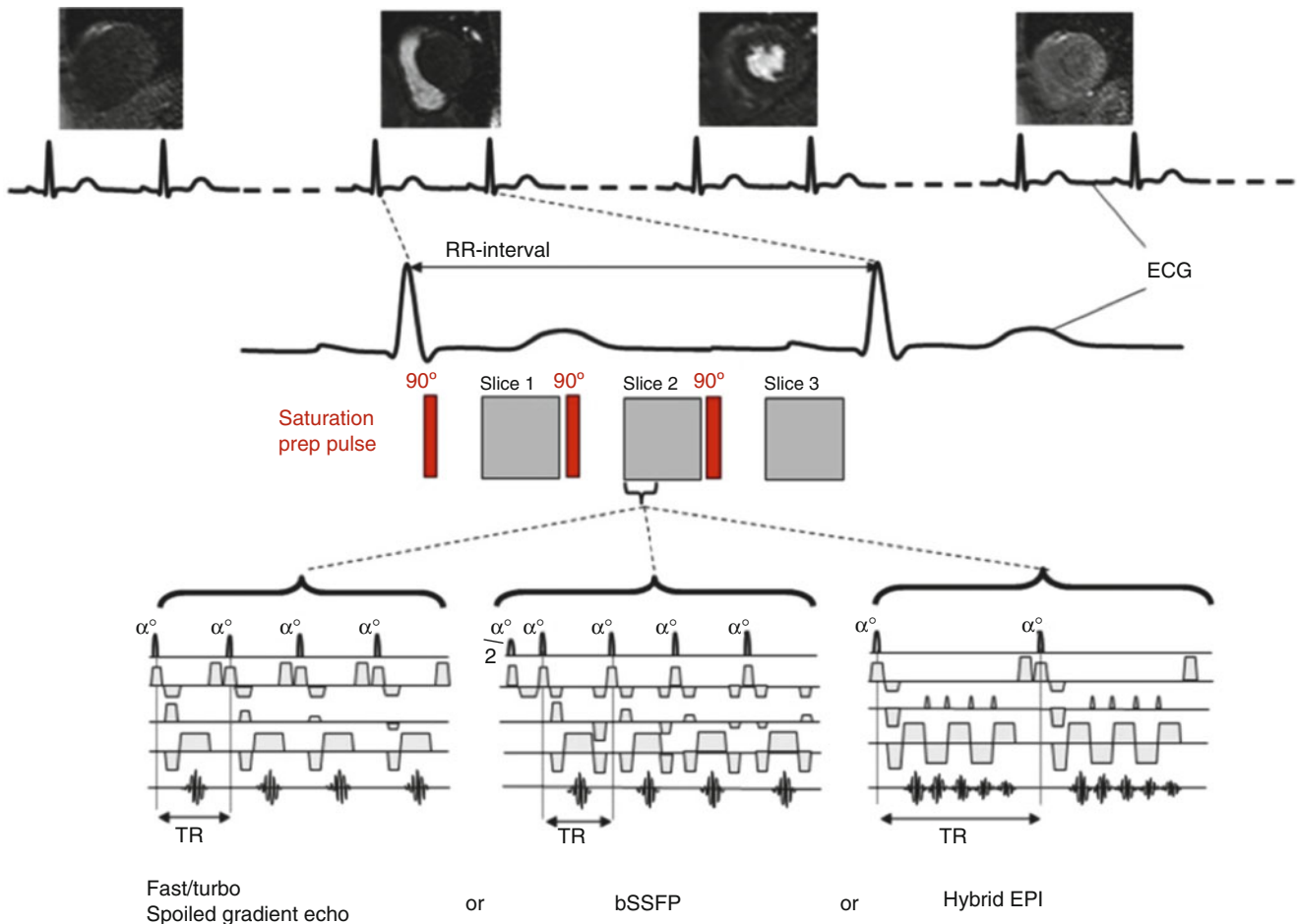


Fig. 14.4 Choice of imaging pulse sequence for myocardial perfusion MRI. Diagram illustrating the choices of data acquisition pulse sequence for myocardial perfusion MRI. A saturation recovery preparation pulse is employed to ensure T1-weighting followed after a delay by the image data acquisition pulse sequence. The most common data acquisition pulse sequences used are fast/turbo spoiled gradient echo

(*FGRE*), balanced steady state free precession (*bSSFP*) or hybrid (or segmented) EPI. The number of slices that can be acquired (in this case three) is limited by the R-R interval, the saturation delay and the length of data acquisition period (From Biglands et al. [15] <http://creativecommons.org/licenses/by/2.0/legalcode>)

Balanced Steady State Free Precession

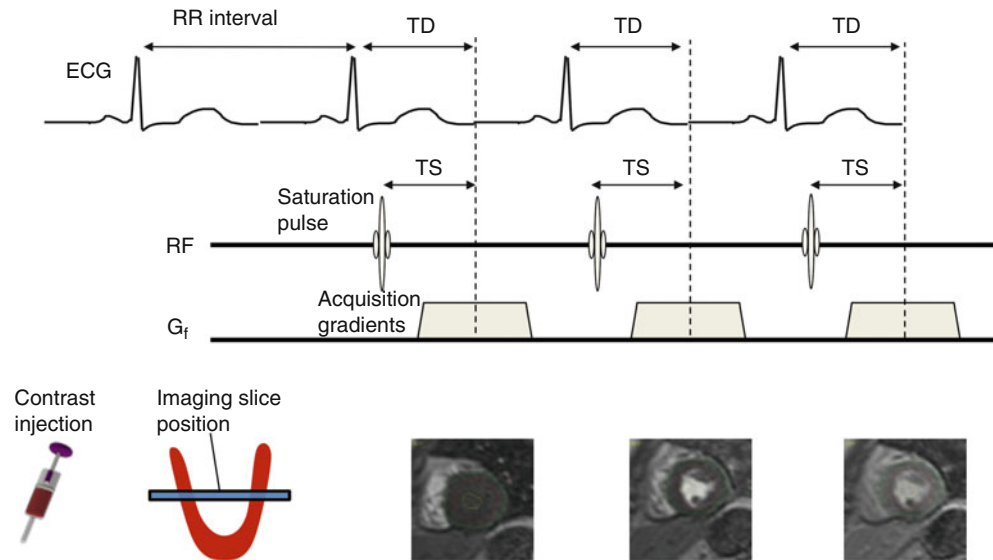
Balanced Steady State Free Precession (*bSSFP*) gradient echo sequences are constructed to protect the transverse magnetization from being spoiled but returned into phase at the end of each TR period when the next rf pulse is applied. Thus, the *bSSFP* sequence reverses the signal de-phased by the applied gradients by means of additional balancing gradients to re-phase the MR signal before each subsequent rf pulse. After a number of repetitions this gives rise to a steady state condition where the transverse magnetization from two or more successive repetition periods incorporate to give a much greater signal. Since the transverse magnetization is generated from multiple TR combination, the magnetization signal amplitude and consequently signal to noise ratio (SNR) for *bSSFP* is much higher in comparison to spoiled gradient echo. The increased signal permits the employment of higher receiver bandwidths, resulting in a shorter TE and

TR compared to spoiled gradient echo pulse sequences and therefore improved imaging efficiency. However, if the magnetic field is not homogenous, the transverse magnetization from several TRs can destroy each other rather than sum together in areas of magnetic field inhomogeneity, causing a higher susceptibility to dark banding artifacts in comparison to spoiled *FGRE*. Shimming and keeping TR as short as possible are therefore crucial when *bSSFP* is used for myocardial perfusion CMR. Unlike spoiled gradient echo sequences, the contrast nature of *bSSFP* sequences is related to the tissue's T_2/T_1 ratio, therefore fluid and fat in particular appearing as brighter than other tissues.

Which Pulse Sequence Is Best?

There is no consensus on the optimal data acquisition pulse sequence for myocardial perfusion CMR. An ideal pulse sequence will have short acquisition time, low susceptibility

Fig. 14.5 Trigger delay and saturation recovery time. Within each RR-interval the trigger delay (TD) sets the point within the cardiac cycle that the image is acquired and the saturation time (TS) sets the time between the saturation – pulse and the acquisition, thereby controlling the T_1 -weighting of the image. In case of multi-slice acquisitions, each slice has a different TD , while TS is usually the same following non-shared saturation prepulses (From Biglands et al. [15] <http://creativecommons.org/licenses/by/2.0/legalcode>)



to artifact and high SNR and contrast to noise ratio (CNR). The different acquisition methods available satisfy these requirements to a different extent [16]. FGRE, EPI and hybrid FGRE-EPI methods are least prone to artifacts and can be very robust in clinical practice. On the other hand, bSSFP generates the highest SNR of the three methods [17] that may allow the detection of perfusion defects with greater sensitivity. In addition, bSSFP acquisition is faster than FGRE, allowing higher spatial and/or temporal resolution. However, of the three sequences SSFP is the most susceptible to artifacts caused by off resonance magnetization and dark rim artifact and its use, particularly at 3 T, can be difficult [18, 19]. The choice of a pulse sequence is therefore often driven by local or vendor-specific expertise and preference.

Contrast Agents

Generally, myocardial perfusion CMR is performed using gadolinium-containing contrast agents in a dose between 0.025 and 0.1 mmol/kg, injected at 3–5 mL/s and followed by at least 30 ml saline flush (3–5 mL/s). The paramagnetic effect of gadolinium causes a shortening in T_1 relaxation time thus resulting in brighter signal of well-perfused myocardial tissue. However, the relationship between contrast agent dose and signal is not linear, especially for higher contrast agent concentrations. In clinical practice doses up to 0.1 mmol/kg body weight are preferred for visual assessment to optimize SNR, although higher contrast dose also causes more dark rim artifacts and is not suitable for quantification. Lower doses (e.g. 0.025 mmol/kg body weight) are more suitable for quantitative and semi-quantitative evaluation, because of the closer linearity of signal versus concentration. However, the image quality for visual assessment is in this case significantly lower.

While induction of hyperemia by adenosine is straightforward and duplicates the approach already established for single-photon emission computed tomography (SPECT), the determination of the optimum CM dose is more challenging. The dose should be as high as possible with the aim to increase signal during first pass. A higher dose (at the same injection speed) will also allow for a higher number of heart beats to be sampled during the first-pass and thus, will provide more data points on a given signal-intensity – time curve. At higher CM doses, it is of particular importance to assure that the pulse sequence used is not susceptible for magnetic field inhomogeneities, which can be induced by the high CM concentrations in the LV cavity during first-pass. Multi-center data demonstrated for a given MR pulse sequence an absence of susceptibility artifacts at the LV subendocardium up to a dose of 0.15 mmol/kg [20]. Currently, doses of 0.075–0.10 mmol/kg are recommended and allow repeating the acquisition at rest after washout of the stressor. Figure 14.5 shows a schematic of perfusion CMR acquisitions.

Practical Considerations in the Design of Perfusion CMR Pulse Sequences

The requirements for design of a myocardial perfusion CMR pulse sequence include strong T_1 -weighting, high spatial and temporal resolution and maximal coverage of the heart. As discussed before, an additional challenge of perfusion CMR is the need for single shot acquisition. Trade-offs therefore have to be made and with numerous approaches being used in clinical practice and research applications. The Society for Cardiovascular Magnetic Resonance has published recommended minimal standards for perfusion CMR, which include [5]:

1. A minimum of three short axis slices (apical, mid and basal) should be acquired at every heartbeat to ensure coverage of all except the most apical left ventricular segment.
2. Slice thickness should be 8 mm. In-plane resolution ≤ 3 mm. Readout temporal resolution between 100 and 125 ms or shorter as available.

These requirements can generally be achieved on commercial scanners using the described dynamic single shot saturation recovery pulse sequences combined with FGRE, EPI or bSSFP readouts and approximately twofold parallel imaging.

It is important to remember that with all these schemes, the typically acquired three slices have to each be acquired in a different cardiac phase in order to accommodate them within an RR interval. This has implications for motion artifacts, which are less pronounced at times of relatively little cardiac motion such as end-diastole and mid-systole. The length of

these cardiac phases changes depending on the patient's heart rate, so that they may differ between patients and even in the same patient between rest and stress acquisitions.

Planning of the three short axis views should be performed according to standardised methods to adapt the inter-slice gap to the dimension of the left ventricle on a per-patient basis (Fig. 14.6). The same procedure is recommended both for perfusion imaging and for dobutamine stress CMR, where three short axis cine sequences are acquired in conjunction with three long axis cines in 2-, 4- and 3-chamber views.

Making Good Images: Practical Considerations

Each perfusion acquisition should be planned thoroughly and at least one non-contrast dummy run should be performed. It is important that this dummy acquisition uses similar breathholding commands as subsequent contrast

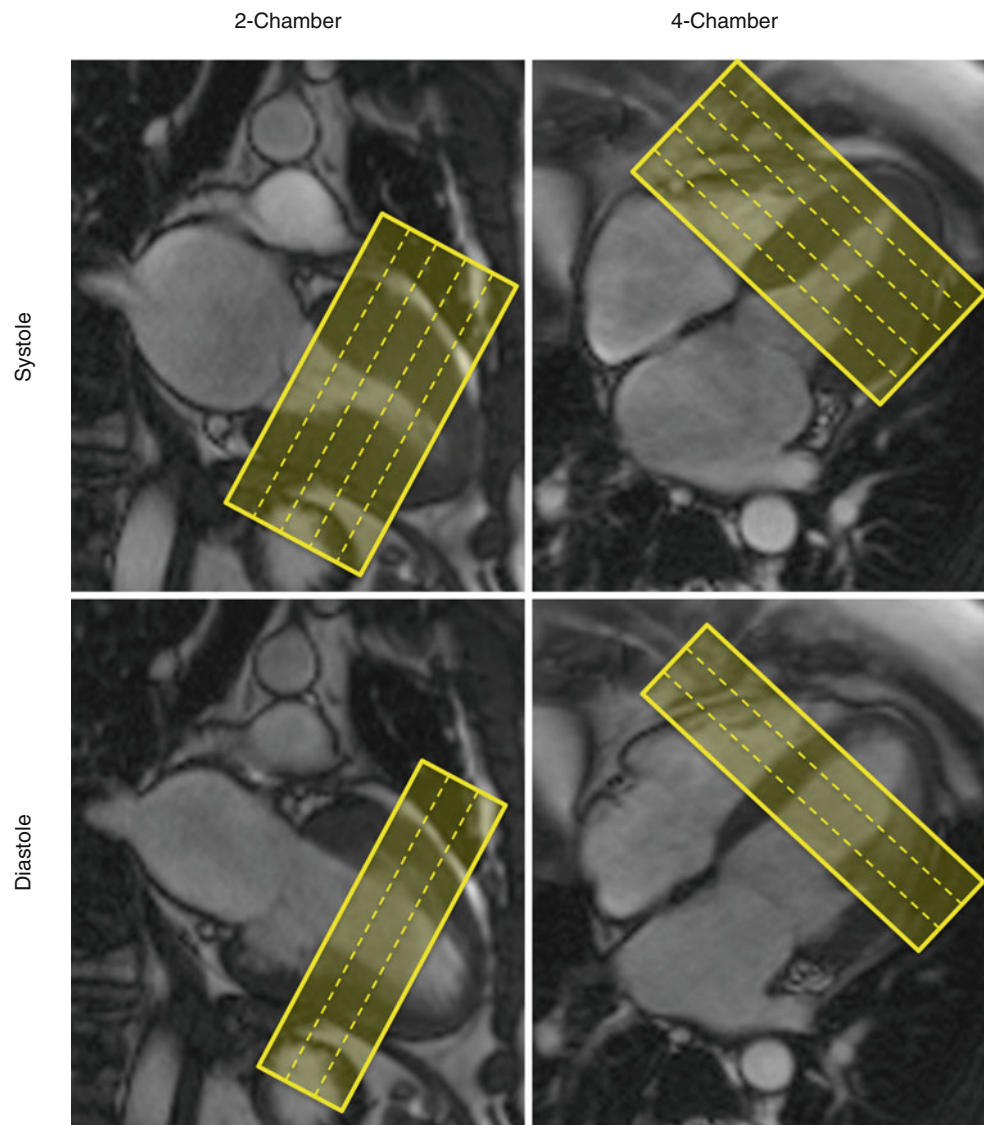


Fig. 14.6 Planning the short axis views for perfusion imaging and dobutamine stress CMR. The slices are prescribed parallel to the plane of the mitral valve, starting from a two-chamber and a four-chamber view. At first, the slab is made of five slices and the slice gap is adjusted to cover from the mitral valve to the endocardium of the apical segment. Once this is complete, the number of slices is reduced to three. The geometry of the slab is maintained, as well as the inter-slice gap and the position of the central slice. However, the outer slices now are positioned to avoid the left ventricular outflow tract and partial volumes effect at the apex, covering 16 standard left ventricular segments and excluding the apical cap

enhanced acquisitions. During pharmacological stress, patients often breathe more deeply and their breathhold position changes. This can move the heart into a different position compared to the planning views, leading to misplacement of the acquired slices.

If a patient's heart rate exceeds the rate a pulse sequence is designed for, for example during pharmacological stress, the operator may choose to make changes to the pulse sequence and for example reduce the number of acquired slices (but maintain at least three short axis slices), reduce the spatial resolution or the saturation prepulse delay, or to use a single saturation prepulse for all slices.

ECG triggering problems can occur during stress acquisitions, related to changes in the patient's chest motion

(leading to movement of ECG cables and motion artifacts), sweating (reducing the contact of electrodes). Some of these tend to be more likely at 3 Tesla. It is important therefore to ensure a highly reliable ECG before commencing a stress CMR study.

Good breath-holding during the stress acquisition will improve the quality of the acquired images. To avoid artifacts related to motion, coaching patients before the scan is essential.

Dark rim artifacts can be minimized by using low dosages of contrast agent or avoiding pulse sequences that are particularly susceptible to such artifacts like bSSFP. In general, higher spatial resolutions obtained with faster sequences are less prone to dark rim artifacts (Fig. 14.7).

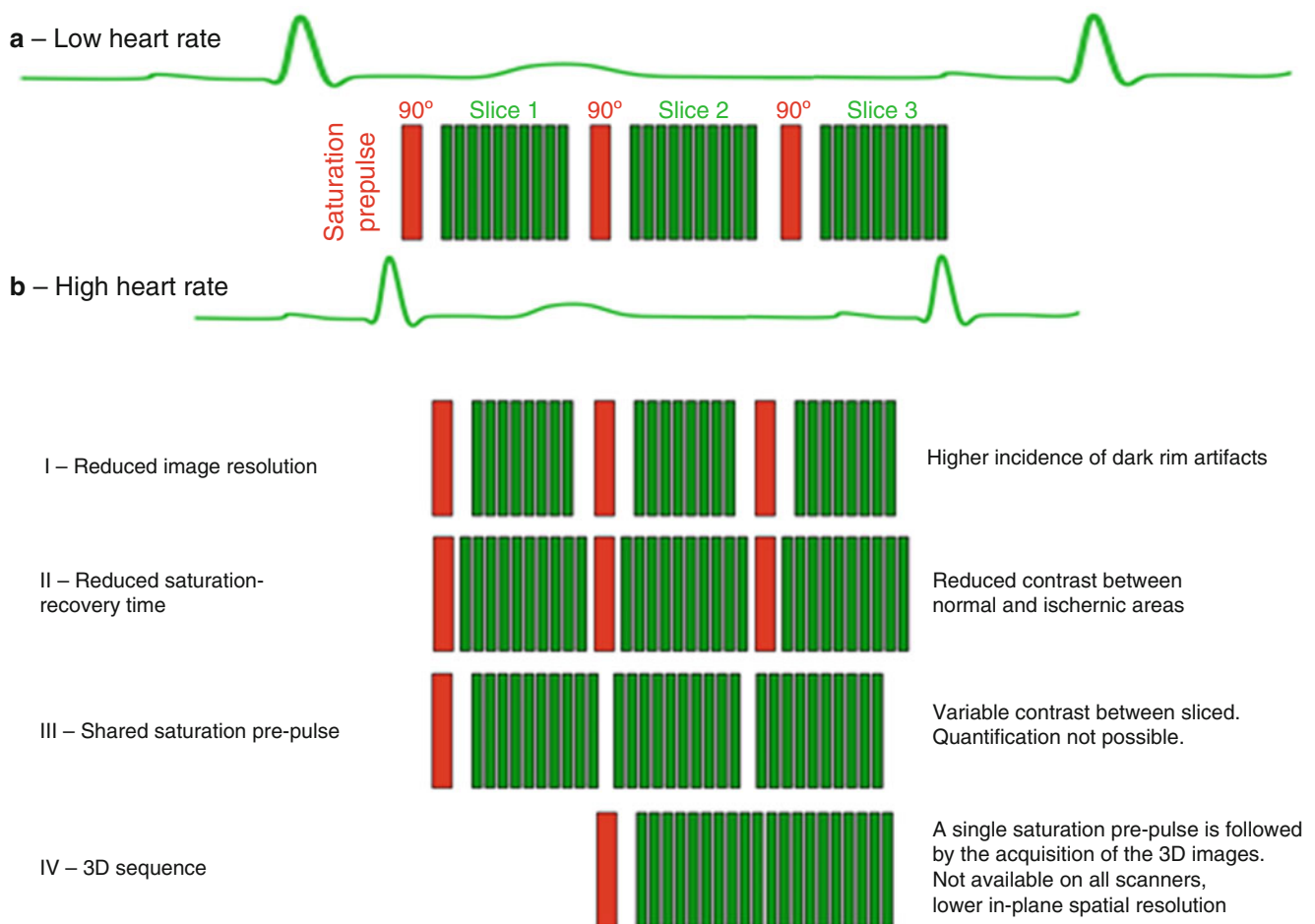


Fig. 14.7 Comparison between a standard perfusion sequence at low (a) and higher (b) heart rate. In order to accommodate for the sequence of saturation prepulses (red) and phase encoding steps for image acquisition (green) in case of increased heart rate, several strategies can be adopted. (I) Reduced image resolution – The speed of image acquisition increases as the number of phase encoding steps is reduced, resulting in a lower spatial resolution and in higher occurrence of dark rim artifacts. (II) Reduced saturation recovery time – Shorter time is allowed for signal to recover following the saturation pre-pulse. While reducing the total acquisition time, this approach can cause a reduction of image contrast between normally perfused and ischemic areas. (III)

Shared saturation prepulse – A single non slice-selective saturation prepulse is applied, reducing significantly the duration of image acquisition. However, variable levels of contrast are expected in different slices, making review of the images more difficult and quantification very challenging. (IV) 3D sequence – New 3D sequences for first-pass perfusion are currently available for research applications and will likely be available as clinical products in the near future. 3D acquisition uses a single saturation pre-pulse to acquire a 3D k-space. Contrast levels are constant throughout the volume and 300–350 ms are enough to complete the acquisition, at the cost of a relatively reduced in plane spatial resolution

Image Interpretation and Analysis

Where available, rest and stress myocardial perfusion CMR images should be reviewed in conjunction with cine and late gadolinium enhanced (LGE) images [7]. All image data should be synchronized and correlated. In contrast to nuclear imaging, myocardial scar is determined from the LGE images and not as a matched rest/stress perfusion defect. Indeed, perfusion in scar may appear normal or near normal on CMR if the scar has residual blood supply and is usually normal on rest perfusion images when performed after stress, due to initial redistribution of the first dose of contrast agent. For visual analysis, window and level should be adjusted to avoid “overspilling” of the LV cavity signal into the myocardium and to ensure that pre-contrast myocardium appears near black, although some signal should still be visible. Perfusion defects are determined by the contrast arrival and first passage through the LV myocardium and by visual analysis are determined by relative comparison between regions, either circumferentially or transmurally. A true perfusion defect should occur first when contrast arrives in LV myocardium and persists beyond peak myocardial enhancement. Because of the high resolution of perfusion CMR images, true perfusion defects are typically most prominent in the subendocardial portion of the myocardium with a transmural gradient towards the epicardium. Evidently, perfusion defects should make biological sense and conform to one or multiple coronary artery distribution territories. Rest perfusion images and late gadolinium enhancement should then be used to exclude image artifacts or areas of scar in the region with abnormal stress perfusion. See Fig. 14.8.

Pitfalls of Analysis: Dark Rim Artifact

First pass myocardial perfusion images can be affected by a dark rim artifact (DRA) at the border between the myocardium and the left ventricular (LV) cavity. These are considered sequence specific artifacts and do not represent true perfusion abnormalities, although their endocardial localization – particularly when using relatively low resolution sequences – can mimic the presence of ischemia. The causes of this artifact have been proposed to include susceptibility, Gibbs ringing and motion effects, or a combination of these factors [21]. Standard pulse sequences have different propensity for DRA and balanced SSFP images tend to be most affected. Radial acquisition strategies tend to be less affected than Cartesian acquisition schemes. Spatial resolution is a major determinant of the extent of the DRA and contrast agent dose and injection speed play another important role, with lower doses and slower injection reducing the artifact [22]. In the design of pulse sequences and imaging protocols, it is therefore possible to minimize the occurrence of the DRA.

However, for practical reasons and because many other factors affect the choice of pulse sequence parameters as outlined above, it is not always possible to eliminate DRA entirely and many images will be affected by this artifact. The possibility of artifacts therefore needs to be considered in the analysis of perfusion CMR images. An example of DRA is shown on Fig. 14.8 in comparison with a true perfusion defect in the RCA territory. Typically, DRA occur when the contrast between the LV blood pool and the myocardium is at its greatest, i.e. generally before contrast washes into the myocardium. The DRA reduces over the subsequent heartbeats as contrast washes into the myocardium and its concentration in the LV blood pool diminishes. When the myocardium reaches its maximal signal intensity, the artifact is generally less prominent. These are important distinguishing features from true perfusion defects, which tend to be most prominent at peak myocardial enhancement, i.e. later in the dynamic data series. Other features of the DRA are its typical location, which is often inconsistent with a physiologically plausible distribution (depending on the pulse sequence used and is consistent location when the same parameters are used in different patients) and its typical extent of 1 pixel width (in the phase encoding direction). See Fig. 14.9.

Dark banding present at stress and at rest with no corresponding scar on LGE images is also indicative of an artifact, but differences in heart rate and baseline contrast mean that the artifact appearance may be different.

Visual myocardial perfusion analysis may be falsely negative in cases of inadequate vasodilator stress during data acquisition.

It is also worth noting that the signal intensity across the image section and thus the heart may vary depending on the distance of myocardium from the surface coil. This can lead to misinterpretation of the images if it is not considered in the analysis.

Quantitative Perfusion Analysis

Myocardial perfusion CMR data can in principle also be analysed quantitatively and absolute myocardial blood flow estimated [23]. From the dynamic contrast enhanced data, MBF can be determined with deconvolution methods which are based on the relative concentration-time courses of the myocardium and an arterial input function (AIF), typically taken from the left-ventricular (LV) blood pool. A key challenge for these calculations is that the contrast concentrations in the AIF are considerably larger than those in the myocardium and that the concentration to signal ratio of MRI contrast agent is non-linear, in particular at higher contrast doses. Because clinical acquisition protocols for perfusion CMR are designed to optimise signal in the myocardium and

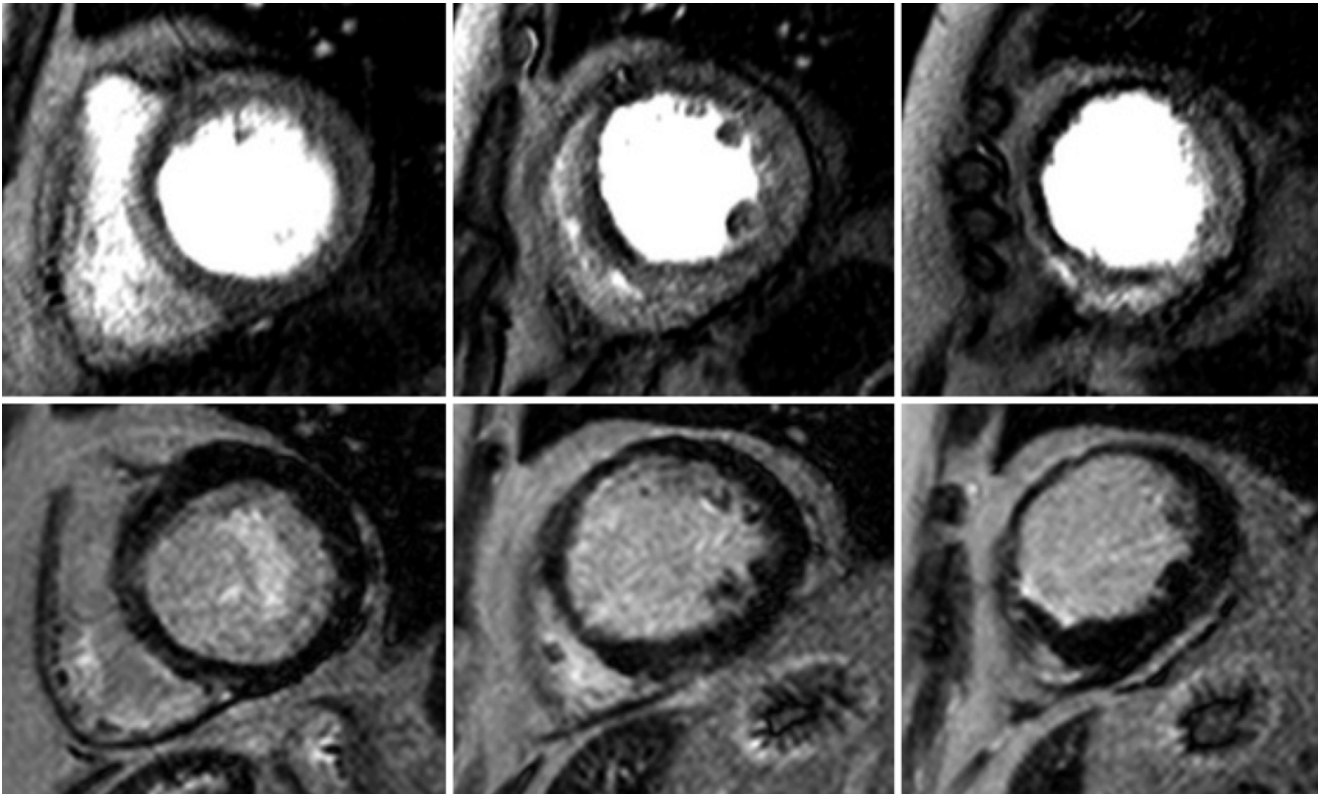


Fig. 14.8 75-year-old patient presenting with angina. Coronary angiography shows occluded mid-LAD. The stress perfusion images showed an extensive perfusion abnormality in the LAD territory at all levels from base (*left*) to apex (*right*). The perfusion defect was more evident in the subendocardial layers but was also extending to the outer

epicardial layers in the affected segments. Late enhancement images (*bottom row*) showed preserved viability in the basal segments, 50 % scar in the mid-LAD segments and 75 % scar in the apical segment supplied by the LAD

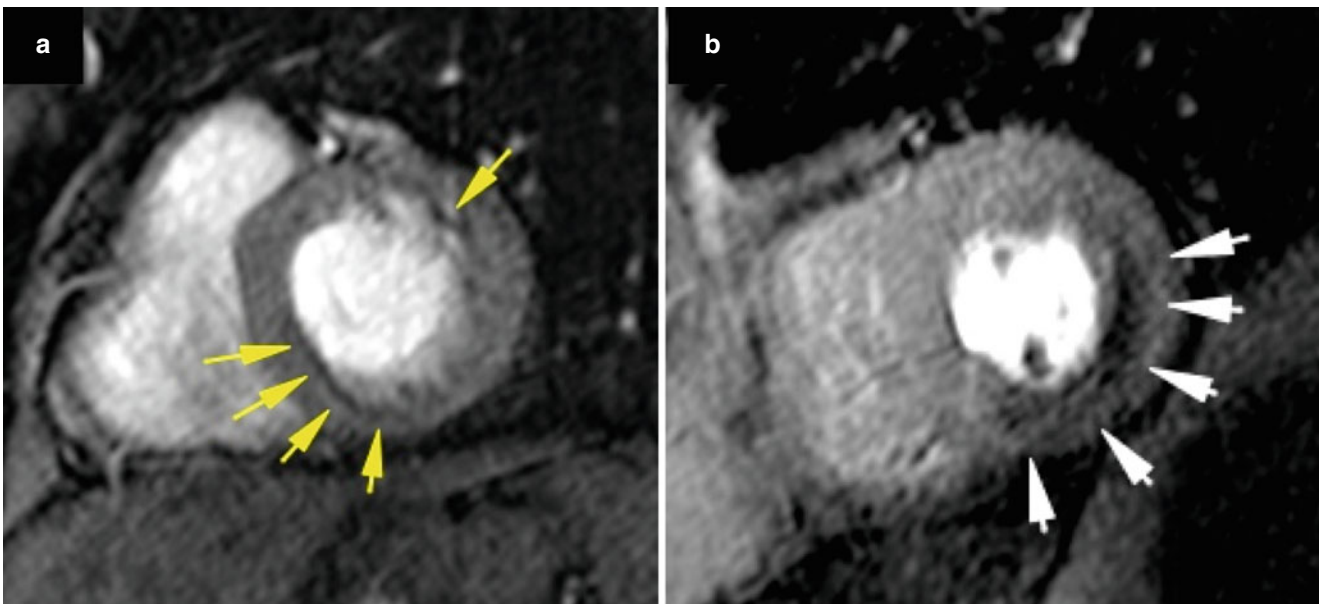


Fig. 14.9 Dark rim artifacts (**a**) versus true perfusion defects (**b**). Note the presence of a relatively thin dark artifact in (**a**). The defect in (**b**) is more transmural, with an epicardial to endocardial gradient and follows a typical coronary perfusion pattern

contrast between normally and abnormally perfused areas, they do not provide a linear relationship between signal enhancement and concentration in the AIF. Mathematical models can be used to address the concentration-signal relationship, but it is preferable to adjust the acquisition method if quantitative analysis is anticipated. For this purpose, it has been proposed to either acquire the AIF with a less T_1 sensitive pulse sequence, typically by using a very short saturation pulse delay for the AIF slice (dual-sequence method) or to use a second lower dose contrast bolus injection to derive the AIF (dual-bolus method).

Clinical Indications

Detection of CAD

Vasodilator stress myocardial perfusion CMR is a highly accurate method for the detection of coronary artery stenosis. In recent meta analyses, the pooled sensitivity of CMR, using a wide variety of pulse sequences, to detect anatomically defined significant CAD on a patient basis was 89 % (95 % CI: 88–91 %) with a specificity of 76 % (95 % CI: 73–78 %) [24]. These values are comparable with PET imaging and higher than for SPECT. In a separate meta analysis comparing CMR with a more appropriate functional endpoint, the invasive standard of fractional flow reserve, sensitivity was 87.7 % (95 % CI, 84.4–90.6 %) and specificity of 88.6 % (95 % CI, 86.7–90.4 %) [25]. These large meta analyses confirm that myocardial perfusion CMR, using conventional and diverse methodology, can play an important clinical role in the management of patients with CAD. This evidence has also led to the inclusion of CMR in recent practice guidelines in the US and Europe [26, 27].

Perfusion-CMR can also be used to risk stratify patients as shown in several single center studies and meta-analyses. In a study by Jahnke et al. in 513 patients a normal scan was associated with a <1 % annual event rate (cardiac death or non-fatal myocardial infarction) [13]. A study of 1,229 patients showed 5-year event free survival of 95.6 % in the patients with a normal perfusion study [28]. The evidence was summarized in a meta-analysis with data from 19 studies, including 15 perfusion CMR studies. Eleven thousand six hundred thirty-six patients were followed up for a mean of 32 months and the event rate of a positive test was 4.9 % vs 0.8 % for a negative stress test ($P < 0.0001$) [29].

Heart Failure

The European Society of Cardiology guidelines for the management of heart failure recommend myocardial perfusion imaging by CMR in patients thought to have CAD, and who are considered suitable for coronary revascularization, to determine whether there is reversible myocardial ischemia and viable myocardium [30].

Developments

Many ongoing developments are likely to further improve myocardial perfusion CMR over the coming year. Innovative data acceleration schemes allow higher acceleration with relatively preserved SNR and are used to further improve spatial resolution, cardiac coverage or both. First studies suggest improved diagnostic performance of these methods. The rapid uptake of 3 Tesla CMR systems is of particular benefit for perfusion CMR in view of the higher SNR provided. Initial studies have suggested myocardial perfusion CMR at 3 Tesla to be highly accurate and to improve the detection of ischemia compared with 1.5 Tesla [31]. See Fig. 14.10.

Acceleration

In order to accelerate perfusion imaging, parallel imaging techniques that exploit the spatial difference of radiofrequency coil sensitivities such as sensitivity encoding (SENSE) are employed as standard in most centers [32], supported by the wider adoption of multi-coil arrays. Practically, the acceleration provided by these methods is limited to two to three fold due to increasing SNR penalties with higher acceleration factors [33]. Prior-knowledge driven methods such as Highly Constrained Back-Projection Reconstruction (HYPR), k - t Broad Linear Speed up Technique (BLAST) and k - t Sensitivity Encoding (SENSE) allow higher acceleration with relatively preserved SNR [34, 35].

With these methods, acceleration is generally achieved by undersampling in both the space and time domains. The resulting alias is resolved with acquisition of low spatial resolution training data sets and the aid of reconstruction model. The speed up in data acquisition can be used to spatial resolution or increased cardiac coverage.

In small clinical studies the use of high resolution (1–2 mm in plane) for perfusion CMR has been demonstrated [20, 36]. At higher resolution, imaging artifacts such as endocardial dark rims, were found to be lower with improvements in image quality. An initial study suggested diagnostic superiority of high versus standard resolution myocardial perfusion CMR, but these data require validation in larger clinical populations [37]. See Fig. 14.11.

Using highly accelerated acquisition schemes, it is also possible to acquire 3D myocardial perfusion CMR data covering the whole heart in each RR interval within a 200 ms acquisition window. Several small single center studies have established the feasibility and accuracy of this approach. Manka et al. studied 146 patients with 3D myocardial perfusion CMR and reported a sensitivity of 91.7 % and a specificity of 74.3 % to detect CAD as defined by QCA [38]. In a second study, the group compared 3D perfusion CMR with FFR in two centers and 120 patients with a sensitivity of 90 %, specificity of 82 % and diagnostic accuracy of 87 % [39].

Other methods in development include ungated data radial acquisition [40]. The advantage of this method is the

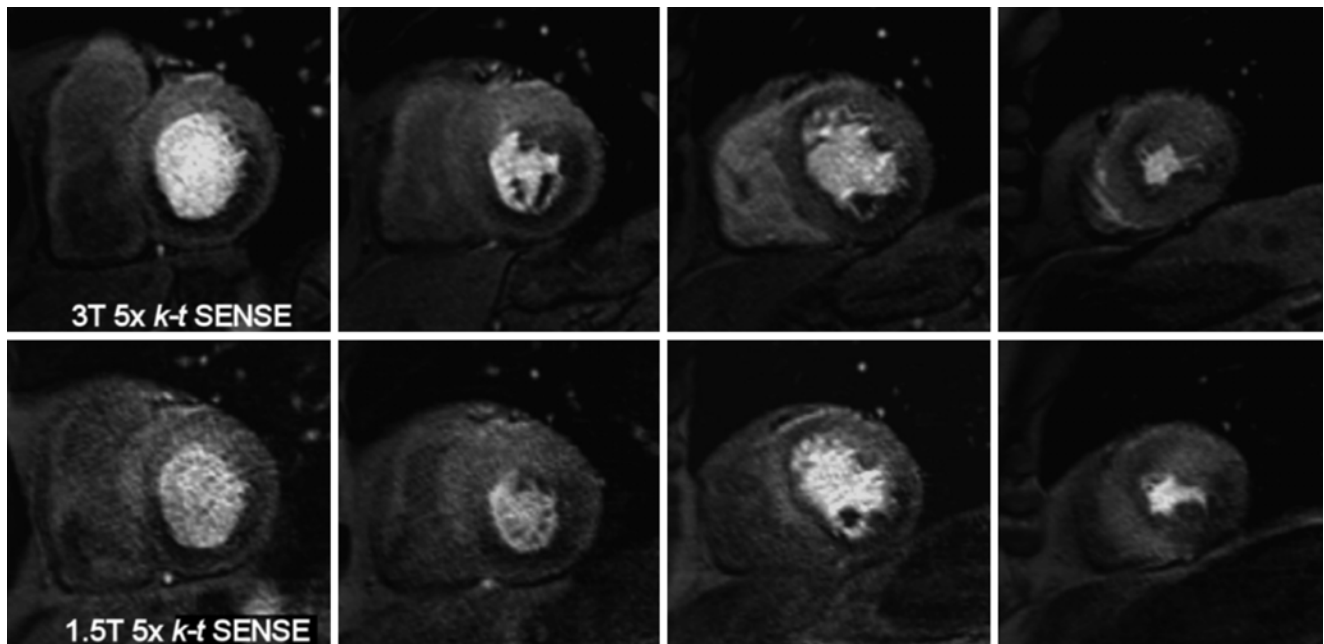


Fig. 14.10 Comparison between 3 and 1.5 Tesla perfusion series in the same patient. k-t Sensitivity encoding accelerated cardiac magnetic resonance per- fusion images at 3 Tesla and 1.5 T in a patient with 3-vessel disease and chronic occlusion of the right coronary artery. Both datasets contain the same diagnostic information, with an area of

subendocardial ischemia in the inferior segments of the left ventricle and a transmural gradient of perfusion, with more severe ischemia in the subendocardial layers of the left ventricle. The image quality is superior at 3 Tesla [43]

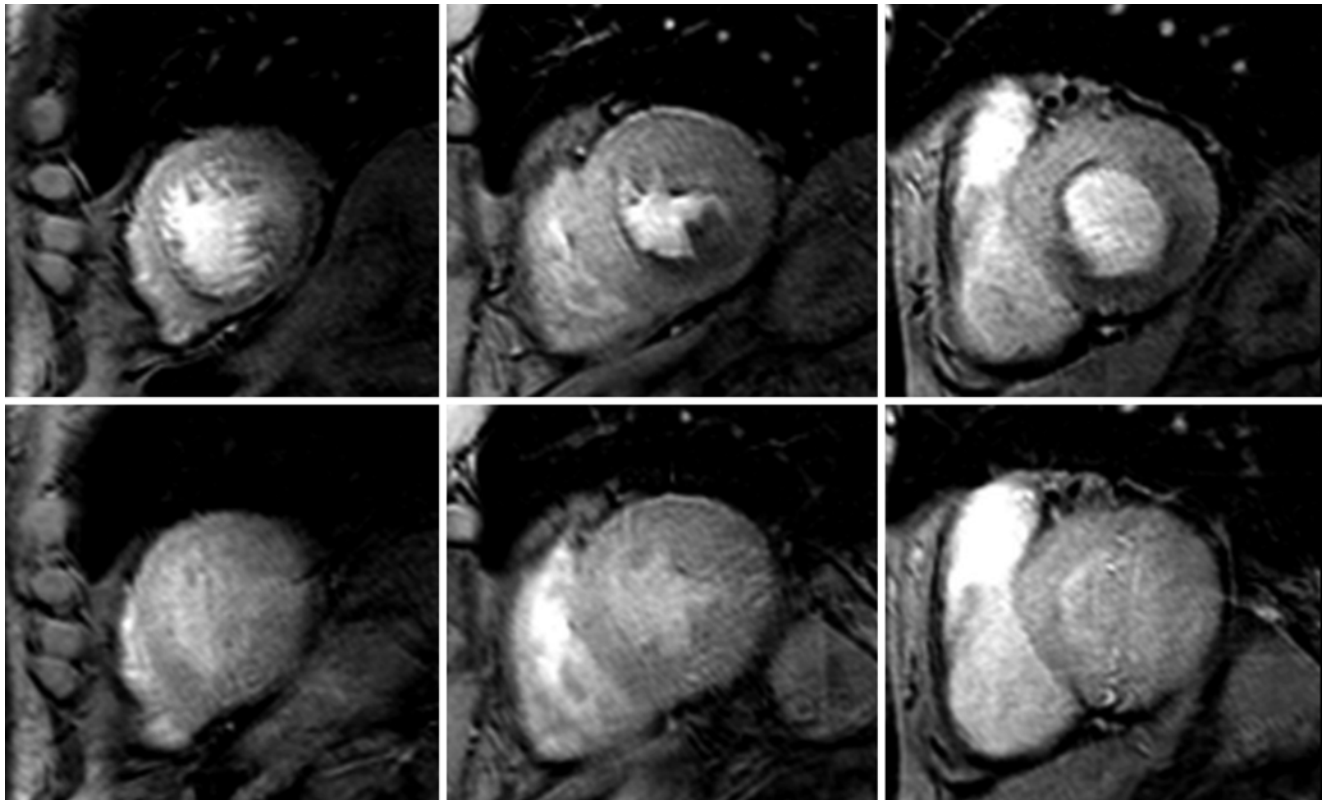


Fig. 14.11 Stress (*top*) and rest (*bottom*) perfusion imaging of a 53-year old diabetic patient presented with breathlessness. Other risk factors included family history for CAD. On the stress images (high-resolution 3 T *kt* BLAST), evidence of a subendocardial perfusion abnormality in the basal inferior, infero-septal and infero-lateral walls

(RCA territory) and basal antero-lateral wall (LCX territory), mid-infero-septal, inferior and infero-lateral and apical inferior. Angiogram showed diffuse and non critical disease in the LAD, dominant RCA with proximal lesion (FFR 0.45), and diseased obtuse marginal branch (FFR 0.73)

fast acquisition of data providing a number of perfusion images adequate for diagnosis without using ECG gating signals and during free breathing. Therefore, it can be potentially used in patients who have arrhythmias, difficulties of gating or unable to perform adequate breath holding. As for many other CMR applications, compressed sensing is emerging as a promising method to accelerate myocardial perfusion CMR [41].

References

- Nesto RW, Kowalchuk GJ. The ischemic cascade: temporal sequence of hemodynamic, electrocardiographic and symptomatic expressions of ischemia. *Am J Cardiol.* 1987;57:23C–30.
- Paetsch I, Jahnke C, Wahl A, Gebker R, Neuss M, Fleck E, Nagel E. Comparison of dobutamine stress magnetic resonance, adenosine stress magnetic resonance, and adenosine stress magnetic resonance perfusion. *Circulation.* 2004;110:835–42.
- Foster EL, Arnold JW, Jekic M, Bender JA, Balasubramanian V, Thavendiranathan P, Dickerson JA, Raman SV, Simonetti OP. MR-compatible treadmill for exercise stress cardiac magnetic resonance imaging. *Magn Reson Med.* 2012;67:880–9.
- Nagel E, Lorenz C, Baer F, Hundley WG, Wilke N, Neubauer S, Sechtem U, van der Wall E, Pettigrew R, de Roos A, Fleck E, van Rossum A, Pennell DJ, Wickline S. Stress cardiovascular magnetic resonance: consensus panel report. *J Cardiovasc Magn Reson.* 2001;3:267–81.
- Kramer CM, Barkhausen J, Flamm SD, Kim RJ, Nagel E. Society for cardiovascular magnetic resonance board of trustees task force on standardized P. Standardized cardiovascular magnetic resonance imaging (cmr) protocols, society for cardiovascular magnetic resonance: board of trustees task force on standardized protocols. *J Cardiovasc Magn Reson.* 2008;10:35.
- Schalla S, Klein C, Paetsch I, Lehmkuhl H, Bornstedt A, Schnackenburg B, Fleck E, Nagel E. Real-time mr image acquisition during high-dose dobutamine hydrochloride stress for detecting left ventricular wall-motion abnormalities in patients with coronary arterial disease. *Radiology.* 2002;224:845–51.
- Schulz-Menger J, Bluemke DA, Bremerich J, Flamm SD, Fogel MA, Friedrich MG, Kim RJ, von Knobelsdorff-Brenkenhoff F, Kramer CM, Pennell DJ, Plein S, Nagel E. Standardized image interpretation and post processing in cardiovascular magnetic resonance: Society for Cardiovascular Magnetic Resonance (SCMR) board of trustees task force on standardized post processing. *J Cardiovasc Magn Reson.* 2013;15:35.
- Wahl A, Paetsch I, Gollersch A, Roethemeyer S, Foell D, Gebker R, Langreck H, Klein C, Fleck E, Nagel E. Safety and feasibility of high-dose dobutamine-atropine stress cardiovascular magnetic resonance for diagnosis of myocardial ischemia: experience in 1000 consecutive cases. *Eur Heart J.* 2004;25:1230–6.
- Nandalur KR, Dwamena BA, Choudhri AF, Nandalur MR, Carlos RC. Diagnostic performance of stress cardiac magnetic resonance imaging in the detection of coronary artery disease: a meta-analysis. *J Am Coll Cardiol.* 2007;50:1343–53.
- Nagel E, Lehmkuhl HB, Bocksch W, Klein C, Vogel U, Frantz E, Ellmer A, Dreyse S, Fleck E. Noninvasive diagnosis of ischemia-induced wall motion abnormalities with the use of high-dose dobutamine stress mri: comparison with dobutamine stress echocardiography. *Circulation.* 1999;99:763–70.
- Korosoglou G, Gitsioudis G, Voss A, Lehrke S, Riedle N, Buss SJ, Zugck C, Giannitsis E, Osman NF, Katus HA. Strain-encoded cardiac magnetic resonance during high-dose dobutamine stress testing for the estimation of cardiac outcomes: comparison to clinical parameters and conventional wall motion readings. *J Am Coll Cardiol.* 2011;58:1140–9.
- Schuster A, Kutty S, Padiyath A, Parish V, Gribben P, Danford DA, Makowski MR, Bigalke B, Beerbaum P, Nagel E. Cardiovascular magnetic resonance myocardial feature tracking detects quantitative wall motion during dobutamine stress. *J Cardiovasc Magn Reson.* 2011;13:58.
- Jahnke C, Nagel E, Gebker R, Kokocinski T, Kelle S, Manka R, Fleck E, Paetsch I. Prognostic value of cardiac magnetic resonance stress tests: adenosine stress perfusion and dobutamine stress wall motion imaging. *Circulation.* 2007;115:1769–76.
- Wellnhofer E, Olariu A, Klein C, Grafe M, Wahl A, Fleck E, Nagel E. Magnetic resonance low-dose dobutamine test is superior to scar quantification for the prediction of functional recovery. *Circulation.* 2004;109:2172–4.
- Biglands JD, Radjenovic A, Ridgway JP. Cardiovascular magnetic resonance physics for clinicians: part II. *J Cardiovasc Magn Reson.* 2012;14:66.
- Kellman P, Arai AE. Imaging sequences for first pass perfusion – a review. *J Cardiovasc Magn Reson.* 2007;9(3):525–37.
- Wang Y, Moin K, Akinboboye O, Reichek N. Myocardial first pass perfusion: steady-state free precession versus spoiled gradient echo and segmented echo planar imaging. *Magn Reson Med.* 2005;54(5):1123–9.
- Fenchel M, Helber U, Simonetti OP, et al. Multislice first-pass myocardial perfusion imaging: comparison of saturation recovery (SR)-TrueFISP-two-dimensional (2D) and SR-TurboFLASH-2D pulse sequences. *J Magn Reson Imaging JMRI.* 2004;19(5):555–63.
- Elkington AG, Gatehouse PD, Cannell TM, et al. Comparison of hybrid echo-planar imaging and FLASH myocardial perfusion cardiovascular MR imaging. *Radiology.* 2005;235(1):237–43.
- Manka R, Vitanis V, Boesiger P, Flammar AJ, Plein S, Kozerek S. Clinical feasibility of accelerated, high spatial resolution myocardial perfusion imaging. *J Am Coll Cardiol Cardiovasc Imaging.* 2010;3:710–7.
- Di Bella EV, Parker DL, Sinusas AJ. On the dark rim artifact in dynamic contrast-enhanced MRI myocardial perfusion studies. *Magn Reson Med.* 2005;54:1295–9.
- Meloni A, Al-Saadi N, Torheim G, Hoebel N, Reynolds HG, De Marchi D, Positano V, Burchielli S, Lombardi M. Myocardial first-pass perfusion: influence of spatial resolution and heart rate on the dark rim artifact. *Magn Reson Med.* 2011;66:1731–8.
- Jerosch-Herold M. Quantification of myocardial perfusion by cardiovascular magnetic resonance. *J Cardiovasc Magn Reson.* 2010;12:57.
- Jaarsma C, Leiner T, Bekkers SC, Crijns HJ, Wildberger JE, Nagel E, Nelemans PJ, Schalla S. Diagnostic performance of noninvasive myocardial perfusion imaging using single-photon emission computed tomography, cardiac magnetic resonance, and positron emission tomography imaging for the detection of obstructive coronary artery disease: a meta-analysis. *J Am Coll Cardiol.* 2012;59:1719–28.
- Desai RR, Jha S. Diagnostic performance of cardiac stress perfusion MRI in the detection of coronary artery disease using fractional flow reserve as the reference standard: a meta-analysis. *AJR Am J Roentgenol.* 2013;201(2):W245–52.
- Task Force Members, Montalescot G, Sechtem U, Achenbach S, Andreotti F, Arden C, Budaj A, Bugiardini R, Crea F, Cuisset T, Di Mario C, Ferreira JR, Gersh BJ, Gitt AK, Hulot JS, Marx N, Opie LH, Pfisterer M, Prescott E, Ruschitzka F, Sabaté M, Senior R, Taggart DP, van der Wall EE, Vrints CJ, ESC Committee for Practice Guidelines, Zamorano JL, Achenbach S, Baumgartner H, Bax JJ, Bueno H, Dean V, Deaton C, Erol C, Fagard R, Ferrari R, Hasdai D, Hoes AW, Kirchhof P, Knuuti J, Kolh P, Lancellotti P,

- Linhart A, Nihoyannopoulos P, Piepoli MF, Ponikowski P, Sirnes PA, Tamargo JL, Tendera M, Torbicki A, Wijns W, Windecker S, Document Reviewers, Knuuti J, Valgimigli M, Bueno H, Claeys MJ, Donner-Banzhoff N, Erol C, Frank H, Funck-Brentano C, Gaemperli O, Gonzalez-Juanatey JR, Hämäläinen M, Hasdai D, Husted S, James SK, Kervinen K, Kolh P, Kristensen SD, Lancellotti P, Maggioni AP, Piepoli MF, Pries AR, Romeo F, Rydén L, Simoons-Sel A, Sirnes PA, Steg PG, Timmis A, Wijns W, Windecker S, Yildirir A, Zamorano JL. ESC guidelines on the management of stable coronary artery disease: the task force on the management of stable coronary artery disease of the European Society of Cardiology. *Eur Heart J*. 2013;34:2949–3003.
27. Fihn SD, Gardin JM, Abrams J, Berra K, Blankenship JC, Dallas AP, Douglas PS, Foady JM, Gerber TC, Hinderliter AL, King 3rd SB, Kligfield PD, Krumholz HM, Kwong RY, Lim MJ, Linderbaum JA, Mack MJ, Munger MA, Prager RL, Sabik JF, Shaw LJ, Sikkema JD, Smith Jr CR, Smith Jr SC, Spertus JA, Williams SV, American College of Cardiology Foundation, American Heart Association Task Force on Practice Guidelines, American College of Physicians, American Association for Thoracic Surgery, Preventive Cardiovascular Nurses Association, Society for Cardiovascular Angiography and Interventions, Society of Thoracic Surgeons. ACCF/AHA/ACP/AATS/PCNA/SCAI/STS Guideline for the diagnosis and management of patients with stable ischemic heart disease: a report of the American College of Cardiology Foundation/American Heart Association Task Force on Practice Guidelines, and the American College of Physicians, American Association for Thoracic Surgery, Preventive Cardiovascular Nurses Association, Society for Cardiovascular Angiography and Interventions, and Society of Thoracic Surgeons. *J Am Coll Cardiol*. 2012;60:e44–164.
 28. Buckert D, Dewes P, Walcher T, Rottbauer W, Bernhard P. Intermediate-term prognostic value of reversible perfusion deficit diagnosed by adenosine CMR: a prospective follow-up study in a consecutive patient population. *JACC Cardiovasc Imaging*. 2013;6(1):56–63.
 29. Lipinski MJ, McVey CM, Berger JS, Kramer CM, Salerno M. Prognostic value of stress cardiac magnetic resonance imaging in patients with known or suspected coronary artery disease: a systematic review and meta-analysis. *J Am Coll Cardiol*. 2013;62:826–38.
 30. McMurray JJ, Adamopoulos S, Anker SD, Auricchio A, Böhm M, Dickstein K, Falk V, Filippatos G, Fonseca C, Gomez-Sanchez MA, Jaarsma T, Køber L, Lip GY, Maggioni AP, Parkhomenko A, Pieske BM, Popescu BA, Rønnevik PK, Rutten FH, Schwitzer J, Seferovic P, Stepinska J, Trindade PT, Voors AA, Zannad F, Zeiher A, ESC Committee for Practice Guidelines, ESC Guidelines for the diagnosis and treatment of acute and chronic heart failure. The Task Force for the Diagnosis and Treatment of Acute and Chronic Heart Failure 2012 of the European Society of Cardiology. Developed in collaboration with the Heart Failure Association (HFA) of the ESC. *Eur Heart J*. 2012;33:1787–847.
 31. Cheng AS, Pegg TJ, Karamitsos TD, Searle N, Jerosch-Herold M, Choudhury RP, Banning AP, Neubauer S, Robson MD, Selvanayagam JB. Cardiovascular magnetic resonance perfusion imaging at 3-tesla for the detection of coronary artery disease: a comparison with 1.5-tesla. *J Am Coll Cardiol*. 2007;49:2440–9.
 32. Plein S, Radjenovic A, Ridgway JP, Barnby D, Greenwood JP, Ball SG, Sivanathan MU. Coronary artery disease: myocardial perfusion MR imaging with sensitivity encoding versus conventional angiography. *Radiology*. 2005;235:423–30.
 33. Pruessmann KP, Weiger M, Boesiger P. Sensitivity encoded cardiac MRI. *J Cardiovasc Magn Reson*. 2001;3(1):1–9.
 34. Ma H, Yang J, Liu J, Ge L, An J, Tang Q, Li H, Zhang Y, Chen D, Wang Y, Liu J, Liang Z, Lin K, Jin L, Bi X, Li K, Li D. Myocardial perfusion magnetic resonance imaging using sliding-window conjugate-gradient highly constrained back-projection reconstruction for detection of coronary artery disease. *Am J Cardiol*. 2012;109:1137–41.
 35. Plein S, Ryf S, Schwitzer J, Radjenovic A, Boesiger P, Kozerke S. Dynamic contrast-enhanced myocardial perfusion MRI accelerated with k-t sense. *Magn Reson Med*. 2007;58:777–85.
 36. Lockie T, Ishida M, Perera D, Chiribiri A, De Silva K, Kozerke S, Marber M, Nagel E, Rezavi R, Redwood S, Plein S. High-resolution magnetic resonance myocardial perfusion imaging at 3.0-tesla to detect hemodynamically significant coronary stenoses as determined by fractional flow reserve. *J Am Coll Cardiol*. 2011;57:70–5.
 37. Motwani M, Maredia N, Fairbairn TA, Kozerke S, Radjenovic A, Greenwood JP, Plein S. High-resolution versus standard-resolution cardiovascular MR myocardial perfusion imaging for the detection of coronary artery disease. *Circ Cardiovasc Imaging*. 2012;5(3):306–13.
 38. Manka R, Jahnke C, Kozerke S, Vitanis V, Crelier G, Gebker R, Schnackenburg B, Boesiger P, Fleck E, Paetsch I. Dynamic 3-dimensional stress cardiac magnetic resonance perfusion imaging: detection of coronary artery disease and volumetry of myocardial hypoenhancement before and after coronary stenting. *J Am Coll Cardiol*. 2011;57(4):437–44.
 39. Manka R, Paetsch I, Kozerke S, Moccetti M, Hoffmann R, Schroeder J, Reith S, Schnackenburg B, Gaemperli O, Wissmann L, Wyss CA, Kaufmann PA, Corti R, Boesiger P, Marx N, Lüscher TF, Jahnke C. Whole-heart dynamic three-dimensional magnetic resonance perfusion imaging for the detection of coronary artery disease defined by fractional flow reserve: determination of volumetric myocardial ischaemic burden and coronary lesion location. *Eur Heart J*. 2012;33(16):2016–24.
 40. Sharif B, Dharmakumar R, Arsanjani R, Thomson L, Bairey Merz CN, Berman DS, Li D. Non-ECG-gated myocardial perfusion MRI using continuous magnetization-driven radial sampling. *Magn Reson Med*. 2014;72:1620–8.
 41. Otazo R, Kim D, Axel L, Sodickson DK. Combination of compressed sensing and parallel imaging for highly accelerated first-pass cardiac perfusion MRI. *Magn Reson Med*. 2010;64:767–76.
 42. Kelle S, et al. Prognostic value of negative dobutamine-stress cardiac magnetic resonance imaging. *Med Sci Mon*. 15(10):MT131–136.
 43. Plein S, Schwitzer J, Suerder D, Greenwood JP, Boesiger P, Kozerke S. k-Space and time sensitivity encoding-accelerated myocardial perfusion MR imaging at 3.0 T: comparison with 1.5 T. *Radiology*. 2008;249(2):493–50.

Rebecca E. Thornhill and Elena Peña

Abstract

Late gadolinium enhancement cardiac magnetic resonance (LGE-CMR) has become a powerful and indispensable tool for the characterization of myocardial fibrosis and scar. LGE images can be acquired using any one of a number of fast T_1 -weighted gradient echo sequences, approximately 10–20 min post-injection of contrast media. As such, LGE imaging is a simple technique that is an integral part of most clinical CMR protocols. In this chapter, we explore the fundamental principles underpinning the technique, beginning with a discussion of gadolinium contrast kinetics in both normal and damaged myocardium. Next, we describe the underlying basis for LGE imaging: nulling the MRI signal associated with normal myocardium, such that fibrotic or scarred tissue becomes conspicuously bright on T_1 -weighted images. The chapter continues by providing a brief history of the evolution of LGE pulse sequence development, highlighting many crucial innovations along the way. Finally, we explore a variety of clinical applications of LGE, including its role in the characterization of infarct scar, in multiple cardiomyopathies, and in the rule-out of infectious or infiltrative disease. Common approaches for quantification and characterization of LGE images are also described. While by no means exhaustive, the goal of this chapter is to provide the cardiovascular imager with an understanding of the basic principles of LGE as well as an appreciation for the versatility and clinical utility of the technique.

Keywords

Late gadolinium enhancement • Myocardial viability • Myocardial infarction • Ischemic heart disease • Dilated cardiomyopathy • Hypertrophic cardiomyopathy • Arrhythmogenic right ventricular cardiomyopathy • Cardiac sarcoidosis • Myocarditis • Cardiac amyloidosis

R.E. Thornhill, PhD (✉)
Department of Radiology, University of Ottawa,
Ottawa, ON, Canada

Clinical Epidemiology Program, Ottawa Hospital Research
Institute, Ottawa, ON, Canada

Department Medical Imaging c/o Laura Lang, The Ottawa
Hospital, Civic Campus,
1053 Carling Ave, Ottawa, ON K1Y 4E9, Canada
e-mail: rthornhill@toh.on.ca

E. Peña, MD
Department of Medical Imaging, The Ottawa Hospital,
Ottawa, ON, Canada

Department of Radiology, University of Ottawa,
Ottawa, ON, Canada

Introduction

Late gadolinium enhancement (LGE) has become the gold standard in vivo imaging test for assessing the presence and extent of a wide range of myocardial abnormalities, most commonly infarct scar but also fibrosis of nonischemic disease and inflammatory and other infiltrative materials. With LGE, image acquisition occurs at a set delay (10–15 min) following the intravenous injection of gadolinium-based contrast media, in order to capture a ‘snapshot’ of the extravascular-extracellular distribution of contrast. The signal from normal (non-fibrotic) myocardium is deliberately “nulled” in LGE imaging, such that areas of accumulated contrast will appear bright. While clinical use of LGE-CMR in cardiovascular practice has expanded considerably in the last decade, the fundamental principle of exploiting the differential distribution of gadolinium-based contrast media in infarcted vs. normal myocardium was established in the mid-1980s [1–5]. In the approximately 30 years since, the LGE technique has undergone an impressive series of improvements, evolving from the low contrast-to-noise (CNR), single-slice, ungated spin-echo implementation of the early 1980s to the current state-of-the-art 3D pulse-sequences that are pushing towards resolving left atrial scar. In this chapter, we will discuss many of the key technical developments along this 30-year path, as well as illustrating how these advancements have enabled an expanding variety of clinical applications.

The Fundamental Principles of Late Gadolinium Enhancement

Compared with other CMR procedures, such as stress imaging, LGE is relatively straightforward. For most indications, LGE can be insinuated into the protocol approximately 12–14 min post-contrast injection and requires little more than 5 min to obtain full cardiac coverage in multiple views. In general, the left ventricle (LV) is best covered by acquiring contiguous short-axis views, from the apex to the level of the mitral valve with standard long axis views (horizontal long axis (HLA) or four-chamber, vertical long axis (VLA) or two-chamber, and three-chamber views). The right ventricle (RV) can also be visualized using short axis LGE images, however, there may be scenarios where axial or HLA views are preferable, for example in arrhythmogenic right ventricular cardiomyopathy (ARVC) or congenital heart disease. Although the details of the LGE protocol may vary depending on the clinical indication, an appreciation for the fundamental principles of the technique will enable cardiovascular imagers to tailor this versatile technique to suit their specific clinical or research needs.

Contrast Kinetics

The first attempts to acquire T_1 -weighted spin-echo images revealed that the T_1 of infarcted myocardium was distinctly prolonged compared to normal myocardium, resulting in regions of decreased signal intensity (‘hypo-enhanced’ regions) [1, 4–7]. The introduction of paramagnetic contrast agents such as Gd-DTPA to cardiac MRI enabled stark delineation of irreversibly injured myocardium. Gadolinium (Gd³⁺) is paramagnetic and exerts an indirect T_1 (and to a lesser extent, T_2) shortening effect on neighboring water protons. The chelator, DTPA, is responsible for the distribution and kinetics of the contrast medium. Healthy cells with intact, selectively permeable cell membranes will exclude Gd-DTPA and therefore this agent is restricted to the extravascular and extracellular spaces (Fig. 15.1) [8, 9]. The loss of membrane integrity in irreversibly injured myocytes (e.g., in myocardial infarction) enables the contrast agent to enter the erstwhile intracellular space and, hence, increase its volume of distribution. Excess accumulation of Gd-DTPA is further exacerbated if there is ongoing ischemia and delayed washout kinetics, due to poor venous drainage [10].

One early approach toward quantifying the accumulation of Gd-DTPA in the myocardium was to immediately follow the bolus-injection by a constant-infusion of the contrast agent [11]. With this technique, equilibrium concentrations of the tracer can be achieved in the tissue, thus making it possible to estimate the partition coefficient (λ) of Gd-DTPA in ml of contrast medium per gram of myocardium [11]. Assuming normal renal clearance, an optimum constant infusion dose can be chosen such that the concentration of contrast agent will reach equilibrium in approximately 15 min, in all but the most severely ischemic regions of myocardium (perfusion <0.05 ml/min/g) [12]. With breakdown of cell membrane integrity, Gd-DTPA can begin to permeate the formerly intracellular space (Fig. 15.1c). Given that sarcolemmal disruption is a defining characteristic of irreversible injury, it follows that the λ in infarcted myocardium would exceed that of normal tissue and, in fact, it has been shown to be more than double that of normal myocardium (0.8 ml/g versus 0.3 ml/g) [11, 13, 14]. This has been validated in the setting of unreperfused infarction by Pereira and colleagues by a significant increase in λ in infarcted tissue as early as 2 days and for at least 3 weeks following permanent LAD occlusion in canine models [15]. When applied to patients with acutely reperfused AMI, λ was found to be inversely correlated to areas of low count-density on resting Tl-201 images [16]. Flacke et al. also demonstrated that λ can differentiate between normal and infarcted myocardium in patients with either acute or chronic myocardial infarction [17]. Considered together, the available evidence supports the conclusion that λ is increased exclusively in irreversibly injured myocardium.

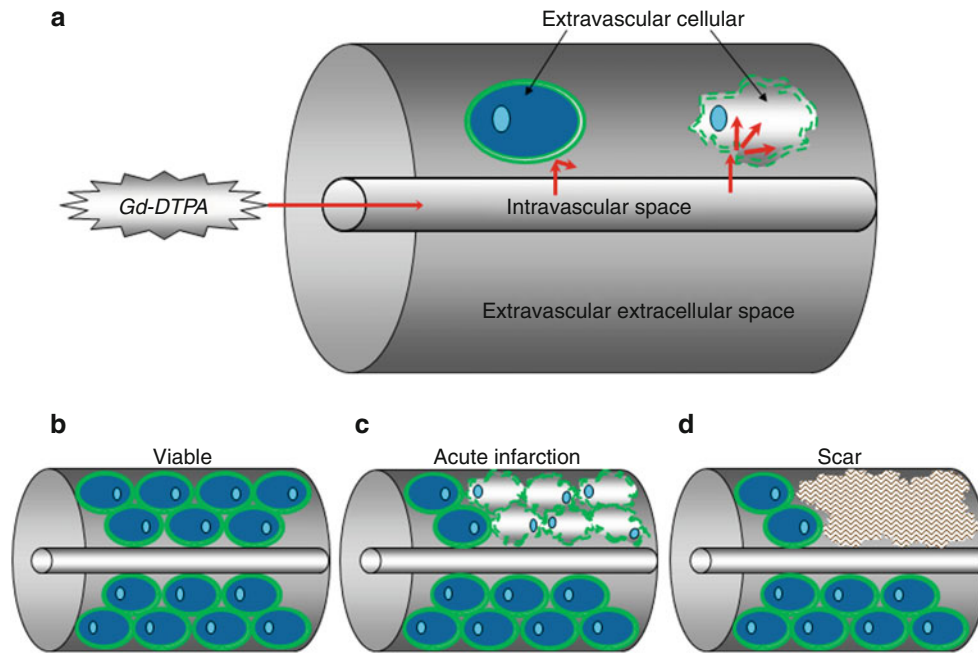


Fig. 15.1 A schematic depicting the distribution of Gd-DTPA contrast in myocardium (a), with two stylized cells, situated within a section of myocardium: a normal cell (*left*), with an intact, selectively permeable cell membrane, and an irreversibly damaged cell (*right*), with disrupted cell membranes. If we introduce an extravascular/extracellular contrast agent such as Gd-DTPA into the intravascular space, Gd-DTPA will not be able to penetrate the cell membrane of healthy myocytes, and there-

fore only distributes to the extracellular space (b). In acutely infarcted tissue, however, breaches in the cell membrane will permit the agent to enter the spaces previously occupied by the cell (c). In chronically infarcted or scarred myocardium (d), the remodelling process also results in a net decrease in the extravascular/cellular compartment, as the lost myocytes are ultimately replaced by mature, collagenous scar, into which Gd-DTPA can accumulate

With respect to dose, the convention at most institutions is to administer a “double dose,” or 0.2 mmol/kg body-weight for all LGE exams. This is to ensure that maximum CNR between healthy and damaged myocardium is achievable at 10–20 min post-injection. Single dose imaging (i.e., 0.1 mmol/kg) will reduce the delay required between injection and image acquisition [18–21]. However, biological clearance of contrast occurs in a non-linear (exponential) fashion and therefore it is still preferable to wait at least 10 min post-injection prior to acquisition, regardless of dose so that areas of hyperenhanced myocardium will appear distinct from the LV or RV blood pools.

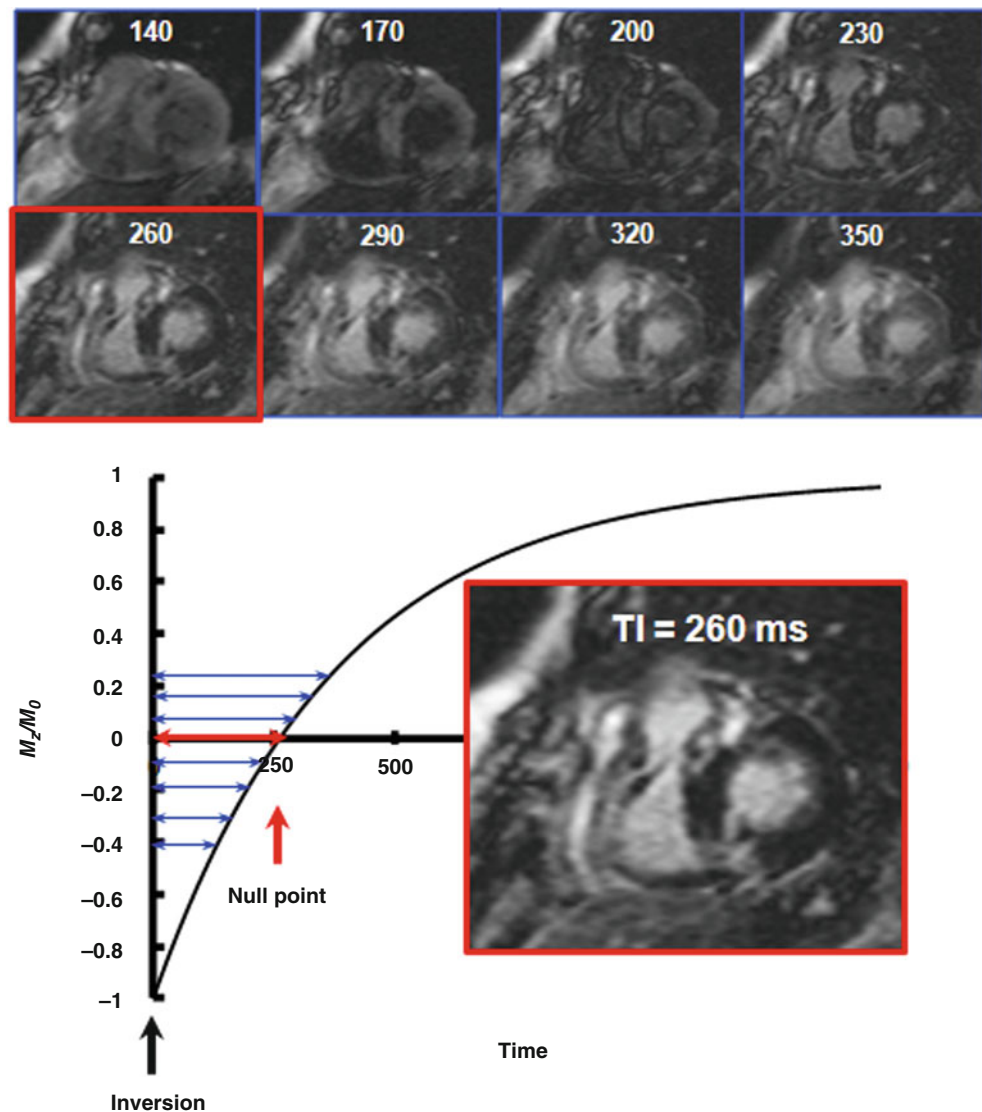
Nulling Normal Myocardium

The goal of LGE imaging is to null the signal contribution of healthy myocardium such that areas of scar or fibrosis are rendered as conspicuous as possible. We accomplish this by exploiting the difference in T_1 between healthy and fibrotic tissues. As such, all LGE sequences are T_1 weighted and most begin by means of a volume inversion preparation pulse. After the inversion pulse, the signal from healthy myocardium will recover according to a longer T_1 time than fibrotic myocardium. During this process, the magnetization from

both healthy and fibrotic myocardium will pass through a point on the recovery curve where their contribution to the MR signal will be zero or “nulled.” Identifying this inversion time (TI) or “null point” precisely for healthy myocardium is crucial for optimization of LGE imaging (Fig. 15.2). When the prescribed TI is too short, the longitudinal magnetization corresponding to normal myocardium will have a negative value during data readout and could potentially appear hyperenhanced relative to infarcted or fibrotic myocardium. Conversely, if the nominal TI is too long, the magnetization associated with normal myocardium will correspond to a point above the zero-crossing and appear gray, but not black (nulled) [22]. While irreversibly injured myocardium will appear hyperenhanced at long TIs, the CNR will be poor, since the discrepancy between the two tissues will be reduced.

There are essentially two different strategies for optimizing the TI: one can perform “test” LGE imaging using an initial “best guess” and then re-acquire in the appropriate direction to iteratively select the optimal inversion time. In practice, it is seldom necessary to perform more than two or three “re-tests” as an experienced technologist will be able to estimate the optimal TI merely from experience and a priori knowledge of the dose of contrast administered. For example, if we assume that normal myocardium has a post-contrast T_1 of 400 ms, then a patient with an R wave to R wave interval (R-R inter-

Fig. 15.2 Application of a “TI scout” sequence to determine the optimal TI for nulling normal myocardium. Eight short-axis scout images are shown (*top*) to illustrate the effect of TI on myocardial enhancement signal intensities in a patient with hypertrophic cardiomyopathy (the TI is indicated on the *top* of each image in ms). After a 180° inversion pulse at Time=0, a series of images with incrementally increasing TIs are acquired during longitudinal relaxation (M_z/M_0). Note the increasing intensity of the fibrotic regions (at the RV-LV hinge points) with increasing TI. The time at which the longitudinal magnetization associated with normal myocardium passes through the $M_z/M_0=0$ (null) point is recorded as the optimal TI. In this example, the optimal TI is determined to be 260 ms



val)=800 ms will require an optimal inversion time of $TI = \ln(2) * T_1 = 0.69 * T_1 = 280$ ms [22]. Alternatively, most vendors provide a so-called “TI scout,” which is usually an inversion recovery prepared cine sequence that systematically acquires test LGE images over a range of TIs (Fig. 15.2), enabling the operator to review and select the optimum inversion time prior to acquisition [23]. When using these sequences, it is important to remain cognizant of the fact that most TI scout sequences utilize a steady-state free precession readout, rather than the spoiled gradient-echo readout common to most LGE acquisitions. In practice, the optimal TI identified by the scout may not effectively match the true ideal required by the LGE sequence.

The Evolution of LGE Pulse Sequence Design

As previously discussed, the basic “recipe” for LGE imaging was first established in the 1980s. The penetration of the

technique into mainstream imaging protocols in the last 10–15 years is primarily due to the near-continuous improvement and innovation in both MR hardware (gradient performance, RF coil sensitivity) and pulse sequence design. These advancements have culminated in the sequences we see on our scanners today: sequences that provide sufficient CNR and spatial resolution to resolve not only subendocardial infarcts, but post-ablation scars in the left atrium—achievements that would have been imponderable in the early days of ungated spin-echo LGE.

The preponderance of initial LGE studies published in the 1980s consisted of inversion-prepared spin-echo and fast (“turbo”) spin-echo sequences [1, 2, 4, 5]. Although these sequences provided the T_1 -weighting needed for delineating areas of gadolinium accumulation, the acquisition times were very long and made breath-holding impractical or impossible. Thus, respiratory artifacts degraded even the most rigorously acquired images. By the mid-to-late 1990s,

most of these spin-echo sequences had been replaced by faster gradient-echo varieties. Saturation- [13, 14, 24, 25] or inversion- preparation [26] provided the T_1 -weighting, along with short TRs and shallow flip-angle readouts. Magnetization-driven “FLASH” (fast low-angle shot) techniques that involved constant RF pulsing also came on the scene at this time [27]. These gradient-echo techniques offered several advantages, as they were sufficiently rapid to be acquired within a reasonable breath-hold, and they could be comfortably repeated, to follow the temporal evolution of contrast accumulation. In fact, the single-shot saturation-prepared fast gradient-echo sequence was used for both perfusion and LGE imaging, and could be acquired either with or without a breath-hold, depending on the post-processing anticipated for quantitative analysis.

Segmented Inversion-Recovery Spoiled Gradient Echo

Unlike perfusion imaging, where the goal is to capture the rapid transit of contrast media during its first pass through the circulation, LGE imaging is performed 10–20 min after administration, to allow for the accumulation of Gd in the extravascular/extracellular space. At this stage, we assume that the contrast has reached equilibrium concentrations in the blood and the tissue. The T_1 s are no longer changing very drastically and thus, it is no longer crucial to read out each image with high temporal resolution. Given that the goal is to obtain the optimum CNR between healthy and injured or fibrotic myocardium, most LGE imaging is now performed with segmented readout pulse sequences, such as the inversion-prepared spoiled gradient-echo sequence introduced by Simonetti et al. in 2001 [28]. This sequence represented a remarkable breakthrough in CNR, with infarct signal intensities 500–600 % greater than normal myocardium [21, 28, 29] (approximately tenfold improvement in CNR relative to T_1 -weighted spin-echo sequences, for example). In this sequence, the initial inversion is achieved using a nonselective 180° pulse, which is typically a hyperbolic secant adiabatic inversion. Slice-selective inversion sequences have also been developed, and may improve edge-detection between healthy myocardium and scar. This could be particularly advantageous for imaging small areas of fibrosis or non-transmural infarcts [30].

A pulse sequence diagram for a typical implementation of the segmented inversion recovery spoiled gradient echo LGE sequence is depicted in Fig. 15.3. Before applying the initial inversion pulse, most scanners allow the technologist to select a variable delay time so that the image readout occurs at mid-diastole, or when we presume the heart is moving the least. We can then begin reading out the first segment of k-space after the pre-determined TI delay. Shallow flip-angle

RF pulses (approximately 20 – 25°) are used during the readout of each line, so that the recovery of the post-inversion magnetization is largely unaffected and in accordance with the nominal TI. The size of the k-space segment (i.e., the number of lines of k-space) that we can read during each R-R interval will necessarily depend on the duration of diastole. In a typical implementation of the sequence [28], with a TR of 8 ms, a segment consisting of 23 lines of k-space can be acquired in 184 ms, which is within the period of mid-diastole for most patients. It is important to be cognizant that the segmented LGE sequences are more sensitive to arrhythmias and variable heart rates than their single-shot counterparts. While gradient-moment refocusing mitigates motion artefact to some extent, the duration of the mid-diastolic phase will also shorten with increasing heart rates, so the number of k-space lines acquired per R-R interval will have to be reduced to further minimize motion artifacts. The heart rate will also dictate sequence planning in terms of selecting the optimal inversion time. Unless the patient’s heart rate is very slow (e.g., <50 bpm), the sequence is triggered every other heartbeat to allow sufficient longitudinal relaxation to occur between inversion pulses. The bulk magnetization $M(t)$ will recover post-inversion according to the following: $M(t) = M_0(1 - 2e^{-t/T_1})$. Thus, if we return to our earlier example with the patient (R-R interval = 800 ms), normal myocardium with a post-contrast $T_1 = 400$ ms will require approximately $4 \times T_1 = 1,600$ ms to recover approximately 96 % of its bulk magnetization.

Phase-Sensitive Inversion-Recovery Imaging

The advent of phase-sensitive reconstruction LGE sequences in 2002 [31] has greatly improved the consistency of image quality over a wide range of TIs, particularly with respect to the CNR between infarcted and normal myocardium [32]. Recall from our earlier discussion that the longitudinal magnetization associated with infarcted or fibrotic myocardium will recover more quickly than that of normal myocardium, since its T_1 is shorter. With conventional magnitude reconstruction, if we prescribe a TI that is too short to null normal myocardium, then the normal myocardium will appear too bright and the CNR between normal and infarcted or fibrotic myocardium will be poor. Even when care is taken to isolate the optimal TI for the first slice (e.g., the first of a short-axis stack covering the LV), the continued clearance of contrast over the 5 min multi-slice acquisition will mean that the T_1 will have increased non-negligibly by the time the final slice is acquired. Phase-sensitive detection is insensitive to small drifts in T_1 , enabling the acquisition of a full complement of high CNR images without the need to interrupt the acquisition to repeat the search for optimal TI. The phase-sensitive detection aspect of this technique involves the acquisition of reference phase maps in between the collection of inversion recovery data (Fig. 15.3, gray inset). These phase images

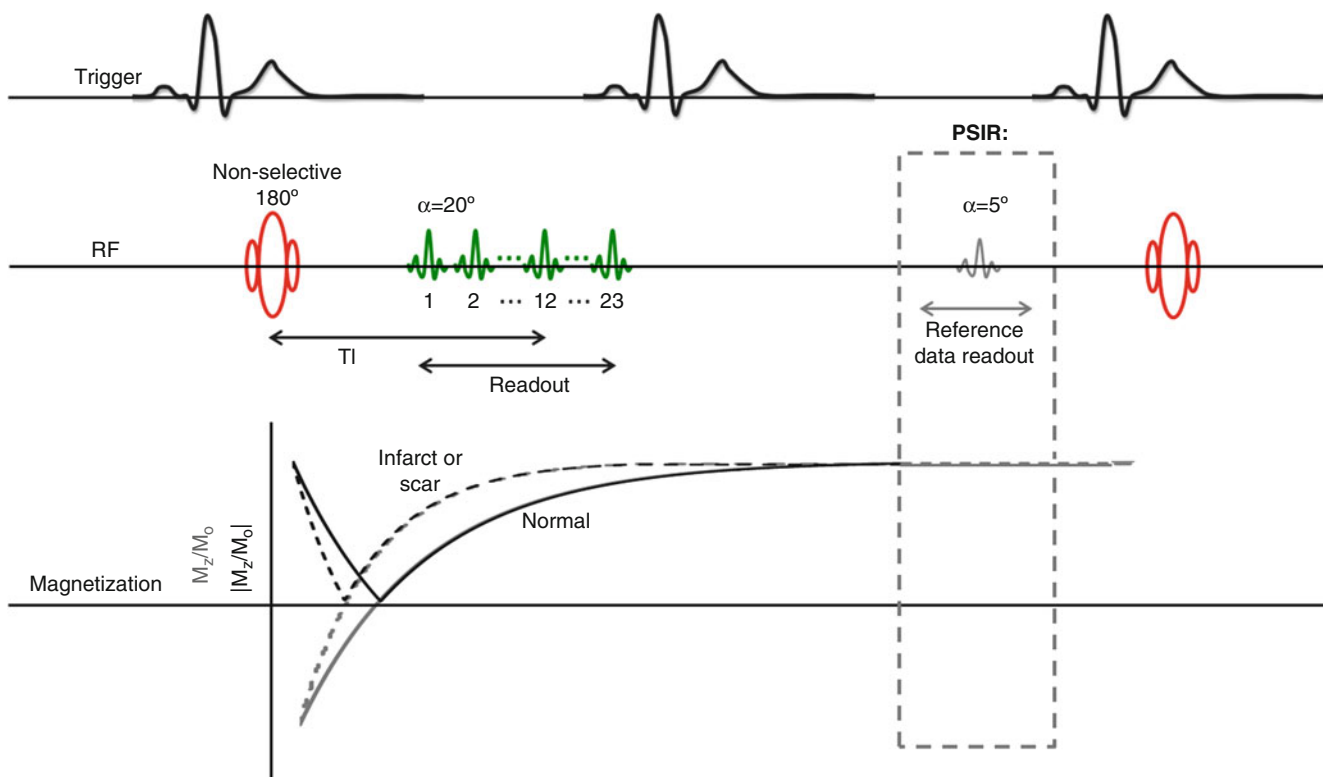


Fig. 15.3 Pulse sequence diagram and associated longitudinal magnetization for a segmented inversion-recovery spoiled gradient echo sequence. The phase-sensitive modification for this sequence is indicated in gray. In both sequences, the non-selective inversion pulse is triggered following a variable delay following detection of the R-wave so that readout occurs at mid-diastole. The first segment of k-space is acquired after the inversion delay TI using shallow flip angle pulses (20°). In this example, each segment consists of 23 lines of k-space. The subsequent segment is collected after allowing for sufficient recovery of longitudinal

magnetization, which for most cases translates to every other heartbeat. In the phase-sensitive modification of this sequence (*gray*), these quiet periods between inversion pulses are used to collect reference images using very shallow RF pulses (5°), so that longitudinal recovery is not unduly disrupted. These reference images are used to remove the background phase from the IR images during reconstruction and restore the signal polarity of the image. For phase-sensitive images, the image intensity is displayed as M_z/M_0 (*gray recovery curves*) rather than the $|M_z/M_0|$ seen in magnitude reconstructed images (*black recovery curves*)

include information regarding background phase as well as surface coil field maps. The phase can be subsequently removed from the IR image during reconstruction to reveal the real component of the inversion recovery image. By restoring the signal polarity of the image, phase-sensitive reconstruction effectively avoids the enhancement artifacts to which magnitude images are prone.

3D and Free-Breathing Techniques

All of the LGE sequences discussed thus far involve 2D imaging, or the acquisition of one 2D slice per breath-hold. Depending on the indication for LGE imaging, comprehensive coverage could potentially involve more than ten breath-holds, which can prove difficult for some patients, particularly those with advanced disease. Fortunately, many scanners are also equipped with 3D LGE sequences, in which the entire LV can be imaged in a single (albeit long) breath-hold. In most implementations, 3D LGE is accomplished using a segmented inversion-recovery gradient echo sequence with shallow flip-angle readout (e.g., 15° rather than the 25°

typical of most 2D acquisitions). In 3D LGE, the inversion pulse is triggered every heartbeat (instead of every second heartbeat), which can potentially degrade CNR due to incomplete magnetization recovery. Approximately 20 contiguous sections are acquired in the z direction, often with the aid of zero-filling and interpolation to maximize spatial resolution in this direction [33]. If the breath-hold required to cover the LV is potentially too long, the LV can be covered in a quasi-3D fashion by dividing the acquisition into three “slabs,” with a commensurate number of manageable breath-holds [34]. While the strategy for finding the optimal TI should be the same as described for 2D LGE, the advantage is that this TI need only be selected once. The correct TI is particularly crucial for 3D imaging, as there is no opportunity to utilize alternate R-R intervals for acquiring reference images for phase-sensitive reconstruction. Additionally, the need to trigger every heartbeat results in greater sensitivity to arrhythmias. Optimization of 3D acquisitions is a subject of considerable ongoing research. While breath-hold 3D slab acquisitions are promising, they may still present difficulties

for some patients. In 2004, Saranathan and colleagues presented a free-breathing 3D LGE alternative, in which a navigator-echo segment is acquired immediately following the gradient echo acquisition [35]. The navigator echo segment is essentially a spin echo sequence that selects a column of spins craniocaudally across the right hemidiaphragm [36]. When combined with their hybrid k-space segmentation scheme, the free-breathing sequence proposed by Saranathan et al. was capable of acquiring 16×5 mm thick sections in less than 2 min.

Common Clinical Applications

LGE has become an undeniably powerful tool for the assessment of many clinical cardiac entities. While much of the early development of LGE imaging was centered on the assessment of post-infarction scar, the technique has become increasingly valuable in the characterization of a wide variety of cardiomyopathies as well as in the rule-out of infectious or infiltrative disease. This section is far from an exhaustive accounting of the myriad applications of LGE imaging. Rather, the intention of the following discussion is to illustrate how the technique has been adapted to address a variety of clinical and research questions.

Acute and Chronic Myocardial Infarction

In many ways, the assessment of myocardial viability and infarct scar was the driving force behind the initial development of LGE imaging. Before the advent of the high CNR segmented inversion-recovery gradient echo techniques, most studies were limited to pre-clinical research in rats [37–42] and dogs [43–47] and small “proof of principle” clinical series [16, 17, 19, 21, 26, 29, 48–52]. The veritable explosion of reports involving LGE imaging in the last decade belies the fact that we owe a great deal of its current appeal to the fundamental basic science and development that preceded this recent popularity.

Many of the early contributions to the development of the technique were focused on establishing the kinetics of MR contrast in ischemic and infarcted myocardium. Specifically, there was a great deal of debate regarding the distribution of Gd-DTPA in areas of reversibly injured myocardium [41, 53]. In a rat model of reperfused infarction, Saeed and colleagues found that Gd-DTPA enhanced regions were 33 % larger than the extent of infarcts identified by triphenyltetrazolium chloride (TTC) staining at day 2 post-reperfusion [40], suggesting that reversibly injured myocardium might also accumulate Gd-DTPA. However, similar studies in canine models such as the one reported by Fieno and colleagues, found excellent agreement between both *in vivo* and

ex vivo gadolinium enhanced images and TTC staining ($r=0.95$) [47], which supports the notion that myocardial hyperenhancement is specific to irreversible injury (infarction). Establishing the “bright equals dead” principle was a key step, as the management of patients with coronary artery disease (CAD) post-infarction is complicated by the presence of both reversibly damaged and infarcted myocardium. The success of revascularization depends on both the existence and extent of viable but dysfunctional myocardium present, as there are few benefits from revascularizing a territory devoid of viable myocardium. Infarction follows a characteristic path or “wavefront” in the myocardium, beginning in subendocardial tissue and progressing towards the subepicardium. Nuclear medicine methods that are often used for assessing myocardial perfusion (e.g., PET, Tl-201, Tc-99m-sestamibi SPECT) lack the ability to resolve transmural variations in viability. LGE CMR, however can identify subendocardial infarcts that would be otherwise missed by Tc-99m-sestamibi SPECT, for example [20]. Choi et al. investigated the relationship between the transmural extent of LGE hyperenhancement and long-term functional improvement in AMI patients at 1 week and 8–12 weeks following reperfused-infarction [18]. In this important work, the authors showed that the extent of the dysfunctional but normally enhancing region at 1 week post-reperfusion was the single best predictor of functional recovery 8–12 weeks post-reperfusion.

In acutely infarcted myocardium, cell membranes lose their integrity and the Gd-DTPA suddenly gains access to what was formerly intracellular space and shortens T_1 to a much greater extent than if the agent was in contact with extracellular space alone. In contradistinction, there does not appear to be an increase in the distribution volume of Gd-DTPA in reversibly dysfunctional myocardium (i.e., “stunned” or “hibernating” myocardium). The ultrastructural changes typical of hibernating myocardial cells include a progressive loss of contractile proteins, which are predominantly replaced by glycogen within the cytoplasm. However, there is no appreciable decrease in cell volume and therefore no evidence of increased gadolinium distribution in hibernating myocardium [51, 54]. Similarly, there does not appear to be any hyperenhancement associated with transiently dysfunctional or “stunned” myocardium [55, 56], which has been confirmed by high-resolution Gd-enhanced imaging of *ex-vivo* specimens.

Although we conceptualize LGE imaging as “viability” or “scar” imaging, there are certainly settings where perfusion has an outsized influence on late enhancement patterns. One such scenario is in unreperfused infarction, where microvascular damage can severely impede contrast wash-in to the myocardium. On LGE images, microvascular obstruction can manifest as a persistent core of hypoenhancement surrounded by hyperenhancement. Interestingly, this core appears to

involute as the infarct heals, regardless of reperfusion status. As the initial inflammation begins to subside and macrophages have left with their cargo of necrotic debris, type I collagen is deposited into the infarcted region. By this point, there should be no residual capillary plugging interfering with Gd-DTPA distribution [57]. Infarct remodelling involves organization of the collagenous scar, with a concomitant loss of myocytes. The net result is a predominantly acellular area, and one that an extravascular/extracellular agent such as Gd-DTPA can occupy in observable volumes (Fig. 15.1d) [58]. Additionally, the potential recruitment of collateral circulation should not be neglected, as it may partially contribute to Gd-DTPA distribution as the infarct matures. Wu et al. demonstrated that LGE hyperenhancement was present in both Q wave and non-Q wave infarcts at 3 months and 14 months following acute myocardial infarction (AMI), and yet none of the patients in the comparison group with idiopathic dilated cardiomyopathy (DCM) exhibited hyperenhancement [21]. This was consistent with the findings reported by Klein et al. in a group of patients with chronic CAD and severely reduced LV function. Klein and colleagues demonstrated that LGE can delineate the location and extent of nonviable myocardium, in close agreement with NH_3 /FDG PET measurements of perfusion and glucose metabolism [51]. In fact, the authors demonstrated that the sensitivity and specificity of hyperenhancement for detecting either transmural or non-transmural scar tissue (as defined by NH_3 /FDG PET mismatch) were 83 % and 88 %, respectively.

Ischemic Cardiomyopathy

The term ischemic cardiomyopathy is often used by clinicians to describe chronic ischemic heart disease, such as that experienced by patients with post-infarction remodelling and LV dysfunction. As with post-infarct LGE, the hyperenhancement associated with “ischemic type” cardiomyopathy has three main characteristics: it always involves the subendocardial layer, it is localized in the territories supplied by the epicardial coronary arteries, and it is consistent with regional wall motion abnormalities (Fig. 15.4). Furthermore, ischemic cardiomyopathy is inconsistent with hyperenhancement located exclusively in the subepicardium or mid-myocardium [59].

When a patient initially presents with LV dysfunction, one of the first objectives is to determine whether the dysfunction arises from an ischemic etiology and if so, the next most important objective is to assess if the myocardium is viable. In a meta-analysis, Allman et al. showed that revascularization may reduce annual mortality in up to 80 % of patients with LV dysfunction and viable myocardium when compared to medical treatment [60]. Kim et al. [29] showed that segments demonstrating ≤ 50 % of transmural extent of hyperenhancement are likely to recover function after revascularization.

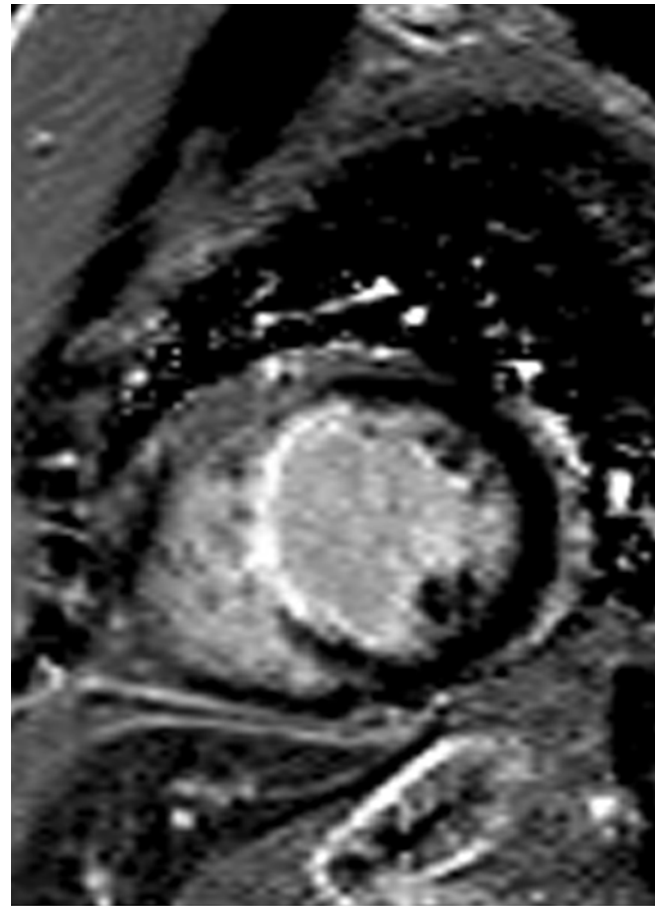


Fig. 15.4 70-year-old woman who presented with dilated cardiomyopathy and an ejection fraction of 35 %. Coronary angiography demonstrated 100 % stenosis in the mid left anterior descending coronary artery. Cardiac MR was performed to assess myocardial viability. Late gadolinium enhancement phase sensitive inversion recovery image in short axis view demonstrates transmural extent of enhancement in the mid septal wall in a left anterior descending artery territory diagnostic of a prior myocardial infarction

Non-ischemic Cardiomyopathies

To increase the likelihood of clinical improvement in patients with cardiomyopathy, proper determination of the etiology is essential as it then guides proper management. While the cause of non-ischemic cardiomyopathies (NICM) can theoretically be confirmed via endomyocardial biopsy, in practice this invasive approach offers limited sensitivity, particularly for conditions in which myocardial fibrosis or infiltrate may be sparse or heterogeneous in distribution [61]. LGE CMR is not only a key tool for differentiating between ischemic and NICM, it is also crucial for differential diagnosis, since several cardiomyopathies have been associated with their own “signature” enhancement patterns. Ultimately, these patterns that are summarized in the following section may also be used to guide endomyocardial biopsy, helping secure a histopathological diagnosis.

Dilated Cardiomyopathy

After a thorough medical history, including family history, and examination with laboratory testing have been conducted, CMR is often considered as an essential part of the diagnostic evaluation for patients with DCM of unknown cause. While echocardiography and CMR both demonstrate ventricular enlargement and decreased systolic function as measured by ejection fraction, McCrohon et al. [62] showed that the midwall enhancement pattern by LGE-CMR typified non-ischemic DCM. Figure 15.5 demonstrates an example of a patient with new onset heart failure and this characteristic enhancement pattern. Of note, 13 % of DCM patients in this cohort previously labeled as nonischemic DCM based on nonobstructive coronary arteries at by invasive angiography actually had subendocardial infarct scar. This suggested a prior myocardial infarction with recanalization or dispersion of an embolic source, with cardiac enlargement and systolic function ensuing as a result of post-infarct adverse remodeling. Midwall enhancement has been identified as an adverse prognostic finding, predicting events such as sudden cardiac death and heart failure with incremental value beyond ejection fraction [63].

Hypertrophic Cardiomyopathy

HCM, typically due to mutations in genes encoding for sarcomeric proteins, is characterized by a cardiac phenotype with myocardial disarray, hypertrophy and fibrosis. Early diagnosis of HCM is crucial, as it remains both the most common cause of SCD among young people [64] and a not infrequent cause of heart failure. Given the varied clinical and phenotypic manifestations of the disease, HCM can pose a considerable diagnostic challenge [65]. Non-invasive markers for focal myocardial fibrosis can potentially track progression to heart failure in patients with HCM and help characterize the risk of SCD. Positive LGE occurs in up to 80 % of patients with HCM [66–68] and represents replacement myocardial fibrosis histologically [29, 69]. The typical LGE pattern in HCM is patchy and in a non-coronary distribution, most commonly associated to the regions of hypertrophy such as the insertion points of the interventricular septum in the classic asymmetric septal hypertrophy phenotype [67, 70–72]. Its presence is an independent predictor of adverse outcomes in HCM [72–76]. An example of the pattern of scarring typically observed in HCM is provided in Fig. 15.6.

Arrhythmogenic Right Ventricular Cardiomyopathy

ARVC is a progressive cardiomyopathy due to fibrofatty replacement of normal myocytes that is associated with right heart failure and SCD. Like HCM, accurate diagnosis of ARVC is important for the prevention of SCD [77, 78]. ARVC is particularly difficult to diagnose, as several of the

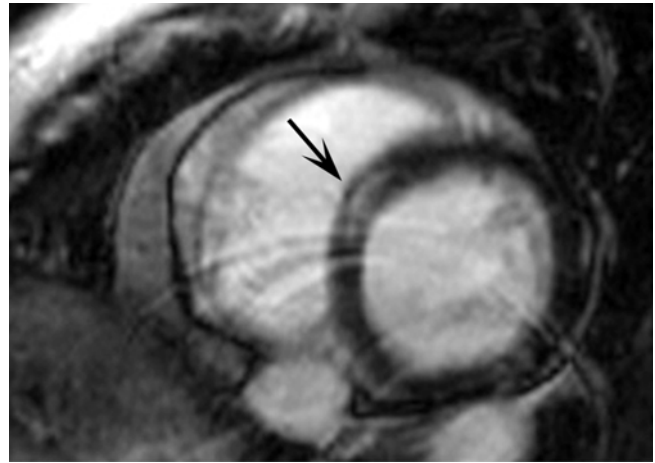


Fig. 15.5 Dilated cardiomyopathy in a 54-year-old man who presented with heart failure. Late gadolinium enhancement magnitude inversion recovery image in a short axis plane demonstrates a characteristic linear mid-myocardial hyperenhancement in the basal septum (*arrow*)

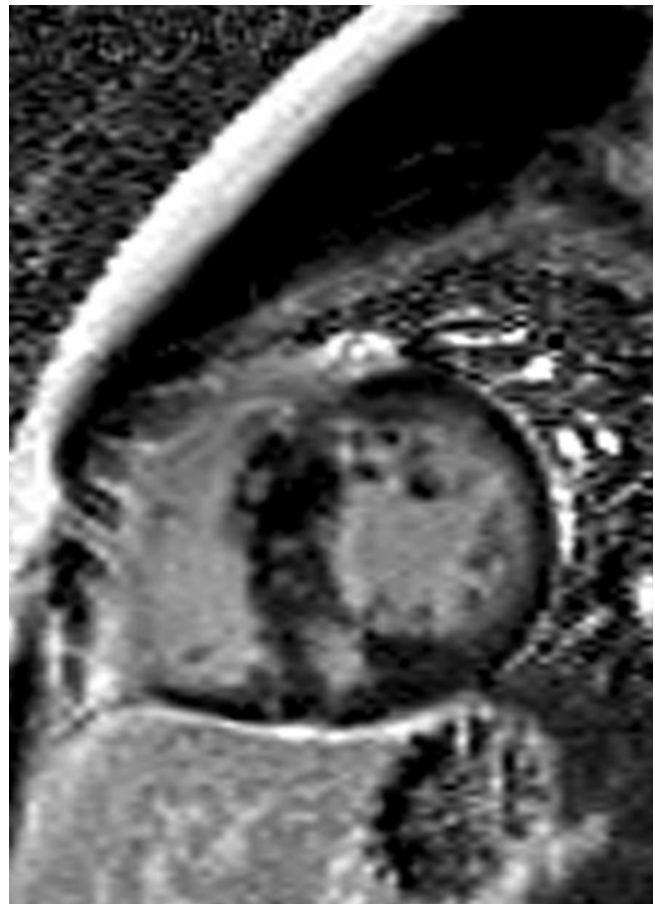


Fig. 15.6 Hypertrophic cardiomyopathy in a 18-year-old man presenting with multiple syncopal episodes. Late gadolinium enhancement phase sensitive inversion recovery image in a short axis plane demonstrates patchy, mid-myocardial enhancement matching the regions of hypertrophy in the septum

presentations of ARVC can mimic that of cardiac sarcoidosis (CS). Furthermore, biopsy for the diagnosis of CS or ARVC is frequently inaccessible owing to the random and patchy distribution of fibrofatty infiltration along the RV septum. It is important to mention that abnormal LGE is not included in the new Task Force Criteria for the diagnosis of ARVC [79], which are based on the presence of increased RV size, decreased RV EF, and RV wall motion abnormalities. Nevertheless, Steckman and colleagues recently reported that LGE hyperenhancement was seen in 73 % of CS and 19 % of ARVC patients, with isolated LV involvement seen only in the CS group [80]. Forty-three percent of the CS group and none of the ARVC group demonstrated intraventricular septum dysfunction or hyperenhancement of the septum. Septal enhancement was observed in 78 % of those with CS and 0 % of those with ARVC. Given the overlap in clinical presentation and high false-negative rate of endomyocardial biopsy, a tool for the accurate differentiation of these conditions is needed.

Cardiac Sarcoidosis

Sarcoidosis is a granulomatous disease affecting multiple systems. It is estimated that 5 % of patients with pulmonary/systemic sarcoidosis also have symptomatic CS [81], which is belied by the higher prevalence observed in necropsy studies [82, 83]. Missing the diagnosis of CS can lead to increased mortality due to SCD or heart failure. LGE MRI findings have been documented in both acute and chronic stages, but enhancement patterns can vary widely [84–87]. While hyperenhancement in CS is often localized to the epicardial zone of the septum, the fibrosis can appear either focal, patchy, or even extend to fully transmural hyperenhancement [87], as observed in the example provided in Fig. 15.7. Also LGE characteristically involves the basal anteroseptal and anterolateral segments of the LV [84]. Early evaluations of LGE in the setting of CS suggested that its sensitivity was significantly inferior to PET [88]. More recent analyses demonstrate that LGE may detect CS at a twofold higher rate than conventional Japanese Ministry of Health criteria (12-lead ECG and either echo, radionuclide perfusion, or cath imaging) [87]. Patel and colleagues [87] found that LGE detected CS in 26 % of patients with biopsy-proven extracardiac sarcoidosis, compared to 12.3 % identified using Japanese Ministry of Health criteria. Furthermore, the authors showed that positive LGE findings were the only independent predictor of adverse clinical events.

Myocarditis

The clinical presentation of myocarditis may mimic acute myocardial infarction in patients with normal coronary arteries on angiogram [89]. Although endomyocardial



Fig. 15.7 48-year-old woman presenting with heart block. Late gadolinium enhancement phase sensitive inversion recovery image in a short axis view demonstrates transmural enhancement in the basal septal and anteroseptal walls (*arrow*) characteristic of cardiac sarcoidosis

biopsy is the standard of reference for the differentiation between these two entities, LGE plays an important role in non-invasively distinguishing both entities [90]. Friedrich and colleagues were among the first to report myocardial enhancement patterns in patients with acute myocarditis [91]. Using a non-breath-hold T_1 -weighted spin-echo pulse sequence, the authors demonstrated 40–50 % greater hyperenhancement in patients with myocarditis, suggesting that LGE even with the low CNR pulse-sequence could identify areas of inflammation. This discrepancy in enhancement was exaggerated to 400 % above normal myocardium when the segmented IR-prepared fast GRE approach was applied to 32 patients with suspected myocarditis [90].

In addition to colocalizing regions of hyperenhancement with histopathologically-confirmed areas of active myocarditis, Marholdt and colleagues observed a distinct geographic pattern from ischemic LGE enhancement, affecting the epicardial quartile of the LV or midwall region [90]. An example of this characteristic enhancement

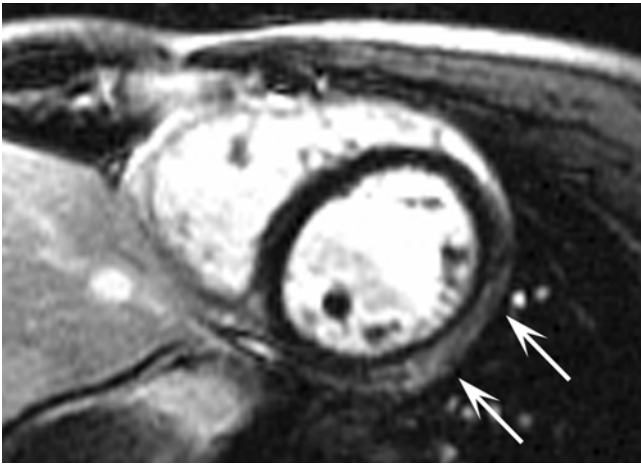


Fig. 15.8 Myocarditis in a 16-year-old male who presented with chest pain and ST elevation on the ECG. Late gadolinium enhancement magnitude inversion recovery image in a short axis view demonstrates subepicardial enhancement in the mid lateral wall (*arrows*) indicative of myocarditis. Note that the subendocardium is nulled, excluding an ischemic cause

pattern is provided in Fig. 15.8. They suggested that the mechanism for LGE during the acute phase of myocarditis is myocardial necrosis, whereas in the more chronic phase, LGE likely represents fibrosis [90]. The areas of LGE may decrease during recovery of myocarditis and can nearly resolve after recovery.

Amyloidosis

Cardiac amyloidosis (CA) is characterized by the interstitial deposition of insoluble amyloid proteins. It presents as a restrictive cardiomyopathy and it is one of the differential diagnoses when assessing patients with diastolic heart failure and myocardial hypertrophy [92]. The gold standard for diagnosing CA is endomyocardial biopsy, but this technique is invasive and has associated risks [93]. A characteristic LGE “amyloid pattern” has been described as diffusely distributed over the entire subendocardial circumference, extending in various degrees into the neighboring myocardium and coupled with a dark black blood pool [94–96]. This distinct pattern of enhancement (Fig. 15.9) is present in approximately 80 % of patients with CA [94, 95, 97] and has shown a sensitivity of 80 % and specificity of 94 % for the diagnosis of CA compared to endomyocardial biopsy [95].

In practice, it can be difficult to establish the appropriate TI for nulling normal myocardium in patients with CA [94], even with the benefit of a TI scout. Maceira et al. reported that blood pool gadolinium clearance was faster than normal in CA patients and that the areas with amyloid deposition demonstrate T_1 s either shorter than or equivalent to those sampled in the blood pool [94]. Additionally, the contrast between normal myocardium and areas of

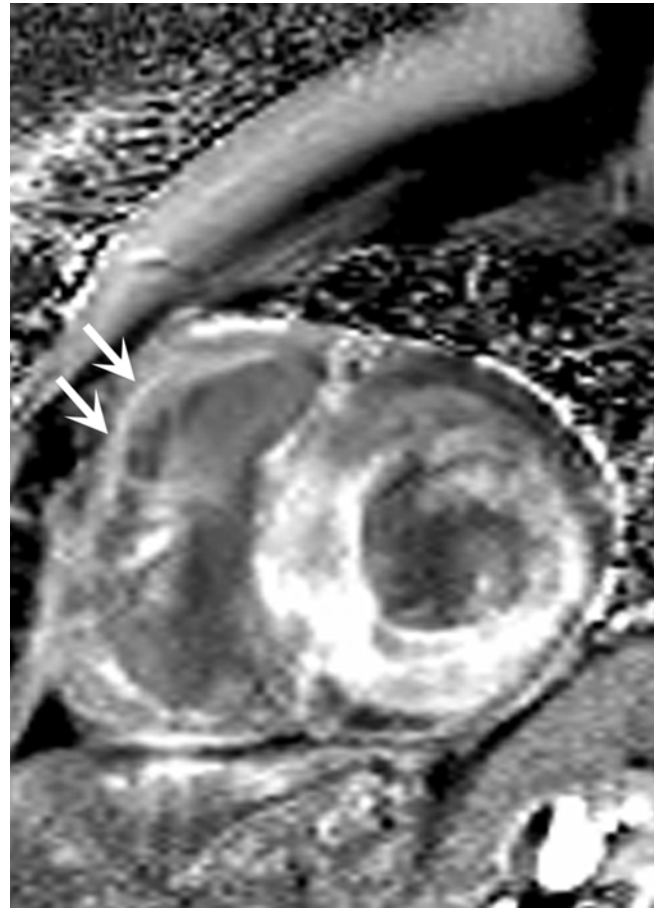


Fig. 15.9 75-year-old man presenting with unexplained severe left ventricular hypertrophy, chronic heart failure and atrial fibrillation. Cardiac MR was performed to exclude an infiltrative cardiomyopathy. Late gadolinium enhancement phase sensitive inversion recovery image in a short axis plane demonstrates diffuse subendocardial enhancement in the left ventricle with a variable extent to the adjacent myocardium. There is also subendocardial enhancement present in the right ventricle (*arrows*). Note that the blood pool shows a characteristic dark appearance commonly observed in cardiac amyloidosis

amyloid deposition becomes markedly reduced approximately 8 min after contrast administration. Thus, LGE images in patients with cardiac amyloidosis are ideally acquired between 5 and 8 min post-injection when the contrast between normal and abnormal myocardium, compared to the typical delay of 10–15 min [94]. Multiple theories have been proposed to explain the contrast kinetics idiosyncratic to CA, the foremost of which is that the marked expansion of the extracellular space is due to accumulation of the interstitial amyloid protein [94, 96, 97], rather than diffuse fibrosis, but this is an active area of investigation. Contemporary quantitative T_1 mapping techniques, covered elsewhere, have greatly reduced uncertainty in the interpretation of LGE images in cardiac amyloidosis.

Other Indications

Cardiac and Pericardial Masses

Evaluation of a cardiac mass is a common indication for cardiac MRI. Although the use of LGE in the evaluation of cardiac masses is beyond the scope of this chapter, we will review its use in the assessment of thrombus since it is the most common cardiac mass. Thrombus is a differential diagnosis for cardiac tumors, and is typically identified in the LV as a result of dysfunction and impaired wall motion following myocardial infarction. LGE imaging can be a helpful technique for differentiating thrombi from masses, since thrombus is avascular and thus, will appear as a mass of low signal intensity on LGE images. It is not uncommon for thrombi to appear as hypoenhanced masses adjacent to areas of hyperenhanced myocardial infarction [98], as shown in Fig. 15.10. The use of LGE imaging with a long TI to null avascular tissue (600 ms) is a strategy to characterize thrombus [99].

Left Atrial Remodeling and Scar

Perhaps one of the most exciting developments in recent years has been application of LGE to the assessment of left atrial remodeling and scar. The left atrium (LA) has long been considered “uncharted territory” in CMR, given its thin walls and potential interference from neighboring fat. The advent of free-breathing 3D LGE schemes enabled researchers to begin exploring LGE as a tool for evaluating LA fibrosis. Peters et al. adapted the sequence proposed by Saranathan and colleagues [35] for evaluating post-ablation LA scar in patients with atrial fibrillation (AF) [100]. By combining the navigator-gated 3D LGE sequence with strategic fat saturation, the authors achieved a voxel size of $1.3 \times 1.3 \times 5$ mm (reconstructed to $0.6 \times 0.6 \times 2.5$ mm), sufficient to visualize focal hyperenhancement caused by pulmonary vein radiofrequency ablation. Oakes and colleagues evaluated a very similar sequence in patients with AF, but performed imaging prior to ablation in order to assess the potential of 3D LGE to predict procedural outcomes [101]. In addition to finding a significant positive correlation between areas of LA fibrosis on LGE and low-voltage regions on electroanatomic maps ($R^2=0.61$, $P<0.05$), the authors indicated that there was a strong association between pre-ablation hyperenhancement and post-procedural recurrence of AF. Specifically, patients who experienced post-procedural AF exhibited hyperenhancement throughout the LA. In contradistinction, the hyperenhancement observed among treatment responders appeared to be restricted to the posterior wall and septum. This important work suggests that 3D LGE shows potential to guide clinicians in predicting who will benefit from catheter ablation of AF.



Fig. 15.10 Anterior myocardial infarction in a 30-year-old man who presented with chest pain, troponin elevation, and echocardiographic abnormalities after receiving a hematopoietic stem cell transplant. Late gadolinium enhancement magnitude inversion recovery image in a four-chamber view demonstrates subendocardial enhancement in the left anterior descending coronary artery territory of distribution (*short arrows*). The mass in the left ventricle does not demonstrate enhancement, indicating an associated intraventricular thrombus (*long arrow*). The combination of a non-enhancing mass adjacent to an area of infarcted myocardium is highly suggestive of a thrombus

Image Interpretation and Quantification

As we have seen, LGE imaging has undergone tremendous technical evolution since its introduction in the early days of cardiac MRI. In view of this pedigree, it is somewhat surprising that there is no consensus about quantification of these images. Many radiologists and cardiologists continue to rely on subjective visual assessment or semi-quantitative techniques for routine interpretation of LGE images. Borrowing the 17 segment AHA model familiar to cardiologists, some clinicians report the extent of hyperenhancement in terms of the approximate area per AHA segment (e.g., 0–25 %, 25–50 %, etc.) [29]. If dedicated post-processing software is available, it is often possible for the analyst to select a reference area of “normal” (ideally nulled) myocardium, such

that all pixels in excess of a pre-defined number of standard deviations of that reference become defined as “hyperenhanced.” Society for Cardiovascular Magnetic Resonance guidelines [102] recommend defining “hyperenhancement” as any myocardial pixel exceeding the mean signal intensity of normal myocardium by more than two standard deviations (SDs), but many programs allow flexible selection of between 2 and 6 SDs. Others have advocated for a “full width at half maximum” (FWHM) technique, in which the scar is selected by the analyst and the threshold for hyperenhancement becomes the value of the 50 % maximum signal intensity within the scar [103]. Flett et al. compared the LGE volumes obtained using seven distinct quantification techniques (manual segmentation, FWHM, or thresholds equal to 2, 3, 4, 5 or 6 SD above normal myocardium) in patients with AMI, chronic MI (CMI), and HCM [104]. The authors discovered that the LGE volumes defined by each of the methods varied substantially, and the most reproducible techniques appeared to depend on the clinical entity under investigation (e.g. AMI, CMI, or HCM). Specifically, the 2-SD threshold resulted in infarct volumes as high as 100 % greater than either the FWHM, 6-SD or manual approaches. The effect of threshold was most apparent in the HCM patients, where hyperenhanced volumes varied from 11 to 29 %. For both infarct-size estimates and HCM fibrosis quantification, the authors recommended either the 6-SD or FWHM thresholds. The limitation of the FWHM approach is that it assumes that maximum hyperenhancement will be localized to the lesion core, which can be problematic in the case of heterogeneous or “patchy” enhancement.

Conclusion

Over the last 30 years, LGE imaging has evolved from a relatively esoteric research interest to an indispensable component of most clinical CMR examinations. While the sequence and implementation may differ depending on availability and indication, a firm understanding of the principles underpinning LGE will assist in providing important diagnostic and prognostic information relevant for patient care.

References

1. Ratner AV, Okada RD, Newell JB, Pohos GM. The relationship between proton nuclear magnetic resonance relaxation parameters and myocardial perfusion with acute coronary arterial occlusion and reperfusion. *Circulation*. 1985;71(4):823–8.
2. Wesbey G, Higgins CB, Lanzer P, Botvinick E, Lipton MJ. Imaging and characterization of acute myocardial infarction in vivo by gated nuclear magnetic resonance. *Circulation*. 1984;69:125–30.
3. McNamara MT, Higgins CB, Ehman RL, Revel D, Sievers R, Brasch RC. Acute myocardial ischemia: magnetic resonance contrast enhancement with gadolinium-DTPA. *Radiology*. 1984;153:157–63.
4. Johnston DL, Brady TJ, Ratner AV, Rosen BR, Newell JB, Pohost GM, Okada RD. Assessment of myocardial ischemia with proton magnetic resonance: effects of a three hour coronary occlusion with and without reperfusion. *Circulation*. 1985;71(3):595–601.
5. Pflugfelder PW, Wisenberg G, Prato FS, Carroll SE, Turner KL. Early detection of canine myocardial infarction by magnetic resonance imaging in vivo. *Circulation*. 1985;71(3):587–94.
6. Bouchard A, Reeves RC, Cranney G, Bishop SP, Pohost GM. Assessment of myocardial infarct size by means of T₂-weighted 1H nuclear magnetic resonance imaging. *Am Heart J*. 1989;117:281–9.
7. Ryan T, Tarver RD, Duerk JL, Sawada SG, Hollenkamp NC. Distinguishing viable from infarcted myocardium after experimental ischemia and reperfusion by using nuclear magnetic resonance imaging. *J Am Coll Cardiol*. 1990;15:1355–64.
8. Wesbey G, Weinmann HJ, Brasch RC, Press WR. Characteristics of gadolinium-DTPA complex: a potential NMR contrast agent. *AJR Am J Roentgenol*. 1984;142:619–24.
9. Prato FS, Wisenberg G, Marshall TP, Uksik P, Zabel P. Comparison of the biodistribution of gadolinium-153 DTPA and technetium-99m DTPA in rats. *J Nucl Med*. 1988;29:1683–7.
10. Judd JR, Kim RJ, Chen EL, Lima JA. Myocardial Gd-DTPA kinetics determine MRI contrast enhancement and reflect the extent and severity of myocardial injury after acute reperfused infarction. *Circulation*. 1996;94(12):3318–26.
11. Diesbourg LD, Prato FS, Wisenberg G, Drost DJ, Marshall TP, Carroll SE, O’Neill B. Quantification of myocardial blood flow and extracellular volumes using a bolus injection of Gd-DTPA: kinetic modeling in canine ischemic disease. *Magn Reson Med*. 1992;23(2):239–53.
12. Tong CY, Prato FS, Wisenberg G, Lee TY, Carroll E, Sandler D, Wills J. Techniques for the measurement of the local myocardial extraction efficiency for inert diffusible contrast agents such as gadopentate dimeglumine. *Magn Reson Med*. 1993;30(14):332–6.
13. Pereira RS, Prato FS, Sykes J, Wisenberg G. Assessment of myocardial viability using MRI during a constant infusion of Gd-DTPA: further studies at early and late periods of reperfusion. *Magn Reson Med*. 1999;42(1):60–8.
14. Pereira RS, Prato FS, Wisenberg G, Sykes J. The determination of myocardial viability using Gd-DTPA in a canine model of acute myocardial ischemia and reperfusion. *Magn Reson Med*. 1996;36:684–93.
15. Pereira RS, Prato FS, Lekx KS, Sykes J, Wisenberg G. Contrast-enhanced MRI for the assessment of myocardial viability after permanent coronary artery occlusion. *Magn Reson Med*. 2000;44(2):309–16.
16. Pereira RS, Wisenberg G, Prato FS, Yvorchuk K. Clinical assessment of myocardial viability using MRI during a constant infusion of Gd-DTPA. *MAGMA*. 2000;11(3):104–13.
17. Flacke SJ, Fischer SE, Lorenz CH. Measurement of the gadopentetate dimeglumine partition coefficient in human myocardium in vivo: normal distribution and elevation in acute and chronic infarction. *Radiology*. 2001;218:703–10.
18. Choi KM, Kim RJ, Gubernikoff G, Vargas JD, Parker M, Judd RM. Transmural extent of acute myocardial infarction predicts long-term improvement in contractile function. *Circulation*. 2001;104:1101–7.
19. Ricciardi MJ, Wu E, Davidson CJ, Choi KM, Klocke FJ, Bonow RO, Judd RM, Kim RJ. Visualization of discrete microinfarction after percutaneous coronary intervention associated with mild creatine kinase-MB elevation. *Circulation*. 2001;103(23):2780–3.
20. Wagner A, Mahrholdt H, Holly TA, Elliott MD, Regenfus M, Parker M, Klocke FJ, Bonow RO, Kim RJ, Judd RM. Contrast-enhanced MRI and routine single photon emission computed tomography (SPECT) perfusion imaging for detection of suben-

- docardial myocardial infarcts: an imaging study. *Lancet*. 2003;361(9355):374–9.
21. Wu E, Judd RM, Vargas JD, Klocke FJ, Bonow RO, Kim RJ. Visualisation of presence, location, and transmural extent of healed Q-wave and non-Q-wave myocardial infarction. *Lancet*. 2001;357(9249):21–8.
 22. Kim RJ, Shah DJ, Judd RM. How we perform delayed enhancement imaging. *J Cardiovasc Magn Reson Off J Soc Cardiovasc Magn Reson*. 2003;5:505–14.
 23. Simonetti O, Chung YC, Lee VS, Laub G. Inversion recovery cine trueFISP for optimizing TI in myocardial infarct imaging. *Proc Intl Soc Mag Reson Med*. 2002;10:2019.
 24. Tong CY, Prato FS, Wisenberg G, Lee TY, Carroll E, Sandler D, Wills J, Drost D. Measurement of the extraction efficiency and distribution volume for Gd-DTPA in normal and diseased canine myocardium. *Magn Reson Med*. 1993;30(3):337–46.
 25. Kim RJ, Fieno DS, Parrish TB, Harris K, Chen E, Simonetti O, Bundy J, Finn JP, Klocke FJ, Judd RM. Relationship of MRI delayed contrast enhancement to irreversible injury, infarct age, and contractile function. *Circulation*. 1999;100:1992–2002.
 26. Rogers WJ, Kramer CM, Geskin G, Hu YL, Theobald TM, Vido DA, Petruolo S, Reichek N. Early contrast-enhanced MRI predicts late functional recovery after reperfused myocardial infarction. *Circulation*. 1999;99(6):744–50.
 27. Judd RM, Reeder SB, Atalar E, McVeigh ER, Zerhouni EA. A magnetization-driven gradient echo pulse sequence for the study of myocardial perfusion. *Magn Reson Med*. 1995;34:276–82.
 28. Simonetti OP, Kim RJ, Fieno DS, Hillenbrand HB, Wu E, Bundy JM, Finn JP, Judd RM. An improved MR imaging technique for the visualization of myocardial infarction. *Radiology*. 2001;218(9):215–23.
 29. Judd R, Kim RJ, Wu E, Rafael A, Chen EL, Parker MA, Simonetti O, Klocke FJ, Bonow RO. The use of contrast-enhanced magnetic resonance imaging to identify reversible myocardial dysfunction. *N Engl J Med*. 2000;343(20):1445–53.
 30. Kim D, Lee VS, Srichai MB. Improved visualization of non-transmural scar using slice-selective inversion-recovery delayed contrast-enhanced MRI: a preliminary report. *NMR Biomed*. 2007;20:121–7.
 31. Kellman P, Arai AE, McVeigh ER, Aletras AH. Phase-sensitive inversion recovery for detecting myocardial infarction using gadolinium-delayed hyperenhancement. *Magn Reson Med*. 2002;47:372–83.
 32. Huber AM, Schoenberg SO, Hayes C, Spannagl B, Engelmann MG, Franz WM, Reiser MF. Phase-sensitive inversion-recovery MR imaging in the detection of myocardial infarction. *Radiology*. 2005;237:854–60.
 33. Kühl HP, Papavasiliu TS, Beek AM, Hofman MBM, Heusen NS, van Rossum AC. Myocardial viability: rapid assessment with delayed contrast-enhanced MR imaging with three-dimensional inversion-recovery prepared pulse sequence. *Radiology*. 2004;230(2):576–82.
 34. Bauner KU, Muehling O, Theisen D, Hayes C, Wintersperger BJ, Reiser MF, Huber AM. Assessment of myocardial viability with 3D MRI at 3 T. *AJR Am J Roentgenol*. 2009;192(6):1645–50.
 35. Saranathan M, Rochitte CE, Foo TKF. Fast, three-dimensional free-breathing MR imaging of myocardial infarction: a feasibility study. *Magn Reson Med*. 2004;51(5):1055–60.
 36. Ehman RL, Felmlee JP. Adaptive technique for high-definition MR imaging of moving structures. *Radiology*. 1989;173:255–63.
 37. Wendland M, Arheden H, Saeed M, Higgins CB, Gao DW, Bremerich J, Wyttenbach R, Dae MW. Measurement of the gadopentetate dimeglumine at echo-planar MR imaging to quantify myocardial infarction: comparison with 99m Tc-DTPA autoradiography in rats. *Radiology*. 1999;211:698–708.
 38. Wendland M, Arheden H, Saeed M, Higgins CB, Gao DW, Ursell PC, Bremerich J, Wyttenbach R, Dae MW. Reperfused rat myocardium subjected to various durations of ischemia: estimation of the distribution volume of contrast material with echo-planar MR imaging. *Radiology*. 2000;215:520–8.
 39. Wendland MF, Saeed M, Lauerma K, Derugin N, Mintorovitch J, Cavagna FM, Higgins CB. Alterations in T₁ of normal and reperfused infarcted myocardium after Gd-BOPTA versus Gd-DTPA on inversion recovery EPI. *Magn Reson Med*. 1997;37:448–56.
 40. Higgins C, Saeed M, Lund G, Wendland MF, Bremerich J, Weinmann H. Magnetic resonance characterization of the peri-infarction zone of reperfused myocardial infarction with necrosis-specific and extracellular contrast media. *Circulation*. 2001;103:871–6.
 41. Oshinski JN, Yang Z, Jones JR, Mata JF, French BA. Imaging time after Gd-DTPA injection is critical in using delayed enhancement to determine infarct size accurately with magnetic resonance imaging. *Circulation*. 2001;104(23):2838–42.
 42. Inoue S, Murakami Y, Ochiai K, Kitamura J, Ishibashi Y, Kawamitsu H, Sugimura K, Shimada T. The contributory role of interstitial water in Gd-DTPA-enhanced MRI in myocardial infarction. *J Magn Reson Imaging*. 1999;9(2):215–9.
 43. Judd RM, Lugo-Olivieri CH, Arai M, Kondo T, Croisille P, Lima JA, Mohan V, Becker LC, Zerhouni EA. Physiological basis of myocardial contrast enhancement in fast magnetic resonance images of 2-day-old reperfused canine infarcts. *Circulation*. 1995;92:1902–10.
 44. Wu KC, Kim RJ, Bluemke DA, Rochitte CE, Zerhouni EA, Becker LC, Lima JA. Quantification and time course of microvascular obstruction by contrast-enhanced echocardiography and magnetic resonance imaging following acute myocardial infarction and reperfusion. *J Am Coll Cardiol*. 1998;32(6):1756–64.
 45. Gerber BL, Rochitte CE, Bluemke DA, Melin JA, Crosille P, Becker LC, Lima JA. Relation between Gd-DTPA contrast enhancement and regional inotropic response in the periphery and center of myocardial infarction. *Circulation*. 2001;104(9):998–1004.
 46. Hillenbrand HB, Kim RJ, Parker MA, Fieno DS, Judd RM. Early assessment of myocardial salvage by contrast-enhanced magnetic resonance imaging. *Circulation*. 2000;102(14):1678–83.
 47. Fieno DS, Kim RJ, Chen E, Lomasney JW, Klocke FJ, Judd RM. Contrast-enhanced magnetic resonance imaging of myocardium at risk: distinction between reversible and irreversible injury throughout infarct healing. *J Am Coll Cardiol*. 2000;36(3):1985–91.
 48. Dendale P, Franken PR, Block P, Pratikakis Y, De Roos A. Contrast enhanced and functional magnetic resonance imaging for the detection of viable myocardium after infarction. *Am Heart J*. 1998;135:875–80.
 49. Ramani K, Judd RM, Holly TA, Parrish TB, Rigolin VH, Parker MA, Callahan C, Fitzgerald SW, Bonow RO, Klocke FJ. Contrast magnetic resonance imaging in the assessment of myocardial viability in patients with stable coronary artery disease and left ventricular dysfunction. *Circulation*. 1998;98(24):2687–94.
 50. Lauerma K, Niemi P, Janatuinen T, Knuuti J, Toivonen L, Aronen HJ. Multimodality MR imaging assessment of myocardial viability: combination of first-pass and late contrast enhancement to wall motion dynamics and comparison with FDG PET—initial experience. *Radiology*. 2000;217(5):729–36.
 51. Klein C, Nekolla SG, Bengel FM, Momose M, Sammer A, Haas F, Schnackenburg B, Delius W, Mudra H, Wolfram D, Schwaiger M. Assessment of myocardial viability with contrast-enhanced magnetic resonance imaging: comparison with positron emission tomography. *Circulation*. 2002;105(2):162–7.
 52. van Voorthuisen A, de Roos A, Doornbos J, van der Wall EE. MR imaging of acute myocardial infarction: value of Gd-DTPA. *AJR Am J Roentgenol*. 1988;150:531–4.
 53. Judd RM, Kim RJ. Imaging time after Gd-DTPA injection is critical in using delayed enhancement to determine infarct size accu-

- rately with magnetic resonance imaging. *Circulation*. 2002;106(2):e6. p. e6; author reply e6, Jul.
54. Lekk K, Prato F, Sykes J, Wisenberg G. The partition coefficient of Gd-DTPA reflects maintained tissue viability in a canine model of chronic significant coronary stenosis. *J Cardiovasc Magn Reson*. 2004;6(1):33–42.
 55. Rehwald WG, Fieno DS, Chen E-L, Kim RJ, Judd RM. Myocardial magnetic resonance imaging contrast agent concentrations after reversible and irreversible ischemic injury. *Circulation*. 2002;105(2):224–9.
 56. Thornhill RE, Prato FS, Pereira RS, Wisenberg G, Sykes J. Examining a canine model of stunned myocardium with Gd-DTPA-enhanced MRI. *Magn Reson Med*. 2001;45(5):864–71.
 57. Sun Y, Weber KT. Infarct scar: a dynamic tissue. *Cardiovasc Res*. 2000;46(2):250–6.
 58. Thornhill RE, Prato FS, Wisenberg G. The assessment of myocardial viability: a review of current diagnostic imaging approaches. *J Cardiovasc Magn Reson*. 2002;4(3):381–410.
 59. White JA, Patel MR. The role of cardiovascular MRI in heart failure and the cardiomyopathies. *Cardiol Clin*. 2007;25(1):71–95. vi.
 60. Allman KC, Shaw LJ, Hachamovitch R, Udelson JE. Myocardial viability testing and impact of revascularization on prognosis in patients with coronary artery disease and left ventricular dysfunction: a meta-analysis. *J Am Coll Cardiol*. 2002;39:1151–8.
 61. Kubo N, Morimoto S, Hiramitsu S, Uemura A, Kimura K, Shimizu K, Hishida H. Feasibility of diagnosing chronic myocarditis by endomyocardial biopsy. *Hear Vessel*. 1997;12:167–70.
 62. McCrohon JA, Moon JCC, Prasad SK, McKenna WJ, Lorenz CH, Coats AJS, Pennell DJ. Differentiation of heart failure related to dilated cardiomyopathy and coronary artery disease using gadolinium-enhanced cardiovascular magnetic resonance. *Circulation*. 2003;108(1):54–9.
 63. Gulati A, et al. Association of fibrosis with mortality and sudden cardiac death in patients with nonischemic dilated cardiomyopathy. *JAMA*. 2013;309(9):896–908. PMID 23462786.
 64. Libby P. Braunwald's heart disease: a textbook of cardiovascular medicine. 8th ed. Philadelphia: Saunders Company; 2007.
 65. Chun EJ, Il Choi S, Jin KN, Kwag HJ, Kim YJ, Choi BW, Lee W, Park JH. Hypertrophic cardiomyopathy: assessment with MR imaging and multidetector CT. *Radiogr Rev Publ Radiol Soc N Am Inc*. 2010;30:1309–28.
 66. Wilson JM, et al. Imaging of myocardial fibrosis in hypertrophic. *Texas Heart Inst J*. 2002;29(3):176–80.
 67. Teraoka K, Hirano M, Ookubo H, Sasaki K, Katsuyama H, Amino M, Abe Y, Yamashina A. Delayed contrast enhancement of MRI in hypertrophic cardiomyopathy. *Magn Reson Imaging*. 2004;22(2):155–61.
 68. Rubinshtein R, Glockner JF, Ommen SR, Araoz PA, Ackerman MJ, Sorajja P, Bos JM, Tajik AJ, Valeti US, Nishimura RA, Gersh BJ. Characteristics and clinical significance of late gadolinium enhancement by contrast-enhanced magnetic resonance imaging in patients with hypertrophic cardiomyopathy. *Circ Heart Fail*. 2010;3(1):51–8.
 69. Kim RJ, Judd RM. Gadolinium-enhanced magnetic resonance imaging in hypertrophic cardiomyopathy. *J Am Coll Cardiol*. 2003;41(9):1568–72.
 70. Maron MS, Maron BJ, Harrigan C, Buros J, Gibson CM, Olivetto I, Biller L, Lesser JR, Udelson JE, Manning WJ, Appelbaum E. Hypertrophic cardiomyopathy phenotype revisited after 50 years with cardiovascular magnetic resonance. *J Am Coll Cardiol*. 2009;54(3):220–8.
 71. Choudhury L, Mahrholdt H, Wagner A, Choi KM, Elliott MD, Klocke FJ, Bonow RO, Judd RM, Kim RJ. Myocardial scarring in asymptomatic or mildly symptomatic patients with hypertrophic cardiomyopathy. *J Am Coll Cardiol*. 2002;40(12):2156–64.
 72. Moon JC, McKenna WJ, McCrohon JA, Elliott PM, Smith GC, Pennell DJ. Toward clinical risk assessment in hypertrophic cardiomyopathy with gadolinium cardiovascular magnetic resonance. *J Am Coll Cardiol*. 2003;41(9):1561–7.
 73. O'Hanlon R, Grasso A, Roughton M, Moon JC, Clark S, Wage R, Webb J, Kulkarni M, Dawson D, Sulaiabek L, Chandrasekaran B, Bucciarelli-Ducci C, Pasquale F, Cowie MR, McKenna WJ, Sheppard MN, Elliott PM, Pennell DJ, Prasad SK. Prognostic significance of myocardial fibrosis in hypertrophic cardiomyopathy. *J Am Coll Cardiol*. 2010;56:431–4.
 74. Adabag AS, Maron BJ, Appelbaum E, Harrigan CJ, Buros JL, Gibson CM, Lesser JR, Hanna CA, Udelson JE, Manning WJ, Maron MS. Occurrence and frequency of arrhythmias in hypertrophic cardiomyopathy in relation to delayed enhancement on cardiovascular magnetic resonance. *J Am Coll Cardiol*. 2008;51(14):1369–74.
 75. Kwon DH, Setser RM, Popović ZB, Thamilarasan M, Sola S, Schoenhagen P, Garcia MJ, Flamm SD, Lever HM, Desai MY. Association of myocardial fibrosis, electrocardiography and ventricular tachyarrhythmia in hypertrophic cardiomyopathy: a delayed contrast enhanced MRI study. *Int J Cardiovasc Imaging*. 2008;24(6):617–25.
 76. Leonardi S, Raineri C, De Ferrari GM, Ghio S, Scelsi L, Pasotti M, Tagliani M, Valentini A, Dore R, Raisaro A, Arbustini E. Usefulness of cardiac magnetic resonance in assessing the risk of ventricular arrhythmias and sudden death in patients with hypertrophic cardiomyopathy. *Eur Heart J*. 2009;30(16):2003–10.
 77. Sen-Chowdhry S, Syrris P, Ward D, Asimaki A, Sevdalis E, McKenna WJ. Clinical and genetic characterization of families with arrhythmogenic right ventricular dysplasia/cardiomyopathy provides novel insights into patterns of disease expression. *Circulation*. 2007;115:1710–20.
 78. Shimada T, Shimada K, Sakane T, Ochiai K, Tsukihashi H, Fukui M, Inoue S, Katoh H, Murakami Y, Ishibashi Y, Maruyama R. Diagnosis of cardiac sarcoidosis and evaluation of the effects of steroid therapy by gadolinium-DTPA-enhanced magnetic resonance imaging. *Am J Med*. 2001;110:520–7.
 79. Marcus FI, McKenna WJ, Sherrill D, Basso C, Bauce B, Bluemke DA, Calkins H, Corrado D, Cox MGPJ, Daubert JP, Fontaine G, Gear K, Hauer R, Nava A, Picard MH, Protonotarios N, Saffitz JE, Sanborn DM, Steinberg JS, Tandri H, Thiene G, Towbin JA, Tsatsopoulou A, Wichter T, Zareba W. Diagnosis of arrhythmogenic right ventricular cardiomyopathy/dysplasia: proposed modification of the Task Force Criteria. *Eur Heart J*. 2010;31:806–14.
 80. Steckman DA, Schneider PM, Schuller JL, Aleong RG, Nguyen DT, Sinagra G, Vitrella G, Brun F, Cova MA, Pagnan L, Mestroni L, Varosy PD, Sauer WH. Utility of cardiac magnetic resonance imaging to differentiate cardiac sarcoidosis from arrhythmogenic right ventricular cardiomyopathy. *Am J Cardiol*. 2012;110(4):575–9.
 81. Ayyala US, Nair AP, Padilla ML. Cardiac sarcoidosis. *Clin Chest Med*. 2008;29:493–508. ix.
 82. Silverman KJ, Hutchins GM, Bulkley BH. Cardiac sarcoid: a clinicopathologic study of 84 unselected patients with systemic sarcoidosis. *Circulation*. 1978;58:1204–11.
 83. Roberts WC, McAllister HA, Ferrans VJ. Sarcoidosis of the heart. A clinicopathologic study of 35 necropsy patients (group 1) and review of 78 previously described necropsy patients (group 11). *Am J Med*. 1977;63:86–108.
 84. Smedema J-P, Snoep G, van Kroonenburgh MPG, van Geuns R-J, Dassen WRM, Gorgels APM, Crijs HJGM. Evaluation of the accuracy of gadolinium-enhanced cardiovascular magnetic resonance in the diagnosis of cardiac sarcoidosis. *J Am Coll Cardiol*. 2005;45(10):1683–90.
 85. Wu Y-W, Tadamura E, Kanao S, Yamamuro M, Marui A, Komeda M, Toma M, Kimura T, Togashi K. Myocardial viability by

- contrast-enhanced cardiovascular magnetic resonance in patients with coronary artery disease: comparison with gated single-photon emission tomography and FDG position emission tomography. *Int J Cardiovasc Imaging*. 2007;23(6):757–65.
86. Ichinose A, Otani H, Oikawa M, Takase K, Saito H, Shimokawa H, Takahashi S. MRI of cardiac sarcoidosis: basal and subepicardial localization of myocardial lesions and their effect on left ventricular function. *AJR Am J Roentgenol*. 2008;191:862–9.
 87. Patel MR, Cawley PJ, Heitner JF, Klem I, Parker MA, Jaroudi WA, Meine TJ, White JB, Elliott MD, Kim HW, Judd RM, Kim RJ. Detection of myocardial damage in patients with sarcoidosis. *Circulation*. 2009;120:1969.
 88. Hiroe M, Hiraga H, Yuwai K. Guideline for diagnosis of cardiac sarcoidosis: study report on diffuse pulmonary disease from the Japanese Ministry of Health and Welfare. Tokyo: Japanese Ministry of Health and Welfare; 1993. p. 23–4.
 89. Angelini A, Calzolari V, Calabrese F, Boffa GM, Maddalena F, Chioin R, Thiene G. Myocarditis mimicking acute myocardial infarction: role of endomyocardial biopsy in the differential diagnosis. *Heart*. 2000;84:245–50.
 90. Mahrholdt H, Goedecke C, Wagner A, Meinhardt G, Athanasiadis A, Vogelsberg H, Fritz P, Klingel K, Kandolf R, Sechtem U. Cardiovascular magnetic resonance assessment of human myocarditis: a comparison to histology and molecular pathology. *Circulation*. 2004;109(10):1250–8.
 91. Friedrich MG, Strohm O, Schulz-Menger J, Marciniak H, Luft FC, Dietz R. Contrast media-enhanced magnetic resonance imaging visualizes myocardial changes in the course of viral myocarditis. *Circulation*. 1998;97:1802–9.
 92. Shah KB, Inoue Y, Mehra MR. Amyloidosis and the heart: a comprehensive review. *Arch Intern Med*. 2006;166:1805–13.
 93. Duston MA, Skinner M, Shirahama T, Cohen AS. Diagnosis of amyloidosis by abdominal fat aspiration. Analysis of four years' experience. *Am J Med*. 1987;82:412–4.
 94. Maceira AM, Joshi J, Prasad SK, Moon JC, Perugini E, Harding I, Sheppard MN, Poole-Wilson PA, Hawkins PN, Pennell DJ. Cardiovascular magnetic resonance in cardiac amyloidosis. *Circulation*. 2005;111(2):186–93.
 95. Vogelsberg H, Mahrholdt H, Deluigi CC, Yilmaz A, Kispert EM, Greulich S, Klingel K, Kandolf R, Sechtem U. Cardiovascular magnetic resonance in clinically suspected cardiac amyloidosis: noninvasive imaging compared to endomyocardial biopsy. *J Am Coll Cardiol*. 2008;51:1022–30.
 96. Syed IS, Glockner JF, Feng D, Araoz PA, Martinez MW, Edwards WD, Gertz MA, Dispenzieri A, Oh JK, Bellavia D, Tajik AJ, Grogan M. Role of cardiac magnetic resonance imaging in the detection of cardiac amyloidosis. *JACC Cardiovasc Imaging*. 2010;3:155–64.
 97. Perugini E, Rapezzi C, Piva T, Leone O, Bacchi-Reggiani L, Riva L, Salvi F, Lovato L, Branzi A, Fattori R. Non-invasive evaluation of the myocardial substrate of cardiac amyloidosis by gadolinium cardiac magnetic resonance. *Heart*. 2006;92:343–9.
 98. Srichai MB, Junor C, Rodriguez LL, Stillman AE, Grimm RA, Lieber ML, Weaver JA, Smedira NG, White RD. Clinical, imaging, and pathological characteristics of left ventricular thrombus: a comparison of contrast-enhanced magnetic resonance imaging, transthoracic echocardiography, and transesophageal echocardiography with surgical or pathological validation. *Am Heart J*. 2006;152:75–84.
 99. Weinsaft JW, Kim HW, Shah DJ, Klem I, Crowley AL, Brosnan R, James OG, Patel MR, Heitner J, Parker M, Velazquez EJ, Steenbergen C, Judd RM, Kim RJ. Detection of left ventricular thrombus by delayed-enhancement cardiovascular magnetic resonance prevalence and markers in patients with systolic dysfunction. *J Am Coll Cardiol*. 2008;52:148–57.
 100. Peters DC, Wylie JV, Hauser TH, Kissinger KV, Josephson ME, Manning WJ. Detection of pulmonary vein and left atrial scar after catheter ablation with three-dimensional navigator-gated delayed enhancement MR imaging: methods: results: conclusion. *Radiology*. 2007;243(3):690–5.
 101. Oakes RS, Badger TJ, Kholmovski EG, Akoum N, Burgon NS, Fish EN, Blauer JJE, Rao SN, DiBella EVR, Segerson NM, Daccarett M, Windfelder J, McGann CJ, Parker D, MacLeod RS, Marrouche NF. Detection and quantification of left atrial structural remodeling with delayed-enhancement magnetic resonance imaging in patients with atrial fibrillation. *Circulation*. 2009;119(13):1758–67.
 102. Kramer CM, Barkhausen J, Flamm SD, Kim RJ, Nagel E. Standardized cardiovascular magnetic resonance imaging (CMR) protocols, society for cardiovascular magnetic resonance: board of trustees task force on standardized protocols. *J Cardiovasc Magn Reson*. 2008;10:1–10.
 103. Amado LC, Gerber BL, Gupta SN, Rettmann DW, Szarf G, Schock R, Nasir K, Kraitchman DL, Lima JC. Accurate and objective infarct sizing by contrast-enhanced magnetic resonance imaging in a canine myocardial infarction model. *J Am Coll Cardiol*. 2004;44(12):2383–9.
 104. Flett AS, Hasleton J, Cook C, Hausenloy D, Quarta G, Ariti C, Muthurangu V, Moon JC. Evaluation of techniques for the quantification of myocardial scar of differing etiology using cardiac magnetic resonance. *JACC Cardiovasc Imaging*. 2011;4(2):150–6.

John N. Oshinski, Anurag Sahu, and Gregory R. Hartlage

Abstract

Phase-Contrast Magnetic Resonance (PCMR) is a technique used to quantitatively measure blood velocity and determine blood flow. In the first section, the technical aspects of the technique are described including the basic physics covering the generation of the phase-based velocity measurements, the specific implementation of the technique in pulse sequences, and MR parameters specific to PCMR. Advanced acquisition methods such as real-time imaging, tissue phase mapping, and 4D PCMR are described, as well as effects of parameter choices on temporal and spatial resolution. The analysis of the PCMR velocity images is explained, specifically highlighting physiologically relevant velocity and flow metrics that can be calculated from the PCMR measurements. In the second section, the clinical applications of PCMR are surveyed, concentrating on the information PCMR can provide as a complementary hemodynamic assessment of systolic and diastolic function to aide both diagnosis and prognosis in patients with cardiovascular disease. Disease conditions highlighted include myocardial disease, valve disease, and vascular disease. Special emphasis is given to congenital heart disease, where a significant number of PCMR applications have been developed.

Keywords

Blood flow • Velocity • Hemodynamics • Phase-contrast

Introduction

Magnetic Resonance Imaging (MRI) can be used to quantitatively measure blood velocity and determine flow [1]. The most widely used technique to quantify blood flow is

Phase-Contrast Magnetic Resonance (PCMR), although other names for this technique exist including; phase velocity mapping, phase velocity encoding, quantitative flow imaging, etc. Other MRI-based techniques to quantify velocity flow include methods to label blood (similar to what is done in tagging), but these techniques are infrequently used [2].

This chapter is divided into two major sections, one section on the technical aspects of PCMR including physics and implementation of PCMR, and a second section on clinical applications of PCMR. The technical methodology section covers: (1) the basic physics of the generation of the phase-based velocity measurements, (2) the implementation of the technique in MR pulse sequences and advanced acquisition methods, (3) the analysis of velocity images and some of the important metrics that can be calculated from the velocity and flow measurements. The clinical application section

J.N. Oshinski, PhD (✉)

Radiology and Imaging Sciences, Emory University
School of Medicine, Atlanta, GA, USA
e-mail: jnoshin@emory.edu

A. Sahu, MD

Division of Cardiology, Emory University Hospital,
Atlanta, GA, USA
e-mail: Anurag.sahu@emory.edu

G.R. Hartlage, MD

Division of Cardiology, Department of Internal Medicine,
Emory University, Atlanta, GA, USA
e-mail: ghartla@emory.edu

covers PCMR in the setting of: (1) myocardial disease, (2) valve disease, and (3) vascular disease, and (4) congenital heart disease.

The Physics of Phase Velocity Measurements

The MR signal results from a rotating magnetization vector that creates a time-varying signal in the radiofrequency (RF) receiver coils that can be measured. The vast majority of MR images are displayed as a measure of the magnitude of the vector from each spatially localized voxel. However, since the signal is time-varying, it has both a magnitude and a phase. The phase difference between two signals can be thought of as a time shift in the signals (Fig. 16.1a). PCMR works by imparting a different phase value to flowing tissue versus static tissue, thereby generating a phase shift between the two signals.

PCMR imparts this phase shift by using a bipolar magnetic field gradient during the signal acquisition. A magnetic field gradient is a linear variation of the main magnetic field in a single direction. The gradient is controlled by a set of electromagnets separate from the main magnetic field. Gradients are characterized by the time they are on (t), the direction of the variation (x , y , or z) and the value representing the slope of the field versus distance (G). The gradient $G_z(t)$ is a gradient with a positive slope value of G in the z -direction for a time t . A bipolar gradient is a gradient that is on for the same amount of time (t) in the positive (G) and negative ($-G$) directions (i.e., first moment=0), Fig. 16.1b. When a bipolar gradient is applied in the direction blood is flowing, the blood will have a phase shift proportional to its motion over the time the gradient is applied. This bipolar gradient has no effect on static tissue, but imparts a phase shift to moving blood that is proportional to its velocity.

If one ignores higher order motion terms such as acceleration, the imparted phase shift is proportional to the blood velocity to within a constant. By acquiring a phase image

with a bipolar gradient (velocity-encoded image) and reference phase image (velocity-compensated image) and subtracting them, the majority of the background phase shift can be removed from the images. The value which relates the measured phase shift after subtraction to the velocity is called the velocity encoding (VENC) value, and is related to the strength and duration of the applied gradients. The formula for the relationship is shown in Eq. 16.1.

$$f_z = g \int G_z(t) r_z(t) dt \quad (16.1)$$

This is the generalized equation for phase shift. If G_z is a known bipolar gradient waveform (area under curve=0), and we assume position of spins is: $r_z(t) = r_0 + v_z t$, the velocity can be determined within a constant. Velocity encoded and non-encoded images are acquired and subtracted to remove much of the residual background phase constant. The velocity encoding value (VENC) is the proportionality constant between velocity and phase that takes into account gradient strength and durations.

An example PCMR image after subtraction along with a corresponding magnitude image from a transverse slice through the ascending aorta at peak systole is shown in Fig. 16.2. The intensity values in the phase images are directly proportional to the velocity of spins within the voxel in the direction of the velocity encoding on a pixel-by-pixel basis. In a PCMR image, mid-grey level represents static tissue, bright signal represents flow toward the head, and the dark signal represents flow toward the feet.

Implementation of PCMR

In the previous section, we presented an overview of how PCMR works to measure velocity. In the following section, we will present few details on the implementation of PCMR and how its implementation may affect clinical measurements.

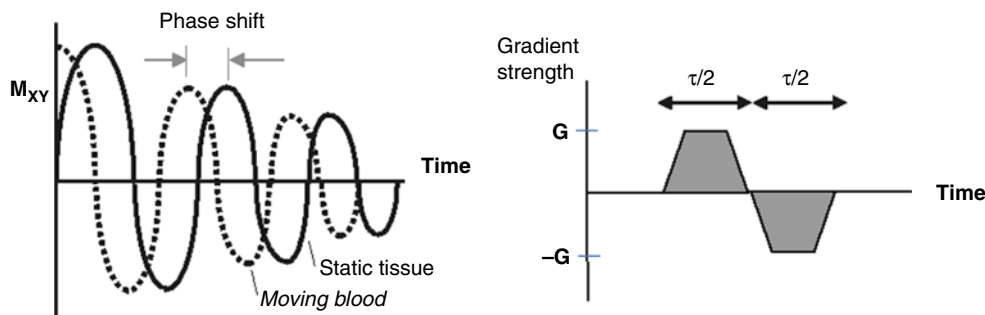


Fig. 16.1 A phase shift of the MR signal relative to static tissue is imparted to moving tissue (a, left) when a bipolar gradient is applied during signal acquisition (b, right). The phase shift can be thought of as

a time shift between the signal from the static and moving spins. A bipolar gradient is a gradient that has positive and negative components with the same area

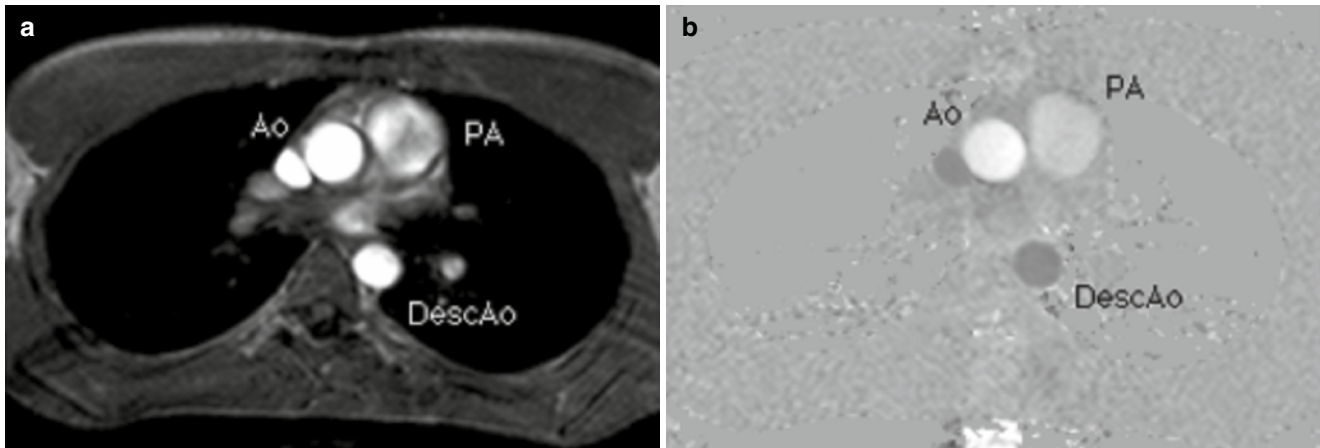


Fig. 16.2 Magnitude (*left*) and phase (*right*) images from a transverse slice through the chest just superior to the aortic valve at peak systole. Velocity is encoded in the foot-to-head direction. In the phase image the ascending aorta (*Ao*) has bright signal, indicating flow toward the head. The descending aorta (*DescAo*) is *dark*, indicating flow toward the feet.

The signal intensity directly represents velocity on a pixel-by-pixel basis. The Pulmonary Artery (*PA*) velocity is lower as the area is higher in the slice location. A region of interest (ROI) is shown around the aorta to indicate the area over which to sum velocity measurements in order to get flow values

PCMR Pulse Sequences

The majority of implementations of PCMR require the use of a rapid, low flip angle, gradient echo sequence. The sequence employs a short repetition time (TR) and a short echo time (TE), which minimizes de-phasing due to the presence of complex flow and increases temporal resolution when cardiac gating is used [3]. The lower flip angle reduces radiofrequency energy deposition and keeps TE as short as possible. In many applications where flow measurements are made in or near the heart, respiratory compensation is required to reduce blurring and ghosting in the images. In order to reduce acquisition time and complete the acquisition in a breath hold, segmented acquisitions strategies are often employed in which several lines of k-space are acquired for each cardiac phase. The larger the number of k-space lines that are acquired per cardiac phase, the shorter the overall acquisition time (Fig. 16.3). The penalty for the shorter overall acquisition time is a longer temporal acquisition window (reducing the true temporal resolution). Variations on this pulse sequence include the use of echo-planar techniques [4], spiral readouts strategies [5], and steady state free precession (SSFP) [6].

Cardiac Gating and Temporal Resolution

In most clinical applications of PCMR, cardiac gating is required so that multiple images at equally spaced time points over the cardiac cycle can be generated and displayed. The gating will allow generation of time versus velocity or time versus flow curves over the cardiac cycle. Prospective cardiac gating means that when the R-wave is detected, a

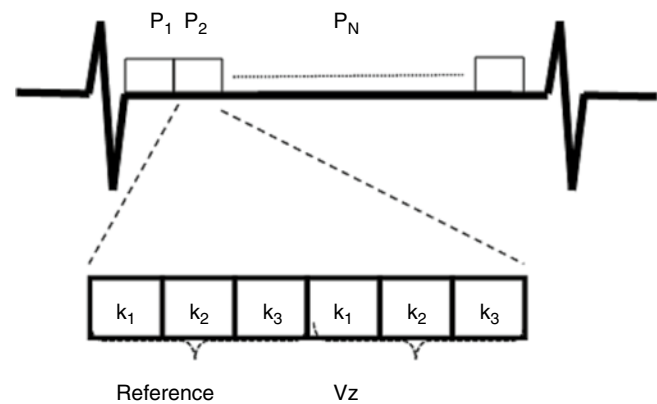
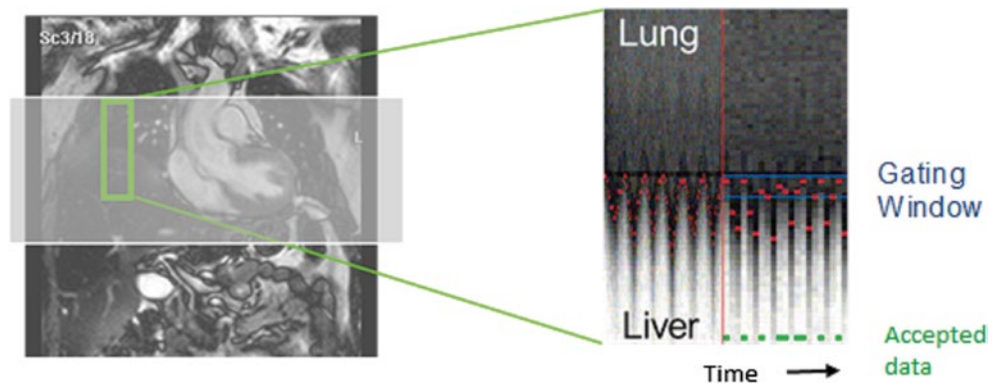


Fig. 16.3 Example of k-space segmentation in PCMR. In the diagram, 3 k-space lines (k_1 , k_2 , k_3) are acquired per cardiac phase ($P_1 \dots P_N$). Because reference (non-encoded) and velocity encoded (V_z) images are acquired, the temporal window is increased and effective temporal resolution is decreased. If more lines are acquired per cardiac phase temporal resolution will decrease (lower number of true cardiac phases), but the scan duration will decrease

sequence is run over a specific time, usually ~90 % of the estimated cardiac cycle. When the next R-wave is detected, the sequence is run again with a new set of phase encoding values, and so on until the entire imaging sequence is complete. Retrospective cardiac gating acquires data continuously and keeps track of the position of the R-wave in relation to the k-space data [7]. When the acquisition is completed, data is binned into temporal phases in relation to the R-wave for reconstruction. The advantage of retrospective gating is that the entire cardiac cycle is reconstructed, prospective gating will miss ~10 % of end-diastole. Retrospective gating also allows for nearly arbitrary reconstruction of the number of phases, however, temporal smoothing occurs during

Fig. 16.4 Schematic illustrating navigator echo gating. Signal from a small region that contains the diaphragm is acquired every heart beat (or more often). The motion of the interface over time represents respiratory motion. The user may set the gating window to accept data from a certain portion of the cardiac cycle



reconstruction. The true temporal resolution of a PCMR scan can be determined by multiplying the TR by the number of segments acquired and by two (for velocity encoded and non-encoded image segments) (Fig. 16.3).

Spatial Resolution

The phase measurement from a voxel is the average phase over the entire voxel. If the pixel contains a mixture of static tissue and moving tissue, the velocity will reflect this average phase value. For flow measurements integrated over the entire vessel area this averaging has little effect on accuracy until there are less than approximately four pixels across the vessel diameter [8]. However, for estimating maximum velocity for pressure gradient calculations, or determining the velocity gradient near the wall for estimating wall shear stress, higher spatial resolution is required [9]. As with any MR sequence, increasing temporal resolution generally will increase acquisition time, decrease signal-to-noise ratio, or decrease spatial resolution.

Respiratory Compensation

As mentioned previously, in most cardiovascular applications, PCMR is executed in a breath hold to mitigate effects of respiratory motion. However, in some applications, either high spatial resolution is required, the patient cannot execute the breath hold, or a 3D volume needs to be covered. In these cases, the scan time exceeds the patient's breath hold duration capacity. Multiple signal averages can be acquired, but this often produces unacceptable image quality results and long scan times. In these cases, a navigator echo respiratory gating scheme can be employed. The navigator echo is a localized excitation beam that produces one-dimensional, time-dependent images. The beam is usually positioned over the right hemi-diaphragm and monitors the respiratory position of the diaphragm. The beam is usually executed at the beginning of the cardiac cycle and a decision is made

whether the diaphragm position is within a user-defined respiratory gating window. If so, the data is used for image reconstruction, if not it is rejected and the k-space line is re-acquired (Fig. 16.4). There are multiple ways to implement navigator echo gating schemes and the gating can be done retrospectively or prospectively. The major applications of navigator echo gated PCMR are in time-resolved 3D imaging (so called 4D PCMR) [10], or in applications that require high spatial resolution such as coronary artery flow measurements [11].

Velocity Encoding Direction

The velocity encoding direction is independent of the slice orientation. Therefore, the velocity of blood (or tissue) can be encoded through the slice, or the velocity in either of the in-plane directions can be encoded. The direction of encoding can be set in the protocol which changes the direction of the bipolar velocity encoding gradient. Note that the velocity encoded in the image phase is the projection (or dot product) of the velocity vector in the direction of the encoding gradient. For example, if the PCMR image slice is off by 30° perpendicular to the velocity direction, then the displayed velocity will be the true velocity multiplied by $\cosine(30^\circ)$, or 0.87, resulting in a velocity error of $\sim 13\%$ from the true value.

Here it is important to understand the difference between velocity and flow. Velocity is the time-rate of change of position in a specific direction of fluid and has the units of length/time (i.e. cm/s). Flow is the rate of volume flux of fluid through a region per unit time and has the units of volume/time (i.e., milliliters/s). Flow requires velocity measurements to be integrated over a cross-sectional area. Therefore, flow can only be determined with through-plane velocity encoding, when estimating peak velocities, care must be taken to align the slice perpendicular to the velocity direction. Flow measurements are less susceptible to this issue as the increase in the vessel area compensates for the decrease in the value of the velocity vector due to misalignment.

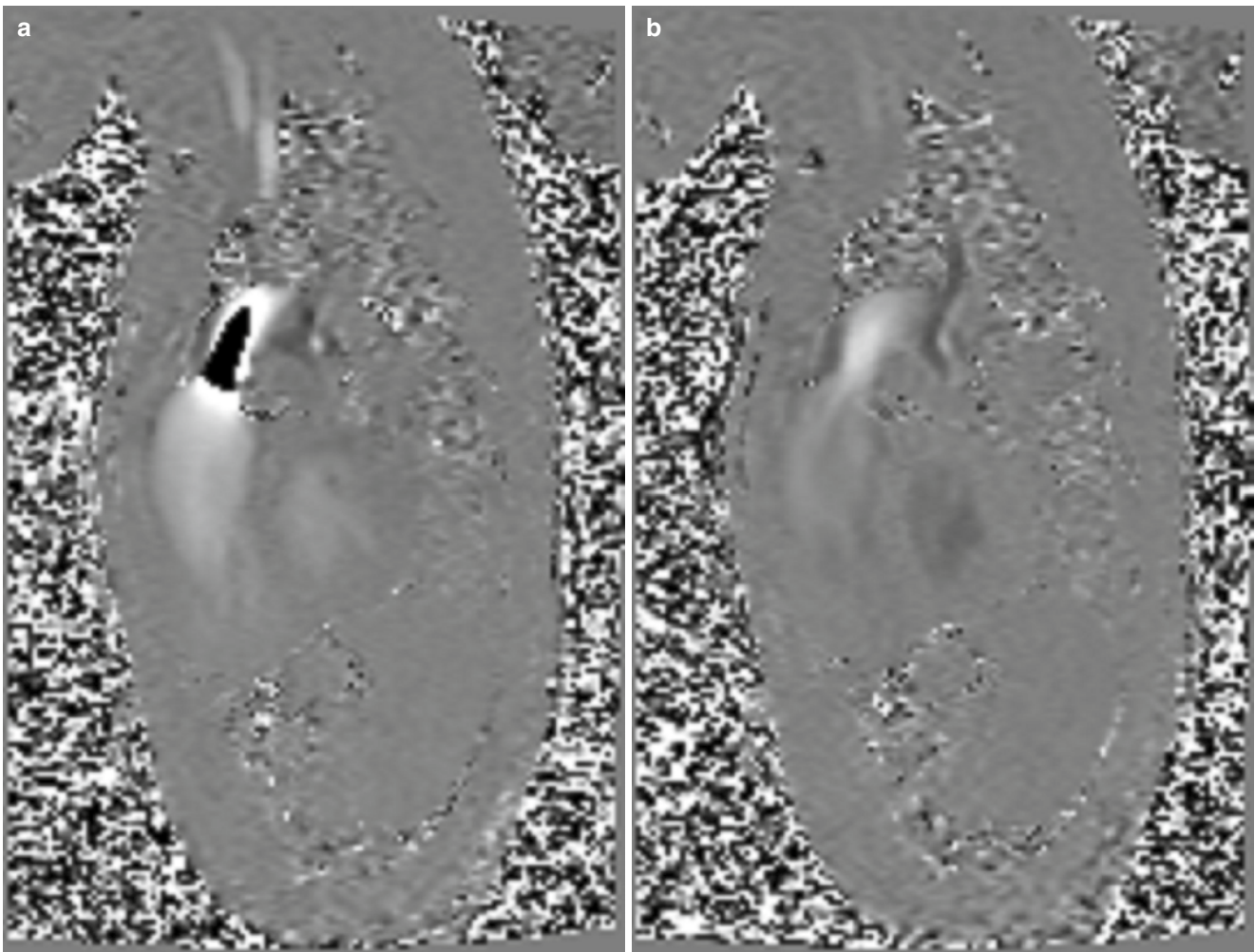


Fig. 16.5 Example of aliasing in the pulmonary artery. On the *left* the VENC value was set too low and the central jet of the flow appears dark, suggesting reverse flow (toward feet). The image on the right was taken with a higher VENC value and the aliasing disappears

Velocity Encoding Value (VENC)

The VENC value is a parameter set by the user and determines the time and magnitude of the applied bipolar velocity encoding gradients. The VENC essentially acts as a relation between the velocity values and the measured phase. If the measured phase exceeds $+180^\circ$, or goes below -180° , it will be assigned a value within the 180° to $+180^\circ$ range since only 360° of phase can be measured. This condition is known as velocity aliasing or velocity wraparound, and an example from a patient is shown in Fig. 16.5. To avoid aliasing, a VENC value must be chosen so that aliasing does not occur. VENC values are displayed as the maximum velocity that can be measured without aliasing. This produces a difficulty in PCMR as the maximum velocity is not known a priori. When a good estimate of the maximum velocity cannot be made, a rapid scan can be done to check if aliasing is present. A VENC

value that exceeds the maximum expected velocity but only by a small amount ($\sim 25\%$) will maximize the ranges of phases used to measure velocity and hence increase the velocity-to-noise ratio. Additionally, it is important to realize that a smaller VENC value requires a larger gradient value, which will increase the echo time and may reduce the number of phases that can be acquired.

Specialized Implementations of PCMR

The majority of PCMR examinations are conducted using a single slice, 2D, ECG gated, cine implementation with velocity encoded through the slice plane to determine vessel flow as described above. However, several recent developments have enabled new applications that expand on this basic implementation and these are described below.

Alternate k-Space Sampling Strategies

Most work in PCMR has been done using standard Cartesian k-space sampling. One of the major problems using PCMR to quantify blood flow is the lengthy acquisition times associated with the technique. Multiple methodologies have been used to reduce acquisition time. Techniques such as vastly under-sampled radial projection reconstruction (VIPR) can be combined with PCMR [12]. PC-VIPR can reduce acquisition time of PC velocity images by sparsely sampling the edges of k-space and more densely sampling the central regions of k-space with a constrained radial sampling strategy. Interleaved spiral acquisition has also been used to reduce temporal resolution of the PCMR velocity measurements. The spiral technique has been used in a single slice, single direction mode to improve temporal resolution. These rapidly acquired images can be used to monitor short duration physiologic changes in cardiac output [13]. A third method to improve the acquisitions time is to use parallel imaging techniques with or without constrained reconstruction.

4D PCMR

The PCMR described previously can be expanded to measure multiple time-resolved velocity directions over a 3D volume (4D PCMR). As previously mentioned, creation of a PCMR image requires two underlying images (flow-encoded and flow compensated). Obtaining multiple directions of velocity increases this time, but advanced encoding strategies can limit the time to a maximum to four times that of the standard gradient echo sequence [14]. Implementing the technique with a 3D acquisition volume allows the voxel size to be reduced over a standard 2D acquisition, and allows for an integrated volume acquisition. Therefore, 4D PCMR can be used to completely define the three-dimensional, time-resolved velocity vector field over a 3D volume in vessels. Having this complete, time-resolved velocity field enables advanced visualization such as plotting streamlines, pathlines, and particle traces. A variety of cardiovascular applications have been examined with 4D PCMR, including ventricular flow and carotid flow, but applications in aortic disease has been a primary focus of many investigators [15, 16]. The major drawback to widespread use of 4D PCMR is the time required for acquisition. Even with parallel imaging techniques, acquiring velocity within the aorta requires ≈ 10 min.

Tissue Velocity Mapping

Similar to what has been done in ultrasound with tissue Doppler imaging (TDI), investigators have used PCMR to map velocity of the left ventricular myocardium rather than the blood flow [17]. This requires a low VENC value and a fairly high spatial resolution acquisition. The disadvantage is

that these low VENC values requires a high velocity encoding gradient to generate adequate phase for the low velocities seen in the myocardial tissue (typically <10 cm/s). The higher gradient increases echo time, often causing susceptibility artifacts in the LV lateral wall, and reduces overall SNR within the image [17–20]. Other issues include the lengthy acquisition time required to cover the entire LV, and issues with large phase shifts from the flowing blood within the left ventricle. Several applications, including measurement of ventricular dyssynchrony have shown promising results [20].

Real-Time PCMR

Because of the need for subtraction of two images in PCMR, development of real-time PCMR has lagged behind other MRI-based real time applications, such as cine imaging of the LV function, or monitoring of needles or catheters in interventional procedures. Using EPI or spiral acquisition and shared encoding strategies have allowed investigators to use real time PCMR to monitor exercise or stress-induced changes in aortic hemodynamics, and diagnosis of congenital and acquired pathology [21]. Because of the complex acquisition strategies and the required post-acquisition subtraction, there is often a delay in displaying the ‘real-time’ PCMR data. Investigators have employed an external dedicated reconstruction hardware to improve the time between delay and acquisition [22, 23].

Pulse Wave Velocity

Pulse wave velocity (PWV) can be used as a measure of arterial stiffness through the Moens-Korteweg equation. The PWV is most often estimated by dividing the distance between two measurement sites by the propagation time of the pressure or flow wave between the two sites. Two slices perpendicular to the aorta are most commonly used for recording locations, but multiple locations using in-plane flow encoding can also be used. A time-marker on the flow waveform must be chosen in order to compare pulse wave arrival times at the sites. High temporal resolution in the PCMR images is critical as the wavespeed is 3–10 m/s in the aorta [24, 25].

Post-processing of PCMR Data

Background Phase Correction

Despite the subtraction of velocity-encoded and non-encoded images, a background phase offset may remain in static tissue, causing static tissue to appear to have a small velocity. The phase offset is caused by concomitant gradients in phase-and by residual eddy currents. The phase offsets can be dependent on

position in the image, but generally are larger as the distance from the iso-center increases. Consideration of the background phase is important because a large background phase can affect the accuracy of flow measurements, especially when calculating quantities such as regurgitant fraction [26]. A variety of techniques have been employed to reduce the background phase or mitigate its effect on quantitative velocity measurements. From the acquisition side, it is important to keep the image slice and vessel near the iso-center of the magnet where effects of inhomogeneity and gradient eddy currents are minimal. From the post-processing side background phase effects can be removed with a background correction algorithm that can be automated, or use user-defined regions of interest placed in static tissue.

Analysis of Velocity Images

By drawing a region of interest curve (ROI) around a vessel, statistics such as average velocity, peak velocity, and a velocity histogram can be determined in a region. One can multiply pixel area times the velocity value in each pixel to obtain flow for each frame. If the regions of interest (ROI's) are drawn for each time frame acquired, one can determine flow as a function of time over the cardiac cycle. Care is usually taken to trace boundaries near the edges of the vessel to eliminate contamination from other vessels, and to eliminate errors in the integration due to inclusion of excess static tissue.

Flow versus time curves can be used to determine clinically relevant quantities such as aortic regurgitant volume, abnormal ventricular filling patterns, cardiac stroke volume, cardiac output, quantification of volumetric flow in left-to-right shunts [27]. Advanced calculations can be done on the velocity maps to create parametric images of wall shear stress, pressure gradient, vorticity, etc.

Clinical Application of PCMR

A multitude of CMR techniques can aid in delineating specific etiologic and pathophysiology. CMR provides gold standard assessment of ventricular mass, volumes, wall motion, and viability via various cine and contrast enhancement techniques. PCMR provides a complementary hemodynamic assessment of systolic and diastolic function, further aiding both diagnosis and prognostication in patients with various cardiac diseases.

Myocardial Disease

Clinical heart failure may arise from impaired myocardial contraction, relaxation, or both conditions. Phase contrast magnetic resonance (PCMR) is useful in assessing the degree of both systolic and diastolic dysfunction due to various

myocardial diseases, as well as impaired ventricular filling. The contribution of various myocardial, valve or shunt lesions to pressure and/or volume overload and secondary myocardial dysfunction can also be evaluated by PCMR.

Cardiac Output

Cardiac output (CO), is the product of stroke volume (SV) and heart rate and is an important clinical parameter in the assessment of patients with heart disease. Reduced CO or cardiac index (CI defined as CO/BSA) is the hallmark of systolic or diastolic dysfunction from any etiology. Traditionally, the most accurate method of measuring CO has relied on invasive cardiac catheterization. CMR offers a non-invasive measurement of CO by both cine ventricular volumetry and PCMR, both with accuracy and precision as comparable to invasive measures. Both CMR methods have established reference values, although cine ventricular volumetry is limited in the case of regurgitant valve disease.

The method of PCMR CO or SV measurement relies on a through-plane velocity measurement and integration of flow volume in one or both of the great vessels as described above. For LVSV measurement, the ascending aorta should be localized in an oblique sagittal scout image to visualize patient specific architecture. The PCMR imaging plane should be set perpendicular to the direction of flow. The location of the imaging plane relative to the aortic annulus is a matter of debate, as some groups recommend a proximal position between the annulus and sinotubular junction, while others recommend the mid-ascending aorta at the level of the main pulmonary artery (PA) bifurcation. The proximal position may be more susceptible to inaccuracies related to valve motion artifacts and complex flow patterns, however, it avoids error related to diastolic coronary flow. Measurement in the mid-ascending aorta, although felt to be more reproducible, may be more affected by aortic compliance, which underestimates regurgitant volume, and reverse coronary diastolic flow, which may account for 0.5–6 % of aortic forward flow. The VENC should initially be set at 200 cm/s.

RVSV is measured in main PA. The main PA should be localized in an oblique axial or coronal scout image to visualize the curvature. The imaging plane should be set perpendicular to the direction of flow, between the pulmonic valve and main PA bifurcation. The VENC should initially be =200 cm/s. Comparison of the SV of the left and right ventricle (RV) may be used to provide an internal control, or to calculate Left-to-right's shunt ratio, if applicable.

Diastolic Dysfunction

Cardiac diastolic dysfunction is an abnormality of ventricular relaxation and occurs in a variety of heart failure etiologies. Diastolic heart failure is a predominant cause of heart failure

symptoms and may precede or accompany systolic dysfunction. Diastolic dysfunction is also a marker of poor outcomes, as patients with diastolic heart failure and preserved systolic function have similar mortality to patients with isolated systolic dysfunction [28, 29]. Diastology is also useful in the clinical management of patients, notably in the estimation of LV filling pressures and guidance of medical therapies.

Clinical diastolic function evaluation is most often performed with Doppler transthoracic echocardiography (TTE). Conventional parameters determined include early and late filling peak velocities of the transmitral flow (E and A waves), E-wave deceleration time (DT), and annular myocardial early longitudinal peak velocity (E') and late longitudinal peak velocity (A'). Pulmonary vein peak systolic (S) and diastolic (D) velocities are a useful adjunct, specifically in the form of the S/D ratio.

CMR can offer a comprehensive evaluation of diastolic function comparable to Doppler TTE with the use of PCMR. PCMR derived diastolic hemodynamics will provide useful information in patients planned to undergo CMR or those with poor TTE windows. Additionally, PCMR may overcome certain limitations of Doppler TTE, including limited field of view, beam angle dependency, and incomplete sampling of eccentric flows.

Transmitral Flow Profiles

Cine CMR imaging in multiple long axis views should be used to visualize the mitral leaflets for planning a PCMR slice location to evaluate transmitral velocity. The PCMR slice should be prescribed at the leaflet tips during diastasis, parallel to the plane of the mitral annulus. Through-plane images should be acquired with retrospective EKG gating. An initial VENC setting around ~200 cm/s is reasonable. However, the correct VENC may vary, between 150 and >300 cm/s, depending on the patient's hemodynamics. After image acquisition, the ROI is traced around the inner contour of the mitral valve (MV) orifice in cross-section on magnitude images, and then transferred to phase images.

Transmitral peak E and A velocity waves are plotted on a flow versus time graph. The DT is calculated by subtracting the time of intersect of the peak E wave with the baseline from the time of intersect of the E wave downslope with the baseline. PCMR derived peak E and A velocity waves correlate well with Doppler TTE techniques, although there is a tendency towards underestimation of magnitude. Assessment of transmitral profiles and E/A ratio, however, have excellent agreement with Doppler TTE for identifying the presence and stage of diastolic dysfunction [30, 31].

Pulmonary Vein Flow Waveform

The right superior pulmonary vein is often the easiest to acquire on cine CMR or scout images, however, any or all visualized pulmonary vein may be imaged. The slice plane

should be perpendicular to flow inside the vein, approximately 1 cm from the ostium. Through-plane PCMR images should be acquired with retrospective EKG gating and a VENC of 100 cm/s. After image acquisition, the ROI is traced around the inner lumen of the pulmonary vein on magnitude images, and then transferred to phase images. Pulmonary vein S and D average velocity waveforms are plotted on a velocity versus time graph to the time-dependent characteristics of the flow. PCMR derived pulmonary vein S/D ratio correlates well with Doppler TTE [32].

Mitral Annular Tissue Velocity

The basal lateral and/or basal septal segments of the mitral annulus can be visualized on long axis cine CMR imaging. A PCMR slice to measure mitral annular velocity should be placed at the lateral and/or septal MV annulus, with care to ensure it the slice does not include mid-left ventricular or left atrial myocardium. Through-plane PCMR images should be acquired with retrospective EKG gating and a VENC of 50 cm/s. After image acquisition, the ROI in the annulus is traced on magnitude images and transferred to phase images.

Mitral annular tissue average velocity waveforms are plotted on a velocity versus time graph to determine time-dependent velocity behavior of the tissue. PCMR derived mitral annular tissue velocities have been found to correlate well with tissue Doppler TTE [30, 33]. The E/E' ratio has been found to correlate well between PCMR and Doppler TTE, as well. Importantly, PCMR derived E/E' correlates strongly with invasive pulmonary capillary wedge pressure by cardiac catheterization with patients with E/E' <8 have PCWP <15 mmHg and those with E/E' >15 having PCWP >15 mmHg [20, 34].

Restrictive Physiology

Restrictive physiology may be a result of progressive diastolic dysfunction or restrictive cardiomyopathy. Restrictive cardiomyopathy often presents with signs of right heart failure including peripheral edema and ascites. Imaging findings include normal or reduced ventricular volumes and normal or near normal ventricular systolic function, often with significantly dilated atria. In this clinical setting, it is important to distinguish restrictive and constrictive physiology. Severe abnormalities of myocardial relaxation and filling, with E/A >2 and mitral annular tissue velocity <4 cm/s, is categorized as restrictive physiology. Moreover, CMR morphologic assessment and tissue characterization provides further analysis of specific causes of restrictive cardiomyopathy such as amyloidosis, sarcoidosis, hemochromatosis, Fabry's disease, endomyocardial fibrosis, and carcinoid heart disease [35].

Pitfalls

Diastolic transmitral hemodynamic profiles and mitral annular tissue velocities may be inaccurate due to large through-plane motion of the annulus over the cardiac cycle.

Specifically, transmitral diastolic velocities and flow may be underestimated. Visual confirmation and manual redrawing of the ROI at each cardiac phase to ensure the appropriate location over each cardiac cycle during post-processing may minimize error. Annular tracking with long-axis cine CMR navigators may provide motion compensation, although this technique is not widely available. The underestimation of peak E and A wave velocity magnitude with PCMR may be related to increased sensitivity of maximal velocity curves to noise or the temporal resolution of PCMR.

Pericardial Disease

CMR provides an accurate assessment of pericardial morphology including thickness, pericardial effusion, acute inflammation and fibrosis. CMR can also provide complementary functional and hemodynamic information on cine PCMR sequences.

Pericardial Constriction

Pericardial constriction occurs when normal ventricular diastolic filling is impeded by a non-compliant pericardium. In the clinical setting, it is critical to distinguish restrictive and constrictive physiology. Although pericardial thickening and even calcification may be present. This finding is not diagnostic of constriction, as constriction may exist without either finding [36, 37].

The hemodynamic hallmark of constriction is dissociation between intracardiac and intrathoracic pressures evidenced by ventricular interdependence and respiratory variations in atrioventricular valve inflow velocities, typically evaluated by Doppler TTE. CMR can provide an assessment similar to that of TTE, including volumetric and functional evaluation, identification of the interventricular septal bounce suggestive of ventricular interdependence and, inferior vena cava (IVC) plethora. Thorough hemodynamic evaluation is essential, as the interventricular septal bounce and IVC plethora may be seen in a variety of other conditions.

Pitfalls

Mitral and tricuspid annular motion with the cardiac cycle and respiration may displace the desired imaging plane on the horizontal long axis images, potentially introducing error into the flow measurements. This can be minimized by visual confirmation of enface inflow orientation with each frame during acquisition and redrawing of the ROI to ensure the appropriate location during post-processing.

Although the use of free-breathing acquisition improves temporal resolution, this may come at the expense of reduced signal-to-noise ratio. Furthermore, maximal velocity curves

may have increased sensitivity to noise as they represent single time point in the cardiac cycle, compared to flow rates, which are estimated from the averaged velocity throughout the cycle. However, given the measurement of respiratory cycle-based velocity variation occurring over hundreds of milliseconds, this is unlikely to have significant impact.

Valve Disease

Left sided valve disease imposes a progressive hemodynamic burden on the heart in the form of pressure overload, volume overload, or both. Established criteria guide physicians in treating patients with left sided valve disease by incorporation of symptoms and cardiac structural changes, in addition to lesion severity as assessed by various imaging techniques. Quantitative assessment of lesion severity is preferred, and may facilitate intervention at an earlier stage prior to potentially irreversible structural changes and limiting symptoms. PCMR provides an accurate non-invasive estimate of hemodynamic profiles across any valve or vascular structure, and allows for precise quantitative results that may be complementary to the anatomic findings of both TTE and cine CMR. Transvalvular velocities, pressure gradients, flow rates, and flow volumes can be directly measured or calculated.

Aortic Stenosis

Aortic stenosis (AS) due to calcific degeneration is the most common valve disease of the elderly. However, congenital and rheumatic aortic valve (AV) disease may present as significant stenosis in children and young adults. Regardless of etiology, progressive narrowing of the AV orifice results in pressure overload of the LV with associated concentric remodeling and elevation of LV filling pressures. Surgical treatment decision is based on lesion severity and patient symptoms. AS is considered severe when the area of the valve orifice is less than 1 cm², the peak velocity is greater than 4 m/s, or the mean transvalvular gradient is more than 40 mmHg. PCMR imaging is useful in determining these structural and hemodynamic findings. Generally, the VENC should be based on the initially estimated severity and can be subsequently adjusted based on the presence of aliasing in the images. Cine CMR also provides complimentary structural assessment of valvular morphology, such as cusp number and fusion, and ventricular remodeling related to chronic pressure overload. Dynamic characterization of the valve orifice area, including morphology (i.e. bicuspid versus tricuspid) and direct measurement of the valve area is possible with PCMR. This method relies on visualization of a distinct boundary identifying high velocity pixels of the jet. The

imaging plane should be parallel to the AV annulus and use a short TE, high temporal resolution cine PCMR sequence.

Quantification of Peak Velocity and Transvalvular Pressure Gradients

The maximum instantaneous velocity (V_{\max}) within the stenotic jet can be obtained on through-plane or in-plane PCMR. Through-plane analysis relies on slice positioning relative to the valve orifice, as the true V_{\max} may be missed if the slice is too far from the valve orifice. Positioning too close to the valve orifice may result in inaccurate V_{\max} from signal loss due to turbulent flow [38]. Conversely, in-plane analysis encompasses the entire longitudinal aspect of the jet, however, severe stenosis may result loss of accuracy due to partial volume averaging and movement of the jet out of the imaging plane. The use of both through-plane and in-plane imaging with sampling of the entire jet is recommended to maximize accuracy.

The peak transvalvular pressure gradient (ΔP) can be calculated using the modified Bernoulli equation and V_{\max} as:

$$\Delta P = 4(V_{\max})^2$$

Measurement of velocities and pressure gradients by PCMR correspond well with both Doppler TTE and cardiac catheterization.

Pitfalls

Partial volume averaging results from increased voxel size due to large slice thickness and causes averaging of velocities from inside and outside of the vena contracta. The net effect of partial volume may be underestimation of the true peak velocity, which has been reported in multiple studies comparing PCMR to Doppler TTE. Generally, thin-section imaging with overlapping and a minimum of 16 voxels covering a cross section volume is adequate to avoid significant partial volume effects [39]. Alignment of the flow jet and imaging plane may be challenging with eccentric high velocity jets and horizontally oriented aortic annuli. Errors related to flow-plane misalignment is proportional to the $\cos \theta$, where θ is the angle of misalignment, thus a small degree of misalignment is associated with a small error. Stenotic AVs are often heavily calcified, which may subject images to significant susceptibility artifact, limiting hemodynamic evaluation at the level of the valve plane.

Aortic Regurgitation

Aortic regurgitation (AR) may arise from primary abnormalities of the aortic valve leaflet or secondary to aortic root dilatation. The primary hemodynamic consequence of chronic AR is progressive LV volume overload which may

remain asymptomatic for years. The timing of surgery for severe AR depends on the presence of symptoms or significant chamber dilatation in asymptomatic patients. Grading of AR has traditionally relied on qualitative and semi-quantitative findings on Doppler TTE or aortic root angiography. Quantitative parameters such as regurgitant jet area, regurgitant volume (RVol), and regurgitant fraction (RF; RVol divided by total LV SV) are the strongest indicators of true lesion severity. A variety of PCMR derived CMR approaches are useful for AR quantification and provide a non-invasive, alternative to traditional methods. AR grading by CMR derived RF is generally accepted as: mild, RF less than 15 %; moderate, RF 16–25 %; moderate to severe 25–48 % and severe, greater than 48 % [40]. Retrospective ECG gating should be utilized to ensure the entirety of diastole is appraised. Cine CMR is used to provide clues as to AR etiology such as jet location and direction, leaflet prolapse or perforation, annular morphology and aortic abnormalities such as root dilatation or aortic dissection. Assessment of LV chamber dimensions is a vital complement to PCMR hemodynamic data.

Calculation of Regurgitant Fraction from Transaortic and Transpulmonic Flows

Direct through-plane measurement of blood flow in the ascending aorta and main PA will provide an assessment of left and right ventricular SVs, respectively, when integrated throughout systole. In the absence of intracardiac shunting or valvular regurgitation, the difference between right and LV volumes by CMR is less than 5 %. This method allows calculation of the RF as:

$$RF = [(LVSV - RVSV) / LVSV] * 100$$

The assessment of LVSV and RVSV by PCMR correlate well with Doppler TTE and invasive cardiac catheterization derived measures [41]. This method assumes isolated AR and is invalid in the case of multivalvular regurgitation.

Quantification of Regurgitant Fraction from Transaortic Flow

An accurate and reproducible method of AR quantification by PCMR is direct through-plane measurement of antegrade and retrograde proximal aortic flow throughout the cardiac cycle. Aortic flow is plotted versus time, and the area inside the curve under the baseline represents diastolic retrograde flow. Systolic antegrade flow, that is LVSV. The Regurgitant Fraction (RF) is calculated as:

$$RF = (RVol / LVSV) * 100$$

It is important to place the slice plane perpendicular to the direction of flow in the aortic root. The plane should be

placed proximal to the coronary ostia, as close to the valve as possible, without artifacts from valve motion and complex flow patterns. This position may also demonstrate the site of regurgitation. Multiple scout views are helpful to account for obliquity and proper placement. This method correlates well with the CMR method of biventricular volumetry, as well as Doppler TTE and aortic root angiography [42].

The presence of valve motion artifacts and complex flow patterns in the proximal root has led some to recommend aortic flow measurement in the mid-ascending aorta at the site of the right PA. However, this position may be more affected by aortic compliance, which underestimates RVol, and reverse coronary diastolic flow, which may account for over 6 % of aortic forward flow [43].

Mitral Stenosis

Mitral stenosis (MS) is caused by restriction of MV opening involving any portion of the mitral apparatus and the result is LV inlet obstruction with a diastolic transvalvular pressure gradient between the left atrium and LV. MS is considered severe when the area of the valve orifice is less than 1 cm² and/or the mean transvalvular gradient is more than 10 mmHg. PCMR provides quantitative hemodynamic information complemented by leaflet, chordae, and annular morphology, planimetered valve area, and abnormal chamber size, such as left atrial enlargement and small LV, seen on cine CMR.

Quantification of Peak Velocity and Transvalvular Pressure Gradient

The calculation of V_{\max} should be performed in multiple in-plane and through-plane positions perpendicular and parallel to the direction of flow. As in AS, through-plane analysis relies on slice positioning relative to the valve orifice, as the true V_{\max} may be missed if the slice is too far from the valve orifice. Positioning too close to the valve orifice may result in inaccurate V_{\max} from signal loss due to turbulent flow. Conversely, in-plane analysis encompasses the entire longitudinal aspect of the jet, but in the setting of severe stenosis may result in loss of accuracy due to partial volume averaging and movement of the jet out of the imaging plane. The use of thin-section imaging may resolve this problem. The use of both through-plane and in-plane imaging with sampling of the entire jet is recommended to maximize accuracy. An initial VENC setting around 200 cm/s is reasonable. However, the correct VENC may vary, between 150 and 400 cm/s, depending on the patient's hemodynamics. The peak transvalvular pressure gradient (ΔP) can be calculated using the modified Bernoulli equation and V_{\max} as:

$$\Delta P = 4(V_{\max})^2$$

The mean transvalvular pressure gradient is obtained by averaging all of the instantaneous velocities over systole. Generally, the mean pressure gradient is about two-third of the peak pressure gradient. Measurements of velocities and pressure gradients by PCMR correspond well with Doppler TTE [44].

Pitfalls

Atrial fibrillation, which is common in MS patients, limits the utility of PCMR quantification due to significant variation in cardiac cycle length. Partial volume effects may result in underestimation of peak velocity and pressure gradients; increased flow states may cause increased peak velocity and pressure gradients similar to AS. Stenotic MVs are often heavily calcified, which may subject images to significant susceptibility artifact, limiting hemodynamic evaluation at the level of the valve plane.

Mitral Regurgitation

Mitral regurgitation (MR) may occur due a primary valve abnormality, such as leaflet prolapse or perforation, or chordal rupture causing a flail leaflet. The etiologies of these abnormalities include, but are not limited to, age related degeneration, myxomatous infiltration, and endocarditis. Alternatively, MR may be secondary to ventricular abnormalities such as papillary muscle dysfunction in ischemic heart disease, or a dilated mitral annulus with dilated cardiomyopathy. A consequence of primary MR is increased LVSV. Surgical intervention for severe MR is predicated by symptoms and structural remodeling, including drop in EF below 60 % and increase in LV end-systolic dimension greater than 4 mm in asymptomatic patients [45]. Currently, Doppler TTE is most commonly used for diagnosis and in the case of poor TTE windows or discrepant results, quantitative parameters such as Regurgitant volume (R_{Vol}) and RF can be obtained by a variety of PCMR derived CMR approaches. MR grading by CMR derived RF is generally accepted as: mild, RF less than 15 %; moderate, RF 16–25 %; moderate to severe 26–48 % and severe, greater than 48 % [40]. Cine CMR provides a complimentary assessment of leaflet, subvalvular, and annular morphology, as well as a gold standard of chamber and volume quantification.

Calculation of Regurgitant Fraction from Cine Volumes and Great Vessel Flows

The most dependable method of MR quantification utilizes a combination of through-plane transaortic, and LVSV measured on cine CMR. The LVSV is the difference of the LV end-diastolic volume and LV end-systolic volume. The difference between the LVSV and aortic valve SV represents the R_{Vol} . The Regurgitant Fraction (RF) is calculated as:

$$RF = [(LVS\dot{V} - \text{semilunar valve } \dot{S}\dot{V}) / LVS\dot{V}] * 100$$

This method correlates well with both Doppler TTE and cardiac catheterization [42, 46]. In the case of significant AR, the transpulmonic SV can be used, providing there is no significant Pulmonary Regurgitation.

Pitfalls

Direct diastolic transmitral flow measurement may be difficult due to valve motion with the cardiac cycle and the three-dimensional “saddle shape” of the mitral annulus. Annular tracking with long-axis cine CMR images may provide motion compensation, although not widely available. A control volume approach can overcome many of these issues, but is time consuming [47].

Prosthetic Valves

Both surgical and percutaneous prosthetic valves can be safely imaged by CMR. Poor visualization due to susceptibility artifact may limit morphologic assessment and measurement of transvalvular velocity and pressure gradients by PCMR, however, downstream hemodynamic assessment remains possible [48, 49]. PCMR is particularly helpful in the assessment of prosthetic valve dysfunction or paravalvular pathology associated with significant regurgitation, as TTE is often limited by significant attenuation from metal containing prostheses.

Methods utilizing cine CMR volumetric analysis and through-plane aortic flow assessment are valid, with additional considerations. Surgical aortic valves generally have a low profile in the aortic root, allowing through-plane flow analysis in proximity to the valve. Transcatheter valves generally have a higher profile within the aorta due to the valve stent frame, with the Edwards Sapien valve extending nearly 1 cm into the aortic root and the Medtronic CoreValve extending 2–3 cm into the aortic root. The nitinol stent frame of the Medtronic CoreValve produces little susceptibility artifact allowing flow analysis in the aortic root.

Vascular Disease

Diseases of the aorta and peripheral vessels are commonly imaged with MRA techniques, however, PCMR provides useful functional information complementary to MRA morphology findings. In the setting of Aortic Dissection, in-plane and through plane views are both useful in distinguishing the true and false lumens. High-velocity flow will be seen in the true lumen, while lower velocities will be seen in the false lumen, often with bidirectional flow. Retrospective gating should be utilized, with an initial VENC

of 150 cm/s. Pressure gradients due to Aortic coarctation or atherosclerotic lesions can be estimated with the modified Bernoulli equation [50].

Congenital Heart Disease

One of the areas where PCMR has been used most extensively is congenital abnormalities. The complex anatomy and often widely varying hemodynamics make PCMR particularly useful. Here we describe how PCMR is used in some of the most common pediatric applications.

Coarctation of the Aorta

Initially thought to be a simple lesion involving narrowing of the aorta at the junction of the distal aortic arch and descending thoracic aorta, coarctation has been recognized to be a complex disorder which requires life-long follow-up and serial imaging even after surgical or interventional treatment [51]. The underlying cause of coarctation is not known though it is believed to be related to postnatal constriction of aberrant ductal tissue.

When using CMR to evaluate the patient with untreated repaired coarctation, it is important to note the nature of the lesion (local stenosis or longer segment stenosis), presence of other associated defects (predominantly bicuspid aortic valve or aortic aneurysm). In the surgically or percutaneously palliated patient, the key to assessment involves an understanding of the type of repair. Resection and end to end anastomosis is the most common type of repair; particularly in the young child. Other types of repair are less common but occasionally are required depending on surgical considerations.

PCMR can provide a hemodynamic assessment of lesion severity and define the presence or absence of collateral blood flow. Due to signal void artifact present in patients who undergo percutaneous stent repair of this lesion, CMR can be limited in the assessment of these patients.

In patients with native coarctation, defining the anatomy of the lesion is the most important portion of the procedure. Unless the imaging planes are properly prescribed, hemodynamic assessment by PCMR will be difficult. MR angiography provides the simplest and most effective way to identify pertinent anatomy. MRA protocol uses 0.1–0.2 mmol/kg of gadolinium contrast injected at 2–3 ml/s using bolus detection with initial acquisition starting once contrast is visualized in the left ventricle. Two repeat acquisitions are then obtained immediately following the initial acquisition. Anatomic planes for hemodynamic evaluation can then be prescribed using the 3-D tool on the work-station. For patients that have contra-indication to gadolinium contrast

other non-contrast techniques are available to provide anatomic data, most notably the use of dark-blood imaging obtained in an axial plane. Prescribing an imaging plane across the ascending aorta through the descending aorta will result in an oblique sagittal view of the thoracic aorta and coarctation segment. This typically prescribes an imaging plane that is inclusive of the ascending aorta, arch, and descending aorta including the coarctation segment.

The most critical aspect of the hemodynamic assessment of the unrepaired coarctation is an assessment of the pressure gradient across the lesion. Traditionally a gradient >20 mmHg is considered to be significant, and this gradient was measured using the difference in systolic blood pressure between the right arm and left leg. This clinical exam is often unreliable in assessment of the true pressure difference particularly in patients with extensive collateral formation. PCMR is an accurate and reproducible method of assessing this gradient. This gradient is best obtained by first obtaining an in-plane flow in the descending thoracic aorta and identifying the segment where maximum velocity occurs. A through plane velocity can then be obtained at this level thereby obtaining a true peak velocity. Using the modified Bernoulli equation, the peak gradient can then be obtained.

Another unique feature of PCMR imaging is the assessment of collateral flow in coarctation. This is usually achieved by a comparison of the measurement of flow in the proximal descending thoracic aorta to the descending thoracic aorta just above the level of the diaphragm. Collateral flow can be assumed to be present if the flow in the descending thoracic aorta just above the diaphragm is greater than the flow in the proximal descending thoracic aorta. This occurs because the intercostal arteries become engorged with blood and other collateral vessels form causing blood flow down the internal mammary arteries and retrograde from the intercostal arteries increasing the flow in the descending thoracic aorta. This creates the characteristic rib notching seen on chest x-ray. The percent increase in flow in the descending thoracic aorta is directly related to the degree of stenosis. Thus, it serves as an indicator of the degree of hemodynamic compromise.

Intracardiac Shunts

Intracardiac shunts are a hallmark of congenital heart disease. In the pediatric realm, atrial septal defects (ASD) represent 1 in 1,500 live births. Most adults who present to a physician with an undiagnosed congenital heart disease do so with an ASD. The management of these defects is dependent on two items measured in tandem – the anatomy of the defect and the physiologic repercussions. CMR is well-suited for the evaluation of ASD shunt anatomy and physiology. Ventricular septal defects (VSD) are the most common

congenital heart lesion and can also be visualized by CMR. Small, isolated ventricular septal defects often close in the pediatric years without intervention and are not present in adulthood. In the developed world, patients with larger VSDs are typically identified early and undergo corrective or palliative surgery.

In-plane PCMR imaging can allow for identification of the defect and visualization of left to right or right to left shunting. Compared with measurements obtained during cardiac catheterization, thru plane PCMR of flow in the proximal great vessels can reliably assess the magnitude of intracardiac left-to-right shunting [52].

Atrial Septal Defects

Secundum atrial septal defects represent the most common type of atrial level defect. They are slightly more common in females and result from defective growth of the septum secundum or excessive resorption of the septum primum. This defect, even in late adulthood, is predominantly left to right in shunt flow as the pulmonary bed has a high capacitance. The presence of right to left shunting is fairly rare even with large defects, but when present suggests pulmonary arterial hypertension.

PCMR can be used to quantify the shunt fraction in patients with this defect by calculating the ratio of pulmonary to aortic flow.

$$Q_p / Q_s = (\text{Pulmonary forward flow} / \text{Aortic forward flow})$$

While Q_p/Q_s is typically a reliable measure for shunt flow there can be some pitfalls. Most notable is significant pulmonary or aortic regurgitation as this negative flow in proximal great vessels would increase the forward flow of the next cardiac cycle increasing the cardiac output and thus altering the Q_p/Q_s calculation. The size of the shunt could be incorrectly increased or decreased. Theoretically, small defects would gain unnecessary importance in the presence of significant pulmonary regurgitation, and larger shunts would appear diminished in the presence of significant aortic regurgitation. Another concern is when the shunt ratio is low (below 1.3) as there is no clear threshold delineating shunt presence from absence by PCMR. Hence while Q_p/Q_s analysis is important in understanding the hemodynamic implications of the shunt; it should not be used in isolation. A thorough interrogation of the atrial septum is required to rule out small secundum defects that appear insignificant by Q_p/Q_s calculation.

Sinus venosus ASDs occur in two forms – inferior and superior. Superior sinus venosus defects are the more common of the two and arise at SVC/RA junction superior to the fossa ovalis. Additionally, there is a significant association of partial anomalous return of the right superior pulmonary vein into the superior vena cava. This leads to an increase in

the degree of left to right shunting as compared to secundum defects. PCMR can be used to quantify the degree of shunting as described for secundum defects above. PCMR, specifically in-plane velocity mapping, can also be used to identify anomalous pulmonary vein flow. This is particularly important as PCMR can reliably detect and quantify these lesions even when other imaging modalities have not readily identified the defect. Inferior sinus venosus defects are much less common and are located at the junction of the right atrium and IVC and is associated with anomalous right inferior pulmonary vein.

Ventricular Septal Defects

While large atrial septal defects rarely lead to pulmonary arterial hypertension (PAH) in the adult, an uncorrected VSD will lead to PAH and subsequent right to left shunting manifesting as a Qp/Qs to <1.

Rarely, adults may present with new symptoms of exercise intolerance as a result of a moderate VSD associated with a left-to-right shunting leading to LV dilation. Unlike ASD which result in right heart enlargement, moderate to large sized VSD will cause left sided ventricular enlargement as the LV receives the excess shunted blood back from the pulmonary circuit. In these cases, where significant pulmonary arterial hypertension has not occurred the shunt fraction will remain >1.5.

Most VSDs identified in adulthood are small restrictive defects that do not alter cardiac hemodynamics. In these cases, shunt fraction by PCMR is undetectable or negligibly increased and RV/LV stroke volumes are similar assuming the absence significant valvular heart disease.

Pulmonary Valve Disorders

Pulmonary valve disorders are typically due to congenital heart disease. Congenital pulmonary stenosis treated in the infant can result in either regurgitation or stenosis. Pulmonary valve assessment is critical in patients with Tetralogy of Fallot (TOF). TOF is the most common cyanotic heart defect and is also one of the most common indications for a congenital CMR exam. The treatment of these patients has changed dramatically with advances in surgical and medical therapy. The original repair involved closure of the ventricular septal defect and resection of muscle from the infundibular region of the right ventricular (RV) outflow tract. In many cases this still resulted in a fair degree of RV outflow obstruction due to reduced pulmonary annulus size. Surgeons compensated for this by using a transannular patch. This relieved the RV outflow tract obstruction but resulted in varying degrees of pulmonic regurgitation, often severe. While severe pulmonic regurgitation can be tolerated well for years to decades it can lead to deleterious effects on the RV and also

lead to potentially fatal arrhythmias. Thus, the question of when to replace the pulmonary valve and how to classify the degree of pulmonic regurgitation is of significant importance in the patient with repaired TOF. Though echocardiography plays a valuable role in this assessment, CMR outperforms echo in this assessment [53]. CMR and PCMR are ideally suited for the evaluation of the pulmonary valve.

Regurgitant fraction (RF) as described previously is defined as the regurgitant flow (ml/beat) divided by the forward flow (ml/beat) and is typically expressed by percentage:

$$RF = (\text{Regurgitant Flow} / \text{Forward Flow}) \times 100 \\ = [(RVSV - LVSV) / RVSV]$$

In pulmonary valve disorders mild regurgitation is classified as <20 %, moderate is 20–40 %, and severe is >40 %. Some consider 30–40 % to represent a subset of patients with moderate to severe regurgitation [53]. Patients with moderate to severe or severe pulmonary regurgitation that are those typically considered for pulmonary valve replacement when appropriate indications are met. CMR criteria for pulmonary valve replacement in *asymptomatic* patients with severe PR include development of at least two of the following criteria [54]:

- (a) RV/LV volume ratio greater than 2:1
- (b) RVEDV index >150 mL/m²
- (c) Large akinetic areas seen along RVOT
- (d) RV ejection fraction <47 %
- (e) RV end-systolic volume index >80 ml/m²
- (f) Left-to-right shunt from residual atrial or ventricular septal defects with pulmonary-to-systemic flow ratio ≥ 1.5
- (g) Severe aortic regurgitation, RF >48 %

For accurate assessment of pulmonary valve flow the imaging plane should be perpendicular to the RVOT at a level just above the pulmonary valve. In order to obtain a true perpendicular imaging plane planning should be done using two separate oblique RVOT views.

In-plane velocity encoding imaging can also be obtained in the RVOT views to help visually assess the degree of regurgitation; though it is not as accurate as through plane estimation which allows for true quantification. A high-velocity jet visualized by in-plane velocity mapping can be useful for locating the appropriate through-plane acquisition. This is particularly important when evaluating pulmonary stenosis. Through-plane flow quantification is significantly more reliable when the imaging plane transects the point of maximum velocity which is typically just downstream from the orifice of the lesion in question. The jet core can be recognized as the area of aliasing on velocity maps (black over white or white over black flow).

The peak pressure gradient across a stenotic lesion can be measured by knowing the maximum peak systolic velocity (V_{\max}) and using the modified Bernoulli equation.

$$\text{Pressure gradient (mmHg)} = 4 \times (V_{\max})^2$$

The grading of pulmonic stenosis is typically defined by either the peak velocity or peak gradient:

Degree of stenosis	Peak velocity (m/s)	Peak gradient (mmHg)
Mild	<3	<36
Moderate	3–4	36–64
Severe	>4	>64

Progression of pulmonary stenosis is rare and patients with a peak gradient below 50 mmHg typically do not progress to severe pulmonic stenosis. When pulmonary stenosis is suspected CMR imaging can provide added value. It is useful in determining the level of obstruction e.g.: infundibular, valvular, or subvalvular as well as help define any associated lesions such as pulmonary artery stenosis, intra-cardiac shunts, or coexisting pulmonary regurgitation. Asymptomatic patients with valvular PS with gradients of greater than 60 mmHg should have relief of the obstruction, most commonly by percutaneous balloon valvuloplasty.

Pulmonary Hypertension

Pulmonary hypertension is defined as an elevated mean pulmonary arterial pressure greater than 25 mmHg at rest. Pulmonary hypertension is often related to elevated left-sided pressures, leading to the diagnosis of pulmonary venous hypertension. Pulmonary arterial hypertension is diagnosed when the mean pulmonary arterial pressure is greater than 25 at rest and the left ventricular end diastole pressure or the mean pulmonary capillary wedge pressure is less than 15 mmHg. The initial work-up typically involves a thorough history/physical, echocardiography, and right heart catheterization. Further diagnostic imaging is then based upon the results of this evaluation.

While echocardiography plays the primary role as the screening tool for patients with PAH, CMR is ideally suited for assessment of the right ventricle and the proximal pulmonary arteries. Hence there has been great interest in the development of CMR and velocity flow mapping in the diagnosis and hemodynamic evaluation of pulmonary arterial hypertension. While it is difficult to use CMR alone to establish a cause for PAH, there are patients who can benefit from information provided by CMR. Patients in research trials or on therapy with PAH drugs may particularly benefit with CMR for serial re-evaluation of RV function and size. The use of PCMR has also been studied in the PAH population and has both its benefits and drawbacks [55, 56].

PCMR, particularly of the tricuspid valve, is limited in the evaluation of PAH. Unlike echocardiography where tricuspid continuous wave Doppler accurately identifies the right ventricular systolic pressure, it is not possible to do so with PCMR. This is a result of fairly rapid dispersion of multiple small jets cores that are too small to be measured either by in plane or through plane flow mapping. PCMR of the pulmonary artery can be used to track cardiac output; additionally PCMR derived flow in the main pulmonary artery has also been used to indirectly assess the hemodynamics of pulmonary hypertension. Pulmonary arterial pressures are inversely correlated with average blood velocity in the main PA. It also appears to have consistent performance across different subgroups of PAH.

PCMR also demonstrates an inhomogeneous flow profile in the pulmonary artery in patients with pulmonary hypertension. Compared to healthy controls, patients with PAH have lower peak systolic velocity and greater retrograde flow after middle to late systole. Retrograde flow observed in patients with PH is also a hemodynamic indication of severity. It is inversely proportional to pulmonary flow volume and directly proportional to pulmonary resistance and cross-sectional area of the vessel. Additionally, 3D magnetic resonance phase-contrast imaging of the main pulmonary artery is a novel tool in the assessment of PAH. Mean pulmonary pressures by 4D PCMRI have been shown to be within 3–4 mmHg of cardiac catheterization derived values [57].

Other metrics have also been studied in CMR for the assessment of pulmonary arterial hypertension. Pulmonary artery strain, acceleration volume, pressure wave velocity, amongst others has been studied with varying degrees of success [58]. The significant number of non-invasive measures many of which require a fair amount of time in calculation and post-processing makes their clinical usefulness limited. The average velocity of main pulmonary artery flow is currently the most clinically useful tool in the hemodynamic evaluation of PAH as it is fairly technically easy to obtain without the need for significant post-processing. Advantages in using an average PA velocity include the lack of assumption of a uniform PA profile which is known to be fairly inhomogeneous in PAH. However, this PA profile is typically obtained by PCMR with breath-hold sequencing which can take in the range of 15–20 s. This can be challenging in patients with pulmonary arterial hypertension particularly if they require supplemental oxygen at baseline. Current real-time non-breathhold flow imaging has not been thoroughly evaluated in this population and thus CMR derived measures are not yet capable of completely replacing right-heart catheterization in the evaluation of PAH.

Conclusion

CMR is routinely used in a variety of cardiovascular abnormalities to quantitatively measure blood velocity and

determine flow. The most widely used technique to quantify blood flow is *Phase-Contrast Magnetic Resonance (PCMR)*, also called phase velocity mapping, phase velocity encoding, quantitative flow imaging, etc. The implementation of PCMR in clinical practice requires understanding of physical principles of image generation, pulse sequences, acquisition methods and analysis. Clinical applications include valvular heart disease, congenital heart disease, vascular disease and myocardial disease.

References

- Morse OC, Singer JR. Blood velocity measurements in intact subjects. *Science*. 1970;170(3956):440–1. PubMed PMID: 5460060.
- Rittgers SE, Fei DY, Kraft KA, Fatouros PP, Kishore PR. Velocity profiles in stenosed tube models using magnetic resonance imaging. *J Biomech Eng*. 1988;110(3):180–4. PubMed.
- Oshinski JN, Ku DN, Pettigrew RI. Turbulent fluctuation velocity: the most significant determinant of signal loss in stenotic vessels. *Magn Reson Med: Off J Soc Magn Reson Med Soc Magn Reson Med*. 1995;33(2):193–9. PubMed.
- Guilfoyle DN, Gibbs P, Ordidge RJ, Mansfield P. Real-time flow measurements using echo-planar imaging. *Magn Reson Med: Off J Soc Magn Reson Med Soc Magn Reson Med*. 1991;18(1):1–8. PubMed.
- Keegan J, Gatehouse PD, Yang GZ, Firmin DN. Spiral phase velocity mapping of left and right coronary artery blood flow: correction for through-plane motion using selective fat-only excitation. *J Magn Reson Imaging*. 2004;20(6):953–60. doi:10.1002/jmri.20208. PubMed PMID: 15558551.
- Markl M, Alley MT, Pelc NJ. Balanced phase-contrast steady-state free precession (PC-SSFP): a novel technique for velocity encoding by gradient inversion. *Magn Reson Med: off J Soc Magn Reson Med Soc Magn Reson Med*. 2003;49(5):945–52. doi:10.1002/mrm.10451. PubMed.
- Spraggins TA. Wireless retrospective gating: application to cine cardiac imaging. *Magn Reson Imaging*. 1990;8(6):675–81. PubMed.
- Tang C, Blatter DD, Parker DL. Correction of partial-volume effects in phase-contrast flow measurements. *J Magn Reson Imaging*. 1995;5(2):175–80. PubMed.
- Oshinski JN, Ku DN, Mukundan Jr S, Loth F, Pettigrew RI. Determination of wall shear stress in the aorta with the use of MR phase velocity mapping. *J Magn Reson Imaging*. 1995;5(6):640–7. PubMed.
- Markl M, Chan FP, Alley MT, Wedding KL, Draney MT, Elkins CJ, Parker DW, Wicker R, Taylor CA, Herfkens RJ, Pelc NJ. Time-resolved three-dimensional phase-contrast MRI. *J Magn Reson Imaging*. 2003;17(4):499–506. doi:10.1002/jmri.10272. PubMed.
- Johnson K, Sharma P, Oshinski J. Coronary artery flow measurement using navigator echo gated phase contrast magnetic resonance velocity mapping at 3.0 T. *J Biomech*. 2008;41(3):595–602. doi:10.1016/j.jbiomech.2007.10.010. PubMed PMID: 18036532, PubMed Central PMCID: PMC2759278.
- Gu T, Korosec FR, Block WF, Fain SB, Turk Q, Lum D, Zhou Y, Grist TM, Haughton V, Mistretta CA. PC VIPR: a high-speed 3D phase-contrast method for flow quantification and high-resolution angiography. *AJNR Am J Neuroradiol*. 2005;26(4):743–9. PubMed.
- Carvalho JL, Nayak KS. Rapid quantitation of cardiovascular flow using slice-selective fourier velocity encoding with spiral readouts. *Magn Reson Med: Off J Soc Magn Reson Med Soc Magn Reson Med*. 2007;57(4):639–46. doi:10.1002/mrm.21196. PubMed.
- Dumoulin CL, Souza SP, Darrow RD, Pelc NJ, Adams WJ, Ash SA. Simultaneous acquisition of phase-contrast angiograms and stationary-tissue images with Hadamard encoding of flow-induced phase shifts. *J Magn Reson Imaging*. 1991;1(4):399–404. PubMed.
- Hope MD, Sedlic T, Dyverfeldt P. Cardiothoracic magnetic resonance flow imaging. *J Thorac Imaging*. 2013;28(4):217–30. doi:10.1097/RTI.0b013e31829192a1. PubMed.
- Markl M, Schnell S, Barker AJ. 4D flow imaging: current status to future clinical applications. *Curr Cardiol Rep*. 2014;16(5):481. doi:10.1007/s11886-014-0481-8. PubMed.
- Van Dijk P. Direct cardiac NMR imaging of heart wall and blood flow velocity. *J Comput Assist Tomogr*. 1984;8(3):429–36. PubMed.
- Delfino JG, Bhasin M, Cole R, Eisner RL, Merlino J, Leon AR, Oshinski JN. Comparison of myocardial velocities obtained with magnetic resonance phase velocity mapping and tissue Doppler imaging in normal subjects and patients with left ventricular dyssynchrony. *J Magn Reson Imaging*. 2006;24(2):304–11. doi:10.1002/jmri.20641. PubMed.
- Delfino JG, Johnson KR, Eisner RL, Eder S, Leon AR, Oshinski JN. Three-directional myocardial phase-contrast tissue velocity MR imaging with navigator-echo gating: in vivo and in vitro study. *Radiology*. 2008;246(3):917–25. doi:10.1148/radiol.2463062155. PubMed.
- Marsan NA, Westenberg JJ, Tops LF, Ypenburg C, Holman ER, Reiber JH, De Roos A, Van der Wall EE, Schalij MJ, Roelandt JR, Bax JJ. Comparison between tissue Doppler imaging and velocity-encoded magnetic resonance imaging for measurement of myocardial velocities, assessment of left ventricular dyssynchrony, and estimation of left ventricular filling pressures in patients with ischemic cardiomyopathy. *Am J Cardiol*. 2008;102(10):1366–72. doi:10.1016/j.amjcard.2008.06.064. PubMed.
- Korperich H, Gieseke J, Barth P, Hoogeveen R, Esdorn H, Peterschroder A, Meyer H, Beerbaum P. Flow volume and shunt quantification in pediatric congenital heart disease by re KOWALIK GT 1-time magnetic resonance velocity mapping: a validation study. *Circulation*. 2004;109(16):1987–93. doi:10.1161/01.CIR.0000126494.66859.A2. PubMed.
- Kowalik GT, Steeden JA, Pandya B, Odille F, Atkinson D, Taylor A, Muthurangu V. Real-time flow with fast GPU reconstruction for continuous assessment of cardiac output. *J Magn Reson Imaging*. 2012;36(6):1477–82. doi:10.1002/jmri.23736. PubMed.
- Lin HY, Bender JA, Ding Y, Chung YC, Hinton AM, Pennell ML, Whitehead KK, Raman SV, Simonetti OP. Shared velocity encoding: a method to improve the temporal resolution of phase-contrast velocity measurements. *Magn Reson Med: Off J Soc Magn Reson Med Soc Magn Reson Med*. 2012;68(3):703–10. doi:10.1002/mrm.23273. PubMed PMID: 22139889, PubMed Central PMCID: PMC3339280.
- Suever JD, Oshinski J, Rojas-Campos E, Huneycutt D, Cardarelli F, Stillman AE, Raggi P. Reproducibility of pulse wave velocity measurements with phase contrast magnetic resonance and applanation tonometry. *Int J Cardiovasc Imaging*. 2012;28(5):1141–6. doi:10.1007/s10554-011-9929-8. PubMed.
- Fielden SW, Fornwalt BK, Jerosch-Herold M, Eisner RL, Stillman AE, Oshinski JN. A new method for the determination of aortic pulse wave velocity using cross-correlation on 2D PCMR velocity data. *J Magn Reson Imaging*. 2008;27(6):1382–7. doi:10.1002/jmri.21387. PubMed.
- Gatehouse PD, Rolf MP, Graves MJ, Hofman MB, Totman J, Werner B, Quest RA, Lin Y, Von Spiczak J, Dieringer M, Firmin DN, Van Rossum A, Lombardi M, Schwitter J, Schultz-Menger J, Kilner PJ. Flow measurement by cardiovascular magnetic resonance: a multi-centre multi-vendor study of background phase offset errors that can compromise the accuracy of derived regurgitant or shunt flow measurements. *J Cardiovasc Magn Reson: Off J Soc Cardiovasc Magn Reson*. 2010;12:5. doi:10.1186/1532-429X-12-5. PubMed PMID: 20074359; PubMed Central PMCID: PMC2818657.

27. Gatehouse PD, Keegan J, Crowe LA, Masood S, Mohiaddin RH, Kreitner KF, Firmin DN. Applications of phase-contrast flow and velocity imaging in cardiovascular MRI. *Eur Radiol*. 2005;15(10):2172–84. doi:10.1007/s00330-005-2829-3. PubMed.
28. Bhatia RS, Tu JV, Lee DS, Austin PC, Fang J, Haouzi A, Gong Y, Liu PP. Outcome of heart failure with preserved ejection fraction in a population-based study. *N Engl J Med*. 2006;355:260–9.
29. Owan TE, Hodge DO, Herges RM, Jacobsen SJ, Roger VL, Redfield MM. Trends in prevalence and outcome of heart failure with preserved ejection fraction. *N Engl J Med*. 2006;355:251–9.
30. Bollache E, Redheuil A, Clement-Guinaudeau S, Defrance C, Perdrix L, Ladouceur M, Lefort M, De Cesare A, Herment A, Diebold B, Mousseaux E, Kachenoura N. Automated left ventricular diastolic function evaluation from phase-contrast cardiovascular magnetic resonance and comparison with Doppler echocardiography. *J Cardiovasc Magn Reson*. 2010;12:63.
31. Rathi VK, Doyle M, Yamrozik J, Williams RB, Caruppanan K, Truman C, Vido D, Biederman RW. Routine evaluation of left ventricular diastolic function by cardiovascular magnetic resonance: a practical approach. *J Cardiovasc Magn Reson*. 2008;10:36.
32. Hartiala JJ, Mostbeck GH, Foster E, Fujita N, Dulce MC, Chazouilleres AF, Higgins CB. Velocity-encoded cine MRI in the evaluation of left ventricular diastolic function: measurement of mitral valve and pulmonary vein flow velocities and flow volume across the mitral valve. *Am Heart J*. 1993;125:1054–66.
33. Buss SJ, Krautz B, Schnackenburg B, Abdel-Aty H, Santos MF, Andre F, Maertens MJ, Mereles D, Korosoglou G, Giannitsis E, Katus HA, Steen H. Classification of diastolic function with phase-contrast cardiac magnetic resonance imaging: validation with echocardiography and age-related reference values. *Clin Res Cardiol*. 2014;103:441–50.
34. Paelinck BP, De Roos A, Bax JJ, Bosmans JM, Van der Geest RJ, Dhondt D, Parizel PM, Vrints CJ, Lamb HJ. Feasibility of tissue magnetic resonance imaging: a pilot study in comparison with tissue Doppler imaging and invasive measurement. *J Am Coll Cardiol*. 2005;45:1109–16.
35. Gupta A, Singh Gulati G, Seth S, Sharma S. Cardiac MRI in restrictive cardiomyopathy. *Clin Radiol*. 2012;67:95–105.
36. Bertog SC, Thambidorai SK, Parakh K, Schoenhagen P, Ozduran V, Houghtaling PL, Lytle BW, Blackstone EH, Lauer MS, Klein AL. Constrictive pericarditis: etiology and cause-specific survival after pericardiectomy. *J Am Coll Cardiol*. 2004;43:1445–52.
37. Talreja DR, Edwards WD, Danielson GK, Schaff HV, Tajik AJ, Tazelaar HD, Breen JF, Oh JK. Constrictive pericarditis in 26 patients with histologically normal pericardial thickness. *Circulation*. 2003;108:1852–7.
38. O'Brien KR, Cowan BR, Jain M, Stewart RA, Kerr AJ, Young AA. MRI phase contrast velocity and flow errors in turbulent stenotic jets. *J Magn Reson Imaging*. 2008;28:210–8.
39. Sondergaard L, Stahlberg F, Thomsen C. Magnetic resonance imaging of valvular heart disease. *J Magn Reson Imaging*. 1999;10:627–38.
40. Gelfand EV, Hughes S, Hauser TH, Yeon SB, Goepfert L, Kissinger KV, Rofsky NM, Manning WJ. Severity of mitral and aortic regurgitation as assessed by cardiovascular magnetic resonance: optimizing correlation with Doppler echocardiography. *J Cardiovasc Magn Reson*. 2006;8:503–7.
41. Kondo C, Caputo GR, Semelka R, Foster E, Shimakawa A, Higgins CB. Right and left ventricular stroke volume measurements with velocity-encoded cine MR imaging: in vitro and in vivo validation. *AJR Am J Roentgenol*. 1991;157:9–16.
42. Cawley PJ, Hamilton-Craig C, Owens DS, Krieger EV, Strugnell WE, Mitsumori L, D'jang CL, Schwaegler RG, Nguyen KQ, Nguyen B, Maki JH, Otto CM. Prospective comparison of valve regurgitation quantitation by cardiac magnetic resonance imaging and transthoracic echocardiography. *Circ Cardiovasc Imaging*. 2013;6:48–57.
43. Chatzimavroudis GP, Oshinski JN, Franch RH, Pettigrew RI, Walker PG, Yoganathan AP. Quantification of the aortic regurgitant volume with magnetic resonance phase velocity mapping: a clinical investigation of the importance of imaging slice location. *J Heart Valve Dis*. 1998;7:94–101.
44. Heidenreich PA, Steffens J, Fujita N, O'Sullivan M, Caputo GR, Foster E, Higgins CB. Evaluation of mitral stenosis with velocity-encoded cine-magnetic resonance imaging. *Am J Cardiol*. 1995;75:365–9.
45. Nishimura RA, Otto CM, Bonow RO, Carabello BA, 3rd Erwin JP, Guyton RA, O'gara PT, Ruiz CE, Skubas NJ, Sorajja P, 3rd Sundt T, Thomas JD. 2014 AHA/ACC guideline for the management of patients with valvular heart disease: executive summary: a report of the American College of Cardiology/American Heart Association Task Force on Practice Guidelines. *J Am Coll Cardiol*. 2014;63:2438–88.
46. Buchner S, Debl K, Poschenrieder F, Feuerbach S, Riegger GA, Luchner A, Djavdani B. Cardiovascular magnetic resonance for direct assessment of anatomic regurgitant orifice in mitral regurgitation. *Circ Cardiovasc Imaging*. 2008;1:148–55.
47. Chatzimavroudis GP, Oshinski JN, Pettigrew RI, Walker PG, Franch RH, Yoganathan AP. Quantification of mitral regurgitation with MR phase-velocity mapping using a control volume method. *J Magn Reson Imaging*. 1998;8:577–82.
48. Botnar R, Nagel E, Scheidegger MB, Pedersen EM, Hess O, Boesiger P. Assessment of prosthetic aortic valve performance by magnetic resonance velocity imaging. *MAGMA*. 2000;10:18–26.
49. Ribeiro HB, Le Ven F, Larose E, Dahou A, Nombela-Franco L, Urena M, Allende R, Amat-Santos I, Ricipito Mde L, Thebault C, Clavel MA, Delarochelliere R, Doyle D, Dumont E, Dumesnil JG, Pibarot P, Rodes-Cabau J. Cardiac magnetic resonance versus transthoracic echocardiography for the assessment and quantification of aortic regurgitation in patients undergoing transcatheter aortic valve implantation. *Heart*. 2014;100:1924–32.
50. Oshinski JN, Parks WJ, Markou CP, Bergman HL, Larson BE, Ku DN, Mukundan Jr S, Pettigrew RI. Improved measurement of pressure gradients in aortic coarctation by magnetic resonance imaging. *J Am Coll Cardiol*. 1996;28:1818–26.
51. Warnes CA. The adult with congenital heart disease: born to be bad? *J Am Coll Cardiol*. 2005;46(1):1–8.
52. Rajiah P, Kanne JP. Cardiac MRI: part 1, cardiovascular shunts. *AJR*. 2011;197(4):W603–20.
53. Mercer-Rosa L, Yang W, Kutty S, Rychik J, Fogel M, Goldmuntz E. Quantifying pulmonary regurgitation and right ventricular function in surgically repaired tetralogy of fallot. A comparative analysis of echocardiography and magnetic resonance imaging. *Circ Cardiovasc Imaging*. 2012;5(5):637–43.
54. Geva T. Repaired tetralogy of Fallot: the roles of cardiovascular magnetic resonance in evaluating pathophysiology and for pulmonary valve replacement decision support. *J Cardiovasc Magn Reson*. 2011;13:9.
55. Kondo C, Caputo GR, Masui T, Foster E, O'Sullivan M, Stulberg MS, Golden J, Chatterjee K, Higgins CB. Pulmonary hypertension: pulmonary flow quantification and flow profile analysis with velocity-encoded cine MR imaging. *Radiology*. 1992;183(3):751–8.
56. Sanz J, Kuschnir P, Rius T, Salguero R, Sulica R, Einstein AJ, Dellagrottagle S, Fuster V, Rajagopalan S, Poon M. Pulmonary arterial hypertension: noninvasive detection with phase-contrast MR imaging. *Radiology*. 2007;243:70–7.
57. Reiter G, Reiter U, Kovacs G, Kainz B, Schmidt K, Maier R, Olschewski H, Rienmueller R. Magnetic resonance-derived 3-dimensional blood flow patterns in the main pulmonary artery as a marker of pulmonary hypertension and a measure of elevated mean pulmonary arterial pressure. *Circ Cardiovasc Imaging*. 2008;1:23–30.
58. Bradlow WM, Simon J, Gibbs R, Mohiaddin RH. Cardiovascular magnetic resonance in pulmonary hypertension. *J Cardiovasc Magn Reson*. 2012;14(1):1–12.

Mehmet Akçakaya and Reza Nezafat

Abstract

Coronary artery disease remains the leading cause of death in the United States, despite significant efforts in prevention and treatment. Coronary artery magnetic resonance imaging is a non-invasive diagnosis technique among patients with suspected anomalous coronary artery disease and coronary artery aneurysms. In this chapter, we will review the imaging strategies for magnetic resonance imaging of coronary arteries and veins. We review techniques for compensating the near-constant motion of the coronaries during both the respiratory and the cardiac cycles, for improving signal-to-noise ratio and contrast-to-noise ratio, advanced methods for accelerated imaging and high-field imaging, and coronary vein imaging.

Keywords

Coronary artery disease • Coronary magnetic resonance imaging • Respiratory motion • Cardiac motion • Motion compensation • Accelerated imaging • High-field imaging • Coronary vein imaging • T_1 contrast • T_2 contrast

Introduction

Coronary artery disease (CAD) remains the leading cause of death in the United States, accounting for one of every six deaths, despite significant efforts in prevention and treatment [1]. Each year approximately 635,000 Americans are estimated to have a new myocardial infarction, and nearly 280,000 to have a recurrent infarction. Furthermore, an additional estimated 150,000 will have their first silent myocardial infarction [1]. The current clinical “gold standard” for the diagnosis of significant (≥ 50 % diameter stenosis) CAD is catheter-based invasive x-ray angiography. More than a million catheter based x-ray coronary angiograms are performed annually in the United States [1], with a higher volume in Europe. However, a recent study of nearly

400,000 patients referred for x-ray coronary angiography showed that only less than 40 % had obstructive CAD, a relatively low yield for an invasive test [2]. Many of these patients without significant CAD were exposed to the potential risks and complications of an invasive test that includes ionizing radiation and iodinated contrast [3, 4]. Furthermore, selected high risk populations such as those patients with aortic valve stenosis, the incidence of subclinical stroke associated with retrograde catheter crossing of the stenotic valve may exceed 20 % [5]. In order to relieve symptoms, percutaneous coronary intervention in single vessel disease is commonly performed, but the greatest impact on mortality occurs with mechanical intervention among patients with left main (LM) and multivessel CAD. Thus, alternative non-invasive imaging modalities, which allow direct visualization of the proximal/mid native coronary vessels for the accurate identification/exclusion of LM/multivessel CAD, are desirable.

Coronary artery magnetic resonance imaging (MRI) has evolved as a non-invasive diagnosis alternative to

M. Akçakaya, PhD • R. Nezafat, PhD (✉)
Department of Medicine, Beth Israel Deaconess Medical Center,
Harvard Medical School, Boston, MA, USA
e-mail: rnezafat@bidmc.harvard.edu

catheter based x-ray angiography among patients with suspected anomalous coronary artery disease and coronary artery aneurysms. Over the past two decades, it has reached sufficient maturity to obviate the need for catheter based x-ray angiography in the discrimination of patients with multivessel disease. Though, coronary multi-detector computed tomography (MDCT) offers superior isotropic spatial resolution and more rapid imaging, coronary MRI, is advantageous to MDCT in several respects, including the absence of ionizing radiation or iodinated contrast, which facilitates follow-up scanning, as well as smaller artifacts related to epicardial calcium. Due to the advantages of coronary MRI and its diagnostic accuracy, it is recommended and deemed appropriate in patients suspected of anomalous coronary artery disease by both the American College of Cardiology and American Heart Association [6, 7]. In this chapter, we will review the imaging strategies for magnetic resonance imaging of coronary arteries and veins.

Coronary Artery MRI

Imaging Sequences

The early approaches to coronary MRI have been based on 2D breath-hold electrocardiogram (ECG) triggered segmented sequences, described nearly two decades ago [8, 9]. Over the past two decades, 3D free-breathing approaches have replaced these sequences, since they enable greater anatomical coverage and higher signal level. Either targeted or whole-heart coverage of the coronary anatomy is possible in 3D coronary MRI. In the targeted technique [10], a double-oblique 3D volume aligned along the major axis of the left or right coronary artery is acquired [11–13]. For the visualization of the left main (LM), left anterior descending (LAD) and left circumflex (LCX) coronary arteries, a 3D volume is interactively prescribed in the axial plane centered about the LM coronary artery, typically with a 30-mm slab with 20 overlapping using a segmented acquisition (Fig. 17.1) [13, 14]. For imaging of the RCA, the imaging plane passing through the proximal, mid and distal coordinates of the RCA is identified and the targeted 3D coronary sequence is repeated in this orientation. In whole-heart coronary MRI [15–29], in a manner analogous to coronary MDCT, an axial (or coronal) 3D volume encompassing the entire heart is sampled in a single acquisition. This facilitates imaging slab prescription and provides more complete anatomical coverage, positioned ~1 cm above the LM and extending to the inferior cardiac border. However, based on single-center trials up to date, it has not been shown to be superior to the targeted approach for CAD assessment (Table 17.1).

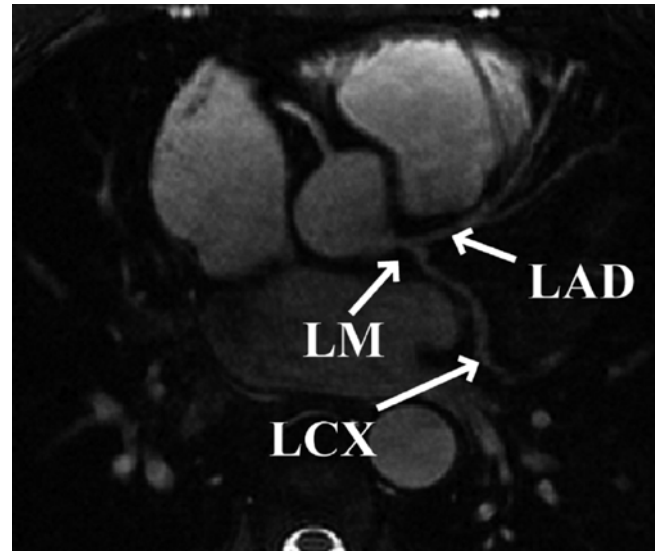


Fig. 17.1 Reformatted coronary MRI of the left coronary system acquired using a targeted free breathing acquisition with real time navigator gating and tracking in a healthy adult subject. The transverse acquisition displays the left main (LM), left anterior descending (LAD) and the left circumflex (LCX) coronary arteries. The in-plane spatial resolution is $0.7 \times 1.0 \text{ mm}^2$

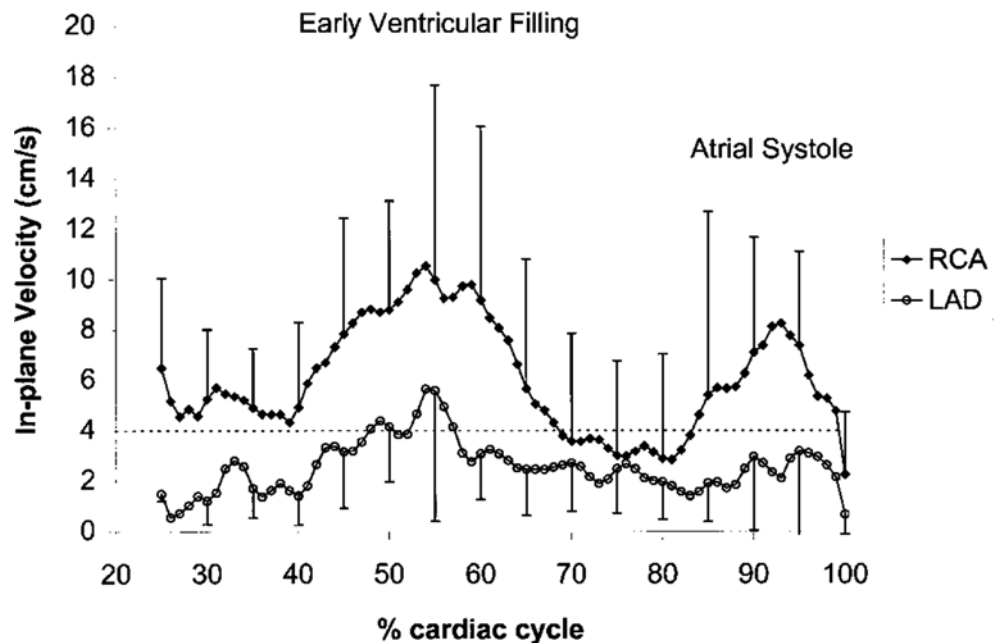
Both gradient echo (GRE) and steady state free precession (SSFP) sequences [38] have been used for targeted thin-slab 3D acquisitions. Thin-slab 3D targeted acquisition with a GRE sequence results in more homogenous blood pool signal, but is heavily dependent on the inflow of unsaturated protons [39]. If coronary flow is slow or stagnant, saturation effects will cause a local signal loss that is often relatively exaggerated as compared with the lumen stenosis. Compared to GRE sequences, SSFP provides intrinsically higher signal due to its balanced gradients and improved blood-myocardium contrast due to its T_1/T_2 weighting [40] with reduced sensitivity to inflow effects. Both GRE and SSFP have been used for targeted 3D coronary MRI, where both have shown similar diagnostic accuracy for CAD [40, 41]. For whole-heart non-contrast coronary MRI at 1.5 T, SSFP appears to be the sequence of choice due to its higher blood-myocardium contrast and superior inflow properties [39].

Even with these technical advances, clinical acceptance of coronary MRI remains challenging due to coronary artery motion, long scan times, limited spatial resolution, suboptimal signal-to-noise-ratio (SNR) and blood-myocardium contrast-to-noise-ratio (CNR). The technical challenges in coronary artery MRI is different than other cardiovascular magnetic resonance (CMR) acquisitions due to unique issues including: (1) small caliber of coronary arteries (3–6 mm diameter), (2) high level of tortuosity, (3) near-constant motion during both the respiratory and the cardiac cycles, and (4) surrounding signal from adjacent epicardial fat and myocardium.

Table 17.1 Diagnostic accuracy of ECG-triggered, free-breathing, targeted 3D and whole-heart coronary MRI with and without contrast agents

Study	Single-center/multi-center	# patients	Sensitivity (%)	Specificity (%)
<i>Non-contrast 3D targeted coronary MRI</i>				
Kim et al. [10]	Multi-center	109	88–98	32–52
Bunce et al. [30]	Single-center	46	50–89	72–100
Sommer et al. [31]	Single-center	107	74–88	63–91
Bogaert et al. [32]	Single-center	21	85–92	50–83
<i>Non-contrast 3D whole-heart coronary MRI</i>				
Jahnke et al. [33]	Single-center	21	79	91
Sakuma et al. [27]	Single-center	39	82	91
Sakuma et al. [26]	Single-center	131	82	90
Pouleur et al. [34]	Single-center	77	100	72
Kato et al. [35]	Multi-center	138	88	72
<i>Contrast enhanced 3D whole-heart coronary MRI</i>				
Yang et al. [36]	Single-center	62	94	82
Yang et al. [37]	Multi-center	272	91	80

Fig. 17.2 Graph depicting the in-plane motion of the right coronary artery (RCA) and the left anterior descending (LAD) coronary artery during the cardiac cycle. The x-axis displays time as a percentage of the R-R interval. Note the image quality of the RCA cross section improves when the acquisition is performed during mid-diastole as compared to early diastole (Reproduced from [47], with permission of Wiley)



Cardiac Motion

Bulk epicardial motion is a major impediment to coronary artery and vein MRI and can be separated into motion related to direct cardiac contraction/relaxation during the cardiac cycle and that due to superimposed diaphragmatic and chest wall motion from respiration. The magnitude of motion from each component may greatly exceed the coronary artery diameter, thereby leading to blurring artifacts in the absence of motion-suppressive methods.

To compensate for bulk cardiac motion, accurate electrocardiographic (ECG) synchronization with QRS detection is required, and vector ECG approaches are preferred [42].

Coronary motion has been characterized using both catheter based x-ray angiography [43, 44] and CMR [45–47] methods during the cardiac cycle. Both the proximal/mid right coronary artery (RCA) and the left anterior descending (LAD) coronary artery display a triphasic pattern (Fig. 17.2), with the magnitude of in-plane motion nearly twice as great for the RCA. Coronary motion is minimal during isovolumic relaxation, approximately 350–400 ms after the R wave, and again at mid-diastole (immediately prior to atrial systole). The LAD diastasis is longer than the RCA, and begins earlier in the cardiac cycle [12]. The duration of the mid-diastolic diastasis period is inversely related to the heart rate and dictates the coronary data acquisition interval.

For coronary artery MRI, the acquisition interval is adapted to the heart rate/diastasis interval using a patient-specific diastasis period. This can be readily identified by the acquisition of high temporal resolution cine dataset orthogonal to the long axis of the proximal/mid RCA and of the LAD. Semi-automated tools to identify the optimal data acquisition window have also been proposed [48, 49]. For patients with a heart rate of 60–70/min, a coronary artery MRI acquisition duration of ~80 ms during each cardiac cycle results in improved image quality [14]. The duration must be further abbreviated (e.g., <50 ms) at higher heart rates, while with bradycardia, the acquisition interval can be expanded to 120 ms or longer. The use of patient-specific acquisition windows serves to reduce overall scan time [50, 51]. Image degradation can be caused by sinus arrhythmia, leading to heart rate variability, which is common especially in younger adults [52]. An adaptive real-time arrhythmia rejection algorithm can correct for heart rate variability, and improves coronary artery MRI quality [49].

Respiratory Motion

The second major challenge for coronary artery MRI is compensation for respiratory motion. With inspiration, the diaphragm may descend up to 30 mm and the chest wall expands – resulting in an inferior displacement and anterior rotation of the heart [53]. Several approaches have been proposed to minimize respiratory motion artifacts, including sustained end-expiratory breath-holding, chest wall bellows, respiratory navigators, fat navigators and self-gating methods.

Prolonged (15–20 s) end-expiratory breath holds were utilized to suppress respiratory motion in initial 2D coronary artery MRI methods [54]. Breath holding offers the advantage of relative ease of implementation in compliant subjects, but it limits the temporal acquisition window, image spatial resolution and anatomic coverage. Additionally, many patients are unable to adequately sustain a breath-hold. Furthermore, slice registration errors (due to variability in end-expiratory diaphragmatic position) are very common as is diaphragmatic drift during the breath hold [54–57] and may occur in up to half of patients [12]. Supplemental oxygen and hyperventilation (separately or in combination) can be utilized to prolong the breath-hold duration [56, 57], but these methods may not be appropriate for all patients, and both diaphragmatic drift and slice registration errors persist [57].

Diaphragmatic respiratory navigators, first proposed by Ehman [58] for abdominal MR imaging, enable free-breathing acquisitions without the stringent time constraints and patient cooperation requirements imposed by multiple breath holds, and thus offer superior spatial resolution opportunities. Although the specifics of navigator implementation varies among CMR vendors, in the ideal implementation, the naviga-

tor can be positioned at any interface that accurately reflects respiratory motion, including the dome of the right hemidiaphragm (Fig. 17.3) [59, 60], the left hemidiaphragm, the anterior chest wall, the anterior free wall of the left ventricle [60, 61], or even through the coronary artery of interest. The navigator should not cause an image artifact and should be temporally located *immediately* preceding the imaging portion of the sequence with data accepted (used for image reconstruction) only when the navigator indicates that the “interface” (e.g., diaphragm position) falls within a user-defined window. The dome of the right hemidiaphragm has become the preferred location [27, 38–40] due to the simplicity and ease in set-up, where the motion of the right hemidiaphragm in the superior-inferior direction can be tracked. From CMR studies of cardiac border position during the respiratory cycle, Wang observed that at end-expiration, the ratio between cardiac and diaphragmatic displacement is ~0.6 for the RCA and ~0.7 for the left coronary artery [53] though there is variability among subjects [20, 42, 43] and position (e.g., supine vs. prone imaging) [23]. This rule-of-thumb offers the opportunity for prospective navigator gating with real-time tracking [60, 62], in which the position of the interface (diaphragm) is determined, and the slice position coordinates can then be shifted in real-time (before the data collection) to appropriately adjust spatial coordinates [63]. This technique allows for the use of wider gating windows and increased navigator efficiency, leading to shorter scan times. Real-time tracking implementation with a 5-mm diaphragmatic gating window is often used resulting in a navigator efficiency approaching 50 % [62]. Coronary artery MRI with real-time navigator tracking has been shown to minimize registration errors (as compared with breath holding) while maintaining or improving the image quality [12, 62]. It should also be noted that the quality of coronary artery MRI is improved by using consistent ECG timing as well as respiratory suppression methodology for both the coronary localizing/motion scout images and for the coronary artery MRI acquisitions [51].

A number of refinements to the navigator method have been proposed. While a “fixed” superior-inferior correction factor of 0.6 (with no left-right or anterior-posterior correction) [44, 45] is commonly used, significant individual variability has been observed [55]. A subject-specific tracking factor has been advocated and shown to improve the quality of coronary images when the subject-specific tracking factor differs from 0.6 [64]. The use of multiple navigator locations, use of leading and trailing navigators, and navigators that provide guidance for affine transformations, i.e. 3D translations and rotations, of the slice prescription for each heart-beat have been proposed [23, 65–67]. The affine transformation permits use of larger navigator windows, and hence higher navigator efficiency. It has also been proposed that the heart itself be tracked [20, 68–70]. For instance, methods that track the epicardial fat to detect the heart position have been proposed

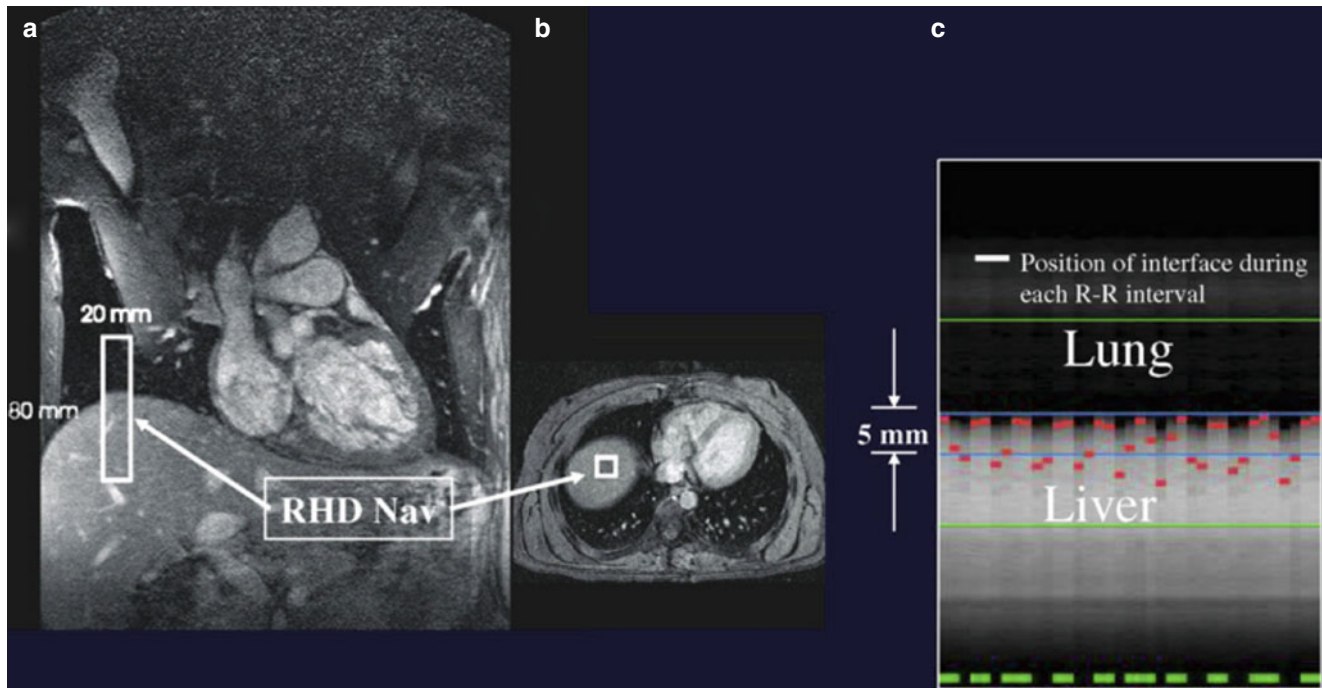


Fig. 17.3 Positioning and utility of the respiratory navigator. Coronal (a) and axial (b) thoracic images for placing the navigator at the dome of the right hemidiaphragm (RHD NAV). (c) Respiratory motion of the lung-diaphragm interface is recorded using a 2-D selective navigator with the lung (superior) and liver (inferior) interface. In this example, the maximum excursion between end-inspiration and end-expiration is

~11 mm. The position of the lung-liver interface at each R-R interval is indicated by the *broken line* in the middle of (c). Data are only accepted if the lung-liver interface is within the acceptance window of 5 mm. Data acquired with the navigator outside of the window are rejected. Accepted data is indicated by the *broken green line* at the bottom of (c)

[71–74]. In addition to navigator gating, respiratory self-gating techniques have been investigated, a method that derive the respiratory position of the heart from the imaging data itself [19, 20, 28, 68, 69, 75, 76], thus avoiding certain issues with navigators such as subject-dependent tracking factor [77] and hysteresis effects [78]. Navigator with fixed scan efficiency has also been recently introduced which results in imaging at a fixed scan time [79]. Novel k-space trajectories and various image reconstruction based method such as cross-correlation of low resolution images have also been proposed for respiratory motion compensation [28, 80–82].

SNR and CNR

The coronary arteries are surrounded by epicardial fat and the myocardium. Thus contrast-to-noise ratio (CNR) can be improved by suppressing the fat and myocardium signal surrounding the coronary arteries. Frequency (spectrally) selective pre-pulses are applied to saturate signal from fat tissue, thereby allowing visualization of the underlying coronary arteries [54, 83]. To differentiate myocardium and the coronary lumen, endogenous contrast preparation techniques are commonly utilized [14, 83–86]. Two methods that can enhance the contrast between the coronary lumen and under-

lying myocardium are T_2 preparation pre-pulses [14, 84, 85, 87] and magnetization transfer contrast [83, 86]. The former is often used for coronary artery MRI as it also suppresses deoxygenated venous blood, while the latter is used for coronary *vein* MRI [57].

The limited signal-to-noise ratio (SNR) in coronary artery MRI, along with constraints on acquisition duration, restricts the spatial resolution in the acquisition. Spatial resolution requirements for clinical coronary artery MRI depend on whether the goal is to identify the origin and proximal course of the coronary artery (e.g., issues of anomalous coronary disease), or whether the goal is to identify focal stenoses in the proximal and middle segments.

The SNR of coronary MRI can be enhanced by higher B_0 field strength [88], larger 3D spatial coverage [29], vasodilator administration, and contrast agents based on gadolinium chelates. The intrinsically higher SNR associated with higher magnetic field strengths may be advantageous for non-contrast coronary MRI. However, additional considerations, such as higher B_1 and B_0 inhomogeneity and higher specific absorption rate, affect certain aspects of coronary MRI, such as the diminished utility of SSFP sequences at 3 T due to increased field inhomogeneity and high specific absorption rate. Hence, GRE sequences, which are less sensitive to field inhomogeneity, as well as localized shimming [89] and

contrast preparation techniques that deal with B_1 inhomogeneities [87, 90] have been advocated.

The increased coverage of whole-heart coronary MRI can potentially improve the SNR but this also increases the scan time. Thus, the SNR gain is often counteracted by the need for accelerated imaging to reduce scan time, which carries an SNR penalty. Despite this penalty, excellent image quality of whole-heart coronary MRI has been shown in several studies [26, 29], and an example from a single-center study [26] is depicted in Fig. 17.4. Furthermore, whole-heart imaging suffers from saturation effects of the inflowing blood magnetization [39]. Another technique to improve SNR in coronary MRI is the administra-

tion of vasodilators, since the increased coronary blood flow secondary to vasodilatation reduces the inflow saturation effects [91, 92]. Figure 17.5 demonstrates impact of sublingual isosorbide dinitrate administration on 3D targeted coronary MRI up to 30 min after drug administration in terms of subjective image quality and objective SNR and vessel sharpness.

The administration of exogenous gadolinium contrast agents (both extracellular [16, 93, 94] and intravascular [95–100]) that shorten the T_1 relaxation time provides an alternative flow-independent approach to improve SNR and CNR. Since conventional extracellular contrast agents, e.g. gadopentetate dimeglumine (Gd-DTPA), diffuse rapidly into

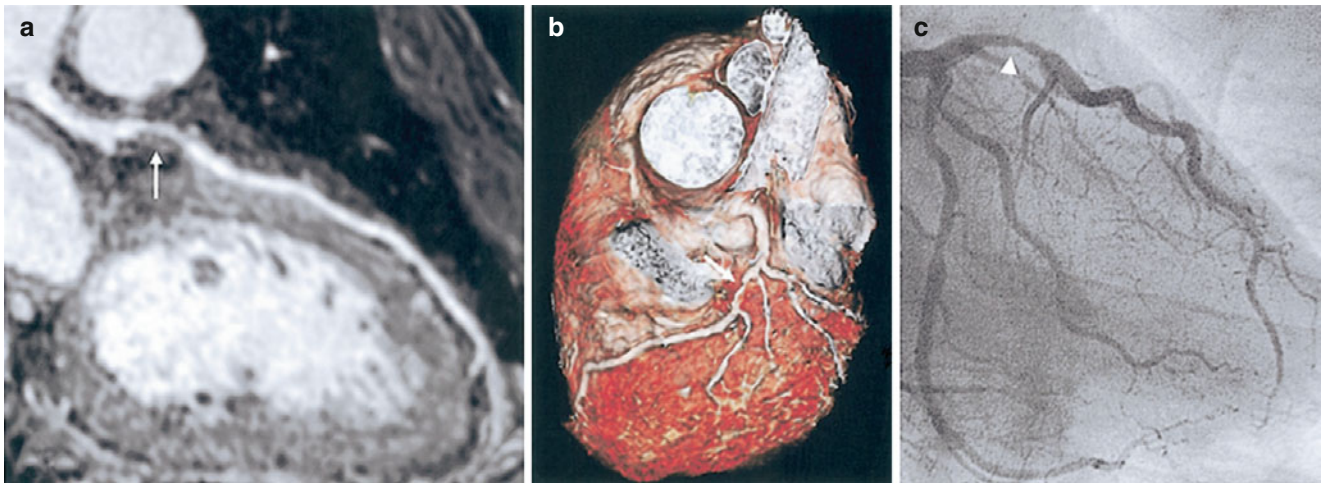


Fig. 17.4 Whole-heart coronary MRI. (a) A stenosis in LAD is visualized using a curved multiplanar reconstruction (*white arrow*). (b) A three-dimensional view of LAD with stenosis is depicted in the volume-

rendered image. (c) X-ray coronary angiography confirms proximal LAD stenosis (*arrowhead*) (Adapted from Ref. [26], with permission of Elsevier)

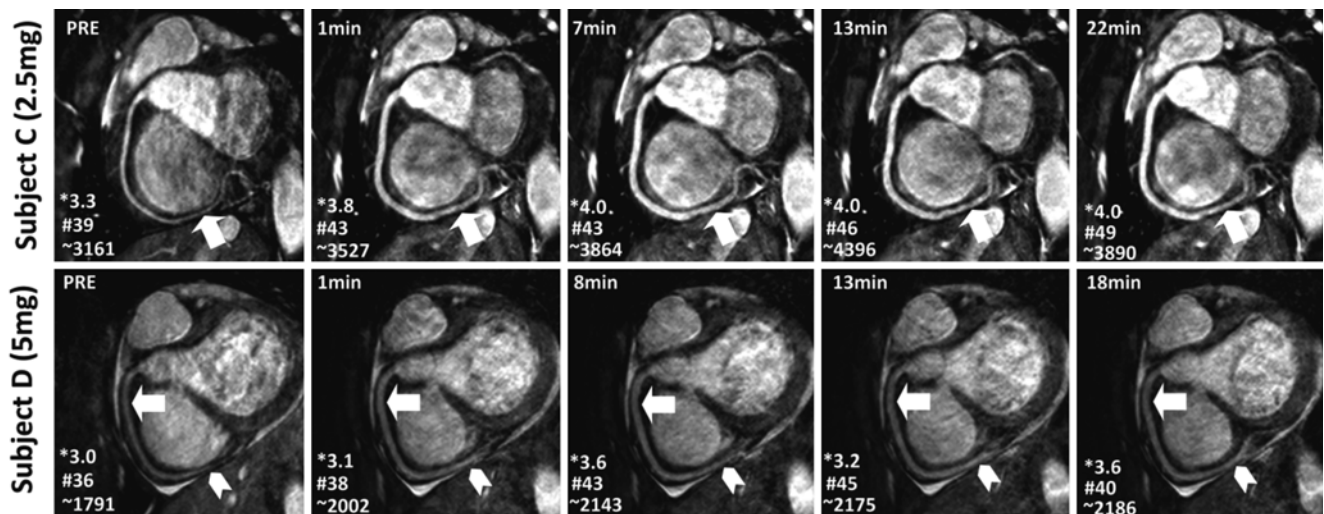


Fig. 17.5 Reformatted images from a targeted 3D coronary MRI of the RCA acquired before and after sublingual isosorbide dinitrate administration on two healthy subjects using a 3D free-breathing SSFP with 2.5 mg (*top row*) and 5 mg doses (*bottom row*) as a function of

time. Improved RCA vasodilation and signal enhancement can be observed in all images post-isosorbide dinitrate (*arrows in top and bottom row*). The enhanced SNR with isosorbide dinitrate also allows for improved visualization of the distal segments

the interstitial space, early contrast-enhanced coronary MRI studies focused on breath-hold technique to take advantage of the first-passage of these agents [94]. However, both the breath-hold and first-pass aspects of such approaches limit the spatial resolution and is unsuitable for whole-heart coronary acquisitions [29]. Following the availability of a high relaxivity extracellular contrast agent, gadobenate dimeglumine (Gd-BOPTA; MultiHance; Bracco Imaging SpA, Milan, Italy), improved whole-heart coronary MRI at 3 T was shown to be feasible using a T_1 -weighted inversion recovery (IR) GRE sequence with a slow infusion of this Gd-BOPTA [16]. An example of contrast-enhanced whole-heart coronary MR image from a CAD patient and the corresponding x-ray angiogram are shown in Fig. 17.6, demonstrating agreement between two modalities in detecting significant stenosis. In a single center trial, 3 T whole-heart coronary MRA with slow infusion of Gd-BOPTA had 93 % sensitivity, 89 % specificity and 90 % accuracy for detecting >50 % diameter stenosis on a per-vessel basis (and 94 %, 82 % and 89 % on a per-patient basis) when compared with x-ray angiography [36]. A bolus infusion of Gd-BOPTA for coronary MRI has also been reported [101], and an example depicted in Fig. 17.7 shows a clear visualization of the three major coronary vessels in the reformatted and 3D volume rendered images. Furthermore, the bolus contrast injection method is advantageous in multiple ways, since it simplifies the initiation time of coronary MRI acquisition compared to slow infusion, and it is compatible with late gadolinium enhancement imaging, which enables the assessment of coronary artery stenosis and myocardium viability using a single bolus contrast injection.

Coronary MRI: Advanced Methods

The sensitivity and specificity of coronary MRI for detection of CAD remain moderate based on single-center [26, 27, 30–34, 36] (Table 17.1) and multi-center [10, 35, 37] studies, despite the tremendous technical improvements in the last two decades. Coronary motion, SNR and CNR remain as major impediments to coronary MRI, and these issues need to be addressed before clinical prime time for coronary MRI. To overcome some of these hurdles, several CMR centers continue with the development and implementation of novel approaches, including non-Cartesian acquisitions, accelerated imaging techniques, coronary vein MRI and higher field imaging.

Non-Cartesian acquisitions provide efficient k-space traversals that lead to incoherent or less visually significant artifacts. Thus, alternative non-Cartesian k-space acquisitions, including spiral and radial coronary MRI have received attention. The use of spiral coronary artery MRI was first reported by Meyer and colleagues [102]. Spiral acquisitions are advantageous to Cartesian acquisitions in several

respects, including a more efficient filling of k-space, enhanced SNR [40, 103], and favorable flow properties. However, there are also drawbacks associated with spiral trajectories, such as increased sensitivity to magnetic field inhomogeneity and longer image reconstruction. Interleaved spiral imaging is typically used due to reduced artifacts [102–105], though a single-shot k-space trajectory can also be employed. Both breath-hold (2D) and free-breathing/navigator-gated acquisitions can be performed with spiral coronary imaging [40, 95, 103, 105]. Compared to conventional Cartesian approaches, single spiral acquisitions (per R-R interval) afford a near threefold improvement in SNR [40, 103]. Hence, acquiring two spirals during each R-R interval will halve the acquisition time, while maintaining superior SNR (vs. Cartesian acquisition) and CNR. Variable density spirals have also shown benefit [82].

Radial trajectories also enable more rapid acquisitions, while decreasing sensitivity to motion. Data in healthy subjects appear promising [40, 106–108] and may be particularly beneficial for coronary wall imaging [70, 109, 110].

Parallel imaging techniques such as generalized autocalibrating partially parallel acquisition (GRAPPA) [111] or sensitivity encoding (SENSE) [112] are the most commonly used clinical acceleration technique for coronary MRI [16, 36, 100, 101]. Resultant acceleration rates of up to twofold while using 5–16 element cardiac-coil arrays, and up-to fourfold acceleration rate using 32-channel coils have been achieved [24, 113]. Currently, parallel imaging is considered the state-of-the-art accelerated imaging technique for whole-heart coronary MRI, and is commonly utilized for clinical imaging.

In addition to the non-Cartesian trajectories [114] described previously, compressed sensing (CS) has emerged as an alternative acceleration technique that exploits the sparsity of the image in a transform domain [115, 116]. CS also requires an incoherent undersampling pattern, which can be achieved by random undersampling of k-space data in the k_y - k_z plane for three-dimensional (3D) Cartesian acquisitions. In high-resolution coronary MRI, an advanced CS-based reconstruction strategy was shown to provide reconstructions with reduced blurring compared to conventional CS techniques [117], and was successfully utilized in contrast-enhanced whole-heart coronary MRI [118]. More recently, for highly-accelerated sub-millimeter resolution whole-heart coronary MRI, CS was shown to outperform parallel imaging at sixfold accelerated imaging in a head-to-head comparison [119], with example images depicted in Fig. 17.8. CS can also be used in conjunction with non-Cartesian imaging, such as with spiral acquisitions to enable whole heart acquisitions in a single prolonged breath-hold [81] or with 3D radial trajectories [108].

Coronary MRI at high fields has been an active area of research, due to potential benefits in SNR and CNR. SNR is directly related to field strength (B_0), and thus 3 T imaging

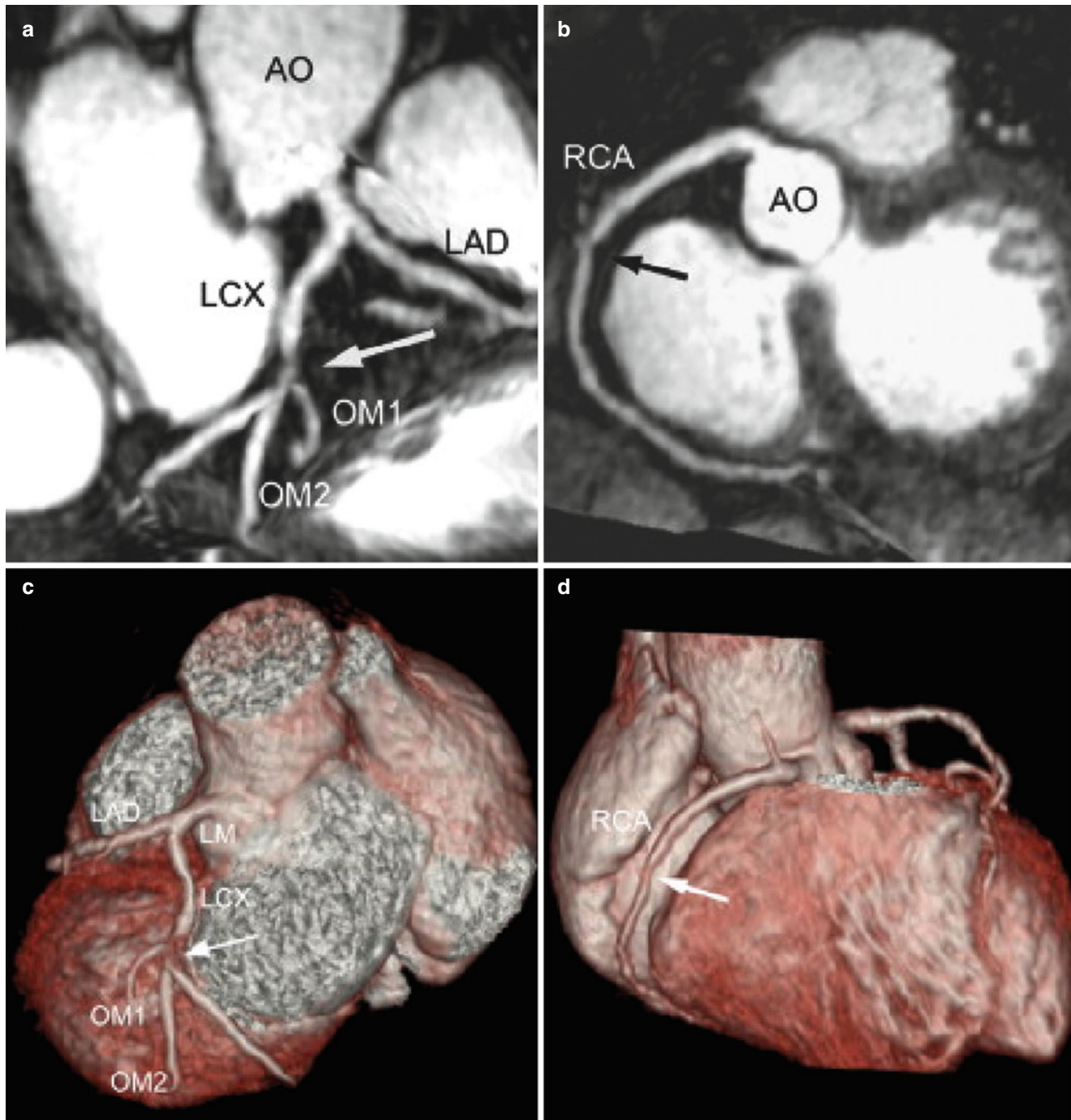


Fig. 17.6 Contrast-enhanced whole-heart 3D coronary MRI with a slow infusion of Gd-BOPTA contrast agent in a patient with atypical chest pain. (**a, b**) Contrast-enhanced whole-heart maximum intensity projection images show a significant stenosis in the proximal LCX and a non-significant stenosis in the middle RCA (*arrows*), respectively.

(**c, d**) The volume-rendered images have the same findings in LCX and RCA (*arrows*). These were consistent with the findings (*arrows*) of conventional coronary angiography (**e, f**). AO aorta, OM obtuse marginal artery (Adapted from Ref. [36], with permission of Elsevier)

would offer the opportunity to double SNR compared to 1.5 T systems [120]. While the vast majority of coronary artery MRI investigations have been performed on 1.5 T systems, clinical 3 T systems are increasingly available and becoming the platform of choice for testing of many advances.

Technical challenges associated with 3 T coronary MRI include increased susceptibility artifacts, field inhomogeneities [87], reduced T_2^* [121, 122], increased specific absorption rate (SAR), T_1 prolongation and the amplified magnetohydrodynamic effect [42]. At 3 T, free breathing

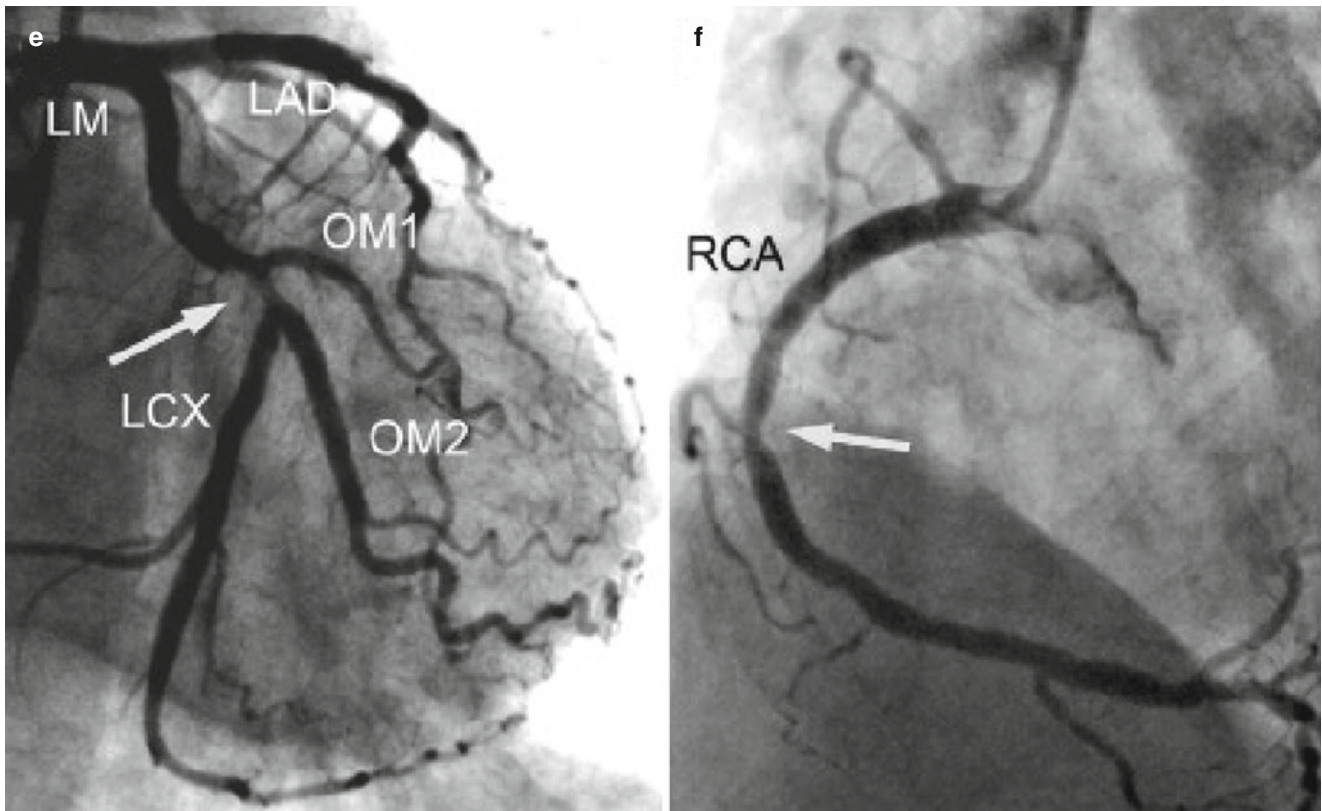


Fig. 17.6 (continued)

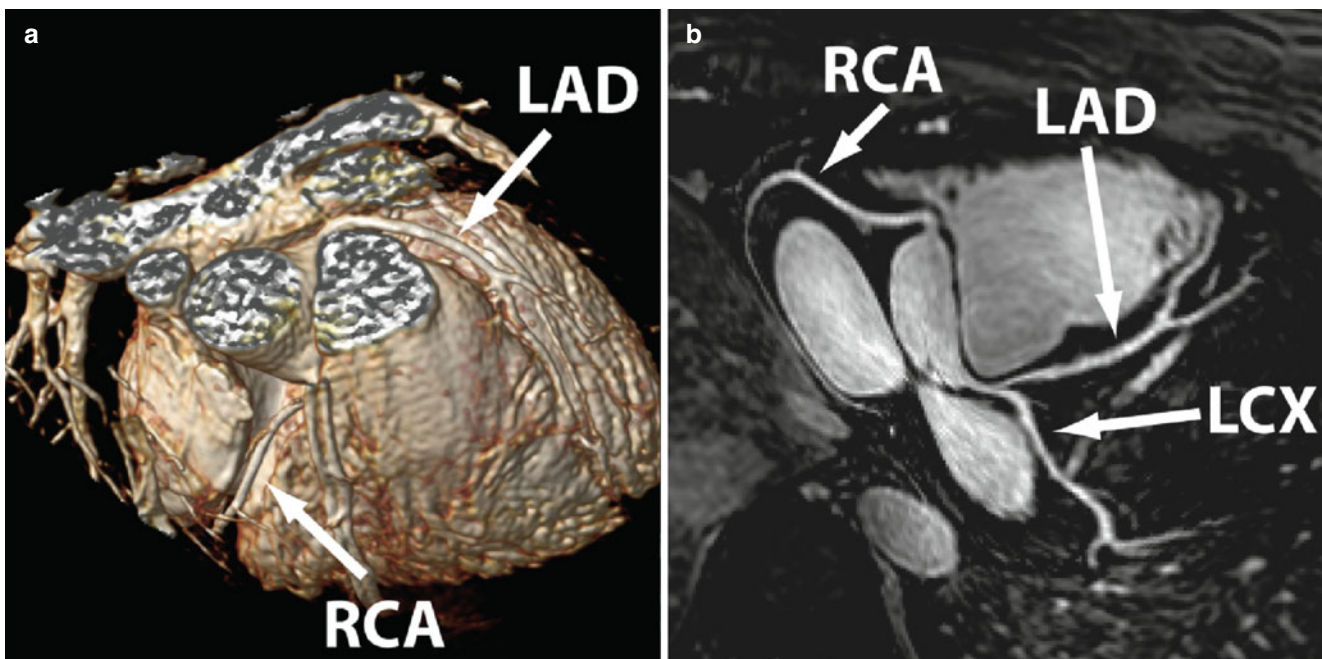


Fig. 17.7 Whole heart SSFP coronary MRI acquired with a bolus injection of Gd-BOPTA. **(a)** 3D volume rendering of the acquisition volume. **(b)** Corresponding reformatted whole-heart image. All three

major coronary arteries and distal branches are clearly depicted. *RCA* right coronary artery, *LAD* left anterior descending, *LCX* left circumflex

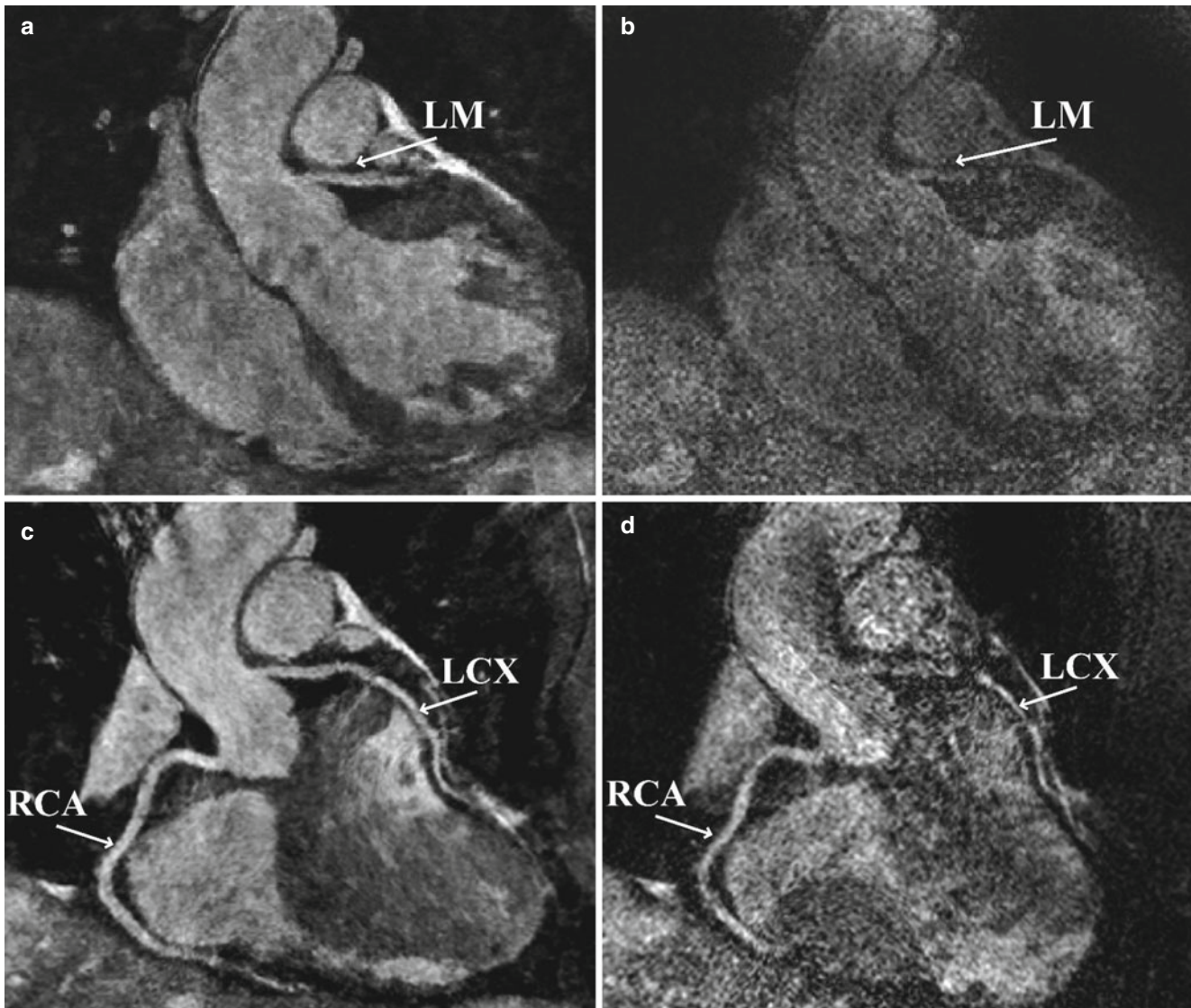


Fig. 17.8 Example images from two separate highly-accelerated sub-millimeter resolution whole-heart coronary MRI. An example coronal slice (*top*) containing a cross-section of the left main (*LM*) shows that SENSE images, acquired with sixfold uniform undersampling (*right*), suffers from noise amplification. In contrast, the LM is clearly

visualized using an advanced CS-based technique (LOST), acquired using sixfold random undersampling (*left*). In the reformatted coronal images (*bottom*), the proximal LCX cannot be tracked due to the high noise level in the SENSE reconstruction, but RCA and LCX branches are visualized with the LOST technique

navigator and breath-hold 3D coronary artery MRI studies in healthy volunteers have demonstrated >50 % improvement in SNR with impressive image quality using segmented k-space gradient echo or SSFP [123], as well as spiral and contrast enhanced methods [88, 124, 125]. Coronary MRI at 3 T using SSFP sequences is challenging due to increased field inhomogeneity and high SAR, thus GRE sequences have become widely used for coronary MRI at 3 T. To reduce the impact of B_1 inhomogeneity at the high field strengths, improved preparation sequences such as adiabatic T_2 magnetization preparation [87, 90] and adiabatic fat saturation have also been utilized. Figure 17.9 shows an example

of coronary MR images acquired at 3 T using improved T_2 magnetization preparation, which suppresses the banding artifact resulting from conventional T_2 magnetization preparation. Despite these technical improvements, there are currently no multi-center data on a head-to-head comparison between 3 and 1.5 T coronary MRI for diagnosing CAD. Coronary MRI at even higher field strengths, such as 7 T [126], is even more challenging. Figure 17.10 shows an example coronary MRI from a healthy subject acquired at 7 T. Several technical issues, including coil design, motion compensation and B_0 and B_1 field inhomogeneity, need to be addressed before clinical evaluation is possible.

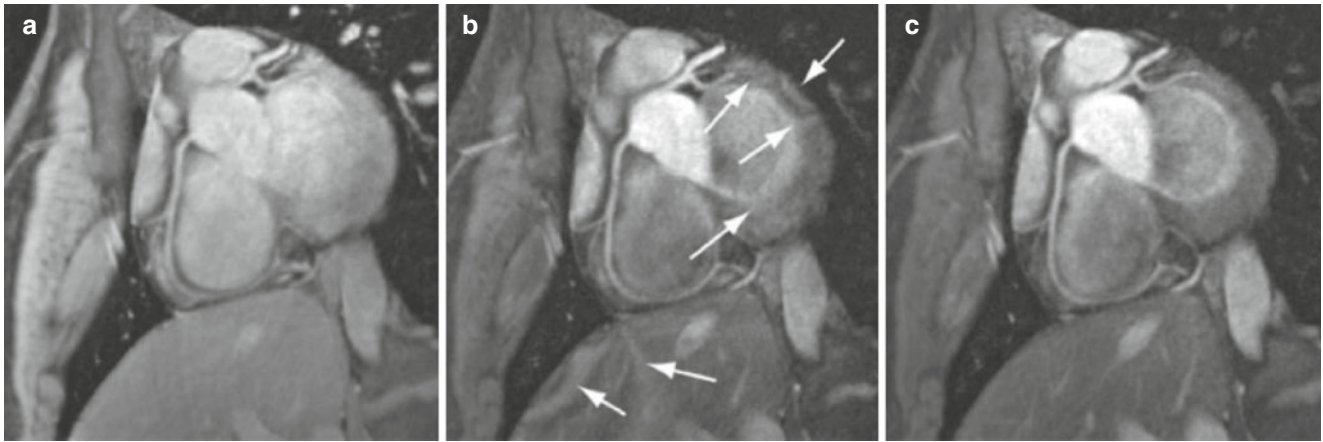


Fig. 17.9 Reformatted 3D coronary MRI of the right coronary artery at 3T (a) acquired with no T_2 -Prep; (b) with T_2 -Prep; (c) with adiabatic T_2 -Prep. Arrows in (b) point to the artifacts resulting from T_2 -Prep

sequence. The banding artifacts are suppressed in (c), where the homogeneity of the signal is also improved

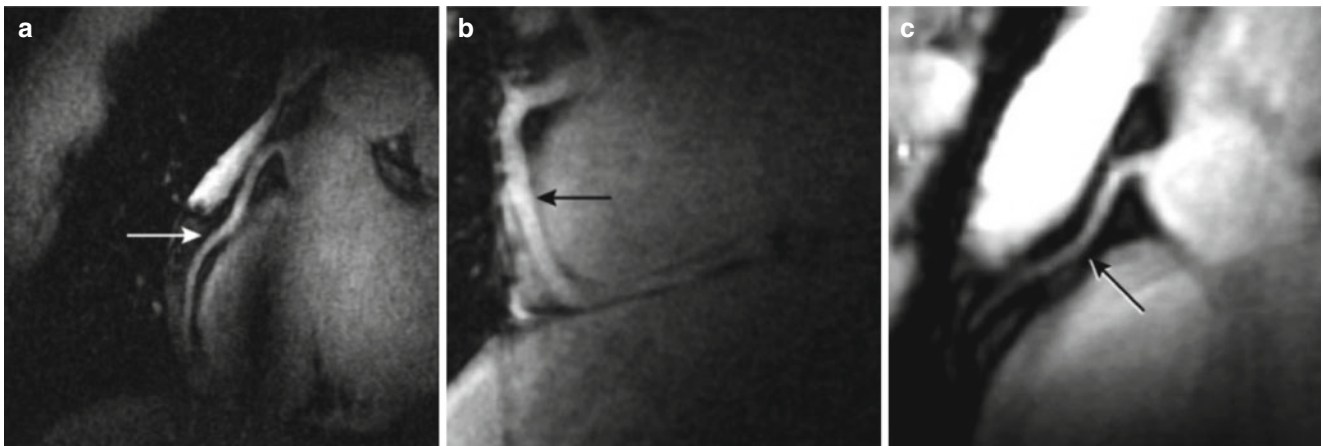


Fig. 17.10 7T coronary MRI of the right coronary artery acquired using a gradient echo imaging sequence. Proximal (a, c) and more distal (b) segments of the RCA are visualized (arrows) (Adapted from Ref. [126], with permission of Wiley)

Coronary Vein MRI

For several interventional cardiac procedures, including epicardial radiofrequency ablation [127, 128], retrograde perfusion therapy in high-risk or complicated coronary angioplasty [129], arrhythmia assessment [130, 131], stem cell delivery [132], coronary artery bypass surgery [133] and cardiac resynchronization therapy (CRT) [134, 135], there has been increased interest in imaging the coronary vein anatomy. In CRT, simultaneous pacing of the right ventricle and left ventricle (LV), or pacing the LV alone, results in hemodynamic improvement and restoration of a more physiological contraction pattern [136]. One of the technical difficulties of CRTs is achieving effective, safe and permanent pacing of the LV. Transvenous coronary sinus pacing is the most common technique as it has the least procedural risk, but it is associated with long procedure times, extensive radiation exposure from

fluoroscopy, implantation failure and LV lead dislodgment. Two of the major difficulties of the transvenous approach are the small number of coronary vein branches adjacent to an appropriate LV wall and the great variability in coronary vein anatomy [135]. Ideally, coronary venous morphology should be assessed noninvasively prior to CRT procedure, to determine whether epicardial or transvenous lead placement would be more appropriate.

The technical challenges of coronary vein MRI are similar to coronary artery MRI, and techniques developed for coronary artery MRI are widely applicable. Notable differences in coronary vein MRI include the magnetization preparation methods and optimal time window for imaging within the cardiac cycle, as well as more modest spatial resolution requirements since information regarding vein anatomy and vessel size are desired, but not focal stenoses. Magnetization transfer preparation has been utilized in coro-

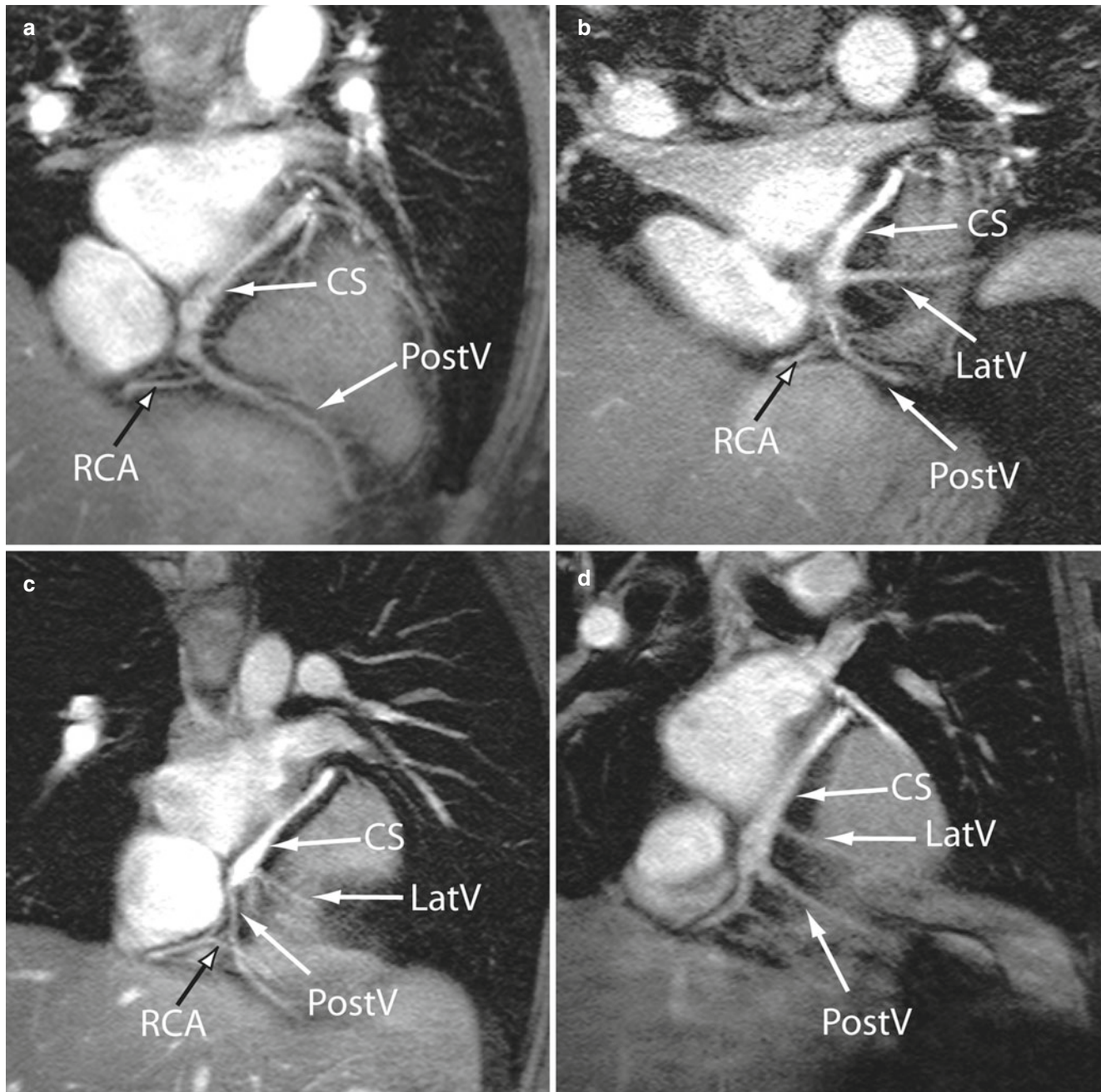


Fig. 17.11 Example coronary vein MRI acquired using magnetization transfer GRE during the systolic rest period, depicting the variations in the coronary venous anatomy in four healthy adult subjects (a-d). Clear variations in the branching point, angle, and diameter of different tribu-

taries of coronary sinus are observed, highlighting the potential for non-invasive assessment of the coronary venous anatomy in cardiac resynchronization therapy. For example, subject (a) has no visible lateral vein (*LatV*)

nary vein imaging, which is different than the T_2 magnetization preparation commonly used in coronary artery MRI, for both targeted [137] and whole-heart [138] approaches. Figure 17.11 shows example coronary vein MRI using a targeted approach with a magnetization transfer preparation sequence. Contrast in coronary vein MRI can be improved by other means, such as the use of intravascular contrast

agents such as gadoleptic acid trisodium salt [139] or the use of high relaxivity extracellular contrast agents such as Gd-BOPTA [101]. For the optimal window of imaging, while coronary artery MRI is commonly performed during mid-diastolic quiescent period, coronary vein MRI is acquired in the end-systolic quiescent period as it coincides with the maximum size of the coronary veins [137].

Conclusion

The current clinical applications of coronary artery MRI are limited to evaluation of coronary anomalies and coronary artery aneurysms. For the evaluation of coronary artery stenosis, coronary MRI is able to assess left main and proximal portions of the epicardial coronary arteries. However, due to technical limitations in spatial resolution the evaluation of distal coronary arteries and small side branches is not adequate for routine clinical use. Ongoing technical advances in image acquisition and post-processing have the potential to improve clinical applications of coronary MRI.

References

- Go AS, et al. Heart disease and stroke statistics – 2013 update: a report from the American Heart Association. *Circulation*. 2013;127(1):e6–245.
- Patel MR, et al. Low diagnostic yield of elective coronary angiography. *N Engl J Med*. 2010;362(10):886–95.
- Johnson LW, et al. Coronary arteriography 1984–1987, a report of the registry of the society for cardiac angiography and interventions. I. Results and complications. *Cathet Cardiovasc Diagn*. 1989;17(1):5–10.
- Davidson CJ, et al. Thrombotic and cardiovascular complications related to nonionic contrast media during cardiac catheterization: analysis of 8,517 patients. *Am J Cardiol*. 1990;65(22):1481–4.
- Omran H, et al. Silent and apparent cerebral embolism after retrograde catheterisation of the aortic valve in valvular stenosis: a prospective, randomised study. *Lancet*. 2003;361(9365):1241–6.
- Hendel RC, et al. ACCF/ACR/SCCT/SCMR/ASNC/NASCI/SCAI/SIR 2006 appropriateness criteria for cardiac computed tomography and cardiac magnetic resonance imaging: a report of the American College of Cardiology Foundation Quality Strategic Directions Committee Appropriateness Criteria Working Group, American College of Radiology, Society of Cardiovascular Computed Tomography, Society for Cardiovascular Magnetic Resonance, American Society of Nuclear Cardiology, North American Society for Cardiac Imaging, Society for Cardiovascular Angiography and Interventions, and Society of Interventional Radiology. *J Am Coll Cardiol*. 2006;48(7):1475–97.
- Hundley WG, et al. ACCF/ACR/AHA/NASCI/SCMR 2010 expert consensus document on cardiovascular magnetic resonance. A report of the American College of Cardiology Foundation Task Force on Expert Consensus Documents. *Circulation*. 2010;121:2462–508.
- Manning WJ, Edelman RR. Magnetic resonance coronary angiography. *Magn Reson Q*. 1993;9(3):131–51.
- Manning WJ, Li W, Edelman RR. A preliminary report comparing magnetic resonance coronary angiography with conventional angiography. *N Engl J Med*. 1993;328(12):828.
- Kim WY, et al. Coronary magnetic resonance angiography for the detection of coronary stenoses. *N Engl J Med*. 2001;345(26):1863–9.
- Stuber M, et al. Breathhold three-dimensional coronary magnetic resonance angiography using real-time navigator technology. *J Cardiovasc Magn Reson*. 1999;1(3):233–8.
- Stuber M, et al. Submillimeter three-dimensional coronary MR angiography with real-time navigator correction: comparison of navigator locations. *Radiology*. 1999;212(2):579–87.
- Stuber M, et al. Double-oblique free-breathing high resolution three-dimensional coronary magnetic resonance angiography. *J Am Coll Cardiol*. 1999;34(2):524–31.
- Botnar RM, et al. Improved coronary artery definition with T2-weighted, free-breathing, three-dimensional coronary MRA. *Circulation*. 1999;99(24):3139–48.
- Bhat H, et al. Whole-heart contrast-enhanced coronary magnetic resonance angiography using gradient echo interleaved EPI. *Magn Reson Med*. 2009;61(6):1388–95.
- Bi X, Carr JC, Li D. Whole-heart coronary magnetic resonance angiography at 3 Tesla in 5 minutes with slow infusion of Gd-BOPTA, a high-relaxivity clinical contrast agent. *Magn Reson Med*. 2007;58(1):1–7.
- Bi X, et al. Coronary artery magnetic resonance angiography (MRA): a comparison between the whole-heart and volume-targeted methods using a T2-prepared SSFP sequence. *J Cardiovasc Magn Reson*. 2006;8(5):703–7.
- Kim YJ, et al. Feasibility and diagnostic accuracy of whole heart coronary MR angiography using free-breathing 3D balanced turbo-field-echo with SENSE and the half-fourier acquisition technique. *Korean J Radiol*. 2006;7(4):235–42.
- Lai P, et al. A respiratory self-gating technique with 3D-translation compensation for free-breathing whole-heart coronary MRA. *Magn Reson Med*. 2009;62:731–8.
- Lai P, et al. A dual-projection respiratory self-gating technique for whole-heart coronary MRA. *J Magn Reson Imaging*. 2008;28(3):612–20.
- Liu X, et al. Contrast-enhanced whole-heart coronary magnetic resonance angiography at 3.0 T: comparison with steady-state free precession technique at 1.5 T. *Invest Radiol*. 2008;43(9):663–8.
- Maintz D, et al. Whole-heart coronary magnetic resonance angiography: value for the detection of coronary artery stenoses in comparison to multislice computed tomography angiography. *Acta Radiol*. 2007;48(9):967–73.
- Nehrke K, et al. Free-breathing whole-heart coronary MR angiography on a clinical scanner in four minutes. *J Magn Reson Imaging*. 2006;23(5):752–6.
- Niendorf T, et al. Toward single breath-hold whole-heart coverage coronary MRA using highly accelerated parallel imaging with a 32-channel MR system. *Magn Reson Med*. 2006;56(1):167–76.
- Okada T, et al. Whole-heart coronary magnetic resonance angiography with parallel imaging: comparison of acceleration in one-dimension vs. two-dimensions. *Eur J Radiol*. 2009;71(3):486–91.
- Sakuma H, et al. Detection of coronary artery stenosis with whole-heart coronary magnetic resonance angiography. *J Am Coll Cardiol*. 2006;48(10):1946–50.
- Sakuma H, et al. Assessment of coronary arteries with total study time of less than 30 minutes by using whole-heart coronary MR angiography. *Radiology*. 2005;237(1):316–21.
- Stehning C, et al. Free-breathing whole-heart coronary MRA with 3D radial SSFP and self-navigated image reconstruction. *Magn Reson Med*. 2005;54(2):476–80.
- Weber OM, Martin AJ, Higgins CB. Whole-heart steady-state free precession coronary artery magnetic resonance angiography. *Magn Reson Med*. 2003;50(6):1223–8.
- Bunce NH, et al. Evaluation of free-breathing three-dimensional magnetic resonance coronary angiography with hybrid ordered phase encoding (HOPE) for the detection of proximal coronary artery stenosis. *J Magn Reson Imaging*. 2001;14(6):677–84.
- Sommer T, et al. Submillimeter 3D coronary MR angiography with real-time navigator correction in 107 patients with suspected coronary artery disease. *Röfo*. 2002;174(4):459–66.
- Bogaert J, et al. Coronary artery imaging with real-time navigator three-dimensional turbo-field-echo MR coronary angiography: initial experience. *Radiology*. 2003;226(3):707–16.
- Jahnke C, et al. Coronary MR angiography with steady-state free precession: individually adapted breath-hold technique versus free-breathing technique. *Radiology*. 2004;232(3):669–76.
- Pouleur AC, et al. Direct comparison of whole-heart navigator-gated magnetic resonance coronary angiography and 40- and 64-slice multidetector row computed tomography to detect the coronary artery stenosis in patients scheduled for conventional coronary angiography. *Circ Cardiovasc Imaging*. 2008;1(2):114–21.

35. Kato S, et al. Assessment of coronary artery disease using magnetic resonance coronary angiography: a national multicenter trial. *J Am Coll Cardiol*. 2010;56(12):983–91.
36. Yang Q, et al. Contrast-enhanced whole-heart coronary magnetic resonance angiography at 3.0-T: a comparative study with X-ray angiography in a single center. *J Am Coll Cardiol*. 2009;54(1):69–76.
37. Yang Q, et al. Assessment of coronary artery disease using 3.0 T magnetic resonance coronary angiography: a national multicenter trial. *J Cardiovasc Magn Reson*. 2013;15 Suppl 1:E5.
38. Deshpande VS, et al. 3D magnetization-prepared true-FISP: a new technique for imaging coronary arteries. *Magn Reson Med*. 2001;46(3):494–502.
39. Nezafat R, et al. Inflow quantification in three-dimensional cardiovascular MR imaging. *J Magn Reson Imaging*. 2008;28(5):1273–9.
40. Maintz D, et al. Coronary MR angiography: comparison of quantitative and qualitative data from four techniques. *AJR Am J Roentgenol*. 2004;182(2):515–21.
41. Ozgun M, et al. Comparison of 3D segmented gradient-echo and steady-state free precession coronary MRI sequences in patients with coronary artery disease. *AJR Am J Roentgenol*. 2005;185(1):103–9.
42. Polson MJ, Barker AT, Gardiner S. The effect of rapid rise-time magnetic fields on the ECG of the rat. *Clin Phys Physiol Meas*. 1982;3(3):231–4.
43. Paulin S. Coronary angiography. A technical, anatomic and clinical study. *Acta Radiol Diagn*. 1964;54(Suppl 233):L+.
44. Wang Y, Vidan E, Bergman GW. Cardiac motion of coronary arteries: variability in the rest period and implications for coronary MR angiography. *Radiology*. 1999;213(3):751–8.
45. Kaji S, et al. Rapid evaluation of left ventricular volume and mass without breath-holding using real-time interactive cardiac magnetic resonance imaging system. *J Am Coll Cardiol*. 2001;38(2):527–33.
46. Hofman MB, Wickline SA, Lorenz CH. Quantification of in-plane motion of the coronary arteries during the cardiac cycle: implications for acquisition window duration for MR flow quantification. *J Magn Reson Imaging*. 1998;8(3):568–76.
47. Kim WY, et al. Impact of bulk cardiac motion on right coronary MR angiography and vessel wall imaging. *J Magn Reson Imaging*. 2001;14(4):383–90.
48. Jahnke C, et al. A new approach for rapid assessment of the cardiac rest period for coronary MRA. *J Cardiovasc Magn Reson*. 2005;7(2):395–9.
49. Leiner T, et al. Correction for heart rate variability improves coronary magnetic resonance angiography. *J Magn Reson Imaging*. 2005;22(4):577–82.
50. Jahnke C, Paetsch I, Gebker R, Schnackenburg B, Bornstedt A, Fleck E, et al. Comparison of individually adapted breath-hold and free-breathing coronary MRA using steady state free precession [abstr]. *J Cardiovasc Magn Reson*. 2004;6:166–7.
51. Plein S, et al. Three-dimensional coronary MR angiography performed with subject-specific cardiac acquisition windows and motion-adapted respiratory gating. *AJR Am J Roentgenol*. 2003;180(2):505–12.
52. Tangcharoen T, et al. Impact of heart rate variability in patients with normal sinus rhythm on image quality in coronary magnetic angiography. *J Magn Reson Imaging*. 2008;28(1):74–9.
53. Wang Y, Riederer SJ, Ehman RL. Respiratory motion of the heart: kinematics and the implications for the spatial resolution in coronary imaging. *Magn Reson Med*. 1995;33(5):713–9.
54. Edelman RR, et al. Coronary arteries: breath-hold MR angiography. *Radiology*. 1991;181(3):641–3.
55. Taylor AM, et al. MR navigator-echo monitoring of temporal changes in diaphragm position: implications for MR coronary angiography. *J Magn Reson Imaging*. 1997;7(4):629–36.
56. Holland AE, Goldfarb JW, Edelman RR. Diaphragmatic and cardiac motion during suspended breathing: preliminary experience and implications for breath-hold MR imaging. *Radiology*. 1998;209(2):483–9.
57. Danias PG, et al. Navigator assessment of breath-hold duration: impact of supplemental oxygen and hyperventilation. *AJR Am J Roentgenol*. 1998;171(2):395–7.
58. Ehman RL, Felmlee JP. Adaptive technique for high-definition MR imaging of moving structures. *Radiology*. 1989;173(1):255–63.
59. Oshinski JN, et al. Two-dimensional coronary MR angiography without breath holding. *Radiology*. 1996;201(3):737–43.
60. Sachs TS, et al. Real-time motion detection in spiral MRI using navigators. *Magn Reson Med*. 1994;32(5):639–45.
61. McConnell MV, et al. Comparison of respiratory suppression methods and navigator locations for MR coronary angiography. *AJR Am J Roentgenol*. 1997;168(5):1369–75.
62. Danias PG, et al. Prospective navigator correction of image position for coronary MR angiography. *Radiology*. 1997;203(3):733–6.
63. McConnell MV, et al. Prospective adaptive navigator correction for breath-hold MR coronary angiography. *Magn Reson Med*. 1997;37(1):148–52.
64. Moghari MH, et al. Subject-specific estimation of respiratory navigator tracking factor for free-breathing cardiovascular MR. *Magn Reson Med*. 2012;67(6):1665–72.
65. McConnell M, et al. Comparison of respiratory suppression methods and navigator locations for MR coronary angiography. *Am J Roentgenol*. 1997;168(5):1369.
66. Nezafat R, et al. Improved spatial-temporal resolution MR coronary blood flow imaging at 3T. *J Cardiovasc Magn Reson*. 2005;7(1):199.
67. Nehrke K, Bornert P. Prospective correction of affine motion for arbitrary MR sequences on a clinical scanner. *Magn Reson Med*. 2005;54(5):1130–8.
68. Lai P, et al. Respiratory self-gated four-dimensional coronary MR angiography: a feasibility study. *Magn Reson Med*. 2008;59(6):1378–85.
69. Larson AC, et al. Preliminary investigation of respiratory self-gating for free-breathing segmented cine MRI. *Magn Reson Med*. 2005;53(1):159–68.
70. Park J, et al. 4D radial coronary artery imaging within a single breath-hold: cine angiography with phase-sensitive fat suppression (CAPS). *Magn Reson Med*. 2005;54(4):833–40.
71. Keegan J, et al. Non-model based correction of respiratory motion using beat-to-beat 3D spiral fat-selective imaging. *J Magn Reson Imaging*. 2007;26(3):624–9.
72. Nguyen T, et al. Free-breathing 3D steady-state free precession coronary magnetic resonance angiography: Comparison of diaphragm and cardiac fat navigators. *J Magn Reson Imaging: JMIR*. 2008;28(2):509.
73. Nguyen T, et al. 2128 Free-breathing steady-state free precession 3D coronary MRA: comparison of diaphragm and cardiac fat navigator techniques. *J Cardiovasc Magn Reson*. 2008;10 Suppl 1: A397.
74. Nguyen T, et al. Free-breathing 3-dimensional steady-state free precession coronary magnetic resonance angiography: comparison of four navigator gating techniques. *Magn Reson Imaging*. 2009;27(6):807–14.
75. Uribe S, et al. Whole-heart cine MRI using real-time respiratory self-gating. *Magn Reson Med*. 2007;57:606–13.
76. Brau AC, Brittain JH. Generalized self-navigated motion detection technique: preliminary investigation in abdominal imaging. *Magn Reson Med*. 2006;55(2):263–70.
77. Danias PG, et al. Relationship between motion of coronary arteries and diaphragm during free breathing: lessons from real-time MR imaging. *AJR Am J Roentgenol*. 1999;172(4):1061–5.

78. Nehrke K, et al. Free-breathing cardiac MR imaging: study of implications of respiratory motion – initial results. *Radiology*. 2001;220(3):810–5.
79. Moghari MH, et al. Free-breathing cardiac MR with a fixed navigator efficiency using adaptive gating window size. *Magn Reson Med*. 2012;68(6):1866–75.
80. Gurney PT, Hargreaves BA, Nishimura DG. Design and analysis of a practical 3D cones trajectory. *Magn Reson Med*. 2006;55(3):575–82.
81. Santos JM, et al. Single breath-hold whole-heart MRA using variable-density spirals at 3T. *Magn Reson Med*. 2006;55(2):371–9.
82. Sussman M, et al. Variable-density adaptive imaging for high-resolution coronary artery MRI. *Magn Reson Med*. 2002;48(5):753–64.
83. Li D, et al. Coronary arteries: three-dimensional MR imaging with fat saturation and magnetization transfer contrast. *Radiology*. 1993;187(2):401–6.
84. Brittain JH, et al. Coronary angiography with magnetization-prepared T2 contrast. *Magn Reson Med*. 1995;33(5):689–96.
85. Shea SM, et al. Three-dimensional true-FISP imaging of the coronary arteries: improved contrast with T2-preparation. *J Magn Reson Imaging*. 2002;15(5):597–602.
86. Balaban RS, Ceckler TL. Magnetization transfer contrast in magnetic resonance imaging. *Magn Reson Q*. 1992;8(2):116–37.
87. Nezafat R, et al. B1-insensitive T2 preparation for improved coronary magnetic resonance angiography at 3 T. *Magn Reson Med*. 2006;55(4):858–64.
88. Stuber M, et al. Preliminary report on in vivo coronary MRA at 3 Tesla in humans. *Magn Reson Med*. 2002;48(3):425–9.
89. Schar M, Kozerke S, Fischer SE, Boesiger P. Cardiac SSFP imaging at 3 Tesla. *Magn Reson Med*. 2004;51(4):799–806.
90. Nezafat R, et al. Spectrally selective B1-insensitive T2 magnetization preparation sequence. *Magn Reson Med*. 2009;61(6):1326–35.
91. Terashima M, et al. Noninvasive assessment of coronary vasodilation using magnetic resonance angiography. *J Am Coll Cardiol*. 2005;45(1):104–10.
92. Hu P, et al. Coronary MR imaging: effect of timing and dose of isosorbide dinitrate administration. *Radiology*. 2010;254(2):401–9.
93. Zheng J, et al. Efficacy of slow infusion of gadolinium contrast agent in three-dimensional MR coronary artery imaging. *J Magn Reson Imaging*. 1999;10(5):800–5.
94. Goldfarb JW, Edelman RR. Coronary arteries: breath-hold, gadolinium-enhanced, three-dimensional MR angiography. *Radiology*. 1998;206(3):830–4.
95. Knuesel PR, et al. Multislice breath-hold spiral magnetic resonance coronary angiography in patients with coronary artery disease: effect of intravascular contrast medium. *J Magn Reson Imaging*. 2002;16(6):660–7.
96. Herborn CU, et al. Coronary arteries: contrast-enhanced MR imaging with SHL 643A – experience in 12 volunteers. *Radiology*. 2003;229(1):217–23.
97. Prompona M, et al. Contrast-enhanced whole-heart MR coronary angiography at 3.0T using the intravascular contrast agent gadofosveset. *Invest Radiol*. 2009;44(7):369–74.
98. Kelle S, et al. Whole-heart coronary magnetic resonance angiography with MS-325 (Gadofosveset). *Med Sci Monit*. 2007;13(11):CR469–74.
99. de Haen C, et al. Gadocoletic acid trisodium salt (b22956/1): a new blood pool magnetic resonance contrast agent with application in coronary angiography. *Invest Radiol*. 2006;41(3):279–91.
100. Tang L, et al. Volume-targeted and whole-heart coronary magnetic resonance angiography using an intravascular contrast agent. *J Magn Reson Imaging*. 2009;30(5):1191–6.
101. Hu P, et al. Contrast-enhanced whole-heart coronary MRI with bolus infusion of gadobenate dimeglumine at 1.5 T. *Magn Reson Med*. 2011;65(2):392–8.
102. Meyer CH, et al. Fast spiral coronary artery imaging. *Magn Reson Med*. 1992;28(2):202–13.
103. Bornert P, et al. Direct comparison of 3D spiral vs. Cartesian gradient-echo coronary magnetic resonance angiography. *Magn Reson Med*. 2001;46(4):789–94.
104. Thedens DR, et al. Fast magnetic resonance coronary angiography with a three-dimensional stack of spirals trajectory. *Magn Reson Med*. 1999;41(6):1170–9.
105. Bornert P, Aldefeld B, Nehrke K. Improved 3D spiral imaging for coronary MR angiography. *Magn Reson Med*. 2001;45(1):172–5.
106. Leiner T, Yeh E, Katsimaglis G, Kissinger KV, Spuentrup E, Manning WJ, et al. Comparison of cartesian and radial balanced GTFE coronary MRA [abstr]. *J Cardiovasc Magn Reson*. 2004;6:75.
107. Weber OM, et al. Free-breathing, three-dimensional coronary artery magnetic resonance angiography: comparison of sequences. *J Magn Reson Imaging*. 2004;20(3):395–402.
108. Nam S, et al. Compressed sensing reconstruction for whole heart imaging with 3D radial trajectories: a GPU implementation. *Magn Reson Med*. 2013;69(1):91–102.
109. Botnar RM, et al. Noninvasive coronary vessel wall and plaque imaging with magnetic resonance imaging. *Circulation*. 2000;102(21):2582–7.
110. Katoh M, et al. MR coronary vessel wall imaging: comparison between radial and spiral k-space sampling. *J Magn Reson Imaging*. 2006;23(5):757–62.
111. Griswold MA, et al. Generalized autocalibrating partially parallel acquisitions (GRAPPA). *Magn Reson Med*. 2002;47(6):1202–10.
112. Pruessmann KP, et al. Advances in sensitivity encoding with arbitrary k-space trajectories. *Magn Reson Med*. 2001;46(4):638–51.
113. Nagata M, et al. Diagnostic accuracy of 1.5-T unenhanced whole-heart coronary MR angiography performed with 32-channel cardiac coils: initial single-center experience. *Radiology*. 2011;259(2):384–92.
114. Bhat H, et al. Contrast-enhanced whole-heart coronary magnetic resonance angiography at 3T with radial EPI. *Magn Reson Med*. 2011;66(1):82–91.
115. Block KT, Uecker M, Frahm J. Undersampled radial MRI with multiple coils. Iterative image reconstruction using a total variation constraint. *Magn Reson Med*. 2007;57(6):1086–98.
116. Lustig M, Donoho DL, Pauly JM. Sparse MRI: the application of compressed sensing for rapid MR imaging. *Magn Reson Med*. 2007;58(6):1182–95.
117. Akcakaya M, et al. Low-dimensional-structure self-learning and thresholding: regularization beyond compressed sensing for MRI reconstruction. *Magn Reson Med*. 2011;66(3):756–67.
118. Akcakaya M, et al. Accelerated contrast-enhanced whole-heart coronary MRI using low-dimensional-structure self-learning and thresholding. *Magn Reson Med*. 2012;67(5):1434–43.
119. Akcakaya M, et al. Accelerated isotropic sub-millimeter whole-heart coronary MRI: compressed sensing versus parallel imaging. *Magn Reson Med*. 2014;71(2):815–22.
120. Wen H, et al. The intrinsic signal-to-noise ratio in human cardiac imaging at 1.5, 3, and 4T. *J Magn Reson*. 1997;125(1):65–71.
121. Noeske R, et al. Human cardiac imaging at 3 T using phased array coils. *Magn Reson Med*. 2000;44(6):978–82.
122. Atalay MK, et al. Cardiac susceptibility artifacts arising from the heart-lung interface. *Magn Reson Med*. 2001;45(2):341–5.
123. Bi X, et al. Three-dimensional breathhold SSFP coronary MRA: a comparison between 1.5T and 3.0T. *J Magn Reson Imaging*. 2005;22(2):206–12.

124. Steen HLJ, Giannitsis E, Katus HA, Stuber M. Comparison of high field magnetic resonance imaging at 1.5T and 3T for coronary artery MRA [abstr]. *J Cardiovasc Magn Reson*. 2004;6:342–4.
125. Bi X, Deshpande V, Simonetti O, Laub G, Li D. Three-dimensional breath-hold coronary MRA: a comparison between 1.5T and 3.0T [abstr]. *J Cardiovasc Magn Reson*. 2004;6:335–6.
126. van Elderen SG, et al. Initial results on in vivo human coronary MR angiography at 7 T. *Magn Reson Med*. 2009;62(6):1379–84.
127. Kusano KF, et al. Catheter ablation of an epicardial accessory pathway via the middle cardiac vein guided by monophasic action potential recordings. *Europace*. 2001;3(2):164–7.
128. Haissaguerre M, et al. Radiofrequency catheter ablation of left lateral accessory pathways via the coronary sinus. *Circulation*. 1992;86(5):1464–8.
129. Kar S, Nordlander R. Coronary veins: an alternate route to ischemic myocardium. *Heart Lung*. 1992;21(2):148–57.
130. Stellbrink C, et al. Transcoronary venous radiofrequency catheter ablation of ventricular tachycardia. *J Cardiovasc Electrophysiol*. 1997;8(8):916–21.
131. Butter C, et al. Human experience with transvenous biventricular defibrillation using an electrode in a left ventricular vein. *Pacing Clin Electrophysiol*. 2002;25(3):324–31.
132. Thompson CA, et al. Percutaneous transvenous cellular cardiomyoplasty. A novel nonsurgical approach for myocardial cell transplantation. *J Am Coll Cardiol*. 2003;41(11):1964–71.
133. Oesterle SN, et al. Percutaneous in situ coronary venous arterialization: report of the first human catheter-based coronary artery bypass. *Circulation*. 2001;103(21):2539–43.
134. de Paola AA, et al. Angiographic and electrophysiological substrates for ventricular tachycardia mapping through the coronary veins I. *Heart*. 1998;79(1):59–63.
135. Singh JP, et al. The coronary venous anatomy: a segmental approach to aid cardiac resynchronization therapy. *J Am Coll Cardiol*. 2005;46(1):68–74.
136. Abraham WT, et al. Cardiac resynchronization in chronic heart failure. *N Engl J Med*. 2002;346(24):1845–53.
137. Nezafat R, et al. Coronary magnetic resonance vein imaging: imaging contrast, sequence, and timing. *Magn Reson Med*. 2007;58(6):1196–206.
138. Stoeck CT, et al. Whole heart magnetization-prepared steady-state free precession coronary vein MRI. *J Magn Reson Imaging*. 2009;29(6):1293–9.
139. Rasche V, et al. Whole-heart coronary vein imaging: a comparison between non-contrast-agent-and contrast-agent-enhanced visualization of the coronary venous system. *Magn Reson Med*. 2007;57(6):1019–26.

Ronald Ouwerkerk

Abstract

This chapter describes an MR technique that can yield information on the metabolism and energy status of the myocardium. MR Spectroscopy (MRS) explores the chemical shift dimension of the MR signal. MR visible nuclei like ^1H - and ^{31}P exhibit slightly shifted resonance frequencies depending on the molecular environment. Thus, compounds can be identified from spectra of these chemical shifts. ^{31}P -MRS was the first method used to investigate cellular metabolism in-vivo, using a simple surface coil. This method was soon adapted for the heart and then used in humans. By observing high-energy phosphate metabolites with ^{31}P -MRS in patients with cardiomyopathies a link was shown between heart failure and changes in the levels of phosphocreatine. Creatine compounds can also be observed with more technically accessible ^1H -MRS techniques. With ^1H -MRS it is also possible to quantify intra-myocellular triglyceride content. These triglycerides are a major fuel for the heart and abnormal levels are linked to obesity and heart failure. A comprehensive but simple description is given on how to acquire and process in-vivo cardiac MRS data in humans. This chapter will focus on ^1H -MRS because this is by far the most accessible technique.

Keywords

- Magnetic resonance spectroscopy • Myocardial metabolism • Creatine • Phosphocreatine
- Triglycerides • Myocardial triglyceride content • ^1H -MRS • ^{31}P -MRS

Introduction

Cardiac ^1H -MRI is a very versatile tool for examining cardiac morphology, function and blood flow. To know more about the effect of cardiovascular disease and possibly the subsequent therapy on the heart we can monitor changes in cardiac function with repeat cardiac MRI examinations. MR Spectroscopy (MRS) of the heart makes it possible to gauge the impact of cardiovascular disease on the metabolism of

the cardiomyocytes. MR visible nuclei like ^1H - and ^{31}P exhibit slightly shifted resonance frequencies depending on the molecular environment. Thus, compounds can be identified from spectra of these chemical shifts. This technique can be used in vivo to measure metabolite levels in living tissue. With MRS it is possible to observe changes in metabolism in disease and we may use this to better understand the development of disease and perhaps even predict outcomes.

Studying Cardiac Metabolism with MR

Magnetic resonance spectroscopy started as an analytical technique that was mainly used in organic chemistry laboratories. MR visible nuclei such as ^1H or ^{31}P exhibit slightly shifted resonance frequencies depending on their molecular environ-

R. Ouwerkerk, PhD
The Biomedical and Metabolic Imaging Branch,
National Institute of Diabetes and Digestive
and Kidney Diseases (NIDDK), Bldg. 10-CRC RM 3-5340
MSC 1263, 10 Center Dr., Bethesda, MD 20892-1263, USA
e-mail: ouwerkerkr@mail.nih.gov

ment. With spectra recorded of these chemical shifts organic compounds can be identified and even quantified. Subsequently equipment got much better, mainly by incorporating the Fourier Transform MR method invented by Nobel prize winner Dr. Richard Ernst, and this analytical technique became an important tool in biochemistry research. In the lab of Dr. George Radda ^{31}P -MRS was first used on in-vivo muscle tissue to gain an insight in the energy metabolism of skeletal muscle [1]. With ^{31}P -MRS it is possible to readily observe changes in the intra-cellular concentrations of adenosine triphosphate (ATP) and phosphocreatine (PCr), respectively the universal energy currency in all cells and the energy buffer and shuttle compound in all excitable tissues. This was the start of a rapid development from animal experiments to MRS in humans. One of the extensions of this research was the use of this technique, in-vivo ^{31}P -MRS, on the human heart to study cardiac energy metabolism in various disease states and during exercise or pharmacological stress [2, 3]. The ^{31}P -MRS technique can even offer more than just a peek at the steady state concentrations of high energy metabolites and how these change with interventions, but it is also possible to measure the creatine kinase mediated flux between ATP and PCr with the use of magnetization transfer techniques [4]. The use of these ^{31}P -MRS techniques is limited to just a handful of research centers in the world. Not only is the extra equipment required expensive, but the experimental setups for ^{31}P -MRS as delivered by the major scanner manufacturers, generally require a lot of fine tuning before a good ^{31}P -MRS exam can be conducted.

^1H -MRS of the Heart

Proton MRS is in principle accessible to a much larger number of MR centers because it does not require special broadband RF amplifiers and receive channels and ^{31}P tuned RF coils. Even so, it is not widely used yet. Still, some sequence adaptations are required to apply the standard ^1H -MRS spectroscopy sequences that are usually set up for ^1H -MRS of the brain, for use in the human heart. However, compared to non-proton methods the required adaptations are minor and certainly worth the trouble.

The information that can be gathered with cardiac ^1H -MRS is not the same as with ^{31}P -MRS. With ^1H -MRS the main identifiable metabolites are triglycerides and creatine. With ^{31}P -MRS only the energy rich PCr is visible but ^1H -MRS also observes the de-phosphorylated species. With ^{31}P -MRS it is extremely difficult to measure absolute concentrations of ATP and PCr, so usually only the ratios of PCr to ATP are reported. It is reasonable to assume that the concentration of ATP remains constant because its cytosolic concentration is tightly regulated. The breakdown product of ATP, adenosine diphosphate (ADP), stimulates mitochondrial ATP synthesis. Also, ADP is very rapidly

re-phosphorylated by creatine kinase, using the PCr as an energy buffer, to keep ATP concentrations constant. Moreover, before ATP concentrations fall, the pumping of sodium and potassium is inhibited to save energy. Thus, we may observe changes in tissue sodium and reduction in PCr before ATP levels change. Of course the assumption of constant ATP levels may not be valid in some disease models. The ideal MRS exam would be a combination of quantitative ^{31}P - and ^1H MRS. This would yield the ratio of creatine and PCr. From this the level of ADP can be inferred and thus the level of mitochondrial stimulation. Such experiments however present enormous technical challenges. Fortunately just ^1H -MRS alone can provide some sensitivity to prolonged abnormal ratios of PCr over creatine. Creatine with the phosphate attached can never leave the cell, but creatine can and does leave the cell. A compromised energy metabolism or a sustained depletion of PCr as a result of increased workload can lead to a depletion in myocardial creatine levels. This happens in ischemia [5], but it has also been shown to happen in other cardiomyopathies [6].

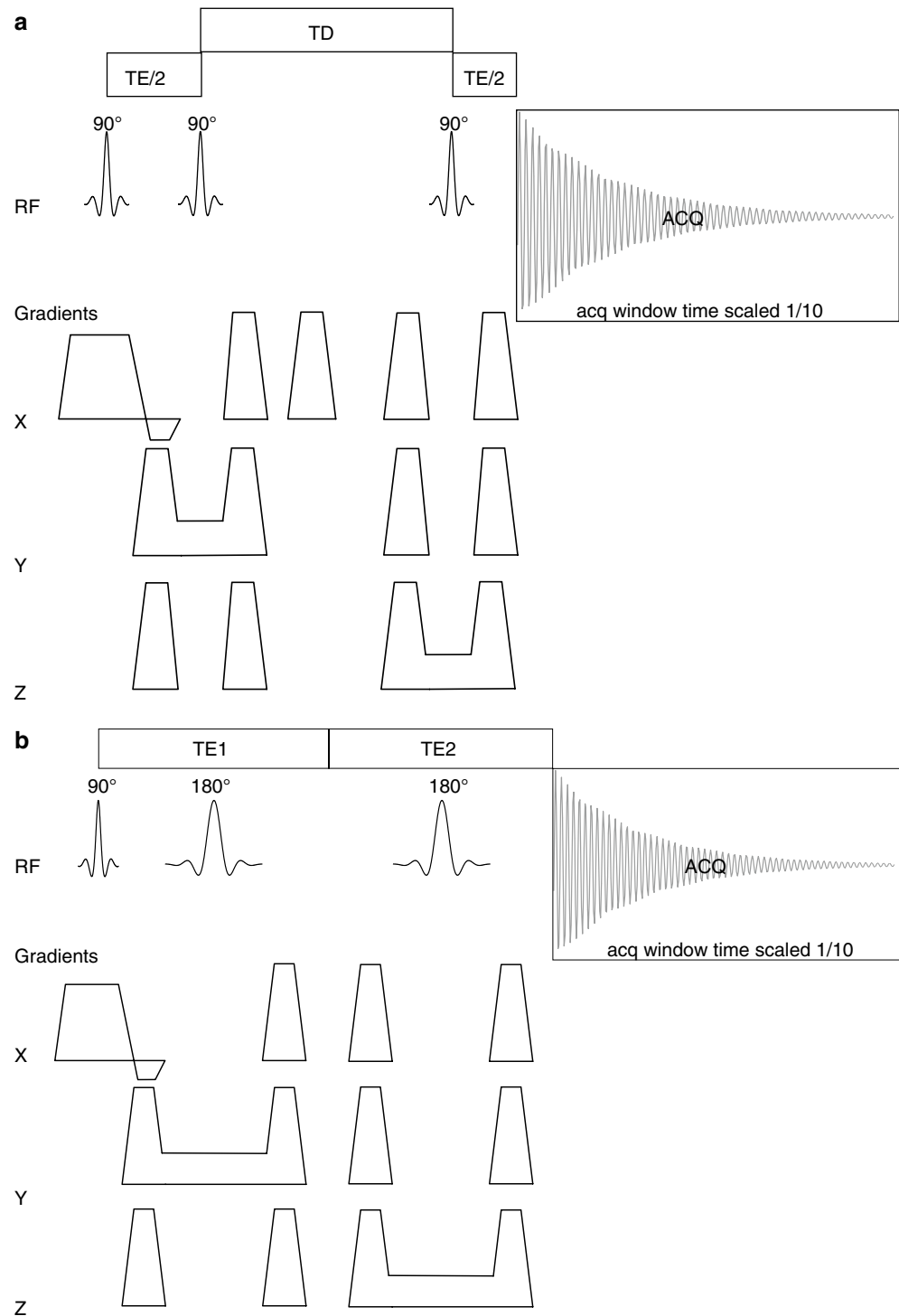
Cardiac Triglyceride Content

The more dominant and most frequently reported signal in ^1H -MRS spectra of the human heart is the lipid signal from intracellular triglycerides. Triglycerides (TG) are stored in healthy myocardium as a fuel for the mitochondrial production of ATP. In the heart the breakdown products of TG, along with lactate when present, are the main fuel for the cardiac muscle. Thus, a certain low level of TG in the heart is healthy, but the levels of cardiac TG can increase to toxic levels due to abnormal fat metabolism and obesity. The triglyceride levels in the heart have been shown to correlate with obesity [7], gauged as body mass index (BMI). The cardiac lipid levels will vary swiftly as a result of fasting or food intake [8] and after exercise [9]. Therefore it is important to consistently scan subjects either post-prandial or fasting. In fasting state the triglyceride levels tend to increase. These changes in cardiac lipid content are just now beginning to be explored. The triglyceride levels in the heart increase with age [10] and is also increased in type 2 diabetes mellitus where it is an independent predictor of cardiac function [11]. Further well-designed experiments and clinical studies will help us understand more about the relation of fat metabolism and cardiac health.

Proton MRS Scan Methods

In this chapter guidelines are provided to allow persons who are familiar with the principles of MR to perform cardiac ^1H -MRS experiments successfully. The last section of this chapter will discuss methods for processing MRS data. Hopefully this chapter will lower the threshold for cardiac MR users for exploring clinical research cardiac ^1H -MRS.

Fig. 18.1 Diagrams of the RF transmit and receive and gradients of the STEAM (a) and PRESS (b) sequences. The data acquisition windows are ten times longer than shown in these diagrams, but otherwise the timings are typical for the sequences set up for the shortest TE possible. The excitation RF refocus and first 180° pulse spoiler gradients are combined to reduce the TE. In STEAM the magnetization is not in the transverse plane in the mixing time TD. This time does not count towards the total TE of the sequence as only (a very small amount of) T_1 relaxation takes place. Transverse relaxation happens only during the two TE/2 periods. The effective TE for the PRESS sequence is the sum of the two spin-echo times TE1 and TE2



The Choice of Localization Pulse Sequence

Pulse sequences used for cardiac ^1H -MRS typically have a number of add-on components. The dominating water signal needs to be suppressed to get reliable metabolite spectra and additional sequence elements may be added to deal with breathing motion. The core of the sequence is a signal localization sequence with some orthogonal slice selective RF pulses to define a volume. Two methods are particularly

suited for single volume localized ^1H -MRS as used in the heart. The first, *point resolved spectroscopy* or PRESS [12], uses two slice selective spin-echoes and a slice selective excitation pulse to define a volume. The other, the *stimulated echo acquisition mode* (STEAM) [13, 14] uses three selective 90° pulses and allows much shorter minimum (TE) times, typically in the 12–20 ms range. Both sequences are shown in Fig. 18.1. STEAM has the added advantage that even at the short TE moving signals, such as the blood signal,

get very effectively suppressed. In cardiac MR imaging STEAM can be used to obtain black-blood images. STEAM does however have the disadvantage that intrinsically the stimulated echo yields 50 % less signal than the spin echo sequence with the two 180° refocusing pulses. This deficit is not recovered by shorter echo times except for resonances with extremely short T_2 . The longer TE of the PRESS sequence are in the order of 25–35 ms and this longer TE also help to reduce the signal from ventricular blood.

Much of the experimental approach of cardiac ^1H -MRS is identical for either PRESS or STEAM. The TEs are different as they should be set close to the minimum achievable for the sequence on the scanner, but the other sequence parameters, such as selected volume size spectral resolution, receiver bandwidth, offset frequency, repetition rate and some others are all optimally set to the same values for both sequences.

Dealing with Motion

The breathing and cardiac motion makes ^1H -MRS far more challenging than single volume brain MRS. First of all it is essential that the sequence be gated to an ECG signal. It is better to spend some time to optimize the ECG than to accept a mediocre signal that causes gating errors. If magnetic field and gradients distort the ECG so much that gating is unreliable a peripheral pulse signal can also be used as a last resort.

The breathing motion can be dealt with in a number of ways [15]. Where available a navigator sequence can be used to monitor the movement of the diaphragm and gate the MRS acquisition to respiratory motion. The most sophisticated version of this is navigator gated and volume tracking ^1H -MRS [16]. Using the navigator set on the top of the diaphragm an estimate is made of the cardiac motion due to breathing and the spectroscopy volume position is adjusted for each scan. This technique is not widely available yet, but navigator gating without volume tracking works OK in most cases.

Some researchers have set up the spectroscopy sequence to record each scan individually and then retroactively adjust the phase and frequency of all the recorded scans before averaging the signals, a technique called constructive averaging [17]. This method can lead to great improvements in reproducibility and signal-to-noise ratio (SNR). But doing this constructive averaging automatically needs a strong signal that is visible in one signal acquisition. Doing it manually at post-processing is an option, but this seriously complicates data analysis when each exam requires 32 or 64 scans to be individually inspected for averaging.

Collecting a large number of averages without the on-the-fly constructive averaging carries the risk that one missed trigger adds a bad signal and ruins the entire spectrum. As a compromise, spectra can be recorded in separate sets of four or eight averages. This allows some four or eight step phase

cycling, which is always advisable to reduce artifacts due to sequence imperfections. Really failed spectra can be discarded and remaining spectra can be constructively added in post processing.

If navigator gating is not available a pressure band can be used to record the breathing motion [18]. This is less reliable and more difficult to set up correctly. Optimize the placement of the belt with an MRI sequence that does have a navigator sequence. Alternatively spectra can be recorded in breath holds. For a useful MRS result several breath holds will be required. Four breath holds each with 6 signals averaged with water suppression and a short one without gives 24 averages. Provided the consecutive breath-holds are consistent this approach can yield good results.

Water Suppression

For all in vivo ^1H -MRS some type of water suppression (WS) is essential. The concentration of creatine and even TG is several orders of magnitude lower than the water signal. Therefore the base of the water peak will severely distort the spectral baseline at the scale of the signals. Also, the water signal can cause interference with some small overtone signals that are caused by acoustic vibrations in the magnet and gradient assembly. These acoustic signals are recognizable as a pair of peaks with opposite phases and equidistant left and right of the water peak.

Pre-saturating the water peak with a series of chemical shift selective pulses, each followed by a crusher gradient pulse, solves both baseline distortion and acoustic side-band problems. There are a number of WS schemes usually designed for ^1H -MRS on the brain. For cardiac MRS the choice is limited to short sequences such as chemical shift selective suppression (CHESS) or the somewhat longer three-RF-pulse WET (water suppression enhanced through T_1 effects) [19, 20].

Optimization of the WS for each individual is not possible due to motion. Fortunately it is not necessary because any residual water signals can be removed in the data processing stage, as will be discussed later in this chapter. Do test various WS schemes and settings on a volunteer to ensure a reasonably good suppression in all subjects. The aim is to consistently get a better than 50-fold reduction in the water peak height.

An important factor for the success of any WS scheme is finding the correct resonance frequency for water. This step is not trivial because often the preparation phases on the scanner are set up for navigator or ECG gated operation. Motion interferes with WS even in the final gated experiment. If the data acquisition part of the sequence is set in late systole the preceding WS pulses, which can take anything between 100 and 250 ms, could end up in a cardiac phase with more motion, especially with rapid heart rates. Therefore

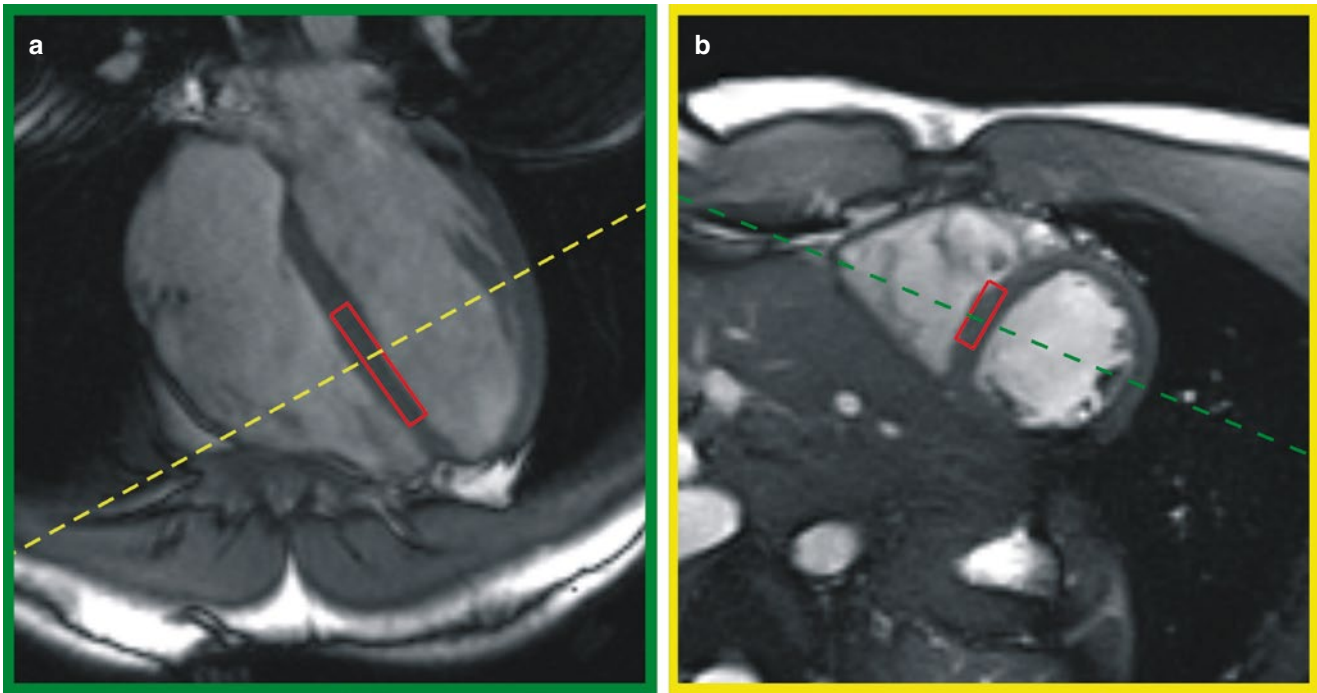


Fig. 18.2 Spectroscopy volume placement on systolic SSFP cine images in (a) four-chamber view and (b) short axis view. The intersection of the volume with the image plane is shown in red, the intersections of the images with each other are shown as dashed green or yellow lines

some water frequency shifts are likely to occur during the WS sequence. These shifts create a variable appearance of the remaining water peak that makes the previously discussed constructive averaging unreliable if it is based on the residual water signal.

Choosing a larger suppression bandwidth for the WS RF pulses reduces the chance of missing the water peak due to motion related frequency shifts. As a bonus, wider the bandwidth shorter the RF pulse, therefore the WS scheme can become shorter and easier to fit in the R-R interval. Depending on field strength and experiences with testing one can set the WS width at 60–80 Hz for 3 T. In the heart we do not expect to observe resonances close to water.

Optimal Data Acquisition Parameters

To reduce the effect of cardiac motion the acquisition window should be kept relatively short compared to the length of a heartbeat. This can be done either by limiting the number of free induction data points or by increasing the bandwidth. The acquisition window should still be long relative to the T_2^* of the observed peaks to avoid truncation of signals. About 1,500 Hz at 256 point resolution is good for a 3 T cardiac ^1H spectrum. This keeps the acquisition time <200 ms and the spectral resolution <6 Hz/point. This is more than enough because the line widths at this field strength will rarely be less than 20 Hz. Time domain fitting methods as

discussed later in the data processing section are less sensitive to MRS signal truncation artifacts, thus safely allowing shorter acquisition windows.

The receive frequency can often be set independent of the center frequency for volume placement. The latter frequency determines the chemical shift at which the volume placement is accurate. The signals of other chemical shifts will be from locations that are slightly shifted in each of the localization dimensions. The bandwidth of the selective RF pulses of the STEAM or PRESS, relative to the chemical shift in Hz sequence determine the amount of shift. At 3 T the chemical shift difference between water and fat is about 400 Hz. Each 4,000 Hz bandwidth pulse will cause a 10 % shift in the volume between water and fat. Shifting the reference frequency for volume placement by -1.7 ppm cuts the volume shift in half. The correct volume prescription will then be halfway between water (at 4.7 ppm) and lipid (at 1.3 ppm) and spot-on for creatine at 3 ppm.

Spectroscopy Volume Placement

The optimal spectrum volume position is the inter-ventricular septum because this uniquely is a region of the left ventricle that is never clad with pericardial fat. The volume is typically placed using a 4-chamber (4CH) scout image and at least three or four short axis (SA) images (see Fig. 18.2). In a 3 T scanner a volume of $6 \times 20 \times 40$ mm delivers enough SNR for good quality spectra with 32 signals averaged (see Fig. 18.3).

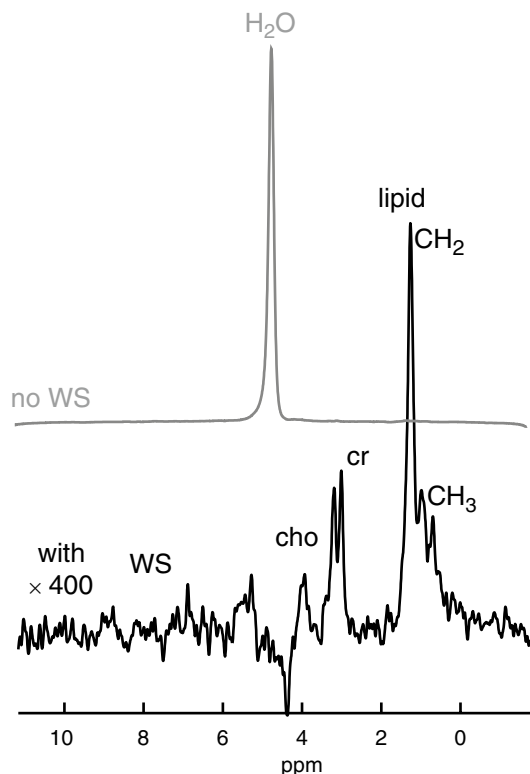


Fig. 18.3 Sample navigator guided PRESS spectra with and without WS. The non WS spectrum (top, grey line), is recorded with 4 signals averaged, the WS spectrum (bottom, black line) was recorded with 32 signals averaged. The WS spectrum is shown with a 400-fold vertical scale magnification. The assigned peaks are (left to right) lipid CH₃ at 0.8–0.9 ppm, lipid CH₂ at 1.2–1.3 ppm. At 3.0 ppm is the combined creatine+phosphocreatine resonance and next to this at 3.25 ppm the resonance for choline compounds

Cine images are used to determine the best delay time and ensure that the volume remains on the septum for the remainder of the cardiac cycle. The actual data acquisition will occupy about 200 ms. The spectroscopy volume dimensions should be the largest volume that fits this location because the SNR is directly proportional to the voxel size. The thickness of the septum limits one dimension to no more than 4–6 mm. The curvature of the left ventricle in the SA image plane limits the second dimension to about 10 mm and the base to apex curvature may limit the remaining dimension to anything between 20 and 40 mm.

Spatial saturation slabs may be prescribed at this point to suppress signals from outside the volume, These Outer Volume Suppression (OVS) slabs can be useful when fat is in close contact with the selected volume, but in cardiac ¹H-MRS they would typically be set on pericardial fat and on

the ribcage. These remote fatty locations should not interfere at all, but as long as the sequence does not come close to SAR limits the inclusion of OVS is not a problem. The OVS does not effectively suppress blood signal because new blood moves in too fast.

Preparation Scans

Much of the sequence optimization for MRI is done automatically. For MRS it is often desirable to go through these steps manually, or at least check the results of these steps. Refer to the scanner manual for instructions, as the default setting is probably automatic background optimization.

By far the most important and difficult step is shimming. As mentioned before, the preparation phase scans are usually not gated. Un-gated manual shimming on a moving target like the heart is virtually impossible. A B₀ field mapping technique with a single (expiration) breath-hold scan is by far the best method. Added bonus is that the same B₀ field map can also be used to optimize the field over the entire heart and get much better results with rapid cine MRI scans using steady state free precession techniques.

The next step is the frequency optimization. Ideally this is done in an expiration breath-hold to best match the position of the heart with the navigator-gated position. The scan-to-scan variations in the offset frequency and line width due to breathing can be observed by running a manual shim sequence.

Finally the transmit RF power needs to be calibrated. Most scanners have only a slab-based optimization. At fields strengths of 3 T and more this is not accurate because the available transmit RF in the heart can be 30 % or more different from the average measured in a transverse slab. A B₁ field mapping technique that can be operated in a breath hold would be best. Lacking such techniques the scanner optimizations will cost some SNR, but fortunately the WS and non-WS will be attenuated by the same factor, so metabolite quantification accuracy will not be severely affected.

Some of the tools that are needed for cardiac ¹H-MRS such as breath-hold B₀ and B₁ field mapping or navigator gated MRS may presently not be available or only be available under a research agreement with the scanner manufacturer. Hopefully it will not take long before these tools are integrated in the commercially available scanner software. Remember that it is our duty to make sure that the scanner manufacturers know there is a demand for it.

MRS Data Processing

An important part of MRS is the data processing. This is not trivial and usually only a basic set of tools is included in the MR scanner software. Scanner based processing is not the best use of scanner time. Even using manufacturer's software on a separate workstation may not be best for speed and accuracy. The use of proper data processing methods is almost as important as having the right scan methods and a good data fitting routine can help retrieve the best possible information from spectra with low SNR.

The popular Mac based MRI processing tool Osirix now has MRS data handling capacity with the SIVIC pug-in and hopefully more plug-ins will become available. Another processing tool that is freely available and widely used in academic institutions is the jMRUI (java Magnetic Resonance User Interface) [21, 22] software package. This is a good starting point for data fitting and pre-processing and includes the time-domain fitting method AMARES (Advanced Method for Accurate, Robust and Efficient Spectral fitting of MRS data) [23], which has the advantage that baseline correction and phasing of the spectra are not critical. The jMRUI package also has a tool for removal of residual water signals from WS spectra: the Hankel single value decomposition HSVD filtering method (see Fig. 18.4). This algorithm automatically finds a predefined number of the strongest resonances. The filter function removes a subset of these signals from a user defined frequency region from the measured data. In Fig. 18.4b the residual water peak in the WS spectrum is partly inverted and skewed due to a shifted WS frequency and too much power in the WS RF pulses. When properly configured the HSVD filter completely removes even this type of line shape.

With the time domain based fit algorithm AMARES the user has to provide initial guesses for resonance frequencies and line widths. A summary of recommended values and settings for AMARES data fitting are given in Tables 18.1 and 18.2. The myocardial lipids resonances can be fitted with a lipid CH₂ peak and lipid CH₃ at 1.3 and 0.9 ppm respectively. All choline containing compounds are fitted with one peak at 3.24 ppm. Creatine and phosphocreatine are indistinguishable at 3 T and below and are fitted with one peak at 3.01 ppm. Optionally one or two peaks for β-CH₂ a peak for CH₂ adjacent to carboxyl or unsaturated lipids at 2 ppm. All peaks should be fitted with soft constraint boundaries. The time domain windowing function is applied to both the measured data and model functions to improve fitting of closely spaced resonances [24]. This filter also allows separated but irrelevant peaks to be ignored in the fit without influencing the result

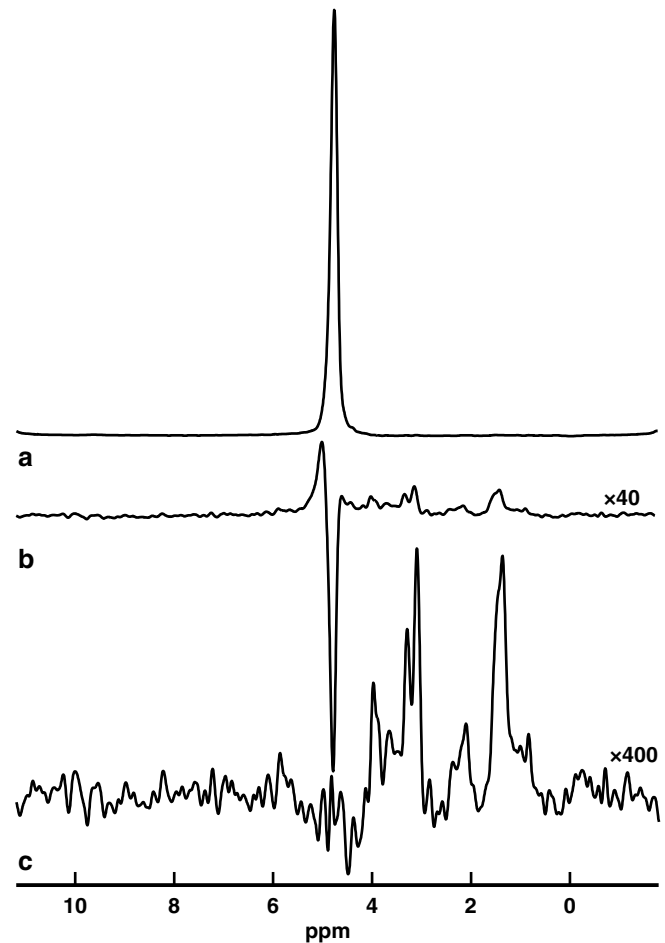


Fig. 18.4 Removal of the water signal with WS and fitted peak subtraction on post-processing. (a) The spectrum recorded without WS. (b) The spectrum recorded with WS. (c) The same spectrum as in (b) after subtracting the (inverted) residual water peak with the HSVD filter function in MRUI. Of the 12 strongest resonances found with HSVD the 5 with chemical shifts between 4.4 and 5 ppm were subtracted from the spectrum in (b) to yield the spectrum in (c). The vertical scales of spectra (b) and (c) were increased by a factor 40 and 400 respectively

(see Fig. 18.5). The zero order phase of the entire spectrum can be a fitted parameter only if all the relative peak phases are fixed at 0° and begin time is fixed or tightly constrained.

Preparing and mastering the data processing steps of ¹H-MRS can be a challenge. The process is not automated and, like the actual ¹H-MRS scanning, it requires a relatively high skill level. However, the cardiac ¹H-MR spectra are a lot simpler than brain ¹H-MR spectra, which contain many more peaks with intricate coupling patterns. Once proper data fit templates are set up the spectral analysis becomes much easier.

Table 18.1 Setting up fit parameters and prior knowledge in the jMRUI user interface for AMARES time domain fitting. The initial estimates (*Starting Values tab*) and soft constraint boundaries (*Prior Knowledge tab*) for human cardiac ^1H -MRS spectra are based on spectra acquired at 3 T

Peak name	Chemical shift [ppm]	Soft constraint limits [ppm]	Line widths [Hz] at 3 T	Soft constraint limits [Hz] at 3 T (optional) ^a
Lipid CH_3	0.9	0.7–1.1	40	0–100 (or 0–3.18)
Lipid CH_2	1.3	1.1–1.5	35	0–100 (or 0–3.18)
Lipid $\beta\text{-CH}_2\text{-a}$	2.0	1.8–2.2	50	0–100 (or 0–3.18)
Lipid $\beta\text{-CH}_2\text{-b}$	2.2	2.0–2.4	50	0–100 (or 0–3.18)
creatine	3.01	2.8–3.15	20	0–50 (or 0–0.785)
choline	3.24	3.15–3.4	35	0–100 (or 0–3.18)

^aWhen with AMARES fitting to a Gaussian line shape in jMRUI versions 5 and earlier, there is a bug in the soft constraint setting for line widths. The desired limits have to be translated to: $\text{input value} = (\text{Desired_Limit_in_Hz})^2 / (1000 * \pi)$. Thus the user input of 0.785 gives an effective limit of 50 Hz and 3.18 yields a limit of 100 Hz

Table 18.2 Recommended settings for overall phase fitting (*Overall Phases tab*) for AMARES time domain fitting of human cardiac ^1H -MRS spectra. The prior knowledge individual peak relative phase setting should be set to fixed at 0° for all peaks (in *Prior Knowledge tab*)

Peak name	Chemical shift [ppm]
Zero order phase	Fitted between -180° and $+180^\circ$
Begin time	Locked at zero or fixed value no more than ± 0.2 ms
Weighting in time domain	ON, begin interval 0, end 10 or 15
Number of points in fit	All the points measured (typically 256)
Ignore initial points	Only with severe baseline roll or offset in the spectra

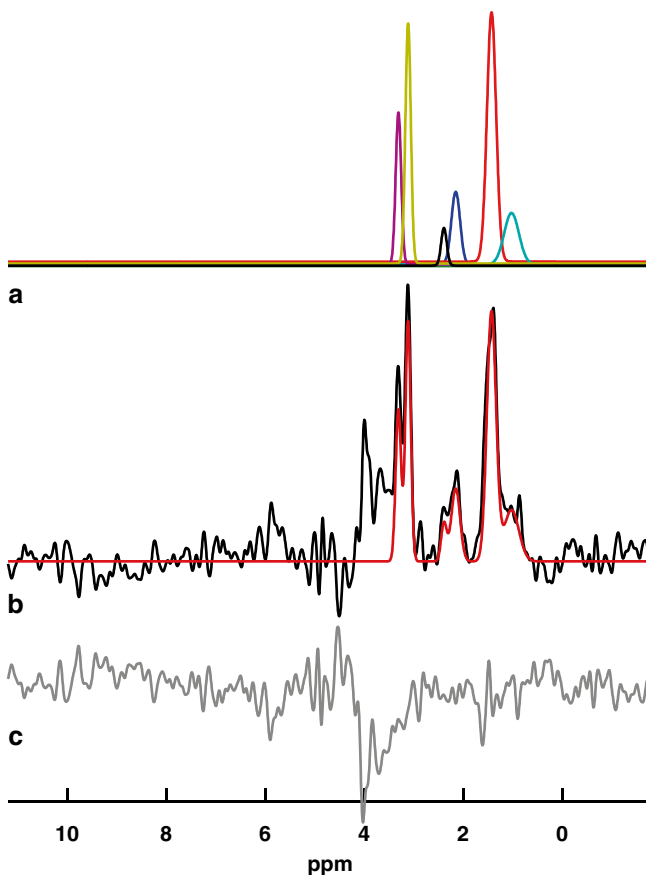


Fig. 18.5 Result of an AMARES time domain fit of a cardiac ^1H -MRS spectrum. **(a)** The spectra of the individual fitted peaks. The fitted peaks are left to right: lipid CH_3 (*turquoise* at 0.9 ppm) and CH_2 (*red* at 1.3 ppm) lipid CH_2 unsaturated adjacent to unsaturated protons or carboxyl and amino acids (*blue* and *black* at about 2 ppm), creatine (*green* at 3 ppm) and choline containing compounds (*purple* at 3.25 ppm). **(b)** The total fitted model spectrum (*red line*) and the measured spectrum (*black*) and **(c)** the residual difference between measured data and fit

Conclusion

There are many aspects of ^1H -MRS that require specific optimization and adaptation for successful use in the human heart. Even so, the investment is manageable and the rewards can be great. Because MR scanners can be used for advanced cardiac ^1H -MRI techniques as well as ^1H -MRS there is great potential for gaining insight into the links between cardiac metabolism and function or morphology.

References

- Ackerman JJ, Grove TH, Wong GG, Gadian DG, Radda GK. Mapping of metabolites in whole animals by ^31P NMR using surface coils. *Nature*. 1980;283(5743):167–70.
- Bottomley PA. MR spectroscopy of the human heart: the status and the challenges. *Radiology*. 1994;191(3):593–612.
- Lamb HJ, Beyerbach HP, Ouwerkerk R, Doornbos J, Pluim BM, van der Wall EE, van der Laarse A, de Roos A. Metabolic response of normal human myocardium to high-dose atropine-dobutamine stress studied by ^31P -MRS. *Circulation*. 1997;96(9):2969–77.
- Weiss RG, Gerstenblith G, Bottomley PA. ATP flux through creatine kinase in the normal, stressed, and failing human heart. *Proc Natl Acad Sci U S A*. 2005;102(3):808–13.
- Bottomley PA, Weiss RG. Non-invasive magnetic-resonance detection of creatine depletion in non-viable infarcted myocardium. *Lancet*. 1998;351(9104):714–8.
- Nakae I, Mitsunami K, Omura T, Yabe T, Tsutamoto T, Matsuo S, Takahashi M, Morikawa S, Inubushi T, Nakamura Y, Kinoshita M, Horie M. Proton magnetic resonance spectroscopy can detect creatine depletion associated with the progression of heart failure in cardiomyopathy. *J Am Coll Cardiol*. 2003;42(9):1587–93.
- Rial B, Robson MD, Neubauer S, Schneider JE. Rapid quantification of myocardial lipid content in humans using single breath-hold ^1H MRS at 3 Tesla. *Magn Reson Med: Off J Soc Magn Reson Med/Soc Magn Reson Med*. 2011;66(3):619–24.
- van der Meer RW, Hammer S, Lamb HJ, Frölich M, Diamant M, Rijzewijk LJ, de Roos A, Romijn JA, Smit JWa. Effects of short-term high-fat, high-energy diet on hepatic and myocardial triglyceride content in healthy men. *J Clin Endocrinol Metab*. 2008;93(7):2702–8.
- Bilet L, van de Weijer T, Hesselink MKC, Glatz JFC, Lamb HJ, Wildberger J, Kooi ME, Schrauwen P, Schrauwen-Hinderling VB. Exercise-induced modulation of cardiac lipid content in healthy lean young men. *Basic Res Cardiol*. 2011;106(2):307–15.
- van der Meer RW, Rijzewijk LJ, Diamant M, Hammer S, Schär M, Bax JJ, Smit JWa, Romijn JA, de Roos A, Lamb HJ. The ageing male heart: myocardial triglyceride content as independent predictor of diastolic function. *Eur Heart J*. 2008;29(12):1516–22.
- Rijzewijk LJ, van der Meer RW, Smit JWa, Diamant M, Bax JJ, Hammer S, Romijn JA, de Roos A, Lamb HJ. Myocardial steatosis is an independent predictor of diastolic dysfunction in type 2 diabetes mellitus. *J Am Coll Cardiol*. 2008;52(22):1793–9.
- Bottomley PA. Spatial localization in NMR spectroscopy in vivo. *Ann NY Acad Sci*. 1987;508:333–48.
- Granot J. Selected volume excitation using stimulated echoes (VEST). Applications to spatially localized spectroscopy and imaging. *J Magn Reson* (1969). 1986;70(3):488–92.
- Frahm J, Merboldt K-D, Hänicke W. Localized proton spectroscopy using stimulated echoes. *J Magn Reson* (1969). 1987;72(3):502–8.
- Fischbach F, Bruhn H. Assessment of in vivo ^1H magnetic resonance spectroscopy in the liver: a review. *Liver Int: Off J Int Assoc Study Liver*. 2008;28(3):297–307.
- Schär M, Kozerke S, Boesiger P. Navigator gating and volume tracking for double-triggered cardiac proton spectroscopy at 3 Tesla. *Magn Reson Med: Off J Soc Magn Reson Med/Soc Magn Reson Med*. 2004;51(6):1091–5.
- Gabr RE, Sathyanarayana S, Schär M, Weiss RG, Bottomley PA. On restoring motion-induced signal loss in single-voxel magnetic resonance spectra. *Magn Reson Med: Off J Soc Magn Reson Med/Soc Magn Reson Med*. 2006;56(4):754–60.
- Szczepaniak LS, Dobbins RL, Metzger GJ, Sartoni-D'Ambrosia G, Arbique D, Vongpatanasin W, Unger R, Victor RG. Myocardial triglycerides and systolic function in humans: in vivo evaluation by localized proton spectroscopy and cardiac imaging. *Magn Reson Med: Off J Soc Magn Reson Med/Soc Magn Reson Med*. 2003;49(3):417–23.
- Zijl PM, Moonen CW. Solvent suppression strategies for in vivo magnetic resonance spectroscopy. In: Rudin M, editor. *In-vivo magnetic resonance spectroscopy I: probeheads and radiofrequency pulses spectrum analysis SE – 3*, vol. 26. Berlin: Springer; 1992. p. 67–108.
- Ogg RJ, Kingsley PB, Taylor JS. WET, a T1- and B1-insensitive water-suppression method for in vivo localized ^1H NMR spectroscopy. *J Magn Reson B*. 1994;104(1):1–10.
- Naressi A, Couturier C, Devos JM, Janssen M, Mangeat C, de Beer R, Graveron-Demilly D. Java-based graphical user interface for the MRUI quantitation package. *MAGMA*. 2001;12(2–3):141–52.
- MRUI home page. <http://sermn02.uab.cat/mrui/>. Published December, 2009. 2011. [Online]. Available: <http://sermn02.uab.cat/mrui/>. Accessed 30 June 2011.
- Vanhamme L, van den Boogaart A, Van Huffel S. Improved method for accurate and efficient quantification of MRS data with use of prior knowledge. *J Magn Reson (San Diego, Calif)*. 1997;129(1):35–43.
- Knijf A, Debeer R, Vanormondt D. Frequency-selective quantification in the time domain. *J Magn Reson*. 1992;97(2):444–50.

Lara Bakhos and Mushabbar A. Syed

Abstract

Gadolinium based contrast agents (GBCA) are routinely used in MRI of cardiovascular system. The two most clinically applicable categories of GBCA are the extracellular and blood pool/intravascular contrast agents with extracellular agents dominating the clinical use. Major indications of GBCA use in cardiac and vascular examinations include assessment of myocardial infarction and viability, myocardial tissue characterization in various forms of non-ischemic cardiomyopathies including dilated cardiomyopathy, hypertrophic cardiomyopathy, sarcoidosis, amyloidosis or myocarditis, myocardial perfusion imaging during stress testing, cardiac mass or thrombus evaluation and magnetic resonance angiography of arteries or veins. There are evolving applications for GBCA that include left atrial scar imaging in patients with atrial fibrillation or coronary artery imaging among others. Dosing of GBCAs depend upon the type of contrast agents and specific imaging protocol. Standardized protocols have been published by the Society for Cardiovascular Magnetic Resonance Imaging and were recently updated in 2013. GBCAs are generally considered safe with a very low incidence of adverse reactions, mostly minor including rash/hives and nausea. Rarely serious side effects may occur including life-threatening anaphylactoid reactions and recently recognized nephrogenic systemic fibrosis (NSF). The incidence of NSF varies with the degree of renal insufficiency. It is estimated that patients with stage 4–5 chronic kidney disease [eGFR <30 ml/min/1.73 m²] have a 1–7 % risk of developing NSF after exposure to GBCA. However, screening for renal impairment to identify patients at risk for NSF and following GBCA use guidelines in these patients has nearly eliminated new NSF cases. Novel contrast agents are in development that could be used in patients with renal dysfunction or as molecular probes in imaging of biological processes at the cellular or subcellular level.

Introduction

Paramagnetic and superparamagnetic metals are used as contrast agents for magnetic resonance imaging (MRI). These contrast agents are coupled with specific MRI sequences to image cardiac and vascular structures and to aid in tissue characterization. Gadolinium is a paramagnetic lanthanide metal that has been widely studied and used as an MRI contrast agent. There are several gadolinium based contrast agents (GBCAs) that are FDA approved in the USA for clinical use. Unlike X-ray contrast agents, MRI contrast agents are not visible by themselves on MRI images; rather

L. Bakhos, MD
Department of Medicine-Cardiology, Stritch School of Medicine,
Loyola University Medical Center, Maywood, IL, USA

M.A. Syed, MD (✉)
Rolf & Merian Gunnar Professor of Medicine, Departments of
Medicine – Cardiology, Radiology, Cell & Molecular Physiology,
Director, Cardiovascular Imaging & Cardiology Fellowship
Program, Stritch School of Medicine, Loyola University Medical
Center, 2160 S. First Ave., Maywood, IL 60513, USA
e-mail: masyed@lumc.edu

affect the tissue signal intensity by interacting with tissue relaxation properties. More recently the discovery and association of nephrogenic systemic fibrosis with GBCAs in patients with advanced kidney disease have limited their widespread application. This chapter provides a concise review of MRI contrast media including basic principles of physics, types of contrast agents available, clinical applications, adverse reactions and use in special populations. A brief description of novel contrast agents is also included.

Basic Principles of MRI Contrast Agents

Magnetic resonance imaging (MRI) signals arise from hydrogen (^1H), which has intrinsic magnetic properties due to its single positively charged proton and is in great abundance in the body. The details of MRI signal generation and image acquisition have been discussed in previous chapters. One of the important advantages of MRI is its ability to differentiate various tissues from one another also termed tissue characterization.

The relative difference in signal intensity between two adjacent tissues is referred to as image contrast and forms the basis for visual perception to differentiate between the two tissues. Contrast media is frequently used to enhance these differences. The intrinsic factors that contribute to contrast are ^1H proton density, the relaxation times of ^1H protons, and magnetic susceptibility [1]. Because it is not possible to change tissue proton density, alteration of tissue relaxation times and susceptibility have been the major determinants of contrast media development, with the former dominating the field.

By shortening relaxation times of the ^1H protons in neighboring water molecules, contrast media increase the strength of the magnetic field in the local environment, which results in either an increase or decrease in signal intensity. Therefore, MR contrast agents enhance intrinsic contrast not by generating signals themselves, but by modifying the amplitude of the signal generated by ^1H protons [1].

All contrast agents shorten both T_1 (longitudinal relaxation time) and T_2 (transverse relaxation time). However, depending on various factors including the agent itself, dose and MRI sequence applied, contrast agents can result in a more T_1 (positive) or T_2 (negative) shortening effect. Agents with a dominant T_1 shortening effect give rise to an increase in signal intensity. Therefore, these agents are referred to as “positive” contrast agents as tissues taking up these agents become bright or hyperintense on T_1 -weighted imaging [2]. Accordingly, agents with a dominant T_2 shortening effect cause a reduction in signal intensity and are referred to as “negative” contrast agents. Among others, paramagnetic gadolinium (Gd)- and manganese (Mn)-based contrast agents are examples of T_1 agents, whereas para-/superparamagnetic large iron oxide particles are examples of T_2 agents [2].

Paramagnetic metal agents contain unpaired electrons in their outer shells. The magnetic field produced by an electron is much stronger than that by a ^1H proton, making these ideal agents to impact tissue T_1 and T_2 relaxation. The number of unpaired electrons directly correlates with the strength of the magnetic moment of the element [3]. Gd^{3+} has seven unpaired electrons, making it an excellent paramagnetic contrast agent and currently the most commonly used in routine clinical practice.

Gadolinium is a lanthanide metal element. In its free form, Gd^{3+} is highly toxic, accumulating in organs by displacing endogenous Fe^{3+} , Zn^{2+} , Cu^{3+} and calcium via transmetallation [4]. Therefore, gadolinium must be complexed to a ligand or chelate before intravenous (IV) administration. The chelate encapsulates the gadolinium, resulting in thermodynamically stable and biologically inert complex at a physiologic pH. The fundamental issue for all contrast agents is their chelation stability that reflects the potential release of free metal ions in vivo. Therefore, the safety of the complex is determined by the properties of the chelate, its binding to Gd, and the stability of the complex [5]. Favorable chelate attributes include selective affinity for Gd^{3+} and slow dissociation [5]. This ensures near-complete renal excretion of the intact complex without biotransformation and prevents toxic interactions between Gd^{3+} ions and endogenous tissues. Macrocyclic chelates are known to provide higher kinetic stability than linear chelates (see Table 19.1).

In addition to its need for safety purposes, the chelate has multiple effects on gadolinium. When gadolinium is bound to a chelate with a large molecular structure, its rate of tumbling slows resulting in an increase in relaxivity [6]. Conversely, chelates decrease the T_1 shortening effect of gadolinium by reducing the interaction between Gd^{3+} ions and ^1H protons [7]. Additionally, the renal excretion of chelated gadolinium increases approximately 500-fold when compared to that of free Gd^{3+} ions [8].

The coordinated water molecule also plays a critical role in contrast enhancement. Its proximity to the gadolinium ion results in efficient relaxation. It undergoes rapid chemical exchange with the solvating water molecules, resulting in a catalytic effect whereby the gadolinium complex shortens the relaxation time of the bulk solution [2]. GBCAs transiently bind to water molecules which results in a shortening of the T_1 relaxation time and the production of a brighter signal. This can be simply quantified by the following equation: [2]

$$1/T_1 = 1/T_{1_0} + R_1 \times [\text{CA}]$$

Where T_1 is the observed relaxation time with contrast agent, T_{1_0} is the relaxation time before addition of the contrast agent, $[\text{CA}]$ is the concentration of the contrast agent, and R_1 is the relaxivity of the GBCA. As demonstrated by this equation, the contrast agent usually increases the relaxation rate

Table 19.1 Properties of FDA approved Gadolinium based contrast agents

Generic name	Gadopentetate dimeglumine	Gadoteridol	Gadodiamide	Gadoversetamide	Gadobenate dimeglumine	Gadoxetate	Gadobutrol	Gadoterate	Gadofosveset trisodium
Trade name	Magnevist	ProHance	Omnican	OptiMARK	MultiHance	Eovist	Gadavist	Dotarem	Ablavar
Manufacturer	Bayer healthcare	Bracco diagnostics	GE healthcare	Mallinckrodt	Bracco diagnostics	Bayer healthcare	Bayer healthcare	Guerbet	Lantheus medical imaging
Label dose	0.1 mmol/Kg (0.2 mL/Kg)	0.1 mmol/Kg (0.2 mL/Kg)	0.1 mmol/Kg (0.2 mL/Kg)	0.1 mmol/Kg (0.2 mL/Kg)	0.1 mmol/Kg (0.2 mL/Kg)	0.025 mmol/Kg (0.1 mL/Kg)	0.1 mmol/Kg (0.1 mL/Kg)	0.1 mmol/Kg (0.2 mL/Kg)	0.03 mmol/Kg (0.12 mL/Kg)
Approval year	1988	1992	1993	1999	2004	2008	2011	2013	2008
Approved indication	Central nervous system Extracranial/extraspinal Tissues Body (excluding the heart)	Central nervous system Extracranial/extraspinal tissues	Central nervous system Body (excluding the heart)	Central nervous system Liver	Central nervous system	Hepatobiliary disease	Disrupted blood brain barrier Central nervous system Breast	Central nervous system	Aortoiliac occlusive disease
Approved age	≥2 years	2–18 years and adults	2–16 years and adults	18–76 years	≥2 years	Adults	≥2 years	≥2 years	Adults
Molecular structure	Linear, ionic	Linear, ionic	Cyclic, nonionic	Linear, nonionic	Linear, nonionic	Linear, ionic	Macrocyclic, nonionic	Macrocyclic, ionic	Linear, ionic
Chelating agent	DTPA	HP-DO3A	DTPA-BMA	DTPA-BMEA	BOPTA	EOB-DTPA	DO3A-butrol	DOTA	Fosveset
Elimination pathway	Renal	Renal	Renal	Renal	Renal (97 %) and biliary (3 %)	Renal (50 %) and biliary (50 %)	Renal	Renal	Renal (91 %) and biliary (9 %)
Serum elimination half-life	96 ± 7.8 min	94 ± 4.8 min	77.8 ± 16 min	104 ± 19.5 min	70–121 ± 15.6–36 min	55–57 min	1.33–2.13 h	1.6 ± 0.2 h	16.3 ± 2.6 h

($1/T_1$) proportionally to the amount of contrast agent [2]. Furthermore, the performance of the contrast agent is highly dependent on its relaxivity (R_1). Of note, although the linear relationship of the equation is maintained at the concentrations used in routine clinical imaging, it is not preserved at the extremes of the concentration spectrum [9]. For example, very high concentrations actually reduce the signal intensity as the T_2 shortening effect of the contrast agent then becomes dominant [9].

Classification of GBCAs

There are several methods with which to classify MRI contrast agents, none of which are all encompassing. The most commonly used contrast agents for cardiovascular imaging are gadolinium based. There are currently nine available GBCAs approved for use by the FDA in the United States. Table 19.1 summarizes the properties of these FDA approved GBCAs.

GBCAs can be further classified into categories based on their biodistribution in tissues, which is determined by the chemical structure of the chelator. The two most clinically applicable categories are the extracellular and blood pool/intravascular contrast agents.

Extracellular Contrast Agents

The first approved GBCAs were extracellular contrast agents (ECCAs). As demonstrated in Table 19.1, each agent has a generic name and a trade name. Despite the complicated nomenclature, these agents share three similar properties in chemical structure. They are gadolinium-based, contain a chelate bound to the gadolinium, and have a single water molecule coordination site to the gadolinium [2].

After intravenous injection, ECCAs distribute rapidly into both the intravascular and extracellular spaces, a process which can be divided into three phases: arterial, venous, and equilibrium phases. Initially, the water-soluble contrast agent distributes into the intravascular space. The arterial phase is the time between contrast arrival in the region of interest and subsequent venous filling [9]. This phase is typically less than 20 s in duration; therefore, the timing of arrival of the contrast bolus with imaging is critical. The arterial phase is followed by venous filling (venous phase). Approximately 10 min later, the extracellular contrast agent redistributes into interstitial spaces, known as the equilibrium phase.

Elimination of contrast agents occurs rapidly and without biotransformation through glomerular filtration in the kidney [1]. The plasma elimination half-life is typically 70–90 min in the setting of normal kidney function with approximately 98 % of the dose being cleared within 24 h [7]. In patients

with renal impairment, the plasma half-life is lengthened. In one study, the elimination half-life of Gadodiamide (Omniscan) increased to 34.2 h in a patient with severe renal insufficiency (GFR 2–10 mL/min) [10]. Hepatic excretion is negligible, even in those with severely reduced renal function except for Gadoxetate (Eovist) which has 50 % biliary excretion making it useful for hepatobiliary disease imaging. Other available ECCAs include Gadopentetate dimeglumine (Magnevist), Gadoteridol (ProHance), Gadodiamide (Omniscan), Gadoversetamide (OptiMARK), Gadobenate dimeglumine (MultiHance), Gadobutrol (Gadavist) and Gadoterate (Dotarem).

Intravascular/Blood Pool Contrast Agents

Extracellular contrast agents are frequently used off-label for MR angiography (MRA) with imaging targeted to their arterial or venous phase as required. However, because of their pharmacokinetic profile, they are not the ideal agents for this use given their short period of peak vascular enhancement before rapid extravasation into the interstitial space. Intravascular or blood pool contrast agents were specifically designed to overcome this limitation through deliberate confinement to the intravascular space, resulting in a longer plasma half-life with prolonged intravascular enhancement [11]. These agents allow for the imaging of multiple vascular beds with a higher intravascular signal than is achievable with the use of ECCAs. Furthermore, the need for bolus timing as with ECCA is eliminated, as the optimal imaging window is significantly longer on the order of tens of minutes as compared to seconds with the use of ECCAs.

The distribution and elimination of a contrast agent can be altered by modifying the size, charge and molecular shape of the ligand relative to the permeability of the capillary bed. The higher the molecular weight of the compound, the slower its elimination half-life and clearance are [1]. Early blood pool agents consisted of gadolinium covalently linked to very large molecules such as polylysine, dextran, and modified bovine serum albumin. These large compounds had restricted diffusion out of the vascular space with good imaging results. However, this resulted in very slow elimination creating concerns about a potential immunologic response in preclinical studies [12]. This led to the revised approach of synthesizing a compound large enough to be partially or completely confined to the vascular compartment in some tissues, but small enough to be eliminated by glomerular filtration. As a point of reference, the capillary beds in myocardial tissue are lined with an uninterrupted layer of endothelial tissue, allowing for diffusion of only small molecules (such as Gd-DTPA, weighted 590 Da), whereas the fenestrations in the glomerular capillaries are 60–70 nm in diameter and allow for passage of any molecule weighing $\leq 20,000$ Da [1].

In December 2008, the FDA approved the use of Gadofosveset (Vasovist or Ablavar, previously known as MS-325), making it the first commercial agent to be approved in this class [13]. Gadofosveset is a unique gadolinium-based contrast agent in that it binds reversibly to serum albumin. Reversible albumin binding serves various purposes: (1) the albumin binding slows extravasation of the contrast agent, thus allowing the contrast agent to remain in the intravascular space for a much longer period of time (plasma half-life approximately 15.5 h), (2) the reversibility still allows a path for excretion, and (3) the relaxivity of the contrast agent is increased four to tenfold by its binding to albumin allowing for the administration of a much smaller dose. In the United States, gadofosveset is FDA approved only for aortoiliac disease in adults with other uses being off-label at present. Compared to traditional ECCAs, blood pool agents allow for both arterial and venous phase imaging, as well as delayed venous imaging and cover a larger anatomic area, e.g. head to foot without re-injection.

There are several other intravascular agents in clinical development, including Gadocoletic acid (also known as B-22956 and B22956/1) which is a Gd-DTPA derivative and binds to albumin. Polymeric gadolinium chelates are also blood pool contrast agents that are in development and exhibit higher relaxivity and more pronounced contrast enhancement than traditional ECCAs [14]. Sometimes, the extracellular contrast agent Gadobenate dimeglumine, Gd-BOPTA (MultiHance) is erroneously categorized as a blood pool agent due to its affinity for albumin, which results in a modest increase in relaxivity relative to the ECF agents [2, 5]. However, as it only binds weakly and transiently to albumin, it should not be classified as such.

Novel/Experimental Contrast Agents

Ferumoxytol

Ferumoxytol (Feraheme, AMAG Pharmaceuticals, Cambridge, MA) is a novel ultrasmall paramagnetic iron oxide (USPIO) nanoparticle, which is FDA approved as an intravenous iron replacement therapy for the treatment of iron deficiency anemia in adult patients with chronic kidney disease. Ferumoxytol has recently been investigated extensively as an intravenous contrast agent in MRI [15]. Ferumoxytol is given as a rapid intravenous injection, has a long half-life on the order of 14–15 h and distributes only in the intravascular compartment behaving as a blood pool agent. Ferumoxytol is made of iron oxide particles surrounded by a carbohydrate coat and as an iron replacement agent it carries no risk of nephrogenic systemic fibrosis (NSF). It has no renal excretion and is cleared by macrophages over several days. It shortens T_1 leading to strong enhancement on T_1 -weighted imaging but also can cause

strong susceptibility artifacts due to shortening of T_2^* . Dilution of the ferumoxytol minimizes its marked T_2^* shortening effects, which can lead to signal loss [16]. Ferumoxytol has been used off-label as a MRA blood pool agent, in the imaging of the carotid arteries, thoracic and abdominal aorta, renal arteries and peripheral arteries and veins. The main advantage is likely to be in patients where GBCAs use is contraindicated, e.g. in patients with end-stage renal disease with or without dialysis where it has been studied extensively as an iron replacement therapy.

Manganese Based Contrast Agents

Manganese (Mn) is a non-lanthanide metal which has been used as a paramagnetic contrast agent in MRI. Manganese ion (Mn^{2+}) works primarily as GBCAs by shortening the T_1 thus leading to increase in signal intensity on T_1 -weighted imaging. Similar to Gd, Mn in its free form is toxic and needs to be chelated before administration. At the cellular level, Mn is transported into the cells through calcium channels and accumulates in the mitochondria [17]. Because of its involvement in mitochondrial function, Mn uptake is based on mitochondrial density in the cell which makes it an attractive contrast agent for liver, pancreas, kidney, heart and other mitochondrial rich organs. Manganese based contrast agents have been studied in Manganese-enhanced MRI (MEMRI) for the assessment of tissue viability. In a study of ten patients with recent myocardial infarction, use of manganese dipyridoxyl diphosphate (MnDPDP) showed increased uptake by normal myocardium compared to infarcted myocardium [18]. In a mouse model of acute and chronic myocardial infarction, MEMRI using $MnCl_2$ was compared with late gadolinium enhancement (LGE) using Gadodiamide [19]. In the acute stage, LGE overestimated infarct size compared to MEMRI and histology (+12.0 % \pm 3.6 %, $P=0.001$) while no difference in infarct size was found in chronic stage. A major drawback of using Mn in free ionic form ($MnCl_2$) is its cellular toxicity (cardiotoxicity, neurotoxicity), however, unlike GBCAs there is no risk of NSF with Mn use. Some toxicity has been observed in animal experiments even with low-affinity chelates. Two Mn based contrast agents, intravenous Mn-DPDP (Teslascan, GE Healthcare) for liver imaging and oral manganese chloride tetrahydrate for gastrointestinal imaging (LumenHance, Bracco Diagnostics) are available for human use.

Molecular MRI Contrast Agents

Molecular imaging is the visualization of biological processes at the cellular or subcellular level [20]. Imaging of the molecular pathways have the potential to transform the current treatment paradigms by providing accurate early diagnosis and treatment follow up which may form the basis of personalized medicine in cardiovascular, cancer and neurological diseases. MRI has the advantage of providing a

comprehensive evaluation of cardiac morphology and function. New technical advances in high-resolution imaging can potentially make MRI an ideal modality for molecular imaging. Studies of carotid plaque imaging by MRI have documented the feasibility to delineate carotid plaque composition by characterizing lipid core, calcification and fibrous cap [21]. Most of carotid plaque characterization studies were conducted by using high-resolution imaging techniques with or without GBCAs, however, *in vivo* imaging of finer molecular processes require the use of molecular probes in the form of novel contrast agents. New contrast agents are being developed for molecular MRI that may aid in the detection of microthrombi or arterial plaques.

Lanza et al. developed a novel fibrin-specific MR contrast agent, which is a ligand-directed, lipid-encapsulated liquid perfluorocarbon nanoparticle (250 nm nominal diameter) that can detect and quantify occult microthrombi within the intimal surface of atherosclerotic vessels with high sensitivity [22]. In subsequent *in vitro* and *in vivo* (canine model of jugular vein thrombus) experiments using this nanoparticle formulated with Gd-DTPA-BOA, they found presence of nanoparticles on the surface of thrombi that produced a high signal (contrast enhancement) on T₁-weighted imaging [23]. Their results suggested that molecular imaging of fibrin-targeted paramagnetic nanoparticles could provide sensitive detection and localization of fibrin with potential for early detection of vulnerable plaques.

Magnetic iron oxide nanoparticles constitute another class of molecular MRI agents also called novel ultrasmall paramagnetic iron oxide (USPIO) nanoparticles. They have a central core of iron oxide, which measures 3–5 nm in diameter surrounded by a dextran, starch, or polymer coat. Ferumoxytol is an example of USPIO used as blood pool agent (see above). Two USPIO have been approved for liver imaging, Feumoxides (Feridex) and Ferrixan (Resovist). There are other USPIO that are in various phases of development or clinical testing. Cross linked iron oxide (CLIO) nanoparticles have been specifically developed for molecular imaging and studied as molecular probes for imaging apoptosis and vascular cell adhesion molecule 1 (VCAM-1) [20]. Their small size and long circulating half-life allows them to penetrate atherosclerotic plaques or myocardial interstitial space.

Applications and Methods for Contrast Administration

As elaborated in other chapters, the use of GBCAs has become an integral component of cardiovascular MRI. Their use is particularly crucial in the diagnosis of cardiomyopathies, the assessment of myocardial viability, the evaluation of myocardial perfusion, the evaluation of cardiac masses

and thrombi, the assessment of congenital heart disease, and the diagnosis of vascular abnormalities. Novel uses under development include the use of contrast agents in coronary artery imaging, T₁ mapping for diffuse myocardial fibrosis, and MRI-guided cardiac interventions.

Dosing of GBCAs in the literature is variable and depends on the indication for its use. Standardized protocols have been published by the Society for Cardiovascular Magnetic Resonance Imaging and were recently updated in 2013 [24]. Contrast volume and injection rates depend upon the scan duration, type of contrast agents and specific imaging protocol (Tables 19.1 and 19.2).

Adverse Effects

GBCAs are generally considered safe with an exceptionally low incidence of adverse reactions. The frequency of all acute adverse events after an injection of a 0.1 or 0.2 mmol/kg dose ranges from 0.07 to 2.4 % [25]. The vast majority of reactions are considered mild as defined by the American College of Radiology (ACR), which includes coldness, warmth or pain at the injection site, nausea, vomiting, headache, flushing, dizziness and mild pruritus (Table 19.3) [26]. In a recent international multicenter registry study that assessed the safety of GBCAs in over 17,000 patients, only 30 acute adverse reactions occurred with an incidence of 0.17 %, all of which were mild [26]. The most frequent adverse reaction was rash/hives (0.05 %), followed by nausea (0.04 %), and anxiety (0.03 %). Reactions resembling an “allergic” response including urticaria and less frequently bronchospasm are very rare and occur with a frequency of 0.004–0.7 % [25]. Although there are reports of severe adverse reactions including life-threatening anaphylactoid reactions and death, they are exceptionally rare [27, 28]. The largest assessment of GBCA safety came in 2013 on the use of Gd-DTPA (Magnevist) in 120 million administrations which reported an incidence of severe reactions of only 0.003 % [28].

Several risk factors have been identified that are associated with an increased frequency of acute adverse reactions to GBCAs. These include a history of asthma or allergy, a faster contrast injection rate, and a prior reaction to a gadolinium-based or iodinated contrast agent [29]. Currently, there are no universal guidelines on the management of patients with these risk factors. The most recent 2013 ACR recommendations include identification of patients with a prior reaction to a GBCA, assessing the need for contrast, determining if an alternative agent can be used, and evaluating the need for premedication with corticosteroids and antihistamines [25]. Treatment of moderate or severe acute adverse reactions to GBCAs is similar to that for reactions to iodinated contrast [25].

Table 19.2 Contrast and chasing bolus doses and injection rates

Indication	Contrast dose (mmol/Kg body weight)	Injection rate	Saline chasing bolus (mL)	Injection rate (mL/s)
Perfusion	0.05–0.1	3–7 mL/s	30	3–7
Late gadolinium enhancement	0.1–0.2		20	
Angiography (carotids, renals, aorta)	0.1–0.2	2–3 mL/s	20	2–3
Time-resolved angiography	0.005	3–5 mL/s	30	3–5
Peripheral angiography	0.2	First 10 mL @ 1.5 mL/s, rest @ 0.4–0.8 mL/s	20	0.4–0.8

Reproduced from Kramer et al. [24]

Table 19.3 Classification of severity and manifestation of adverse reactions to contrast media

Mild	
Signs and symptoms appear self-limited without evidence of progression (e.g., limited urticaria with mild pruritus, transient nausea, 1 episode of emesis) and include:	
Nausea, vomiting	Pallor
Cough	Flushing
Warmth	Chills
Headache	Sweats
Dizziness	Rash, hives
Shaking	Nasal stuffiness
Altered taste	Swelling: eyes, face
Itching	Anxiety
<i>Treatment:</i> Requires observation to confirm resolution and/or lack of progression and may require treatment in some cases. Patient reassurance is usually helpful.	
Moderate	
Signs and symptoms are more pronounced. Moderate degree of clinically evident focal or systemic signs or symptoms, including:	
Tachycardia/bradycardia	Bronchospasm, wheezing
Hypertension	Laryngeal edema
Generalized or diffuse erythema	Mild hypotension
Dyspnea	
<i>Treatment:</i> Clinical findings in moderate reactions frequently require prompt treatment. These situations require close, careful observation for possible progression to a life-threatening event.	
Severe	
Signs and symptoms are often life-threatening and include:	
Laryngeal edema (severe or rapidly progressing)	Convulsions
Profound hypotension	Unresponsiveness
Clinically manifest arrhythmias	Cardiopulmonary arrest
<i>Treatment:</i> Requires <i>prompt</i> recognition and aggressive treatment; manifestations and treatment frequently require hospitalization.	

Reproduced with permission from Bruder et al. [26, p. 1173]

Nephrogenic Systemic Fibrosis (NSF)

GBCAs are considered non-nephrotoxic at clinically recommended doses for MRI and MRA and historically, were considered safe in patients with impaired renal function [30]. In 2000, Cowper and colleagues reported 15 dialysis patients that presented with ‘scleromyxoedema-like’ cutaneous lesions which he later termed nephrogenic fibrosing dermatopathy (NFD) [31, 32]. In 2003, systemic involvement of the disease was identified in a subset of patients with NFD, resulting in the adoption of the term nephrogenic systemic fibrosis (NSF) [33]. In 2006, Grobner was the first to identify

the link between GBCA exposure to this rare, but potentially fatal disease [34]. Shortly thereafter, the FDA issued a black box warning on the product labeling of all GBCAs.

NSF is a rare disorder characterized by fibrosis, most often involving the skin resulting in thickening and hardening. In its more severe form, NSF can result in systemic fibrosis of connective tissue, lungs, liver and heart leading to debilitating contractures, multi-organ dysfunction and occasionally death [35]. After GBCA exposure, the time of onset of NSF symptoms is within 12 months in a vast majority of patients, although in rare cases have appeared years after the last reported exposure [36]. It has no predilection for race or

gender. It can occur in any age group but tends to most commonly affect the middle-aged population. At the time of writing of this chapter, there were over 380 cases of NSF identified in the NSF registry [37].

The incidence of NSF varies with the degree of renal insufficiency. It is estimated that patients with stage 4–5 chronic kidney disease (CKD) [eGFR <30 mL/min/1.73 m²] have a 1–7 % risk of developing NSF after exposure to GBCAs [25, 38]. However, patients with an eGFR 15–29 mL/min/1.73 m² only account for approximately 3 % of the all reported NSF cases, most of whom had an eGFR closer to 15 mL/min/1.73 m² [25, 38]. In the reported cases of NSF occurring in patients with an eGFR >30 mL/min/1.73 m², it was subsequently determined that those patient were in acute renal failure at the time of administration which resulted in a temporal lag between eGFR and actual GFR [38]. In 2009, this led the FDA to reverse the position taken in 2006 in which it determined that moderate renal impairment (CKD stages 1–3) was also a risk factor for NSF. To date, there have been no reported cases of NSF in patients with normal renal function.

Other identified risk factors include acute kidney injury (AKI) accounting for 12–20 % of confirmed NSF cases, high dose GBCA, and multiple GBCA exposures [38, 39]. Initial research observed several NSF cases in patients with hepatorenal syndrome and in the perioperative liver transplantation period. This prompted the FDA to issue a warning against the use of GBCAs in patients with acute renal insufficiency of any severity due to the hepatorenal syndrome or in the perioperative liver transplantation period. However, subsequent research has not verified this risk. Accordingly, ACR's current recommendation is that hepatic disease in the absence of AKI or severe CKD should no longer be considered a factor for NSF [25].

Although the link between NSF and the exposure to GBCAs in the setting of severe renal impairment is widely accepted, the exact pathogenesis is unknown. The leading hypothesis relates to the dissociation of gadolinium from its chelate due to prolonged elimination times in patients with impaired renal function. By a process known as transmetalation, the toxic, free gadolinium then binds with other anions, resulting in an insoluble precipitate that deposits in tissues and triggers an immunologic response and fibrotic cascade [40]. This hypothesis was reinforced by studies demonstrating the presence of gadolinium on tissue biopsy in patients with NSF [41] and prompted the focus of research to shift to the properties of the agents themselves.

It has since been demonstrated that the incidence of NSF not only varies with the severity of renal insufficiency, but also with the dose and type of GBCA used. One study reported the incidence of NSF after gadolinium administration without screening for renal function was zero of 74,124 patients after receiving standard dose of GBCA and 15 of 8,997 patients who received high dose (≥ 0.2 mmol/Kg) [42]. Of 301 dialysis

patients that underwent contrast-enhanced MRI, 12 cases of NSF developed in 210 patients after receiving high-dose GBCA and none in the 94 patients that received single-dose GBCA yielding an odds ratio of 12:1 [43]. This data suggests that the risk of NSF may be significantly reduced by limiting the dose of gadolinium to a minimum whenever possible. In 2010, this data prompted the FDA to recommend that label doses of GBCAs not be exceeded in any patient.

Along those same lines, it was noted that there were differences in the number of reports cases of NSF among the various GBCAs [25, 38]. This raised the question of whether or not the propensity for the GBCA to dissociate from its chelates is a factor in the development of NSF. Where a specific agent was identified, the agent most associated with NSF was the least thermodynamically stable contrast agent, Gadodiamide (Omniscan) [38, 42]. This agent is followed by Gadopentetate (Magnevist) and Gadoversetamide (Optimark). Similarly, there appears to be a much lower incidence of NSF among those who received the more stable agents, Gadobenate (Multihance) and Gadoteridol (Prohance) [38, 42]. The data for recently introduced GBCAs Gadofosveset (Ablavar) and Gadoxetic acid (Eovist) is limited. These findings prompted both the FDA and ACR to classify the various GBCAs into different risk groups based on reported rates of NSF association.

Based on the current level of understanding, there are several measures that should be taken to reduce the risk of NSF prior to GBCA administration. First and foremost, patients at risk for NSF need to be identified prior to injection. This includes any patient on dialysis, those with severe or end-stage CKD (eGFR <30 mL/min/1.73 m²), AKI, as well as those with an eGFR from 30 to 40 mL/min/1.73 m² as levels may fluctuate.

A screening method should be instituted to identify conditions that may be associated with renal impairment. For outpatient testing, the ACR proposed various risk factors that would warrant pre-administration eGFR testing including the following co-morbidities: age >60, renal disease (including a history of dialysis, kidney transplant, solitary kidney, kidney surgery, renal carcinoma), hypertension requiring medical therapy, and diabetes [25]. Patients with one or more risk factor for compromised renal function generally need repeat eGFR within 2–6 weeks of MRI if the initial eGFR was >60 unless the initial eGFR was within 6 months and patient has been stable. If the initial eGFR was 30–59 mL/min/1.73 m² then this should be repeated within 2 weeks and within 1 week if it was below 30 mL/min/1.73 m².

For all inpatients, it is recommended that an eGFR level be obtained within 2 days of GBCA administration and AKI should be ruled out by the ordering health care professional [25].

Once a patient at risk for NSF is identified, an alternative diagnostic modality should be considered. If there is no alternative and the clinical indication is compelling enough, informed consent should be obtained from both the patient and the referring physician. In this scenario, a GBCA with a

lower incidence of NSF should be used (see above). Furthermore, only the lowest possible dose necessary to answer the clinical question should be used and should not exceed the recommended single dose.

Although there is no evidence to suggest dialysis protects from NSF, studies have demonstrated that GBCAs can be dialyzed [44]. Thus, it is recommended that patients on chronic hemodialysis should undergo a prompt post-procedural session [25, 38]. However, there is insufficient evidence to support the initiation of dialysis after GBCA administration in other at-risk patients who are not already on chronic dialysis.

The institution of such simple precautions has already had a profound impact on the incidence of NSF, resulting in a near elimination of new cases [45, 46].

Serum Calcium Determinations

Although GBCAs do not cause actual reductions in serum calcium, they can interfere with some calcium assay methods resulting in spuriously low serum calcium levels [33, 34]. Specifically, only Gadoversetamide (OptimMARK) and Gadodiamide (Omniscan) have been shown to interfere with the reagent used in colorimetric assay methods. Alternative methods including non-colorimetric and ionized calcium assays are not impacted. Other agents have not demonstrated this same phenomenon.

Extravasation

In one study of over 28,000 administrations, the incidence of extravasation was 0.05 % [47]. One study that evaluated the relative toxicities of four GBCAs when extravasated in soft tissue demonstrated that agents with higher osmolality caused the greatest tissue damage in laboratory animals [48]. However, when compared to equal volumes of iodinated contrast media, GBCAs were overall less toxic to the skin and subcutaneous tissue. Furthermore, because of the small volumes typically administered for MRI, the likelihood of significant injury from extravasation is exceedingly low [25].

Special Populations

The administration of GBCAs in the following unique populations is of special concern and requires additional discussion.

Pregnancy

In animal models, GBCAs have been shown to cross the placenta, appearing in the fetal bladder within 11 min after IV

administration [49]. These agents are subsequently excreted via the urine into the surrounding amniotic fluid and reabsorbed by fetal swallowing [49]. It is this extended period of exposure that is of particular concern given the potential risk of the gadolinium chelate to dissociate and result in fetal exposure to toxic free gadolinium.

Several studies have thus been performed to evaluate both the amount and duration of fetal exposure after maternal GBCA administration. A study in a mouse model found that the mean half-life in the fetal tissue and amniotic fluid were 4 and 5 h, respectively, with only trace amounts of gadolinium detectable in the fetus and none detectable in the amniotic fluid at 48 h [49].

After confirming fetal exposure to GBCAs, several studies were performed to evaluate the potential impact of such exposure. When administered at high and/or repeated doses in animal models, several adverse effects have been demonstrated including fetal growth retardation, fetal loss and teratogenicity [50, 51].

Studies assessing the effects of GBCAs on the human fetus have been limited. To date, there have been no known adverse human fetal effects after giving clinically recommended doses of GBCAs during pregnancy [25]. In one prospective study, there were no adverse effects on pregnancy and neonatal outcome in 26 pregnant women exposed to gadolinium derivatives in the first trimester [52].

However, given the adverse effects shown in animal studies and the inability to perform larger, well-controlled human studies, all FDA-approved gadolinium chelates are classified as "Pregnancy Category C" and should only be used during pregnancy when the study results are considered critical and the benefits justify the potential fetal risks [25]. In this circumstance, one of the agents considered low risk for the development of NSF should be used and at the lowest possible dose.

Breastfeeding

The literature on the excretion of GBCAs into breast milk and the subsequent gastrointestinal absorption is limited. Theoretical risks include direct toxicity from free gadolinium and allergic sensitization or reaction. However, it has been shown that <0.04 % of the maternal dose is excreted into the breast milk in the first 24 h, and estimated that <1 % of the contrast medium is subsequently absorbed from the infant's gastrointestinal tract [25, 53, 54]. This would result in an expected systemic dose absorbed by the infant from the breast milk of <0.0004 % of the maternal dose, an amount far less than the permissible dose in neonates [25]. As a result, current ACR recommendations suggest that it is probably safe for a mother to continue breast-feeding after receiving GBCAs [25]. Ultimately, an informed decision to abstain from breastfeeding should be left up to the mother, although there is no value in doing so beyond 24 h [25].

Pediatrics

Although the guidelines for the use of GBCAs in the adult and pediatric population are generally similar, the majority of clinical safety data regarding GBCAs have been obtained in adults. Numerous clinical trials have included subgroup analysis of adverse events in the pediatric population. In the Prohance database of phase I–III clinical trials, which included 119 pediatric patients out of 2,656 injections, there was no correlation between age and the adverse event rate [55]. As in adults, most reactions are mild. Although rare, allergic-like reactions to GBCAs in children do occur with one study documenting a 0.04 % allergic-like reaction rate [56]. As of September 2012, 23 pediatric cases of NSF had been reported, the youngest of which was 6 years old [57]. Although there are no evidence-based guidelines for the prevention of NSF in children, ACR recommends using the adult guidelines for identifying patients and administering GBCAs in the presence of impaired renal function [25].

It is important to note that of the currently approved GBCAs, no agent is approved for administration to individuals less than 2 years of age due to the relative immaturity of the renal system in neonates and infants.

Conclusion

GBCAs are routinely used in cardiovascular MRI including perfusion, late gadolinium enhancement and MRA applications. Use of these agents in cardiac MRI is considered off-label as no agent has FDA approval for cardiac indications. Although most of GBCAs are extracellular agents, blood pool/intravascular agents are increasingly being used in MRA. NSF is a rare but serious complication of GBCAs in patients with stage 4 or 5 kidney disease with limited treatment options. However, screening for renal impairment to identify patients at risk for NSF and following GBCA use guidelines in these patients has nearly eliminated new NSF cases. Novel MRI contrast agents are being developed and tested that may have no risk of NSF (non-gadolinium based agents) and/or will be used as molecular probes in molecular imaging.

References

- Ni Y. MR contrast agents for cardiac imaging. In: Bogaert J, Dymarkowski S, Taylor AM, Muthurangu V, editors. *Clinical cardiac MRI*. 2nd ed. Berlin: Springer-Verlag; 2012. p. 31–51.
- Caravan P. Cardiovascular magnetic resonance contrast agents. In: Manning WJ, Pennell DJ, editors. *Cardiovascular magnetic resonance*. 2nd ed. Philadelphia: Saunders Elsevier; 2010.
- Runge VM, Clanton JA, Lukehart CM, Partain CL, James Jr AE. Paramagnetic agents for contrast-enhanced NMR imaging: a review. *AJR Am J Roentgenol*. 1983;141(6):1209–15.
- Bellin MF, Vasile M, Morel-Precetti S. Currently used non-specific extracellular MR contrast media. *Eur Radiol*. 2003;13(12):2688–98. Epub 2003 Jun 19.
- Sirol M, Rajagopalan. Contrast agents in MR angiography. In: Mukherjee D, Rajagopalan S, editors. *CT and MR angiography of the peripheral circulation*. London: Informa UK Ltd; 2007.
- Tóth É, Vauthey S, Pubanz D, Merbach AE. Water exchange and rotational dynamics of the dimeric gadolinium(III) complex [BO{Gd(DO3A)(H(2)O)}(2)]: a variable-temperature and -pressure (17)O NMR study(1). *Inorg Chem*. 1996;35(11):3375–9.
- Oksendal AN, Hals PA. Biodistribution and toxicity of MR imaging contrast media. *J Magn Reson Imaging*. 1993;3(1):157–65.
- Cacheris WP, Quay SC, Rocklage SM. The relationship between thermodynamics and the toxicity of gadolinium complexes. *Magn Reson Imaging*. 1990;8(4):467–81.
- Ersoy H, Rybicki F, Prince M. Contrast agents for cardiovascular MRI. In: Kwong R, editor. *Cardiovascular magnetic resonance imaging*. New Jersey: Humana Press; 2008.
- Joffe P, Thomsen HS, Meusel M. Pharmacokinetics of gadodiamide injection in patients with severe renal insufficiency and patients undergoing hemodialysis or continuous ambulatory peritoneal dialysis. *Acad Radiol*. 1998;5(7):491–502.
- Edelman RR. Contrast-enhanced MR, imaging of the heart: overview of the literature. *Radiology*. 2004;232(3):653–68. Epub 2004 Jul 29.
- Caravan P, Ellison JJ, McMurry TJ, Lauffer RB. Gadolinium(III) chelates as MRI contrast agents: structure, dynamics, and applications. *Chem Rev*. 1999;99(9):2293–352. <http://pubs.acs.org/doi/pdf/10.1021/cr980440x>.
- Grist TM, Korosec FR, Peters DC, Witte S, Walovitch RC, Dolan RP, Bridson WE, Yucel EK, Mistretta CA. Steady-state and dynamic MR angiography with MS-325: initial experience in humans. *Radiology*. 1998;207:539–44.
- Xu Q, Zhu L, Yu M, Feng F, An L, Xing C, Wang S. Gadolinium (III) chelated conjugated polymer as a potential MRI contrast agent. *Polymer*. 2010;51:1336–40.
- Bashir MR, Bhatti L, Marin D, Nelson RC. Emerging applications of ferumoxytol as a contrast agent in MRI. *J Magn Reson Imaging*. 2014;41:884–98.
- Li W, Tutton S, Vu AT, et al. First pass contrast enhanced magnetic resonance angiography in humans using ferumoxytol, a novel ultrasmall superparamagnetic iron oxide (USPIO)-based blood pool agent. *J Magn Reson Imaging*. 2005;21:46–52.
- Pan D, Schmieder AH, Wickline SA, Lanza GM. Manganese-based MRI contrast agents: past, present and future. *Tetrahedron*. 2011;67:8431–44.
- Skjold A, Amundsen BH, Wiseth R, Stoylen A, Haraldseth O, Larsson HBW, Jynge P. Manganese dipyridoxyl diphosphate (MnDPDP) as a viability marker in patients with myocardial infarction. *J Magn Reson Imaging*. 2007;26:720–7.
- Skardal K, Rolim NPL, Haraldseth O, Goa PE, Thuen M. Late gadolinium enhancement in the assessment of infarcted mouse heart: a longitudinal comparison with manganese-enhanced MRI. *J Magn Reson Imaging*. 2013;38:1388–94.
- Sosnovik DE, Nahrendorf M, Weissleder R. Molecular magnetic resonance imaging in cardiovascular medicine. *Circulation*. 2007;115:2076–86.
- Toussaint J, LaMuraglia G, Southern J, Fuster V, Kantor HL. Magnetic resonance images lipid, fibrous, calcified, hemorrhagic, and thrombotic components of human atherosclerosis in vivo. *Circulation*. 1996;94:932–8.
- Lanza G, Trousil R, Wallace K, et al. In vivo efficacy of fibrin targeted perfluorocarbon contrast system following intravenous injection reflects prolonged systemic half-life and persistent acoustic contrast effect. *Circulation*. 1997;95(suppl I):1–457.

23. Flacke S, Fischer S, Scott MJ, Fuhrhop RJ, Allen JS, McLean M, Winter P, Sicard GA, Gaffney PJ, Wickline SA, Lanza GM. Novel MRI contrast agent for molecular imaging of fibrin. *Circulation*. 2001;104:1280–5.
24. Kramer CM, Barkhausen J, Flamm SD, Kim RJ, Nagel E. Society of cardiovascular magnetic resonance and board of trustees task force on standardized protocols. *J Cardiovasc Magn Reson*. 2013;15:91.
25. ACR Manual on Contrast Media. Version 9. 2013. http://www.acr.org/~media/ACR/Documents/PDF/QualitySafety/Resources/Contrast%20Manual/2013_Contrast_Media.pdf.
26. Bruder O, Schneider S, Nothnagel D, Pilz G, Lombardi M, Sinha A, Wagner A, Dill T, Frank H, van Rossum A, Schwitter J, Nagel E, Senges J, Sabin G, Sechtem U, Mahrholdt H. Acute adverse reactions to gadolinium-based contrast agents in CMR: multicenter experience with 17,767 patients from the EuroCMR registry. *JACC Cardiovasc Imaging*. 2011;4(11):1171–6.
27. Knopp MV, Balzer T, Esser M, Kashanian FK, Paul P, Niendorf HP. Assessment of utilization and pharmacovigilance based on spontaneous adverse event reporting of gadopentetate dimeglumine as a magnetic resonance contrast agent after 45 million administrations and 15 years of clinical use. *Invest Radiol*. 2006;41(6):491–9.
28. Matsumura T, Hayakawa M, Shimada F, Yabuki M, Dohanish S, Palkowitsch P, Yoshikawa K. Safety of gadopentetate dimeglumine after 120 million administrations over 25 years of clinical use. *Magn Reson Med Sci*. 2013;12(4):297–304. Epub 2013 Oct 29.
29. Nelson KL, Gifford LM, Lauber-Huber C, Gross CA, Lasser TA. Clinical safety of gadopentetate dimeglumine. *Radiology*. 1995;196(2):439–43.
30. Prince MR, Arnoldus C, Frisoli JK. Nephrotoxicity of high-dose gadolinium compared with iodinated contrast. *J Magn Reson Imaging*. 1996;6(1):162–6.
31. Cowper SE, Robin HS, Steinberg SM, Su LD, Gupta S, LeBoit PE. Scleromyxoedema-like cutaneous diseases in renal-dialysis patients. *Lancet*. 2000;356(9234):1000–1.
32. Cowper SE, Su LD, Bhawan J, Robin HS, LeBoit PE. Nephrogenic fibrosing dermatopathy. *Am J Dermatopathol*. 2001;23(5):383–93.
33. Ting WW, Stone MS, Madison KC, Kurtz K. Nephrogenic fibrosing dermatopathy with systemic involvement. *Arch Dermatol*. 2003;139(7):903–6.
34. Grobner T. Gadolinium – a specific trigger for the development of nephrogenic fibrosing dermatopathy and nephrogenic systemic fibrosis? *Nephrol Dial Transplant*. 2006;21(4):1104–8. Epub 2006 Jan 23.
35. Cowper SE. Nephrogenic systemic fibrosis: an overview. *J Am Coll Radiol*. 2008;5(1):23–8. doi:10.1016/j.jacr.2007.08.013.
36. Shabana WM, Cohan RH, Ellis JH, et al. Nephrogenic systemic fibrosis: a report of 29 cases. *AJR Am J Roentgenol*. 2008;190:736–41.
37. Cowper SE. Nephrogenic systemic fibrosis [ICNSFR Website]. 2001–2013. Available at <http://www.icnsfr.org>. Accessed 11/16/2014.
38. Gadolinium-Based Contrast Agents & Nephrogenic Systemic Fibrosis FDA Briefing Document. Joint Meeting of the Cardiovascular and Renal Drugs and Drug Safety and Risk Management Advisory Committee [<http://www.fda.gov/downloads/AdvisoryCommittees/CommitteesMeetingMaterials/Drugs/DrugSafetyandRiskManagementAdvisoryCommittee/UCM190850.pdf>]. Accessed 20 Sept 2011.
39. Sadowski EA, Bennett LK, Chan MR, Wentland AL, Garrett AL, Garrett RW, Djamali A. Nephrogenic systemic fibrosis: risk factors and incidence estimation. *Radiology*. 2007;243:148–57.
40. Perazella MA. Nephrogenic systemic fibrosis, kidney disease, and gadolinium: is there a link? *Clin J Am Soc Nephrol*. 2007;2(2):200–2. Epub 2007 Feb 7.
41. High WA, Ayers RA, Chandler J, Zito G, Cowper SE. Gadolinium is detectable within the tissue of patients with nephrogenic systemic fibrosis. *J Am Acad Dermatol*. 2007;56(1):21–6.
42. Prince MR, Zhang H, Morris M, MacGregor JL, Grossman ME, Silberzweig J, DeLapaz RL, Lee HJ, Magro CM, Valeri AM. Incidence of nephrogenic systemic fibrosis at two large medical centers. *Radiology*. 2008;248(3):807–16.
43. Broome DR, Girguis MS, Baron PW, Cottrell AC, Kjellin I, Kirk GA. Gadodiamide-associated nephrogenic systemic fibrosis: why radiologists should be concerned. *AJR Am J Roentgenol*. 2007;188(2):586–92.
44. Okada S, Katagiri K, Kumazaki T, Yokoyama H. Safety of gadolinium contrast agent in hemodialysis patients. *Acta Radiol*. 2001;42(3):339–41.
45. Martin DR, Krishnamoorthy SK, Kalb B, Salman KN, Sharma P, Carew JD, Martin PA, Chapman AB, Ray GL, Larsen CP, Pearson TC. Decreased incidence of NSF in patients on dialysis after changing gadolinium contrast-enhanced MRI protocols. *J Magn Reson Imaging*. 2010;31(2):440–6. doi:10.1002/jmri.22024.
46. Altun E, Martin DR, Wertman R, Lugo-Somolinos A, Fuller 3rd ER, Semelka RC. Nephrogenic systemic fibrosis: change in incidence following a switch in gadolinium agents and adoption of a gadolinium policy – report from two U.S. universities. *Radiology*. 2009;253(3):689–96. doi:10.1148/radiol.2533090649. Epub 2009 Sep 29.
47. Cochran ST, Bomyea K, Sayre JW. Trends in adverse events after IV administration of contrast media. *AJR Am J Roentgenol*. 2001;176(6):1385–8.
48. Runge VM, Dickey KM, Williams NM, Peng X. Local tissue toxicity in response to extravascular extravasation of magnetic resonance contrast media. *Invest Radiol*. 2002;37(7):393–8.
49. Mühler MR, Clément O, Salomon LJ, Balvay D, Autret G, Vayssettes C, Cuénod CA, Siauve N. Maternofetal pharmacokinetics of a gadolinium chelate contrast agent in mice. *Radiology*. 2011;258(2):455–60.
50. Rofsky NM, Pizzarello DJ, Duhaney MO, Falick AK, Prendergast N, Weinreb JC. Effect of magnetic resonance exposure combined with gadopentetate dimeglumine on chromosomes in animal specimens. *Acad Radiol*. 1995;2(6):492–6.
51. Okuda Y, Sagami F, Tirone P, Morisetti A, Bussi S, Masters RE. Reproductive and developmental toxicity study of gadobenate dimeglumine formulation (E7155) (3) – study of embryo-fetal toxicity in rabbits by intravenous administration. *J Toxicol Sci*. 1999;24 Suppl 1:79–87.
52. De Santis M, Straface AF, Cavaliere B, et al. Gadolinium periconceptional exposure: pregnancy and neonatal outcome. *Acta Obstet Gynecol*. 2007;86:99–101. Birchard KR – *AJR Am J Roentgenol* 2005;184:452–458.
53. Wang PI, Chong ST, Kielar AZ. Imaging of pregnant and lactating patients: part 1. Evidence-based review and recommendations. *AJR Am J Roentgenol*. 2012;198:778–84.
54. Kubik-Huch RA, Gottstein Alame NM, Frenzel T, et al. Gadopentetate diglumine excretion into human breast milk during lactation. *Radiology*. 2000;216:555–558.
55. Yoshikawa K, Davies A. Safety of ProHance in special populations. *Eur Radiol*. 1997;7 Suppl 5:246–50.
56. Dillman JR, Ellis JH, Cohan RH, Strouse PJ, Jan SC. Frequency and severity of acute allergic-like reactions to gadolinium containing i.v. contrast media in children and adults. *AJR Am J Roentgenol*. 2007;189:1533–8.
57. Nardone B, Saddleton E, Laumann AE, Edwards BJ, Raisch DW, McKoy JM, Belknap SM, Bull C, Haryana A, Cowper SE, Abu-Alfa AK, Miller FH, Godinez-Puig V, Dharmidharka VR, West DP. Pediatric nephrogenic systemic fibrosis is rarely reported: a RADAR report. *Pediatr Radiol*. 2014;44(2):173–80.

Parmede Vakil, Octavia Bane, Charles G. Cantrell,
and Timothy J. Carroll

Abstract

The Development of Contrast Enhanced Magnetic Resonance Angiography represents a major success in the development of diagnostic imaging. In the short time since its inception CE-MRA, has replaced the more invasive X-ray angiography as the front line-diagnostic imaging modality. The prevalence of vascular disease in developed countries and the aging of the population has made CE-MRA a multi-billion dollar market. We discuss many of the newer approaches to CE-MRA that are reducing the scan time to allow for higher resolution scans with improved ease of use and diagnostic accuracy.

Keywords

Angiography • MRI • Physics • Dynamic imaging

Introduction

Contrast Enhanced MR Angiography (CE-MRA) is a technique for imaging blood vessels using contrast agents, which are delivered intravenously during imaging. The contrast bolus briefly enhances the signal in the vascular bed of interest. It was first introduced in 1993 by Prince et al. [1] and has been improved upon by many researchers [2–12]. This chapter discusses the basics of CE-MRA and the recent developments made in the field.

P. Vakil, PhD • C.G. Cantrell • T.J. Carroll, PhD (✉)
Departments of Biomedical Engineering and Radiology,
Northwestern University, Chicago, IL, USA

Department of Radiology, Northwestern Memorial Hospital,
737 N. Michigan Avenue, Suite 1600, Chicago, IL 60611, USA
e-mail: t-carroll@northwestern.edu

O. Bane, PhD
Departments of Biomedical Engineering and Radiology,
Northwestern University, Chicago, IL, USA

Mount Sinai Hospital, Translational and Molecular Imaging
Institute, New York, NY, USA

Contrast Agents

Gadolinium Agents

See Chap. 19 for detailed discussion. Gadolinium (Gd) is a highly paramagnetic element with seven unpaired electrons in its outer f orbital. This property causes shortening of T_1 relaxation of protons in surrounding tissue. The T_1 shortening is described by the following equation,

$$\frac{1}{T_1} = \frac{1}{T_{1_0}} + R_1 \times [Gd],$$

where T_{1_0} is the longitudinal relaxation time of blood without Gd, T_1 is the shortened longitudinal relaxation time of blood in the presence of Gd, and R_1 is the relaxivity of Gd, which is multiplied by the concentration of [Gd].

Since the gadolinium itself is highly toxic, it must be chelated before it can be injected into the vessels. Currently there are several different chelates widely used for first-pass CE-MRA including Gd-DTPA (Magnevist), gadodi- amide (Omniscan), gadobenate (Multihance), and

gadobutrol (Gadovist). These compounds are permeable through the blood vessel walls, enhancing tissue signals as well. Chelates that are not permeable through the vessel walls, called intravascular agents, also exist (gadofosveset trisodium).

Gadofosveset trisodium (sometimes referred to by trade names, Vasovist and Ablavar) is a gadolinium-based, T_1 -shortening contrast agent that, unlike other Gd chelates, binds reversibly to serum albumin, in a proportion of 80–90 % for humans [13]. In 2010, it obtained FDA approval for MRA in the United States and has been used for over a decade in Europe for angiographic applications. Albumin binding hinders leakage of gadofosveset, and increases its half-life, so that the T_1 shortening effect is observed up to 4 h post-injection, and interpretable steady-state images can be obtained up to an hour post injection [13]. The reversible binding allows excretion through the kidneys, or uptake by hepatocytes [14]. Excretion of unbound agent by the kidneys makes repeat injections feasible, unlike with other intravascular contrast agents [15].

The albumin bond also slows down the rotation rate of the complex, which enhances its relaxivity (T_1 -shortening effect, in mmol/L/s) six to ten times compared to other non-binding Gd-chelates [13], and four to tenfold compared to unbound gadofosveset [14]. As consequence of the high relaxivity/relaxation rate $1/T_1$, and the long half life in the blood vessels, the gadofosveset dosage necessary for high quality perfusion imaging is much lower than that of Gd-DTPA (0.03 mmol/kg vs 0.1 mmol/kg).

Gadofosveset is particularly advantageous to MRA, because images can be acquired with the first pass of the contrast agent bolus, as well as in steady-state (1–5 min to up to 1 h post injection) [16]. Steady-state MRA with gadofosveset allows the acquisition of bright, high resolution images of the smaller branches of the vasculature [17].

Ferumoxytol

Ferumoxytol is an ultrasmall paramagnetic iron oxide (USPIO) which has obtained FDA approval as an injectable iron supplement for the treatment of severe anemia in patients with advanced kidney disease. It has been used off-label as a MRA blood pool agent, in the imaging of the carotid arteries, thoracic and abdominal aorta, and peripheral vessels. Initial studies have shown the feasibility of first-pass and steady-state MRA in humans, with the initial concentration of 537.2 μmol elemental Fe/mL diluted four (134.3 μmol Fe/mL) or eightfold (67.1 μmol Fe/mL). The highest dose for MRA was 71.6 $\mu\text{mol}/\text{kg}$, injected at a rate of 1 mL/s. Dilution of the contrast agent minimizes its marked T_2^* shortening effects, which can lead to signal loss [18, 19].

Injection

Contrast agent is injected as a bolus during the scan using a power injector, which delivers an accurate dose and injection rate. Typically, 0.1 mmol/kg (considered single dose) is injected at 0.5–5 mL/s. Saline flush immediately follows to clear the venous access and push the contrast agent further into the circulation.

Due to the time delay between bolus injection and the appearance of contrast in the vessels of interest (passage of bolus from venous system to the heart, lungs, and aorta), conventional CE-MRA protocols required an initial timing run to measure lag time in order to precisely align the acquisition of the center of k-space to the peak of the bolus, thereby maximizing SNR. However, with radial acquisition with sliding window reconstruction, no timing of the injection is necessary because each radial line transverses the center of k-space. This will be discussed in further detail below.

Bolus Timing and Venous Overlay

Typically, a 20 mL bolus of contrast agent is injected into the veins over a short time interval (5–10 s). The goal of arterial CE-MRA is to image the maximum arterial enhancement, achieved when the injection bolus first passes through the artery of interest at its peak concentration. Therefore, acquisition speed is the main design criterion for first-pass CE-MRA pulse sequences. Usually, CE-MRA pulse sequences are spoiled gradient-echo pulse sequences that minimize TE and TR, and very often use partial k-space acquisitions in two or three directions. CE-MRA venography does not have this time constraint, which permits the acquisition of high SNR and spatial resolution images after the veins enhance.

Single phase CE-MRA sequences use the entire acquisition time to obtain data for one set of 3D images, in order to increase spatial resolution and coverage. This method requires timing of the bolus arrival, typically using a test bolus or fluoroscopic triggering (bolus tracking).

Time-resolved MRA images the volume of interest at different moments in time, which allows visualization of the various stages of signal enhancement in the vessels. Time resolved MRA frees the operator from having to measure the bolus circulation time (time from injection to peak arterial enhancement in the vessel of interest). However, since multiple acquisitions of the imaging volume have to be performed into a time interval comparable to the circulation time of the bolus, acquisition speed is even more important than in single phase CE-MRA. To decrease acquisition time, parallel imaging (SENSE) or partial k-space updating methods such as keyhole imaging or TRICKS are used. The keyhole method updates the center of k-space periodically, while TRICKS reacquires high-spatial-frequency data that contain the imaging information on small vessels.

Basic CE-MRA Technique

Data Acquisition

SPOiled Gradient Recalled echo (SPGR) sequence is used for CE-MRA. SPGR pulse sequences are T_1 -weighted making them well suited for imaging the T_1 shortening effects of gadolinium contrast agent. Additionally, the short TR and TE in SPGR sequences enable them to image the fast moving contrast bolus [20]. Multiple phases or repetitions are acquired for dynamic imaging. Often, a pre-contrast volume is acquired before injecting the contrast agent bolus for subtraction in order to isolate the vessels from the background tissues. The MR acquisition is extremely lengthy compared to X-Ray angiography. A typical protocol of $TR=3$ ms, 192×192 pixel resolution, and 24 slices results in almost 14 s of acquisition time just for a single volume. Even with the lengthy acquisition time, the spatial resolution and signal-to-noise ratio cannot match those of X-ray angiography. Section below will address the improvements to accelerate the acquisition of MRA data.

Gradient Echo Imaging

Spoiled GRE

SPGR sequences are known by different names, depending on the vendor: spoiled gradient echo (SPGR), T_1 fast field echo (T_1 -FFE), and Fast Low-Angle Shot (FLASH). In each TR interval, the RF excitation converts the longitudinal magnetization into transverse magnetization, which is rephased by a gradient echo. If perfect spoiling is achieved, the transverse magnetization is zero before the new TR begins (there is no residual transverse magnetization from previous TR intervals). After a sufficient number of excitation pulses are applied, the longitudinal magnetization reaches steady state, and the FLASH signal at steady-state is dependent on T_1 , T_2^* and the flip angle:

$$S_{ss} = \frac{M_0 \sin \theta (1 - E_1) e^{-TE/T_2^*}}{1 - \cos \theta E_1}$$

The FLASH signal is maximized at a flip angle called the Ernst angle:

$$\theta_E = \cos^{-1} \left(e^{-TR/T_1} \right)$$

Since the Ernst angle increases monotonically as the ratio TR/T_1 increases, TR values much shorter than T_1 are an advantage, not a trade-off, to signal intensity. In SPGR sequences, much shorter TR values ($TR \ll T_1$) are possible compared to spin echo pulse sequences, since no lengthy period of time is required for T_1 recovery.

Spoiling

Due to the short TR ($TR \ll T_1$), of SPGR pulse sequences, residual transverse magnetization following each TR interval affects subsequent acquisitions thereby introducing a hybrid of T_1 and T_2 weighting to the image contrast. A combination of a time-varying gradients and RF phase cycling can be used to eliminate this effect. Gradient spoiling typically refers to a phase-encoding rewinder and a constant moment spoiler on the read-out axis. RF phase cycling shifts the RF excitation pulses according to a preset schedule. Spoiling in SPGR pulse sequences is addressed differently in non-Cartesian scans as the readout direction is changing with each projection acquisition. Spoiling residual transverse magnetizations equally at the end of each read out interval requires balancing of gradient moments. A simple method of accomplishing this may be to first rewind all gradients to the origin and subsequently wind the magnetization to the same point in k-space along the k_x or k_y axis. Two methods for doing this are shown in Fig. 20.1. This ensures the net magnetization at the end of each TR interval is at the same point in k-space [19].

Balanced Steady-State Free Precession Imaging

Balanced steady-state free precession (bSSFP) (true-FISP: *True Fast Imaging with Steady-State Free Precession*; FIESTA: *fast imaging employing steady-state excitation*; FFE: *balanced fast field echoes*) is a method for performing flow-independent MRA. In bSSFP, image acquisition is sped up by recycling, instead of spoiling, the transverse magnetization after each TR. There are two conditions for achieving steady-state free precession: firstly, the RF pulses over several TR intervals have to have the same phase in the rotating frame, or a simple phase cycle such as sign alternation [21], and secondly, the phase accumulated by the transverse magnetization must be the same in each TR interval. To avoid dephasing of the transverse magnetization, the area under the gradient waveforms must be zero (gradients are completely balanced – see Fig. 20.2).

The signal equation when steady-state has been achieved is given by the following equation:

$$M_{ss} = \frac{M_0 \sin \theta (1 - E_1) e^{-TE/T_2}}{1 - (E_1 - E_2) \cos \theta - E_1 E_2}$$

where $E_1 = \exp(-TR/T_1)$ and $E_2 = \exp(-TR/T_2)$.

The signal equation illustrates the T_2/T_1 contrast specific to bSSP imaging. Thus, media with large T_2/T_1 , such as blood and fluids, will appear brighter in bSSFP images, which makes bSSFP naturally suitable for imaging blood vessel. The T_2/T_1 contrast can be further enhanced by choice of the optimal flip angle, $\alpha_{opt} = \arccos \left(\frac{T_1}{T_2} - 1 \right) / \left(\frac{T_1}{T_2} + 1 \right)$, with expected T_1 and T_2 of the tissue to be imaged. At the optimal flip angle, the signal amplitude is proportional to the square root of T_2/T_1 :

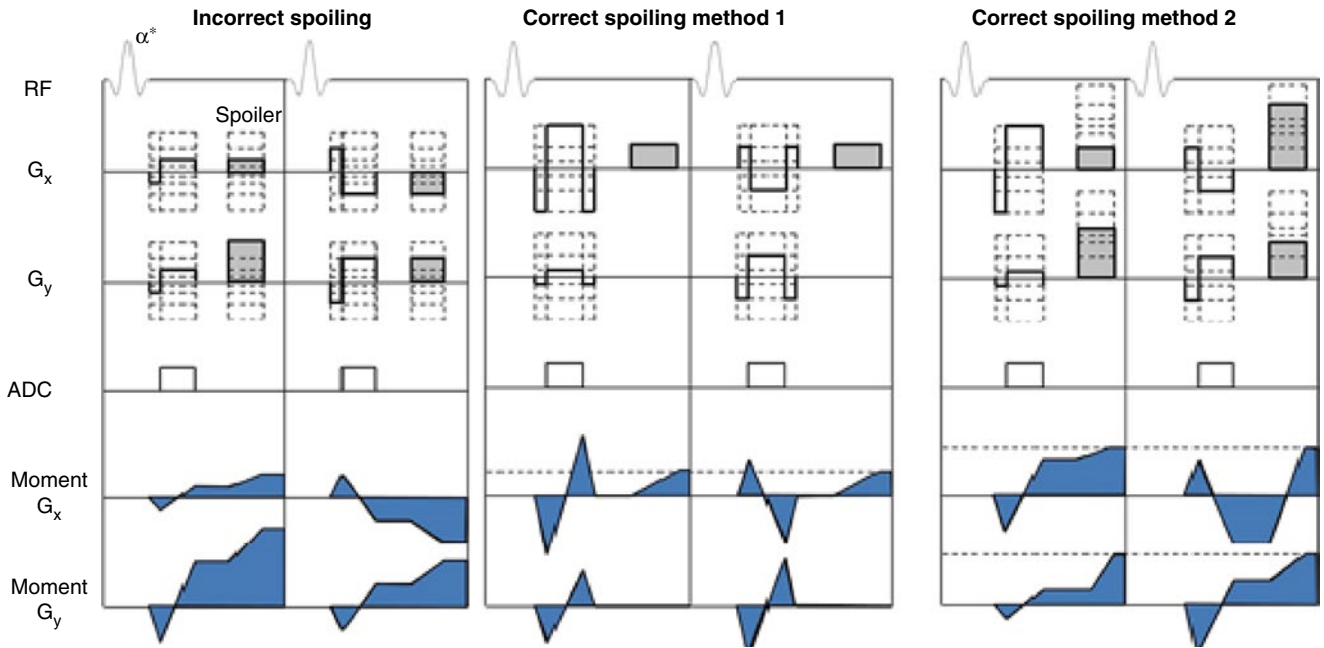


Fig. 20.1 Pulse sequence diagrams of consecutive projections in pseudo-random radial FLASH acquisitions showing examples of incorrect spoiling and two correct spoiling methods. Incorrect spoiling results in unbalanced gradient moments visualized in the blue shaded moment plots. The initial projection has a net positive moment accrual along G_x while the second projection has a net negative moment accrual along G_x . In each of

the corrected spoiling methods, the magnetization is wound out to the same point in k-space resulting in balanced gradient moments among consecutive projections. In method 1, the G_x and G_y gradients are rewound and a constant spoiler is played along G_x . In method 2, the spoiler moment is adjusted in accordance with the projection angle, ensuring equal positive moments along G_x and G_y at the end of the TR interval

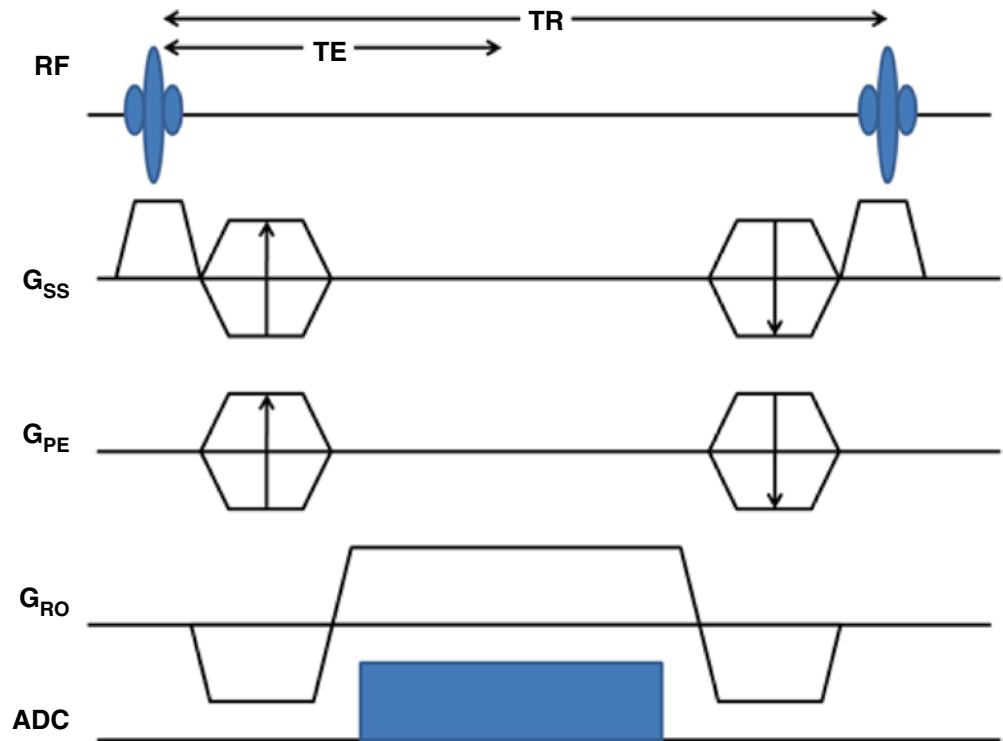


Fig. 20.2 Pulse sequence diagram for a balanced steady-state free precession (bSSFP) pulse sequence

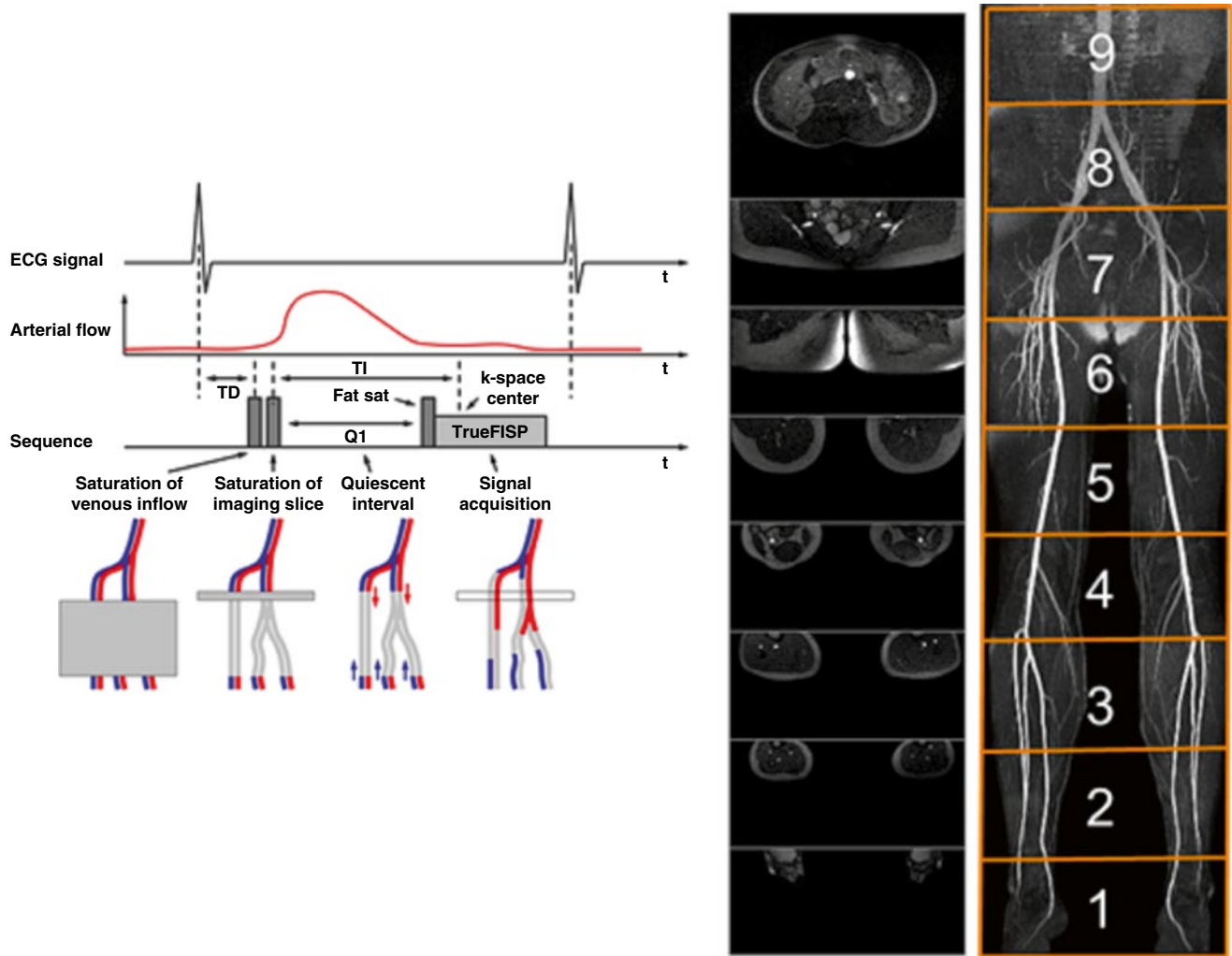


Fig. 20.3 Multi station QISS images acquired without the use of contrast agent showing the vasculature from the abdomen to the pedal arch (Images Courtesy of Dr. Robert Edelman, M.D.)

$$M_{ss} = \frac{1}{2} M_0 \sqrt{\frac{T_2}{T_1}}$$

However, the same contrast mechanism makes other tissues with large T_2/T_1 , such as fat, appear hyperintense, which requires the use of fat suppression methods during bSSFP imaging.

QISS

Quiescent interval single shot (QISS) [22] is a bSSFP-based, cardiac gated pulse sequence form MRA that takes advantage of the bright blood contrast in bSSFP while suppressing fat, venous inflow and background tissue. Following the ECG R-wave, 90° slice selective saturation pulses are played to null the longitudinal magnetization of tissues within the slice. Another 90° tracking pulse is played to saturate the venous spins. The quiescent interval corresponds to peak systolic flow, which allows the signal to be replenished by

the inflowing spins of the arterial blood. The quiescent period is followed by a chemical shift – selective fat saturation RF pulse and an RF $\alpha/2$ catalyzation pulse that forces the magnetization into steady-state free precession. bSSFP read-out follows these preparation pulses. A two-center trial in 53 patients referred for lower extremity MRA found QISS to have equivalent diagnostic accuracy as CE-MRA and DSA [1]. See Fig. 20.3 for multi station QISS images acquired without the use of contrast agent showing the vasculature from the abdomen to the pedal arch.

Data Reconstruction

The simplest data reconstruction of CE-MRA datasets begins with calculating the 2D Fourier transform of the Cartesian data. In the case of a 3D acquisition a 1D Fourier transform is performed as well in the slice direction. To depict blood

vessels without tissue overlay, subtraction is utilized. Usually, the first volume is then subtracted from the subsequent volumes to subtract any background tissues. Maximum intensity projections (MIP), where the highest values are selected in the slice direction, are derived from the subtracted volumes to obtain images similar to X-Ray DSA.

Applications and Developments in CE-MRA

Many developments have been made and significant research is still in progress to improve the performance of CE-MRA. The ultimate goal is to replace the invasive X-Ray DSA, which has superior temporal resolution and image quality. The following improvements enabled faster acquisition, reduced artifacts, increased signal, and better dynamic information. Some of the improvements discussed here are well suited for CE-MRA, but are not limited to MRA and are applicable to other MR imaging techniques.

Partial Fourier

The simplest way of accelerating acquisition is acquiring less data in violation of the Nyquist criteria. Partial Fourier is a method to only acquire a fraction of the full k -space. The k -space consists of spatial frequency information in positive and negative directions. Most of the image energy is located in the lower spatial frequencies, close to the center of the k -space. Taking advantage of this idea, the k -space is acquired asymmetrically about the origin, as shown on Fig. 20.4, taking the high frequency data from only one side of the k -space. This idea can be used in all dimensions. Each echo can be asymmetrically sampled. Phase encoding steps can be reduced. For 3D imaging with Fourier encoding in slice direction, less slices can be imaged. The parts of k -space not acquired can be either zero-filled or calculated using the fact that the k -space representation of a real image is Hermitian, meaning the opposite side of the k -space is the complex conjugate of the other side. Filling the missing k -space using Hermitian symmetry is called homodyne method.

However, partial Fourier results in decreased SNR, since high frequency noise variance is increased while the low frequency signal remains the same. Also it has been shown that zero-filled k -space have higher SNR than homodyne processed since high frequency components are not collected [23]. However, the homodyne method retains more high frequency information which may be useful. It has been reported that 62.5 % partial acquisition resulted in about 75 % decrease in SNR using homodyne method [24]. This may be an acceptable tradeoff when rapid imaging is of higher priority.

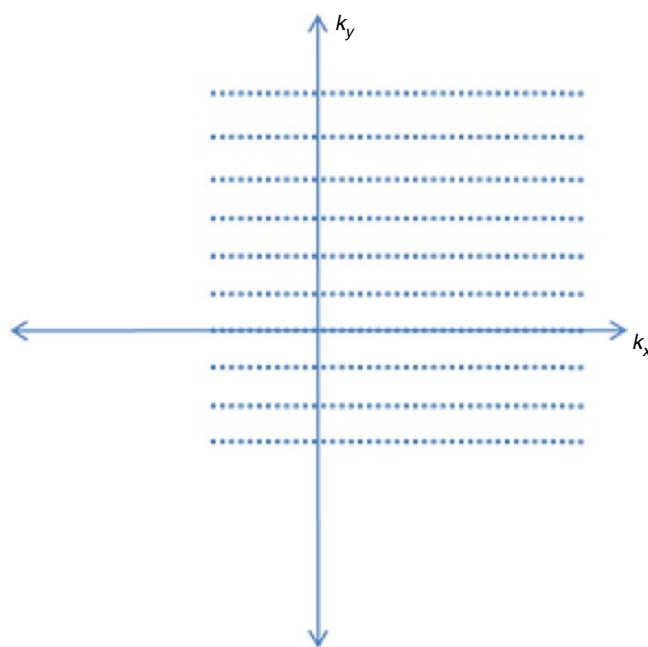


Fig. 20.4 Partial Fourier acquisition in k_y and k_x

Acquisition Ordering

Instead of collecting data by linearly traversing the k -space, the acquisition order can be modified to optimize image quality. Centric acquisition collects the phase encoding lines starting from the center of k -space and outward in the order of proximity to the center. This ordering is useful when timing the bolus arrival since the center of k -space, which has most of the image energy, needs to be acquired at the peak phase. The centric scheme can be applied to both phase encoding and slice select directions. The elliptical-centric ordering takes centric acquisition further to 3D and acquires the data in the order close to the origin of k -space. In other words, the readout with the smallest $kr = \sqrt{kz^2 + ky^2}$ value gets acquired first [4]. Although the centric ordering schemes improve the imaging protocol by making it easier to time the peak contrast arrival, there are no substantial improvements in speed or image quality from the technique itself.

Also utilizing the fact that the central parts of k -space contain more information, the Keyhole method is a technique that samples the center of k -space more often than the outer parts of the k -space [25, 26]. Initially, a full k -space image is acquired as a reference. Then for subsequent dynamic series only the central part of the k -space, or 'keyhole data', are imaged. Later, the keyhole data is combined with the high frequency data from the reference image using various methods. The keyhole technique increases the acquisition rate because it reduces the amount of high spatial frequencies acquired, but the high frequency components are never truly updated. High frequency information such as smaller vessels or aneurysms may be misrepresented.



Fig. 20.5 Maximum Intensity Projection through a 3D image volume selected from the peak arterial phase of a 3D TRICKS image provides clinically relevant information on the presence of a carotid artery stenosis equivalent to more invasive X-Ray DSA (Images courtesy of Dr. Patrick Turski, M.D.)

Similar to Keyhole technique, the Time Resolved Imaging of Contrast KineticS (TRICKS) is another method [27] that samples the center of k -space more often than the outer regions. In this technique, the k -space is divided into sections, A, B, C, and D, for example, with the A section being the central part and B, C, and D sections being the outer parts, in order of proximity. The use of 3DTRICKS provided information as well as high quality non-invasive angiograms. In Fig. 20.5 a patient with a high grade carotid artery stenosis images with X-ray DSA and 3D TRICKS demonstrates the excellent depiction of a moderate stenosis in the distal carotid artery of a patient.

Then the data is acquired in the order, ABACADABA-CAD..., until the end of the scan. This technique addresses the problem of not updating high frequency information in the Keyhole technique. But because of the extra acquisition time needed, TRICKS has not been shown to be fast enough for some applications, such as intracranial AVMs [28].

Parallel Imaging

Parallel Imaging, a technique used in all areas of MRI, is used to accelerate imaging time by using multiple coils that each acquire different information and later combine to form one image. Compared to using one coil or having multiple channels all acquire the same information and averaging the data, parallel imaging reduces the imaging time roughly by the factor of the number of channels since each channel only acquires a part of the image. In most cases, this is done by undersampling phase encodes, which produces aliased images. Then parallel reconstruction techniques are applied to extract an unaliased image. The techniques can be divided into two broad categories, image space and k -space techniques.

An image space technique, partially Parallel Imaging with Localized Sensitivities (PILS) [29] uses the prior knowledge of the coil sensitivities that cover distinct regions in image space phase encoding direction. Unaliased regions with reduced FOV are combined to form the final image. This technique is restricted to localized coil sensitivities, which leads to the discussion of Sensitivity Encoding, or SENSE [30]. The SENSE technique also uses prior knowledge of coil sensitivities which are not assumed to be localized. Each aliased pixel is a sum of intensities from different parts of the image, weighted by the coil sensitivity. Then, if the sensitivity weighting is known, a linear system with the number of equations and variables equal to the number of coils is derived. Solving this system yields the final image.

A k -space technique, SMASH (Simultaneous Acquisition of Spatial Harmonics), also uses prior knowledge of sensitivity values but solves for missing phase encoding lines instead of image intensities [31]. Instead of prior estimation of coil sensitivities, Auto-SMASH uses additional calibration scans to estimate the sensitivity values to combine the coils [32]. GRAPPA (Generalized Autocalibrating Partially Parallel Acquisitions) uses similar acquisition technique but produces multiple coil images which are combined using magnitude reconstruction [33].

Parallel imaging, in return for faster imaging, results in degraded SNR by at least by the square root of the reduction factor R , the factor by how much the phase encoding steps are reduced.

Contrast Enhanced EPI

Echo Planar Imaging (EPI), is a multi-echo GRE sequence that uses a series of “blips” to acquire several lines of k -space during a single RF pulse. By sampling multiple k -space lines per RF, multi-echo GRE sequences decrease the amount of time required to fill k -space and thus increase imaging speed. However, these methods are complicated by different effective echo times (TE_{eff}) caused by sampling intervals along the echo train. Consequently, conventional EPI techniques can suffer from lower SNR and reduced spatial resolution.

In a clinical environment reduced imaging times are beneficial for a variety of reasons including decreased motion artifacts resulting in higher quality images and increased exam success rates. For cardiac imaging this is even more pronounced, as imaging protocols often must be completed during a patient breath-hold. Consequently, the speed of EPI makes it a useful imaging protocol. To increase SNR and spatial resolution inherent in conventional EPI protocols, contrast enhanced (CE) imaging is often used. T_1 shortening agents (such as those discussed earlier in this chapter) increase the longitudinal regrowth rate, and thus increase the transverse signal intensity following an RF pulse. In CE-EPI, a slow injection rate of a T_1 shortening agent is used to increase blood signal intensity and image contrast.

Radial Imaging

Most MRI data is sampled on a rectilinear grid [34] using spin-warp imaging. This Cartesian method of sampling was adopted due to its reliability against inhomogeneity-inducing scanner imperfections in the static magnetic field. With recent advances in scanner hardware and consequent improvements in static field homogeneities, clinical and research protocols utilizing non-Cartesian sampling schemes have been increasingly explored. In the coming paragraphs we will address a very popular non-Cartesian sampling technique called radial sampling.

Although radial trajectories have recently become a popular focus in MRI research, it is in fact a relatively old technique, developed and used by Paul Lauterbur in his first MRI acquisitions in 1980 [35]. Instead of acquiring k -space lines orthogonally in Cartesian k -space, radial spokes are acquired in equal angular spaces, as shown on Fig. 20.6.

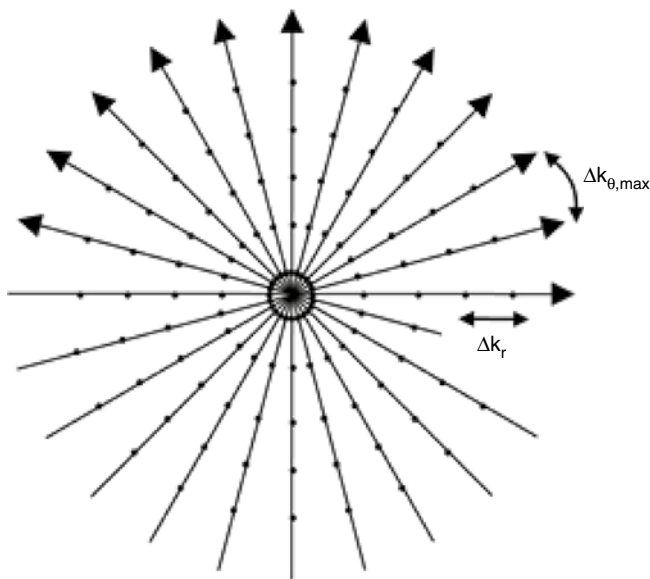


Fig. 20.6 Radial k -space trajectory

Every radial spoke, or projection, acquires N_r read out points in accordance with Nyquist criteria. As a result, the radial trajectory oversamples the center of k -space and undersamples the edges. The oversampling of low-frequency central k -space has known advantages in time-resolved imaging [18], however larger numbers of projections are required to meet the minimum Nyquist criteria. Those criteria state that the largest spacing between adjacent k -space samples must be no larger than $1/FOV$. For points on adjacent spokes at the edge of k -space where the spacing is largest we have

According to Nyquist theory we must have $\Delta k_{\max} < 1/FOV$ and $\Delta k_r = 1/FOV$. The number of projections required to meet Nyquist criteria within the FOV is therefore

$$\Delta k_{\max} = \frac{N_r \pi}{2N_p} \Delta k_r$$

According to Nyquist theory we must have $\Delta k_{\max} < 1/FOV$ and $\Delta k_r = 1/FOV$. The number of projections required to meet Nyquist criteria within the FOV is therefore

$$N_p \geq \frac{\pi}{2} N_r$$

Acquiring fewer than $N_{p,\text{opt}}$ results in a reduction of the artifact-free FOV [36].

Benefits for MRA

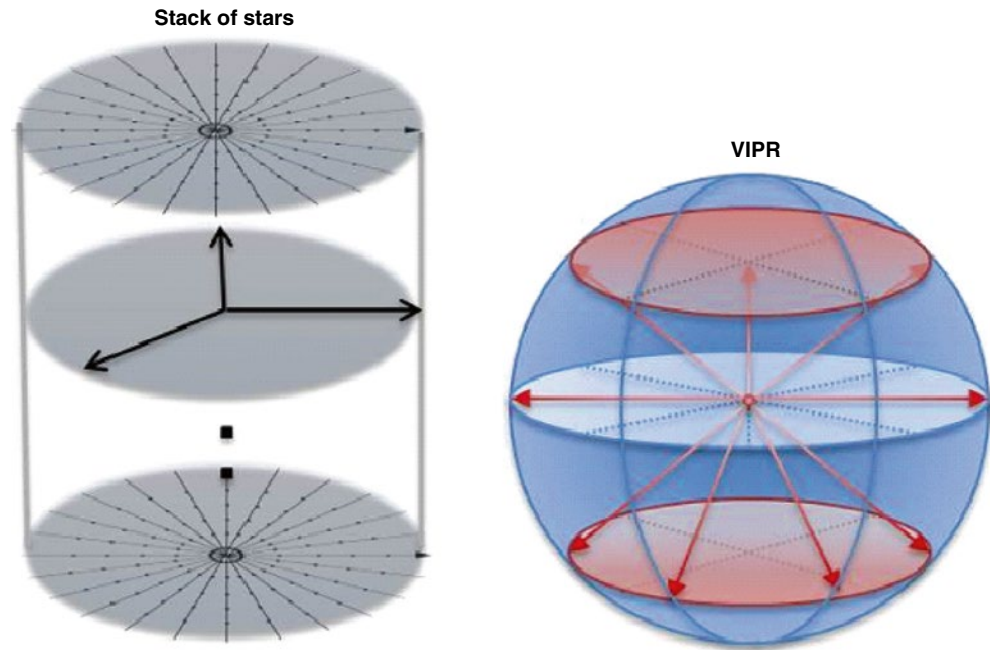
Two popular strategies for sampling 3D k -space with radial trajectories include cylindrical sampling with a radial stack of stars or spherical sampling using the true radial VIPR sequence as shown in Fig. 20.7.

In each scheme there is a reduction in the total amount of sampled space relative to a cube sampled on a 3D Cartesian grid. For example a cylindrical sampling scheme acquires 21.5 % less sampling and spherical sampling 47.6 % less sampling relative to a cube.

Radial trajectories sample the center of k -space often and at regular time intervals. This has an averaging effect, which serves to reduce motion artifacts evident in Cartesian sampling schemes [37]. In addition, studies have shown that Cartesian acquisitions can distort the bolus profile during the vascular time course depending on the direction of travel relative to the gradient read out direction, while radial acquisitions produce more uniform bolus profiles regardless of bolus direction [18].

Because of the radial geometry, the lower frequency parts of the k -space are sampled more densely than the high frequency parts, as shown in Fig. 20.4. It was shown that radial imaging is less susceptible to motion artifacts since each readout contains data for the center of the k -space. However,

Fig. 20.7 3D Radial K-space sampling schemes include stack of stars or cylindrical sampling and “true radial” or VIPR sampling



in order to meet the Nyquist criterion for the high frequency data, where the samples are farther apart, the imaging time takes longer than the Cartesian sampling by a factor of $\pi/2$, or roughly 1.5 times longer, for a radial image of comparable quality [38]. But the radial undersampling artifacts appear as streaks rather than aliasing, which may be acceptable in some applications.

Reconstruction

Data acquired on Cartesian rectilinear grids are easily reconstructed into images using a simple inverse Fourier transformation. However, data sampled by radial trajectories must first be re-sampled onto a Cartesian grid in order for the Fourier Transform to be utilized. Acquired non-Cartesian data is first interpolated by convolution with a smoothing function and then re-sampled onto a Cartesian grid. The entire process including the inverse Fourier Transform is called gridding. Radially sampled data is sometimes reconstructed using filtered backprojection, similar to the reconstruction of computed tomography data; however, this method is considerably less commonly used than gridding and will not be addressed here.

The interpolative process of gridding uses a convolution kernel and accounts for differences in sampling density. Since k-space data is non-zero for a finite space, sampling theory informs us that any point can be sampled accurately with SINC interpolation at or above Nyquist sampling frequency. This results in multiplication by a RECT function in the image domain and hence suppresses aliasing. However, since the SINC function has infinite extent, the calculation of each new k-space point requires the multiplication of all points with the

SINC function, a process which is time-intensive. For that reason, a convolution kernel that has finite extent is utilized. However, the corresponding Fourier transform is not finite, potentially resulting in image aliasing. The choice of interpolation kernels therefore trades off speed and accuracy. Finally, convolution in k-space amounts to multiplication in the image domain resulting in shading in the reconstructed image. For this reason, the final image is typically divided by the Fourier transform of the convolution kernel.

Kaiser-Bessel Kernel

Considerable efforts have undergone the identification of the best convolution kernel in terms of speed and accuracy. Many agree that the Kaiser-Bessel window is the most precise for k-space convolution in terms of accuracy of the reconstructed image, determined with comparison to SINC interpolation using least-squares metrics [39]. The 1D Kaiser-Bessel function is given by the equation

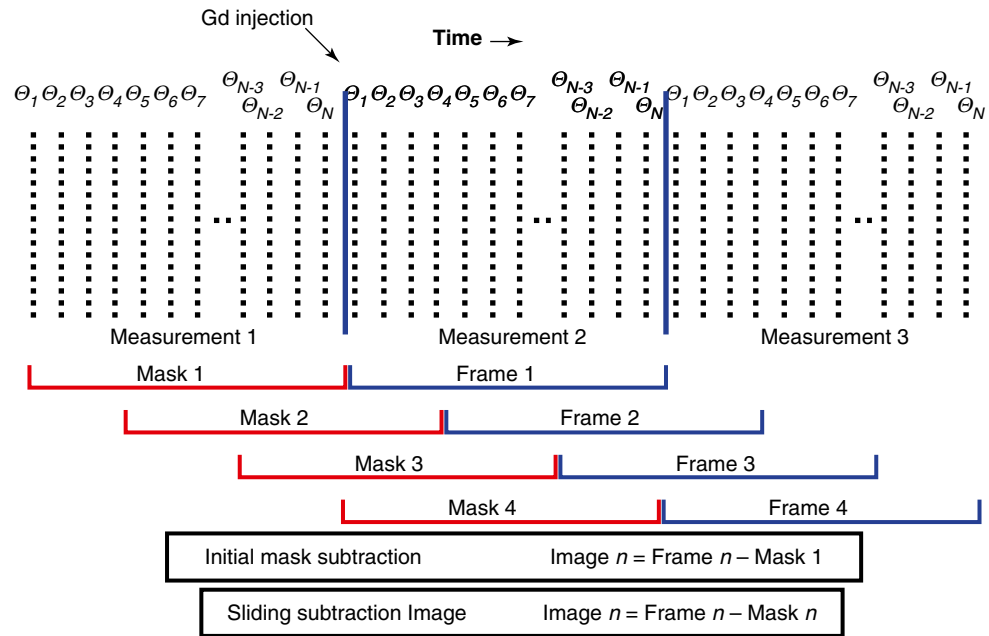
$$KB(k) = \frac{1}{w} I_0 \left(b \left[1 - (2k/w)^2 \right] \right) \text{RECT}(2k/w)$$

Where w is the width of the kernel, b a scaling parameter, I_0 , a zero-order modified Bessel function of the first kind and $\text{RECT}(x)$ a rectangle function defined by

$$\text{RECT}(x) = \begin{cases} 1, & |x| \leq 1 \\ 0, & |x| > 1 \end{cases} \quad \text{RECT}(x) = \begin{cases} 1, & |x| \leq 1 \\ 0, & |x| > 1 \end{cases}$$

The width parameter w is typically chosen to be 2–4 k-space samples. Increasing w suppresses aliasing artifacts in the image domain, but also increases the computation time.

Fig. 20.8 Radial Sliding Window Reconstruction with Sliding Mask. The N radial acquisitions $\theta_1 \dots \theta_N$ make up one measurement repetition. Intermediate frames are reconstructed by sharing echoes from two consecutive measurements that fall in the sliding time window. Sliding mask subtraction uses a subtraction mask reconstructed in a similar manner that follows the frame. Conventional subtraction, or initial mask, uses Mask 1 for all frames



Sampling Density

Since the data is denser as it gets closer to the origin, filters such as Ram-Lak are used to weight radial points accordingly during the re-gridding process. Then 2D Fourier transform is performed on the re-gridded data. There are a number of algorithms for calculating the sampling density with the most popular being an iterative approach proposed by Pipe [40].

Sliding Window Reconstruction

Even with partial Fourier techniques in all three dimensions, a typical MRA requires approximately 10 s to acquire one 3D volume. This results in a frame rate of 0.1 frame/s, whereas X-Ray DSA uses 3–6 frames/s to capture the hemodynamics.

A technique to achieve higher frame rate is to use sliding window reconstruction, first developed by Riederer [41]. This method reconstructs intermediate frames between the actual measurements by combining echoes from two consecutive volumes. After the first measurement is reconstructed, it is updated by replacing the “oldest” k -space lines of the image with the corresponding lines from the next measurement. After the updated volume is reconstructed, it is again updated by replacing the next “oldest” k -space lines, which are now the “oldest” in the latest frame. When all the lines are replaced, the image will be equal to the second measurement. This process is repeated with the second and third measurements.

This technique is suitable for radial acquisition since each line has information about the center of k -space, so each update is equivalent. The slice loop needs to be inside the angular loop of course, to update projections. For Cartesian acquisitions, each phase encoding line contains different

spatial frequencies. Therefore it would not capture motion smoothly since the center of k -space not sampled as often. Figure 20.8 shows a diagram of the radial sliding reconstruction.

Each update could be as small as one projection, which could result in a frame rate of about 12 frames/s for an acquisition with 128 projections per image. However, although the image is *updated* more often, the update rate is not the true temporal resolution. Each image still contains about 10 s of dynamic information, whereas in X-Ray DSA, each frame is acquired instantaneously. The direct result of having 10 s of dynamic information is temporal blurring of the images. In order to increase the true temporal resolution, acquisition time needs to be shortened.

One approach to mitigate the effects of temporal blurring is sliding mask subtraction which can be used in addition to the sliding window reconstruction. Conventional subtraction in CE-MRA datasets uses an initial pre-contrast acquisition as the “mask” volume, which is subtracted from every subsequent contrast acquisition. While the imaging acquisition continues the temporal separation between the mask and the imaging slice increases. In pulse sequences with long imaging times, this can result in blurring of arterial and venous phases. Utilizing a mask which advances synchronously in time with the imaging acquisition improves the arterial and venous separation [18]. This is especially useful for diagnosis of vascular diseases which feature high flow pathology such as arteriovenous malformations and fistulas. A comparison of Radial Sliding Window view share MRI to x-ray DSA found that sliding window MRA was able to predict Spetzler-Martin grade, AVM size and the topology of feeding arteries and draining veins equivalent to Xray

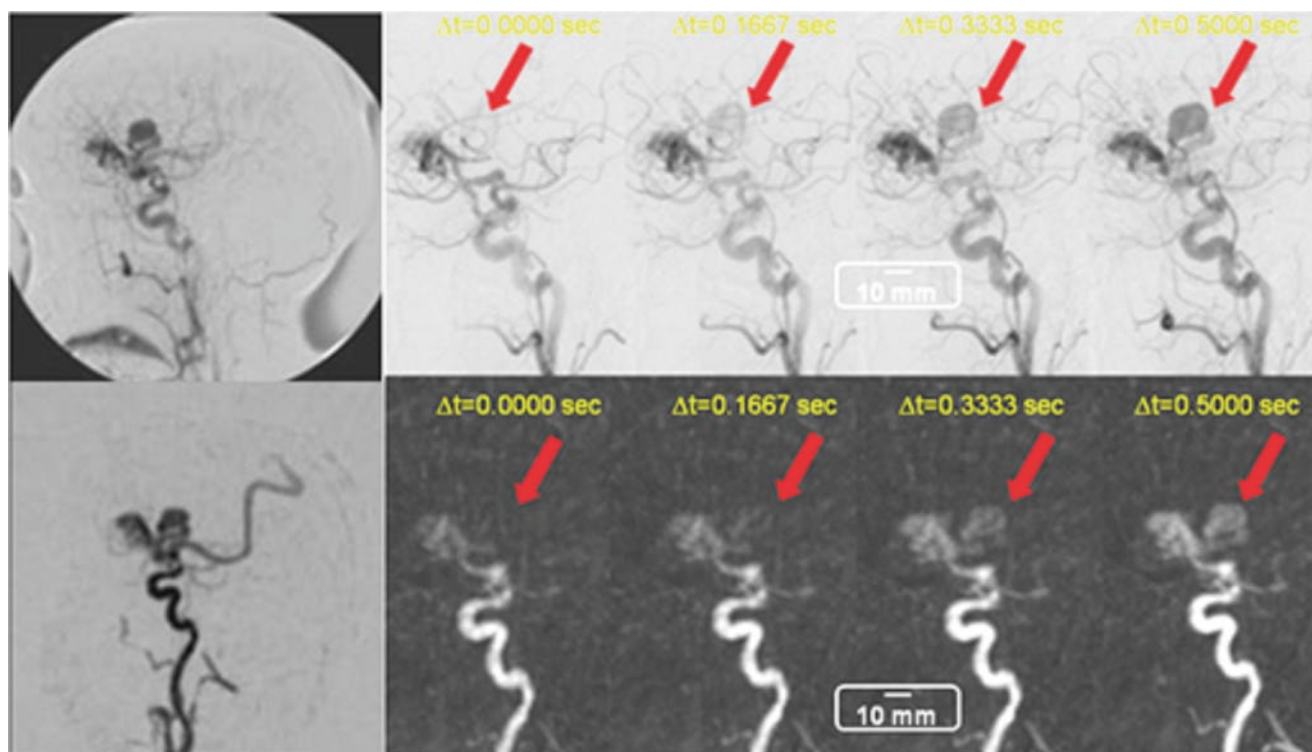


Fig. 20.9 Intracranial arteriovenous malformation visualized with both 2D X-Ray DSA (*top*) and radial stack of stars CE-MRA with sliding window reconstruction (*bottom*). The use of radial stack of stars sampling and sliding window reconstruction allows identical frame rates between

the two imaging modalities (6 frames/s). This allows comparable depiction of flow dynamics in the vascular pathology without the need for intracranial catheter placement and risk of injury associated with X-ray DSA (Images Courtesy Dr. Christopher Eddleman, M.D., Ph.D.)

DSA. Figure 20.9 show a comparison in a angiographically observed AVM with adjacent arterialized vein (i.e. verix) [46]. Radial data can be reconstructed in one of two ways: Using filtered-backprojection (also known as projection reconstruction or PR) and regridding.

The filtered backprojection method utilizes the central slice theorem and applies the idea of computed tomography (CT) reconstruction. The central slice theorem states that the 1D Fourier Transform of a projection through a 2D object onto a line is equal to the parallel slice through the origin (the central slice) of the object's 2D Fourier Transform. The radial projection acquired in k -space from the MRI scan is the central slice of the 2D Fourier Transform. Then, that radial data can be inverse Fourier transformed into image space projection. When all the radial lines have been transformed into projections, they can be filtered and Radon transformed to complete an image similar to CT filtered backprojection.

The regridding method simply transfers the radial k -space data onto the Cartesian coordinates. Since the radial and Cartesian data points do not exactly overlap, some sort of interpolation is performed. Since the data is denser as it gets closer to the origin, filters used in the filtered backprojection method, such as Ram-Lak, are also used in regridding. Then 2D Fourier transform is performed on the regridded data.

It was previously shown that while the filtered backprojection method results in higher SNR but regridding has superior spatial resolution [42].

Radial Imaging Errors

There are errors associated with radial imaging. One error is from gradient delays. To sample echoes radially, the x and y gradients need to turn on at the same time. But there exists some delay in turning on the gradients in the order of few microseconds. Moreover, the delays are different for each gradient coil and the model of the MR scanner. These delays cause the radial lines to be centered incorrectly, offset from the origin. Plus, the radial lines in different projection angles do not intersect at a single point. These errors appear as streaks at the edges and uneven shading on the images. For Cartesian trajectories, the gradient delays do not result in any artifacts.

The gradient delay can be corrected by several different ways. One method involves measuring gradient delay for each of the scanner and adjusting the gradient amplitude during the scan [43]. If the delays are known, gradient amplitudes can be calculated to make adjustments so that the projection intersects the origin. Image-based post processing

Table 20.1 Summary of k-space sampling techniques

Technique	Motion artifact susceptibility	Sliding window reconstruction compatibility	Coherence of aliasing artifact due to undersampling	Reconstruction considerations	Scan time ^a
Stack of stars	Reduced	Yes	Minimal coherence	Regridding, sampling density compensation, fourier transform	Intermediate
VIPR	Least	Yes	Incoherent	Regridding, sampling, density compensation, fourier transform	Most
Cartesian	Severe	No	Greatest coherence	Simple fourier transform	Least

^aAssuming nyquist criteria are met

methods are also available, where the algorithm iteratively corrects the images based on user defined constraints [44].

Another type of artifacts in radial imaging is clockshift errors. The phases of the numeric crystal oscillator of the scanner sometimes may not align with the phase of the echo. This results in no visible errors for Cartesian imaging, since readout direction is always the same and because phase shift is constant. But for radial imaging, the readout direction changes for each scan. The varying phase shifts for each readout cause artifacts resembling halos around the objects. Similar to gradient delays, the phase shifts can also be measured and corrections can be applied prior to scanning. Table 20.1 shows a summary of k-space sampling techniques.

Highly Constrained Projection Reconstruction (HYPR)

Highly Constrained Projection Reconstruction is a recent topic of interest, which was developed to increase the temporal resolution of projection reconstruction. HYPR achieves high frame rate by reconstructing only a few number of projections which contain good temporal information but poor SNR, and combining those images with a composite image which has high SNR but poor temporal information. Mistretta reported acceleration factor of about 100 with the same SNR as regular filtered back-projection methods using this technique [45].

However, the accuracy of temporal information represented by this technique is an area of active research. Furthermore, combining limited projection images and the composite makes the SNR calculation difficult, and it is still under debate.

Conclusion

Contrast Enhanced MR Angiography remains an active area of research due to the rising incidence of vascular disease. Recent successes are overshadowed by new approaches, based on sound physics principles which are engineered to allow for clinical ease of use. Techniques

for time-resolved imaging and newer approaches to image acceleration allow for improved spatial resolution and overall image quality to add confidence to increasingly subtle clinical findings based on MRA.

References

1. Prince MR, et al. Dynamic gadolinium-enhanced three-dimensional abdominal MR arteriography. *J Magn Reson Imaging*. 1993;3(6): 877–81.
2. Earls JP, et al. Breath-hold single-dose gadolinium-enhanced three-dimensional MR aortography: usefulness of a timing examination and MR power injector. *Radiology*. 1996;201(3):705–10.
3. Maki JH, et al. The effects of time varying intravascular signal intensity and k-space acquisition order on three-dimensional MR angiography image quality. *J Magn Reson Imaging*. 1996;6(4): 642–51.
4. Wilman AH, et al. Fluoroscopically triggered contrast-enhanced three-dimensional MR angiography with elliptical centric view order: application to the renal arteries. *Radiology*. 1997;205(1): 137–46.
5. Foo TK, et al. Automated detection of bolus arrival and initiation of data acquisition in fast, three-dimensional, gadolinium-enhanced MR angiography. *Radiology*. 1997;203(1):275–80.
6. Ho KY, et al. Peripheral vascular tree stenoses: evaluation with moving-bed infusion-tracking MR angiography. *Radiology*. 1998;206(3):683–92.
7. Hany TF, et al. Contrast-enhanced magnetic resonance angiography of the renal arteries. Original investigation. *Invest Radiol*. 1998; 33(9):653–9.
8. Meaney JF, et al. Stepping-table gadolinium-enhanced digital subtraction MR angiography of the aorta and lower extremity arteries: preliminary experience. *Radiology*. 1999;211(1):59–67.
9. Korosec FR, et al. Contrast-enhanced MR angiography of the carotid bifurcation. *J Magn Reson Imaging*. 1999;10(3):317–25.
10. Kruger DG, et al. Continuously moving table data acquisition method for long FOV contrast-enhanced MRA and whole-body MRI. *Magn Reson Med*. 2002;47(2):224–31.
11. Finn JP, et al. Thorax: low-dose contrast-enhanced three-dimensional MR angiography with subsecond temporal resolution – initial results. *Radiology*. 2002;224(3):896–904.
12. Carr JC, et al. Preoperative evaluation of the entire hepatic vasculature in living liver donors with use of contrast-enhanced MR angiography and true fast imaging with steady-state precession. *J Vasc Interv Radiol*. 2003;14(4):441–9.

13. Hennes S, Keating GM. Gadofosveset. *Drugs*. 2006;66(6):851–7.
14. Eldredge HB, et al. Species dependence on plasma protein binding and relaxivity of the gadolinium-based MRI contrast agent MS-325. *Invest Radiol*. 2006;41(3):229–43.
15. Kraitchman DL, et al. MRI detection of myocardial perfusion defects due to coronary artery stenosis with MS-325. *J Magn Reson Imaging*. 2002;15(2):149–58.
16. Goyen M. Gadofosveset-enhanced magnetic resonance angiography. *Vasc Health Risk Manag*. 2008;4(1):1–9.
17. Grist TM, et al. Steady-state and dynamic MR angiography with MS-325: initial experience in humans. *Radiology*. 1998;207(2):539–44.
18. Cashen TA, et al. 4D radial contrast-enhanced MR angiography with sliding subtraction. *Magn Reson Med*. 2007;58(5):962–72.
19. Vakil P, et al. Magnetization spoiling in radial FLASH contrast-enhanced MR digital subtraction angiography. *J Magn Reson Imaging*. 2012;36(1):249–58.
20. Maki JH, Chenevert TL, Prince MR. Three-dimensional contrast-enhanced MR angiography. *Top Magn Reson Imaging*. 1996;8(6):322–44.
21. Bernstein M, King K, Zhou X. *Handbook of MRI pulse sequences*. Amsterdam/Boston: Elsevier Academic Press; 2004.
22. Edelman RR, et al. Quiescent-interval single-shot unenhanced magnetic resonance angiography of peripheral vascular disease: technical considerations and clinical feasibility. *Magn Reson Med*. 2010;63(4):951–8.
23. Hurst GC, et al. Signal-to-noise, resolution, and bias function analysis of asymmetric sampling with zero-padded magnitude FT reconstruction. *Magn Reson Med*. 1992;27(2):247–69.
24. Noll DC, Nishimura DG, Macovski A. Homodyne detection in magnetic resonance imaging. *IEEE Trans Med Imaging*. 1991;10(2):154–63.
25. van Vaals JJ, et al. “Keyhole” method for accelerating imaging of contrast agent uptake. *J Magn Reson Imaging*. 1993;3(4):671–5.
26. Jones RA, et al. K-space substitution: a novel dynamic imaging technique. *Magn Reson Med*. 1993;29(6):830–4.
27. Korosec FR, et al. Time-resolved contrast-enhanced 3D MR angiography. *Magn Reson Med*. 1996;36(3):345–51.
28. Carroll TJ. The emergence of time-resolved contrast-enhanced MR imaging for intracranial angiography. *AJNR Am J Neuroradiol*. 2002;23(3):346–8.
29. Griswold MA, et al. Partially parallel imaging with localized sensitivities (PILS). *Magn Reson Med*. 2000;44(4):602–9.
30. Pruessmann KP, et al. SENSE: sensitivity encoding for fast MRI. *Magn Reson Med*. 1999;42(5):952–62.
31. Sodickson DK, Manning WJ. Simultaneous acquisition of spatial harmonics (SMASH): fast imaging with radiofrequency coil arrays. *Magn Reson Med*. 1997;38(4):591–603.
32. Jakob PM, et al. AUTO-SMASH: a self-calibrating technique for SMASH imaging. *Simultaneous Acquisition of Spatial Harmonics. MAGMA*. 1998;7(1):42–54.
33. Griswold MA, et al. Generalized autocalibrating partially parallel acquisitions (GRAPPA). *Magn Reson Med*. 2002;47(6):1202–10.
34. Edelstein WA, et al. Spin warp NMR imaging and applications to human whole-body imaging. *Phys Med Biol*. 1980;25(4):751–6.
35. Lauterbur PC. Progress in n.m.r. zeugmatography imaging. *Philos Trans R Soc Lond B Biol Sci*. 1980;289(1037):483–7.
36. Scheffler K, Hennig J. Reduced circular field-of-view imaging. *Magn Reson Med*. 1998;40(3):474–80.
37. Glover GH, Pauly JM. Projection reconstruction techniques for reduction of motion effects in MRI. *Magn Reson Med*. 1992;28(2):275–89.
38. Peters DC, et al. Undersampled projection reconstruction applied to MR angiography. *Magn Reson Med*. 2000;43(1):91–101.
39. Jackson JI, et al. Selection of a convolution function for Fourier inversion using gridding [computerised tomography application]. *IEEE Trans Med Imaging*. 1991;10(3):473–8.
40. Zwart NR, Johnson KO, Pipe JG. Efficient sample density estimation by combining gridding and an optimized kernel. *Magn Reson Med*. 2012;67(3):701–10.
41. Riederer SJ, et al. MR fluoroscopy: technical feasibility. *Magn Reson Med*. 1988;8(1):1–15.
42. Lauzon ML, Rutt BK. Polar sampling in k-space: reconstruction effects. *Magn Reson Med*. 1998;40(5):769–82.
43. Peters DC, Derbyshire JA, McVeigh ER. Centering the projection reconstruction trajectory: reducing gradient delay errors. *Magn Reson Med*. 2003;50(1):1–6.
44. Lee KJ, et al. Method of generalized projections algorithm for image-based reduction of artifacts in radial imaging. *Magn Reson Med*. 2005;54(1):246–50.
45. Mistretta CA, et al. Highly constrained backprojection for time-resolved MRI. *Magn Reson Med*. 2006;55(1):30–40.
46. Eddleman CS, et al. 4D radial acquisition contrast-enhanced MR angiography and intracranial arteriovenous malformations: quickly approaching digital subtraction angiography. *Stroke*. 2009;40(8):2749–53.

Ioannis Koktzoglou, Ruth P. Lim, Oisín Flanagan,
and Robert R. Edelman

Abstract

Non-contrast-enhanced magnetic resonance angiography (NEMRA) refers to the class of magnetic resonance angiographic techniques that do not use contrast agents for displaying blood vessels within the body. NEMRA comprises several techniques and has many clinical applications. Each NEMRA technique is designed to visualize arteries or veins based on blood flow or the physical properties of blood. This chapter summarizes the motivations for using NEMRA (in place of contrast-enhanced magnetic resonance angiography), and reviews various methods for NEMRA that are either commercially available or have been described in the academic literature. Covered NEMRA methods include time of flight, arterial spin labeling, gated subtractive imaging, inflow inversion recovery, quiescent interval slice selective velocity selective angiography, phase contrast and flow independent angiography. The physical underpinnings and applications of each NEMRA method are reviewed, and the advantages and limitations of each technique are discussed.

Keywords

MRA • Magnetic resonance • Angiography • Venography • MRI • Non-contrast • Nonenhanced

Introduction

Non-contrast enhanced magnetic resonance angiography (MRA), or “nonenhanced” MRA, is performed using a diverse body of techniques, with each technique designed to

visualize arteries or veins on the basis of various physical properties and physiological states. Nonenhanced methods for MRA originated nearly 30 years ago and have evolved greatly since. Modern techniques for nonenhanced MRA, enabled in large part by considerable advancements in MRI

I. Koktzoglou, PhD (✉)

Department of Radiology, Evanston Hospital, NorthShore
University HealthSystem, Walgreen Jr. Bldg, G507, 2650
Ridge Ave, Evanston, IL 60201, USA

The University of Chicago Pritzker School of Medicine,
Chicago, IL, USA
e-mail: ikoktzoglou@gmail.com

R.P. Lim, MD

Department of Radiology, Austin Health,
145 Studley Rd, Melbourne/Heidelberg, VIC 3084, Australia

The University of Melbourne, Melbourne, Victoria, Australia
e-mail: ruth.lim@austin.org.au

O. Flanagan, MD

Northwestern University Feinberg School of Medicine,
Chicago, IL, USA

NorthShore University HealthSystem, Walgreen Jr. Bldg,
G507, 2650 Ridge Ave, Evanston, IL 60201, USA
e-mail: oisinflanagan@gmail.com

R.R. Edelman, MD

Department of Radiology, Evanston Hospital, NorthShore
University HealthSystem, Walgreen Jr. Bldg, G507, 2650
Ridge Ave, Evanston, IL 60201, USA

Northwestern University Feinberg School of Medicine,
Chicago, IL, USA
e-mail: redelman@northshore.org

hardware and software, are now faster, more robust and, when used appropriately, provide diagnostic images in most instances.

Although contrast-enhanced MRA (CE-MRA) is widely regarded as being superior to nonenhanced MRA in terms of imaging speed, accuracy and robustness in the diagnosis of vascular disease, there has been resurgence in the research and development of improved methods for nonenhanced MRA. This resurgence has been spurred by economic and safety considerations of contrast agents. In nations where the cost of contrast agent is substantial compared with the cost of the MRI exam, elimination of the contrast material is helpful in reducing medical costs. The association of gadolinium-based contrast agents with nephrogenic systemic fibrosis (NSF), a rare but potentially fatal disorder in patients with advanced renal insufficiency, has also sparked efforts to reduce or altogether eliminate the use of contrast agents in MRA examinations.

Nonenhanced MRA has other advantages besides reducing costs and eliminating the risk of NSF. Unlike CE-MRA which usually can only be applied once in each exam, nonenhanced MRA can be repeated in the case of technical error. Nonenhanced MR angiograms acquired before contrast injection can also serve as invaluable backup examinations when CE-MRA images are rendered non-diagnostic due to patient motion or operator error.

This chapter aims to survey several types of nonenhanced MRA techniques. These techniques include time of flight angiography, subtractive arterial spin labeling, advanced inflow and outflow techniques, flow-independent methods, and phase contrast. The typical implementations, capabilities, limitations and applications of these nonenhanced MRA techniques are discussed.

Time of Flight Angiography

Overview and Physical Principles

Time of flight (TOF) angiography refers to a category of nonenhanced MRA techniques which suppresses (i.e. saturates) non vascular background tissue and preferentially displays arterial spins flowing into the vasculature being imaged [1, 2]. These techniques consist of either 2D or 3D gradient-echo sequences which use relatively short interecho spacings and flip angles chosen to maximize vascular display.

In its simplest form, TOF MRA is performed by applying a gradient-echo imaging sequence perpendicular to the target vasculature as shown in Fig. 21.1. As the inflowing blood enters the imaging slice, it experiences multiple imaging RF pulses and progressively becomes saturated as it traverses through the vasculature. Background tissue is substantially

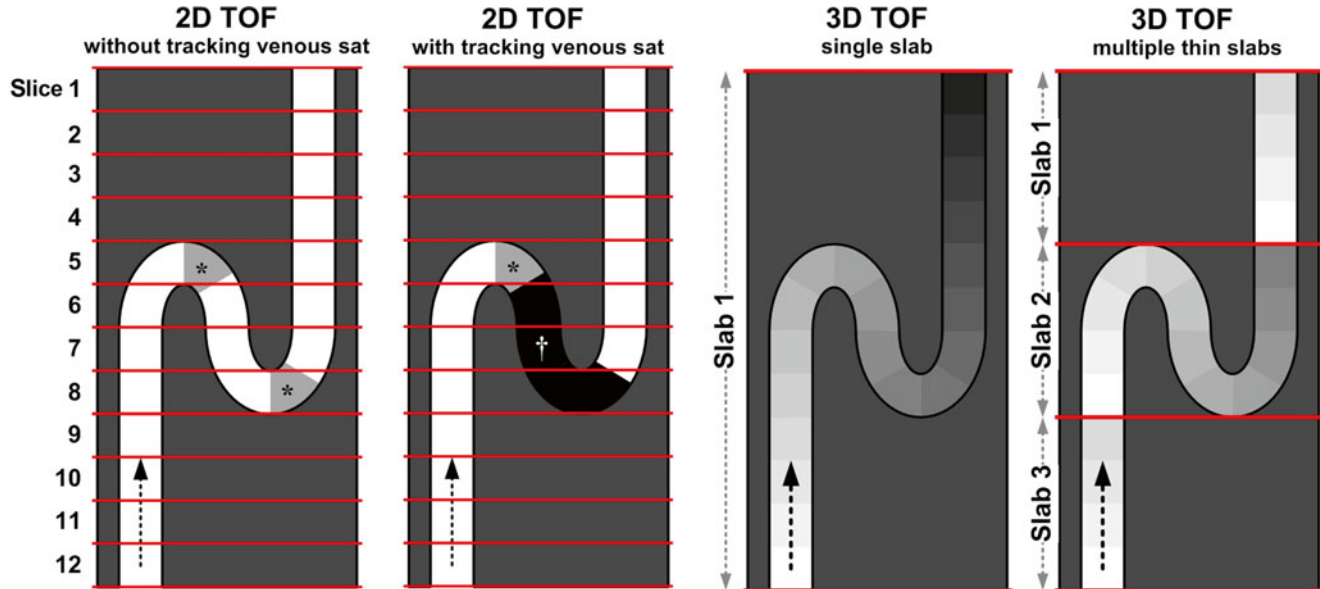
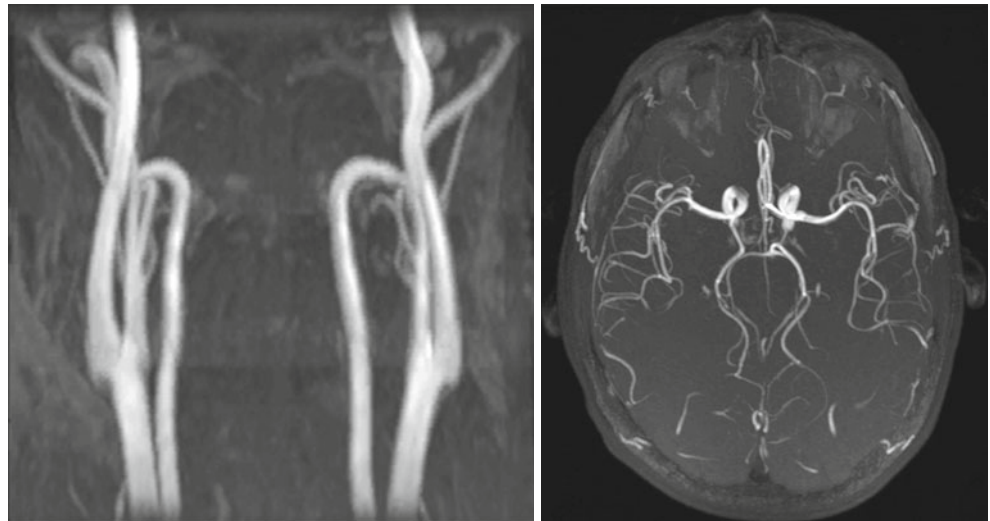


Fig. 21.1 Diagrams showing the basic principles of 2D and 3D time of flight (TOF) angiography. A tortuous artery traversing through tissue is shown; *arrows* show the direction of arterial flow and brightness corresponds to the signal observed at MR imaging. Horizontal red lines demarcate slices and slabs for 2D and 3D TOF MRA, respectively. Stationary tissue experiences repeated RF pulses, which saturate its magnetization and suppress its appearance. Blood vessels experience inflow enhancement, which render them hyperintense. The degree of arterial hyperintensity diminishes as arterial spins flow farther into the

slab and become saturated; this effect is best appreciated with single-slab 3D TOF MRA (third column). With 2D TOF MRA (first column), horizontally directed vessel segments are partially saturated and vascular contrast is diminished (*); the use of tracking venous saturation immediately above the imaging slice suppresses arterial segments containing retrograde flow (†, second column). Saturation of inflowing arterial magnetization during 3D TOF MRA can be lessened with the acquisition of multiple overlapping or adjacent thin slabs (fourth column)

Fig. 21.2 3D time of flight (TOF) MR angiograms obtained in the carotid arteries (*left panel*; coronal maximum intensity projection) and intracranial arteries (*right panel*; transversal maximum intensity projection) at 1.5 Tesla



suppressed because its magnetization experiences repeated imaging RF pulses and, unlike arterial blood, does not experience inflow enhancement. With TOF MRA, additional saturation RF pulses may be applied downstream of the slice or slab to suppress the appearance of inflowing venous spins. Example TOF angiograms obtained in the neck and head are shown in Fig. 21.2.

With TOF MRA, arterial signal and contrast with respect to surrounding background tissue depends on several factors including the longitudinal relaxation times (T_1 s) of arterial blood and prevailing background tissue (which depend on the magnetic field strength), the effective thickness of the imaging slice or slab which corresponds to the distance arterial blood must travel within the slab, the interecho spacing, the imaging flip angle, and the velocity of inflowing arterial blood. For a fixed interecho spacing and slab thickness, the use of larger flip angles with 3D TOF MRA improve background suppression but reduce the conspicuity of vessels located deeper within the slab.

Compared to 3D TOF MRA, 2D TOF imaging reduces inflow requirements for achieving optimal arterial opacification. Accordingly, 2D TOF MRA protocols typically use larger flip angles and achieve better arterial-to-background contrast than 3D TOF MRA methods. On the other hand, 3D TOF MRA can provide higher resolution in the slice direction than 2D TOF MRA. In either implementation, placement of the imaging slice (for 2D TOF) or slab (for 3D TOF) perpendicular to the blood vessels minimizes inflow requirements and optimizes vascular signal.

Suppression of non-vascular background signal during TOF imaging is achieved through the repeated application of imaging RF pulses. Compared with TOF imaging at 1.5 T, 3.0 T imaging provides improved background tissue suppression due to longer T_1 relaxation times. Additional suppression of

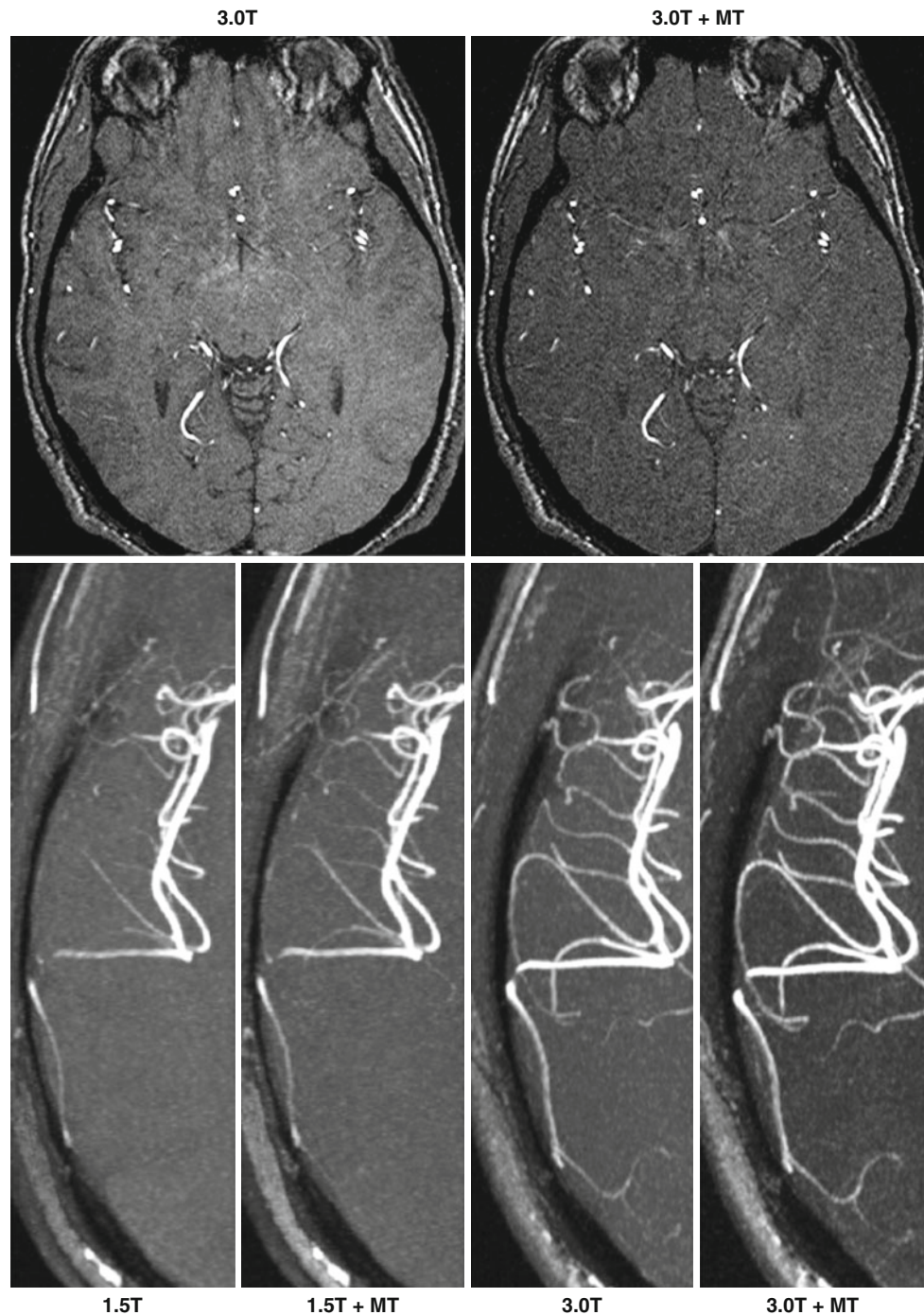
background tissue with significant macromolecular content (such as muscle or gray matter) is possible by applying magnetization transfer RF pulses within the echo train. The impact of 3 T imaging and magnetization transfer RF pulses on the arterial contrast of 3D TOF MRA is shown in Fig. 21.3.

Although traditional TOF methods use single-echo readouts, some studies in the brain have explored dual-echo TOF techniques to improve arterial-to-background contrast or provide additional venographic information. By acquiring a TOF angiogram with the first gradient echo and dephasing the appearance of flowing spin in the second echo, the appearance of background tissue can be suppressed by subtracting the image derived from the second echo from that of the first echo. Alternatively, the second echo can be used for dark-blood venography (bright-blood venography with inversion of the grayscale) because it is sensitive to shortened T_2^* from deoxygenated blood in cerebral veins.

Advantages, Limitations and Technical Considerations

Advantages of TOF MRA include widespread availability on commercial MRI systems at 1.5 T as well as 3.0 T, and good opacification of arteries containing rapid or continuous flow, such as the carotid and intracranial arteries. Drawbacks of TOF MRA include relatively slow acquisition times which prohibit routine screening of long vascular lengths, and imaging artifacts. Artifacts encountered with TOF MRA include arterial signal degradation in vessels containing turbulent, slow, or retrograde flow (which can be exacerbated by tracking venous saturation RF pulses), tortuous vessels, artifacts due to motion, and signal loss in vascular segments with severe stenosis.

Fig. 21.3 Impact of magnetization transfer contrast (*MT*) and magnetic field strength on 3D TOF MRA of the intracranial arteries. *Top panel:* axial source images show that magnetization transfer improves the suppression of brain parenchyma. *Bottom panel:* axial maximum intensity projection (MIP) images show the improved arterial display and background tissue suppression obtained at higher field strength, and the improvements associated with magnetization transfer contrast at 1.5 T and 3.0 T (Reprinted from Thomas et al. [21] with permission from John Wiley and Sons)



Applications of Time of Flight MRA

Time of flight MRA is most commonly applied to neurovascular imaging where a relatively small anatomical coverage is required, and where flow is fairly rapid and continuous and there is little physiological motion. Multiple overlapping thin slab acquisition (MOTSA) 3D TOF MRA is used to evaluate the intracranial vessels, combining some of the benefits of 3D TOF MRA while minimizing flow saturation

effects. With the use of parallel imaging, acquisition times of the order of 3–4 min can be achieved.

Common neurovascular applications include imaging for steno-occlusive intracerebral disease, in the setting of suspected acute cerebral infarction/ischemia. TOF MRA can be performed at the same examination as diffusion and perfusion weighted imaging to identify infarct and ischemic penumbra. Another common application is in the assessment of cerebral aneurysms, including screening patients predisposed to

aneurysm formation, assessment of known aneurysms and post-treatment follow up, particularly for previous endovascular coil occlusion. Improved performance at 3.0 T compared to 1.5 T has been reported, as higher spatial resolution is achievable. Susceptibility artifact related to previously surgically clipped aneurysms may preclude identification of small volume recanalization. TOF MRA performance is poorer in acute non-traumatic subarachnoid hemorrhage, due to challenges of patient clinical status and presence of blood in the subarachnoid space.

Other potential applications include screening for occult vascular malformations, or evaluation of the extracranial carotid and vertebral arteries for dissection or steno-occlusive disease as an alternative or adjunct examination where contra-indications to CT or MR with contrast exist.

2D TOF MR venography is also used in the assessment of dural venous sinus thrombosis. Similar to in arterial ischemia, a comprehensive MR examination can be performed that enables direct visualization of thrombus, as well as evaluation of potential complications including venous infarct or intracerebral hemorrhage.

Apart from anatomic assessment, TOF MRA can also be applied for determining flow directionality, which may be helpful in suspected subclavian steal, where reversal of flow in the ipsilateral vertebral artery is observed, or in body imaging, including assessment of directionality of portal vein flow in portal hypertension.

One potential pitfall of TOF MRA is that any tissues with short T_1 relaxation times (including intracellular and extracellular methemoglobin) may fail to be suppressed by excitation pulses and be mistaken for flow. As such, intracerebral hematoma may for example be mistaken for a giant cerebral aneurysm, or may mask an underlying vascular malformation if images are not interpreted in conjunction with other sequences, where lack of flow at the same location should enable differentiation. Also, turbulent, slow or in-plane flow can lead to overestimation of stenosis due to saturation effects.

Subtractive Arterial Spin Labeled Angiography

Overview and Physical Principles

Arterial spin labeling (ASL) is an approach for nonenhanced MR angiography that acquires two image sets which are later subtracted. The image sets differ only in the magnetization states of arterial spins. The process by which this difference in arterial magnetization is imparted is referred to as ‘labeling.’ Subtraction of the image sets displays the labeled arteries and provides complete suppression of background signal.

The first reports of ASL for nonenhanced MR angiography were made in the mid and late 1980s [3–5]. Early

implementations of ASL for MR angiography used spin-echo and gradient-echo readouts, but most modern implementations now utilize readouts that are faster and more SNR-efficient. Two popular readouts meeting these criteria are balanced steady-state free precession imaging (bSSFP) and fast spin-echo (FSE) imaging.

As will be explained, labeling of arterial magnetization in ASL MRA can be performed in two ways. Arterial spin labeling can be achieved by either applying RF pulses to alter arterial magnetization, or relying on flow-related dephasing made possible by magnetic field gradients.

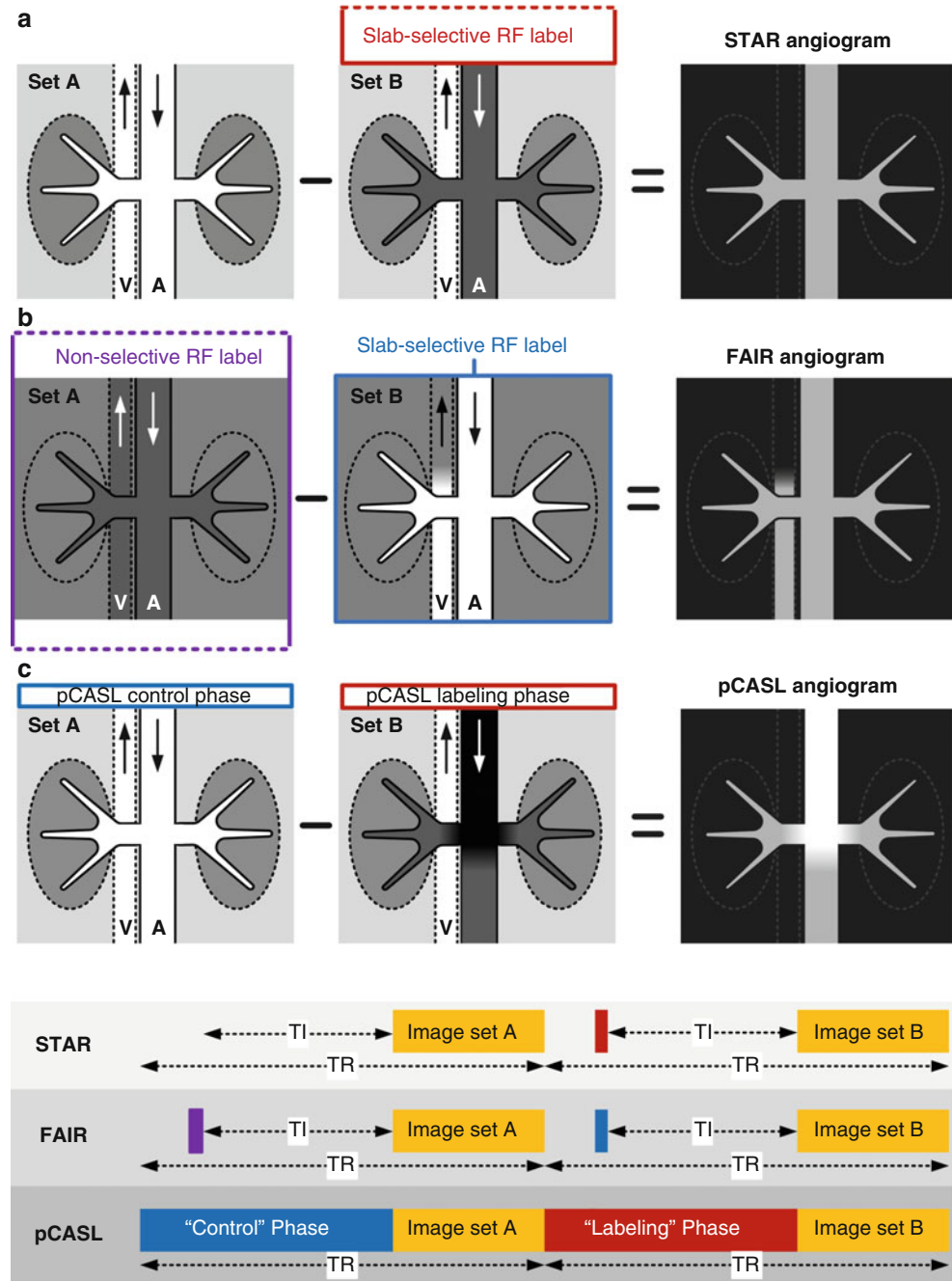
Arterial Spin Labeling with Radiofrequency Pulses

Labeling of arterial spins with inversion RF pulses is often considered the most traditional form of arterial spin labeling. This variation of arterial spin labeling is often referred to as ‘pulsed’ ASL. In its most basic form, this method consists of applying an inversion recovery RF pulse, typically of adiabatic type, to arterial spins flowing into the target vasculature, followed by an inversion delay time (TI), and an imaging readout. The difference of this data set and one acquired without the inversion RF pulse selectively displays the labeled arterial spins on a background of no signal. This labeling approach is often referred to as “Signal Targeting with Alternating inversion Recovery” (STAR) [6]. An illustration of STAR ASL MRA is shown in Fig. 21.4a.

Another approach for pulsed arterial spin labeling is “Flow Alternating Inversion Recovery” (FAIR) (Fig. 21.4b) [7]. This approach applies a slice selective inversion RF pulse to the target vasculature in one set and a non-selective inversion RF pulse to the second data set. Subtraction of the data sets displays vascular spins flowing into the target region. Compared with STAR, FAIR ASL may, depending on venous orientation and flow rate, display venous flow into the target region which can be undesirable. As compared to STAR, the FAIR approach better equalizes magnetization transfer effects between the two acquired data sets, which can improve the suppression of background tissue. This magnetization transfer effect, however, is usually not a concern with nonenhanced ASL MRA because of its small magnitude compared to the large signal within arteries.

Unlike pulsed arterial spin labeling, which applies short RF inversion pulses at a fixed TI time before imaging, another class of ASL techniques apply a continuous stream of RF energy for spin labeling. These methods are referred to as “continuous” or “pseudo-continuous”. Whereas continuous arterial spin labeling requires the use of a separate labeling RF coil which limits widespread use in the clinical setting, pseudo-continuous arterial spin labeling (also referred to as “pulsed-continuous” arterial spin labeling) can

Fig. 21.4 Illustration of (a) STAR, (b) FAIR, and (c) pCASL techniques for nonenhanced MRA. For each technique, a cross-sectional view of the imaging slab is shown containing a cartoon of the aorta (A) and inferior vena cava (V). STAR and FAIR utilize either selective or non-selective inversion RF pulses for spin labeling. During pCASL MRA, RF labeling is applied to a thin plane upstream of the arterial anatomy under interrogation. RF energy applied during the pCASL “control” phase is effectively inert and leaves inflowing arterial blood largely unperturbed. RF energy applied during the pCASL “labeling” phase inverts inflowing arterial magnetization. With all techniques, subtraction of the two acquired data sets produces a MR angiogram with excellent background suppression. Sequence timing diagrams are shown at the bottom. TR repetition time, TI inversion time



be applied without additional hardware requirements [8]. An implementation of pseudo-continuous ASL (pCASL) is shown in Fig. 21.4c. Compared to pulsed techniques, pCASL can provide larger arterial signal to noise ratio (SNR) in regions near the pseudo-continuous labeling plane where short effective inversion times are realized. Drawbacks of pCASL include increased RF energy deposition compared with pulsed approaches, and increased sensitivity to off-resonance as well as flow velocity which can reduce labeling efficiency and arterial SNR. Example MR angiograms obtained with pulsed and pseudo-continuous ASL are shown in Fig. 21.5.

Arterial Spin Labeling with Gradient Dephasing

Another means for labeling arterial spins during ASL is based on differential flow between systole and diastole in vessels containing pulsatile flow. This approach, originally referred to as gated subtraction angiography [3, 5], subtracts data sets acquired in systole and diastole. Brisk flow during systole results in the dephasing of arterial spins during the echo train and renders arteries dark. Conversely, arterial signal is preserved in diastole due to slow flow. Subtraction displays the arterial anatomy (Fig. 21.6). A commercially

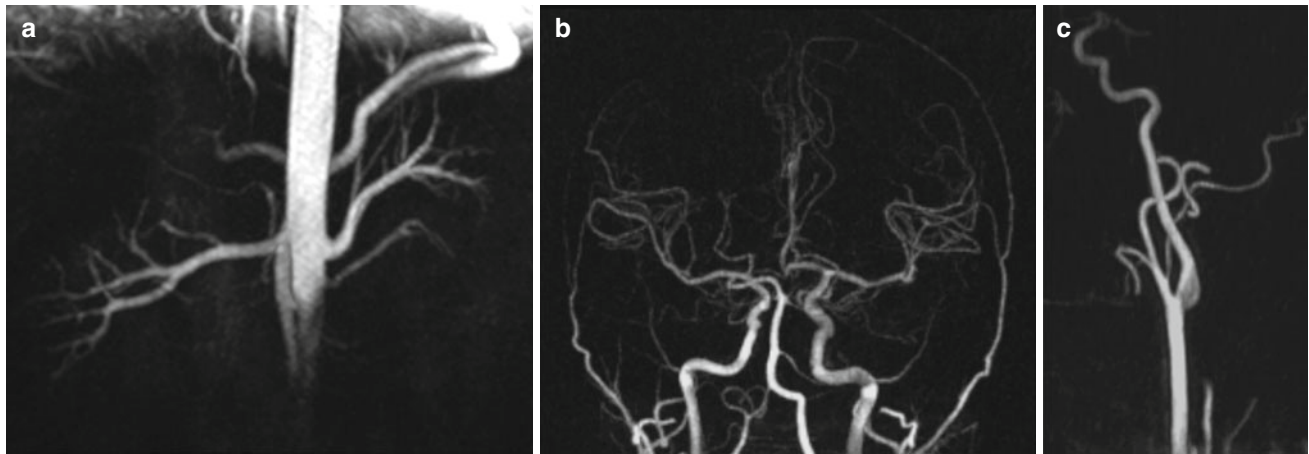
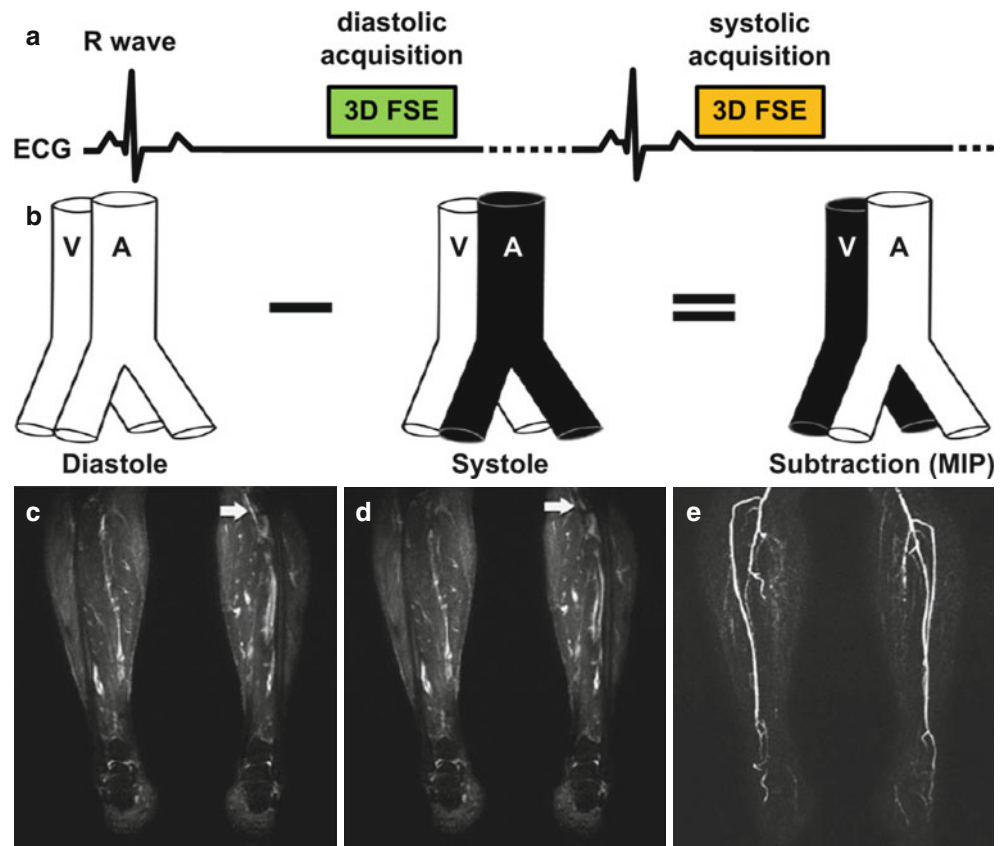


Fig. 21.5 Examples of arterial spin labeled MR angiography acquired using a bSSFP readout at 1.5 T. (a) Nonenhanced renal MR angiogram obtained with STAR arterial spin labeling and respiratory gating. (b)

Intracranial and (c) extracranial carotid MR angiograms obtained with combined pseudo-continuous and pulsed arterial spin labeling. All images are maximum intensity projections

Fig. 21.6 Illustration of a cardiac-gated subtractive MRA sequence known as Native SPACE in the lower extremities. (a) The sequence consists of a 3D fast spin-echo (FSE) readout that is acquired in both diastole and systole. Typically, data from one cardiac phase (e.g. diastole) is acquired one slice-encoding step at a time until completion before acquiring data from the complementary cardiac phase (systole). The expected vascular signal of the sequence is shown in (b). Imaging gradients do not dephase arterial or venous signal in diastole when flow is slow (c), but dephase fast arterial flow in systole (d). Subtraction of systolic from diastolic images produces a nonenhanced MR angiogram (e) (Reprinted from Lim et al. [22] with permission from John Wiley and Sons)

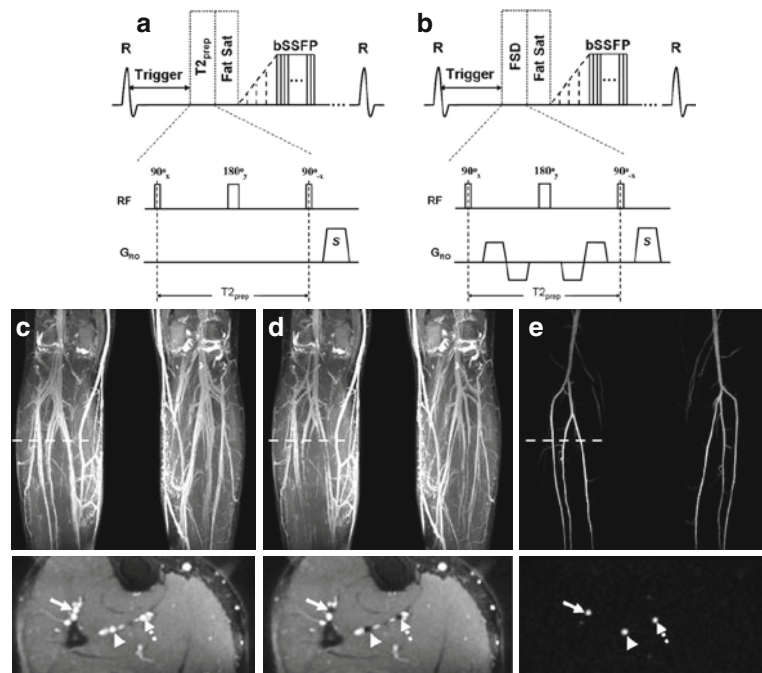


available technique for nonenhanced MRA using this labeling scheme is gated subtraction FSE imaging [9], which is also known as “Fresh Blood Imaging” (FBI), “Native Sampling Perfection with Application optimized Contrasts using different flip-angle Evolutions” (Native SPACE), “Delta Flow”, and “Trance”. The flow sensitivity of this technique can be tailored with partial Fourier sampling, adjustment of the refocusing flip angle, additional gradient

lobes for flow compensation or spoiling, and by orientation of the frequency encoding axis. Specifically, reduced dephasing and signal loss is achieved with the use of partial Fourier acquisition, larger spin-echo refocusing RF pulse flip angles, flow compensation gradients, and by aligning the phase-encoding axis parallel to the arterial flow direction.

With gated subtraction FSE imaging, dephasing of arterial spins during systole is accomplished by gradients within

Fig. 21.7 Illustration of a gated subtractive 3D bSSFP MRA sequence known as flow sensitive dephasing (FSD) in the lower extremities. The sequence acquires data in (a) diastole and (b) systole; flow sensitization is applied by a FSD magnetization preparation that precedes image acquisition. When imaging is performed in diastole, the FSD preparation applies no dephasing gradients along the readout direction, which results in bright arteries and veins (c). Conversely, in systole, flow spoiling gradients are applied which results in arteries appearing dark (d); veins containing slow flow are not dephased and remain hyperintense. Subtraction of the imaging data produces a nonenhanced MR angiogram (e) with no background signal (Reprinted from Fan et al. [23] with permission from John Wiley and Sons)



the imaging readout. Dephasing of arterial spins during systole may also be achieved by applying specially designed magnetization preparations before the imaging readout [10]. Figure 21.7 shows the design of one such sequence. Using RF and gradient pulses, these magnetization preparations spoil arterial signal based on its velocity or acceleration, leaving signal from stationary or non-pulsatile tissue unaltered. These approaches are most frequently applied before imaging readouts, such as bSSFP, which preserve arterial signal even during phases of substantial flow. Names of these techniques include “Flow Sensitive Dephasing” (FSD) and “Acceleration Dependent Vascular Anatomy for Non-Contrast-Enhanced MRA” (ADVANCE-MRA). With these methods, the degree of flow spoiling depends on the timing, duration, and strength of the gradient lobes applied. Gradients may also be applied along multiple axes to enhance flow spoiling and improve angiographic detail.

Advantages, Limitations and Technical Considerations

Main drawbacks of ASL MRA include increased motion sensitivity and doubled scan time compared with non-subtractive nonenhanced MRA techniques. For scans requiring cardiac gating, knowledge of the systolic and diastolic phases of fast and slow flow is important to optimize image quality and avoid artifacts. This information can be obtained with phase contrast imaging or preparatory scans that survey several phases of the cardiac cycle. For gated subtractive techniques, abnormal flow patterns in patients with vascular

disease can complicate the acquisition of dark-blood and bright-blood contrasts in systole and diastole, which can lead to image artifacts.

Some ASL methods for MRA require gating while others do not. In particular, ASL techniques based on differential RF pulses often do not require cardiac gating when coupled with readouts that preserve arterial signal during brisk flow, such as bSSFP. This is especially true in vascular beds containing predominantly continuous flow such as the carotid and intracranial arteries. Conversely, techniques that use imaging readouts that are sensitive to fast flow, such as FSE, generally require cardiac gating.

Applications of Arterial Spin Labeled Angiography

Although not often used in clinical practice, arterial spin labeling can be used to image a variety of vascular beds. In the evaluation of peripheral vascular disease without the use of contrast agents, gated subtractive FSE and flow dephased methods may be used. Of these methods, gated subtractive FSE imaging is the only technique that is commercially available. However, both gated techniques have good reported accuracy for imaging peripheral vascular disease in the distal lower extremities. Both gated techniques have potential for imaging the hands and feet, where contrast-enhanced MRA can be challenging due to slow arterial flow and short arterial to venous transit times.

In the evaluation of intracranial vascular disease, ASL can provide for time-resolved display of arterial flow patterns

which may be helpful for assessing the functional significance of various disorders, including arterial occlusions, stenoses, and arteriovenous malformations. This information can be used to supplement the static MR angiograms obtained with 3D TOF MRA. In the carotid arteries, ASL can display arterial stenosis, but more validation is needed to assess the accuracy of the method and the merits and weaknesses of the technique in comparison with 2D and 3D TOF MRA.

Arterial spin-labeled MRA of the renal arteries is feasible but, as with the use of ASL in other vascular territories, large validation studies are lacking. In imaging the renal arteries, there is stiff competition from non-subtractive techniques such as inflow inversion recovery (IFIR) which are faster, less sensitive to motion, and have been better validated. ASL imaging has also been found capable of displaying portal venous anatomy.

Advanced Flow-Dependent Angiography

Overview and Physical Principles

Other than TOF and ASL techniques, a few non-subtractive flow-dependent nonenhanced MRA techniques have found increased utilization and development in recent years. Although these techniques still depend on the presence of flow for angiography, as is the case with traditional TOF MR angiography, they differ substantially from TOF in their implementation, timing and display of arterial anatomy. These methods are reviewed here.

Inflow Inversion-Recovery Angiography

Inflow inversion-recovery (IFIR) refers to a technique in which angiographic contrast is obtained by inflow of unsaturated arterial spins into the target vasculature and suppression of background spins through application of an inversion-recovery prepulse [11]. Figure 21.8 shows a timing diagram for such a sequence. Unlike traditional TOF MRA which applies a train of series of largely interrupted RF pulses separated by a short time interval, the IFIR method applies a slab-selective inversion pulse followed by a substantial inversion time (TI). This TI time, which is selected to ensure adequate inflow into the vascular anatomy under interrogation and an adequate degree of background suppression, is followed by a rapid imaging readout with a short interecho spacing.

As compared with ASL imaging, the IFIR method does not use signal subtraction. This reduces scan time and sensitivity to motion artifact in exchange for imperfect background suppression. Because angiographic contrast with the IFIR method is predicated on inflow, it is most-often applied

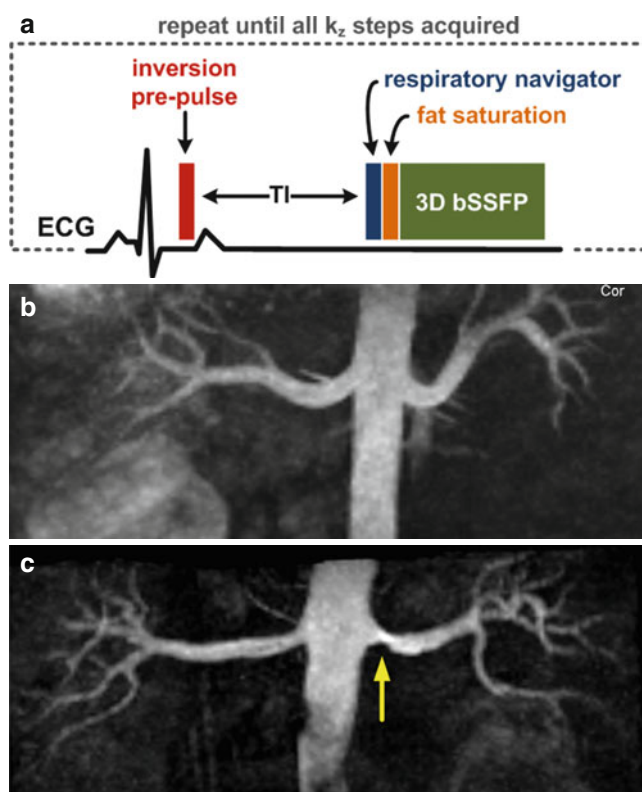


Fig. 21.8 Inflow inversion-recovery (IFIR) MR angiography. (a) Pulse sequence diagram for a cardiac- and navigator-gated implementation of renal IFIR. The slice-selective inversion pre-pulse is applied early in the cardiac cycle axially over the renal arteries. The TI time accommodates fresh inflow of arterial magnetization into the axial imaging slab and suppresses the appearance of background signal inverted by the pre-pulse. Navigator-gating eliminates respiratory motion artifact and fat saturation suppresses the appearance of abdominal and perivascular fat. (b) IFIR in a 24 year old healthy male subject. The renal arteries are well depicted despite the presence of some background signal. (c) IFIR in a 51 year old patient with a left renal artery stenosis (arrow)

to image arterial beds containing brisk flow, such as the renal and carotid arteries. The typical imaging readout is either bSSFP or FSE (half-Fourier or flow-compensated), to maintain signal from flowing spins. Minimization of inflow requirements is achieved by positioning the upstream edge of the inversion recovery slab close to the arterial anatomy under interrogation.

When imaging the renal arteries, one optimal implementation of IFIR applies two oblique sagittal inversion slabs over the left and right renal arteries. Prospective navigator or respiratory bellows gating is used to compensate for respiratory motion. Typical inversion times for the IFIR technique in the renal arteries range from 0.5 to 0.7 s; repetition times are usually 1 R-R interval. Trade names for this renal imaging technique include “Time-Spatial Labeling Inversion Pulse” (TimeSLIP), “NATIVE trueFISP” and “Inhance Inflow IR.”

Other variants of IFIR methods exist. In lieu of applying a spatially-selective inversion RF pulse, alternate

implementations first apply a non-selective inversion RF pulse, followed by a slice-selective inversion pulse to the inflowing blood pool prior to its entry into the target vascular anatomy. This approach is often referred to as “outflow” MRA instead of “inflow” MRA.

Quiescent Inflow Slice-Selective Angiography

Quiescent inflow slice-selective (QISS) angiography is a non-subtractive nonenhanced MRA technique introduced for imaging the peripheral arteries [12]. As shown in Fig. 21.9, the QISS sequence applies an in-plane radiofrequency (RF) saturation pulse to suppress static tissue, as well as a tracking venous RF saturation pulse to suppress venous signal. After a waiting period of a few hundred milliseconds, data are acquired using a bSSFP readout. The sequence is ECG-gated to ensure that data are acquired during diastole, whereas the waiting period (“quiescent interval”) spans systole. One slice is acquired per RR interval. A complete peripheral arterial study can be completed in less than 10 min.

QISS MRA normally acquires a single slice per RR interval. However, exam time can be shortened by a factor of 2–3 by acquiring multiple slices in rapid succession within a single RR interval in conjunction with a highly undersampled radial k-space trajectory (Fig. 21.10). Unlike Cartesian k-space trajectories, radial k-space trajectories permit the use of high undersampling factors without degradation of spatial resolution, so long as the data are sparse. The combination of fat saturation and in-plane saturation ensures QISS data are always sparse, which minimizes radial streak artifacts from undersampling. For multi-slice radial QISS, the venous saturation RF pulse, in-plane saturation RF pulse, and quiescent interval are applied only once prior to the first slice regardless of the number of slices. The chemical shift-selective fat saturation pulse and $\alpha/2$ catalyzation are applied prior to the bSSFP readout for each concurrently acquired slice. For a 2-slice radial QISS acquisition, the thickness of the in-plane saturation RF pulse is doubled and the position adjusted to span the two slices that are concurrently acquired.

Conventional QISS approaches provide only static images of blood vessels. A cine display of blood flow patterns, along with a high-resolution static display of vessel anatomy, can be obtained simultaneously by using QISS with a golden radial k-space trajectory. This “cine QISS” implementation depicts the onset and propagation of arterial flow in the peripheral arteries. With a single shot readout, scan time is equivalent to standard QISS. Multi-shot imaging improves the temporal fidelity at the expense of scan time. The highly constrained projection reconstruction (HYPR) algorithm can be used to improve the SNR and quality of the time-resolved MR angiogram. Initial patient studies have shown the method can depict delayed arrival of the pulse wave due to a hemodynamically significant stenosis.

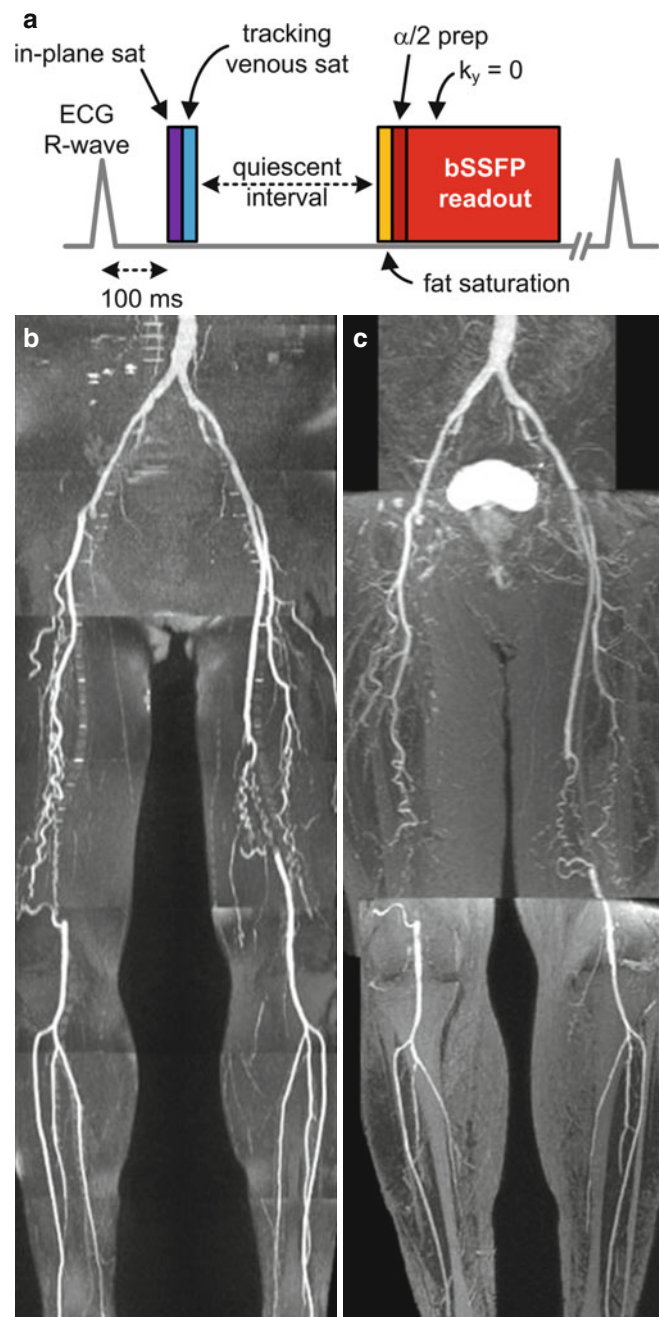
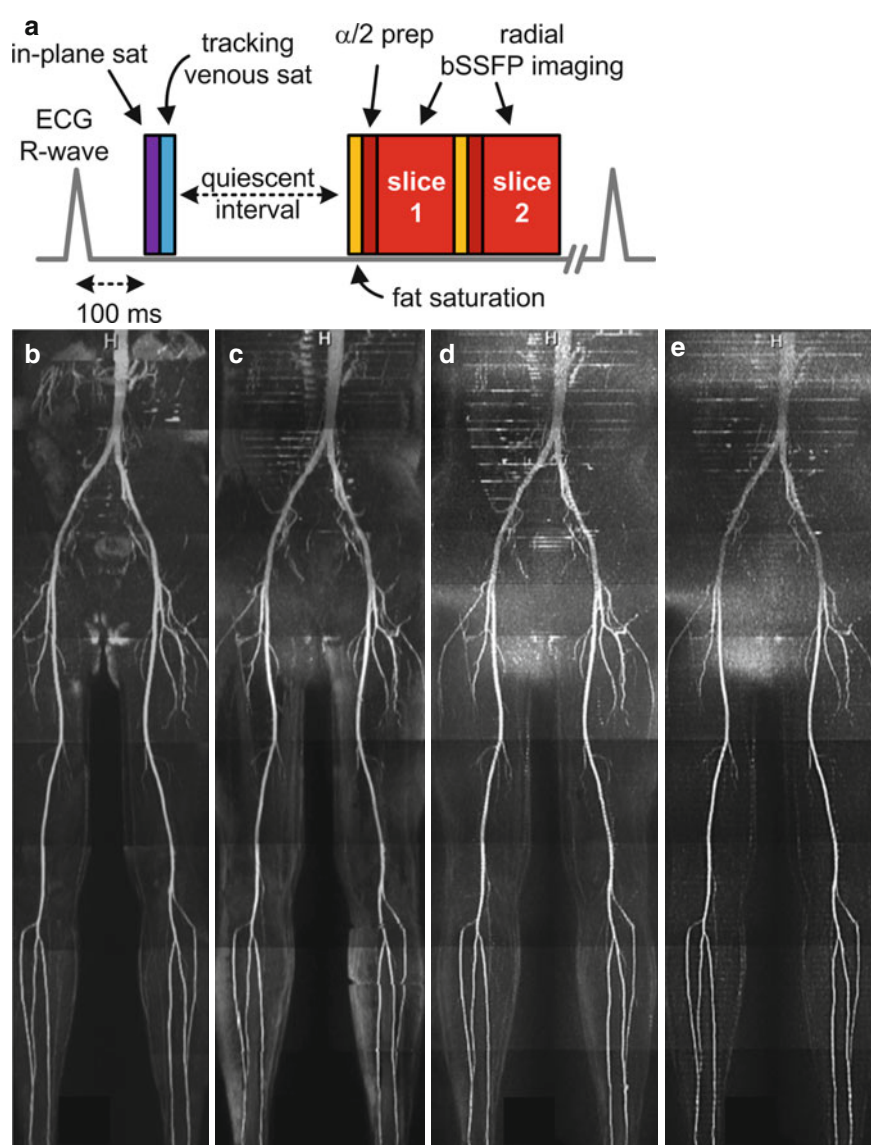


Fig. 21.9 Quiescent-inflow slice-selective (QISS) MR angiography. (a) QISS pulse sequence diagram. (b) Nonenhanced QISS MR angiogram obtained in a patient with bilateral superficial femoral artery occlusions (scan time ≈ 6 min) correlates well with the (c) contrast-enhanced MRA study, shows most of the collateral vessels, and better shows the calf vessels than the contrast-enhanced study. Images are maximum intensity projections (Reprinted from Edelman et al. [12] with permission from John Wiley and Sons)

Velocity Selective Angiography

Velocity selective angiography is a cardiac gated technique for nonenhanced MRA that applies a velocity selective inversion preparation to enhance the display of arterial anatomy

Fig. 21.10 Multi-slice radial QISS MR angiography. (a) Pulse sequence timing diagram showing a two slice implementation. Representative MIP images obtained with (b) Cartesian QISS with 93 lines, total scan time ~6 min; (c) two-slice radial QISS with 46 views, total scan time ≈ 3 min; (d) three-slice radial QISS with 32 views, total scan time ≈ 2 min; (e) single-slice radial QISS with 60 views, two signal averages (scan time ≈ 12 min), and large, single-element body coil for signal reception. Body coil radial QISS used an acceleration factor of 10 without the need for phased array coils as would be required for Cartesian-based parallel imaging techniques (Reprinted from Edelman et al. [24] with permission from John Wiley and Sons)



[13]. When applied at the appropriate phase of the cardiac cycle, the velocity selective module inverts stationary and slow moving background spins while leaving flowing spins unperturbed. After waiting a delay time to suppress background spins, imaging renders the arteries, which were unaffected by the velocity selective preparation, bright. A velocity selective preparation module, a pulse sequence diagram for performing velocity selective angiography, and a resulting angiogram are shown in Fig. 21.11.

Advantages, Limitations and Technical Considerations

Compared to subtractive arterial spin-labeled MRA, inflow inversion-recovery MRA offers shorter acquisition times and is considerably less sensitive to motion artifact. As such, IFIR is preferred to ASL MRA for imaging of arteries

experiencing respiratory or cardiac motion. With IFIR, the extent of inflow is often traded for the degree of background suppression. In particular, the use of long inflow/inversion times, which provide greater inflow of spins into the anatomy of interest, generally provide poorer arterial-to-background contrast due to T_1 -mediated recovery of background tissue signal.

QISS offers advantages over gated subtractive ASL techniques in the evaluation of peripheral arterial disease. Due to the lack of subtraction and use of saturation recovery, QISS is highly robust with minimal sensitivity to patient motion and cardiac arrhythmias. It has the particular advantage of enabling a simple and efficient workflow, thereby eliminating the need for scout imaging (for instance, to optimize trigger delays or the degree of flow spoiling) or special technologist expertise.

Compared to IFIR MRA, velocity selective MRA is not limited by inflow into the vascular anatomy and can provide

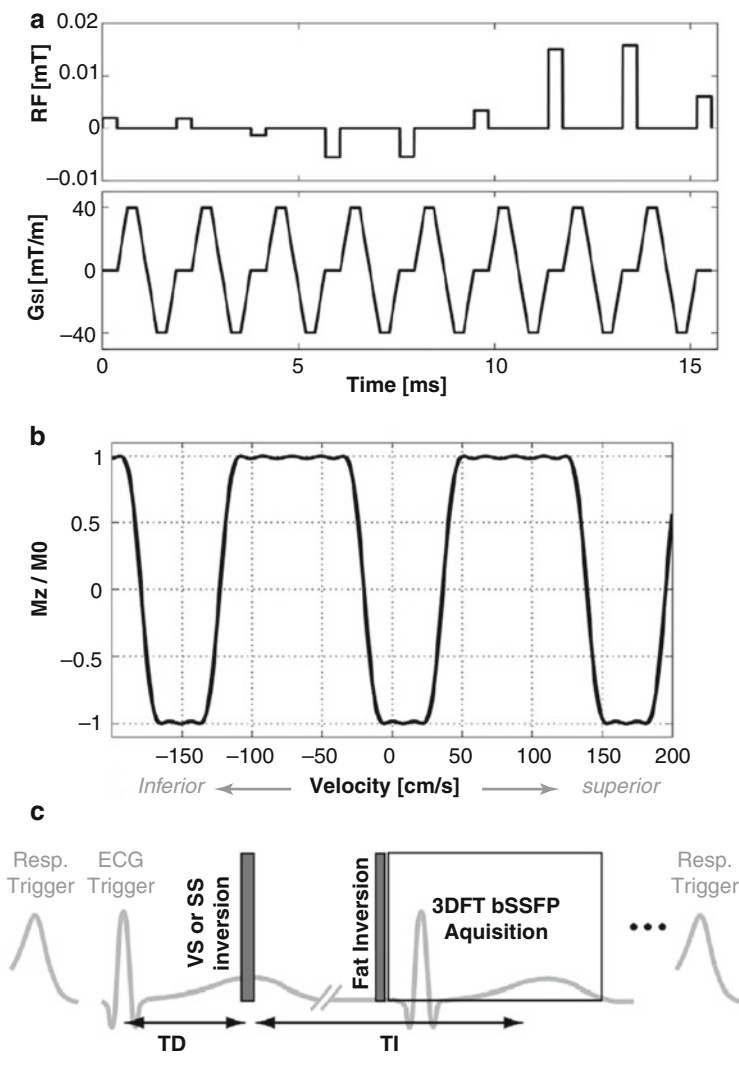


Fig. 21.11 Velocity-selective MR angiography. (a) Example gradient and RF pulse activity for a velocity selective preparation that inverts stationary and slow moving spins and leaves more rapidly flowing spins unperturbed. (b) Plot showing the dependence of the inversion efficiency on flow velocity for the preparation shown in (a). (c) Pulse sequence

diagram for velocity selective angiography of the renal arteries. The velocity selective (VS) module is applied during a phase of rapid flow. (d) Maximum intensity projection of a velocity-selective MR angiogram of the renal and aortoiliac arteries of a healthy subject (Reprinted from Shin et al. [13] with permission from John Wiley and Sons)

display of a longer extent of vascular anatomy. On the other hand, velocity selective MRA is more dependent on the use of cardiac gating than IFIR MRA because it is predicated on applying a velocity selective preparation at a suitable phase of the cardiac cycle. Velocity selective MR angiography also requires appropriate tuning of the velocity selective preparation for optimal arterial display.

Applications of Advanced Flow-Dependent Angiography

Inflow inversion-recovery MRA has been applied most commonly to assessment of the renal arteries, with a number of

centers reporting excellent sensitivity and good specificity for identification of hemodynamically significant renal artery stenosis compared against contrast enhanced MRA. A study in chronic kidney disease (CKD) patients where IFIR MRA was compared against digital subtraction angiography demonstrated high sensitivity and specificity. Spatial resolution and coverage limitations may render it less sensitive to identification of accessory renal arteries, of concern in potential renal donors. However, a potential advantage of IFIR renal MRA is in improved visualisation of the segmental renal arteries compared with contrast-enhanced MRA, where parenchymal enhancement may impair visualization of the intrarenal arteries. It offers a commercially available alternative to contrast-enhanced MRA or CTA in patients with

moderate to severe renal impairment. The technique has also been applied to assessment of stenosis in transplant renal arteries with perfect sensitivity and high specificity.

IFIR MRA has also been described for hepatic vascular assessment although it is not currently in widespread clinical use. The technique enables hepatic artery assessment, potentially useful in treatment planning for liver transplant or percutaneous chemoembolization of hepatic malignancies. Similarly, portal venous assessment with IFIR is also possible, where both FSE and SSFP readouts have been explored. Better branch portal vein visualization has been reported with FSE readout, likely due to relatively lower signal of hepatic parenchyma leading to improved vessel contrast.

Similarly, the extracranial supra-aortic arteries can be imaged using IFIR MRA, due to relatively limited required craniocaudal coverage and fast arterial flow. Preliminary studies with both balanced SSFP and FSE readouts have been described, with FSE potentially less impacted by inhomogeneous magnetic field (B_0) that is problematic in this region. However, clinical studies evaluating accuracy of the technique for extracranial carotid artery imaging are lacking.

Given its dependence on flow, IFIR becomes less reliable in low flow states including where cardiac output is low, placing limitations on inflow during the inversion time. This can be combated by lengthening the selected inversion time, at the expense of signal recovery of background tissue. Imaging at 3.0 T, where there are longer T_1 tissue relaxation times, may therefore benefit arterial visualization at equivalent or longer inversion times to 1.5 T. For body applications, patients with unpredictable respiratory patterns are also challenging; this can prolong imaging times and result in poor respiratory motion compensation.

QISS is an accurate technique for evaluating the peripheral arteries (from the level of the renal arteries to the ankles) in patients with known or suspected peripheral arterial disease at 1.5 T and 3.0 T. Good accuracy with respect to contrast-enhanced MRA and digital subtraction angiography has been found, with the method demonstrating high sensitivity, specificity as well as positive and negative predictive values.

Flow-Independent Angiography

Overview and Physical Principles

Unlike other methods for nonenhanced MRA that require flowing blood to generate angiographic contrast, flow-independent methods derive angiographic contrast by exploiting the MRI properties of the blood pool. These MRI properties include its spin-lattice relaxation time

Table 21.1 MR relaxation constants leveraged by flow-independent MRA

Tissue	T_1 (ms)	T_2 (ms)	T_1/T_2
Blood	1200	100–200*	6.0–12.0
Muscle	900	50	18.0
Fat	250	60	4.2
Gray matter	950	100	9.5

Magnetic resonance relaxation time for hydrogen protons in various tissues at 1.5 Tesla

*Depends on oxygen saturation; lower and higher values are for venous and arterial blood, respectively

(T_1), spin-spin relaxation time (T_2), and proton spin-density. Because differences in spin-density between the blood pool and most tissues in the body are small, differences in T_1 and T_2 contribute most significantly to the contrast provided by flow-independent MRA techniques. Table 21.1 lists the T_1 and T_2 relaxation times for blood as well as for other tissues including skeletal muscle, fat, brain matter, and cerebrospinal fluid. Substantial differences in T_1 , T_2 , and the ratio of T_1/T_2 exist between the blood pool and other tissues. Flow-independent MRA methods leverage at least one of these properties to preferentially visualize arteries and veins. Some methods even use these properties to suppress the appearance of unwanted tissues such as muscle and fat.

Balanced Steady State Free Precession Imaging

Although early reports of flow-independent MRA used spin-echo and gradient-echo readouts [14, 15], balanced steady-state free precession (bSSFP) imaging is the prevailing modern method for performing flow-independent MRA [16]. This technique is also referred to as “True Fast Imaging with Steady-state Precession” (trueFISP), “Fast Imaging Employing State-state Acquisition” (FIESTA), or “balanced Fast Field Echoes” (bFFE). The pulse sequence details for bSSFP imaging are provided in Chap. 6. Tissues with large T_2/T_1 ratios, such as blood, fluids, and fat are enhanced in bSSFP images, while others having short T_2 s and long T_1 s (e.g. muscle) are suppressed. Due to the large T_2/T_1 ratio of arterial and venous blood, both arteries and veins are well depicted.

A strength of bSSFP imaging for flow-independent MRA is its fast, high SNR readout which enables efficient, high spatial resolution imaging of the vasculature. Compared with TOF MRA, flow-independent MRA using a bSSFP readout may provide better depiction of slow and static flow as well as small branch vessels. Limitations with respect to TOF MRA include greater sensitivity to B_0 inhomogeneity and the hyperintense appearance of fat.

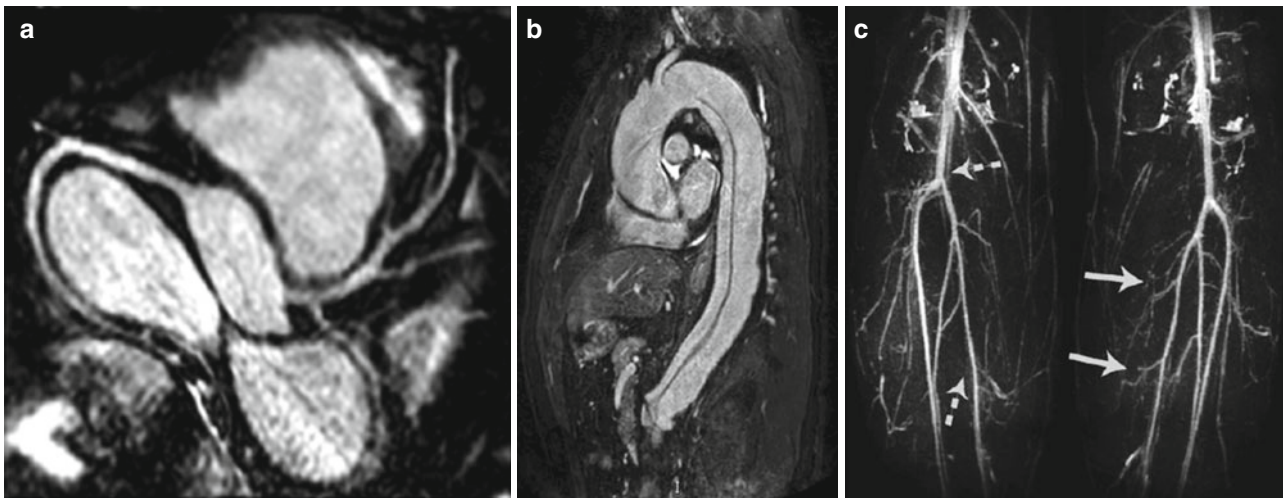


Fig. 21.12 Examples of nonenhanced flow-independent MRA. Coronary (a) and aortic (b) angiograms acquired with segmented, cardiac- and navigator-gated bSSFP sequences. T_2 preparation and chemically selective fat saturation were used to suppress the appearances of background and fat tissues (Figures reprinted from Henningsson et al. [25] and Amano et al. [26] with the permission of

John Wiley and Sons, respectively). (c) Flow-independent peripheral MR angiogram obtained using an inversion-recovery and T_2 -prepared multi-echo bSSFP sequence. Fat was suppressed using the “Iterative Decomposition of water and fat with Echo Asymmetry and Least-squares estimation” (IDEAL) algorithm (Reprinted from Cukur et al. [27] with permission from John Wiley and Sons)

Magnetization-Prepared Balanced Steady State Free Precession Imaging

A drawback of bSSFP imaging is that fat and fluids appear bright and often preclude evaluation of the vasculature with standard maximum intensity projection processing. The conspicuity of these non-vascular tissues can be suppressed with the use of segmented bSSFP imaging incorporating magnetization preparation modules. Magnetization preparations routinely applied with segmented bSSFP imaging for flow-independent MRA include chemically selective fat saturation and T_2 preparation, which suppress the appearance of fat and muscle, respectively.

Other strategies enabling bSSFP-based flow-independent MRA include the application of non-selective inversion-recovery for suppression of long T_1 fluids, the use of long inter-echo bSSFP spacings for separating arterial and venous spins based on oxygen saturation, and multi-echo Dixon methods for fat suppression [17]. The appearance of fat during bSSFP imaging may also be suppressed with the use of masking algorithms that leverage the phase difference between fat and water spins at compatible interecho spacings (≤ 4.6 ms at 1.5 T). Example flow-independent MR angiograms obtained with magnetization-prepared 3D bSSFP techniques are shown in Fig. 21.12.

Subtractive Methods Using Balanced Steady State Free Precession Imaging

Subtraction-based bSSFP techniques have also been proposed for flow-independent angiography. Compared to non-subtractive bSSFP acquisitions, the advantage of subtractive

bSSFP techniques is their ability to provide better if not complete suppression of unwanted signal from background tissue.

One subtractive technique for flow-independent MRA is “Signal Targeting Alternative Radiofrequency and Flow-Independent Relaxation Enhancement” (STARFIRE) [18]. Figure 21.13a, b shows two pulse sequence diagrams STARFIRE flow-independent MRA. The technique consists of an interleaved acquisition of two bSSFP readouts, with one readout preceded by a non-selective inversion RF pulse. With use of an inversion time (TI) of at least three times the T_1 of fat, subtraction of the two data sets suppresses the appearance of fat, while preserving signal from the long T_1 and T_2 blood pool. Muscle is suppressed primarily on the basis of its short T_2 . Typical timing parameters for STARFIRE at 1.5 T include a TI of between 0.9 and 1.2 s and a sequence repetition time (TR) between 2.0 and 3.0 s.

Figure 21.13c, d shows images acquired with the STARFIRE technique in the lower extremities. Complex subtraction of acquired data is typically preferred over subtraction of magnitude images since the former reduces partial volume artifacts, the appearance of off-resonance banding artifacts, and improves image quality when parallel imaging is used. Nonetheless, magnitude subtraction can be useful for suppressing the appearance of fluids.

Advantages, Limitations and Technical Considerations

The main strength of flow-independent MRA is its ability to depict vessels containing very slow or stationary blood that

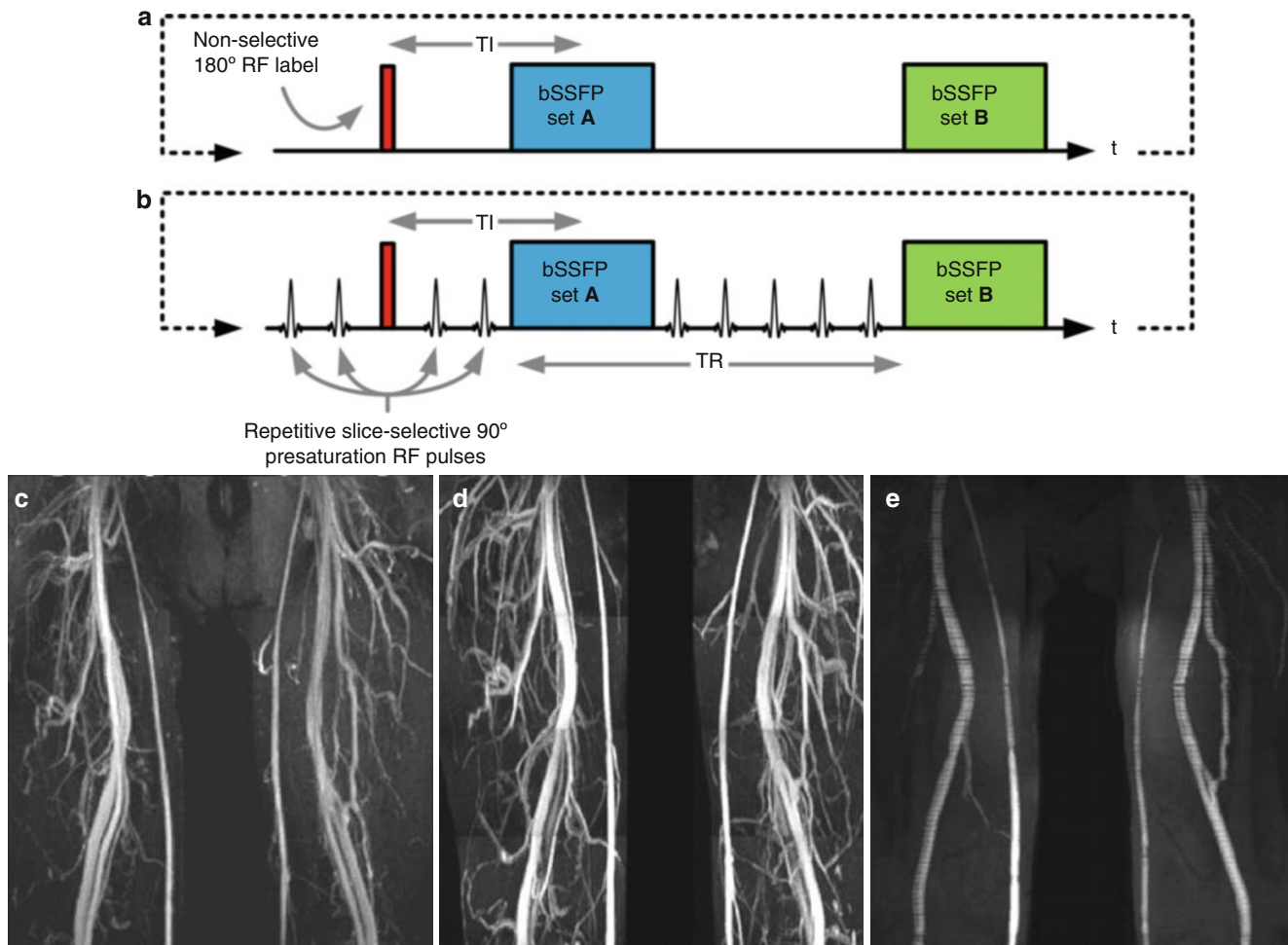


Fig. 21.13 STARFIRE flow-independent nonenhanced MRA. Pulse sequence diagrams for STARFIRE imaging depicting (a) both arteries and veins and (b) arteries or veins. Subtraction of image set A from B is performed (not shown). Repetitive tracking saturation pulses in (b) suppress the appearance of veins or arteries. (c) Coronal STARFIRE MRA of the thighs (using the sequence configuration shown in (a))

displays arteries and veins together. (d) Four slab axial STARFIRE with arterial saturation provides a venogram. (e) Corresponding venogram obtained with 2D TOF MRA with tracking arterial saturation lacks the detail of the STARFIRE venogram (Reprinted from Edelman and Koltzoglou [18] with permission from the Radiological Society of North America)

would otherwise be difficult to image with inflow or time-of-flight techniques. Flow-independent nonenhanced methods are also particularly useful for depicting vessels with complex morphology, such as the coronary arteries. A practical advantage of bSSFP imaging, the principal flow-independent method, is its widespread availability on modern clinical MRI systems.

A main drawback of flow-independent bSSFP-based MRA is its sensitivity to off-resonance which can result in image artifacts at tissue interfaces or near metallic implants. Other limitations include incomplete suppression of veins, inconsistent venous contrast that is dependent on both the main magnetic field strength and the oxygen saturation level, and suboptimal suppression of other background tissues such as edema and fluids. The use of inversion-recovery to suppress long- T_1 tissues often significantly prolongs the acquisition time and reduces arterial SNR. As with ASL techniques,

drawbacks of subtractive flow-independent methods include increased sensitivity to misregistration artifact and longer scan times due to the collection of two data sets.

Applications of Flow-Independent Angiography

The main application of flow-independent MRA is the nonenhanced evaluation of the coronary arteries using a cardiac-gated segmented, magnetization-prepared bSSFP sequence. Coronary multidetector CTA is more commonly used in the assessment of the coronary artery disease (CAD), due to speed of acquisition and higher spatial resolution that enables more accurate evaluation of distal coronary segments. However, coronary bSSFP MRA using both ECG and respiratory gating offers a viable

radiation-free alternative that is particularly useful in younger patients. For example, it is useful for evaluation of anomalous coronary artery anatomy and vasculitides including Kawasaki disease. It can also be used in the evaluation of CAD patients who have undergone coronary artery bypass grafting, due to the often larger caliber of the graft vessels, and combined with myocardial viability assessment in patients with suspected recurrent stenocclusive disease.

The technique can also be applied to evaluation of the thoracic aorta, with several centers describing improved aortic root quality compared with non-gated contrast enhanced thoracic MRA.

Flow independent angiography is also useful for depicting veins containing slow flow that are difficult to image using flow-dependent methods. These techniques can be used in the imaging of venous thrombosis.

Potential challenges for coronary imaging include cardiac arrhythmias and irregular respiratory patterns, which may lead to motion degradation and increase the overall acquisition time of the technique. Image acceleration techniques including two-dimensional parallel imaging have made breath-hold coronary MRA a possibility. Susceptibility artifact related to implanted metal such as sternotomy wires or mechanical valves may also preclude accurate assessment of adjacent coronary segments. For venous thrombosis, due to T_2/T_1 weighting of steady state free precession imaging, there is the possibility that thrombus with relatively short T_1 may not be appreciated, due to similar signal to adjacent blood.

Phase Contrast Angiography

Overview and Physical Principles

Unlike other nonenhanced MRA techniques that derive angiographic contrast from the magnitude of the MRI signal, phase contrast (PC) MRA derives angiographic contrast from the phase of the MRI signal. As explained in Chap. 16, magnetic field gradients impart a first order moment at the echo time and can impart a phase that is proportional to velocity of flowing blood. This phase information, when acquired along three orthogonal axes, can be used for nonenhanced MRA.

One methodology by which these gradient-induced flow-related phase shifts can generate a MR angiogram is shown in Fig. 21.14 [19, 20]. Flow-encoded data are first acquired along three orthogonal axes. The complex difference between these three sets of data and a non-flow encoded reference data set is computed, followed by a square root sum of squares reconstruction. The result yields a PC MR angiogram in which flowing blood is hyperintense and stationary background signal is suppressed. Suppression of random phase differences from areas of low MR signal can be achieved by multiplying the angiogram by the magnitude of the reference data set.

Advantages, Limitations and Technical Considerations

Advantages of PC MRA include excellent background suppression, reduced saturation of slow flow as compared with

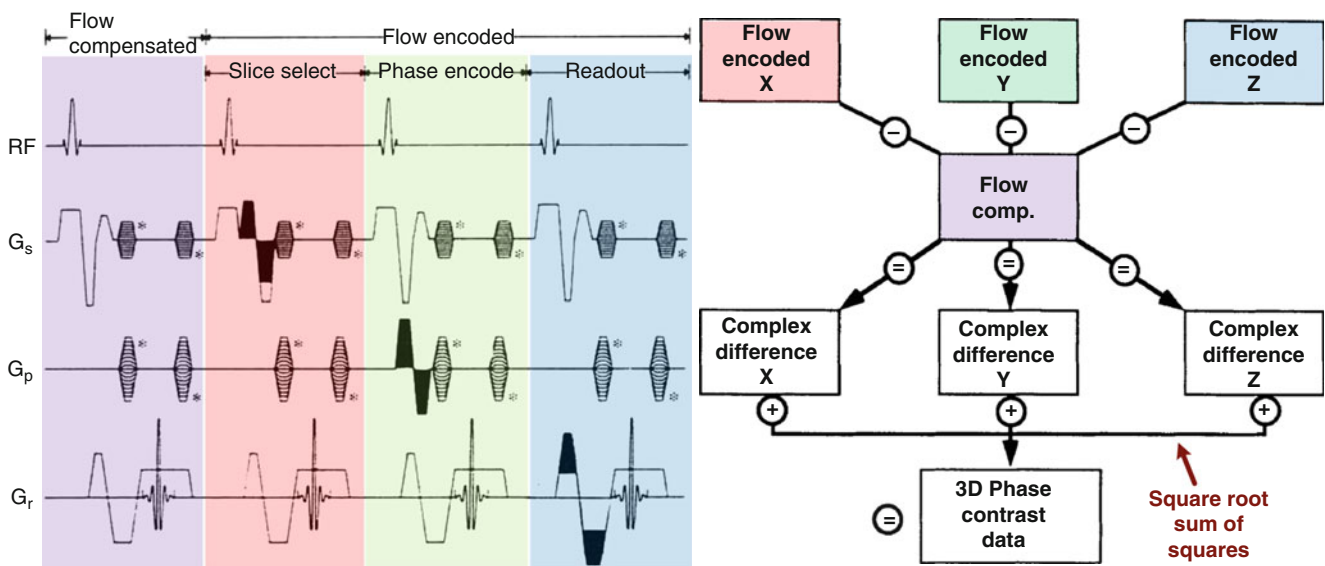


Fig. 21.14 Pulse sequence diagram (left) and reconstruction algorithm (right) for 3D phase contrast MRA. In the pulse sequence, a flow compensated gradient-echo line is acquired and followed by flow encoded lines in the slice, phase and readout directions. Flow encoding is accomplished by applying a bipolar gradients (shown in black) along

each gradient axis. During reconstruction, the complex difference of the flow encoded and reference data are computed, and these data are combined into a 3D phase contrast MR angiogram using a square root sum of squares algorithm (Reprinted from Hausmann et al. [20] with the permission from John Wiley and Sons)

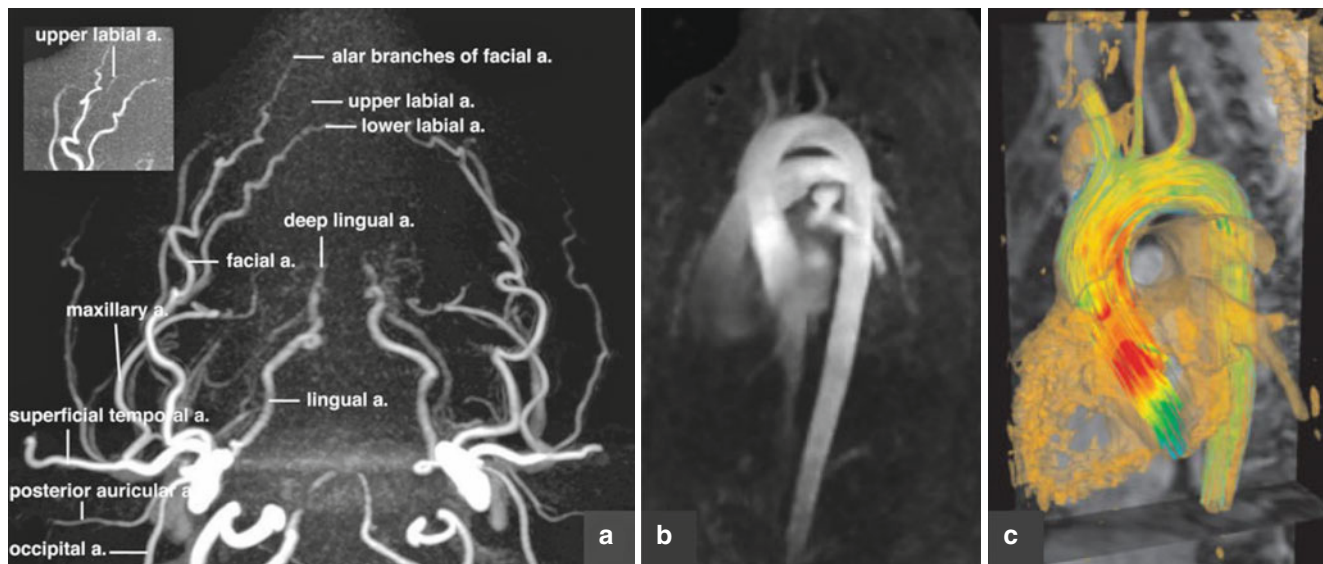


Fig. 21.15 Examples of PC MR angiography. (a) Axial MIP image shows the branches of the external carotid artery and the excellent background suppression obtainable with a 3D PC MRA sequence (Reprinted from Sumi et al. [28] with permission from John Wiley and Sons). (b) MR angiogram of the thoracic aorta acquired with a 4D PC MRA

sequence. (c) 3D blood flow visualization of the thoracic aorta with superimposed flow streamlines during systole provided by 4D PC MRA. Colors indicate the velocity of blood flow (Figures reprinted from Bock et al. [29] with permission from John Wiley and Sons)

TOF MRA (which uses larger excitation flip angles), and the ability to quantify arterial flow velocity in three dimensions. Compared to other nonenhanced MRA techniques, the main limitation of PC MRA is the long scan time due need to acquire two to four image sets (for one- to three-dimensional flow encoding, respectively). The prolonged scan time often renders the method sensitive to artifacts from patient motion. Parallel imaging or undersampled non-Cartesian trajectories can be used to reduce scan times.

An important consideration when using PC MRA is the need to select a velocity encoding sensitivity (VENC) that avoids phase aliasing while maximizing velocity to noise ratio. Proper selection of a suitable VENC can sometimes be difficult a priori because the optimal VENC can vary substantially between patients. Other limitations of PC MRA include imperfections due to eddy current effects, Maxwell (concomitant) gradient effects, and spatially-varying background phase offsets.

Applications of Phase Contrast Angiography

Examples of phase contrast MRA are shown in Fig. 21.15. In addition to standard 2D and 3D imaging of intracranial, carotid and vertebral arteries, it can demonstrate the direction of flow in the vertebral arteries and provide hemodynamic evaluation of carotid atherosclerosis. As the technique directly measures flow, it is less susceptible than TOF MRA to high signal artifact from tissues with short T_1 such as fresh thrombi which is important in evaluation of arterial dissection or intracerebral

arteriovenous malformations. The intravascular signal loss on 3D PC MRA at hemodynamically significant stenoses secondary to intravoxel phase dispersion from turbulent flow can also be used to estimate the hemodynamic significance of stenosis.

PC MRA can also be used to measure flow volumes, velocities, and allows for estimation of pressure gradients across stenoses in various pathologies, including congenital abnormalities such as pulmonary artery hypoplasia and aortic coarctation. Phase contrast MRA is also useful in aortic dissection to help characterize the false lumen, which normally shows slower flow than the true lumen; it may also demonstrate entry and exit sites between the true and false lumens. PC MRA of the aortic root and pulmonary trunk can also help evaluate intra and extracardiac shunts.

The emerging technique of four-dimensional PC imaging comprises three-dimensional spatial encoding, three-dimensional velocity encoding and time. Its advantage lies in providing additional hemodynamic information in areas such as evaluation of aortic flow in aortic valve disease and flow dynamics in intracranial aneurysms. It also allows assessment of complex parameters such as volumetric spatial-temporal velocity distribution, vorticity, and wall shear stress which may be useful for estimating risk in these conditions.

Conclusion

In conclusion, nonenhanced MR angiography can be performed using a large and diverse collection of established and emerging techniques. The clinical application largely drives the selection of the appropriate method for nonenhanced MRA, with several nonenhanced techniques

found to be accurate and dependable for the assessment of various vascular beds. With continued refinement of existing techniques, development of altogether new approaches and further clinical validation, nonenhanced MRA is expected to gain greater acceptance and play a larger role in the evaluation of vascular disease in clinical practice.

References

- Masaryk TJ, Modic MT, Ruggieri PM, Ross JS, Laub G, Lenz GW, Tkach JA, Haacke EM, Selman WR, Harik SI. Three-dimensional (volume) gradient-echo imaging of the carotid bifurcation: preliminary clinical experience. *Radiology*. 1989;171(3):801–6.
- Parker DL, Yuan C, Blatter DD. MR angiography by multiple thin slab 3D acquisition. *Magn Reson Med*. 1991;17(2):434–51.
- Wedeen VJ, Meuli RA, Edelman RR, Geller SC, Frank LR, Brady TJ, Rosen BR. Projective imaging of pulsatile flow with magnetic resonance. *Science*. 1985;230(4728):946–8.
- Dixon WT, Du LN, Faul DD, Gado M, Rossnick S. Projection angiograms of blood labeled by adiabatic fast passage. *Magn Reson Med*. 1986;3(3):454–62.
- Meuli RA, Wedeen VJ, Geller SC, Edelman RR, Frank LR, Brady TJ, Rosen BR. MR gated subtraction angiography: evaluation of lower extremities. *Radiology*. 1986;159(2):411–8.
- Edelman RR, Siewert B, Adamis M, Gaa J, Laub G, Wielopolski P. Signal targeting with alternating radiofrequency (STAR) sequences: application to MR angiography. *Magn Reson Med*. 1994;31(2):233–8.
- Kim SG. Quantification of relative cerebral blood flow change by flow-sensitive alternating inversion recovery (FAIR) technique: application to functional mapping. *Magn Reson Med*. 1995;34(3):293–301.
- Dai W, Garcia D, de Bazelaire C, Alsop DC. Continuous flow-driven inversion for arterial spin labeling using pulsed radio frequency and gradient fields. *Magn Reson Med*. 2008;60(6):1488–97.
- Miyazaki M, Takai H, Sugiura S, Wada H, Kuwahara R, Urata J. Peripheral MR angiography: separation of arteries from veins with flow-spoiled gradient pulses in electrocardiography-triggered three-dimensional half-Fourier fast spin-echo imaging. *Radiology*. 2003;227(3):890–6.
- Korosec FR, Grist TM, Polzin JA, Weber DM, Mistretta CA. MR angiography using velocity-selective preparation pulses and segmented gradient-echo acquisition. *Magn Reson Med*. 1993;30(6):704–14.
- Wytenbach R, Braghetti A, Wyss M, Alerci M, Briner L, Santini P, Cozzi L, Di Valentino M, Katoh M, Marone C, Vock P, Gallino A. Renal artery assessment with nonenhanced steady-state free precession versus contrast-enhanced MR angiography. *Radiology*. 2007;245(1):186–95.
- Edelman RR, Sheehan JJ, Dunkle E, Schindler N, Carr J, Koktzoglou I. Quiescent-interval single-shot unenhanced magnetic resonance angiography of peripheral vascular disease: technical considerations and clinical feasibility. *Magn Reson Med*. 2010;63(4):951–8.
- Shin T, Worters PW, Hu BS, Nishimura DG. Non-contrast-enhanced renal and abdominal MR angiography using velocity-selective inversion preparation. *Magn Reson Med*. 2013;69(5):1268–75.
- Wright GA, Nishimura DG, Macovski A. Flow-independent magnetic resonance projection angiography. *Magn Reson Med*. 1991;17(1):126–40.
- Brittain JH, Olcott EW, Szuba A, Gold GE, Wright GA, Irrazaval P, Nishimura DG. Three-dimensional flow-independent peripheral angiography. *Magn Reson Med*. 1997;38(3):343–54.
- Fuchs F, Laub G, Othomo K. TrueFISP – technical considerations and cardiovascular applications. *Eur J Radiol*. 2003;46(1):28–32.
- Cukur T, Lee JH, Bangerter NK, Hargreaves BA, Nishimura DG. Non-contrast-enhanced flow-independent peripheral MR angiography with balanced SSFP. *Magn Reson Med*. 2009;61(6):1533–9.
- Edelman RR, Koktzoglou I. Unenhanced flow-independent MR venography by using signal targeting alternative radiofrequency and flow-independent relaxation enhancement. *Radiology*. 2009;250(1):236–45.
- Dumoulin CL, Souza SP, Walker MF, Wagle W. Three-dimensional phase contrast angiography. *Magn Reson Med*. 1989;9(1):139–49.
- Hausmann R, Lewin JS, Laub G. Phase-contrast MR angiography with reduced acquisition time: new concepts in sequence design. *J Magn Reson Imaging*. 1991;1(4):415–22.
- Thomas SD, Al-Kwif O, Emery DJ, Wilman AH. Application of magnetization transfer at 3.0 T in three-dimensional time-of-flight magnetic resonance angiography of the intracranial arteries. *J Magn Reson Imaging*. 2002;15(4):479–83.
- Lim RP, Hecht EM, Xu J, Babb JS, Oesingmann N, Wong S, Muhs BE, Gagne P, Lee VS. 3D nongadolinium-enhanced ECG-gated MRA of the distal lower extremities: preliminary clinical experience. *J Magn Reson Imaging*. 2008;28(1):181–9.
- Fan Z, Sheehan J, Bi X, Liu X, Carr J, Li D. 3D noncontrast MR angiography of the distal lower extremities using flow-sensitive dephasing (FSD)-prepared balanced SSFP. *Magn Reson Med*. 2009;62(6):1523–32.
- Edelman RR, Giri S, Dunkle E, Galizia M, Amin P, Koktzoglou I. Quiescent-inflow single-shot magnetic resonance angiography using a highly undersampled radial k-space trajectory. *Magn Reson Med*. 2013;70(6):1662–8.
- Henningson M, Smink J, Razavi R, Botnar RM. Prospective respiratory motion correction for coronary MR angiography using a 2D image navigator. *Magn Reson Med*. 2013;69(2):486–94.
- Amano Y, Takahama K, Kumita S. Non-contrast-enhanced MR angiography of the thoracic aorta using cardiac and navigator-gated magnetization-prepared three-dimensional steady-state free precession. *J Magn Reson Imaging*. 2008;27(3):504–9.
- Cukur T, Shimakawa A, Yu H, Hargreaves BA, Hu BS, Nishimura DG, Brittain JH. Magnetization-prepared IDEAL bSSFP: a flow-independent technique for noncontrast-enhanced peripheral angiography. *J Magn Reson Imaging*. 2011;33(4):931–9.
- Sumi T, Sumi M, Van Cauteren M, Kimura Y, Nakamura T. Parallel imaging technique for the external carotid artery and its branches: comparison of balanced turbo field echo, phase contrast, and time-of-flight sequences. *J Magn Reson Imaging*. 2007;25(5):1028–34.
- Bock J, Frydrychowicz A, Stalder AF, Bley TA, Burkhardt H, Hennig J, Markl M. 4D phase contrast MRI at 3 T: effect of standard and blood-pool contrast agents on SNR, PC-MRA, and blood flow visualization. *Magn Reson Med*. 2010;63(2):330–8.

Florian von Knobelsdorff-Brenkenhoff,
Matthias Alexander Dieringer,
and Jeanette Schulz-Menger

Abstract

There are many research activities to improve and extend cardiovascular MRI techniques. This chapter introduces a selection of developments that has the potential to enrich the clinical application in the future. Under the first topic of myocardial tissue characterization, parametric mapping is described, which comprises the pixelwise quantification of myocardial T_1 , T_2 and T_2^* relaxation times. Furthermore, cardiac diffusion magnetic resonance imaging that provides non-invasive visualization of tissue microstructure is described, as well as techniques to analyze fat within the myocardium are elucidated. The second topic deals with the analysis of myocardial mechanics and introduces tissue phase mapping, feature tracking, DENSE and SENC that provide insights into the three-dimensional motion of the left ventricle. The third topic focuses on blood flow assessment: 4D-flow is described, which enables the visualization and quantification of flow patterns, as well as novel techniques for real-time flow quantification. The last part provides insight into achievements and outlooks of cardiovascular MRI at ultrahigh magnetic field strength.

Keywords

T_1 -mapping • T_2 -mapping • T_2^* -mapping • Tissue phase mapping • Feature tracking • Diffusion imaging • 4D-flow • Ultrahigh field

Introduction

Cardiovascular Magnetic Resonance (CMR) is well accepted in clinical routine, integrated in clinical guidelines and is often crucial for decision making.

Whereas the current standards allow for robust daily clinical work, the potential of CMR may not be fully exploited. CMR has – based on its native tissue contrast – the capability to differentiate pathologies with a high spatial and/or temporal

resolution. Nevertheless, the need to decide between spatial or temporal resolution is hampering some applications. Novel accelerated imaging techniques are designed to overcome these limitations as described in the chapter on fast imaging.

From the cardiologist's point of view, the main advantage of CMR is the capability to detect myocardial injury already in subclinical disease stages, to differentiate between causes beyond the scope of other imaging modalities, and to analyze the heart in its relation to other anatomical structures, such as vessels. Hence, the cardiovascular system can be analyzed comprehensively within one scan. In this perspective, the new developments are playing a crucial role. The following chapter focuses on techniques, which are expected to support the clinical applications. Within each section the current stages of advanced CMR techniques are described, but we encourage the reader to enhance and renew the knowledge in this fast developing field at least yearly. Particularly, parametric

F. von Knobelsdorff-Brenkenhoff, MD, PhD
M.A. Dieringer, PhD • J. Schulz-Menger, MD (✉)
Department of Cardiology and Nephrology, Cardiovascular MRI – Experimental and Clinical Research Center, a joint cooperation between Charité Medical Faculty and Max-Delbrueck Center for Molecular Medicine, and HELIOS Clinics Berlin-Buch, Lindenberger Weg 80, 13125 Berlin, Germany
e-mail: jeanette.schulz-menger@charite.de

mapping techniques are a major advance and it is expected that they will supplement or even replace visual assessments as well as semi-quantitative methods by providing a standardized and objective quantification. Current advanced CMR techniques have the potential to impact the field based on the assessment of myocardial mechanics including detection of fiber structure, as it may give new insights into preclinical disease. The balance and the interaction between clinical needs and technical developments are crucial for further proving the clinical applicability of emerging technologies.

Myocardial Tissue Characterization

Parametric Mapping

CMR offers various techniques to assess the myocardial tissue by T_2 - and T_1 -weighted images with and without contrast enhancement. Most of these evaluations are qualitative or semi-quantitative, require reference tissue, and become obvious only if several adjacent pixels are affected creating a focal abnormality, while diffuse changes are often missed. Parametric mapping offers the chance to quantify the T_1 -, T_2 - or T_2^* -relaxation time for each image pixel. This could lead to a more objective interpretation based on predefined thresholds and enables the detection of diffuse tissue changes.

T_2^* -mapping has already been established in the clinical arena to assess myocardial iron load in patients with thalassemia. Iron as a paramagnetic substance increases the local magnetic field inhomogeneity, which leads to a shortening of the T_2^* relaxation time. T_2^* -mapping requires a set of spoiled gradient multi-echo images of a single mid-left ventricular short axis slice that can be acquired during one breath-hold. Arranging the signal intensity of each image pixel over the corresponding echo time allows for extraction of T_2^* by an exponential fit, which yields a T_2^* -map. The quantification of the T_2^* time in a septal region of interest has been shown to impact therapy and prognosis [1, 2].

T_1 -mapping is currently evolving rapidly. The principle is based on the acquisition of a set of single-shot images with different inversion times using an inversion-recovery (IR) sequence. From the signal intensity of each image plotted against the corresponding inversion time, T_1 can be derived for each pixel, which is then summarized in one T_1 -map [3]. This can be done both with native myocardium, and after contrast enhancement. Several acquisition schemes are available, each with specific benefits and drawbacks such as length of breath-hold, precision, accuracy and reproducibility [3–7]. Myocardial T_1 -relaxation time at 1.5 T is about 1,000 ms/500 ms (native/contrast-enhanced) [4, 8] and at 3 T about 1,150 ms/400 ms [9], but differences between sequences, scanners, contrast agent, contrast dosing and timing have to be considered. Native T_1 relaxation times seem to

increase in myocardium with acute inflammation or acute infarction as well as amyloid deposition, while they decrease in lipid storage like Fabry disease and in iron overload. Contrast-enhanced T_1 relaxation times are lower in areas with fibrosis and necrosis [8, 10–12]. Based on T_1 relaxation times of the myocardium and of blood obtained pre- and post-contrast and with consideration of the hematocrit determined from a blood sample, the extracellular volume fraction (ECV) can be calculated [13]. ECV in normal hearts is about 25 % (range 20–30 %) [14], whereas it is elevated for instance in amyloid, myocardial infarction, hypertrophic cardiomyopathy and aortic stenosis [15]. Compared to conventional late enhancement imaging, T_1 -mapping promises to detect diffuse myocardial abnormalities, as no reference myocardium is needed. Furthermore, the quantitative approach should reduce observer dependency and facilitate follow-up assessment. However, the individual variability and the narrow threshold between diseased and healthy myocardium in some diseases has to be considered [9] (Fig. 22.1).

T_2 -mapping is based on the acquisition of a set of single-shot images with different echo times or a set of images with different T_2 preparation times. The arrangement of the signal intensities of each image pixel over the different echo times or preparation times again facilitates the pixelwise quantification of T_2 from an exponential fit, which is then summarized in one T_2 -map [16]. Mean myocardial T_2 -relaxation time at 1.5 T is about 55 ms [17] and at 3 T about 45 ms [9], but differences between sequences and scanners have to be considered. In contrast to T_1 , T_2 theoretically does not change over field strengths, however stronger magnetic susceptibilities at higher field strengths lead to an increased signal loss over time by diffusion effects. T_2 relaxation times have been observed to increase in acutely injured and inflammatory myocardium like in acute myocardial infarction, myocarditis and Takotsubo cardiomyopathy [18, 19]. Thereby, T_2 relaxation times are about 12 ms longer in the involved myocardium compared to remote segments due to the increased free water content (Fig. 22.1).

As an outlook, the term “magnetic resonance fingerprinting” has recently been introduced to measure various tissue parameters of the brain within one MR acquisition [20]. If this concept can be translated to the myocardium, it has the potential to complement parametric mapping of the myocardium. This technique promises to also measure peripheral parameters, such as magnet field and transmission field non-uniformities, which can be pronounced at higher magnetic field strengths.

Cardiac Diffusion MRI

The assessment and visualization of tissue microstructure has moved into the focus of magnetic resonance research during the past years. Diffusion MRI provides non-invasive

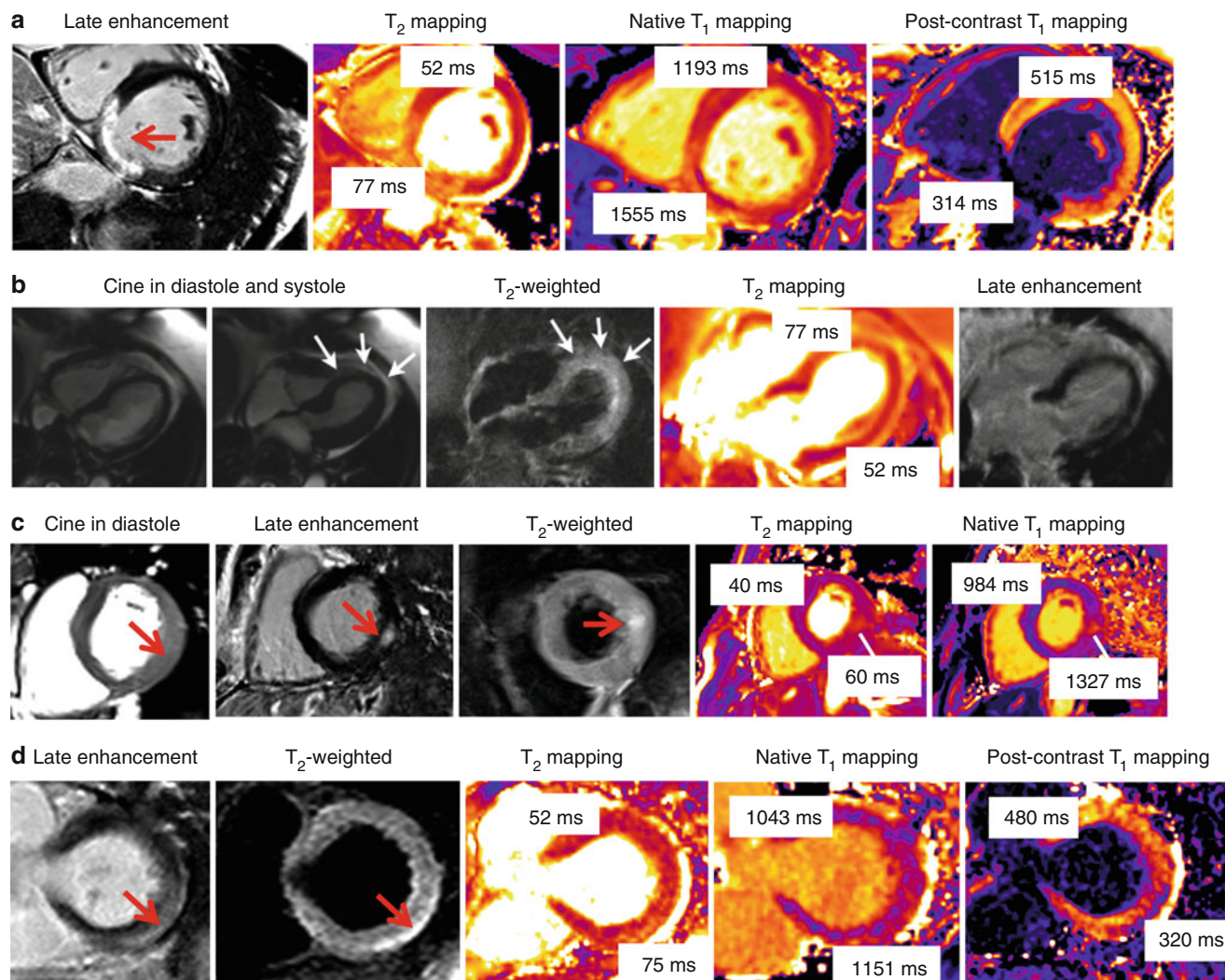


Fig. 22.1 Examples of parametric mapping in various diseases. **(a)** Acute myocardial infarction imaged at 3 T: Late enhancement with transmural myocardial infarction. T_2 - and native T_1 mapping with elevated T_2 and T_1 relaxation times in the infarcted area, whereas postcontrast T_1 relaxation time is reduced there. **(b)** Takotsubo cardiomyopathy obtained at 1.5 T: Cine imaging shows apical ballooning. In the apex, T_2 -weighted imaging shows increased signal intensity, and on T_2 mapping a regional elevation of T_2 relaxation times, while there is no corresponding necrosis in the late enhancement images. **(c)** Anderson Fabry Disease (3 T): Cine imaging shows inferolateral hypertrophy. Late enhancement detects intramural signal increase. T_2 -weighted

imaging defines myocardial edema there, also represented by the elevated T_2 -relaxation time on T_2 mapping. On native T_1 mapping, T_1 relaxation time in the myocardium (excluding the late enhancement region) is significantly reduced compared to normal (984 ms vs. 1,157 ms [9]), which is typical for Fabry disease [11]. In the area of late enhancement, native T_1 relaxation time is elevated. **(d)** Myocarditis (1.5 T): Late enhancement imaging shows the typical subepicardial inferolateral signal increase. On T_2 -weighted imaging, regional edema is detectable. T_2 - and native T_1 -mapping show elevated T_2 and T_1 relaxation times there, while postcontrast T_1 relaxation time is reduced

means to extract structural tissue information and can be used to depict tissue fiber architecture [21, 22]. This technique uses strong, hardware demanding motion encoding magnetic field gradients. Molecular motion along these gradients leads to a pronounced dephasing of the magnetization and thus a loss of signal. Diffusion MRI exploits the fact that water molecules predominantly move along tissue fibers and nerves, which allows their visualization. Diffusion tensor imaging (DTI [23]), q-ball imaging [24], and diffusion spectrum imaging (DSI [25]) are techniques based on diffusion

weighted MRI that aim at the characterization of tissue by assessing fractional tissue diffusion anisotropy, mean diffusivity, and by determining the angular alignment of the tissue fibers. Conventionally, at least two different diffusion weightings are required together with a set of different diffusion directions to provide angular resolution.

MR tractography is the visualization of the tissue fibers in a tractogram. This technique uses three-dimensional modeling of data collected by diffusion MRI and is already well established for neural fiber tracking in the brain. Histological

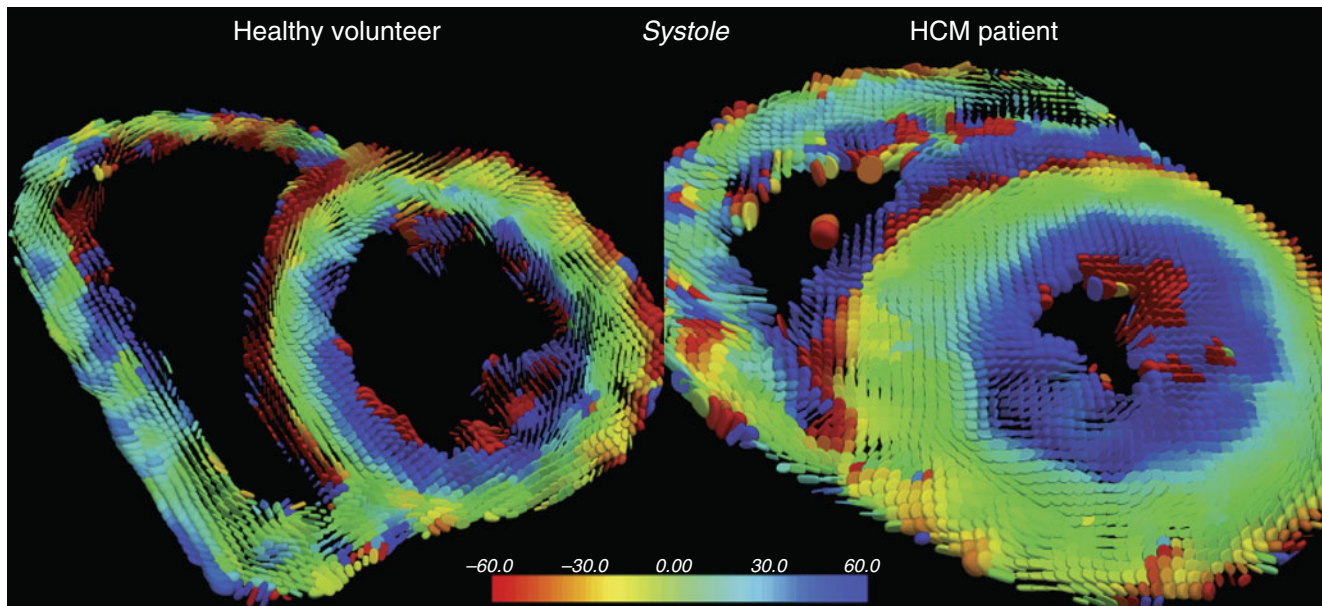


Fig. 22.2 In vivo cardiac diffusion tensor imaging of a patient with hypertrophic cardiomyopathy and a healthy volunteer. Superquadric glyph maps color coded helix angle (Image courtesy of the

Cardiovascular Biomedical Research Unit at the Royal Brompton Hospital, Imperial College of London, UK)

studies have shown that myofiber tracts at the endocardium form a right handed helical structure (positive angle), mid-myocardial fibers are circumferential (zero angle), and epicardial myofibers show a left-handed helical structure (negative angle) [26, 27]. These fiber tracts form laminar sheets that allow the heart muscle to contract. Figure 22.2 shows the fiber architecture of the left ventricle of a human adult heart ex-vivo [28]. Initial in-vivo results have already been presented in early studies using data retrieved from two-dimensional acquisitions [29]. The quantification of microscopic molecular diffusion in-vivo by diffusion MRI in the heart is however challenged by its superposition of cardiac and respiratory motion as well as by signal-to-noise constraints. With the improvement in MR hardware and imaging techniques, human whole-heart in-vivo diffusion quantification and tractography are on their way [30].

Cardiac diffusion MRI techniques are promising for the assessment of cardiac diseases that exhibit structural damage and remodeling of the myofibers, including myocardial infarction and hypertrophic cardiomyopathy. There is evidence that the heart muscle structure on a cellular level is linked to whole-organ functionality [31, 32] and provides essential biological information.

Myocardial Fat Detection

Detection of myocardial fat was one of the first applications in myocardial tissue differentiation applying spin echo sequences with and without fat suppression. It is a basic tool in intra- and

para-cardiac mass assessment by differentiation fat and water. The simplest example is the distinction of lipoma and cysts. Besides basic applications, clinicians expect significant diagnostic advances based on the detection of fatty infiltration in the right ventricle, e.g. in arrhythmogenic right ventricular cardiomyopathy (ARVC). This disease has a certain risk profile especially in young patients and athletes; so far an accurate noninvasive differentiation is lacking. But, most cardiac injuries including ARVC have different compounds including but not limited to fat. In ARVC, fibro-fatty infiltration is a key finding seen in autopsy and is considered crucial for diagnosis [33]. However, conventional CMR-techniques only allow fat or fibrosis detection by applying non-contrast-enhanced or contrast-enhanced techniques. Diagnosis is challenged by the fact that both pathologies appear bright in widely used late gadolinium enhancement (LGE) techniques.

Recently published techniques offer the opportunity to overcome this limitation. Kellman et al. described a multi-echo dixon fat and water separation method for cardiac application [34], which were discussed in detail recently [35]. Nezafat et al. presented a validation from phantom experiments to initial patient studies applying fat-water separating techniques [36].

First clinical applications have shown promising results. Several groups have described the presence of LGE in dilated cardiomyopathy as a prognostic marker related to clinical outcomes. Lu et al. were able to detect fat deposition within scar tissue and showed a relation to a worse remodeling of the left ventricle in this cohort. Patients with fat deposition showed higher ventricular volumes and a larger scar size [37]. The

described sequence was also applied in patients with different risks for atrial fibrillation following the ARIC risk score. The ARIC risk score was developed in a trial evaluating the **Atherosclerosis Risk in Communities**. Atrial fibrillation is a common phenomenon in the aging society and the different therapeutic options are not well stratified and are suffering from different challenges. One missing piece is the non-invasive characterization of the atrial wall, as the atrial wall can also consist of fat and/or fibrosis compounds. Tereshchenko et al. have shown that the fatty substrate in the atrial walls including the septal wall has an association with the ARIC risk score [38].

Besides the dedicated technique, the interest in fat detection is also reflected by a recently published postprocessing algorithm, which is based on standard cardiac CINE imaging. The bright fat-signal in the pre-contrast cine does have certain clinical value, but does not allow for the differentiation of fat and fibrosis [39].

Fatty alterations of the myocardial tissue are not only known in cardiomyopathies, but also in coronary artery disease mainly in chronic myocardial infarction, and in valvular disease. That knowledge is based on basic work in pathology, whereas experiences in noninvasive detection by CMR are limited. The fast and reliable detection and differentiation of fat and fibrosis is expected to be a major step to enhanced risk stratification.

It should be mentioned that cardiac spectroscopy to quantify myocardial triglycerides (MTG) by magnetic resonance proton spectroscopy (MRS) seems to open a new area in risk stratification of the healthy population. Conservative risk factors for coronary artery disease are well-known and widely established, but are often not sufficient. Several groups already published MTG-MRS results at 1.5 and 3 T. As expected, MRS has a higher SNR at 3 T, potentially leading to higher accuracy [40]. Several technical challenges affect the application of MTG-MRS including navigator-gating [41]. Despite the fact that the MTG-distribution is inhomogeneous throughout the myocardium as shown *ex vivo* [42], several groups have shown the impact of different conditions on diagnosis. MTG is not only a predictor for the development of diastolic dysfunction in different known risk diseases like diabetes mellitus [43], but also in the healthy aging population as shown for men [44]. In obese female a correlation to the cardiorespiratory fitness was shown [45] and the influence of moderate dietary induced weight loss was detectable [46]. Nevertheless, MTG-MRS needs significant technical improvement in terms of reliability and reproducibility for application in daily clinical routine.

Myocardial Mechanics Analysis

Almost all cardiac diseases have an impact on cardiac function. Assessing systolic myocardial function is mainly based on quantifying ventricular ejection fraction and visually

determining the presence of wall motion abnormalities. These parameters are often abnormal only late in the course of the disease and they tend to overlook regional abnormalities. Diastolic dysfunction accounts for a high percentage of patients with heart failure, but its assessment is a challenge. Therefore, attempts are being made to evaluate systolic and diastolic motion of the myocardium in detail using various new approaches. These efforts include myocardial tagging [47, 48], phase-contrast velocity encoding [49], displacement encoding (DENSE [50]), strain encoding (SENC [51]), and a combinations of these techniques.

Tissue Phase Mapping

Tissue phase mapping measures the velocity of the myocardial motion using time-resolved three-directional phase contrast imaging. Longitudinal, circumferential and radial velocities can be obtained [52]. Image acquisition is mainly done with respiratory navigator and ECG-gating, with a temporal resolution as high as possible. Postprocessing requires segmentation of myocardial segments, finally enabling the calculation of peak systolic and diastolic velocities, time-to-peak periods, as well as composite parameters like myocardial twist. Differences between men and women, old and young, as well as normotensive and hypertensive patients have been reported [53, 54].

Feature Tracking

Feature tracking is comparable to speckle tracking used in echocardiography. Specific software loads conventional steady state free precession cine images to detect features, such as the apparent cavity boundary or tissue patterns related to the endocardial contour. The software tracks these features from image to image and thus quantifies myocardial deformation over the cardiac cycle in radial, longitudinal and circumferential direction. Derived parameters are strain, displacement, velocity and twist that can be determined globally or on a segmental level [55]. While the post-processing is fast and easy to use, concerns have been raised regarding inter-study reproducibility of some parameters [56]. Hence, further studies are needed to finally demonstrate the value of this tool.

DENSE and SENC

Another advanced technique for cardiac wall motion assessment is *Displacement Encoding via Stimulated Echoes* (DENSE), which directly encodes the displacement of the myocardium into the pixel phase. DENSE provides black-blood T_1 -weighted images and allows the reconstruction of displacement vector maps. These vector maps can be used to calculate

cardiac strain in pixel resolution. Displacement can be assessed for any arbitrary direction, e.g. two in-plane and one through-plane direction to assess three-dimensional myocardial displacement, but only one at a time. Fast imaging techniques allow multiple directions in one breath-hold, while spatial resolution is only limited by voxel size. Signal loss due to tissue perfusion and intra-voxel dephasing however limits the encoding duration. Therefore the encoding duration has to be adapted to the encoding strength to ensure that these detrimental effects are not dominant. More advanced versions of this technique include strain mapping throughout the whole cardiac cycle (cine DENSE [57]), which offers tissue tracking with a high spatio-temporal resolution.

Strain encoded MR imaging (SENC) encodes myocardial longitudinal strain from two cardiac short axis acquisition. This technique is based on the MR tagging principle, but uses tag lines parallel to the imaging plane. Evaluation of spectral peaks in the frequency domain enables calculation of the myocardial strain for the desired cardiac phase.

Blood Flow Assessment

4D Flow

Blood flow measurements based on two-dimensional phase contrast acquisitions are established tools in CMR, for instance to assess valvular heart disease or shunts. The 4D-flow technique is a further development and comprises a time-resolved

three-directional phase contrast measurement [58]. Image acquisition is typically done with a navigator correcting for respiratory motion, and ECG-gating. Contrast agent and higher field strength improve the image quality. Image data can be post-processed to visualize blood flow direction and patterns. Vortex as well as helix formation can be evaluated, and complex blood transfer for instance in congenital heart disease can be visualized [59]. Furthermore, quantitative information can be extracted, such as flow velocities, volumes, wall shear stress or pulse wave velocity. Most experience has been collected with the assessment of the thoracic aorta [60, 61]. For example, patients with bicuspid aortic valve show marked differences in blood flow pattern and distribution of peak systolic wall shear stress in the ascending aorta compared to healthy controls, which may contribute to aneurysm formation [62]. Additionally, intracardiac flow and non-cardiac vessel regions have also been explored [63]. Thus, 4D flow provides a new dimension of hemodynamic information that has not been accessible until now and has a great potential to help us better understand cardiovascular diseases (Fig. 22.3).

Real-Time Flow

Blood flow quantification plays an important role in many heart diseases including valvular disorders and cardiac shunts. Unlike Doppler-Echocardiography, phase contrast (PC) MRI can assess blood flow from any direction and independently from the patients' anatomy. Similar to functional

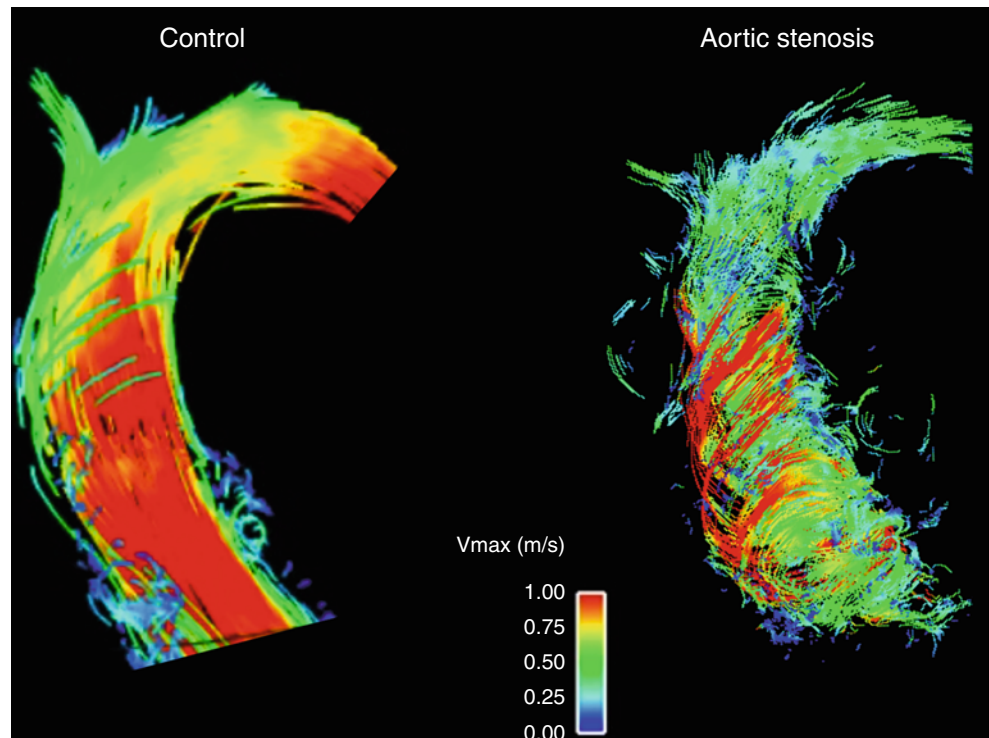


Fig. 22.3 4D-flow measurement of the ascending aorta. Compared to the healthy control (*left*), the patient with severe aortic stenosis showed pronounced vortex and helix formation of the blood flow

cardiac cine imaging, conventional PC-MRI collects segmented data over several heartbeats, which requires a regular heart rhythm. Fast MR sequence concepts together with accelerated data acquisition schemes were introduced that enable flow quantification in real-time without the need for splitting the data into segments [64, 65].

These concepts are promising for the quantification of blood flow in arrhythmic or uncooperative patients, as the data originates from the individual heartbeats rather than being averaged over several heartbeats. Furthermore, the real-time concept allows for the assessment of intra-individual changes in blood flow. Early techniques were challenged by a limited spatial and temporal resolution. As data acquisition acceleration techniques and scanner hardware improve, especially RF receiver coils and magnetic field gradients, faster data acquisition allows for increased spatio-temporal resolution [66].

Ultrahigh Magnetic Field Strength

CMR at 3 Tesla is now routinely performed in clinical settings. CMR at 7 T has several challenges and requires dedicated coil development, sequences development and understanding the potential safety issues.

Higher magnetic field strengths come along with an intrinsic signal-to-noise gain, which is proportional to the strength of the static magnetic field. The key driving force to strive for higher magnetic fields is this inherent advantage. The increased signal-to-noise ratio may be exploited for better spatial and temporal resolution. In human brain, histology-like images are being acquired and new techniques are about to extend the current knowledge in different disorders [67]. Also orphan diseases are likely to experience a more in depth understanding [68].

As the field strength increases, also the Larmor frequency increases and so the wavelength of the radio frequency pulses used for MRI shorten. At 7 T, the RF wavelength in cardiac tissue is approx. 13 cm (compared to approx. 54 cm at 1.5 T), which is already in the range of the human heart size. The resulting wave length effects evoke interferences causing local amplification or weakening of the transmit RF field, which finally result in heterogeneous flip angle distributions and thus heterogeneous signal intensities that can markedly deteriorate image quality at ultra-high fields.

Another challenge for cardiac imaging at ultra-high magnetic fields is the increased energy deposition in tissue, which can lead to local tissue heating. Traditional RF transmit body coils used at clinical magnetic field strengths are facing limitations at higher fields. Rather, local multi-channel transmit RF coil concepts with higher transmission efficiency are pursued that are less affected by this limitation. Additionally, multi-channel coils enable RF-shimming, a procedure to improve homogeneity of the RF transmit field by modulating RF pulse amplitudes and phases for each channel.

To overcome these problems for cardiac ultrahigh-field MRI, RF coils tailored for cardiac imaging are needed. Various RF coil designs with initial experiences have been presented by numerous groups [69, 70]. Regarding cardiac morphology and function assessment, results at 7 Tesla using spoiled gradient echo sequences are not only comparable to the 1.5 T gold standard that uses balanced steady-state free precession sequences, but also allows higher spatial resolution while maintaining diagnostic image quality.

Cardiac triggering using conventional ECG is difficult at higher field strengths due to the magneto-hydrodynamic effect. Alternative gating approaches like acoustic triggering helps to overcome this and enable robust cine imaging [71].

Despite all the expected problems first cardiac images were published in 2009 [72]. In 2010, von Knobelsdorff et al. published the first larger group of volunteers showing that cardiac chamber quantification of the left ventricle is reliable and applicable using very thin slices [73] (Fig. 22.4). Similar results were published by Suttie et al. in 2012 [74]. One would expect that the right ventricular imaging could also benefit from high resolution to characterize its thin free wall. Initial results of RV imaging at 7 T were recently published by our group [75].

However, these “bread and butter” applications should only be considered the first step. The exciting promise is the step towards myocardial tissue characterization. Quantification of the myocardial deoxygenation was already tested at 1.5 Tesla, but the application at 7 Tesla seems to detect an oxygenation gradient within the myocardium [76, 77]. Myocardial spectroscopy is one of the interesting applications in magnetic resonance, as it allows for the understanding of metabolic variations. Rodgers et al. were the first to apply phosphor-MRS in the heart. [78] Fat imaging has been performed at 7 T using a 16-channel coil [79]. Another exciting recent application is the non-contrast MRA in the lower extremities showing the superiority of 7 Tesla in this first study [80].

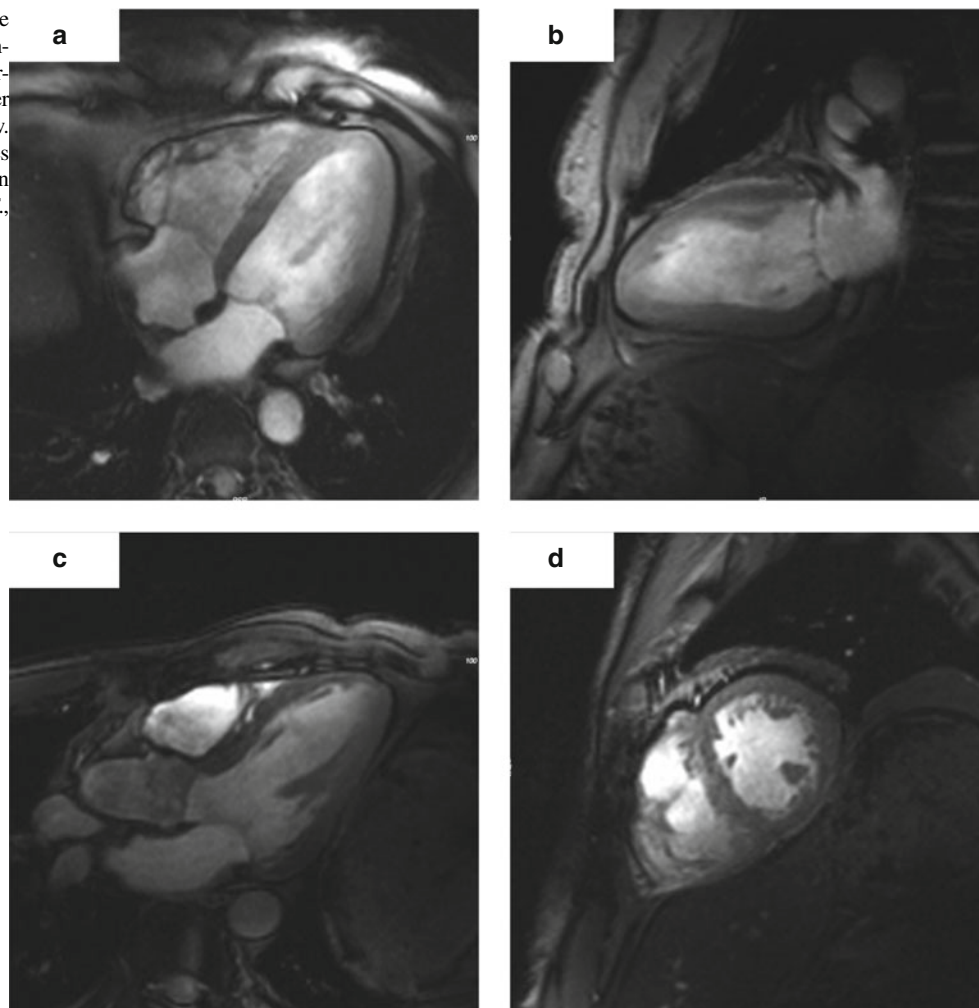
New applications are one aspect of the current research. Simultaneously, safety aspects have to be reevaluated again. To give one example, a significant number of patients with CAD have one or more coronary stents. First simulations that analyze stent heating are offering encouraging results [81].

The potential of CMR at 7 T is currently not fully determined. But against the assumptions less than 10 years ago, the beating heart is visible at 7 Tesla and it offers new exciting avenues in CMR applications.

Outlook

The future in the field of CMR technology including higher field strengths, accelerated imaging, and increased temporal and spatial resolution including 3D-assessment.

Fig. 22.4 Gradient echo cine images of the heart of a healthy volunteer obtained at 7 T. (a) Four-chamber view. (b) Two-chamber view. (c) Three-chamber view. (d) Short-axis view (The images were obtained at the Berlin Ultrahigh Field Facility (B.U.F.F., head Prof. Thoralf Niendorf))



Therapeutic options in most of the cardiovascular diseases continue to evolve due to changing population demographics and aging. Therefore, we need not only awareness of sex differences, but also of the ageing process. CMR has the capability to characterize myocardial changes early and to detect the interaction between the whole cardiovascular system. CMR applications in clinical routine have to be based on the development of standards including protocols and postprocessing [2, 82]. Clinicians are trained to use quantification for patient guidance – e.g. laboratory parameters. CMR has the capability to offer quantification for diffuse myocardial disease and intravascular alterations [60]. The establishment of accurate vendor independent and well proven mapping based quantification offers a step into non-invasive histological characterization of myocardial diseases.

An intelligent stepwise approach will benefit CMR place in the current multimodality environment. The most effective way will be an early interaction between physicists, engineers and clinicians to identify the unique capabilities of CMR. The future is not all about beautiful images or

resolution, but it is all about improving patient care by better understanding of disease pathophysiology.

References

1. Carpenter JP, He T, Kirk P, Roughton M, Anderson LJ, de Noronha SV, Sheppard MN, Porter JB, Walker JM, Wood JC, Galanello R, Forni G, Catani G, Matta G, Fucharoen S, Fleming A, House MJ, Black G, Firmin DN, St Pierre TG, Pennell DJ. On t_2^* magnetic resonance and cardiac iron. *Circulation*. 2011;123:1519–28.
2. Schulz-Menger J, Bluemke DA, Bremerich J, Flamm SD, Fogel MA, Friedrich MG, Kim RJ, von Knobelsdorff-Brenkenhoff F, Kramer CM, Pennell DJ, Plein S, Nagel E. Standardized image interpretation and post processing in cardiovascular magnetic resonance: society for cardiovascular magnetic resonance (scmr) board of trustees task force on standardized post processing. *J Cardiovasc Magn Reson: Off J Soc Cardiovasc Magn Reson*. 2013;15:35.
3. Messroghli DR, Radjenovic A, Kozerke S, Higgins DM, Sivanathan MU, Ridgway JP. Modified look-locker inversion recovery (moli) for high-resolution t1 mapping of the heart. *Magn Reson Med: Off J Soc Magn Reson Med Soc Magn Reson Med*. 2004;52:141–6.

4. Piechnik SK, Ferreira VM, Dall'Armellina E, Cochlin LE, Greiser A, Neubauer S, Robson MD. Shortened modified look-locker inversion recovery (shmoll) for clinical myocardial t1-mapping at 1.5 and 3 t within a 9 heartbeat breathhold. *J Cardiovasc Magn Reson: Off J Soc Cardiovasc Magn Reson.* 2010;12:69.
5. Chow K, Flewitt JA, Green JD, Pagano JJ, Friedrich MG, Thompson RB. Saturation recovery single-shot acquisition (sasha) for myocardial t mapping. *Magn Reson Med: Off J Soc Magn Reson Med Soc Magn Reson Med.* 2014;71(6):2082–95. doi:10.1002/mrm.24878.
6. Weingartner S, Akcakaya M, Basha T, Kissinger KV, Goddu B, Berg S, Manning WJ, Nezafat R. Combined saturation/inversion recovery sequences for improved evaluation of scar and diffuse fibrosis in patients with arrhythmia or heart rate variability. *Magn Reson Med: Off J Soc Magn Reson Med Soc Magn Reson Med.* 2013. doi:10.1002/mrm.24761.
7. Kellman P, Hansen MS. T1-mapping in the heart: accuracy and precision. *J Cardiovasc Magn Reson: Off J Soc Cardiovasc Magn Reson.* 2014;16:2.
8. Messroghli DR, Walters K, Plein S, Sparrow P, Friedrich MG, Ridgway JP, Sivanathan MU. Myocardial t1 mapping: application to patients with acute and chronic myocardial infarction. *Magn Reson Med.* 2007;58:34–40.
9. von Knobelsdorff-Brenkenhoff F, Prothmann M, Dieringer MA, Wassmuth R, Greiser A, Schwenke C, Niendorf T, Schulz-Menger J. Myocardial t1 and t2 mapping at 3 t: reference values, influencing factors and implications. *J Cardiovasc Magn Reson: Off J Soc Cardiovasc Magn Reson.* 2013;15:53.
10. Ferreira VM, Piechnik SK, Dall'Armellina E, Karamitsos TD, Francis JM, Ntusi N, Holloway C, Choudhury RP, Kardos A, Robson MD, Friedrich MG, Neubauer S. T(1) mapping for the diagnosis of acute myocarditis using cmr: comparison to t2-weighted and late gadolinium enhanced imaging. *JACC Cardiovasc Imaging.* 2013;6:1048–58.
11. Sado DM, White SK, Piechnik SK, Banyersad SM, Treibel T, Captur G, Fontana M, Maestrini V, Flett AS, Robson MD, Lachmann RH, Murphy E, Mehta A, Hughes D, Neubauer S, Elliott PM, Moon JC. Identification and assessment of anderson-fabry disease by cardiovascular magnetic resonance noncontrast myocardial t1 mapping. *Circ Cardiovasc Imaging.* 2013;6:392–8.
12. Karamitsos TD, Piechnik SK, Banyersad SM, Fontana M, Ntusi NB, Ferreira VM, Whelan CJ, Myerson SG, Robson MD, Hawkins PN, Neubauer S, Moon JC. Noncontrast t1 mapping for the diagnosis of cardiac amyloidosis. *JACC Cardiovasc Imaging.* 2013;6:488–97.
13. Flett AS, Hayward MP, Ashworth MT, Hansen MS, Taylor AM, Elliott PM, McGregor C, Moon JC. Equilibrium contrast cardiovascular magnetic resonance for the measurement of diffuse myocardial fibrosis: preliminary validation in humans. *Circulation.* 2010;122:138–44.
14. Kellman P, Wilson JR, Xue H, Bandettini WP, Shanbhag SM, Druey KM, Ugander M, Arai AE. Extracellular volume fraction mapping in the myocardium, part 2: initial clinical experience. *J Cardiovasc Magn Reson: Off J Soc Cardiovasc Magn Reson.* 2012;14:64.
15. Sado DM, Flett AS, Banyersad SM, White SK, Maestrini V, Quarta G, Lachmann RH, Murphy E, Mehta A, Hughes DA, McKenna WJ, Taylor AM, Hausenloy DJ, Hawkins PN, Elliott PM, Moon JC. Cardiovascular magnetic resonance measurement of myocardial extracellular volume in health and disease. *Heart (Br Card Soc).* 2012;98:1436–41.
16. Giri S, Chung YC, Merchant A, Mihai G, Rajagopalan S, Raman SV, Simonetti OP. T2 quantification for improved detection of myocardial edema. *J Cardiovasc Magn Reson.* 2009;11:56.
17. Wassmuth R, Prothmann M, Utz W, Dieringer M, von Knobelsdorff-Brenkenhoff F, Greiser A, Schulz-Menger J. Variability and homogeneity of cardiovascular magnetic resonance myocardial t2-mapping in volunteers compared to patients with edema. *J Cardiovasc Magn Reson: Off J Soc Cardiovasc Magn Reson.* 2013;15:27.
18. Thavendiranathan P, Walls M, Giri S, Verhaert D, Rajagopalan S, Moore S, Simonetti OP, Raman SV. Improved detection of myocardial involvement in acute inflammatory cardiomyopathies using t2 mapping. *Circ Cardiovasc Imaging.* 2012;5:102–10.
19. Verhaert D, Thavendiranathan P, Giri S, Mihai G, Rajagopalan S, Simonetti OP, Raman SV. Direct t2 quantification of myocardial edema in acute ischemic injury. *JACC.* 2011;4:269–78.
20. Ma D, Gulani V, Seiberlich N, Liu K, Sunshine JL, Duerk JL, Griswold MA. Magnetic resonance fingerprinting. *Nature.* 2013;495:187–92.
21. Stejskal EO, Tanner JE. Spin diffusion measurements: spin echoes in the presence of a time-dependent field gradient. *J Chem Phys.* 1965;42:288.
22. Le Bihan D, Breton E, Lallemand D, Grenier P, Cabanis E, Laval-Jeantet M. Mr imaging of intravoxel incoherent motions: application to diffusion and perfusion in neurologic disorders. *Radiology.* 1986;161:401–7.
23. Basser PJ, Mattiello J, LeBihan D. Mr diffusion tensor spectroscopy and imaging. *Biophys J.* 1994;66:259–67.
24. Tuch DS. Q-ball imaging. *Magn Reson Med.* 2004;52:1358–72.
25. Wedeen VJ, Hagmann P, Tseng WY, Reese TG, Weisskoff RM. Mapping complex tissue architecture with diffusion spectrum magnetic resonance imaging. *Magn Reson Med.* 2005;54:1377–86.
26. Streeter Jr DD, Spotnitz HM, Patel DP, Ross Jr J, Sonnenblick EH. Fiber orientation in the canine left ventricle during diastole and systole. *Circ Res.* 1969;24:339–47.
27. Streeter Jr DD, Hanna WT. Engineering mechanics for successive states in canine left ventricular myocardium. II. Fiber angle and sarcomere length. *Circ Res.* 1973;33:656–64.
28. Mekkaoui C, Porayette P, Jackowski MP, Kostis WJ, Dai G, Sanders S, Sosnovik DE. Diffusion MRI tractography of the developing human fetal heart. *PLoS ONE.* 2013;8:e72795.
29. Edelman RR, Gaa J, Wedeen VJ, Loh E, Hare JM, Prasad P, Li W. In vivo measurement of water diffusion in the human heart. *Magn Reson Med.* 1994;32:423–8.
30. Sosnovik DE, Mekkaoui C, Huang S, Chen HH, Dai G, Stoeck CT, Ngoy S, Guan J, Wang R, Kostis WJ, Jackowski MP, Wedeen VJ, Kozzerke S, Liao R. Microstructural impact of ischemia and bone marrow-derived cell therapy revealed with diffusion tensor mri tractography of the heart in vivo. *Circulation.* 2014;129:1731–41.
31. Wu MT, Tseng WY, Su MY, Liu CP, Chiou KR, Wedeen VJ, Reese TG, Yang CF. Diffusion tensor magnetic resonance imaging mapping the fiber architecture remodeling in human myocardium after infarction: correlation with viability and wall motion. *Circulation.* 2006;114:1036–45.
32. Wu MT, Su MY, Huang YL, Chiou KR, Yang P, Pan HB, Reese TG, Wedeen VJ, Tseng WY. Sequential changes of myocardial microstructure in patients postmyocardial infarction by diffusion-tensor cardiac mr: correlation with left ventricular structure and function. *Circ Cardiovasc Imaging.* 2009;2:32–40. 36 p following 40.
33. Marcus FI, McKenna WJ, Sherrill D, Basso C, Bauce B, Bluemke DA, Calkins H, Corrado D, Cox MG, Daubert JP, Fontaine G, Gear K, Hauer R, Nava A, Picard MH, Protonotarios N, Saffitz JE, Sanborn DM, Steinberg JS, Tandri H, Thiene G, Towbin JA, Tsatsopoulou A, Wichter T, Zareba W. Diagnosis of arrhythmogenic right ventricular cardiomyopathy/dysplasia: proposed modification of the task force criteria. *Circulation.* 2010;121:1533–41.
34. Kellman P, Hernando D, Shah S, Zuehlsdorff S, Jerecic R, Mancini C, Liang ZP, Arai AE. Multiecho dixon fat and water separation method for detecting fibrofatty infiltration in the myocardium. *Magn Reson Med: Off J Soc Magn Reson Med Soc Magn Reson Med.* 2009;61:215–21.

35. Kellman P, Hernando D, Arai AE. Myocardial fat imaging. *Curr Cardiovasc Imaging Rep.* 2010;3:83–91.
36. Havla L, Basha T, Rayatzadeh H, Shaw JL, Manning WJ, Reeder SB, Kozerke S, Nezafat R. Improved fat water separation with water selective inversion pulse for inversion recovery imaging in cardiac MRI. *J Magn Reson Imaging: JMRI.* 2013;37:484–90.
37. Lu M, Zhao S, Jiang S, Yin G, Wang C, Zhang Y, Liu Q, Cheng H, Ma N, Zhao T, Chen X, Huang J, Zou Y, Song L, He Z, An J, Renate J, Xue H, Shah S. Fat deposition in dilated cardiomyopathy assessed by CMR. *JACC Cardiovasc Imaging.* 2013;6:889–98.
38. Tereshchenko LG, Rizzi P, Mewton N, Volpe GJ, Murthy S, Strauss DG, Liu CY, Marchlinski FE, Spooner P, Berger RD, Kellman P, Lima JA. Infiltrated atrial fat characterizes underlying atrial fibrillation substrate in patients at risk as defined by the atrial fibrillation risk score. *Int J Cardiol.* 2014;172:196–201.
39. Goldfarb JW, Arnold-Anteraper S. Water-fat separation imaging of the heart with standard magnetic resonance bssfp cine imaging. *Magn Reson Med: Off J Soc Magn Reson Med Soc Magn Reson Med.* 2014;71:2096–104.
40. Venkatesh BA, Lima JA, Bluemke DA, Lai S, Steenbergen C, Liu CY. Mr proton spectroscopy for myocardial lipid deposition quantification: a quantitative comparison between 1.5t and 3t. *J Magn Reson Imaging: JMRI.* 2012;36:1222–30.
41. van der Meer RW, Doornbos J, Kozerke S, Schar M, Bax JJ, Hammer S, Smit JW, Romijn JA, Diamant M, Rijzewijk LJ, de Roos A, Lamb HJ. Metabolic imaging of myocardial triglyceride content: reproducibility of 1h mr spectroscopy with respiratory navigator gating in volunteers. *Radiology.* 2007;245:251–7.
42. Liu CY, Liu YC, Venkatesh BA, Lima JA, Bluemke DA, Steenbergen C. Heterogeneous distribution of myocardial steatosis – an ex vivo evaluation. *Magn Reson Med: Off J Soc Magn Reson Med Soc Magn Reson Med.* 2012;68:1–7.
43. Rijzewijk LJ, van der Meer RW, Smit JW, Diamant M, Bax JJ, Hammer S, Romijn JA, de Roos A, Lamb HJ. Myocardial steatosis is an independent predictor of diastolic dysfunction in type 2 diabetes mellitus. *J Am Coll Cardiol.* 2008;52:1793–9.
44. van der Meer RW, Rijzewijk LJ, Diamant M, Hammer S, Schar M, Bax JJ, Smit JW, Romijn JA, de Roos A, Lamb HJ. The ageing male heart: myocardial triglyceride content as independent predictor of diastolic function. *Eur Heart J.* 2008;29:1516–22.
45. Haufe S, Engeli S, Budziarek P, Utz W, Schulz-Menger J, Hermsdorf M, Wiesner S, Otto C, Haas V, de Greiff A, Luft FC, Boschmann M, Jordan J. Cardiorespiratory fitness and insulin sensitivity in overweight or obese subjects may be linked through intrahepatic lipid content. *Diabetes.* 2010;59:1640–7.
46. Utz W, Engeli S, Haufe S, Kast P, Bohnke J, Haas V, Hermsdorf M, Wiesner S, Pofahl M, Traber J, Luft FC, Boschmann M, Jordan J, Schulz-Menger J. Moderate dietary weight loss reduces myocardial steatosis in obese and overweight women. *Int J Cardiol.* 2013;167:905–9.
47. Zerhouni EA, Parish DM, Rogers WJ, Yang A, Shapiro EP. Human heart: tagging with mr imaging – a method for noninvasive assessment of myocardial motion. *Radiology.* 1988;169:59–63.
48. Axel L, Dougherty L. Mr imaging of motion with spatial modulation of magnetization. *Radiology.* 1989;171:841–5.
49. Moran PR. A flow velocity zeugmatographic interlace for nmr imaging in humans. *Magn Reson Imaging.* 1982;1:197–203.
50. Aletras AH, Ding S, Balaban RS, Wen H. Dense: displacement encoding with stimulated echoes in cardiac functional MRI. *J Magn Reson.* 1999;137:247–52.
51. Osman NF, Sampath S, Atalar E, Prince JL. Imaging longitudinal cardiac strain on short-axis images using strain-encoded MRI. *Magn Reson Med.* 2001;46:324–34.
52. Jung B, Foll D, Bottler P, Petersen S, Hennig J, Markl M. Detailed analysis of myocardial motion in volunteers and patients using high-temporal-resolution mr tissue phase mapping. *J Magn Reson Imaging: JMRI.* 2006;24:1033–9.
53. Foll D, Jung B, Schilli E, Staehle F, Geibel A, Hennig J, Bode C, Markl M. Magnetic resonance tissue phase mapping of myocardial motion: new insight in age and gender. *Circ Cardiovasc Imaging.* 2010;3:54–64.
54. Foell D, Jung B, Germann E, Staehle F, Bode C, Markl M. Hypertensive heart disease: MR tissue phase mapping reveals altered left ventricular rotation and regional myocardial long-axis velocities. *Eur Radiol.* 2013;23:339–47.
55. Augustine D, Lewandowski AJ, Lazdam M, Rai A, Francis J, Myerson S, Noble A, Becher H, Neubauer S, Petersen SE, Leeson P. Global and regional left ventricular myocardial deformation measures by magnetic resonance feature tracking in healthy volunteers: comparison with tagging and relevance of gender. *J Cardiovasc Magn Reson: Off J Soc Cardiovasc Magn Reson.* 2013;15:8.
56. Morton G, Schuster A, Jogiya R, Kutty S, Beerbaum P, Nagel E. Inter-study reproducibility of cardiovascular magnetic resonance myocardial feature tracking. *J Cardiovasc Magn Reson: Off J Soc Cardiovasc Magn Reson.* 2012;14:43.
57. Kim D, Gilson WD, Kramer CM, Epstein FH. Myocardial tissue tracking with two-dimensional cine displacement-encoded mr imaging: Development and initial evaluation. *Radiology.* 2004;230:862–71.
58. Markl M, Kilner PJ, Ebbers T. Comprehensive 4d velocity mapping of the heart and great vessels by cardiovascular magnetic resonance. *J Cardiovasc Magn Reson.* 2011;13:7.
59. Markl M, Geiger J, Kilner PJ, Foll D, Stiller B, Beyersdorf F, Arnold R, Frydrychowicz A. Time-resolved three-dimensional magnetic resonance velocity mapping of cardiovascular flow paths in volunteers and patients with fontan circulation. *Eur J Cardiothorac Surg: Off J Eur Assoc Cardiothorac Surg.* 2011;39:206–12.
60. von Knobelsdorff-Brenkenhoff F, Trauzeddel RF, Barker AJ, Gruettner H, Markl M, Schulz-Menger J. Blood flow characteristics in the ascending aorta after aortic valve replacement—a pilot study using 4d-flow mri. *Int J Cardiol.* 2014;170:426–33.
61. Harloff A, Simon J, Bredecke S, Assefa D, Helbing T, Frydrychowicz A, Weber J, Olschewski M, Strecker C, Hennig J, Weiller C, Markl M. Complex plaques in the proximal descending aorta: an underestimated embolic source of stroke. *Stroke.* 2010;41:1145–50.
62. Barker AJ, Markl M, Burk J, Lorenz R, Bock J, Bauer S, Schulz-Menger J, von Knobelsdorff-Brenkenhoff F. Bicuspid aortic valve is associated with altered wall shear stress in the ascending aorta. *Circ Cardiovasc Imaging.* 2012;5:457–66.
63. Rodriguez Munoz D, Markl M, Moya MR JL, Barker A, Fernandez-Golfín C, Lancellotti P, Zamorano Gomez JL. Intracardiac flow visualization: current status and future directions. *Eur Heart J Cardiovasc Imaging.* 2013;14:1029–38.
64. Eichenberger AC, Schwitter J, McKinnon GC, Debatin JF, von Schulthess GK. Phase-contrast echo-planar mr imaging: real-time quantification of flow and velocity patterns in the thoracic vessels induced by valsalva's maneuver. *J Magn Reson Imaging.* 1995;5:648–55.
65. Gatehouse PD, Firmin DN, Collins S, Longmore DB. Real time blood flow imaging by spiral scan phase velocity mapping. *Magn Reson Med.* 1994;31:504–12.
66. Joseph AA, Merboldt KD, Voit D, Zhang S, Uecker M, Lotz J, Frahm J. Real-time phase-contrast mri of cardiovascular blood flow using undersampled radial fast low-angle shot and nonlinear inverse reconstruction. *NMR Biomed.* 2012;25:917–24.
67. Dieringer MA, Deimling M, Santoro D, Wuerfel J, Madai VI, Sobesky J, von Knobelsdorff-Brenkenhoff F, Schulz-Menger J, Niendorf T. Rapid parametric mapping of the longitudinal relaxation time t1 using two-dimensional variable flip angle magnetic resonance imaging at 1.5 tesla, 3 tesla, and 7 tesla. *PLoS ONE.* 2014;9:e91318.

68. Sinnecker T, Dorr J, Pfueller CF, Harms L, Ruprecht K, Jarius S, Bruck W, Niendorf T, Wuerfel J, Paul F. Distinct lesion morphology at 7-t mri differentiates neuromyelitis optica from multiple sclerosis. *Neurology*. 2012;79:708–14.
69. Vaughan JT, Snyder CJ, DelaBarre LJ, Bolan PJ, Tian J, Bolinger L, Adriany G, Andersen P, Strupp J, Ugurbil K. Whole-body imaging at 7t: preliminary results. *Magn Reson Med*. 2009;61:244–8.
70. Dieringer MA, Renz W, Lindel T, Seifert F, Frauenrath T, von Knobelsdorff-Brenkenhoff F, Waiczies H, Hoffmann W, Rieger J, Pfeiffer H, Ittermann B, Schulz-Menger J, Niendorf T. Design and application of a four-channel transmit/receive surface coil for functional cardiac imaging at 7t. *J Magn Reson Imaging: JMRI*. 2011; 33:736–41.
71. Frauenrath T, Hezel F, Renz W, d'Orth Tde G, Dieringer M, von Knobelsdorff-Brenkenhoff F, Prothmann M, Schulz Menger J, Niendorf T. Acoustic cardiac triggering: a practical solution for synchronization and gating of cardiovascular magnetic resonance at 7 tesla. *J Cardiovasc Magn Reson*. 2010;12:67.
72. Snyder CJ, DelaBarre L, Metzger GJ, van de Moortele PF, Akgun C, Ugurbil K, Vaughan JT. Initial results of cardiac imaging at 7 tesla. *Magn Reson Med*. 2009;61:517–24.
73. von Knobelsdorff-Brenkenhoff F, Frauenrath T, Prothmann M, Dieringer MA, Hezel F, Renz W, Kretschel K, Niendorf T, Schulz-Menger J. Cardiac chamber quantification using magnetic resonance imaging at 7 tesla--a pilot study. *Eur Radiol*. 2010;20: 2844–52.
74. Suttie JJ, Delabarre L, Pitcher A, van de Moortele PF, Dass S, Snyder CJ, Francis JM, Metzger GJ, Weale P, Ugurbil K, Neubauer S, Robson M, Vaughan T. 7 tesla (t) human cardiovascular magnetic resonance imaging using flash and ssfp to assess cardiac function: validation against 1.5 t and 3 t. *NMR Biomed*. 2012;25:27–34.
75. von Knobelsdorff-Brenkenhoff F, Tkachenko V, Winter L, Rieger J, Thalhammer C, Hezel F, Graessl A, Dieringer MA, Niendorf T, Schulz-Menger J. Assessment of the right ventricle with cardiovascular magnetic resonance at 7 tesla. *J Cardiovasc Magn Reson*. 2013; 15:23.
76. Hezel F, Thalhammer C, Waiczies S, Schulz-Menger J, Niendorf T. High spatial resolution and temporally resolved t2* mapping of normal human myocardium at 7.0 tesla: an ultrahigh field magnetic resonance feasibility study. *PLoS ONE*. 2012;7:e52324.
77. Meloni A, Hezel F, Positano V, Keilberg P, Pepe A, Lombardi M, Niendorf T. Detailing magnetic field strength dependence and segmental artifact distribution of myocardial effective transverse relaxation rate at 1.5, 3.0, and 7.0 t. *Magn Reson Med*. 2014;71:2224–30.
78. Rodgers CT, Clarke WT, Snyder C, Vaughan JT, Neubauer S, Robson MD. Human cardiac p magnetic resonance spectroscopy at 7 tesla. *Magn Reson Med*. 2014;72:304–15.
79. Thalhammer C, Renz W, Winter L, Hezel F, Rieger J, Pfeiffer H, Graessl A, Seifert F, Hoffmann W, von Knobelsdorff-Brenkenhoff F, Tkachenko V, Schulz-Menger J, Kellman P, Niendorf T. Two-dimensional sixteen channel transmit/receive coil array for cardiac mri at 7.0 t: design, evaluation, and application. *J Magn Reson Imaging*. 2012;36:847–57.
80. Johst S, Orzada S, Fischer A, Schafer LC, Nassenstein K, Umutlu L, Lauenstein TC, Ladd ME, Maderwald S. Sequence comparison for non-enhanced mra of the lower extremity arteries at 7 tesla. *PLoS ONE*. 2014;9:e86274.
81. Santoro D, Winter L, Muller A, Vogt J, Renz W, Ozerdem C, Grassl A, Tkachenko V, Schulz-Menger J, Niendorf T. Detailing radio frequency heating induced by coronary stents: a 7.0 tesla magnetic resonance study. *PLoS ONE*. 2012;7:e49963.
82. Kramer CM, Barkhausen J, Flamm SD, Kim RJ, Nagel E. Society for Cardiovascular Magnetic Resonance Board of Trustees Task Force on Standardized P. Standardized cardiovascular magnetic resonance (cmr) protocols 2013 update. *J Cardiovasc Magn Reson: Off J Soc Cardiovasc Magn Reson*. 2013;15:91.

Index

- A**
Absolute quantification, 187–190
Accelerated imaging technique, coronary MRI, 251
Acquisition for cardiac unified T2 edema (ACUT2E), 175
Acquisition ordering, CE MRA, 288
Acquisition time, 136
 GRE imaging, 33
 SE imaging, 34
Acquisition window (AW), 133
ACR. *See* American College of Radiology (ACR)
Active implants, cardiac MR with cardiovascular devices, 124–125
ACUT2E. *See* Acquisition for cardiac unified T2 edema (ACUT2E)
Acute myocardial infarction, LGE imaging, 217–218
Adenosine, myocardial perfusion CMR, 198
Aliasing artifact, 104, 112
American College of Radiology (ACR), 117, 276
American Society for Testing Materials (ASTM), 117
Amyloidosis, LGE imaging, 221
Analog-to-digital (AD) converter, 21
Aorta coarctation, phase-contrast magnetic resonance, 238–239
Aortic regurgitation (AR), 236–237
Aortic stenosis (AS), 235–236
 peak velocity quantification, 236
 pitfalls, 236
 transvalvular pressure gradients, 236
Apparent spatial resolution, 46
Apparent temporal resolution (TR_{apparent}), 138
AR. *See* Aortic regurgitation (AR)
Arrhythmias
 artifact, 101
 bSSFP cine and, 102
 ECG-gating for CMR, 139–141
 in LGE, 101
Arrhythmogenic right ventricular cardiomyopathy (ARVC), 318
 LGE imaging, 219–220
 Task Force Criteria, 220
Arterial spin labeling (ASL)
 cardiac perfusion scans, 181, 190
 MRA
 advantages, 304
 applications, 304
 with gradient dephasing, 302–304
 limitations, 304
 overview, 301–302
 physical principles, 301–302
 technical considerations, 304
Artifacts, 97
 to advanced cardiac imaging methods, 111–112
 aliasing/wraparound, 104
 arrhythmia, 101
 b0-field inhomogeneities, 106–110
 blood flow, 102–103
 breathing motion, 98–99
 cardiac motion, 98–102
 chemical shift effect, 104–106
 definition, 98
 inversion pulse ghosting, 110–111
 non-Cartesian approaches, 112
 spin-echo blood flow, 102
 truncation, 103–104
 T vs. 3 T, 112–113
ARVC. *See* Arrhythmogenic right ventricular cardiomyopathy (ARVC)
AS. *See* Aortic stenosis (AS)
ASD. *See* Atrial septal defects (ASD)
ASL. *See* Arterial spin labeling (ASL)
ASTM. *See* American Society for Testing Materials (ASTM)
Asymmetric echo, 48
Atrial septal defects (ASD), 239–240
AW. *See* Acquisition window (AW)
- B**
Balanced steady-state free precession (bSSFP), 196, 285–287
 artifacts at 3 T, 89
 and B0 inhomogeneities, 109
 chemical shift artifacts, 151
 clinical applications, 156–157
 dummy heartbeat, 151
 GRE and, 100
 high field MRI, 91
 imaging, 34, 37–40
 inflowing blood, 150–151
 magnetization-prepared, 310
 myocardial perfusion CMR, 200
 non-contrast enhanced MRA, 309–310
 off resonance effects, 151–152
 parameter selection, 152
 pulse sequences, 195
 saturation effect, 150
 signal equation, 150
 SNR efficiency, 151
 steady state, 94
 steady state time, 151
 subtractive methods using, 310
B0-field inhomogeneities, 106–110
 bSSFP and, 109
 h-EPI and, 108–110

- Bipolar gradient, 228, 312
- Black-blood imaging
 - basic concepts, 162
 - bright-blood artifacts, 165–166
 - FSE readout, 162–163
 - important, 162
 - multiple phase encoding, 162–163
 - STIR, 165–166
- Black-blood preparation, 29–30
- Block Regional Interpolation Scheme for k-space (BRISK), 52
- Blood flow, 187, 188, 190
 - artifacts, 102–103
- Blood flow assessment, CMR
 - 4D-flow technique, 320
 - real-time flow, 320
- Blood oxygen level dependent (BOLD) contrast, 88, 94, 180, 190
- Blood pool contrast agents, 274–275
- Blood suppression, 165
- Bolus timing, contrast agent, 284
- Bradycardia, ECG-gating for CMR, 139
- Breastfeeding, and GBCA, 279
- Breathing motion, artifacts, 98–99
- Bright-blood artifacts, 165
- BRISK. *See* Block Regional Interpolation Scheme for k-space (BRISK)
- bSSFP. *See* Balanced steady-state free precession (bSSFP)

- C**
- CA. *See* Cardiac amyloidosis (CA)
- CAD. *See* Coronary artery disease (CAD)
- Cardiac amyloidosis (CA), 221
- Cardiac cycle, 26, 169–171
 - ECG and, 132–133
- Cardiac diffusion MRI, 316–318
- Cardiac gating
 - phase-contrast magnetic resonance, 227–228
 - prospective, 227
 - retrospective, 227–228
- Cardiac imaging
 - breath-holding, 154–155
 - parallel imaging techniques, 156
 - purpose of, 133
 - retrospective gating, 155
 - segmented k-space, 152–154
 - view sharing, 155–156
- Cardiac magnetic resonance (CMR) pulse sequence
 - bSSFP imaging, 37–39
 - definition, 25–26
 - fast spin echo imaging, 36–37
 - fast spoiled gradient echo, 34
 - features of, 26
 - gradient-recalled echo, 31–33
 - magnetization preparation
 - black-blood preparation, 29–30
 - fat suppression, 28–29
 - T₁-weighted preparations, 26–27
 - T₂-weighted preparations, 27–28
 - multi-gradient recalled echo, 33–34
 - spin echo imaging, 34–36
 - structure of, 26, 30–31
- Cardiac mass, LGE, 222
- Cardiac motion, 26
 - artifacts, 98–102
 - dark-blood imaging, 101
 - myocardial perfusion, 100
 - poor triggering, 101
 - coronary MRI, 247–248
 - magnetic resonance spectroscopy, 266
- Cardiac output (CO), phase-contrast magnetic resonance, 233
- Cardiac resynchronization therapy (CRT), 254
- Cardiac sarcoidosis, LGE imaging, 220
- Cardiac self-gating, 142–143
- Cardiac synchronization, fast imaging, 65–66
- Cardiomyopathy
 - ARVC, 219–220, 318
 - DCM, 219, 237, 318
 - HCM, 219, 318
 - ischemic, 218
 - NICM, 218–220
 - restrictive physiology, 234
- Cardiovascular devices
 - active implants, 124–125
 - device implantation, 123
 - passive implants, 123–124
 - patient screening, 122
 - terminology and labeling, 122–123
- Cardiovascular magnetic resonance (CMR) imaging, 149, 181, 184, 315
 - active implants, 124–125
 - blood flow assessment, 320–321
 - device implantation, 123
 - ECG-gating for (*see* Electrocardiographic (ECG)-gating for CMR)
 - fast imaging, 64
 - gradient echo cine images, 322
 - high field MRI, 87
 - advantages, 88
 - applications, 90–93
 - challenges, 88–90
 - novel techniques, 93–94
 - myocardial mechanics analysis
 - DENSE, 319–320
 - feature tracking, 319
 - SENC, 319–320
 - tissue phase mapping, 319
 - myocardial perfusion (*see* Myocardial perfusion imaging, CMR)
 - myocardial tissue characterization
 - cardiac diffusion MRI, 316–318
 - myocardial fat detection, 318–319
 - parametric mapping, 316
 - passive implants, 123–124
 - patient screening, 122
 - stress testing, 193
 - contraindications to drugs used, 194
 - dobutamine, 194–197
 - ergometer stress, 194
 - pulse sequences, 195
 - vasodilator stress, 195
 - terminology and labeling, 122–123
 - ultrahigh magnetic field strength, 321
- Carotid plaque imaging, by MRI, 276
- Cartesian sampling, for real-time imaging, 55–56
- Center for Devices and Radiological Health (CDRH), 122
- Central nervous system (CNS), MRI safety, 119
- Cerebrospinal fluid (CSF), and pleural effusion ghosting, 110–111
- Chemical shift, 88
- Chemical shift artifacts, 104–106
 - b-SSFP fat-water signal cancellation, 105–106
 - h-EPI, 105
 - TSE, 105
- Chronic myocardial infarction, LGE imaging, 217–218
- Cine imaging
 - bSSFP, 149, 152–154
 - k-spaces, 69

in patient with pacemaker, 157
 prospectively triggered imaging, 69
 retrospectively gated imaging, 69
 SSFP, 157

CMR. *See* Cardiovascular magnetic resonance (CMR) imaging

CMR pulse sequence. *See* Cardiac magnetic resonance (CMR) pulse sequence

CNR. *See* Contrast-to-noise ratio (CNR)

Coarctation of aorta, phase-contrast magnetic resonance, 238–239

Compressed sensing, 79–81

Congenital heart disease
 coarctation of aorta, 238–239
 intracardiac shunts
 atrial septal defects, 239–240
 ventricular septal defects, 240
 pulmonary hypertension, 241
 pulmonary valve disorders, 240–241

Continuous update with random encoding (CURE), 53–54

Contractile function, 165

Contrast agent
 bolus timing and venous overlay, 284

CE MRA
 ferumoxytol, 284
 gadolinium, 283–284
 injection, 284

dynamic scan, 197

ECCAs, 274

elimination of, 274

GBCA (*see* Gadolinium based contrast agents (GBCA))

MRI, 272, 274

myocardial perfusion CMR, 199

positive, 272

X-ray, 271

Contrast enhanced EPI, 289–290

Contrast-Enhanced MR Angiography (CE MRA), 92, 283, 298
 acquisition ordering, 288
 contrast agents
 ferumoxytol, 284
 gadolinium, 283–284
 injection, 284
 data acquisition, 285
 data reconstruction, 287–288
 gradient echo imaging
 bSSFP, 285–287
 quiescent interval single shot, 287
 spoiled GRE, 285
 spoiling, 285
 parallel imaging, 289–290
 partial Fourier acquisition, 288
 radial imaging, 290
 benefits for, 290–291
 errors, 293–294
 HYPR, 294
 Kaiser-Bessel Kernel, 291
 sampling density, 292
 sliding window reconstruction, 292–293
 single phase, 284

Contrast media, 271, 272, 277

Contrast-to-noise ratio (CNR), 180
 coronary MRI, 249–251, 253

Coronary angiography, 218, 247, 250

Coronary artery disease (CAD), 193
 detection of, 206
 magnetic resonance imaging, 245
 acquisition interval, 248
 advanced methods, 251–256

cardiac motion, 247–248
 contrast-to-noise ratio, 249–251
 free breathing acquisition, 246
 high-resolution, 252
 imaging sequences, 246–247
 issues of, 246–247
 real-time navigator tracking, 248
 respiratory motion, 248–249
 signal-to-noise ratio, 249–252
 subject-specific tracking factor, 248
 targeted 3D, 251
 whole-heart, 246, 247, 250, 252–254, 256

Coronary MR angiography (coronary MRA), 92

Coronary multi-detector computed tomography (MDCT), 246

Coronary vein MRI, 255–256

Creatine, 264, 266, 267, 269

CRT. *See* Cardiac resynchronization therapy (CRT)

CURE. *See* Continuous update with random encoding (CURE)

D

Dark-blood venography, 299

Dark rim artifact (DRA), 185, 204, 205

Data acquisition
 CE MRA, 285
 ECG-gating
 basic concepts, 133
 prospectively gated segmented acquisition, 136–137
 prospectively gated segmented-cine acquisition, 137–138
 retrospectively gated segmented-cine acquisition, 138
 single-shot prospectively-gated sequence, 133–135
 myocardial perfusion CMR, 200–201

Data reconstruction, CE MRA, 287–288

DCE-MRI. *See* Dynamic contrast-enhanced MRI (DCE-MRI)

DCM. *See* Dilated cardiomyopathy (DCM)

DENSE. *See* Displacement Encoding via Stimulated Echoes (DENSE)

Device implantation, CMR, 123

Diastolic dysfunction, 233
 mitral annular tissue velocity, 234
 pitfalls, 234–235
 pulmonary vein flow waveform, 234
 restrictive physiology, 234
 transmitral flow profiles, 234

Dilated cardiomyopathy (DCM)
 with heart failure, 219
 LGE imaging, 219, 237, 318
 in women, 218

Dipyridamole, myocardial perfusion CMR, 198

Displacement Encoding via Stimulated Echoes (DENSE), 319–320

Dobutamine, myocardial perfusion CMR, 199

Dobutamine stress CMR, 194–195
 functional assessment, 197
 ideal cine approach for, 196
 perfusion imaging and, 202
 prognostic value of, 197
 safety of, 196

Double inversion, 162

Double IR strategy, 29–30

DRA. *See* Dark rim artifact (DRA)

Dynamic contrast-enhanced MRI (DCE-MRI), 82

E

ECCAs. *See* Extracellular contrast agents (ECCAs)

ECG signal. *See* Electrocardiographic (ECG) signal

- ECG-triggering, 133
- Echo-planar imaging (EPI), 22–23, 289–290
 fast imaging, 68
 myocardial perfusion CMR, 199
- Echo time, 31
- Echo-train length (ETL), 36–37
- Electrocardiographic (ECG)-gating for CMR
 apparent temporal resolution, 138
 arrhythmias, 141
 cardiac cycle, 132–133
 cardiac self-gating, 142–143
 data acquisition, 133–138
 goal, 133
 implementation, 138
 induced currents, 140–141
 interpreting ECG tracing, 133
 lead placement configuration, 132
 magnetohydrodynamic effect, 139, 140
 poor signal, 138
 prospective gating, 133
 segmented acquisition, 136–137
 segmented-cine acquisition, 137–138
 single-shot acquisition, 133–135
 pulse oximetry-gating, 139
 real-time imaging, 141, 142
 retrospective gating, 133
 segmented-cine acquisition, 138
 setup, 132–133
 single-shot/segmented acquisitions, 133
 vectorcardiography, 140, 141
- Electrocardiographic (ECG) signal, 26
- Electrophosphenes, 121
- EPI. *See* Echo-planar imaging (EPI)
- Ergometer stress, 194
- Ernst angle (α_E), 147
- ETL. *See* Echo-train length (ETL)
- European Society of Cardiology, 206
- Extracellular contrast agents (ECCAs), 274
- Extracellular volume (ECV) imaging, 172
- Extravasation, GBCA adverse effects, 279
- F**
- Fast-field echo (FFE). *See* Gradient-recalled echo (GRE)
- Fast gradient recalled echo (FGRE)
 myocardial perfusion CMR, 199
 stress wall motion assessment, 196
- Fast imaging
 cardiac and respiratory synchronization, 65–66
 cardiovascular magnetic resonance imaging, 64
 cine imaging, 69
 prospectively triggered, 69
 retrospectively gated, 69
 compressed sensing, 79–81
 functional imaging, 81–82
 k-t methods, 79
 morphological cardiac imaging, 81
 multi-echo GRE, 69
 multi-echo sequences, 67
 myocardial perfusion imaging, 82–84
 non-Cartesian trajectories, 78–79
 parallel imaging, 72–73
 GRAPPA, 75
 limitations, 77–78
 PILS, 73–74
 SENSE, 74–75
 pulse sequences, 64–65
 segmented acquisitions, 68
 single-echo gre sequences, 66
 single-shot TSE/FSE, 68
 k-space lines
 keyhole imaging, 71–72
 partial/half Fourier, 70–71
 rectangular field-of-view, 71
 reducing, 70
 view-sharing, 71
 zero-filling, 70
 turbo spin echo/fast spin echo, 67–68
 vascular imaging, 84–85
 viability imaging, 84
 VIPR/HYPR, 79
- Fast low-angle shot (FLASH) sequence, 34, 183
- Fast spin echo (FSE), 36–37, 162, 174
 fast imaging, 67–68
 single-shot, 68
- Fast spoiled gradient echo, 34
- Fat suppression (FS), 28–29
- Feature tracking, myocardial mechanics analysis, 319
- Ferumoxytol
 contrast agents, 284
 GBCA, 275
- FGRE. *See* Fast gradient recalled echo (FGRE)
- FID. *See* Free-induction decay (FID)
- Field-of-view (FOV), 19, 71
- FLASH sequence. *See* Fast low-angle shot (FLASH) sequence
- Flow-dependent MRA
 advantages, 307–308
 applications, 308–309
 inflow inversion-recovery, 305–306
 limitations, 307–308
 physical principles, 305
 quiescent inflow single-shot, 306
 technical considerations, 307–308
 velocity selective angiography, 306–307
- Flow imaging, 92. *See also* Phase-contrast magnetic resonance
- Flow-independent MRA
 advantages, 310–311
 applications, 311–312
 bSSFP, 309–310
 limitations, 310–311
 overview and physical principles, 309
 technical considerations, 309–311
- Food, Drug and Cosmetic Act of 1938, 116
- 4D-flow technique, blood flow assessment, 320
- Fourier imaging, partial/half, 70–71
- Fourier space, 14
- Fourier transform, 18
- Fractional echo, 48
- Free-breathing techniques, 216–217, 246
- Free-induction decay (FID), 7–8, 146
- Frequency resolution, and SNR, 94
- Frequency space. *See* Fourier space
- FSE. *See* Fast spin echo (FSE)
- Full width at half maximum (FWHM)
 LGE image, 222
 limitation, 223
- Functional imaging, 81–82
- FWHM. *See* Full width at half maximum (FWHM)

G

- Gadofosveset, 275, 284
- Gadolinium based contrast agents (GBCA), 187, 283–284
 - adverse effects, 276
 - extravasation, 279
 - nephrogenic systemic fibrosis, 277–279
 - serum calcium determinations, 279
 - in animal models, 279
 - applications and methods, 276
 - breastfeeding and, 279
 - extracellular contrast agents, 274
 - FDA approved, 273
 - intravascular/blood pool contrast agents, 274–275
 - novel/experimental contrast agents
 - ferumoxytol, 275
 - manganese based contrast agents, 275
 - molecular MRI contrast agents, 275–276
 - pediatric population, 280
 - during pregnancy, 280
- Gd-BOPTA, for coronary MRI, 251–253
- Gd-DTPA
 - in myocardium, 212, 213
 - in rat model, 217
- Generalized Autocalibrating Partially Parallel Acquisition (GRAPPA), 76, 289
- Gibbs ringing, 46, 103–104
- Gradient dephasing, ASL MRA with, 302–304
- Gradient echo (GRE), 146
 - bSSFP, 149
 - CE MRA
 - bSSFP, 285–286
 - quiescent interval single shot, 286
 - spoiled GRE, 285
 - spoiling, 285
 - coronary MRI, 246, 249, 257
 - echoes, 146
 - FID, 146
 - SPGR, 146–149
- Gradient-echo pulse sequence. *See* Gradient-recalled echo (GRE)
- Gradient fields, MRI safety, 118
- Gradient-recalled echo (GRE), 32–33
 - and bSSFP, 100
- Gradients, and k-space, 19–21
- GRE. *See* Gradient-recalled echo (GRE)

H

- Half-Fourier Acquisition Single-shot Turbo spin Echo imaging (HASTE), 49, 71
- Half Fourier imaging, 70–71
- Heart failure, clinical indications, 206
- Heart rate (HR), and R-R interval, 133
- Heart rhythm, 133
- Hemodynamic support devices, 125
- High field MRI, CMR, 87
 - advantages, 88
 - applications, 90–93
 - challenges, 88–90
 - novel techniques, 93–94
- Highly Constrained Projection Reconstruction (HYPR), 79, 294
- High-resolution coronary MRI, 251
- ¹H-MRS of heart, 262
 - AMARES time domain fitting, 267–268
 - cardiac metabolism with, 261–262
 - choice of localization pulse sequence, 263–264

- data processing, 267–268
- dealing with motion, 264
- optimal data acquisition parameters, 265
- scans preparation, 266
- volume placement, 265–266
- water suppression, 264–265
- Hybrid Echo-Planar Imaging (h-EPI), 100, 108–110
- Hybrid-EPI technique, 199
- Hypertrophic cardiomyopathy (HCM), 318
 - diagnosis, 219
 - LGE imaging, 219
 - in men, 219
- HYPR. *See* Highly Constrained Projection Reconstruction (HYPR)

I

- ICDs. *See* Implantable cardioverter defibrillators (ICDs)
- IFIR. *See* Inflow inversion recovery (IFIR)
- Image space
 - data properties in, 15–16
 - k-space and, 44
- Imaging procedure, 8
- Implantable cardioverter defibrillators (ICDs), 124–125
- Implanted cardio defibrillators (ICDs), 88
- Indian ink artifact, 105
- Induced currents, ECG-gating for CMR, 140–141
- Inflow inversion recovery (IFIR), 307
- Inflow inversion-recovery MRA, 307–308
- International Commission on Non-Ionizing Radiation Protection (ICNIRP), 117
- Intracardiac shunts
 - atrial septal defects, 239–240
 - ventricular septal defects, 240
- Intravascular/blood pool contrast agents, 274–275
- Intra-view motion, artifacts, 98
- Inversion pulse ghosting, artifacts, 110–111
- Inversion recovery (IR) approach, 164
- Inversion-recovery (IR) approach, 27
- Inversion time (TI), 27, 214
- Ischemic cardiomyopathy, 218

J

- Japanese Ministry of Health, 220

K

- Kaiser-Bessel Kernel, 291
- Keyhole imaging, 71–72
- Keyhole technique, 284, 288–289
 - temporal resolution, 51–52
- k-t Broad-use Linear Acquisition Speed-up Technique (k-t BLAST), 80
- k-t methods, 79
- k-t SENSE, 79

L

- Larmor frequency, 4
- Late-gadolinium enhancement (LGE), 34, 167, 212
 - arrhythmias in, 101
 - breathing artifacts, 99
 - cardiac masses, 222
 - clinical applications

- Late-gadolinium enhancement (LGE) (*cont.*)
 acute/chronic myocardial infarction, 217–218
 cardiac sarcoidosis, 220
 ischemic cardiomyopathy, 218
 myocarditis, 220–221
 non-ischemic cardiomyopathies, 218–220
 evolution of pulse sequence design, 214–215
 fundamental principles
 contrast kinetics, 212–213
 evolution of pulse sequence design, 214–215
 nulling normal myocardium, 213–214
 phase-sensitive inversion-recovery imaging, 215–216, 221
 3D and Free-Breathing Techniques, 216–217
 FWHM technique, 223
 image interpretation and quantification, 222–223
 for infarct imaging, 92
 left atrial remodeling and scar, 222
 microvascular obstruction, 217
 pericardial masses, 222
 single-shot sequence, 135
 Late gadolinium enhancement cardiac magnetic resonance (LGE-CMR), 212
 LGE. *See* Late-gadolinium enhancement (LGE)
 Longitudinal relaxation of spin, 5–6
 Look-Locker technique, 170–171
 Lymphocyte, MRI safety, 122
- M**
- Magnetic field
 inhomogeneity, 89
 nuclear spin in, 4
 Magnetic resonance, 162, 172
 Magnetic resonance angiography (MRA), 85. *See also specific types*
 benefits for, 290–291
 time-resolved, 284
 Magnetic resonance imaging (MRI), 150, 162, 181, 184, 185, 190
 cardiac diffusion, 316–318
 carotid plaque imaging by, 276
 contrast agents, 272, 274
 coronary artery disease, 245
 acquisition interval, 248
 advanced methods, 251–256
 cardiac motion, 247–248
 contrast-to-noise ratio, 249–252
 coronary vein MRI, 255–256
 free breathing acquisition, 246
 high-resolution, 251
 imaging sequences, 246–247
 issues of, 246–247
 real-time navigator tracking, 248
 respiratory motion, 248–249
 signal-to-noise ratio, 249–252
 subject-specific tracking factor, 248
 targeted 3D, 251
 whole-heart, 246, 247, 250–254, 256
 coronary vein, 255–256
 GBCA (*see* Gadolinium based contrast agents (GBCA))
 issues and regulations, 116
 acoustics, 119
 gradient fields, 118
 injuries and deaths, 117–118
 lymphocyte studies, 122
 patient monitoring, 120
 peripheral nerve stimulation, 118–119
 physiological and sensory effects, 120–122
 radiofrequency heating, 119–120
 static magnetic fields, 118
 NMR and, 115–116
 nonsignificant risk, 117
 screening questionnaire, 117
 terminology and labeling, 122–123
 Magnetic resonance proton spectroscopy, 319
 Magnetic resonance spectroscopy (MRS)
 AMARES time domain fitting, 267–268
 cardiac metabolism with, 261–262
 choice of localization pulse sequence, 263–264
 data processing, 267–268
 dealing with motion, 264
 optimal data acquisition parameters, 265
 scans preparation, 266
 volume placement, 265–266
 water suppression, 264–265
 Magnetization preparation in CMR
 black-blood preparation, 29–30
 definition, 26
 fat suppression, 28–29
 T₁-weighted preparations, 26–27
 T₂-weighted preparations, 27–28
 Magneto-hydrodynamic (MHD) effect, 120, 139, 140
 Magnetophosphenes, 121
 Manganese based contrast agents, 275
 Manganese dipyridoxyl diphosphate (MnDPDP), 275
 Manganese-enhanced MRI (MEMRI), 275
 Mapping, 168, 176
 MBF. *See* Myocardial blood flow (MBF)
 Medical Device Agency (MDA), 119
 Medical Devices Amendments of 1977, 116
 Medtronic Core Valve, 238
 MEMRI. *See* Manganese-enhanced MRI (MEMRI)
 mGRE. *See* Multi-gradient recalled echo (mGRE)
 Mitral annular, tissue velocity, 234
 Mitral regurgitation (MR)
 pitfalls, 238
 regurgitant fraction calculation, 237–238
 Mitral stenosis (MS), 237
 MnDPDP. *See* Manganese dipyridoxyl diphosphate (MnDPDP)
 Moens-Korteweg equation, 232
 Molecular MRI contrast agents, 275–276
 MOLLI approach, 170–171
 Morphological cardiac imaging, 81
 MR. *See* Mitral regurgitation (MR)
 MRI. *See* Magnetic resonance imaging (MRI)
 MRS. *See* Magnetic resonance spectroscopy (MRS)
 MR tractography, 317
 MS. *See* Mitral stenosis (MS)
 Multi-contrast imaging
 GRE imaging, 33
 SE imaging, 34
 Multi-echo GRE, 69
 Multi-echo sequences, 67
 Multi-gradient recalled echo (mGRE), 33–34
 Myocardial blood flow (MBF), 193
 Myocardial disease
 cardiac output, 233
 diastolic dysfunction, 233
 mitral annular tissue velocity, 234
 pitfalls, 234–235
 pulmonary vein flow waveform, 234
 restrictive physiology, 234
 transmitral flow profiles, 234
 Myocardial fat detection, 318–319

- Myocardial infarction
 - LGE imaging, 217–218
 - in men, 222
- Myocardial mechanics analysis, CMR
 - DENSE, 319–320
 - feature tracking, 319
 - SENC, 319–320
 - tissue phase mapping, 319
- Myocardial perfusion imaging, 82–84
 - and cardiac motion artifacts, 100
 - CMR
 - basic principles, 197–198
 - clinical indications, 206
 - dark rim artifact, 204, 205
 - design of, 201–202
 - developments, 206–207
 - practical considerations, 202–203
 - CMR pulse sequences
 - bSSFP, 200
 - challenges, 199
 - contrast agents, 201
 - data acquisition, 200–201
 - echo planar imaging, 199
 - FGRE, 199
 - imaging, 200
 - T1-weighting, 199
 - quantitative perfusion analysis, 204, 206
 - stress agents
 - adenosine, 198
 - dipyridamole, 198
 - dobutamine, 199
 - physiological stress, 199
 - regadenoson, 198–199
 - emerging techniques
 - ASL, 190
 - BOLD, 190
 - non-linearity, 190
 - image analysis
 - absolute quantification, 187–190
 - AIF, 188–190
 - contrast dose, 187
 - quantitative approaches, 186
 - semi-quantitative, 187
 - prospectively gated single-shot sequence., 135
 - pulse sequence
 - acceleration techniques, 184–185
 - artifacts, 185
 - DRA, 185
 - image readout, 182–184
 - motion corrections, 185
 - multiple slices, 184
 - pulse preparations, 181–182
 - requirements, 181
 - 1.5T vs 3T, 185–186
- Myocardial tissue characterization
 - CMR
 - cardiac diffusion MRI, 316–318
 - myocardial fat detection, 318–319
 - parametric mapping, 316
 - TSE for, 95
- Myocardial viability, 217
- Myocarditis
 - clinical presentation, 220
 - LGE imaging, 220–221
 - in men, 221
- Myocardium, 169, 172
- N**
- National Radiological Protection Board (NRPB), 116–117
- Nephrogenic systemic fibrosis (NSF)
 - gadolinium-based contrast agents, 298
 - GBCA adverse effects, 277–279
 - incidence of, 278
- Nominal spatial resolution, 46
- Non-Cartesian acquisitions, coronary MRI, 251
- Non-Cartesian trajectories, 78–79
- Non-contrast enhanced MRA
 - advanced flow-dependent angiography
 - advantages, 307–308
 - applications, 308–309
 - inflow inversion-recovery, 305–306
 - limitations, 307–308
 - overview, 305
 - physical principles, 305
 - quiescent inflow single-shot, 306
 - technical considerations, 307–308
 - velocity selective angiography, 306–307
 - arterial spin labeling
 - advantages, 304
 - applications, 304
 - with gradient dephasing, 302–304
 - limitations, 304
 - overview, 301–302
 - physical principles, 301–302
 - technical considerations, 304
 - flow-independent angiography
 - advantages, 310–311
 - applications, 311–312
 - bSSFP, 309–310
 - limitations, 310–311
 - overview and physical principles, 309
 - technical considerations, 310–311
 - modern techniques, 297
 - phase contrast angiography
 - advantages, 312–313
 - applications, 313
 - limitations, 312–313
 - overview, 312
 - physical principles, 312
 - technical considerations, 312–313
 - time of flight angiography
 - advantages, 299
 - applications of, 300
 - limitations, 299
 - overview, 298–299
 - physical principles, 298–299
 - technical limitations, 299
- Non-ischemic cardiomyopathies (NICM), 218
 - arrhythmogenic right ventricular cardiomyopathy, 219–220
 - dilated cardiomyopathy, 219
 - hypertrophic cardiomyopathy, 219
- Non-selective 180° inversion pulse, 29–30
- Novel/experimental contrast agents, GBCA
 - ferumoxytol, 275
 - manganese based contrast agents, 275
 - molecular MRI contrast agents, 275–276
- NRPB. *See* National Radiological Protection Board (NRPB)
- NSF. *See* Nephrogenic systemic fibrosis (NSF)
- Nuclear magnetic resonance (NMR), and MRI safety, 116–117
- Nuclear spin, in magnetic field, 4
- Null point, 163
- Number of views per segment (NVS), 54–55

- O**
Occupational Safety and Health Administration (OSHA), 119
Osirix, 267
- P**
PA. *See* Pulmonary artery (PA)
PAH. *See* Pulmonary arterial hypertension (PAH)
Parallel imaging
 acquisition time, 72–73
 CE MRA, 289–290
 GRAPPA, 75
 limitations, 77–78
 PILS, 73–74
 SENSE, 74–75
Parallel imaging with localized sensitivities (PILS), 73–74, 289
Paramagnetic contrast agents, 212, 272, 275
Parametric mapping
 in diseases, 316
 myocardial tissue characterization, 316
Partial echo, 48
Partial Fourier acquisition, 47–49, 288
Partial Fourier fraction, 48
Partial Fourier imaging, 70–71
Passive implants, cardiac MR, 123–124
PCMR. *See* Phase-contrast magnetic resonance (PCMR)
Peak velocity
 aortic stenosis, 236
 mitral stenosis, 237
 pulmonic stenosis grading, 241
Pediatric population, gadolinium based contrast agents, 280
Perfusion, 180, 181. *See also* Myocardial perfusion
Pericardial disease
 pericardial constriction, 235
 pitfalls, 235
Peripheral nerve stimulation (PNS), 118–119
PH. *See* Pulmonary hypertension (PH)
Phase-contrast imaging, 52–53
Phase-contrast magnetic resonance (PCMR), 227
 alternate k-space sampling strategies, 232
 cardiac gating and temporal resolution, 229–230
 clinical application, 233
 congenital heart disease
 coarctation of aorta, 238–239
 intracardiac shunts, 239–240
 pulmonary hypertension, 241
 pulmonary valve disorders, 240–241
 4D PCMR, 232
 implementation, 228–232
 myocardial disease
 cardiac output, 233
 diastolic dysfunction, 233–235
 pericardial disease, 235
 physics of phase velocity measurements, 228
 post-processing data, 232–233
 pulse sequences, 229
 pulse wave velocity, 232
 real-time, 232
 respiratory compensation, 230
 spatial resolution, 230
 tissue velocity mapping, 232
 valve disease
 aortic regurgitation, 236–237
 aortic stenosis, 235–236
 mitral regurgitation, 237–238
 mitral stenosis, 237
 prosthetic valves, 238
 vascular disease, 238
 velocity encoding
 direction, 230
 value, 231
Phase contrast MRA
 advantages, 312–313
 applications, 313
 limitations, 312–313
 overview, 312
 physical principles, 312
 technical considerations, 312–313
Phase-sensitive inversion-recovery LGE imaging, 215, 221
Phase velocity, measurements, 228
Phosphenes, 121
Phosphocreatine (PCr), 262, 267
Physiological stress, 199
PILS. *See* Parallel Imaging with Localized Sensitivities (PILS)
Pleural effusion ghosting, 110–111
³¹P-MRS, 261–262
PNS. *See* Peripheral nerve stimulation (PNS)
Point resolved spectroscopy (PRESS), 263–266
Positive contrast agents, 272
Pregnancy, GBCA during, 280
PRESS. *See* Point resolved spectroscopy (PRESS)
Pressure gradient, 241
 aortic coarctation, 238
 transvalvular, 236, 237
Prospective ECG-gating, 133
 segmented acquisition, 136–137
 segmented-cine acquisition, 137–138
 single-shot acquisition, 133–135
Prospective triggering, 56
Proton density, contrast produced by, 7
Pulmonary arterial hypertension (PAH), 240, 241
Pulmonary artery (PA)
 aliasing in, 231
 PCMR, 241
Pulmonary hypertension (PH), 241
Pulmonary stenosis
 congenital, 240
 progression, 241
Pulmonary valve disorders
 phase-contrast magnetic resonance, 240–241
 regurgitant fraction calculation, 240
 Tetralogy of Fallot, 240
Pulmonary vein, flow waveform, 234
Pulmonic stenosis, grading of, 241
Pulse oximetry-gating, ECG, 139
Pulse sequence
 acceleration techniques, 184–185
 artifacts, 185
 CMR
 black-blood preparation, 29–30
 bSSFP imaging, 37–39
 definition, 25–26
 fast spin echo imaging, 36–37
 fast spoiled gradient echo, 34
 fat suppression, 28–29
 features of, 26
 gradient-recalled echo, 31–33
 multi-gradient recalled echo, 33–34
 spin echo imaging, 34–36
 structure of, 26, 30–31
 T₁-weighted preparations, 26–27
 T₂-weighted preparations, 27–28
 constraints, 181
 design

- LGE evolution, 214–215
 - segmented inversion-recovery spoiled gradient echo sequence, 215, 216
 - DRA, 185
 - FSE readout, 162–163
 - ¹H-MRS, 263–264
 - image readout, 182–184
 - motion corrections, 185
 - MR pulse sequence, 25–26
 - multiple slices, 184
 - myocardial perfusion CMR, 200
 - bSSFP, 200
 - challenges, 199
 - contrast agents, 201
 - data acquisition, 200–201
 - echo planar imaging, 199
 - FGRE, 199
 - imaging, 200
 - T1-weighting, 199
 - null signal point, 163–164
 - optimization, 64–65
 - phase-contrast magnetic resonance, 229
 - pulse preparations, 181–182
 - requirements, 181
 - RF pulses, 25
 - STIR, 165–166
 - stress wall motion assessment, 195
 - 1.5T vs 3T, 185–186
 - Pulse wave velocity (PWV), 232
- Q**
- QISS. *See* Quiescent interval single shot (QISS)
 - Quantification, 181, 186–190
 - Quantitative perfusion analysis, 204, 206
 - Quiescent inflow single-shot (QISS), 306
 - Quiescent interval single shot (QISS), 287
- R**
- Radial imaging, CE MRA, 290
 - benefits for, 290–291
 - errors, 293–294
 - HYPRES, 294
 - Kaiser-Bessel Kernel, 291
 - sampling density, 292
 - sliding window reconstruction, 292–293
 - Radial k-space trajectories, 23
 - Radial Sliding Window, 292
 - Radiation Protection Division of the Health Protection Agency (HPA), 117
 - Radio frequency (RF), 4
 - heating, 119–120
 - imaging procedure, 8
 - pulse, 5, 6
 - receiver coil, 5, 7
 - slice selection gradient and, 8–11
 - transverse magnetization, 6
 - Radiofrequency pulses (RF)
 - ECG-gating for CMR, 139
 - Radiological Protection Act of 1970, 116
 - Raw data, 42
 - Readout gradient, 20
 - Real-time cine imaging, 158
 - Real-time flow, blood flow assessment, 320–321
 - Real-time imaging, 55–58
 - ECG-gating for CMR, 141, 142
 - Receiver bandwidth (rBW), 21, 64
 - Refocused gradient echo imaging, 145
 - Regadenoson, myocardial perfusion CMR, 198–199
 - Regurgitant fraction (RF), 240
 - aortic regurgitation, 236–237
 - mitral regurgitation, 237–238
 - Repetition time (TR), 31, 136
 - Respiratory compensation, 230
 - Respiratory gating, 98
 - Respiratory motion, 248–249
 - Respiratory synchronization, 65
 - Retrospective cardiac gating, 229–230
 - Retrospective ECG-gating, 133, 138
 - Retrospective gating, 55, 56
 - RF. *See* Regurgitant fraction (RF)
 - RF field inhomogeneity at 3 T, 90
 - RF pulse phase cycling, 147
 - R-R interval, 26, 133
- S**
- SAR. *See* Specific absorption rate (SAR)
 - Sarcoidosis, LGE imaging, 220
 - Sarcolemmal disruption, 212
 - Saturation recovery (SR) preparation, 27
 - Saturation time (TS), 199
 - SCD, 219, 220
 - Segmented acquisition, prospectively gated, 136–137
 - Segmented-cine acquisition, prospectively gated, 137–138
 - Segmented EPI technique, 199
 - Segmented imaging, 39, 54–55
 - Segmented k-space, 152–154
 - SE imaging. *See* Spin echo (SE) imaging
 - Self-gating techniques, ECG-gating for CMR, 141–142
 - SENSE. *See* Sensitivity encoding (SENSE)
 - Sensitivity encoding (SENSE), 74–75, 185, 289
 - Serum calcium determinations, 279
 - Short T1 inversion recovery (STIR), 29, 165
 - Signal equation, and k-Space, 14–15
 - Signal generation of MRI
 - excitation of spins, 4–5
 - Larmor frequency, 4
 - MRI signal, 3–4
 - nuclear spin, 4
 - primary sources of, 3
 - signal acquisition
 - free induction decay, 7–8
 - imaging procedure, 8
 - slice selection, 8–11
 - spatial encoding, 9
 - spatial localization, 8
 - spin relaxation
 - contrast produced by proton density, 7
 - longitudinal relaxation, 5–6
 - T₁ differences among tissues, 6
 - T₂ differences among tissues, 7
 - transverse relaxation, 6–7
 - Signal intensity, 59
 - Signal-to-noise ratio (SNR), 14, 65
 - coronary MRI, 249–251, 253
 - definition, 58
 - factors affecting, 58–59
 - frequency resolution and, 94
 - GRE imaging, 33
 - high field MRI, 87, 88
 - imaging acquisition time, 59
 - measurement, 59

- Signal-to-noise ratio (SNR) (*cont.*)
 - protocol settings, 58
 - SE imaging, 35
 - signal intensity, 59
 - tradeoffs, 60–61
 - transverse relaxation time, 58
 - voxel size, 58–59
- Simultaneous Acquisition of Spatial Harmonics (SMASH), 289
- Single-echo GRE sequences, 66–67
- Single phase CE MRA, 284
- Single photon emission computed tomography (SPECT), 179
- Single-shot acquisition, 133–135
- Single-shot FSE, 68
- Single-shot prospectively-gated sequence, 133–135
- Single-shot TSE, 68
- Singular value decomposition (SVD), 188
- Slew rate (SR), 118
- Slice selection, 8–11
- Slice-selective inversion sequences, late gadolinium enhancement, 215
- Slice-selective 180° RF inversion pulse, 29–30
- SMASH. *See* Simultaneous Acquisition of Spatial Harmonics (SMASH)
- SNR. *See* Signal-to-noise ratio (SNR)
- Society for Cardiovascular Magnetic Resonance Imaging, 276
- k-Space
 - filling
 - GRE imaging, 33
 - SE imaging, 35
 - formalism
 - acquisition and reconstruction process, 14
 - data properties in, 15–16
 - EPI, 22–23
 - errors in, 17
 - field-of-view, 19
 - gradients and, 19–21
 - matrix sizes and artifacts, 16–17
 - radial, 23
 - receiver bandwidth, 21
 - sampling grids in, 18
 - sampling trajectories, 21–22
 - signal equation and, 14–15
 - spatial frequencies, 15
 - spatial resolution, 18–19
 - spiral, 23
 - lines, fast imaging
 - keyhole imaging, 71–72
 - partial/half Fourier, 70–71
 - rectangular field-of-view, 71
 - reducing, 70
 - view-sharing, 71–72
 - zero-filling, 70
 - partial Fourier acquisition, 288
 - radial trajectory, 290
 - sampling strategies, 232
 - sampling techniques, 294
 - SMASH, 289
 - spatial resolution, 42–44
 - boxcar function, 46
 - on image quality, 44–46
 - and image space, 44
 - and reconstructed image, 43
- Spatial encoding, 9
- Spatial frequencies, 15
- Spatial localization, 8
- Spatial resolution, 18–19, 181
 - field of view, 42
 - k-space, 42–44
 - on image quality, 44–46
 - and image space, 44
 - nominal vs. apparent, 46
 - partial Fourier, 47–49
 - phase-contrast magnetic resonance, 230
 - pixel resolution, 42
 - tradeoffs, 60–61
 - two and three dimensions, 41–42
 - zero filling, 47
- Specific absorption rate (SAR), 120, 150
 - GRE imaging, 33
 - SE imaging, 35
- Specific absorption ratio (SAR), 88
- Spectroscopy
 - MRS (*see* Magnetic resonance spectroscopy (MRS))
 - PRESS, 263–266
- SPGR. *See* Spoiled gradient-recalled acquisition (SPGR)
- Spin
 - alignment of, 4
 - excitation, 4–5
 - in magnetic field, 4
 - precess, 4–5
 - relaxation
 - contrast produced by proton density, 7
 - longitudinal relaxation, 5–6
 - T₁ differences among tissues, 6
 - T₂ differences among tissues, 7
 - transverse relaxation, 6–7
- Spin-echo blood flow artifacts, 102
- Spin echo (SE) imaging, 28, 34–36
- Spiral coronary artery MRI, 251
- Spiral k-space trajectories, 23
- Spoiled gradient echo imaging
 - chemical shift artifact, 148–149
 - clinical applications, 157–158
 - dummy heartbeats, 148
 - gradient spoiling, 146–147
 - GRAPPA, 148
 - inflowing blood, 147
 - off-resonance effects, 149
 - parameter selection, 149
 - RF spoiling, 147
 - saturation and in-flow effects, 147
 - signal equation, 147
 - SNR considerations, 148
 - steady state, 147–148
- Spoiled gradient-recalled acquisition (SPGR), 34, 285
- Static magnetic fields, MRI safety, 118
- Steady-state free precession (SSFP), 150, 174, 184
 - coronary artery MRI, 246, 249, 253, 254
- Stimulated echo acquisition mode (STEAM), 263–264
- Stimulated echoes, 146
- STIR. *See* Short T1 inversion recovery (STIR)
- Strain encoding (SENC), 319–320
- Stress agents, myocardial perfusion CMR
 - adenosine, 198
 - dipyridamole, 198
 - dobutamine, 199
 - physiological stress, 199
 - regadenoson, 198–199
- Stress modes
 - dobutamine stress CMR, 194–195
 - ergometer stress, 194
 - vasodilator stress, 195

- Stress testing
 - in cardiology practice, 193
 - CMR, 193
 - contraindications to drugs used, 194
 - dobutamine, 194–197
 - ergometer stress, 194
 - pulse sequences, 195
 - vasodilator stress, 195
 - magnetic–hydrodynamic effect, 194
 - safety considerations, 194
- Subject-specific tracking factor, coronary MRI, 248
- SVD. *See* Singular value decomposition (SVD)

- T**
- Tachycardia
 - ECG-gating for CMR, 140
- T₂ decay
 - GRE imaging, 33
 - SE imaging, 34
- Temporal resolution, 181
 - BRISK, 52
 - CURE, 53–54
 - definition, 49
 - field-of-view, 56
 - keyhole, 51–52
 - phase-contrast imaging, 52–53
 - real-time imaging, 55–58
 - segmented imaging, 54–55
 - signal-to-noise ratio, 57
 - tachycardia, 141
 - tradeoffs, 60–61
 - view-sharing, 50–51
- Temporal resolution (TR)
 - free-breathing acquisition, 235
 - phase-contrast magnetic resonance, 229–230
- Tetralogy of Fallot (TOF), 240
- 3D late gadolinium enhancement (LGE), 216–217
- 3D TRICKS, 289
- Time of flight (TOF) MRA
 - advantages, 299
 - applications of, 300
 - limitations, 299
 - overview, 298–299
 - physical principles, 298–299
 - technical limitations, 299
- Time-resolved angiography with stochastic trajectories (TWIST), 54
- Time Resolved Imaging of Contrast Kinetics (TRICKS), 284, 289
- Time-resolved MRA, 284
- Tissue characterization
 - native T1, 170
 - T1 relaxation
 - ECV measurement, 172
 - inversion recovery, 168–169
 - look-locker technique, 170–172
 - saturation recovery, 168
 - tissue-contrast method, 170
 - T2 relaxation
 - ACUT2E, 175–176
 - characteristics, 176
 - gradient echo, 174
 - imaging protocols, 176
 - pulse sequence, 174
 - spin echo, 174
- spins experience reasons, 173
- SSFP techniques, 174–175
- T2-prep, 175
- transverse plane, 173
- Z-axis relaxation, 168–172
- Tissue phase mapping, 319
- Tissue velocity mapping, 232
- T₂ mapping
 - GRE imaging, 33
 - SE imaging, 34
- T1-mapping, myocardial tissue characterization, 316
- T2-mapping, myocardial tissue characterization, 316
- TOF MRA. *See* Time of flight (TOF) MRA
- T₂-preparation period (time), 28
- TR. *See* Temporal resolution (TR)
- Transmit field inhomogeneity, 89
- Transmitral flow, 234
- Transvalvular pressure gradients
 - aortic stenosis, 236
 - mitral stenosis, 237
- Transverse relaxation of spin, 6–7
- T1 relaxation
 - ECV measurement, 172
 - inversion recovery, 168–169
 - look-locker technique, 170–172
 - saturation recovery, 168
 - time of spin, 6
 - tissue-contrast method, 170
- T2 relaxation
 - ACUT2E, 175–176
 - characteristics, 176
 - gradient echo, 174
 - imaging protocols, 176
 - pulse sequence, 174
 - spin echo, 174
 - spins experience reasons, 173
 - SSFP techniques, 174–175
 - T2-prep, 175
 - time of spin, 7
 - transverse plane, 173
- Trigger window (TW), 133
- Triglycerides (TG), 262
- Truncation artifacts. *See* Gibbs ringing
- TSE chemical shift artifacts, 105
- Turbo spin echo (TSE), 98, 174
 - fast imaging, 67–68
 - for myocardial tissue characterization, 93
 - single-shot, 68
- T₂-weighted preparations, 27–28
- T1-weighting, myocardial perfusion CMR, 199

- U**
- Ultrahigh magnetic field strength, 321
- Ultrasmall paramagnetic iron oxide (USPIO), 284

- V**
- Valve disease
 - aortic regurgitation, 236–237
 - aortic stenosis, 235–236
 - mitral regurgitation, 237–238
 - mitral stenosis, 237
 - prosthetic valves, 238
- Vascular disease, phase-contrast magnetic resonance, 238
- Vascular imaging, 85–86

Vasodilator stress CMR, 195, 206
Vastly undersampled isotropic projection imaging (VIPR), 79
Vastly undersampled radial projection reconstruction (VIPR), 232
VCG. *See* Vectorcardiography (VCG)
VCG artifacts, 196
Vectorcardiogram (VCG) gating, 120
Vectorcardiography (VCG), 139, 141
Velocity encoding (VENC)
 direction, 230
 value, 228, 231
Velocity selective MRA, 307–308
VENC. *See* Velocity encoding (VENC)
Venography
 dark-blood, 299
 3D TOF MR, 301
Ventricular septal defects (VSD), 239, 240
Vessel wall imaging, 93
Viability imaging, 84
Viable myocardium, 197
View-sharing, 71
 temporal resolution, 50–51
VSD. *See* Ventricular septal defects (VSD)

W

Wall motion-stress CMR, 196
Water suppression (WS)
 magnetic resonance spectroscopy, 264–265
 optimization, 264
 PRESS spectra, 266
 removal of water signal with, 267
Whole-heart coronary MRI, 246, 247, 250–254, 256
Wraparound artifacts, 104
WS. *See* Water suppression (WS)

X

X-ray
 contrast agents, 271
 coronary angiography, 247, 250

Z

Z-axis relaxation, 168–172
Zenith-Cook iliac stent, 123
Zero-filling, 47–49, 70